MARID VII

Marine and River Dune Dynamics

Rennes, France
3 - 5 April, 2023

Organizing Committee:

Dr Alexandre Valance, IPR, Université de Rennes 1, France
Dr Alain Crave, Rennes, Géosciences Rennes, Université de Rennes 1, France
Dr Thierry Garlan, French Hydrographic Office, France
Dr Aurélien Gangloff, French Hydrographic Office, France
Céline Thébault, IPR, Université de Rennes 1, France
Amandine Poirier, IPR, Université de Rennes 1, France
Nathalie Mabic, IPR, Université de Rennes 1, France

Scientific Committee:

Dr Thierry Garlan, French Hydrographic Office, France
Dr Alexandre Valance, University of Rennes 1, France
Dr Alain Crave, University of Rennes 1, France
Dr Aurélien Gangloff, French Hydrographic Office, France
Prof Dr Alain Trentesaux, University of Lille, France
Dr Sophie Le Bot, Rouen University, France
Prof Dr Suzanne Hulscher, Twente University, Netherlands
Prof Dr Maarten Kleinhans, Utrecht University, Netherlands
Prof Dr Jim Best, University of Illinois, United States of America
Prof Dr Dan Parsons, University of Hull, United Kingdom
Prof Dr Vera Van Lancker, Royal Belgian Institute of Natural Sciences, Belgium
Dr Marc Roche, Federal Public Service Economy, Self-employed, SME's and Energy, Belgium
Dr Katrien Van Landeghem, Bangor University, United Kingdom
Dr Jaco Baas, Bangor University, United Kingdom
Prof Dr Christian Winter, Kiel University, Germany
Dr Alice Lefebvre, MARUM, University of Bremen, Germany
Prof Marco Colombini, University of Genoa, Italy

This publication should be cited as follows:
Valance, A., Garlan, T., Crave A., and Gangloff, A. (Eds), 2023. MARID VII. Seventh International Conference on Marine and River Dune Dynamics. Rennes, France, 3-5 April 2023. University of Rennes 1 and Shom. 344 p.

MARID VI is organised and sponsored by

IPR - Institut de Physique de Rennes Bât 11A, Campus Beaulieu, Université de Rennes 1, 35 042 Rennes Cedex, France	
Shom - French Hydrographic and Oceanographic Office STM/Department of Marine Geology, 13 rue du Chatellier, 29228 Brest Cedex 2, France	
Géosciences Rennes Bât.15, Campus Beaulieu Université de Rennes 1 35042 Rennes, France	

And sponsored by

Université de Rennes 1 Campus Beaulieu, 35 042 Rennes Cedex, France	Université de Rennes
OSUR - Observatoire des Sciences de l'Univers de Rennes Bâtiment 15, Campus de Beaulieu, 35042 Rennes CEDEX	Observatoire des Sciences de l'Univers de Rennes Terre, Écosystèmes et Sociétés
CNRS – Centre National de Recherche Scientifique	cnrs

Preface & Welcome

Welcome to MARID VII, the seventh edition of the Marine and River Dune Dynamics conference series.

In 2000, a workshop on marine sand wave dynamics was organised by the French Naval Hydrographic and Oceanographic Office (Shom) and the University of Lille 1 (France) under the aegis of the North Sea Hydrographic Commission. After the success of this first workshop, conferences covering marine and river dune dynamics were organised in 2004 (University of Twente, Enschede, the Netherlands), in 2008 (University of Leeds, United Kingdom), in 2013 (Royal Belgian Institute of Natural Sciences, Bruges Belgium), in 2016 (Caernarfon, University of Bangor, North Wales, UK) and in 2019 (Bremen, University of Bremen, Germany). Now known by the acronym MARID, these conferences provide state-of-the-art overviews and discussions on fundamental and applied knowledge of marine and river bedforms.

Bedforms are ubiquitous and dynamic features on a movable bed, which have been observed in many subaqueous environments, such as rivers, beaches, estuaries, tidal inlets, shallow seas, and deep waters. They are active morphodynamic elements which both reflect and influence hydrodynamic and sediment dynamics processes at various spatiotemporal scales. The study of their presence, size and movement is directly relevant for a wide range of applied and fundamental research. The processes governing bedform formation, dynamics and preservation have still not been unravelled adequately and the MARID VII delegates will outline progress derived from field observations, modelling studies and laboratory experiments across a wide number of disciplines, including earth sciences, oceanography, engineering, hydrography and biology.

MARID VII is held in Rennes, France, organised by the Institute of Physics of Rennes and Geosciences Rennes Laboratory (University of Rennes 1) and the French Naval Hydrographic and Oceanographic Office (Shom). In keeping with the previous MARID conferences, we maintain the concept of a small, focused event with only plenary sessions to stimulate discussion among disciplines and methodology. Scientific sessions are taking place in Amphitheater TA Beaulieu (Pôle Numérique Rennes Bretagne) on 3 and 4 April 2023 including talks from keynote speakers and oral and poster presentations by delegates. On 5 April the field trip to the Mont-Saint-Michel Bay will permit convivial exchange between participants on the sediment dynamics.

We hope that MARID VII will lead to fruitful and productive discussions, which in turn should help and guide future collaborations to further investigate marine and river bedforms. The short format of the MARID conferences has proven to be ideally suited for such networking activities.

We wish you an enjoyable conference!

Alexandre Valance, Thierry Garlan, Alain Crave & Aurélien Gangloff

Invited keynotes		
Authors	**Title**	**Pages**
B. Andreotti O. Duran, A. Fourrière, P. Claudin	A unified model of bedforms across the turbulent roughening transition	I-II
V. R. M. Van Lancker F. Francken, L. Kint, G. Montereale Gavazzi	Tracking the human influence on the modern sedimentary system of the North Sea	III-IV
N. M. Vriend	Bedform dynamics: interaction, attraction and repulsion of dunes	V-VI

Oral presentations		
Authors	**Title**	**Pages**
M. Becker, G. Herrling, K. Krämer, A. Lefebvre, A. Zorndt, F. Kösters, C. Winter	Dune orientation controlled by estuarine circulation in the Outer Weser estuary, German Bight, North Sea	9-16
D. Casalbore, A. Bosman, C. Romagnoli, F.L. Chiocci	Crescent-shaped bedforms on submarine volcanic flanks: the case of Salina (Aeolian Islands, Italy)	39-46
W.N. Cassol, S. Daniel, D. Pham Van Bang	The influence of underwater dunes in spatiotemporal analysis of the hydrodynamic of the Saint-Lawrence River	47-54
J. Chauchat, A. Salimi-Tarazouj, T.J. Hsu, P. Traykovski,	A numerical study on ripple evolution and migration using a two-phase flow model	55-58
P. Claudin, B. Andreotti	Hydrodynamical regimes in turbulent flows over a wavy surface and dissolution instability	59-62
P. Daguinos, N. Le Dantec, P. Le Roy, D. Menier, G. Jouet, A. Ehrhold, M. Franzetti, A. Trotot	Dunes morphodynamics superimposed on sand banks in a shallow macro-tidal environment: the example of the Haut Fond de Ouessant	63-68
J.H. Damveld, R. van der Meijden, B.W. Borsje, S.J.M.H. Hulscher	Episodical sand wave migration: analysis of high temporal resolution bathymetry	75-80
S. de Lange, D. Murphy, R. Bradley, R. Schrijvershof, K. Waldschläger, R. Kostaschuk, J. Venditti, T. Hoitink	Bedform response to mean shear stress in the fluvial to tidal transition zone	87-94
T.A.G.P. van Dijk, J. Best, S. Krause, U. Schneidewind, E. van Onselen, P. van Rijnsoever, M. Karaoulis, L. Haverson, M.G. Kleinhans, J. Stam	Dune preservation and microplastics distribution over time, River Waal, Netherlands	101-108

Oral presentations		
Authors	**Title**	**Pages**
N. Durand, P. Tassi, O. Blanpain, A. Lefebvre	Understanding marine dune dynamics in a shallow shelf sea using sediment mobility indices	109-116
D. Frank-Gilchrist, A. Penko, M. Palmsten, J. Calantoni	Vortex trapping of sand grains over ripples under oscillatory flow	117-124
A. Gilletta de Saint Joseph, J. Chauchat, C. Bonamy, M. Robert	Hydrodynamic simulations of flow around a pile using turbulence-resolving models	125-134
W.S. Kearney, A.M. Penko	The Naval Seafloor Evolution Architecture: a platform for predicting dynamic seafloor roughness	135-140
K. Krämer, M. Becker, C. Winter	Bedform transition in a sediment starved environment (SW Baltic Sea)	141-148
K. Van Landeghem, C. McCarron, R. Whitehouse, M. Clare, C. Unsworth	ECOWind-ACCELERATE: accelerated seabed mobility around offshore windfarms	149-154
A. Lefebvre, R. Bernhard, L. Scheiber, E. Miramontes	What is a dune? Towards a homogenisation of the nomenclature of bedforms	163-170
A. Lefebvre, J. Cisneros	The influence of lee side shape on flow above bedforms	171-176
L.R. Lokin, J.J. Warmink, S.J.M.H. Hulscher	The influence of sediment transport formulae on modelling river dune development	177-182
M.Y. Louge, A. Valance, J. Fang, S. Harnett, F. Porté-Angel, P. Chasle	Anomalous evolution of aerodynamic roughness and shear velocity on large flows	183-188
A. Mathieu, A. Salimi-Tarazouj, T.-J. Hsu, C. Bonamy, J. Chauchat	Simulation of bedform formation using an Eulerian two-phase flow model	189-194
C. Narteau, S. Courrech du Pont	Coexistence of two dune growth mechanisms	203-210
A. Nnafie, H.E. de Swart, T. Verwaest	Modelling effects of shoreface-connected sand ridges on the shoreline evolution: Application to the Belgium coast	225-230
P.H.P. Overes, B.W. Borsje, A.P. Luijendijk, S.J.M.H. Hulscher	Exploring the main drivers of sand wave dynamics	231-238
Y. Plancke, G. Vos Flanders, D. Meire	The residual sand and mud transport in the Schelde-estuary, based on the calculation of the sediment balance	239-244
A.J.H. Reesink, L. Colombera, D. Das, R.A. Duller, V. Ganti, N.P. Mountney, D.R. Parsons	What is the representative elementary volume of preserved dune deposits?	253-260

Oral presentations		
Authors	**Title**	**Pages**
A. Rivière, A. Maison	Potential thermal impact of wind farms within a dynamic seabed	261-262
A.E. Robert, N. Quillien, M. Bacha, C. Caulle, M. Nexer, B. Parent, T. Garlan, E. Feunteun, A. Carpentier, R. Amara, N. Desroy	Dynamic of the benthic ecosystem of bedform areas assessed via structural diversity, functional diversity and isotopic diversity	263-270
M. Roche, F. Barette, K. Degrendele, A.S. Piette	Multibeam echosounder backscatter strength signature of dune fields in the Belgian part of the North Sea	271-278
W.M. van der Sande, P.C. Roos, T. Gerkema, S.J.M.H. Hulscher	Nonlinear modeling of estuarine sand dunes: first results with unidirectional flow	279-286
L. Scheiber, A. Lefebvre	The influence of geometric definitions on dune characteristics	293-298
C. Unsworth, M.A. Austin, K. Van Landeghem, A. Couldrey, R. Whitehouse	Renewable infrastructure in a field of dunes: changes to near bed turbulence & sediments	299-306
M. Vah, M. Ouzaouit, H. Besnard, A. Jarno, B. Morvan, F. Marin	Bedload quantification by passive acoustic measurement: case of an isolated dune	307-312
T.J. van Veelen, P.C. Roos, S.J.M.H. Hulscher	On elevation and migration: a model for sandbank dynamics in sediment-scarce seas	321-326
C. Winter, G. Díaz-Mendoza, M. Becker, K. Krämer	Sedimentology of a large field of lunate shaped bedforms in the Fehmarn Belt, Baltic Sea	327-330
X. Wu, J. Malarkey, F. Fernández, J. H. Baas, D. R. Parsons	Clay winnowing associated with wave–current ripple dynamics on cohesive sand–clay beds	331-338
J.Y. Zomer, B. Vermeulen, A.J.F. Hoitink	Interaction between two scales of fluvial bedforms and its impact on sediment transport dynamics	339-344

Posters		
Authors	**Title**	**Pages**
I. Abroug, P. Weill, N. Abcha	Morphology and dynamics of subaqueous dunes generated under unidirectional flow	1-8
A.C. Bennis, M. Boutet, F. Dumas, L. Furgerot, A. Gangloff, E. Lagniel, S. Le Bot, D. Mouazé, L. Perez, G. Porcile, B. Tessier	MORPHODUNES, a new project dedicated to the 3D morphodynamics of sub-marine sand dunes for safety and maritime activities.	17-24
P. Daguinos, P. Le Roy, D. Menier, N. Le Dantec, A. Ehrhold, G. Jouet, M. Franzetti	Morphological and internal variability of sand banks on a macro tidal dispersive shelf	69-74
J. Daynac, P. Bessin, S. Pochat, R. Mourgues	Deep Learning: A new tool for mapping and analysis dunes (e.g. Rub'Al Khali sand sea)	81-86
S. de Lange, S. van de Veen, I. Niesten, D. Boelee, K. Waldschläger, T. Hoitink	Influence of silt in sand-silt mixtures on dynamic near-equilibrium bedform geometry	95-100
K. Bobiles, C. Carstensen, I. Holzwarth, E. Miramontes, A. Lefebvre	Characterisation of flow dynamics over estuarine bedforms: An experimental approach	25-30
S. Le Bot, M. Bary, M. Fournier, A. Husté, N. Michelet, O. Blanpain, M. Nexer, T. Garlan	Marine dune morphodynamics and sediment fluxes (off Dunkirk, France). Spatio-temporal variability and relations with hydrodynamic forcings	155-162
N. Michelet, M. Bary, O. Blanpain, S. Le Bot, M. Nexer, A. Lefebvre	Estimation of marine dune migration using a three-dimensional numerical modelling	195-202
C. Narteau, P. Lü, P. Claudin, Z. Dong, S. Rodriguez, C. Gadal, S. Courrech du Pont	Direct validation of the dune instability theory	211-216
M. Nexer, T. Garlan, A. Lefebvre, N. Quillien, A. Gangloff, O. Blanpain, S. Le Bot, M. Bacha, M. Bary, N. Durand, A. Gilletta de Saint Joseph, N. Michelet, A. Gangloff, A. Robert	Study marine dunes in an offshore windfarm context	217-224
L. Portos-Amill, P.C. Roos, J.H. Damveld, S.J.M.H. Hulscher	Tidal sand waves on the lower shoreface: effects on basin-scale hydrodynamics	245-252
A. Bosman, C. Pellegrini, C. Romagnoli	Bedforms and morpho-bathymetric evolution of tributary channels in the Po River delta (Italy)	31-38
L. Scheiber, C. Jordan, T. Schlurmann	Dune scaling in the Tien River, Vietnamese Mekong Delta	287-292
A. Valance, S. Kiki, N. Le Dantec	Two-dimensional subaqueous dune dynamics under unidirectional flows	313-320

KEYNOTE

A unified model of bedforms across the turbulent roughening transition

B. Andreotti, *Laboratoire de Physique de l'Ecole Normale Supérieure*
O. Duran, *Department of Ocean Engineering, Texas A&M University*
A. Fourrière, *BGR - Federal Institute for Geosciences and Natural Resources*
P. Claudin, *Laboratoire de Physique et Mécanique des Milieux Hétérogènes*

ABSTRACT The emergence of bedforms as result of the coupling between fluid flow and sediment transport is a remarkable example of self-organized natural patterns. The size of subaqueous and aeolian bedforms generated by unidirectional water or wind flows, like ripples, dunes or compound bedforms, have been shown to depend on grain size, water depth and flow velocity. In the last decade, this variety of morphologies, previously classified according to their size, has gradually been understood in terms of mechanical and hydrodynamical mechanisms. Do ripples and dunes form by linear instability or nonlinear processes like pattern-coarsening? What determines their time and length scales, so different in air and water? What are the similarities and differences between aeolian and subaqueous patterns? What is the influence of the mode of transport: bedload, saltation or suspension? Can bedforms emerge under any hydrodynamical regime, laminar and turbulent?

Guided by these questions, a unified description of bedform growth and saturation will be discussed, with emphasis on the hydrodynamical regime in the inner layer and the relaxation phenomena associated with particle transport. It provides a physical explanation for bedform formation that disentangles the different regimes and show that the transition from ripples to dunes is associated, under water, with an anomalous hydrodynamic response to relief in the range of wavelength exciting the turbulent transition. This anomaly gradually disappears in the rough regime. The model is tested using a quantitative, yet reductionist, numerical model that couples hydrodynamics over a modulated bed to sediment transport and resolves both initial and mature bedforms. Numerical predictions are tested for subaqueous and aeolian bedforms, for which all components of the theory are independently calibrated. The resulting classification of hydrodynamical regimes provides a new mechanistic framework to compare ripples and dunes in different environments.

Finally, the effect of the free surface will be discussed, comparing ripples (downstream propagating transverse bedforms), chevrons and bars (bedforms inclined with respect to the flow direction) and anti-dunes (upstream propagating bedforms), and focusing on the mechanisms involved in the early stages of their formation. In the subcritical regime (Froude number F smaller than unity), the same instability produces ripples or chevrons depending on the influence of the free surface. The transition from transverse to inclined bedforms is controled by the ratio of the saturation length Lsat, which encodes the stabilising effect of sediment transport, to the flow depth H. These results suggest that alternate bars form in rivers during flooding events, when suspended load dominates over bed load. In the supercritical regime $F > 1$, the transition from ripples to anti-dunes is also controlled by the ratio Lsat/H. Anti-dunes appear around resonant conditions for free surface waves, a situation for which the sediment transport saturation becomes destabilising. This resonance turns out to be fundamentally different from the inviscid prediction. Their wavelength selected by linear instability mostly scales on the flow depth H, which is in agreement with existing experimental data.

REFERENCES

[1] Charru F., Andreotti B. & Claudin P. 2013 Ripples and dunes, Annual Review of Fluid Mechanics 45, 469

[2] Andreotti B., Claudin P., Devauchelle O., Duran O. & Fourrière A. 2012 Bedforms in a turbulent stream: ripples, chevrons and antidunes, J. Fluid Mech. 690, 94-128.

[3] Duran O., Andreotti B., Claudin P. & Winter C. 2018 Turbulent and roughening transitions affect bedforms, Nature Geoscience, 12, 345.

KEYNOTE

Tracking the human influence on the modern sedimentary system of the North Sea

V.R.M. Van Lancker, *Operational Directorate Natural Environments, Royal Belgian Institute of Natural Sciences, Brussels, Belgium*
F. Francken, *OD Nature, Royal Belgian Institute of Natural Sciences, Brussels, Belgium*
L. Kint, *OD Nature, Royal Belgian Institute of Natural Sciences, Brussels, Belgium*
G. Montereale Gavazzi, *OD Nature, Royal Belgian Institute of Natural Sciences, Brussels, Belgium*

ABSTRACT Marine ecosystems are affected by a multitude of drivers and pressures, both natural and anthropogenic. Biodiversity is to a large extent driven by the nature and dynamics of sediments, making the monitoring of changes of broad habitat types (BHT), such as mandated by the Marine Strategy Framework Directive (2008/56/EC), a valuable approach. This is linked to safeguarding the integrity of the seafloor and requires from European Member States to assess physical disturbance and loss of benthic habitats in a quantitative and spatially-explicit manner. In Belgium, we have taken the challenge of conducting shelf-wide BHT impact assessments, necessitating new ways of monitoring, setting-up assessment frameworks, making use of best available data, and promoting collaborative efforts [1].

Seabed mapping is essential for BHT change assessments. Methodology-wise rapid evolutions take place, mostly linked to the use of acoustic remote sensing and seafloor classification [2]. Whilst at the smaller scale, typically linked to case-by-case and/or application-oriented approaches, maps can be produced with good predictive power, more regional BHT maps have much lower accuracy because of integration of more fragmented data collected over a wide time span, and consequently also because of the variety of technologies and gear used over time [3]. Uncertainties in the data chain are amplifying, and when analysing depth changes, differences are usually within the confidence envelope of the measurements [4]. However, for some species, typically those associated to gravel beds, centimetric burial by sands, if irreversible, results in habitat loss.

In this keynote, we go back to the basics, i.e., the seabed itself of which diverse bedforms and features are now unveiled by increasing availability of very-high resolution (e.g., 1m) bathymetry. Examples will be given, mostly from analyses of datasets from Flemish Hydrography (agentschapmdk.be/en) covering a range of North Sea habitats. Interpretation calls for multidisciplinary cooperation since, apart its sediments, seabed nature reflects geology, morphology, biology, human influence, and modern-day processes. To cope with measurement-related error margins in change assessments, new approaches are being developed: e.g., defining geological markers, analysing pattern and bedform complexity changes. From this, more advanced workflows will be renewed, ideally based on common initiatives, and connecting to international networks such as EMODnet.eu, GeoHab.org, and the Geological Service for Europe (eurogeosurveys.org).

KEY WORDS: bedforms, seabed features, sediments, subsurface geology, geological markers, anthropogenic activity, sustainability, seabed mapping

REFERENCES

[1] Van Lancker, V., Kint, L. & Montereale Gavazzi, G. , 2018. D6 Fysische verstoring en verlies, pp. 1-24. In: Belgische Staat. Actualisatie van het monitoring programma voor de Belgische mariene wateren. https://odnature.naturalsciences.be/msfd/nl/assessments/2018/page-d6

[2] Pijanowski, B.C., & Brown, C.J., 2022. Grand challenges in acoustic remote sensing: discoveries to support a better understanding of our changing planet. Frontiers in Remote Sensing, 2, 51.

[3] Kint, L., Hademenos, V., De Mol, R., Stafleu, J., van Heteren, S., & Van Lancker, V., 2021. Uncertainty assessment applied to marine subsurface datasets. Quarterly Journal of Engineering Geology and Hydrogeology, 54(1).

[4] Montereale-Gavazzi, G., Roche, M., Lurton, X., Degrendele, K., Terseleer, N., & Van Lancker, V., 2018. Seafloor change detection using multibeam echosounder backscatter: Case study on the Belgian part of the North Sea. Marine Geophysical Research, 39(1): 229-247

KEYNOTE

Bedform dynamics: interaction, attraction and repulsion of dunes

N.M. Vriend, *Paul M. Rady Mechanical Engineering, University of Colorado at Boulder, Boulder, USA*
K.A. Bacik, *Centre for Networks and Collective Behaviour, Dpt. of Mathematical Sciences, University of Bath, UK*

ABSTRACT In desert landscapes, we observe individual sand dunes of different sizes, with a characteristic length scale of up to kilometers, which seamlessly interact with each other and their environment. Can we capture the interaction behaviour of these large objects with simple physical laws? Processes in the field occur over long times and are difficult to investigate in detail, but we are able to scale the physics down to the laboratory. During the presentation, we will explore a unique, recirculating laboratory experiment in which we create and trace aqueous dunes over long times, and investigated three distinct research questions.

We explore the interaction between two dunes of different sizes, leading to either coalescence (merging) or ejection (repulsion) of bedforms and present a phase-space diagram outlining the possible interaction outcomes derived from experiments and cellular automaton simulations [1,2].

An interesting question is what happens in the long-time behaviour [3]: will the system obtain a perfect symmetry in all configurations, or are there certain initial conditions which produce a stable non-symmetrical long-time outcome? We find that the secret ingredient is “turbulence”: for slow flows with a low level of turbulence, the dunes will display fast-slow dynamics before equilibrating symmetrically, but for high levels of turbulence in fast flows, we find an asymmetric attractor. This indicates that dune-dune interactions can either stabilize or destabilize the size and spacing of large dune fields.

Lastly, we place objects in the path of our model dunes and explore the outcome. We observe that both object size and shape matter whether a sand dune is blocked or able to overcome an obstacle and reform on the other side [4]. We discover that a modal decomposition of the flow field (without sediment or dunes present!) can predict the collision outcome, which has interesting applications for reducing and halting dune encroachment.

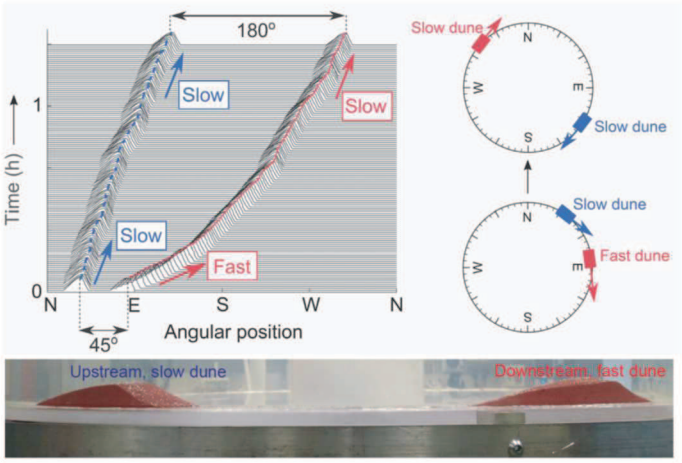

Figure 1: Two equal size dunes, placed 45 degrees apart, drift to antipodal positions over long times.

The central mystery of this research topic is the interplay between small-scale granular physics and large-scale landscape features. The fascinating observation is that certain length-scales change by an order of magnitude or more, but the underlying physics remains the same.

KEY WORDS: subaqueous dunes, sediment transport, dune interactions

REFERENCES

[1] P.A. Jarvis, K.A. Bacik, C. Narteau, N.M. Vriend, "Coarsening dynamics of 2D subaqueous dunes" (2022), Journal of Geophysical Research – Earth Surface 127, e2021JF006492.

[2] K.A. Bacik, S. Lovett, C.P. Caulfield, N.M. Vriend, "Wake-induced long range dune-dune repulsion" (2020), Physical Review Letters 124, 054501.

[3] K.A. Bacik, C.P. Caulfield, N.M. Vriend, "Stability of the Interaction between Two Sand Dunes in an idealized Laboratory Experiment" (2021), Physical Review Letters 127, 154501.

[4] K.A. Bacik, P. Canizares, C.P. Caulfield, M.J. Williams, N.M. Vriend, "Dynamics of migrating sand dunes interacting with obstacles" (2021), Physical Review Fluids 6, 104308.

Morphology and dynamics of subaqueous dunes generated under unidirectional flow

I. Abroug *Normandie université, UNICAEN, UNIROUEN, CNRS, UMR 6143 M2C, 14000 Caen, France – iskander.abroug@unicaen.fr*
P. Weill *Normandie université, UNICAEN, UNIROUEN, CNRS, UMR 6143 M2C, 14000 Caen, France – pierre.weill@unicaen.fr*
N. Abcha *Normandie université, UNICAEN, UNIROUEN, CNRS, UMR 6143 M2C, 14000 Caen, France – nizar.abcha@unicaen.fr*

ABSTRACT: The flow velocity over mobile sandy dunes subjected to unidirectional current was investigated using a UB-Lab 2C, an acoustic velocity profiler newly developed by UBERTONE. A space-localized wavelet approach was used in order to detect the temporal evolution of the main dune's wavelength. The acoustic tool has provided promising results concerning the flow and sediment dynamics over migrating dunes.

1 INTRODUCTION

Dunes in natural marine environments are subject to various, complex and unsteady hydrodynamic forcings. Understanding and forecasting their morphology and dynamics is an important task, especially when interacting with marine structures, as the bedform-related roughness strongly influences sediment transport. In shallow waters and intertidal environments in particular, subaqueous dunes are strongly influenced by waves which combine with unidirectional or reversing currents. Their morphology can also be strongly modified by extreme events. Physical experiments in flumes constitute a common approach to the study of natural systems that helps to test independently the influence of each forcing occurring in nature. To date, most of the physical experiments conducted on marine dunes in flumes have been performed under unidirectional steady current (Blom et al., 2003; Boguchwal and Southard, 1990; Bridge and Best, 1988; Kleinhans, 2004; Naqshband et al., 2014), or under long-period oscillating flows in tunnel flumes (Perillo et al., 2014). Thus, there is still a need to explore how dunes grow in the presence of currents interacting with short-period waves, longer storm waves or extreme events, and to understand how waves modify the dune morphology, in comparison with current-only dynamic equilibrium morphology.

In this paper, we present preliminary experiments of a study which aims at understanding, using physical experiments, the response of dunes to wave-current interactions. We report the development, equilibrium morphology and flow structure of dunes under unidirectional current, a simple flow condition which will serve as a comparison for future experiments using combined flows. Dune growth and equilibrium morphology was surveyed thanks to a laser distance meter, and a space-localized wavelet approach was used in order to detect the temporal evolution of the main dune's wavelength. Quantitative information on flow structure and sediment transport was obtained by deploying the UB-Lab 2C, a new acoustic Doppler profiler manufactured by UBERTONE, which provides high spatial and temporal measurement of both two-component flow velocity and sediment concentration profiles over the entire water column.

The information of sediment concentration can be derived from the UB-Lab 2C backscatter intensities following the

methodology of Hurther et al. (2011). This offers the ability to explore sediment flux profiles in the suspension layer. The inversion from intensity to concentration is done by iterating downwards from the emitter while accounting for the signal attenuation occurring along the water depth, as described in detail by Batteridge et al. (2008) and Thorne and Hurther (2014). The interpretation of the acoustic backscatter intensity requires calibration of the system. In this study, dimensionless concentration results will be given as to date, the calibration system is still under development.

2 MATERIAL AND METHODS

The present data were acquired within the MOdelling of marine DUnes: Local and Large-scale EvolutionS in an OWF context (MODULLES) project. The tests have been carried out in the wave and current circulating flume of the M2C laboratory located in Caen (France). The flume is 16 m long, 0.5 m wide and 0.5 m deep, and is equipped with a piston type wave maker and a centrifugal pump for water recirculation.

In order to ensure the uniformity of the flow, a 20 cm-high honeycomb was installed at the entrance of the flume, followed by a 1 m-long pebble bed to ensure the fast development of a turbulent boundary layer. A sediment trap was also installed at the end of the flume to collect the bedload sediment. The longshore coordinate x was defined as 0 at the beginning of the sandy bed (Figure 1), increasing toward the other end of flume and the still water depth was 0.3 m. For present tests, a coarse sand of median diameter D_{50} = 0.6 mm and relative density $s = \rho/\rho s = 2.65$ is selected based on the bedform phase diagram (Southard and Boguchwal, 1990).

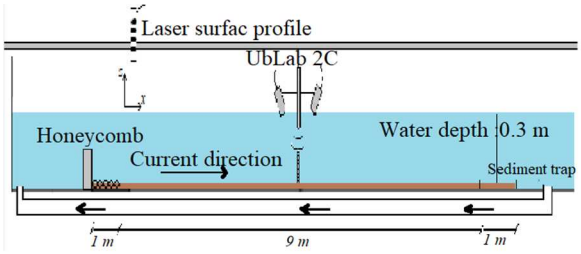

Figure 1. A schematic showing the experimental setup in the test section of the water flume.

The flow velocity was measured with the totally submerged UB-Lab 2C. The UB-Lab 2C allows to acquire co-located two (2C) instantaneous velocity profiles with three transducers (2 emitters and 1 receiver). The two instantaneous velocity components are denoted (u,v) along the directions (x,z) respectively. Figure 2 shows a comparison between a velocity profile u(z) given by the UB-Lab 2C and a velocity profile given by the two well established instruments, the PIV and the ADV.

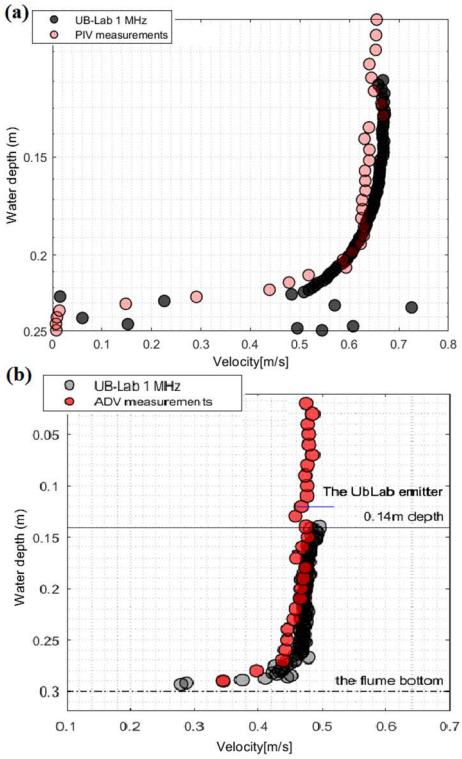

Figure 2. Comparison between velocity profiles u(z) given by the UB-Lab 2C and (a) PIV measurements (b) ADV. The averaging time for the two acoustic tools is 2 minutes and 30 s for the optical tool. The sampling frequency is 20 Hz for UB-Lab 2C, 100 Hz for the ADV and 200 Hz for the PIV.

The experimental procedure was conducted as follows. First, the sandy bed installed over 9 m was flattened to reach a thickness of 10 cm (around 0.5m^3 of sand). The uniform current U = 0.65 m/s was then generated in the flume and UB-Lab 2C flow and concentration measurements were performed. Experiments were stopped every 15 minutes to collect the sand trapped downstream and to reinject it upstream, as the sediment was not recirculated automatically. The overall duration of the experiment was around 300 min.

The 9m-long sandy bed topography was surveyed every 15 minutes along 5 parallel longitudinal transects, using a laser distance-meter mounted on a carriage. The longitudinal profiles were then interpolated to obtain maps of the bottom topography.

3 RESULTS AND DISCUSSION

3.1 Topography evolution of dunes

Starting from plane bed, ripples appeared instantaneously as the flow was introduced in the flume. Dunes subsequently developed and finally a steady state condition was obtained where the dunes migrated through the flume with a relatively constant speed. Figure 3 shows 20 selected maps of the bed evolution in time along the effective measuring section of the flume. Quasi equilibrium state is here defined as the moment when dunes morphologic characteristics (mean wavelength and height) does not change substantially.

Topographic instantaneous profiles are overlaid chronologically at regular time intervals (i.e., 15 min) in order to plot the space-time diagram (Figure 4) which was used to calculate the dune velocity (U ~ 2 m/h) at equilibrium.

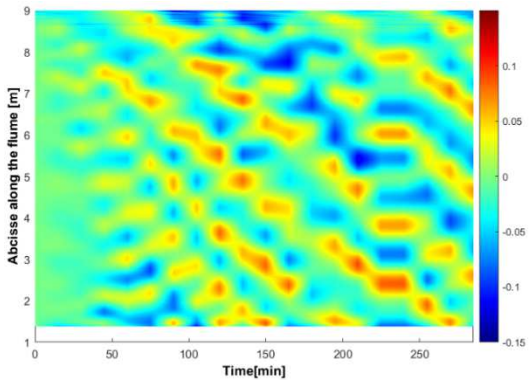

Figure 4. The space-time diagram which reflects the topography along time.

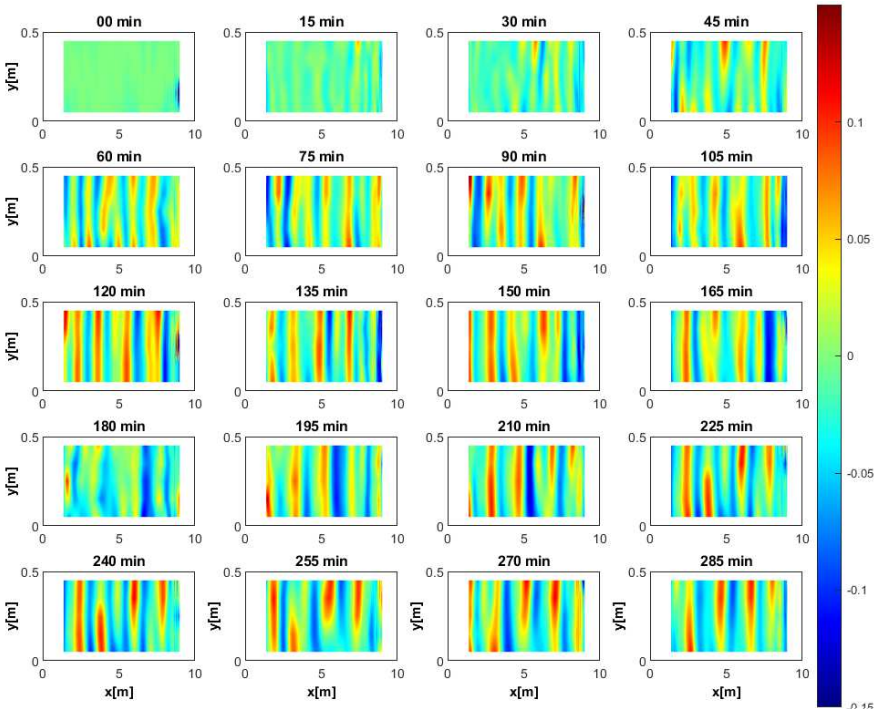

Figure 3. Bed temporal evolution along the flume.

3.2 Wavelet analysis

Wavelet analysis was used to study spatial series bed elevation profiles acquired every 15 min. The objective is to be able to account for the variability of the signal frequency at the different positions along the study section. The continuous wavelet transform $WT(a,\tau)$ of the topography spatial signal, $x_n(t)$, is defined as a convolution integral of $x_n(t)$ with a mother wavelet, $\psi^*_{a,\tau}$ that is translated and scaled along the signal:

$$WT(a,\tau) = \int_{-\infty}^{+\infty} x_n \, \psi^*_{a,\tau} \, dx \quad (1)$$

where the asterisk indicates the complex conjugate, $\psi(a,\tau)$ represents the mother wavelet function dilated by a factor τ and scaled by a factor a, and dx the spacing. The mother wavelet can be dilated by a factor τ and scaled by a factor a. Scales can be written as fractional powers of two:

$$a_i = a_0 2^{i\delta}, i = 1, 2, 3 \ldots M \quad (2)$$

$$M = \frac{1}{\delta} log_2\left(\frac{N\Delta t}{a_0}\right) \quad (3)$$

Where $a_0 = 0.005$ is the smallest resolvable wavelength, M the largest wavelength, and δ the scale factor. The selected scale factor was $\delta = 0.0005$, giving a total of 382 wavelengths. The space sampling and the number of points were, respectively, $\Delta x = 0.005$ m and $N = 2000$. The selection of the mother wavelet was made based on several tests performed in the data. Finally, a complex Morlet mother wavelet was used, in accordance with the suggestion by Cataño-Lopera et al. (2009) and with the results obtained by Gutierrez et al. (2013) in the analysis of the capability of different mother wavelets to retrieve ripple periodicities from synthetic signals. The complex Morlet wavelet can be interpreted as a sine wave multiplied by a gaussian envelope.

The wavelet transform WT (a,τ) is here displayed as a 2D colour plot (Figure 5) showing wavelength versus space (distance along the flume), with the colours representing the magnitudes of $|WT(a,\tau)|^2$. Initially, between 30 and 75 min, the evaluated wavelengths corresponded to wavelengths ranging between 1 m and 1.4 m, which is a currently accepted length criteria to define dunes in the literature (Ashley, 1990). Figure 5 shows that the most energetic wavelengths vary temporally. From 30 to 200 min, the extremes correspond to wavelengths of around 1.2 m and 1.6 m. With increasing time (t > 200

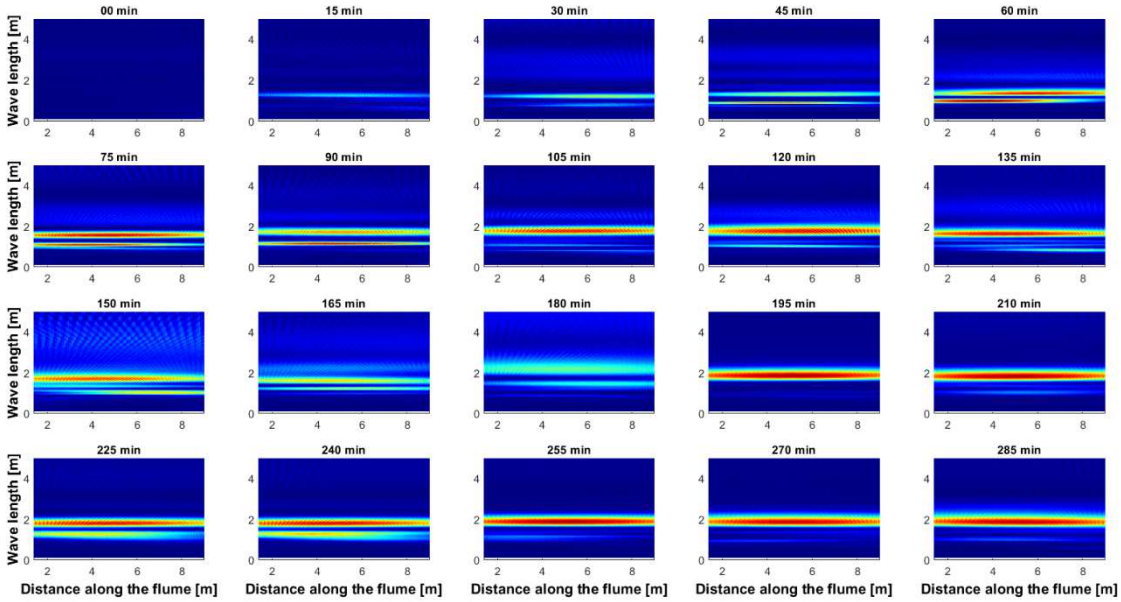

Figure 5. Wavelet magnitude for dunes resulting from steady current during the 285 min of experiments and their corresponding mean wave power for each wavelength.

min), a noticeable energetic band centred at λ = 1.8 m appears. Figure 6 summarizes the temporal evolution of the λ – distance along the flume relation. It is found that at t > 200 min, no noticeable changes are observed in the dune's main wavelength and height (~ 9.5 cm).

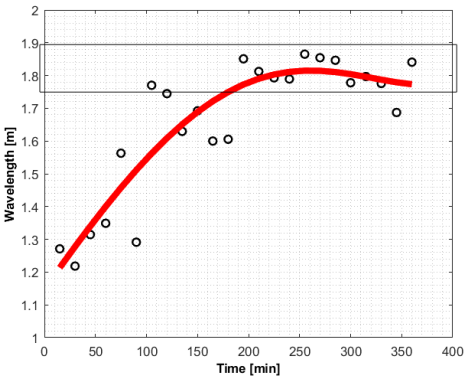

Figure 6. Temporal evolution of dune's wavelengths.

3.3 Flow and concentration analysis

The UB-Lab 2C probe was placed downward-looking at x = 7 m and the dunes migrated underneath it with a relatively constant velocity. The acoustic tool provides flow velocity and sediment concentration profiles of 23 cm length and pulse repetition frequency (PRF) of 900Hz at high spatial (3 mm) and temporal resolution (20 Hz).

The sediment concentration estimation is based on a statistical model of the recorded squared voltage (Equation 4). It is derived from semi-theoretical and experimental determinations of the acoustical backscattering and attenuation properties and it is valid under incoherent scattering conditions (Thorne and Hurther, 2014).

$$C = \left(\frac{r\Psi}{K_s R}\right)^2 V_{rms}^2 e^{4r(\alpha_\omega + \alpha_s)} \qquad (4)$$

r is the range from the emitter which varies between 0.05 m and 0.3 m, Ψ represents the departure from the signal spreading within the transducer nearfield and R is the system constant. K_s represents the sediment backscattering properties, α_s is the attenuation due to suspended sediment scattering and α_ω is the sound attenuation due to water absorption. A typical example of the relative root-mean-square backscatter signal V_{rms} is shown in Figure 7. The first 0.09 m data are not shown because this part of measurements is contaminated by the crosstalk between the transmitter and the receiver during the acquisition. Figure 7 shows a decreasing trend of the backscattered signal with depth due to the r^{-1} term in Equation 4.

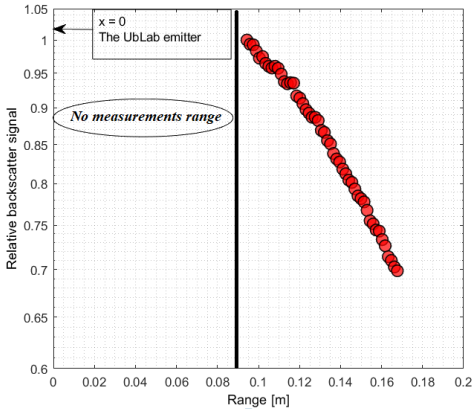

Figure 7. Typical measurements of the relative backscatter signal with range in the flume.

Bed elevation were extracted from the UB-Lab 2C backscattered signal intensity. One example of the bed detection is shown in Figure 8. The sudden and large increase of the backscattered signal intensity corresponds to the bottom echo, and agrees well with the location of zero-velocity on the horizontal velocity profile.

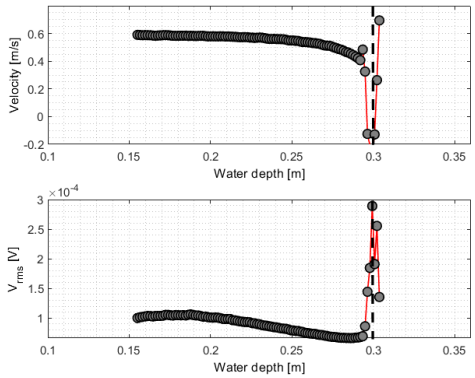

Figure 8. Example of bed detection based on mean backscattered signal intensity profile (bottom) and mean streamwise velocity profile (top).

Figure 9a shows the contour map of the mean streamwise flow velocity $\bar{u}$ evolution with time. The position of the dune topography is

detected thanks to the UB-Lab 2C backscattered signal and is represented by a solid black line. The flow is from right to left. From Figure 9a, we can distinguish three main flow features over the migrating dune. The first feature concerns the presence of a zone of deceleration in the lee side zone. Negative streamwise velocities (counter-currents) are localized in the through region, and associated to the recirculating cell. The second feature is the presence of an acceleration zone in the stoss side region of the dune with high streamwise velocities. The third feature is the development of a millimetric internal boundary layer on the dune crest. These results are qualitatively similar to those found in Naqshband et al. (2014).

Figure 9b shows the contour maps of the mean vertical $\bar{v}$ flow velocities along the migrating dune. The main feature in this figure is the presence of positive vertical velocities almost along the entire migrating dune.

Figure 9c represents the contour map of the dimensionless sediment concentration along the migrating dune. Two zones of high sediment concentration are observed. These are associated to (1) the lee side of the dune, where significant sediment deposition occurs by avalanching from the crest, and by settling in the decelerating recirculation zone; (2) the boundary layer reattachment point, where significant erosion occurs during turbulent bursts.

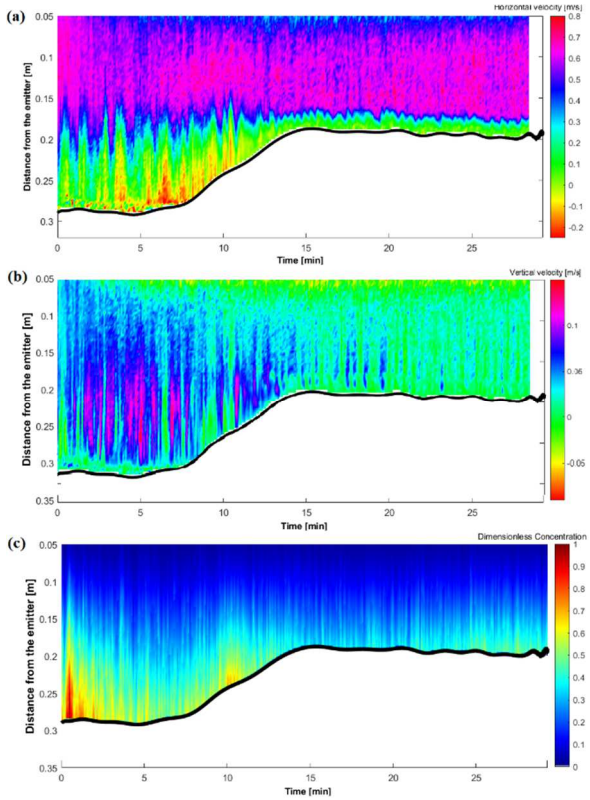

Figure 9. (a) Contour map of the mean streamwise flow velocity $\bar{u}$. (b) Contour map of the mean vertical flow velocity $\bar{v}$. (c) Contour map of the mean dimensionless sediment concentration. The solid black line shows the dune profile.

4 CONCLUSIONS AND PERSPECTIVES

This paper presents a study of the morphology, dynamics, flow structure and sediment concentration over a migrating dune under unidirectional current, using physical experiments. The wavelet approach was used to quantify the mean dune wavelength and its evolution with time. It takes into account the variability of the wavelengths along the flume extension, and so, it permits the identification of the dune wavelengths in different sections. This study strengthens the utility of the UB-Lab 2C acoustic tool in detecting flow and concentration features over migrating dunes.

For the near future, we plan to perform the calibration of the backscattered signal in order to obtain quantitative results concerning the concentration and the flux above the migrating dune. Morever, in order to expand results found in this study, new tests involving the presence of regular and irregular waves propagating on the

background of a steady current will be performed. To our knowledge, there has not yet been flume experiments investigating dune dynamics under extreme waves. Therefore, there is a strong need to conduct experiments on dune dynamics in the presence of group focused waves in order to derive general formulation and deepen our knowledge of dune morphodynamics under nonlinear forcings.

5 ACKNOWLEDGEMENT

This study is funded by the Normandy region, and is part of the project named "MOdelling of marine DUnes: Local and Large-scale EvolutionS in an OWF context (MODULLES), supported by France Energies Marine (FEM).

6 REFERENCES

Ashley, G. M., 1990. Classification of large-scale subaqueous bedforms: A new look at an old problem -SEPM bedforms and bedding structures. Journal of Sedimentary Petrology, 60(1):160–172.https://doi.org/10.2110/jsr.60.160.

Batteridge, K.F.E., Thorne, P.D., Cooke, R.D., 2008. Calibrating multi-frequency acoustic backscatter systems for studying near-bed suspended sediment transport processes. Continental Shelf Research, 28(2), 227-235. Doi.org/10.1016/j.csr.2007.07.007.

Blom, A., Ribberink, J.S., Vriend, H.J., 2003. Vertical sorting in bed forms: Flume experiments with a natural and a trimodal sediment mixture. Water Resources Research 39(2). doi:10.1029/2001WR001088.

Boguchwal, L.A., Southard, J.B., 1990. Bed configurations in steady unidirectional water flows; Part 1. Scale model study using fine sands. Journal of Sedimentary Research 60(5), 649-657. Doi.org/10.1306/212F923C-2B24-11D7-8648000102C1865D.

Bridge, J.S., Best, J.L., 1988. Flow, sediment transport and bedform dynamics over the transition from dunes to upper-stage plane beds: implications for the formation of planar laminae. Sedimentology 35, 753–763. Doi.org/10.1111/j.1365-3091. 1988.tb01249. x.

Cataño-Lopera, Y.A., Abad. J.D., García, M.H., 2009. Characterization of bedform morphology generated under combined flows and currents using wavelet analysis. Ocean Engineering, Volume 36, Issues 9–10, 617-632. doi.org/10.1016/j.oceaneng.2009.01.014.

Gutierrez, R. R., Abad, J.D., Parsons, D., Best, J ., 2013. Discrimination of bedform scales using robust spline filters and wavelet trans-forms: Methods and application to synthetic signals and the Rio Parana, Argentina. Journal of Geophysical Research. Earth Surf.,118, 1400–1418. doi:10.1002/jgrf.20102.

Hurther, D., Thorne, P.D., 2011. Suspension and near-bed load sediment transport processes above a migrating, sand-rippled bed under shoaling waves. Journal of Geophysical Research.,116, C07001, doi:10.1029/2010JC006774.

Kleinhans, M.G., 2004. Sorting in grain flows at the lee side of dunes. Earth-Science Reviews 65, 75–102. Doi.org/10.1016/S0012-8252(03)00081-3.

Naqshband, S., Ribberink, J.S., Hurther, D., Hulscher, S.J.M.H., 2014. Bed load and suspended load contributions to migrating sand dunes in equilibrium. Journal of Geophysical Research: Earth Surface. 119, 1043-1063. Doi.org:10.1002/2013JF003043.

Perillo, M.M., Best, J.L., Garcia, M.H., 2014. A new phase diagram for combined-flow bedforms. Journal of sedimentary research., 84(4), 301-313. Doi: https://doi.org/10.2110/jsr.2014.25.

Southard, J.B., Boguchwal, L.A., 1990. Bed configuration in steady unidirectional water flows; Part 2, synthesis of flume data. Journal of Sedimentary Research, 60, 658-679. Doi.10.1306/212F9241-2B24-11D7-8648000102C1865D.

Thorne, P.D., Hurther, D., 2014. An overview on the use of backscattered sound for measuring suspended particle size and concentration profiles in non-cohesive inorganic sediment transport studies. Continental Shelf Research, Volume 73, 97-118. doi.org/10.1016/j.csr.2013.10.017.

Dune orientation controlled by estuarine circulation in the Outer Weser estuary, German Bight, North Sea

M. Becker *Institute of Geosciences, CAU Kiel, Germany – marius.becker@ifg.uni-kiel.de*
G. Herrling *LKN, State Agency for Coastal Defense, National Park and Marine Conservation, Schleswig-Holstein, Kiel, Germany – gerald.herrling@lkn.landsh.de*
K. Krämer *Institute of Geosciences, CAU Kiel, Germany – knut.krämer@ifg.uni-kiel.de*
A. Lefebvre *MARUM, Center for Marine Environmental Sciences, University of Bremen, Germany – alefebvre@marum.de*
A. Zorndt *BAW, Federal Waterways Engineering & Research Institute, Hamburg, Germany – anna.zorndt@baw.de*
F. Kösters *BAW, Federal Waterways Engineering & Research Institute, Hamburg, Germany – frank.koesters@baw.de*
C. Winter *Institute of Geosciences, CAU, Kiel, Germany – christian.winter@ifg.uni-kiel.de*

ABSTRACT: Several years of monthly bathymetric surveys in the Weser estuary, Germany, show how the local effect of discharge on dune shape and orientation varies along the estuarine channel. Upstream located dunes are flood oriented during low discharge and ebb oriented during high discharge. The opposite is observed in the outer estuary during high discharge conditions, despite an increase of the depth-averaged ebb current velocity all along the channel. Model results suggest that this behavior is due to discharge related changes of the salt intrusion, and the related displacement of the brackish zone. During high discharge, estuarine circulation then alters the velocity structure in the outer estuary, then changing the bed load transport balance and dune orientation.

1 INTRODUCTION

While the emergence and migration of subaqueous dunes in unidirectional flow are well understood, much less is known about the dynamics of tidal dunes. This is especially the case for estuarine systems, where the velocity structure is complicated by baroclinic processes and asymmetries in mean tidal flow velocities.

For example, Hendershot et al. (2016) studied the shape of low-angle dunes on the tidal timescale, looking specifically at lee side angles and bedform height. On a longer timescale, Prokicki et al. (2022) found dune orientation to change in response to a displacement of the fluvial-tidal transition zone in the Lower Columbia River, US, during low discharge conditions. Lefebvre et al. (2021) described significant seasonal changes of steep slip face angles in the lower reaches of the Weser estuary. They indicated that discharge has an impact on dune asymmetry also in the outer estuary and suggested to explore the underlying mechanisms.

The Weser estuary does not exhibit a tidal-fluvial transition zone but is characterized by increasing tidal range from roughly 2.5 m in the outer estuary to more than 4 m at the weir. The weir is located 10 km upstream of river km 0, as used in the figures below. See Lefebvre et al. (2021) for a more detailed description of the dune distribution along the estuary.

2 DUNE PARAMETER EXTRACTION

Parameters describing the dune shape were determined based on an extensive bathymetric data set, acquired approximately every month by the local waterway and shipping administration (WSV).

Available data cover the years from 2008 to 2018. Altogether, 2190 grid files were provided and processed. The spatial resolution is 2 x 2 m. To generate bed elevation profiles (BEPs) grids were interpolated along the thalweg and along several profiles parallel to the thalweg. The lateral distance between the parallel profiles is 10 m. The number of profiles was defined to laterally cover the measured across-channel width.

Dunes in BEPs were identified by zero up and down crossing, roughly following Van der Mark et al. 2008. Bed elevations fluctuations smaller than 10 m were removed applying an appropriate low pass filter. A length scale of 250 m was used for detrending. Dune height was calculated as the distance of the crest to a straight line connecting the two troughs. Not all trough-crest-trough successions represent valid bedforms. Those are removed, using only feature heights between 0.3 m and 5 m, feature length between 15 m and 250 m, and a height to length ration between 0.01 and 0.2.

These steps work well for regular dunes. In case of irregular dunes, not all shapes are favorably detected and the zero crossing method introduced some typical cases of misidentified dunes, e.g. those with two local elevation maxima closer to the crest, or superimposed dunes. It is assumed that the use of parallel BEPs and the depiction of the same dune by several instances leads to statistically representative dune dimensions and directions.

Each grid is then associated with the date of acquisition, and each dune retrieved from BEPs is associated with an along-channel location in terms of river km. It occurred that the same location was measured twice with only a few days in between the two measurements, often as a result of overlaps between adjacent areas to be mapped, which could not be covered on the same day. Then, some locations were not measured for several weeks or even months, generating gaps in the presumably monthly time series for each location. Choosing a time interval of roughly one week (quarter month) combines data collected closely in time, but preserves the mentioned gaps, which allows specific treatment of these in the subsequent analysis.

Gaps in bathymetric data also exist spatially, in along-channel direction, meaning that at a certain point in time not all locations along the estuary were measured. Mean or median dune parameters were determined using an along-channel distance of 500 m. This steps still preserves the spatial variability of dune shape on the estuarine scale, but also preserves gaps, which can then be specifically treated in the analysis, such as for gaps in time.

Since each individual dune may be represented by many of the parallel BEPs, a minimum number of 250 values per 500 m was defined in order to determine median or mean dune parameters. In case of a channel width of 250 m, 25 parallel BEPs are processed.

If dunes crests reach across the entire channel, the same dune is found in all lines, and a minimum of 10 dunes must be located along the 500 m river stretch. Dunes in the Weser are irregularly distributed. Smaller dunes are abundant and should not be neglected in the analysis. As a result, the threshold of 250 values yields along-channel intervals to exhibit dunes, which are not typical dune fields, but may only contain a stretch of smaller dunes at the side of the navigation channel.

3 DUNE ORIENTATION

Here, changes in dune shape are more important than changes in length and height. This is because dune asymmetry is related to the respective face angles, certainly depending on the direction of net bedload transport and therefore on the regime of the tidal flow, often characterized as ebb or flood dominant by basic features of the tidal flow, such as depth averaged or peak ebb and flood velocities.

The spatial and temporal variability in dune asymmetry is shown in Figure 1. Asymmetry is given in terms of the face length asymmetry, which is the ratio between upstream and downstream face length. A remarkable number of dunes is in fact more symmetric than ebb-directed, as originally expected, especially in the regions up to km 10 and between km 55 and 105.

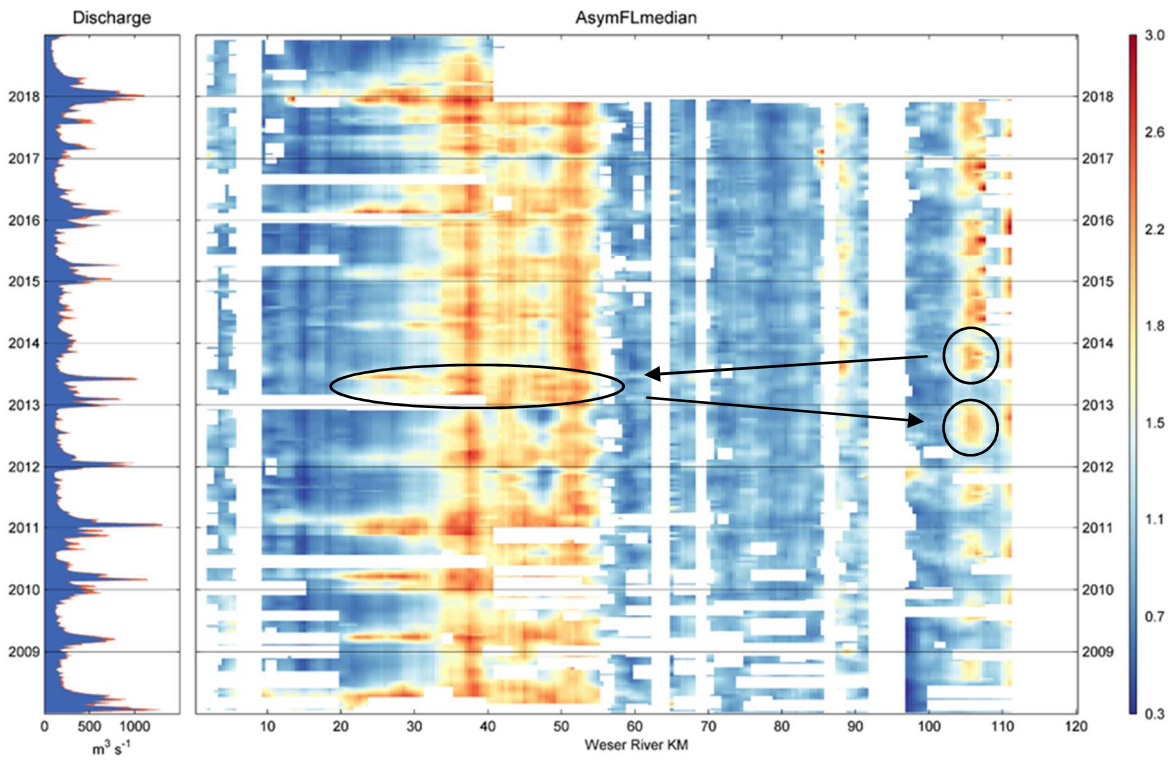

Figure 1. Median face length asymmetry in relation to discharge. Values are given in terms of the ratio of upstream versus downstream face length (FL). Symmetrical dunes exhibit a value of 1. Values exceeding 1 are ebb-directed. Encircled are examples of the occurrence of more flood directed dunes. River km increase downstream.

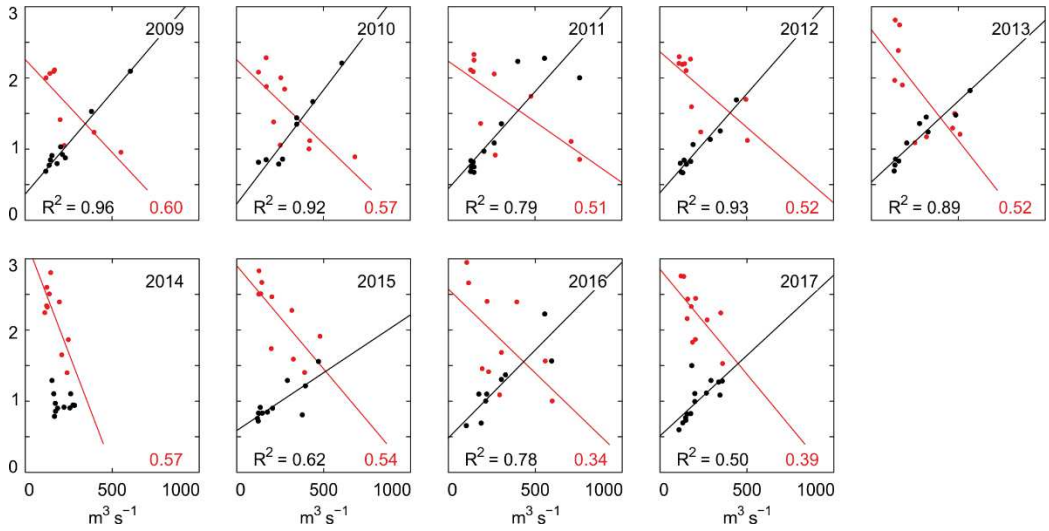

Figure 2. Face length asymmetry versus discharge, for each hydraulic year. Discharge is averaged for four weeks preceding the date associated with each data point of face length asymmetry. Results from km 25 (km 106) are shown in black (red). The typical discharge peak is missing in 2014, and dunes in the inner estuary are predominantly symmetric throughout the year. Note that no correlation line is given for km 25.

Mainly flood directed dunes are found between km 10 to 20. In the region between km 20 and 35, changes in dune asymmetry are related to discharge peaks, causing a change from symmetric or flood-directed to ebb-directed shapes. The opposite behavior is found e.g. around km 107, where dunes develop an ebb-directed shape during periods of

low discharge. The response of dune shape to discharge variations therefore depends on the location within the estuary. Such spatial variations of dune shape response are expected to occur in a funnel-shaped, partially-mixed estuary with a strong barotropic tide. The tidal asymmetry might vary along the channel and in time, and it is presumed, as said, that dune shape reflects the effect of that tidal asymmetry on residual bed load transport.

Dune parameter and discharge are correlated for each hydraulic year separately. Figure 2 shows an example of two different along-channel locations. The slope of the corresponding linear regression is a first estimation of the dune response to discharge variations, neglecting lag effects.

The correlation coefficient in Figure 2 is consistently higher in the inner compared to the outer estuary, indicating the control of discharge on dune asymmetry to decrease downstream. Regression slopes determined for different hydraulic years are interpreted as the response of a parameter to change with discharge and averaged at each location. The regressions show the oppositional behavior of dune asymmetry in the inner and in the outer estuary.

Clearly, low discharge causes dunes to develop flood-directed shapes in the inner and ebb-directed shapes in the outer estuary. The contrary seems to occur during high discharge conditions. It remains to determine in which particular way hydrodynamics change in response to high discharge in the outer estuary.

4 HYDRODYNAMIC MODEL

The analysis of changes of the velocity structure in response to discharge is based on results from a 3D numerical model (UNTRIM2, BAW). The simulation period is from 2019 May to 2020 April. Model results are available for 16 cross-sections, located along the channel between km 30 and km 105, in along-channel steps of approximately 5 km. The vertical resolution is 0.5 m. Across-channel horizontal resolution and corresponding mesh cell size are variable. The number of across-channel mesh cells ranges from 8 (far upstream) to 52 (outer estuary).

The model was validated with respect to variations of the salt intrusion and the vertical density stratification, based on ship-based measurements during the simulation period and data from several stations of salinity, distributed along the estuary. Parameters used here, as obtained from model results, are the near-bed residual velocity, the salt flux, stratification, and the tidal velocity asymmetry.

The near-bed residual velocity was determined as the minimum value of the residual velocity profile. This profile is based on tidal velocities projected with respect to the ebb current direction. A negative, upstream-directed near-bed velocity should indicate an estuarine exchange flow to effect the residual velocity profile, probably somewhere along the brackish zone.

The salt flux was decomposed using the flux decomposition method of Becherer et al. (2016), there used to decompose fluxes of suspended sediment, here applied to salinity. To perform the decomposition, salinity and velocity were interpolated vertically on a sigma grid and corrected for the tidally varying vertical layer spacing, to preserve continuity of the flux. The decomposition then splits the subtidal or net salt flux into three components, taking into account intratidal variations of the vertical profiles of current velocity and salinity.

It is arguable if the salt flux components, resulting from this decomposition, can be addressed as to represent the influences of distinct mechanisms, which would be the tidal pumping flux, the barotropic flux, and the contribution due to exchange flow (Becherer et al. 2016). These flux components have been addressed differently across literature (e.g. Geyer et al. 2001, Burchard et al. 2017, Dijkstra et al. 2022). Here only the contribution due to the exchange flow is used.

Stratification is quantified by the potential energy anomaly (Simpson et al. 1978, Burchard and Hofmeister 2008), as determined from the vertical density distribution and subsequently used to show variations of stratification in response to changes of discharge.

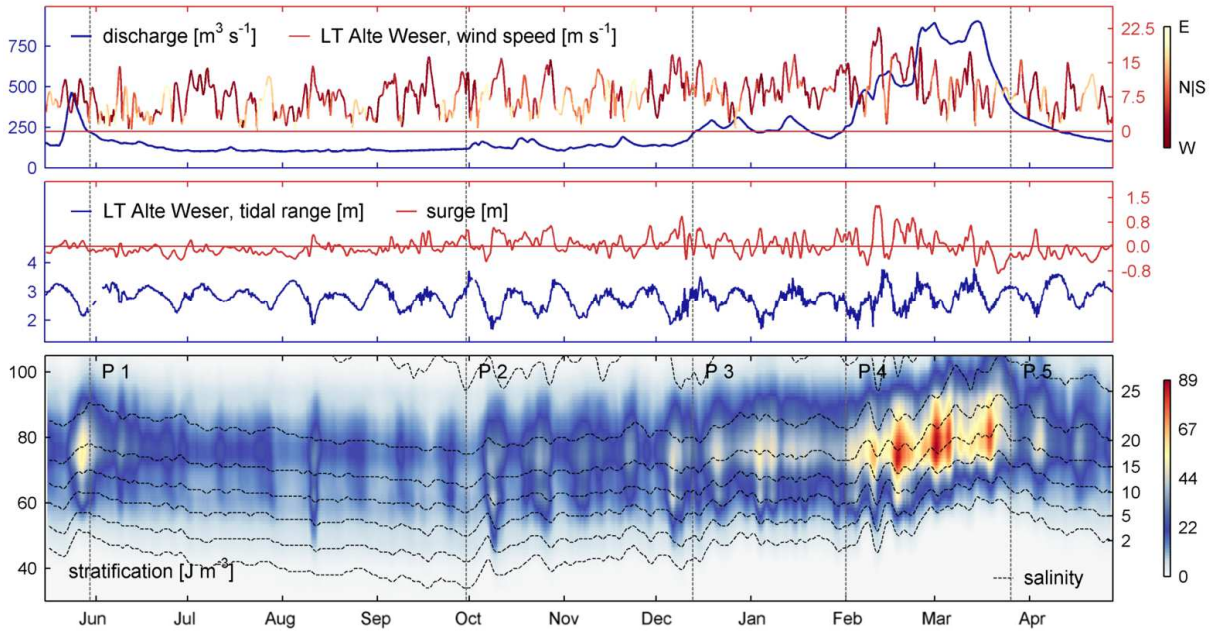

Figure 3. Stratification, discharge, tidal range, wind, and surge during the simulation period. Stratification is plotted in terms of the potential energy anomaly. In the top panel, wind speed is color coded with respect to wind direction, red colors indicate westerly winds. The surge was determined by harmonic analysis, subtracting the reconstructed tidal signal from the measured elevation (Pawlowicz, 2002). Wind and water level elevation (tidal range) are as measured in the Outer Weser, at lighthouse (LT) Alte Weser. Salinity at isohalines is indicated by y-axis labels on the right side of the bottom panel. X-axis labels indicate river km.

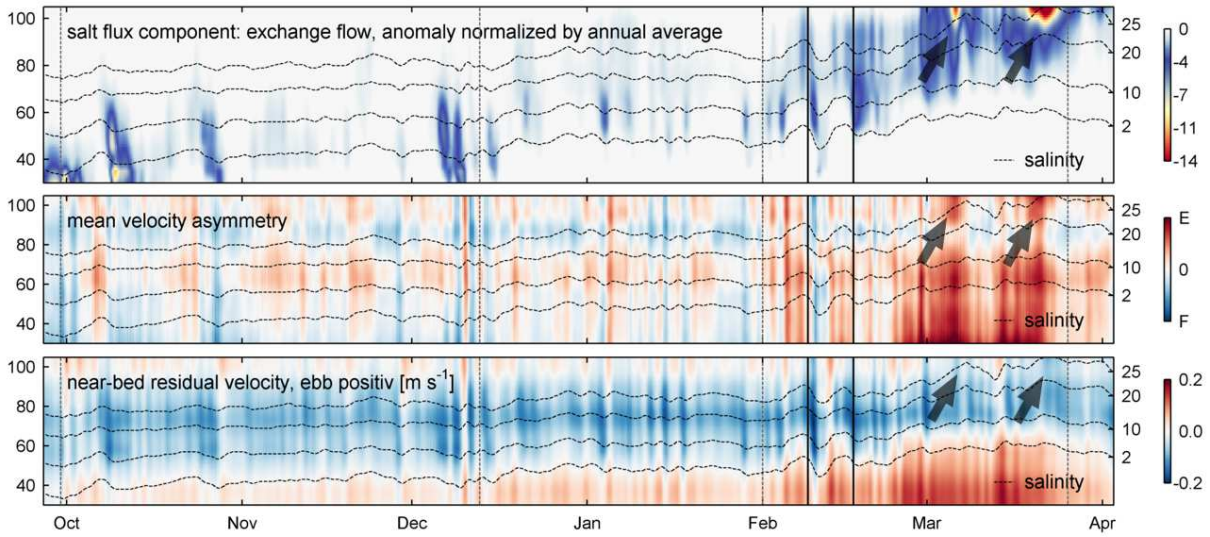

Figure 4. Salt flux due to exchange flow, velocity asymmetry and near-bed velocity between the periods P2 and P4. See text and Figure 3 for explanation of the periods. The exchange flow component of the salt flux is given as its deviation from the annual average, normalized by that annual average. To show the along-channel variations during the simulation period, the annual average and the respective deviations are determined for each location along the river. Arrows point to two distinct discharge peaks during P4. Black vertical lines indicate two storm surges, which affected water levels in the German Bight and occurred during the main increase of discharge.

The tidal velocity asymmetry was calculated as follows. For each tidal phase the velocity was depth and cross-sectionally averaged, in the same flux-preserving way along sigma layers as applied to determine salt flux components. The average ebb velocity was then related to the sum of the ebb and flood velocity, which yields an asymmetry estimate around the value of 0.5. Values exceeding 0.5 indicate ebb velocity dominance

Figure 3 shows the salt intrusion and stratification along the variations of environmental conditions during the simulation period. Stratification is based on the along-channel profile and averaged over two tidal cycles. Isohalines indicate how the salt intrusion changes on various time scales, mainly in response to changes of the discharge.

5 DISCHARGE AND CIRCULATION

The time series is split into periods, each characterized by a certain stratification, discharge and salt intrusion. The maximum of stratification is located around river km 70 during low discharge. Stratification increases during neap tides, certainly in response to lower than average tidal current velocities and less mixing. Stratification increases significantly during times of high discharge in March 2020, during P4 and P5. Then, the salt intrusion decreases and the brackish zone is displaced further downstream, such as the location of maximum stratification.

Figure 4 presents evidence for the change of the vertical velocity structure in the outer estuary, which occurs in response to the increased discharge. While the mean velocity asymmetry indicates increased ebb-dominance, the near-bed velocity is flood-directed, downstream of km 85. In addition, the effect of the exchange flow on the salt flux increases substantially in the outer estuary, especially during the two discharge peaks. The implications are discussed, as follows.

6 DISCUSSION

To start it is noted that the mean velocity asymmetry downstream of km 85 does not reflect the velocity structure close to bed, and cannot be interpreted as to indicate any favorable direction of bed sediment transport. The deviation between the dominant directions inferred from the velocity asymmetry and the near-bed residual current are due to the nature of the estuarine tidal shear flow, which is shown to effect also the salt flux, by the exchange flow component. Here it is not analyzed, which particular process would then be responsible for the changes of the residual flow profile. Processes involved are complex and their understanding underwent substantial corrections in the past decades (e.g. Dijkstra et al. 2020).

However, results show a spatial correlation between the along-channel location of the salt intrusion and stratification on one hand, and the change of the velocity structure on the other hand. Note that also the maximum along-channel density gradient is displaced downstream, accordingly. This indicates that the exchange flow profile, emerging in the outer estuary during high discharge, is controlled by processes related to and driven by the estuarine along-channel and vertical density structure, e.g. by the subtidal, gravitational circulation, by tidal straining and by associated tidal asymmetries in stratification and mixing.

The reversal of dune orientation requires at least a change of the bed load transport balance. Certainly, this change would be induced by the altered direction of the near-bed residual velocity, as it is found in model results during high discharge conditions.

Both the reversal of dune orientation as well as the change of the near-bed velocity occur downstream of km 85. It is concluded that effects due to estuarine circulation, or rather the displacement of its effective location, determine the shape of dunes in the outer Weser estuary. Similar conclusions were drawn by Berne et al. (1993) for the Gironde estuary, who suggested that the migration direction of large dunes was influenced by estuarine circulation. Following up on the Gironde case, van der Sande et al. (2021) applied an analytical model of estuarine flow and linear stability analysis, diagnostically imposing an along-channel salinity gradient, which introduced the development of gravitational circulation in their model. There, a relatively low

eddy viscosity and low river flow was required to induce upstream dune migration. They, however, note that the migration direction of dunes was not necessarily the same as the direction of net sediment transport. In that sense, several aspects remain to be explored. The simulated bed shear stress and bed load sediment transport have not been analyzed, such as along-channel variations of the properties of bed sediments. Lateral processes affecting the along-channel velocity structure were neglected. Lag-effects between discharge, the salt intrusion and changes in dune shape were not considered.

Here is to say that data processed for this study show no indications for week-long lags as reported by Allen (1976), who revisited data acquired by Nasner (1974) in the Weser estuary. It is expected that bed load transport responds relatively quickly to a change in discharge and the corresponding change in current velocity.

How the new bed load transport then leads to a change in dune asymmetry and ultimately in dune direction depends on the pre-existing dune shape. This defines the mass of sediment required to be transported, which is essentially Allen's "intrinsic resistance of individual bedforms to any kind of change". Note that in case of the Weser, all measured discharge peaks must have sufficiently altered the transport balance, as they all induced changes in dune asymmetry, not only in the Outer Weser, but all along the estuarine channel.

7 REFERENCES

Allen, J. R. L., 1976. Time-lag of dunes in unsteady flows: An analysis of Nasner's data from the River Weser, Germany. Sedimentary Geology, 15(4), 309-321

Becherer, J., Flöser, G., Umlauf, L., Burchard, H., 2016. Estuarine circulation versus tidal pumping: Sediment transport in a well-mixed tidal inlet. Journal of Geophysical Research: Oceans, 121(8), 6251-6270

Becker, M., Schrottke, K., Bartholomä, A., Ernstsen, V., Winter, C., Hebbeln, D., 2013. Formation and entrainment of fluid mud layers in troughs of subtidal dunes in an estuarine turbidity zone. Journal of Geophysical Research: Oceans, 118(4), 2175-2187

Berne, S., Castaing, P., Le Drezen, E., Lericolais, G., 1993. Morphology, internal structure, and reversal of asymmetry of large subtidal dunes in the entrance to Gironde Estuary (France). Journal of Sedimentary Research, 63(5), 780-793

Burchard, H., Hofmeister, R., 2008. A dynamic equation for the potential energy anomaly for analysing mixing and stratification in estuaries and coastal seas. Estuarine, Coastal and Shelf Science, 77(4), 679-68

Burchard, H., Schuttelaars, H.M., Ralston, D.K., 2017. Sediment Trapping in Estuaries. Annual Review of Marine Science

Dijkstra, Y. M., Schuttelaars, H. M., Kranenburg, W. M., 2022. Salt Transport Regimes Caused by Tidal and Subtidal Processes in Narrow Estuaries. Journal of Geophysical Research: Oceans, 127(12)

Geyer, W. R., Woodruff, J. D., Traykovski, P., 2001. Sediment transport and trapping in the Hudson River estuary. Estuaries and Coasts, 24(5), 670-679.

Geyer, W. R., MacCready P., 2014. The Estuarine Circulation. Annual Review of Fluid Mechanics, 46(1), 175-197

Hendershot, M. L., Venditti, J. G., Bradley, R. W., Kostaschuk, R. A., Church, M., Allison, M. A., 2016. Response of low-angle dunes to variable flow. Sedimentology, 63(3), 743-760

Lefebvre, A., Herrling, G., Becker, M., Zorndt, A., Krämer, K., Winter, C., 2022. Morphology of estuarine bedforms, Weser Estuary, Germany. Earth Surface Processes and Landforms, 47(1), 242-256

Nasner, H., 1974. Über das Verhalten von Transportkörpern im Tidegebiet. Mitteilungen des Franzius-Instituts für Wasserbau und Küsteningenieurwesen, 40, 1-140

Prokocki, E. W., Best, J. L. , Perillo, M. M. , Ashworth, P. J., Parsons, D. R., Sambrook Smith, G. H., Nicholas, A. P., Simpson, C. J., 2022. The morphology of fluvial-tidal dunes: Lower Columbia River, Oregon/Washington, USA. Earth Surface Processes and Landforms, 47(8), 2079-2106

Simpson, J. H., Allen, C. M., Morris, N. C. G., 1978. Fronts on the Continental Shelf. Journal of Geophysical Research, 83, 4607-4614

Van der Mark, C. F., Blom, A., Hulscher, S. J. M. H., 2008. Quantification of variability in bedform geometry. Journal of Geophysical Research, 113(F03020), 11

Van der Sande, W. M., Roos, P., C., Gerkema, T., Hulscher, S. J. M. H., 2021. Gravitational Circulation as Driver of Upstream Migration of Estuarine Sand Dunes. Geophysical Research Letters 48(14)

MORPHODUNES, a new project dedicated to the 3D morphodynamics of sub-marine sand dunes for safety and maritime activities.

A.-C. Bennis, *UNICAEN, CNRS, UNIROUEN, UMR M2C 6143, Caen (FR) - ac.bennis@unicaen.fr*
M. Boutet, *CNRS, UNICAEN, UNIROUEN, UMR M2C 6143, Caen (FR) - martial.boutet@unicaen.fr*
F. Dumas, *Shom, STM/REC, Brest, France - franck.dumas@shom.fr*
L. Furgerot, *UNICAEN, CNRS, UNIROUEN, UMR M2C 6143, Caen (FR) - lucille.furgerot@unicaen.fr*
A. Gangloff, *Shom, STM/SEDIM, Brest, France - aurelien.gangloff@shom.fr*
E. Lagniel, *UNICAEN, CNRS, UNIROUEN, UMR M2C 6143, Caen (FR) - emilie.lagniel@unicaen.fr*
S. Le Bot, *UNIROUEN, CNRS, UNICAEN, UMR M2C 6143, Rouen (FR) - sophie.lebot@univ-rouen.fr*
D. Mouazé, *UNICAEN, CNRS, UNIROUEN, UMR M2C 6143, Caen (FR) - dominique.mouaze@unicaen.fr*
L. Perez, *CNRS, UNICAEN, UNIROUEN, UMR M2C 6143, Caen (FR) - laurent.perez@unicaen.fr*
G. Porcile, *UNICAEN, CNRS, UNIROUEN, UMR M2C 6143, Caen (FR) - gaetano.porcile@unicaen.fr*
B. Tessier, *CNRS, UNICAEN, UNIROUEN, UMR M2C 6143, Caen (FR) - bernadette.tessier@unicaen.fr*
P. Weill *UMR CNRS M2C, University of Caen Normandie, Caen, France - pierre.weill@unicaen.fr*

ABSTRACT: Here is presented a new project, MORPHODUNES, dealing with the sub-marine sand dune morphodynamics. It is funded by Shom (French Navy) to develop a fully-coupled 3D hydro-morphodynamic model able to simulate the dune migration over the continental shelf according to the metocean forcings, sediment characteristics and seabed morphology. The first part of the project is related to the physical modelling of an idealized and realistic field of dunes at laboratory scale. The laboratory measurements of the flow characteristics and bed topography will be used to validate and calibrate the hydro-morphodynamic model for some specific processes (e.g. sur-imposed bedforms and impacts). The second part of the project is devoted to the analysis of field data. These data are recorded by Shom in Iroise/Celtic sea, near the Brest harbour during the project. Sedimentary fluxes, bed morphology and thickness of the mobile zone, sediment response of the hydrodynamic condition swill be determined from this analysis. The third part is dedicated to the set-up, validation, and calibration of the hydro-morphodynamic model for the study site thanks to the in-situ data and their analysis. This work will be based on several diagnoses for hydrodynamics and morphodynamics (e. g. flow characteristics, wavelength and height of dunes, asymmetry index, crest sinuosity). At the end, the model should be as much as possible independent of the site conditions to be used to simulate dune morphodynamics in 3D at another location in the world for the marine safety and navigation.

1 INTRODUCTION

Tidal sand dunes are mostly present in tidal channels or mouths (e.g. Kostaschuk & Best, 2015) as well as over the continental shelf in areas with a moderate mean depth and a tidal current, which is constrained by the site geometry or channelized (e. g. Le Bot and Trenteseaux, 2004; Ferret et al., 2010).Their characteristics (e. g. wavelength, height, shape, sediment vertical sorting) depend on many factors, including tidal range and tidal prism, ocean wave energy, sediment grain size, and the amount of mobile sediment (e. g. Fitzgerald, 1996).

Due to the generation of tidal sand dunes by a well-directed tidal flow, their dynamics have been often modelled in two-dimension vertical (e. g. Doré et al., 2016, 2018). In areas where the current varies little in the water column, two-dimension horizontal modelling (e.g. Ma et al., 2019) is usually performed. However, some cases require to

use three-dimensional (3D) modelling for hydrodynamics when the hydrodynamic forcing is 3D or/and the dune morphology is 3D. For the moment, very few studies have been published in a realistic environment for the 3D case.

A pioneer study was initiated by Goll et al., (2016) for river dunes. The hydrodynamic model Telemac3D was used in combination with the Sisyphe module for morphodynamics (Villaret et al., 2013). They have simulated the movement of a sand dune field forced by a 3D flow in the Elbe River (Germany).

A recent study by Herrling et al., (2021), using Delft3D, simulated idealized 3D scenario for the sand dune dynamics in the Weser Estuary (Germany). They highlighted the need to consider dune-induced directional bed roughness in numerical models of estuarine and tidal environments.

From our knowledge and to date, no study exists for the 3D modelling of realistic sand dune fields on the continental shelf. The MORPHODUNES project, presented here, is dedicated to this.

In this context, this paper aims to explain the methodology forseen in MORPHODUNES to answer the following scientific questions and then provide a fully-coupled 3D hydro-morphodynamic model to the scientific community:

- How do the 3D hydrodynamics drive sediment transport and impact the sand dune morphology?
- When should 3D rather than 2D hydrodynamics be considered?
- What is the impact of winter storms on tidal dune dynamics?

After a short introduction in Section 1, physical modelling activities are presented in Section 2. The study site and field measurements are described in Section 3. The numerical modelling part, through the presentation of the numerical models and the calibration, validation steps, is detailed in Section 4. A brief conclusion is provided in Section 5.

2 PHYSICAL MODELLING

At a first step, some laboratory experiments will be conducted to identify key processes and assess the capability of the hydro-sedimentary model to simulate the sand dune morphodynamics. A first set of experiments will focus on the hydrodynamics above fixed concrete dunes of variable surface roughness. A second set will deal with the morphodynamics of sediment dunes in live-bed conditions. The experimental set-up and test cases are presented below.

2.1 Experimental set-up

Figure 1. Wave-current flume of the University of Caen (M2C lab.)

The experiments will be conducted in a 16 m-long, 0.5 m-wide and 0.5 m-deep current flume, equipped with a centrifugal pump for water recirculation (Fig. 1). In order to ensure the uniformity of the flow, a honeycomb will be installed at the entrance of the flume, followed by a 1 m-long pebble bed to ensure the fast development of a turbulent boundary layer. For live-bed experiments, a sediment trap will be installed at the end of the flume to collect the bedload sediment, to be reloaded regularly upstream. The topography of the sediment bed will be surveyed every 15 minutes along 5 parallel longitudinal transects, using a laser distance-meter mounted on a carriage. The longitudinal profiles will then be interpolated to obtain maps of the bottom topography. Flow measurements under live-bed conditions will be monitored using the UBERTONE acoustic Doppler velocity profiles UB-Lab 2C. The probe will be placed downward-looking at a fixed position, with the dunes migrating underneath. It will provide two-dimensional flow velocity profiles (u,w) at a spatial resolution of 2-3 mm, and a sampling rate

between 20 and 50 Hz. The suspended sediment concentration will be estimated from the intensity of the backscattered signal (Thorne and Hurther, 2014), after calibration with the appropriate sediment. The flow dynamics over the fixed concrete dunes will be investigated using PIV at a sampling frequency of 200 Hz.

2.2 Test cases

2-D fixed dunes (scaled in situ topography) will be built in smooth concrete panels. Local change of the micro roughness will be insured by rough bands (parallel to dune crests) of glued sand. Similitude scaling will be focused on reproducing the main flow features, including turbulence, at the seabed. Velocity profiles, vorticity and turbulence features will be quantified thanks to high frame rate PIV system. Spatial equivalent roughness will be then determined along the varying macro and micro morphology and will be correlated with the dynamic of the flow.

Experiments in live-bed conditions will be performed using a bimodal quartz sand. The dunes morphology will evolve naturally from an initial 10 cm-thick flat bed, under stationary flow conditions, until a dynamic equilibrium is reached. Several flow velocities will be tested within the field of stability of dunes, in order to quantify the dune morphology variability in response to hydrodynamic forcing. A qualitative analysis of segregation of the bi-modal sediment will be performed thanks to sidewall photographies and cross-sections.

3 STUDY SITE AND FIELD MEASUREMENTS

3.1 Study site

The study site is in the exit channel of the Bay of Brest in Iroise Sea (western-most part of Brittany, NW France; Fig. 2).

Tidal regime is semi-diurnal with macrotidal conditions (average tidal range of 4.7 m). Tidal currents are constrained by the bathymetry of channel and reach 2.3 m/s during the ebb (SW orientation) and 2 m/s during the flood (NE orientation). This part can be also dominated by the swell mostly during south-west storm events (Grégoire, 2016).

The study area consists in two fields of medium to large dunes, composed of gravelly shelly fine to coarse sands (Grégoire et al., 2016) for a total area of 2,3 km^2. The water depth is comprised between 25 and 40m (LAT). Bedload transport is important during spring tides (around 1.10-6 $m^3/m/s$) with residual fluxes oriented towards the W-SW, direction of the tidal ebb-dominated residual current (Grégoire et al., 2016). Dune migration rates are estimated from their asymmetry index (Xu et al., 2008) to be around 4-6 m/yr (Grégoire et al., 2016).

3.2 Field campaigns and future analysis

Bathymetric data are acquired since 2022 every one to two weeks to describe the dune short-term morphodynamics. Bathymetric DEMs and DODs will be produced. The data will be analyzed with GIS tools to quantify dune morphometric parameters and migration rates. Sediment fluxes will be estimated using empirical formulas for sediment transport (e.g. van Rijn, 1984), « dune tracking » formula (e.g. Simons et al., 1965; Schmitt and Mitchell, 2014) and through the quantification of displaced sediment volumes between two bathymetric surveys (e.g. Claude et al., 2012).

Grain-size and seismic data will allow to characterize dune sedimentary environment and analyze the internal architecture of dunes (erosion-deposition structures) and the thickness of the active layer. Acquisition of current velocity and wave data during the bathymetric monitoring will allow to try to put forward relations between hydrodynamics and dune morphodynamics.

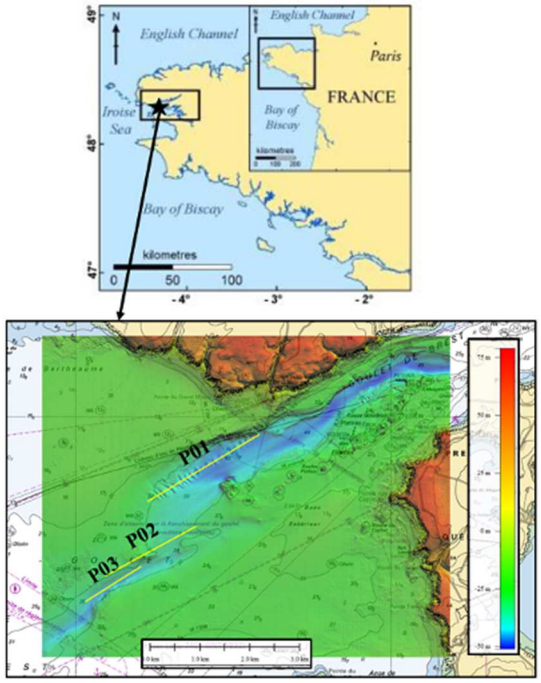

Figure 2. Location (top) and bathymetry (bottom) of the study area. P01 to P03 are the bathymetric profiles surveyed every 1 or 2 weeks.

4 NUMERICAL MODELLING

In this section, the fully-coupled 3D hydro-morphodynamic model is described through all its component models. Then, the methodology for improving, calibrating, and validating the coupled model thanks to the laboratory and in-situ measurements is presented.

4.1 Hydrodynamic model

This study uses the hydrodynamic model, CROCO, which is currently developed by IRD, Ifremer, INRIA, Shom and CNRS (https://www.croco-ocean.org). It solves the primitive equations of the ocean under the Boussinesq assumptions and with/without hydrostatic assumption. It computes the coastal dynamics at different scales in time and space. CROCO is also in capacity to simulate air-sea, sea-bottom and sea-ice interactions by its coupling with atmospheric, morphodynamic or ice numerical models (e.g. Pianezze et al., 2018). This coupling is managed by the automatic coupler OASIS (Valcke et al., 2015).

In a cartesian framework (x,y,z), the governing equations for horizontal momentums are:

$$\frac{\partial u}{\partial t} + \vec{\nabla}.\left(\vec{\mathbf{v}}u\right) - fv = -\frac{\partial \phi}{\partial x} + \mathcal{F}_u + \mathcal{D}_u$$

$$\frac{\partial v}{\partial t} + \vec{\nabla}.\left(\vec{\mathbf{v}}v\right) + fu = -\frac{\partial \phi}{\partial y} + \mathcal{F}_v + \mathcal{D}_v$$

and the continuity equation is:

$$\vec{\nabla}.\vec{\mathbf{v}} = \frac{\partial u}{\partial x} + \frac{\partial v}{\partial y} + \frac{\partial w}{\partial z} = 0$$

Where $\vec{\mathbf{v}}=(u,v,w)$ is the 3D flow velocity vector. The vertical velocity (w) is computed thanks to the continuity equation. f is the Coriolis parameter, $\mathcal{D}_u$ and $\mathcal{D}_v$ are the diffusive terms, $\mathcal{F}_u$ and $\mathcal{F}_v$ are the forcing terms, g is the gravity acceleration, ϕ is the dynamic pressure (more details about CROCO in Jullien et al., 2022).

The time-evolution of passive tracers (e.g. temperature, salinity) is governed by:

$$\frac{\partial C}{\partial t} + \vec{\nabla}.\left(\vec{\mathbf{v}}C\right) = \mathcal{F}_C + \mathcal{D}_C$$

where C is the tracer concentration. $\mathcal{F}_C$ and $\mathcal{D}_C$ are the source and diffuse terms, respectively.

The non-hydrostatic solver will be used in particular at local scale to simulate the flow separation downstream the dune crest.

CROCO will be coupled to WAVEWATCH-III (WAVEWATCH-III, 2019), a spectral wave model, and to MUSTANG (Le Hir et al., 2011), a sediment and morphodynamic module. This allows to understand how the sub-marine dunes move according to the metocean conditions.

4.2 Spectral wave model

The spectral wave model, WAVEWATCH-III, developed by NOAA/NCEP and Ifremer, is coupled to

CROCO to simulate the wave-induced circulation, changes in bottom friction and impacts on sediment transport.

This model computes the generation, propagation, and dissipation of ocean waves at the ocean surface for a phase-averaged flow. It solves the equation of conservation of the wave action (N) such that:

$$\frac{\mathrm{D}N}{\mathrm{D}t} = \frac{S}{\sigma}$$

where σ is the intrinsic wave frequency and S contains all the physics required to represent ocean wave behavior (more details in WAVEWATCH-III, 2019). Here, the most significant source terms will be those for wave-atmosphere interactions (particularly for studying storm effects on dune morphodynamics), wave breaking, wave-bottom interactions, scattering of waves by bottom features.

4.3 Sediment and morphodynamic model

The sediment and morphodynamic model, named MUSTANG and developed by Ifremer (e.g. Le Hir et al., 2011), is used here. It computes the sediment concentration in the water column, which is modulated by the hydrodynamic forcing. An update of the bottom morphology is done at each time step.

In a cartesian framework (x,y,z), it solves the advection-diffusion equation:

$$\frac{\partial C}{\partial t} + \nabla(\mathbf{u}\,C) = \frac{\partial}{\partial x}\left(D_H \frac{\partial C}{\partial x}\right) + \frac{\partial}{\partial y}\left(D_H \frac{\partial C}{\partial y}\right) + \frac{\partial}{\partial z}\left(D_V \frac{\partial C}{\partial z}\right) + \frac{\partial w_s C}{\partial z}$$

where C is the sediment concentration and w_s is the vertical settling velocity.

This module computes the erosion (E) and deposive (D) fluxes such that:

$$E = E_0\left(1 - \frac{\tau}{\tau_{ce}}\right)^n \quad \text{if } \tau > \tau_{ce}$$
$$= 0 \quad \text{if } \tau < \tau_{ce}$$

and

$$D = w_s C^b,$$

where τ is the bottom shear stress, τ_{ce} is the critical shear stress and n is a constant set to 1.5. C_b is the concentration at the bottom (calculated from a Rouse profile).

The bottom shear stress and the settling velocity are estimated using Soulsby and Whitehouse (1997) and Soulsby (1997).

This module is able to generate sand dunes and their movement as shown in Rivier et al. (2016).

4.4 Validation and calibration

The hydro-sedimentary model will be first tested against laboratory measurements for the test cases described in section 2. Then, the model will be used to simulate the dynamics at the study site scale.

4.4.1 Simulations at the laboratory scale

At this scale, two different versions of CROCO will be set-up, a non-hydrostatic and hydrostatic version. These versions allow us to represent different vertical hydrodynamics. For a strong vertical velocity, the vertical acceleration of the flow becomes non-negligible and therefore the hydrostatic assumption is broken. The turbulent activity will be parameterized with classical turbulent closures for RANS modelling (e.g. k-ε or k-ω). In addition, DNS simulations will be tested to try to simulate all the turbulent structures with a characteristic length-scale greater than the mesh size. Indeed, the turbulent activity near the bottom, particularly in the bottom boundary layer, is a key factor for the dune dynamics and it is therefore important to represent it as accurately as possible

For experiments using a rigid bottom, purely hydrodynamic simulations will be performed using only CROCO. Because of the water is mainly oriented towards the longitudinal direction, the model will be run in 2DV (two-dimension vertical). The bottom rugosities will be considered in the simulations by using parameterizations or they will be solved explicitly thanks to their integration in the bathymetry file.

For experiments using a mobile bed, MUSTANG will be coupled to CROCO. The bed load being the key process in the dune dynamics, it will be studied in-depth using the works of Rivier et al., 2017 and Mengual et Le Hir, 2018. 2DV and 3D (if necessary) simulations with CROCO-MUSTANG will be set-up and run for a bi-modal sediment.

Numerical results will be analyzed and compared to measurements for the flow velocity at different points (on and off the dunes), sea surface height, and near-bottom turbulence characteristics. In case of mobile bed, the time evolution of the bed, the bed thickness and the flow velocity near the bed will be also analyzed.

According to the comparison results, the model could be improved to represent significant processes like the near-bed turbulence and its impact on sediment transport, for example.

4.4.2 Simulations at the study site scale

Based on the previous work at the laboratory scale, a realistic configuration of CROCO-WWIII-MUSTANG will be set-up and applied to the dune fields located at the entrance of the Brest Harbour (Fig. 2).

The impact of the metocean forcings (e.g. tide, wind, wave) on the hydro-sedimentary environment will be assessed as well as the influence of the extreme events (e.g. winter storms) on the sediment transport. Different boundary fields from European and American databases (e.g. Copernicus or CFSR) will be tested.

Cross-comparisons with existing datasets (CANDHYS for waves, MAREL for sea water level or others) and with new data (e.g. flow velocity, bed topography, granulometry and sediment sorting) recorded during the project (more details in section 3) will be carried out to estimate the capability of the model to reproduce the dynamics induced by tide (e.g. flood and ebb flow, tide asymetry), ocean waves (e.g. Stokes drift, wave orbital velocity) and turbulence (e.g. horizontal and vertical mixing) and coupling effects (e.g. wave-induced current, wave-enhancement of the bottom stress). Then, tide, wave, turbulence and coupling effects on sediment transport and bed morphology will be assessed for: i) wavelength and height of dunes, ii) location of the dune crests, iii) dune asymmetry index, iv) length and slope of the dune sides, v) sinuosity of the dune crestline.

The main novelty here is to consider 3D computed hydrodynamics in interaction with a realistic 3D dune field. The modification of the flow in all the directions by the sand dunes could be simulated as well as the effects of 3D hydrodynamic processes.

5 CONCLUSIONS

In this project, thanks to an exceptional dataset, particularly for the bottom topography, we could be able to identify the driving mechanisms of the sand dune dynamics and their internal structure. Moreover, an innovative fully-coupled 3D hydro-morphodynamic model will be developed and assessed, which can be deployed in the future by the scientific community to study other sand dune fields around the world and preserve marine safety and navigation.

6 ACKNOWLEDGEMENTS

Authors thank the Shom for the funding and data acquisition. Authors acknowledge the Centre Régional Informatique et d'Applications Numériques de Normandie (CRIANN) for the computational facilities throughout the use of the super-computer Myria.

7 REFERENCES

Claude, N., Rodrigues, S., Bustillo, V., Bréhéret, J.G., Macaire, J.J., Jugé, P., 2012. Estimating bedload transport in a large sand-gravel bed river from direct sampling, dune tracking and empirical formulas. Geomorphology, 179, 40–57.

Doré, A., Bonneton P., Marieu V., and Garlan T., 2016. Numerical modeling of subaqueous sand dune morphodynamics, J. Geophys. Res. Earth Surf., 121, 565–587

Doré, A., Bonneton, P., Marieu, V. and Garlan, T., 2018. Observation and numerical modeling of tidal dune dynamics. Ocean Dynamics 68, 589–602.

Ferret, Y., Le Bot, S., Tessier, B., Garlan, T., and Lafite, R., 2010. Migration and internal architecture of marine dunes in the eastern English Channel over 14- and 56-year intervals: the influence of tides and decennial storms. Earth Surface Processes and Landforms, 35(12), 1480-1493.

Fitzgerald, D. M., 1996. Geomorphic variability and morphologic and sedimentologic controls on tidal inlets. Journal of Coastal Research, 23, 47-71.

Goll A., 2016. 3D numerical modelling of dune formation and dynamics in inland waterways. PhD in Fluid mechanics, Université Paris-Est, 195.

Gregoire, G., Ehrhold, A., Le Roy, P., Jouet, G., Garlan, T., 2016. Modern morpho-sedimentological patterns in a tide-dominated estuary system: the Bay of Brest (west Britanny, France). Journal of Maps, 12(5), 1152-1159.

Gregoire, G., 2016. Dynamique sédimentaire et évolution holocène d'un système macrotidal semi-fermé : l'exemple de la rade de Brest. PhD in Sedimentology, Université de Bretagne occidentale, 295.

Herrling, G., Becker, M., Lefebvre, A., Zorndt, A., Krämer, K., Winter, C., 2021. The effect of asymmetric dune roughness on tidal asymmetry in the Weser estuary. Earth Surface Processes and Landforms, 46 (11), 2211– 2228.

Jullien S., Caillaud M., Benshila R., Bordois L., Cambon G., Dumas D., Le Gentil S., Lemarié F., Marchesiello P., Theetten S., Dufois F., Le Corre M., Morvan G., Le Gac S., Gula J., & Pianezze J., 2022. CROCO Technical and Numerical Documentation, Tech. Report, IRD/IFREMER/INRIA/Shom/UT3.

Kostaschuk, R., Best, J., 2005. Response of sand dunes to variations in tidal flow: Fraser Estuary, Canada. J. Geophys. Res., 110, F04S04.

Le Bot, S., Trenteseaux, A., 2004. Types of internal structure and external morphology of submarine dunes under the influence of tide- and wind-driven processes (Dover Strait, northern France). Marine Geology, 211, 143-168.

Le Hir P., Cayocca F., Waeles B., 2011. Dynamics of sand and mud mixtures: a multiprocess-based modelling strategy. Continental Shelf Research, 31(10), 135-149

Mengual, B., Hir, P.L., Cayocca, F., and Garlan, T. (2017). Modelling Fine Sediment Dynamics: Towards a Common Erosion Law for Fine Sand, Mud and Mixtures. Water, 9, 564.

Pianezze, J., and Coauthors, 2018. A new coupled ocean-waves-atmosphere model designed for tropical storm studies: Example of tropical cyclone bejisa (2013–2014) in the south-west indian ocean. Journal of Advances in Modeling Earth Systems, 10 (3), 801–825.

Rivier A., Le Hir P., Bailly Du Bois P., Laguionie P., Morillon M., 2017. Numerical modelling of heterogeneous sediment transport: new insights for particulate radionuclide transport and deposition. Proceedings of Coastal Dynamics 2017 in Part 26 Modelling of coastal sediment transport, 1767-1778.

Schmitt, T., Mitchell, N.C., 2014. Dune-associated sand fluxes at the nearshore termination of a banner sand bank (Helwick Sands, Bristol Channel). Continental Shelf Research, 76, 64-74.

Simons, D.B., Richardson, E. V, Nordin, C.F., 1965. Bedload equation for ripples and dunes, Geological Survey Professional Paper 462-H. USGS, Washington. 9 pp.

Soulsby R., 1997. Dynamics of marine sands: a manual for practical applications. Thomas Telford.

Soulsby R., Whitehouse R., 1997. Threshold of sediment motion in coastal environments. In: Pacific Coasts and Ports' 97: Proceedings of the 13th Australasian Coastal and Ocean Engineering Conference and the 6th Australasian Port and Harbour Conference; Volume 1, Centre for Advanced Engineering, University of Canterbury, p 145

Thorne, P.D., Hurther, D., 2014. An overview on the use of backscattered sound for measuring suspended particle size and concentration profiles in non-cohesive inorganic sediment transport studies. Continental Shelf Research, 73, 97-118.

Valcke, S., Craig T., and Coquart L., 2015. OASIS3-MCT User Guide. Tech. rep., CERFACS.

Van Rijn, L.C., 1984. Sediment transport, part I: bed load transport. J. Hydraul. Eng., 110(10), 1431-1456.

Villaret, C., Hervouet J.-M., Kopmann R., Merkel U., and Davies A. G., 2013. Morphodynamic modeling using the Telemac finite-element system. Computers & Geosciences, 5(0):105–113.

WAVEWATCH-III, Development Group, 2019. User manual and system documentation of WAVEWATCH-III, version 6.07. Tech. Rep. 333, NOAA/NWS/NCEP/MMAB.

Ma X., Yan J., Song Y., Liu X., Zhang J., Traykovski P. A., 2019. Morphology and maintenance of steep dunes near dune asymmetry transitional areas on the shallow shelf (Beibu Gulf, northwest South China Sea). Marine Geology, 412, 37-52.

Xu, J. P., Wong, F. L., Kvitek, R., Smith, D. P., Paull, C. K., 2008. Sandwave migration in Monterey submarine canyon, Central California. Marine Geology, 248(3), 193-212

Characterisation of flow dynamics over estuarine bedforms: An experimental approach

K. Bobiles *MARUM, University of Bremen, Leobener Str. 8, 28359 Bremen, Germany; Faculty of Geosciences, University of Bremen, Klagenfurter Str. 2-4, 28359 Bremen, Germany – knsbobiles@gmail.com*
C. Carstensen *Federal Waterways Engineering and Research Institute (BAW), Wedeler Landstr. 157, 22559 Hamburg, Germany – christina.carstensen@baw.de*
I. Holzwarth *Federal Waterways Engineering and Research Institute (BAW), Wedeler Landstr. 157, 22559 Hamburg, Germany – ingrid.holzwarth@baw.de*
E. Miramontes *MARUM, University of Bremen, Leobener Str. 8, 28359 Bremen, Germany; Faculty of Geosciences, University of Bremen, Klagenfurter Str. 2-4, 28359 Bremen, Germany – emiramon@uni-bremen.de*
A. Lefebvre *MARUM, University of Bremen, Leobener Str. 8, 28359 Bremen, Germany – alefebvre@marum.de*

ABSTRACT: In many estuaries, large bedform fields develop due to the strong hydrodynamics and high availability of sandy sediment. Flow above these bedform fields differs fundamentally from unidirectional flow above well-known angle-of-repose (30° slope) triangular bedforms which until now have been the focus of laboratory and numerical modelling studies. Estuarine bedforms are mainly low-angle dunes, with mean lee slopes of 5 to 20°. Flow properties over such gentle slopes are currently not precisely characterised. To address this, this study aims at characterising flow properties over estuarine bedforms through flume experiments and numerical simulations. A series of experiments will be carried out in a large flume facility at the BAW in Hamburg, Germany and high-resolution numerical simulations of flow over three-dimensional bedform fields will complement the flume experiments.

1 INTRODUCTION

Traditionally, the effect that bedforms have on the flow has been investigated over two-dimensional (2D) bedforms having an angle-of-repose (30°) lee side and a triangular shape. These bedforms are representative of dunes observed in flumes and small rivers. Over such bedforms, the flow separates at the crest and recirculates over the steep lee side. A turbulent wake develops along the shear layer between the separated and overlying flow and dissipates downstream (Kwoll et al., 2016). Such bedform generates a high form roughness which can be several orders of magnitude stronger than the grain roughness (Van Rijn, 1984). Therefore, they constitute a major factor in the calculation and prediction of hydrodynamics and sediment transport. Recently, it has been demonstrated that in large rivers, bedforms are mainly low-angle dunes with an average lee side slope of around 10° (Cisneros et al., 2020). Although river dunes are mainly low-angle, the flow above such low-angle bedforms has until now received little attention. This is also the case for estuarine dunes found at the confluence of river mouth and sea.

Bedforms have been observed in various estuaries around the world. Dalrymple and Rhodes (1995) give a thorough review of the early work related to estuarine bedform dynamics, with a focus on bedforms found in the outer, marine-dominated part of estuaries. In tidal environments, flow reverses from one tidal phase to the next. Therefore, the positions of the stoss and lee sides switch during a tidal cycle. Similar to bedforms

found in large rivers, the shape of tidal bedforms is thought to control flow separation, turbulent wake and, therefore, bedform roughness and sediment transport. Bedforms found in estuarine and tidal environments have been reported to have mean lee sides angles smaller than the angle-of-repose, however, portions of the lee sides as steep as 25-30° suggest that flow separation may happen over restricted portions of the lee slope (Aliotta and Perillo, 1987, Lefebvre et al., 2013). On the contrary to river bedforms, estuarine bedforms have their steepest slope situated close to the crest (Fenster et al., 1990, Dalrymple and Rhodes, 1995, Lefebvre et al., 2021). Until now, bedforms with such a shape have not been systematically studied and it is unknown how flow properties over estuarine bedforms differ to that over river bedforms. Furthermore, estuarine bedforms found in nature are three-dimensional with sinuous crestlines and irregular dimensions. The influence of crestline sinuosity on unidirectional flow has been documented (Maddux et al., 2003, Venditti, 2007, Lefebvre, 2019). However, it has not been specifically investigated yet in tidal environments where flow reversal affects the relation between hydrodynamics and morphology. With this, it is also necessary to characterise the flow properties over natural estuarine bedforms where an effect of flow reversal is expected to occur.

2 OBJECTIVES OF THE STUDY

This study further characterises the flow dynamics above estuarine bedforms. This objective is accomplished with two experimental approaches:

(1) High-resolution measurements of flow above representative estuarine bedforms.

For this, physical experiments will be carried out in the flume at Federal Waterways Engineering and Research Institute (BAW) Hamburg. Each experiment will investigate flow properties (flow velocities, turbulence, turbulence structures) above a set of representative estuarine bedforms, whose shapes were chosen to represent the range of bedform geometries observed in the Weser Estuary.

(2) Numerical simulations of flow properties (mean flow and turbulence) above a natural estuarine bedform field.

Numerical simulations will be carried out over a natural bedform field to complement the flume experiments. The numerical simulations will focus on the effect of three-dimensionality and natural estuarine morphology on tidal flows.

This study is significant for a wide range of fundamental and applied research in shallow and deep water. Most of the knowledge of flow properties has been acquired above simplified angle-of-repose bedforms. This knowledge, however, is likely not transferable to flow properties above natural low to very low angle dunes. The results of this present study can be used to better predict the interaction between bedforms, flow and sediment movement in estuaries.

3 PLANNED EXPERIMENTS

3.1. Flume experiments

Laboratory experiments will be conducted at the facilities of BAW Hamburg. The experimental flume is a recirculating flume consisting of two straight sections connected at their respective ends by a semi-circular area to form a closed recirculating channel. The total length of the flow channel is 220 m in which the above ground channel section has a length of 80 m, width of 1.5 m and a maximum water depth of 1 m. A maximum flow velocity of 1 m/s can be generated in two opposite directions.

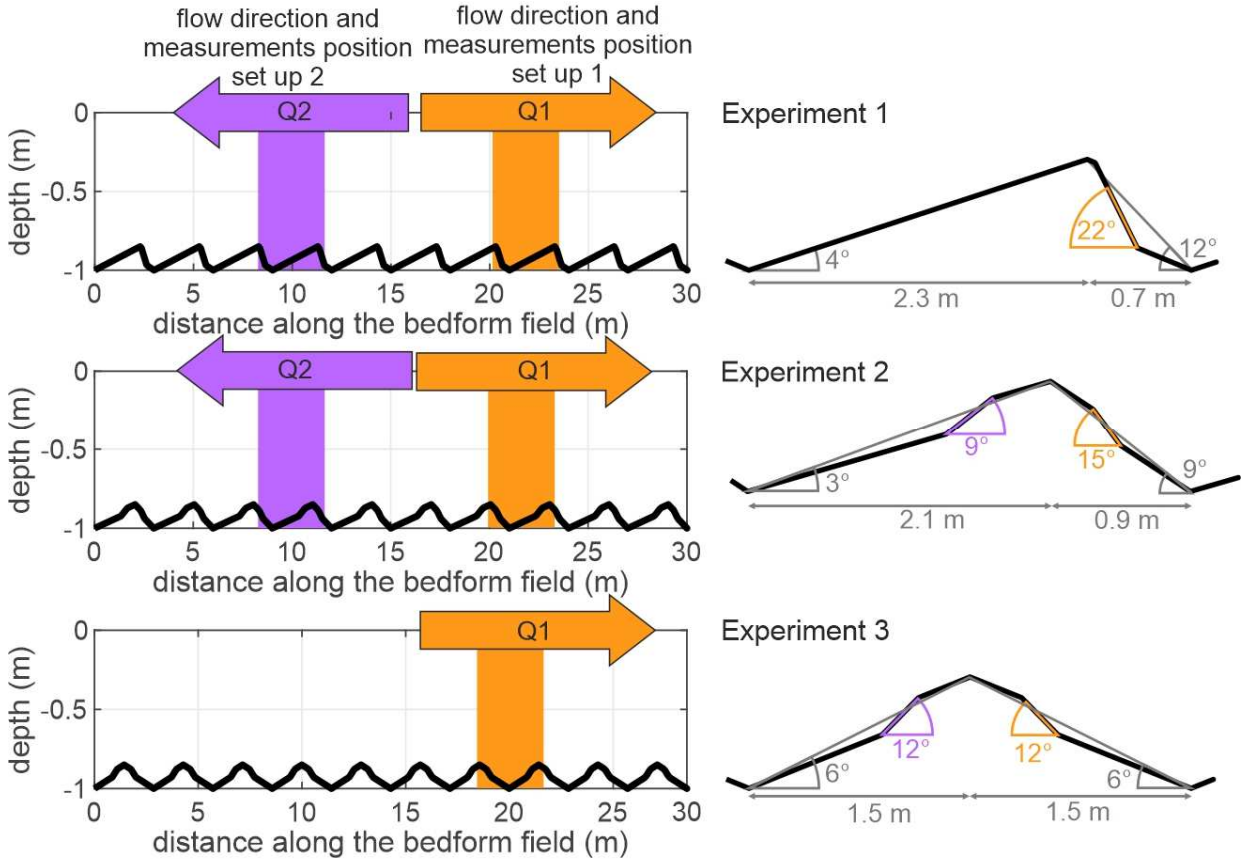

Figure 1. Experimental design of the flume experiments

For all the experiments, a set of 10 prototype bedforms will be installed in the flume to represent a bedform field. The dimensions of the bedforms are based on bedform characteristics as measured from the bathymetry data of the Weser Estuary (Lefebvre et al., 2021). To allow comparison between experiments, mean water depth, bedform length and height are kept constant for all the experiments and only the shape of the bedform is changed. Importantly, the position of the steepest part of the bedform sides will be close to the crest to mimic the shape of a natural estuarine and marine bedform (Figure 1). The dimensions of the bedforms are scaled down by a factor of 15 compared to field measurements.

A high-resolution flow measurement is conducted for all the three experiments using an acoustic device above the 7th bedform (Figure 1) where the flow is already fully adapted to the bedform field. For all three experiments hydrodynamic quantities will be investigated including the mean streamwise and vertical flow velocities to define the zone of permanent flow separation, the turbulent kinetic energy (TKE) to define the turbulent wake, the intermittency factor (IF, percentage of the measured time series at one point occupied by the reversed flow) to define the zone of temporary flow separation and the vertical gradient of the time-averaged streamwise velocity to define the zone of the shear layer.

The novelty of these high-resolution flow measurements compared to previous studies is that the investigated bedform shapes will be representative of estuarine bedforms and not triangular or river bedforms. It will be the first time that flow will be measured in detail over very low angle dunes. A variety of maximum lee side slopes will be investigated (9°, 12°, 15° and 22°). These include the slopes where flow separation is changing from absent to intermittent to permanent. Since the bedforms are relatively large compared to other flume experiments,

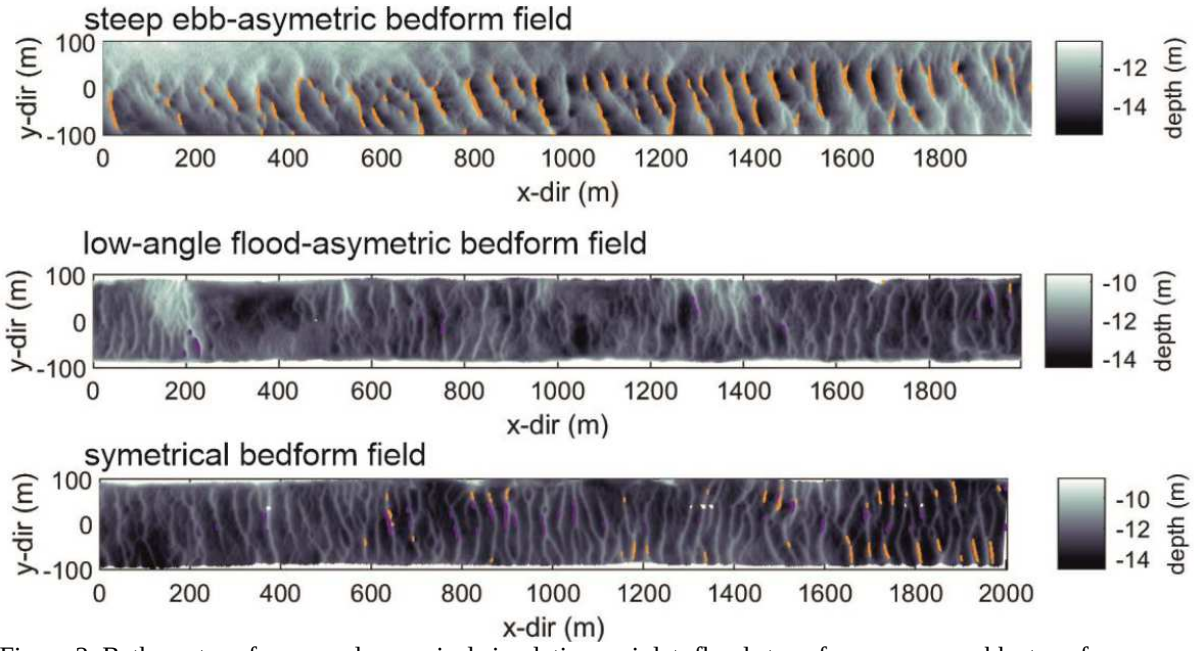

Figure 2. Bathymetry of proposed numerical simulations; violet: flood steep faces, orange: ebb steep faces

measurements can be taken close to bed and even a small flow separation can be detected.

3.2. Numerical modelling

In addition to the flume experiments, numerical modelling will be carried out to address the effects of three dimensionality and bedform sinuosity which are not captured in the prototype bedforms due to scaling issues typically encountered in a physical experiment. The numerical modelling will be done using the DELFT-3D model with bathymetry data based on the Weser Estuary with a grid resolution of 2 m (Lefebvre et al., 2021).

Three straight sections, about 2-3 km long and 200 m wide (Figure 2), will be investigated: (1) bedform field with steep ebb-oriented dunes; (2) bedform field with low-angle flood-oriented dunes; (3) bedform field with symmetrical dunes. These bedform fields were chosen both to represent the variety of bedforms observed in the Weser Estuary and to study similar morphologies already investigated in the flume (i.e., steep asymmetric, asymmetric, and symmetric bedforms in the estuary) to complement the physical experiments.

For each section, two simulations will be carried out, each with the current velocity imposed in opposing direction, in order to model the ebb and flood phases. This setup will allow to investigate the differences and properties of flow separation and turbulence depending on bedform orientation compared to the flow direction.

Numerical outputs at the end of simulation include the horizontal (U, V) and vertical (W) velocities and TKE. As a first step for the numerical analysis, the depth-, streamwise- (U) and cross- (V) averaged flow properties can be examined in order to provide an overview of the effect of the 3D morphology on averaged flow properties. Next, the presence and size of the flow separation zone (i.e. the region in which the flow going upstream is compensated by the flow going downstream), the shear layer (i.e. the steep portion of the mean velocity gradient which shows a change in velocity between the regions within and above the flow separation zone), the turbulent wake (i.e. the zone of high TKE) and the secondary circulation (i.e. the zones with strong crosswise flow velocity) will be investigated. Furthermore, bed shear stress along the bedform fields will allow to investigate the local effects of

bedforms on flow and, thus, predict sediment transport pathways. These quantities will then be compared to the bedform morphology.

Furthermore, the flume experiments will also be used to validate the model over low angle bedforms. For this case, numerical models can be set up at a flume scale and the results of the physical and numerical simulations can then be directly compared.

4 CONCLUSIONS

A detailed high-resolution experimental approach, both physical and numerical, is presented to characterise the flow dynamics over low angle estuarine bedforms. The proposed flume experiments are the first in which flow over very low angle dunes, resembling that of estuarine bedforms, will be measured in detail and in high-resolution owing to the large flume facility at BAW Hamburg.

Furthermore, a high-resolution numerical modelling using the DELFT-3D model is also proposed to complement the results of the flume experiments. Special attention is given to the three-dimensionality of the bedform to better represent the flow properties over bedform typically found in a natural tidal estuary.

This study aims to add to the present knowledge on flow dynamics over estuarine bedform which is, rather, not fully elaborated yet at present. Also, the results of this study may be utilized to better understand the mutual interaction among bedforms, flow and sediment movement in tidal estuary.

5 ACKNOWLEDGEMENT

Kevin Bobiles is supported by the German Research Foundation (Deutsche Forschungsgemeinschaft, DFG), project no. 504378711. Alice Lefebvre is funded through the Cluster of Excellence ‘The Ocean Floor – Earth’s Uncharted Interface’.

6 REFERENCES

Aliotta, S., Perillo, G.M.E., 1987. A sand wave field in the entrance to Bahia Blanca Estuary, Argentina. Marine Geology 76, 1-14. doi: https://doi.org/10.1016/0025-3227(87)90013-2

Cisneros, J., Best, J., Van Dijk, T., De Almeida, R.P., Amsler, M., Boldt, J., Freitas, B., Galeazzi, C., Huizinga, R., Ianniruberto, M., Ma, H.B., Nittrouer. J.A., Oberg, K., Orfeo, O., Parsons, D., Szupiany, R., Wang, P., Zhang, Y.F., 2020. Dunes in the world’s big rivers are characterized by low-angle lee-side slopes and a complex shape. Nature Geoscience 13, 156-+. doi: https://doi.org/10.1038/s41561-019-0511-7

Dalrymple, R.W., Rhodes, R.N., 1995. Chapter 13 Estuarine Dunes and Bars, in Perillo, G.M.E (ed.). Developments in Sedimentology. Elsevier, 359-422

Fenster, M.S., Fitzgerald, D.M., Bohlen, W.F., Lewis, R.S., Baldwin, C.T., 1990. Stability of giant sand waves in eastern Long Island Sound, U.S.A. Marine Geology 91, 207-225. doi: https://doi.org/10.1016/0025-3227(90)90037-K

Kwoll, E., Venditti, J.G., Bradley, R.W., Winter, C., 2016. Flow structure and resistance over subaquaeous high- and low-angle dunes. Journal of Geophysical Research: Earth Surface 121, 545-564. doi: https://doi.org/10.1002/2015JF003637

Lefebvre, A., Herrling, G., Becker, M., Zorndt, A., Kramer, K., Winter, C., 2021. Morphology of estuarine bedforms, Weser Estuary, Germany. Earth Surface Processes and Landforms. doi: https://doi.org/10.1002/esp.5243

Lefebvre, A., 2019. Three-Dimensional Flow Above River Bedforms: Insights from Numerical Modeling of a Natural Dune Field (Rio Parana, Argentina). Journal of Geophysical Research: Earth Surface 124, 2241-2264. doi: https://doi.org/10.1029/2018jf004928

Maddux, T.B., Nelson, J.M., McLean, S.R., 2003. Turbulent flow over three-dimensional dunes: 1. Free surface and flow response. Journal of Geophysical Research: Earth Surface 108. doi: https://doi.org/10.1029/2003JF000017

Van Rijn, L.C., 1984. Sediment transport, Part III: Bed forms and alluvial roughness. Journal of hydraulic engineering 110, 1733-1754.

Venditti, J.G., 2007. Turbulent flow and drag over fixed two- and three- dimensional dunes. Journal of Geophysical Research 112, F04008. doi: https://doi.org/10.1029/2006JF000650

Bedforms and morpho-bathymetric evolution of tributary channels in the Po River delta (Italy)

A. Bosman *Institute of Environmental Geology and Geoengineering (IGAG), National Research Council (CNR), Rome, Italy – alessandro.bosman@cnr.it*
C. Pellegrini *Institute of Marine Sciences (ISMAR), National Research Council (CNR), Bologna, Italy – claudio.pellegrini@cnr.it*
C. Romagnoli *Department of Biological, Geological and Environmental Sciences (BIGEA), University of Bologna, Italy – claudia.romagnoli@unibo.it*

ABSTRACT: Repeated high-resolution multibeam bathymetry surveys were carried out in 2016 in the Po della Pila (North Adriatic Sea, Italy) delta and tributary channels in order to verify the geomorphological features of the riverbed related to morpho-sedimentary processes. The morpho-bathymetric data allowed to observe and map widespread bedforms fields in the alluvial, non-cohesive deposits of the riverbed consisting of dunes with wavelengths ranging from 8 m to 20 m. Repeated bathymetric surveys, carried out after hours and days along the river thalweg, have shown the migration of the bedforms, enabling the estimation of the average rate. We document the rapid geomorphological changes affecting these ephemeral features and the riverbed, also in relation with changes in the average flow discharge rate occurred during the surveys. This was particularly evident after a major flood, when in a few days the riverbed underwent partial reworking and the bedform migration rate was higher.

1 INTRODUCTION

The Po River is the longest river of Italy (673 km) with a medium flow of 1540 m^3/sec and a watershed of 71.000 km^2. It originates in the western Alps and outflows into the North Adriatic Sea (Fig. 1), where microtidal conditions are present. At its mouth, the river splits into five sub-branches. The Po della Pila is the most active branch of the delta, discharging about 61 % of the total flow of the Po and being responsible for the growth of the recent most delta lobe (Bosman et al. 2020). In historical times, the whole Po delta system has been subjected to extensive anthropogenic impacts, mostly due to land use and freshwater management. Since 1950, in fact, the Po delta has undergone a strong degradation and partial retreat, mainly due to the lack of sediment supply caused by the exploitation of inert material in the riverbed and the hydraulic regulation of watercourses, and subsidence due to the extraction of fluids (Stefani et al. 2005). Climatic change impacts are also affecting the Po River, such as marked drought conditions, enhancing the salt intrusion in the delta and fluvial area. In the framework of the RITMARE Project, funded by the Italian Ministry (MIUR), the Po della Pila delta and tributary channels have been the subject of repeated, high-resolution multibeam bathymetric surveys. The main mouth channel of Po della Pila (Busa Dritta) and two smaller channels (Busa di Tramontana and Busa di Scirocco (see Fig. 1) have been surveyed, showing the occurrence of widespread bedforms fields in the non-cohesive deposits of the riverbed. These features have been mapped and analysed from a morphological point of view. Furthermore, the comparison of time-lapsed, high-resolution bathymetric data acquired along the river thalweg some days after the first survey allowed to observe the short-term

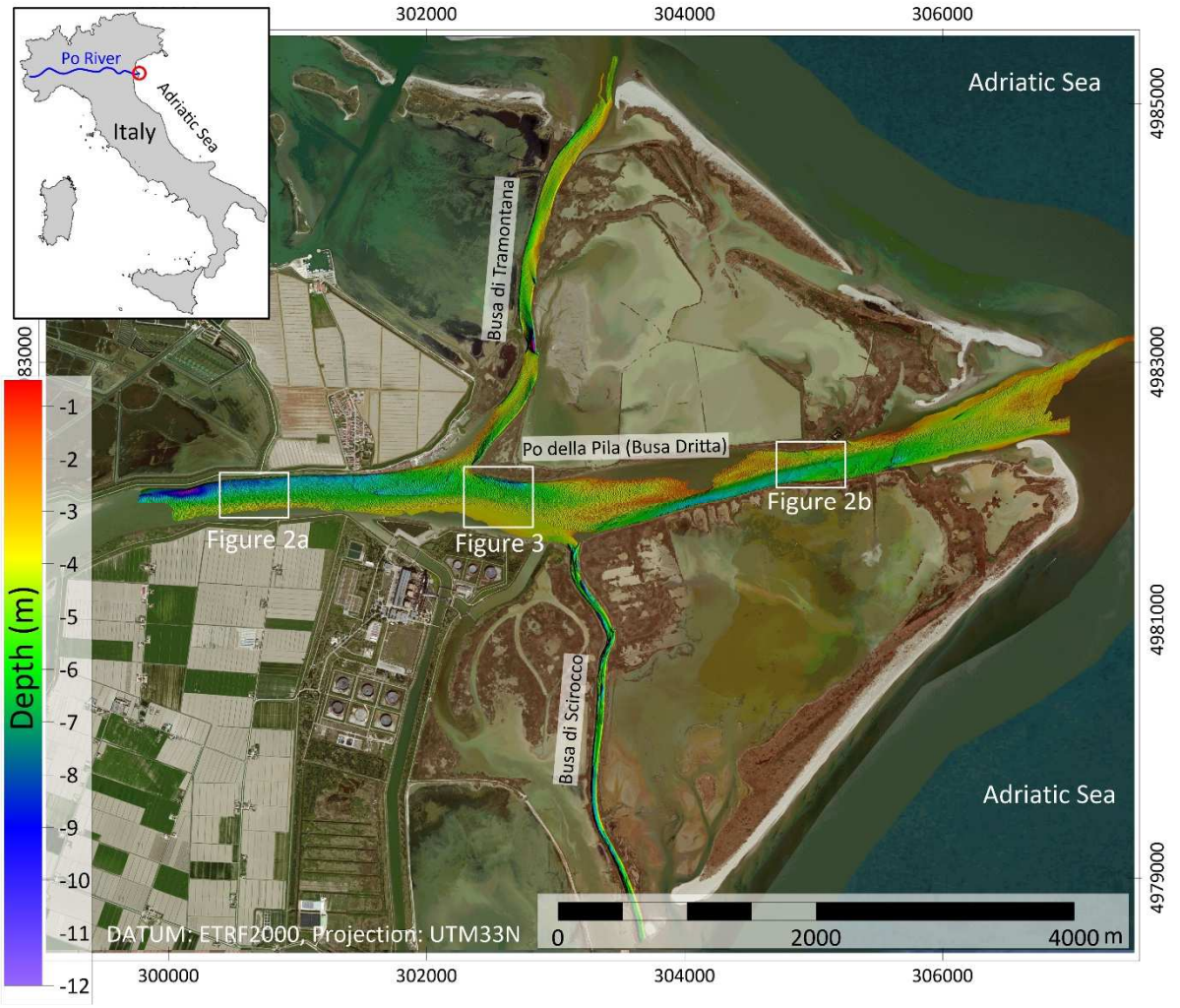

Figure 1. High-resolution Digital Elevation Model of the Po della Pila delta area, investigated by means of multibeam geophysical surveys. The location of the following figures is indicated by boxes. Red circle in the inset indicates the study area.

morphological changes of the bedforms, and to estimate their migration rate at daily scale.

2 DATA AND METHODS

In May 2016, three repeated high-resolution multibeam surveys were carried out along the Po River. High-resolution multibeam data was acquired with a Kongsberg EM2040 single head system, with the frequency that was set to 300 kHz. It was hull-mounted on the vessel 1213 belonging to the Italian Hydrographic Office and allowed a bathymetric coverage between 0.5 m and 7 m water depth. The positioning system was a Kongsberg Seapath 330, corrected with a Fugro HP Differential Global Positioning System (horizontal accuracy: 0.2 m). A Kongsberg Seatex Inertial Motion Reference Unit MRU 5 was used to correct pitch, roll, heave and yaw movements. Sound velocity profiles were collected with a Monitor SVP Valeport sound velocity profiler. For the surveys, a local tidal station belonging to the regional agency of the River Po network was used to measure and correct sea level changes during the surveys (https://www.agenziapo.it/content/monitoraggio-idrografico-0).

All multibeam data were processed using Caris Hips and Sips hydrographic software for bathymetric geophysical correction while QPS-FMGT for backscatter processing and data analysis. During the geophysical survey, a targeted sediment sampling was also carried out by means of a Van Veen grab, and grain-size analyses were obtained with a laser granulometer Malvern Mastersizer 3000.

3 MORPHOMETRY AND BACKSCATTER DATA ANALYSIS

The Po della Pila riverbed is characterized by a shallow depth (mostly within a few metres) and a mainly sub-flat morphology, with local depressions where the depth is locally > 10 m (Fig. 1).

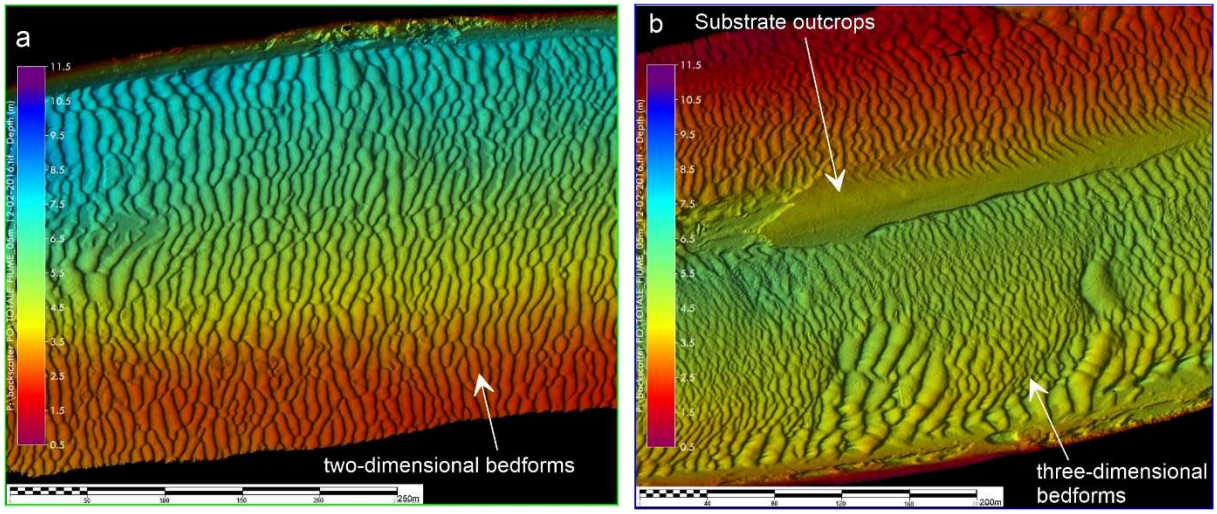

Figure 2. High-resolution Digital Elevation Model of the Busa Dritta tributary channel, showing a uniform distribution of bedforms along the thalweg (a). The bedforms are generally two-dimensional with elongated crests and rarely have three-dimensional shape (b) in correspondence with hydraulic narrowing and deepening of the channel. See Figure 1 for location.

In the studied area, the Busa Dritta channel has a width between 240 and 450 m and a depth between about 1 and 10 m, gradually increasing towards the northern side, on the hydrographical left (Fig. 2a) or towards the southern side on the hydrographical right (Fig. 2b) closer to the river mouth. The thalweg is entirely characterized by bedforms (Fig. 2), apart from locally depressed areas where the substrate crops out (Fig. 2b). The bedforms have different wavelengths, ranging from a minimum of 8 m to a maximum of 20 m, with an average value of about 10 m. They are asymmetrical in cross-section, with a slope of about 3°-5° upstream (stoss side) and of 15°-20° downstream (lee side). The height of the bedforms is approximately constant and ranges from 0.2 m to 0.5 m. The bedform shape is usually two-dimensional (Fig. 2a) with mostly linear or slightly sinuous crests, aligned perpendicular to the slight slope gradient of the river bed (Fig. 1), and transversal with respect to the flow direction. They rarely have three-dimensional shape (Lefebvre, 2019) and locally show a crescentic shape in correspondence with hydraulic narrowing and deepening of the channel (Fig. 2b). Considering their size, these bedforms can be classified as river dunes (Bosman & Orlando 2017).

Backscatter data, recorded through the multibeam survey (Fig. 3a), show that the bedforms crests are overall characterized by medium-low intensity values, while the deepest part of the troughs show higher values. These differences might be explained in terms of sediment texture.

4 SAMPLES

Grain size analyses of samples collected in 2016 on lower- and higher- backscatter areas, supported the interpretation of backscatter intensity as mostly related to the grain size of the sediment lying on the seabed. In particular, sample BF1 (location in Fig. 3a) collected at 3.8 m water depth in a sector with well-developed bedforms, in correspondence of

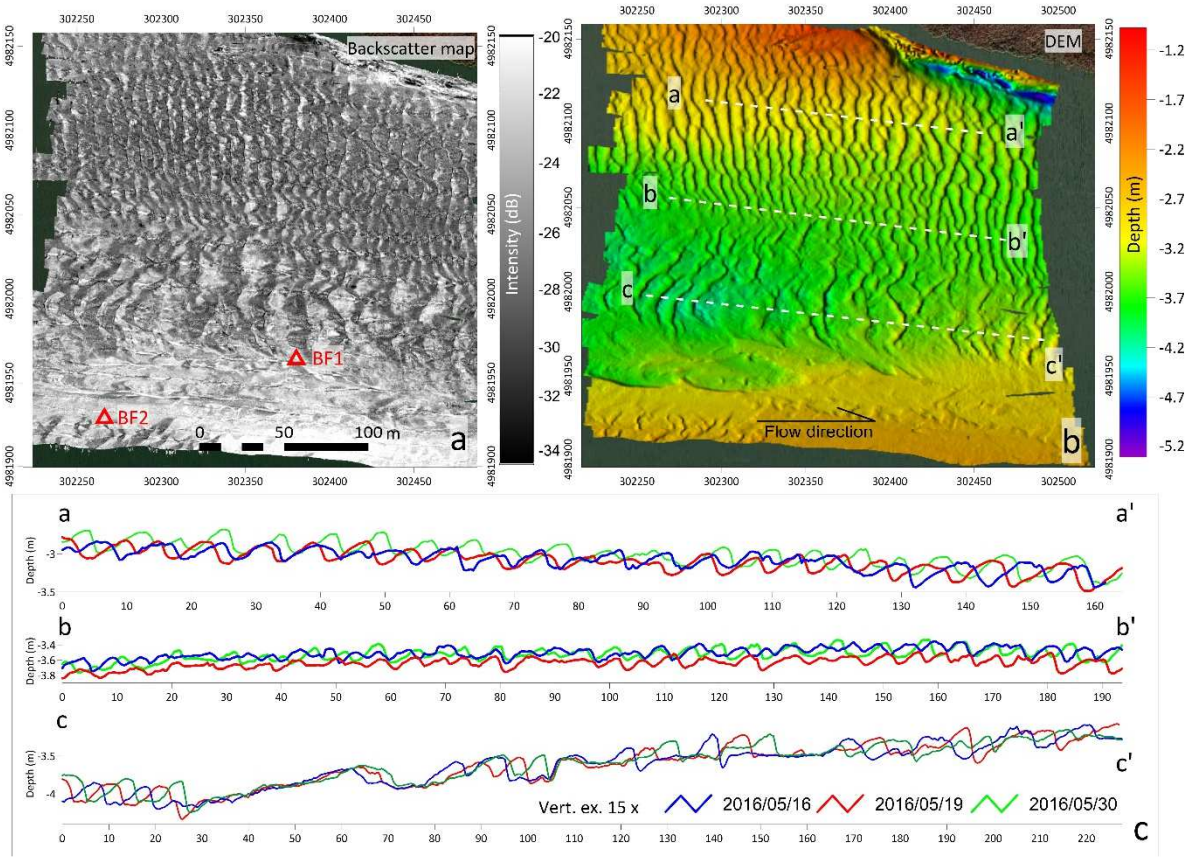

Figure 3. Comparison between bathymetry (b) and backscatter intensity data (a) in the monitored area. See Figure 1 for location. a) The backscatter intensity shows a clear zonation, in relation with the sediment texture: medium-low backscatter areas correspond to the dunes' crest, while higher backscatter indicates coarse sediments located in the trough. Red triangles indicate the location of the sampling sites c) Bathymetric sections (see location in a) show the migration of the dunes, 3 and 14 days (red and green profiles, respectively) after the first survey of May 16 (blue profile).

higher backscatter intensity (values from -23 dB and -26 dB; light grey on the map), resulted to be a muddy sand, mostly composed of fine sand (59.3%) with a muddy fraction of 40.7%). Conversely, sample BF2 (location in Fig. 2a) collected at 3.4 m depth from a smoother area of the channel seabed, slightly raised with respect to the channel thalweg and characterized by slightly lower backscatter intensity (values from -27 dB to -30 dB; dark grey tones on time lapse analysis the map) resulted composed by finer-grained sediment, i.e. sandy mud. In detail, mostly muddy sediment (mud 71%) with lower percentage of sand (29%) was sampled at the river bed lying above a sandier substrate (sand 45.3%, mud 54.7%).

5 TIME-LAPSE ANALYSIS

The possibility of collecting repeated high-resolution bathymetric data in the same river bed area of about 260 x 300 m, allowed to characterize the bedforms dynamic. The multibeam data were collected with the same operating procedures on three different days, on the 16th, 19th and 30th of the May 2016. The data recorded 3 and 14 days after the first survey show a significant mobility of bedforms, likely in response to different conditions of hydraulic regime. Bathymetric sections illustrated in figure 3 C show, in fact, how the dunes have a strong mobility along the entire investigated area, both in the central part of the riverbed (section b-b') and near the

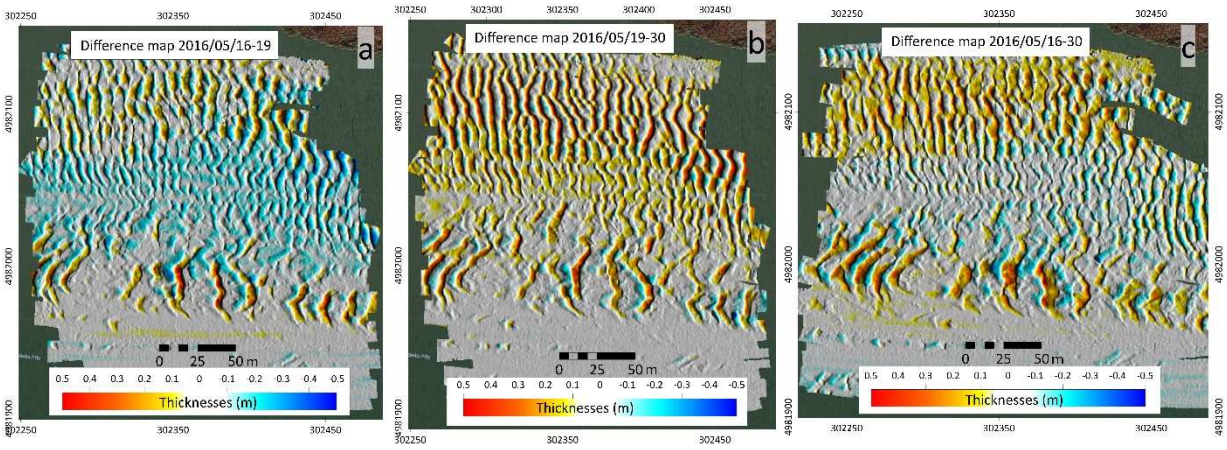

Figure 4. Difference maps between the bathymetric surveys conducted 3, 11 and 14 days after the first survey (a, b and c, respectively). The maps show differences in the seabed up to tens of centimetres, mostly due to the dune migration. A generalized lowering of the riverbed in the central part (section b-b' in Figure 3c) is visible between the first and second survey (map a), while an overall accumulation occurs between the second and the third (map b).

natural banks (sections a-a' and c-c'). The dunes migrate differently along bathymetric sections (Fig. 3c).

Bathymetric residues (difference maps in Fig. 4) obtained as the difference among the Digital Elevation Models (DEMs) collected during three days of the survey, show a meter-scale migration of the dunes throughout the investigated section.

The difference between the DEMs relating to the days of May, 16 and 19 (3 days of difference) show a variable migration of the dune crests between 2 m and 4 m, which corresponds to an estimated average velocity of 4 cm per hour. The difference between the DEMs of May 19 and May 30 (11 days of difference) shows, instead, a variable migration from 4 m to 5.5 m which corresponds to about 2 cm per hour. These values, although averaged on different time spans, suggest a slower rate in the dune migration after May 19, as river discharge reach value < 2000 m^3/sec. Finally, using the difference between DEMs collected in the first (May 16) and the last day of the survey (May 30), an average velocity of about 1.5 cm per hour can be obtained. These differences are attributable to the different hydraulic regime occurring during the bathymetric surveys.

By considering the average flow discharge and the hydrometric level recorded on the Po River at the Pontelagoscuro station (blue line and red line, respectively in Fig. 5) a river flood event is recognizable on 2016/05/16. The flow discharge amount changed, in fact, from about 2792 m3/sec on May 16 to 1793 m^3/sec on May 19, while after this date a markedly lower flow discharge (gradually decreasing to about 1200 m^3/sec) was measured. Similarly, the hydrometric level shows a difference of about 3 m between May 16 and May 19 (Fig. 5). The effects of this major flood event are also recognizable on morphologies: between the first and second surveys (May, 16-19) the central part of the riverbed underwent a marked reworking and lowering of some tens of cm (Figs. 4a, 3c section b-b').

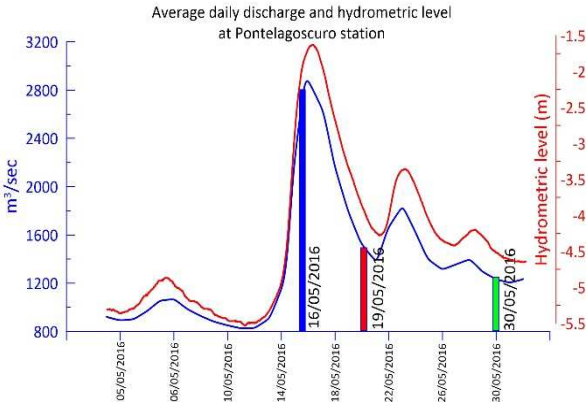

Figure 5. Average discharge and hydrometric level at Pontelagoscuro station located on the final tract of the Po River (from Arpae Emilia Romagna https://simc.arpae.it/dext3r/). Colored bars correspond to the dates of the high-resolution multibeam bathymetry surveys.

6 DISCUSSION & CONCLUSIONS

Bedforms in fluvial and marine environments are commonly considered as cyclic depositional and erosional features formed during bedload transport processes, being controlled by flow velocity, grain size and water depth (Yang et al. 2022 and references therein). Widespread bedform fields have been observed in the riverbed of the Po della Pila, the most active branch of the Po delta. Their shape is similar to that of typical bedforms of river environments (Nittrouer et al. 2008; Bosman et al. 2017) with wavelengths ranging from 8 m to 20 m and heights of a few decimetres. The different intensity of backscattering also appeared to be related to the sediment texture, as also confirmed by the results of grain size analyses. High-resolution multibeam bathymetric monitoring allowed to understand bedforms dynamic at time span of a few days, that strongly derive from the hydrological conditions of the river. Therefore, they are not relict bedforms, but active dunes with variable migration rate, according to the discharge of the river with mobility of a few centimeters (2-4 cm) per hour. Nevertheless, their morphological variations and mobility support the occurrence of a solid transport (bed load) towards the river mouth, capable of feeding the submerged lobe of Po della Pila (Bosman et al. 2020; Trincardi et al., 2020). Despite the Po delta is presently affected by a marked degradation, mostly due to the reduction in sediment transport for anthropogenic and natural (climatic) factors (Stefani et al. 2005), local progradation in response to main flooding events has been recently claimed for the northern portion of the Po della Pila on the base of satellite images (Ninfo et al. 2018) and marine surveys (Bosman et al. 2020). More frequent bedload measurements are requested to better quantify the solid transport in the Po River bed. It is undoubtedly necessary to repeat bathymetric surveys at least annually, to verify the evolutionary state of the submerged sectors (erosion/deposition) of the river and of the delta area, since monitoring only based on remote sensing techniques is insufficient to understand the complex physical processes acting on a fragile and vulnerable of the Po della Pila system.

7 ACKNOWLEDGMENTS

The data used in this study were collected aboard the boat 1213 of the Italian Hydrographic Office and we would like to thank the captains, crews and participants of the oceanographic cruises. We also acknowledge the Venice University for supporting the grain size analyses. Research surveys and part of the scientific equipment were funded by the National Ritmare Project (La Ricerca ITaliana per il MARE).

8 REFERENCES

Bosman, A., Romagnoli, C., Madricardo, F., Correggiari, A., Fogarin, S., Trincardi, F., 2020. Short-term evolution of Po della Pila delta lobe from high-resolution multibeam bathymetry (2013-2016). Estuarine, Coastal and Shelf Science 233, 106533.https://doi.org/10.1016/j.ecss.2019.106533

Bosman, A., & Orlando, L., 2017. Bedforms on the Lowermost Reach of the Tiber River (Rome, Italy): Preliminary Results from Integrated Geophysical Surveys and Samplings. Atlas of Bedforms in the Western Mediterranean. doi:10.1007/978-3-319-33940-5_16

Lefebvre, A., 2019. Three-dimensional flow above river bedforms: Insights from numerical modeling of a natural dune field (Río Paraná, Argentina). Journal of Geophysical Research: Earth Surface, 124, 2241–2264. doi. org/10.1029/2018JF004928

Yang, Y., Liu, M., Xu, J., and Xu, W., 2022. Migrating sandwaves riding on relict dunes of Taiwan shoal, northern South China Sea. Front. Earth Sci. 10:975220. doi: 10.3389/feart.2022.975220

Nittrouer, J.A., Allison, M.A., and Campanella, R., 2008. Bedform transport rates for the lowermost Mississippi River. Journal of Geophysical Research, VOL. 113, F03004, doi:10.1029/2007JF000795

Ninfo, A., Ciavola, P., & Billi, P., 2018. The Po Delta is restarting progradation: geomorphological evolution based on a 47-years Earth Observation dataset. Sci Rep 8, 3457 -2018. doi.org/10.1038/s41598-018-21928-3

Stefani, M., & Vincenzi, S., 2005. The interplay of eustasy climate and human activity in the late Quaternary depositional evolution and sedimentary architecture of Po Delta system. Mar. Geol., 22-2232-, V-VI, 19-48

Trincardi, F., Amorosi, F., Bosman, A., Correggiari, A., Madricardo, F., Pellegrini, C., 2020. Ephemeral rollover points and clinothem evolution in the

modern Po Delta based on repeated bathymetric surveys. Basin Research. doi.org/10.1111/bre.12426

Crescent-shaped bedforms on submarine volcanic flanks: the case of Salina (Aeolian Islands, Italy)

D. Casalbore *Department of Earth Sciences, Sapienza University of Rome, Italy; Institute of Environmental Geology and Geoengineering, National Research Council, Rome, Italy – daniele.casalbore@uniroma1.it.*
A. Bosman *Institute of Environmental Geology and Geoengineering, National Research Council, Rome, Italy – alessandro.bosman@cnr.it*
C. Romagnoli *Department of Biological, Geological and Environmental Sciences, University of Bologna, Italy; Institute of Environmental Geology and Geoengineering, National Research Council, Rome, Italy – claudia.romagnoli@unibo.it*
F.L. Chiocci *Department of Earth Sciences, Sapienza University of Rome, Italy; Institute of Environmental Geology and Geoengineering, National Research Council, Rome, Italy – francesco.chiocci@uniroma1.it*

ABSTRACT: Salina is the highest island of the Aeolian Archipelago, representing the upper part of a large submarine stratovolcano. The submarine eastern flank of Salina is morphologically dominated by different bedforms fields located between ~50 and ~600 m water depths. Bedforms have wavelengths ranging from some tens to few hundreds of meters and wave heights of some meters at maximum. Their crestlines are roughly parallel to the isobaths, with sinuous to arcuate/crescentic shape in plan-view, while their cross-sections are commonly asymmetric downslope, with short and steep lee sides. Bedform size tend to increase with water depth, especially in correspondence of marked break-in-slopes or within wider channels developed at the base of the edifice. Based on their similarities in size and geometry with bedforms found in other submarine volcaniclastic systems, canyons and fan-deltas, these features have been interpreted as migrating cyclic steps.

1 INTRODUCTION

In the last few decades, extensive seafloor mapping studies performed on the submarine portions of insular volcanoes and seamounts have exponentially increased our knowledge on the geological processes shaping their flanks. However, most of these studies mainly focused on the characterization of large-scale geomorphic features associated with sector collapses or caldera eruptions (e.g., Mitchell et al. 2002; Wright & Gamble 1999), often overlooking smaller-scale features associated with more frequent mass-wasting processes. This bias is also due to the rapid decrease in resolution with depth of hull-mounted multibeam systems as well as to the paucity of shallow-water surveys around volcanic islands (Casalbore et al. 2021 and reference therein). Seafloor mapping of shallow-water areas is, in fact, a time-consuming and expensive task because of the limited lateral coverage of multibeam swath in the first hundreds of meters. On the other hand, the available studies in shallow-waters areas (also through time-lapse surveys) have evidenced widespread small-scale landslide scars, erosive channels and bedform fields, indicating a highly dynamic environment in terms of mass-wasting processes and associated sedimentary gravity flows (e.g., Babonneau et al. 2013, Clare et al 2018; Casalbore et al. 2020, 2021 and reference therein).

In this study, we describe and discuss the main features of small-scale bedforms fields recently identified along the eastern submarine flank of Salina Island (Aeolian archipelago) between few tens of meters down to over 400 m water depths (Casalbore

et al. 2016, 2021). The analysis is based on high-resolution multibeam bathymetries, integrated by seafloor grabs, collected during the 2010 "EOLARC" and 2013 "Thygraf" cruises onboard the R/V Urania (National Research Council).

2 STUDY SITE

Salina is the highest island of the Aeolian archipelago, reaching a maximum elevation of 962 m above sea level (asl, herafter) at Monte Fossa delle Felci (MFF in Fig. 1).

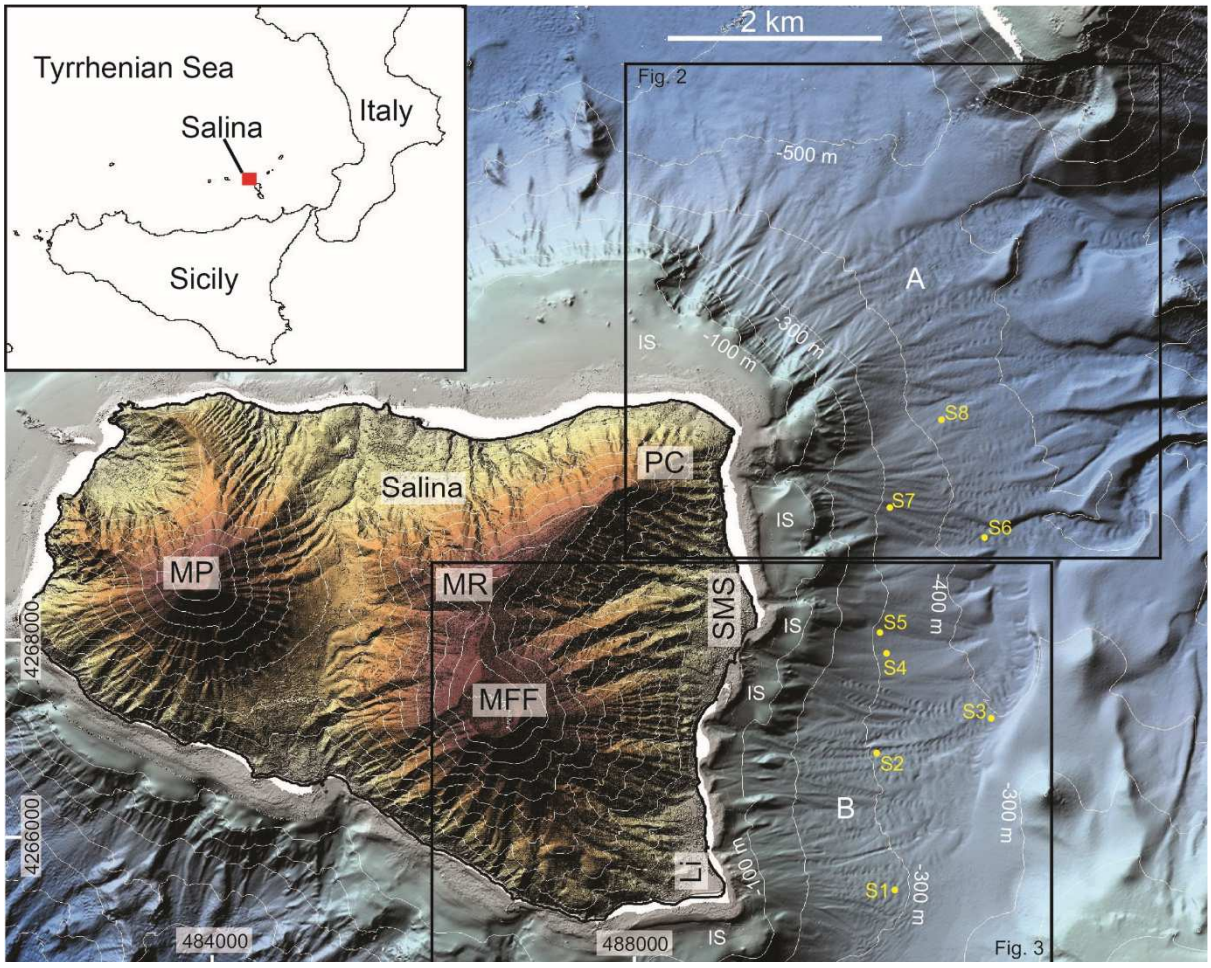

Figure 1 Shaded relief map (artificial light from NW) and contour lines (equidistance of 100 m) of Salina Island and its eastern and north-eastern submarine flanks, with the location of the described features and seafloor grabs (S1-S8, see also Table 1). MP: Monte dei Porri, MFF: Monte Fossa delle Felci, MR: Monte Rivi, PC: Pizzo Capo, SMS: Santa Marina Salina, Li: Lingua; IS: insular shelf. Coordinates are in UTM WGS84 33N.

The island is the tip (~16% as surface) of a large submarine volcanic edifice, extending down to 1300 m water depth (Casalbore et al. 2016). Together with Lipari and Volcano, Salina is part of an NNW-SSE elongated volcanic belt linked with the offshore continuation of the regional "Tindari-Letojanni" strike-slip fault system (Ventura, 2013). The subaerial volcanic activity of Salina spans between ~244 and 15.6 ka, displaying an overall E-W migration of active vents through time (Lucchi et al. 2013). The NE part of Salina is mostly characterized by basaltic lava flows and strombolian scoriae belonging to the Pizzo Capo composite volcano (~244-226 ka, PC in Fig. 1). South of Pizzo Capo, basaltic to dacitic pyroclastic successions and lava flows, emplaced between 160-121 ka, formed the eastern flank of Monte Rivi (MR) and Monte Fossa delle Felci stratocones. Three orders of raised marine terraces, located at 50, 25-30 and 10-12 m asl and attributed to the Last Interglacial peaks,

cut the lower part of the early stratocones, witnessing a general uplift since (at least) 124 ka, with average rates of 0.35 m/ka (Lucchi et al. 2019 and reference therein).

The NE coastal area is generally characterized by steep and up to 65-m high sea cliffs, engraved on a thick succession of strombolian scoriae around Pizzo Capo (Romagnoli et al. 2018). Differently, sea cliffs are markedly lower (< 26 m) or totally absent along the eastern flank of Monte Fossa delle Felci. This volcanic flank is largely carved by a network of narrow and steep subaerial creeks, locally forming thick epiclastic slope fans at its foot, where Santa Marina Salina and Lingua small villages are built (SMS and Li in Fig. 1).

The submarine morphology of the eastern Salina flank is characterized by a narrow insular shelf (around Pizzo Capo, Fig. 1) being almost absent on the eastern flank of Monte Fossa delle Felci) (Romagnoli et al. 2018). A network of submarine erosive channels indents the shelf edge at variable depths: a) around 80-100 m wd in the NE part (Pizzo Capo), where the shelf is larger and better preserved, b) up to 5-10 m wd in the SE sector, where the shelf is almost absent or dismantled (Casalbore et al. 2016).

3 RESULTS

Morpho-bathymetric data allow us to recognize two main areas (A and B in Fig. 1) characterized by bedforms fields located on the submarine flanks of the Pizzo Capo and Monte Fossa delle Felci stratocones, respectively (Fig. 1).

In area A, coaxial trains of arcuate or crescent-shaped bedforms are recognized at depths higher than 320 m, down to over 600 m (Fig. 2). They commonly start as narrow (50-150 m wide) and shallow (a few meters deep) channelized features that erode an overall convex-downward morphology related to the presence of one or more (coalescent) fan-shaped deposits. These deposits are, in turn, associated upslope with erosive channels that mainly indent the insular shelf edge around 80-100 m wd, (locally up to 15-25 m wd). The recognized bedforms have wavelengths of ~20-150 m and wave heights of ~0.5-5 m; their wave parameters generally increase downslope, especially when the narrow channels merge within wider and flat-bottomed, more sinuous channels. The latter develop at the base of the submarine flank, in correspondence of a marked decrease of slope gradients from 7°-8° to value less than 4°. In cross-section, bedforms are generally symmetric or (mostly) downslope asymmetric, with a gently sloping stoss side followed by a shorter and steeper lee side. In area A, three grabs (Table 1) recovered sandy sediments (S6 and S7 in Fig. 1) or silty sand (S8).

In area B, bedforms are present from ~45 to ~430 m wd, displaying a larger variability in size and plan-view shapes (Fig. 3). Shallower bedforms start as isolated coaxial trains in the first 150-200 m wd, forming narrow channelized features within the main erosive channels that carve the steep (> 10°) volcanic flank from shallow-water (up to 5-10 m wd). These bedforms are mostly arcuate or crescent-shaped in plan-view and downslope asymmetric in cross-section; they have wavelengths of few tens of meters and wave heights < 1 m. At greater depths, bedforms are widespread and commonly tend to increase their wave parameters downslope. The maximum concentration of bedforms is observed-between 150-200 m and 300-340 m wd, where they display sinuous or arcuate/crescentic shape in plan-view. The sinuous bedforms are mainly associated with the development of fan-shaped deposits at the foot of erosive channels, in correspondence of an abrupt decrease of slope gradients to values less than 6°-8°. Differently, arcuate or crescent-shaped bedforms are commonly related to narrow and erosive channelized features superimposed on the fan-shaped deposits (Fig. 3). At depths greater than 300-340 m wd, the coaxial trains of bedforms merge downslope within a wider and flat-bottomed channel running at the base of the volcanic flank. Here, bedforms are arcuate or crescent-shaped in plan-view, reaching wave lengths of ~200 m and wave heigh of ~6 m; their lateral extent largely increase, extending on almost all the channel's width. In the area

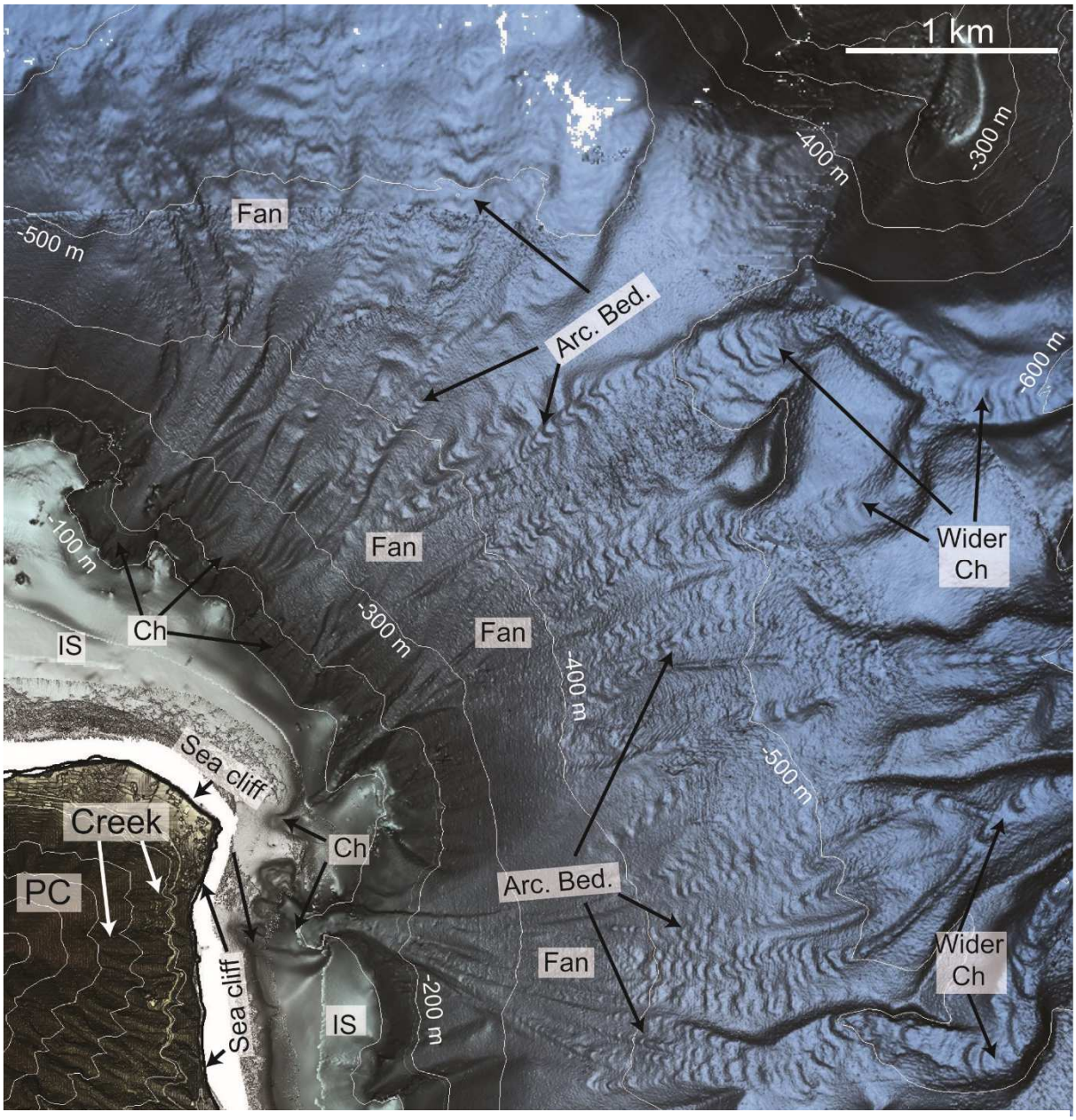

Figure 2 Shaded relief map (azimuthal artificial light) and contour lines (equidistance of 100 m) of area A (location in Fig. 1) in front of Pizzo Capo (PC), where minor creeks hanging on steep and high sea cliffs are present. In the facing marine area, the insular shelf (IS) is indented by channels (Ch), passing downslope to fan-shaped features and wider channels, locally characterized by coaxial trains of arcuate bedforms indicated by arrows (Arc. Bed.).

B, five grabs recovered sandy sediment, with variable percentage of silty or gravelly component (S1 to S5 in Fig. 1 and Table 1).

4 DISCUSSION AND CONCLUSIONS

The previous morpho-bathymetric analysis has shown how small-scale bedforms are widespread on the submarine E flank of Salina. Similar features were also observed on the northern submarine flank of Salina (Casalbore et al., 2021). They can be related to extensive mass-wasting processes and associated sedimentary gravity flows affecting the area, as testified by their linking with erosive channels and fan-shaped deposits. These features witness an efficient transport of volcaniclastic sediment (mostly

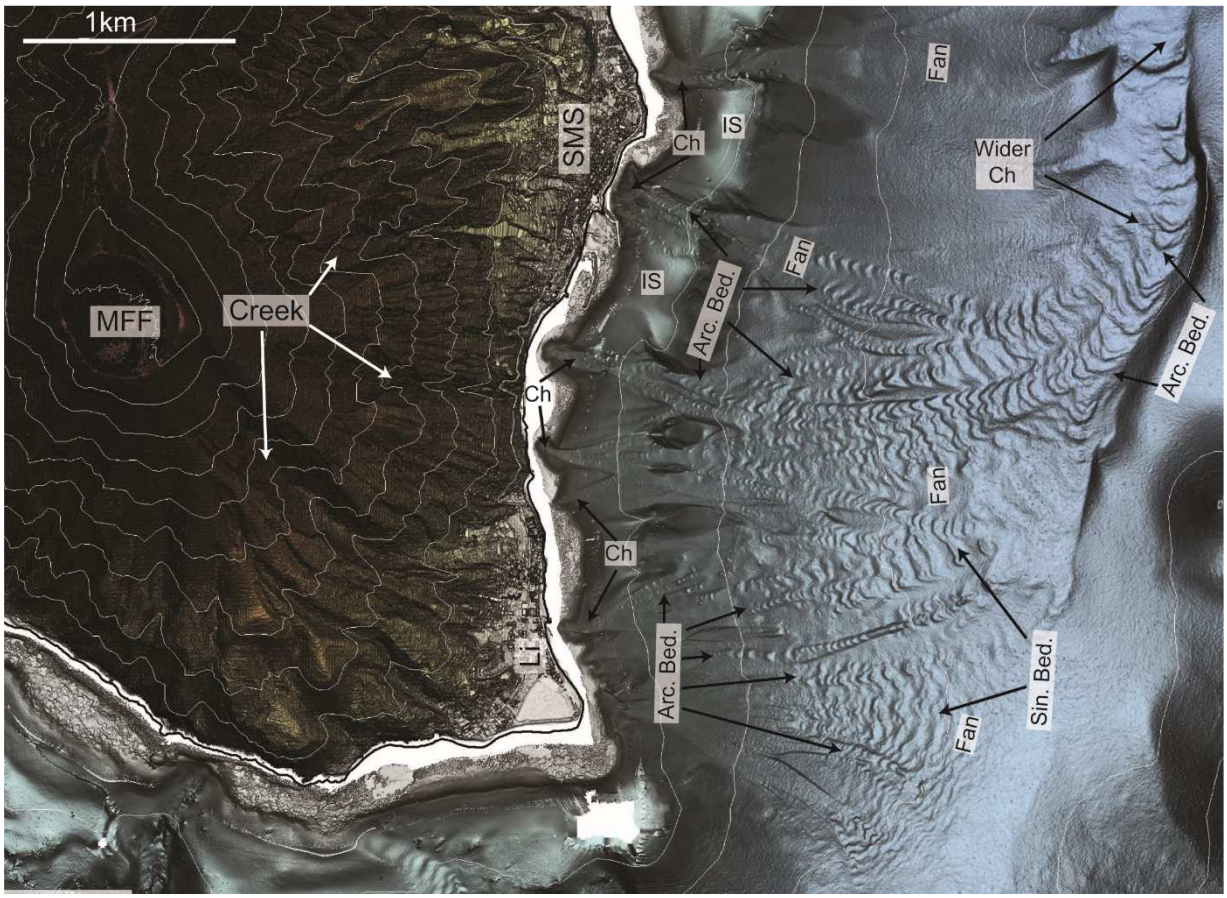

Figure 3 Shaded relief map (azimuthal artificial light) and contour lines (equidistance of 100 m) of area B (location in Fig. 1) along the eastern flank of Monte Fossa delle Felci (MFF), largely carved by a network of steep creeks, locally forming detrital cones at the coast. In the facing marine area, the narrow or totally absent insular shelf (IS)is indented by erosive channels (Ch) , passing downslope to fan-shaped features and wider channels. Both features are characterized by the occurrence of arcuate and sinuous bedforms (Arc. and Sin. Bed., respectively).

sandy) along the submarine flanks, where pyroclastic units crop out.

The observed bedforms share similarities in size and geometry with those recognized within active canyons and fan-deltas in continental margins (e.g., Hughes-Clarke 2016) and other submarine volcanic settings (Casalbore et al. 2021), so they are similarly interpreted as upper-flow regime bedforms due to turbidity currents. Based on their different morphology and location, the arcuate or crescent-shaped bedforms found within channelized features may be tentatively interpreted as transportation or net-erosional cyclic steps, while the sinuous bedforms recognized on fan-shaped features as net-depositional cyclic steps, according to the recent aggradation-based classification of Slootman & Cartigny (2020). However, we are aware that seismic profiles able to image the inner geometry of the bedforms, coupled with more extensive seafloor sampling, should be required to better support such morphology-based inferences. Data also show a strong relationship between the development, change in size and/or geometry of the bedforms and marked variations in slope gradients along the submarine flank. These, in fact, can favour the development of hydraulic jumps in the sedimentary gravity flow, or locally change its parameters (e.g., Postma et al. 2009; Slootman & Cartigny 2020).

A further point of discussion deals with the different distribution of the bedforms in the two areas A and B, which can be related to a complex interplay between marine erosional retrogressive processes and the subaerial dismantling of pyroclastic materials from the

Sample	% gravel	%sand	% silt	% clay
S1	0,05	72,98	18,86	8,11
S2	8,6	85,01	4,80	1,59
S3	0,21	94,32	4,15	1,32
S4	1,07	55,62	30,41	12,9
S5	16,91	57,54	17,68	7,87
S6	0,8	89,26	7,15	2,79
S7	18,75	78,71	1,93	0,61
S8	0,1	39,23	42,38	18,29

Table 1 shows the percentages of gravel, sand, silt and clay in the recovered samples (location in Fig. 1)

E flank of the island through a network of narrow and steep creeks. In the NE area, where the shelf is wider and the few subaerial creeks hang above the high coastal cliffs, bedforms are mostly limited at greater depths and their formation is less directly linked to subaerial processes. They could be instead more likely associated with small-scale slope failures affecting the shelf edge. Alternatively, the formation of these bedforms could be related to past conditions, when the sea-level was lower than at present. Differently, along the E flank of Monte Fossa delle Felci, the morphological link between the subaerial and submarine drainage network is more evident and favored by the very limited extension (or lacking) of the insular shelf, the presence of lower sea cliffs or coastal detrital slope fans. Narrow and steep creeks are commonly considered prone to the development of hyperpycnal flows, especially in the case of sudden and heavy rains which may occur in the semi-arid climate characterizing Southern Italy (Sabato & Tropeano 2004). In addition, it should be considered that most of the submarine channel heads are located at 5-10 meters wd, so they can both intercept the longshore drift and/or be affected by storm-wave loading, thus increasing the probability of small-scale failures in coastal deposits.

In summary, the present study shows how the steep and uneven flanks of insular stratovolcanoes are very prone to the development of upper-flow regime bedforms. Particularly, those observed on the E flank of Salina show an impressive variability in size, plan-view geometry and cross-section at small spatial scale and can be considered a natural laboratory for identifying the main factors controlling the formation and development of small-scale bedforms.

5 ACKNOWLEDGEMENT

Multibeam bathymetry was collected in the framework of the Italian MaGIC (Marine Geohazards along the Italian Coasts) Project. We would like to acknowledge crews of R/V Urania (CNR) together with the researchers and students that have took part to the oceanographic cruises. We acknowledge Ministero dell'Ambiente e della Tutela del Territorio e del Mare-Geoportale Nazionale with license Creative Commons 3.0 Italy (CC BY-SA-3.0IT) for providing the terrestrial LIDAR data. Research activities of Daniele Casalbore were also supported by funding provided by the "Progetto di Ateneo 2021", Sapienza University of Rome.

6 REFERENCES

Babonneau, N., Delacourt, C., Cancouët, R., Sisavath, E., Bachèlery, P., Mazuel, A., …& Villeneuve, N., 2013. Direct sediment transfer from land to deep-sea: insights into shallow multibeam bathymetry at La Réunion Island. Marine Geology 346, 47-57.

Casalbore, D., Bosman, A., Romagnoli, C., & Chiocci, F. L., 2016. Morphology of Salina offshore (southern Tyrrhenian sea). Journal of Maps 12(5), 725-730.

Casalbore, D., Passeri, F., Tommasi, P., Verrucci, L., Bosman, A., Romagnoli, C., & Chiocci, F. L., 2020. Small-scale slope instability on the submarine flanks of insular volcanoes: The case-study of the Sciara del Fuoco slope (Stromboli). International Journal of Earth Sciences 109(8), 2643-2658.

Casalbore, D., Clare, M. A., Pope, E. L., Quartau, R., Bosman, A., Chiocci, F. L., …& Santos, R., 2021. Bedforms on the submarine flanks of insular volcanoes: new insights gained from high resolution seafloor surveys. Sedimentology 68(4), 1400-1438.

Clare, M. A., Le Bas, T., Price, D. M., Hunt, J. E., Sear, D., Cartigny, M. J., ... & Cronin, S. 2018. Complex and cascading triggering of submarine landslides and turbidity currents at volcanic islands revealed from integration of high-resolution onshore and offshore surveys. Frontiers in Earth Science 6, 223.

Hughes Clarke, J. E. 2016. First wide-angle view of channelized turbidity currents links migrating cyclic steps to flow characteristics. Nature communications 7(1), 1-13.

Lucchi, F., Gertisser, R., Keller, J., Forni, F., De Astis, G., & Tranne, C. A., 2013. Eruptive history and magmatic evolution of the island of Salina (central Aeolian archipelago). Geological Society, London, Memoirs 37(1), 155-211.

Lucchi, F., Ricchi, A., Romagnoli, C., Casalbore, D., & Quartau, R., 2019. Late Quaternary paleo sea level geomorphological markers of opposite vertical movements at Salina volcanic island (Aeolian Arc). Earth Surface Processes and Landforms 44(12), 2377-2395.

Mitchell, N. C., Masson, D. G., Watts, A. B., Gee, M. J., & Urgeles, R., 2002. The morphology of the submarine flanks of volcanic ocean islands: A comparative study of the Canary and Hawaiian hotspot islands. Journal of Volcanology and Geothermal Research 115(1-2), 83-107.

Postma, G., Cartigny, M., & Kleverlaan, K., 2009. Structureless, coarse-tail graded Bouma Ta formed by internal hydraulic jump of the turbidity current? Sedimentary Geology 219(1-4), 1-6.

Romagnoli, C., Casalbore, D., Ricchi, A., Lucchi, F., Quartau, R., Bosman, A., ... & Chiocci, F. L., 2018. Morpho-bathymetric and seismo-stratigraphic analysis of the insular shelf of Salina (Aeolian archipelago) to unveil its Late-Quaternary geological evolution. Marine Geology 395, 133-151.

Sabato, L., & Tropeano, M., 2004. Fiumara: a kind of high hazard river. Physics and Chemistry of the Earth, Parts A/b/c, 29(10), 707-715.

Slootman, A., & Cartigny, M. J., 2020. Cyclic steps: Review and aggradation-based classification. Earth-Science Reviews 201, 102949.

Ventura, G., 2013. Kinematics of the Aeolian volcanism (Southern Tyrrhenian Sea) from geophysical and geological data. Geological Society, London, Memoirs 37(1), 3-11.

Wright, I. C., & Gamble, J. A., 1999. Southern Kermadec submarine caldera arc volcanoes (SW Pacific): caldera formation by effusive and pyroclastic eruption. Marine Geology 161(2-4), 207-227.

The influence of underwater dunes in spatiotemporal analysis of the hydrodynamic of the Saint-Lawrence River

W.N. Cassol *Université Laval, Québec, QC, Canada – willian-ney.cassol@scg.ulaval.ca*
S. Daniel *Université Laval, Québec, QC, Canada - sylvie.daniel@scg.ulaval.ca*
D. Pham Van Bang *Institut National de la Recherche Scientifique, Québec QC, Canada - damien.pham_van_bang@inrs.ca*

ABSTRACT: The Estuary of the Saint-Lawrence River is a high-energy fluvial sedimentary environment with the second largest annual discharge in North America (Hudon & Carignan, 2008). With the high dynamism in the Estuary, significant changes can be observed in the seafloor surface near Quebec City on a daily time scale. The hydrodynamics and the seafloor morphology of this complex section of the Saint-Lawrence is paradoxically poorly documented. In this paper, we present the results of a bathymetric survey in the vicinity of Quebec City, highlighting the sedimentary structures present there and their mobility.

1 INTRODUCTION

The data acquired from MultiBeam EchoSounder (MBES) surveys can be used for multiple applications. These datasets with high-resolution and accuracy are involved in the study of the seafloor morphology, the inspection of underwater structures and the safe navigation in navigation channels. In this context, the study of the dynamics related to underwater sedimentary structures such as underwater dunes has an important role. Such study can be an intricate task, starting with the extraction of these structures from Digital Bathymetric Models (DBM). Indeed, dunes are fuzzy objects, as many landforms. Therefore, their identification performed by human operators can be subjective, since the perception of the dunes varies from user to user depending on their background and experience.

Different approaches have been proposed in the literature to automatically segment and characterize dunes from the seafloor surface. Debese et al. (2016) and Ogor (2018) have proposed the identification of these structures from TIN (Triangulated Irregular Network). The first considered geodesic morphometry to extract the salient features of the dunes (i.e. crest line and troughs). The latter considered differential geometry to identify the crest lines of the dunes, which are used as seed regions to extract the whole structure. Di Stefano & Mayer (2018) and Cassol et al. (2021; 2022) have proposed approaches to segment dunes from a regular gridded DBM. Both performed a morphometric analysis of the DBM with the geomorphons algorithm (Jasiewicz & Stepinski, 2012). While the first work extracts the dunes through an aggregation of the DBM cells according to their geomorphon class, the latter considered an OBIA (Object-Based Image Analysis) approach, which shall be further discussed in this paper.

A spatiotemporal analysis of the dynamics associated to the dunes can be conducted once they have been extracted from multi temporal DBMs (i.e. DBM at different dates). Thibaud et al. (2013) have proposed a spatiotemporal analysis of dune migration through graph-based model. This approach considered two consecutive periods, as suggested by Del Mondo et al. (2010), with time being a discrete criterion associated to each survey. Duffy & Hughes Clarke (2005) considered a cross correlation method to study the process of dunes migration in marine context. Similar to the previous

approach, they considered two consecutive datasets of the study area to observe the directional vector of dunes migration. Although there is some work in the literature on the spatiotemporal analysis of sedimentary structures, there is still a lack of knowledge on the features to extract and track to characterize the migration, especially in highly dynamic environments. Moreover, to our knowledge, there is no end-to-end automated approach to remove the operator from the process in order to provide greater objectivity and efficiency of analysis. This paper attempts to fill some of these knowledge gaps.

Based on a temporal bathymetric database, this paper proposes an analysis of the mobility of the dunes in the estuary of the Saint-Lawrence River. Such an analysis is crucial when proposing a new hydrodynamic model specific for the Saint-Lawrence River Estuary. Indeed, the mobility of these sedimentary structures on the seafloor is intimately related to the hydrodynamics and environmental factors as well as the characteristics of the dunes, as suggested by Kenyon (1970) and Le Bot (2001).

This paper is organized in three sections. The first section presents the methodology of extraction and spatiotemporal analysis of dunes from a DBM. The second section presents the results and discussion of the segmentation, characterization and spatiotemporal analysis of the dunes. The last section proposes some conclusion with prospects for future research related to the spatiotemporal evolution of dunes and hydrodynamic model.

2 SPATIOTEMPORAL ANALYSIS OF THE DUNES

This section described our proposed methodology to monitor the spatiotemporal mobility of underwater dunes. The first step addresses the determination of the relevant time scale for the acquisition of bathymetric data. This scale needs to be adjusted according to the environmental context and previous knowledge of the dynamism of the study area. Indeed, in marine environments the acquisition can be done with an interval of months or even years (Le Bot, 2001, Garlan, 2007), while in estuarine environments the acquisition of bathymetric data may be done daily, as further discussed in this paper.

Once the bathymetric data have been acquired and processed, a DBM is created from which the dunes are segmented using Cassol et al. (2021, 2022) method. Unlike existing methods in the literature, this approach does not involve any manual intervention to delineate landforms, which limits subjectivity, cumbersomeness and sources of error in the analysis of the surface as well as in the delimitation of the seafloor objects. The key principle relies on the formalization of the underwater dune object through a conceptual model that considers the underwater dunes can be identified on the seafloor by three salient features, namely, the crest line, the stoss trough and the lee trough. The crest line is the linear feature located in the higher zone of the dune. This feature is the upper bound of both sloping sides of the dune (i.e. stoss and lee sides). The stoss and lee troughs represent the boundary of the dune objects, being also represented by linear features. These troughs bound the stoss and lee sides, respectively.

Considering the formalized dune model, a morphometric analysis can be carried out on the DBM using the Geomorphon algorithm (Jasiewicz & Stepinski, 2012). This analysis aims to identify the three salient features previously mentioned. Then, the crest line of each dune on the DBM is matched with its corresponding lee and stoss troughs. This matching is done by searching the troughs nearest to the crest lines. The search is conducted in the orthogonal direction of the crest line orientation with a predefined range distance limit. Afterwards, the dune object is created by aggregating the pixels located in the area between the crest line and the troughs. Mathematical morphology and image processing are used to extract and better delineate the dune object. The result of

is the dune object identified by the same label as its crest line.

Once the dunes have been segmented from the DBM, these structures can be characterized calculating a series of morphological descriptors. These descriptors consider the dune object segmented itself as well as its salient features. The main descriptors considered in the characterization are the dune orientation, depth, width, height, stoss and lee angles, stoss and lee widths and the symmetry index of the dunes. More details about the segmentation approach and the estimation of the morphological descriptors can be found in, respectively, Cassol et al. (2021) and Cassol et al. (2022).

A spatiotemporal analysis of the mobility of the dunes is performed once they have been extracted from the DBM. It consists of a manual extraction of several cross-sectional profiles through which the mobility of the dunes on the seafloor surface and their displacement can be observed and quantified. The dune objects, their related morphological descriptors as well migration scheme can be further integrated in a hydrodynamic model. Figure 1 synthetizes the steps of the proposed spatiotemporal analysis of underwater dunes.

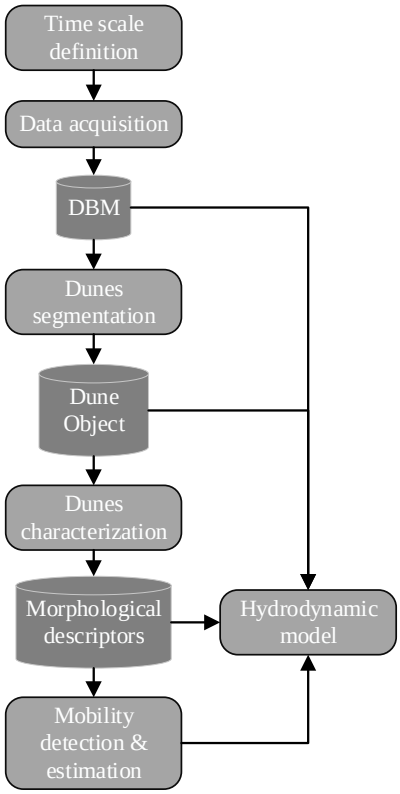

Figure 1. Approach for the spatiotemporal analysis of underwater dunes.

3 RESULTS AND DISCUSSION

3.1 Saint-Lawrence Fluvial Estuary DBM

The Fluvial Estuary of the Saint-Lawrence River is a high-dynamic environment with a length of 400km with a width of a few kilometres in Quebec City and 70km downstream (i.e. Île aux Coudres). The seafloor depth ranges down to 60m. The dimensions are such that the conditions prevailing near Quebec city are highly complex. The tidal signal is asymmetric due to a strong competition between bottom friction and convergence effects. This region of the river is also characterized by a complex seafloor topography with different physical agents being responsible for the high dynamism, such as tide, waves, wind, ship waves, and ice (Drapeau, 1992). The studied area can be observed in Figure 2.

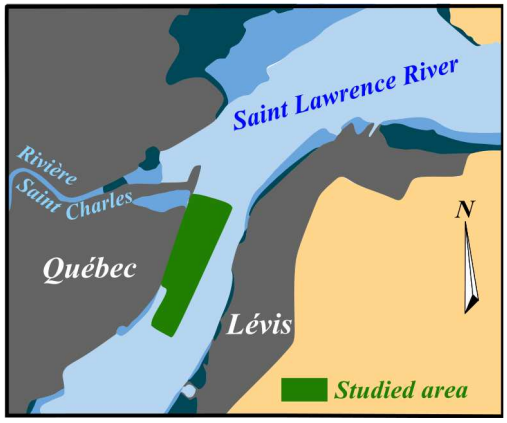

Figure 2. Study area of the Saint-Lawrence Estuary in Québec City. In green, the field of dunes surveyed. Maximum extension of 2.2km X 450m.

The MBES data used to generate the DBM considered in this paper was acquired from July 11th – July 14th, 2022. The data acquisition system consisted in a Kongsberg EM2040 MBES, an Applanix POS-MV320 and two GNSS antennas (Trimble GA830 and 540AP) embedded in the Louis-Edmond-Hamelin vessel. The field of dunes near Québec City was surveyed daily between 9:00 am and 12:00pm in the four days of acquisition. A DBM generated from the

MBES data acquired can be observed in Figure 3 with the crest lines of the dunes in red.

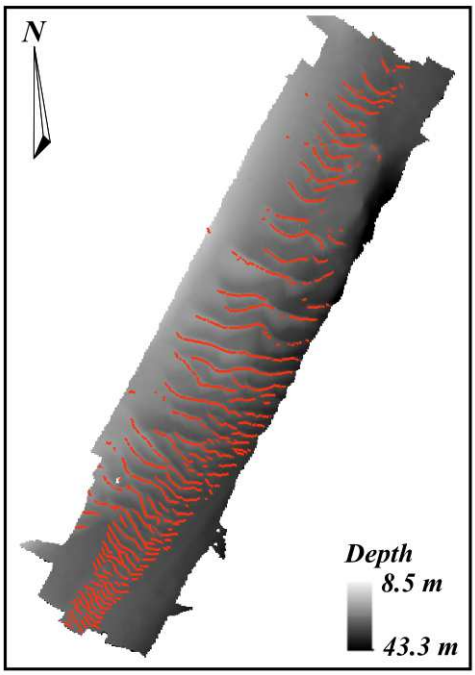

Figure 3 – DBM generated from July 13th MBES data with a resolution of 1m. In red, the crest line of dunes.

3.2 Dunes segmentation

The underwater dunes presented in the four DBM were segmented considering the approach described in the previous section. A total of 561 dunes were segmented over the four surfaces. Since the covered area of the survey was not exactly the same, 144 dunes were segmented in July 11th, 136 dunes in July 12th, 129 dunes in July 13th and 152 dunes in July 14th. An example of the dunes segmented can be observed in Figure 4. In this figure, we observe that larger dunes are located in the centre of the surveyed area while small dunes are observed in the north and south zones of the DBM. To analyse the performance of the segmentation of these sedimentary structures from acquired data, a ground truth was built manually segmenting dunes from each daily DBM. Therefore, three measures were computed to assess the performance, namely the true positive, false positive and false negative rate. A true positive is considered when a minimum of 50% of the segmented dune coincides with its area in the ground truth. A false positive is considered when the area of the segmented dune coincides less than 50% with the ground truth or when this structure does not have a related dune in the ground truth. A false negative is when the segmentation approach fails to segment a dune existing in the ground truth (adapted from Nguyen et al., 2020). The performance of the segmentation can be observed in Figure 5.

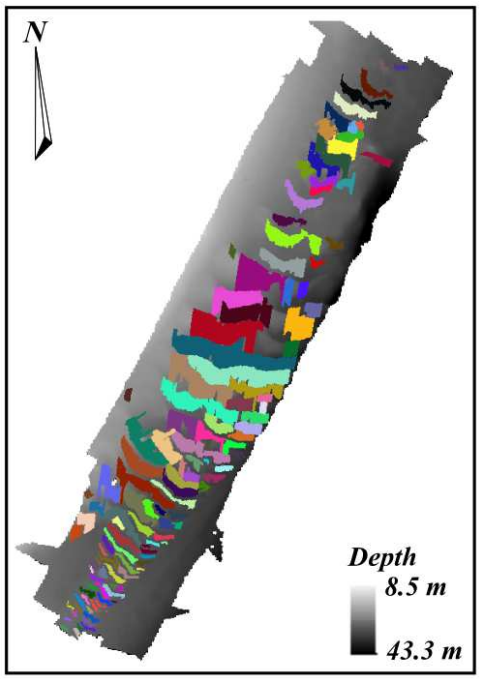

Figure 4 – Segmented dunes from the DBM. The dune objects are coloured on the DBM.

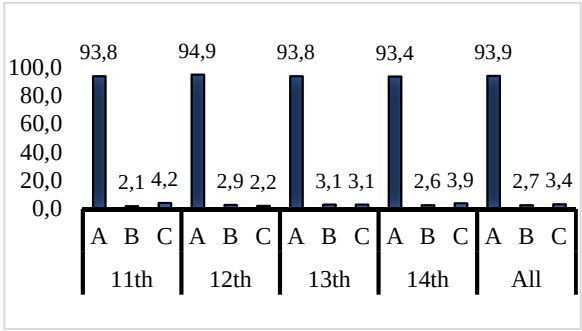

Figure 5 – Performance of the segmentation. A represents the true positive of each acquisition day, B the false positive and C the false negative. All considers the 561 segmented dunes overs the four days of acquisition.

The performance index over the four days of acquisition are similar to the overall performance considering the four days of acquisition. In the latter, 93.9% of the dunes

were well segmented with 2.7% of false positive and 3.4% of false negative. The false positive is essentially associated with small dunes that the salient features are difficult to detect from the DBM due to its resolution of 1m. The false negative is essentially associated with dunes partially surveyed on the acquisition.

3.3 Dunes characterization

Once the dunes have been segmented from the DBM, they can be characterized using morphological descriptors. Their values are displayed as histograms in Figure 6 and 7.

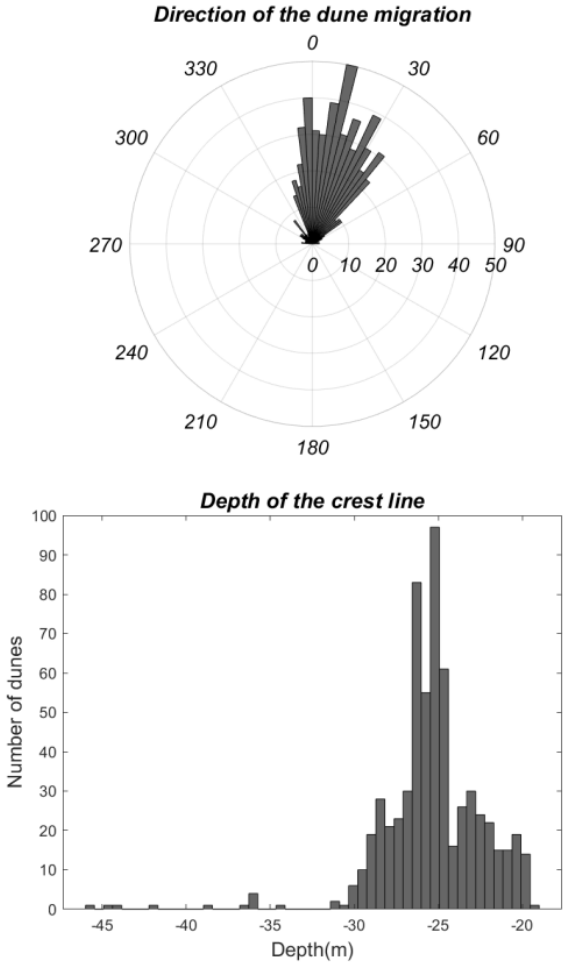

Figure 6 – Histograms of direction of dunes migration and depth.

According to the orientation of the dunes (cf. Fig. 6), their migration direction can be assessed as being approximatively 12.5° (i.e. median value), which is coincident with the main current of the Saint-Lawrence River in the study area. The dunes have a depth ranging from 19.5m to 45.7m (cf. Fig. 6), with a median depth value of 25.3m. The height of dunes ranges from 4cm up to 4.5m (cf. Fig. 7), with a median value of 0.77m. They have a width varying from 1.85m up to 100m (cf. Fig. 7) with a median value of 27m.

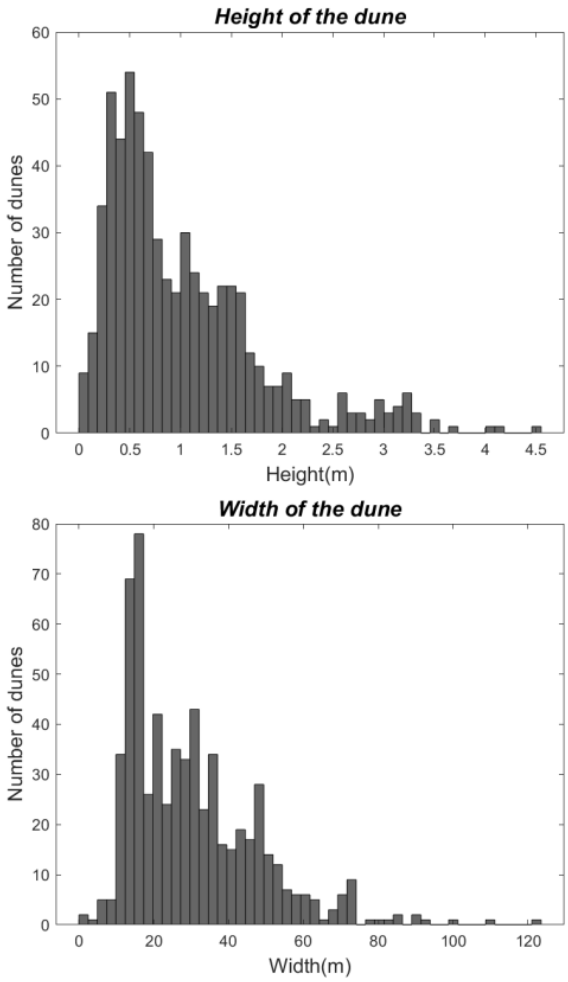

Figure 7 - Histograms of height and width of dunes.

We have also estimated the wavelength value (i.e. distance between the crest line of two consecutive dunes) and the density for this surveyed field of dunes. The median wavelength value, considering the four days of surveying, is 44m and the dunes density is up to 89% of the seafloor in this studied area. Considering these values for the morphological descriptors, the dunes of the study area are predominantly large dunes, as suggested by the dunes classification in Ashley (1990).

3.4 Spatiotemporal analysis of dunes

A spatiotemporal analysis of the mobility of the dunes in the Saint-Lawrence Estuary is proposed through different cross-section profiles. Figure 8 illustrates two profiles with underwater dunes present in DBM of July 11th and July 14th. We observe that the underwater dunes segmented in our study area are subjected to a migration rate up to 1m/day in different zones of the DBM. Indeed, the migration dynamic of large dunes differ from the small and medium dunes. The latter are located in the south region of our study zone (cf. Fig. 8 P1), migrated by traction on the seafloor, resulting in a difference up to 4m between July 11th and July 14th. A different dynamic can be observed in the centre of our study zone, with larger dunes migrating through an erosion-deposition regime (cf. Fig.8 P2).

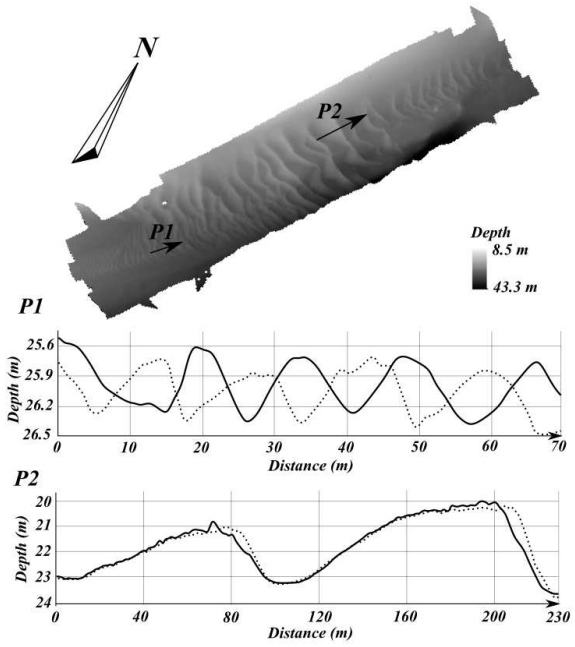

Figure 8 – DBM surface indicating profiles P1 and P2. The dotted line represents the profile from DBM generated with data acquired in July 11th and the black line data of July 14th.

4 CONCLUSION

This paper proposed a methodology to monitor the spatiotemporal mobility of underwater dunes in the Estuary of the Saint-Lawrence River. It consisted in the comparison of cross-sectional profiles through daily DBM in the same studied area. Two distinct types of displacement of dunes have been observed, the traction of small and medium dunes and erosion-deposition of larger dunes (cf. Fig. 8). This dynamic of migration is intimately related to hydrodynamic and environmental factors (e.g. current velocity, tidal information, grain size). Therefore, future works should consider a multisource approach to better analyse the mobility of dunes. Indeed, the information regarding these multiple factors may be helpful to better understand the dynamism of these structures on the seafloor surface.

Spatiotemporal information of underwater dune will be further analysed with respect to the tidal current. A 3D hydrodynamic model is under development yet. The model is based on the finite element method and will result on extension of an existing 2D depth integrated model which has been validated on field measurements (Matte et al. 2017a, 2017b). The newly developed 3D model will provide access to unmeasured flow velocities during the bathymetry investigation (i.e. July 2022) and complete information to better analyse the mobility of observed dunes (Hulscher, 1996). This information may be helpful to understand the correlation between the hydrodynamic and environmental factors with the morphological descriptors estimated for the dunes, as suggested by Kenyon (1970) and Le Bot (2001).

5 ACKNOWLEDGEMENT

The authors would like to thank Université Laval and INRS for providing access to equipment and laboratories to conduct this research. In addition, they would like to thank Réseau Québec Maritime for their financial support. We must thank QPS for their help with post-processing of bathymetric data and Qimera license. We must thank Réseau Québec Maritime and REFORMAR for the financing and organization of the MBES campaign in July 2022.

6 REFERENCES

Ashley, G.M., 1990. Classification of large-scale subaqueous bedforms: A new look at an old problem. Journal of Sedimentary Research 60, 160-172. doi:10.2110/JSR.60.160

Cassol, W. N., Daniel, S., Guilbert, É., 2021. A segmentation Approach to Identify Underwater Dunes from Digital Bathymetric Models. Geosciences, 11, n°9: 361. doi: 10.3390/geosciences11090361.

Cassol, W. N., Daniel, S., Guilbert, É., 2022. An approach for the automatic characterization of underwater dunes in fluviomarine context. Geosciences, 12, 89. doi : 10.3390/geosciences12020089

Debese, N., Jacq, J.J., Garlan, T. 2016. Extraction of sandy bedforms features through geodesic morphometry. Geomorphology, 267, 82–97. doi: 10.1016/j.geomorph.2016.05.013

Del Mondo, G., Stell, J. G., Claramunt, C., Thibaud R., 2010. A graph model for spatiotemporal evolution. Journal of Universal Computer Science, vol.16. 21 pages.

Di Stefano, M., Mayer, L.A., 2018. An automatic procedure for the quantitative characterization of submarine bedforms. Geosciences, 8, 28, doi:10.3390/geosciences8010028

Drapeau, G., 1992. Dynamique sédimentaire des littoraux de l'estuaire du Saint Laurent. Géographie Phys. Quat. 46, 233–242. doi:

Duffy, G. P., Hughes-Clarke, J. E., 2005. Application of spatial cross-correlation to detection of migration of submarine sand dunes. Journal of geophysical research, vol. 110. 11 pages.

Garlan, T., 2007. Study on Marine Sandwave Dynamics. International Hydrographic Review, Vol. 8, n°2, 26-37.

Hudon, C., Carignan, R. 2008. Cumulative impacts of hydrology and human activities on water quality in Sr. Lawrence River (Lake Saint-Pierre, Quebec, Canada). Canadian Journal of fisheries and aquatic sciences, vol. 65, 1165-1180

Hulscher, S., 1996. Tidal-induced large-scale regular bed form patterns in a three-dimensional shallow water model. J. Geophys. Res., Vol. 101, NO. C9, 20727-20744

Jasiewicz, J., Stepinski, T.F., 2012. Geomorphons - A pattern recognition approach to classification and mapping of landforms. Geomorphology, 182, 147–156. doi: 10.1016/j.geomorph.2012.11.005.

Kenyon, N.H., 1970. Sand Ribbons of European tidal Seas. Mar. Geol., 9, 25–39.

Le Bot, S., 2001. Morphodynamique de Dunes Sous-Marines Sous Influence des Marées et des Tempêtes. Processus Hydro-Sédimentaires et Enregistrement. Exemple du Pas-de-Calais. Ph.D. Thesis, Université de Lille I.

Matte, P., Secretan, Y., Morin, J. (2017a). Hydrodynamic modeling of the St. Lawrence fluvial estuary. I: Model setup, calibration, and validation. J. Waterw. Port. Coast. Ocean Eng. 143 (5), 04017010. https://doi.org/10.1061/(ASCE)WW.1943-5460.0000397.

Matte, P., Secretan, Y., Morin, J. (2017b). Hydrodynamic modeling of the St. Lawrence fluvial estuary. II: Reproduction of Spatial and Temporal Patterns. J. Waterw. Port. Coast. Ocean Eng. 143 (5), 04017011. https://doi.org/10.1061/(ASCE)WW.1943-5460.0000394.

Nguyen, T.H., Daniel, S., Guériot, D., Sintès, C., Le Caillec, J.M., 2020. Super-resolution-based snake model—an unsupervised method for large-scale building extraction using airborne LiDAR data and optical image. Remote Sens., 12, 1702.

Ogor, J., 2018. Design of Algorithms for the Automatic Characterization of Marine Dune Morphology and Dynamics. Ocean, Atmosphere. Ph.D. Thesis, ENSTA-Bretagne.

Thibaud, R., Del Mondo, G., Garlan, T., Mascret, A., Carpentier, C., 2013. A spatio-temporal graph model for marine dune dynamics analysis and representation. Transctions in GIS, 17 (5), 742-762. doi: 10.1111/tgis.12006

A numerical study on ripple evolution and migration using a two-phase flow model

A. Salimi-Tarazouj *Center for Applied Coastal Research, University of Delaware, USA – alisalim@udel.edu*
T.J. Hsu *Center for Applied Coastal Research, University of Delaware, USA – thsu@udel.edu*
P. Traykovski *Woods Hole Oceanographic Institution, USA – ptraykovski@whoi.edu*
J. Chauchat *LEGI, University of Grenoble Alpes, France – julien.chauchat@univ-grenoble-alpes.fr*

ABSTRACT: The evolution of ripple geometries and their equilibrium states due to different wave forcing parameters are investigated by a Reynolds-averaged two-phase model, SedFoam, in a two-dimensional domain. Modeled ripple geometries, for a given uniform grain diameter, show a good agreement with ripple predictors that include the wave period effect explicitly, in addition to the wave orbital excursion length (or wave orbital velocity amplitude).

1 INTRODUCTION

Oscillatory flow motions of surface wave near seabed can generate a wide range of bedforms. Bedforms are essential due to their effect on the seabed roughness and wave-current driven onshore/offshore sediment transport. Field and laboratory observation on onshore/offshore sediment transport in orbital ripple regime suggested that under onshore velocity skewed waves, suspended load above the ripple was offshore directed while onshore transport occurred as ripple migration. These complex processes associated with suspended load and ripple migration pose a challenge to conventional single-phased sediment transport models as they require assumptions and empirical treatments in modeling suspended load and bedload. We present a novel numerical model that is able to resolve sediment transport over ripples and ripple migration altogether in a Eulerian two-phase modeling framework, called SedFoam. With a two-equation k-epsilon closure, interphase drag and particle stresses, the model can resolve full profiles of sediment concentration and particle/fluid velocities. Particularly, a careful consideration of particle stresses in the high concentration of fluid-solid transition is essential to the resulting ripple steepness and migration speed.

2 GOVERNING EQUATIONS AND NUMERICAL MODEL

The two-phase model sedFoam (Chauchat et al. 2017) (https://github.com/SedFoam/sedfoam) is used to simulate the formation and evolution of ripples in oscillatory flows using the Reynolds-averaged k-ε turbulence model.

In the Eulerian two-phase flow formalism, coupled mass and momentum conservation equations for the fluid and the solid phases are solved. The mass conservation for the fluid and the solid phase are given by

$$\frac{\partial(1-\phi)}{\partial t}+\frac{\partial(1-\phi)u_i^f}{\partial x_i}=0 \qquad (1)$$

$$\frac{\partial\phi}{\partial t}+\frac{\partial\phi u_i^s}{\partial x_i}=0 \qquad (2)$$

respectively with x the position vector, $i=1,2,3$ representing the streamwise, vertical and spanwise components, ϕ the filtered sediment concentration and u^f and u^s the fluid and solid Favre filtered velocities.

The fluid and solid momentum conservation equation are written as

$$\begin{aligned}&\frac{\partial\rho^f(1-\phi)u_i^f}{\partial t}+\frac{\partial\rho^f(1-\phi)u_i^f u_j^f}{\partial x_j}=\\&-(1-\phi)\frac{\partial p^f}{\partial x_i}+\frac{\partial}{\partial x_i}\left[T_{ij}^f\right]\\&-I_i+\rho^f(1-\phi)g_i+(1-\phi)f_i^v\end{aligned} \qquad (3)$$

$$\frac{\partial \rho^s \phi u_i^f}{\partial t} + \frac{\partial \rho^s \phi u_i^s u_j^s}{\partial x_j} = -\phi \frac{\partial P^f}{\partial x_i} - \frac{\partial P^s}{\partial x_i} + \frac{\partial}{\partial x_i}\left[T_{ij}^s\right] + I_i + \rho^s \phi g_i + \phi f_i^v \quad (4)$$

with ρ^f and ρ^s the fluid and solid densities and P^f and P^s the fluid ans solid phase pressures. The effective fluid and solid stress tensors T^f and T^s are given by

$$T_{ij}^f = \rho^f (1-\phi)\nu^f \left(\frac{\partial u_j^f}{\partial x_i} + \frac{\partial u_i^f}{\partial x_j} - \frac{2}{3}\frac{\partial u_k^f}{\partial x_k}\delta_{ij}\right) \quad (5)$$

$$T_{ij}^s = \rho^s \phi \nu^s \left(\frac{\partial u_j^s}{\partial x_i} + \frac{\partial u_i^s}{\partial x_j} - \frac{2}{3}\frac{\partial u_k^s}{\partial x_k}\delta_{ij}\right) \quad (6)$$

where ν^f and ν^s are the fluid and solid phases viscosities, g is the acceleration of gravity and f^v a volume force driving the flow.

The momentum exchange term between the two phases I is modelled using the semi-empirical drag law from Ding and Gidaspow (1990). The interested reader is referred to Chauchat *et al.* (2017) for more details about the model and the closures.

3 RESULTS AND DISCUSSION

Figure 1 shows the typical domain characteristics and boundary conditions. At the top domain boundary, a free-slip (i.e., Neumann) boundary condition is used for both the fluid and sediment field quantities. At the bottom boundary, a no-slip boundary is used for the velocities of both phases while a zero-gradient boundary is used for the other quantities. For the pressure field, a fixed zero value is specified at the top boundary, and at the bottom boundary of the domain, a zero gradient condition is imposed.
Periodic boundary conditions are specified at the two lateral boundaries to minimize computational domain length and Lx i is set to be the same as the measured equilibrium ripple reported by van der Werf et al. (2007). The domain length specified such that it includes n = 3 ripples. For initial ripple height η_i, we specify a much larger value than that measured ripple height. The domain height is set to be Lz = 0.5 m in all the simulations.

The oscillatory flow is driven by a prescribed horizontal pressure gradient which generates a free-stream velocity time series following the Stokes second-order wave.
In table 1, four cases are presented corresponding to different wave forcing conditions and the same sand diameter (d_{50}=440 μm, s=ρ_s/ ρ_f =2.65). The ripple profile at different wave cycle is shown in figure 2 a for case 1, the ripple height slightly reduces and the ripple migrates onshore. By tracking the position of the ripples crest it is possible to deduce the migration speed of the ripple which is shown in figure 2b for case 1 and 2. The numerical model predicts no migration for the symmetric wave case 2 (as expected) and a migration rate of 14-15 mm/min for case 1 which is very comparable with the measured value of 18 mm/min by van der Werf *et al.* (2007). This first result validate the two-phase flow approach for simulation of ripple migration by asymmetric waves. More details can be found in Salimi-Tarazouj *et al.* (2021a).

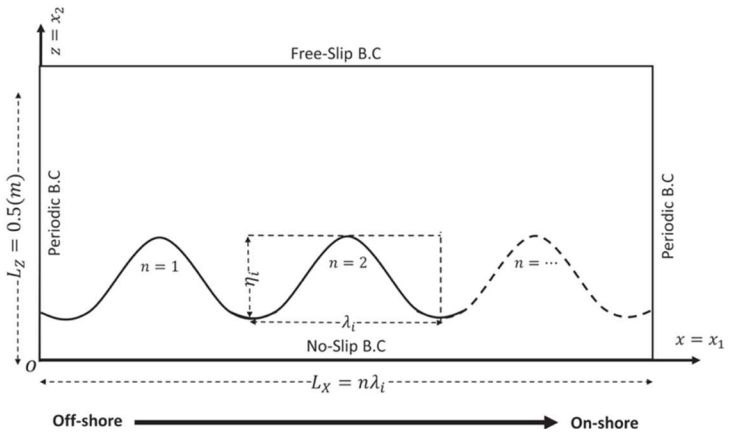

Figure 1: Schematic plot of the model domain and initial ripple bed profile

Table 1: Parameters for numerical configurations

Case #	Waves (order)	T (s)	U_m (m/s)	λ_e (m)	η_e/λ_e (-)
1	2nd	5	0.54	0.41	0.19
2	1st	5	0.48	0.46	0.17
3	1st	3	0.48	0.23	0.17
4	1st	3	0.8	0.345	0.13

The morphodynamical evolution of the ripple is the result of the small imbalance in the sediment fluxes during a wave period. Figure 3 and 4 show the period-averaged dimensionless vorticity field (Ω/ω) and the dimensionless sediment flux (ψ).

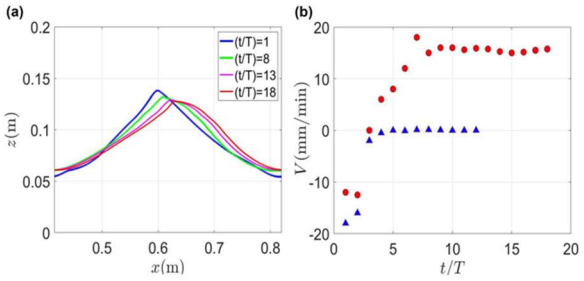

Figure 2: (a) Ripple profile for the middle ripple in Case 1 at different wave cycle. (b) Ripple migration rate as a function of the number of wave's cycle for the middle ripple in Case 1 (red circles) and Case 2 (blue triangles).

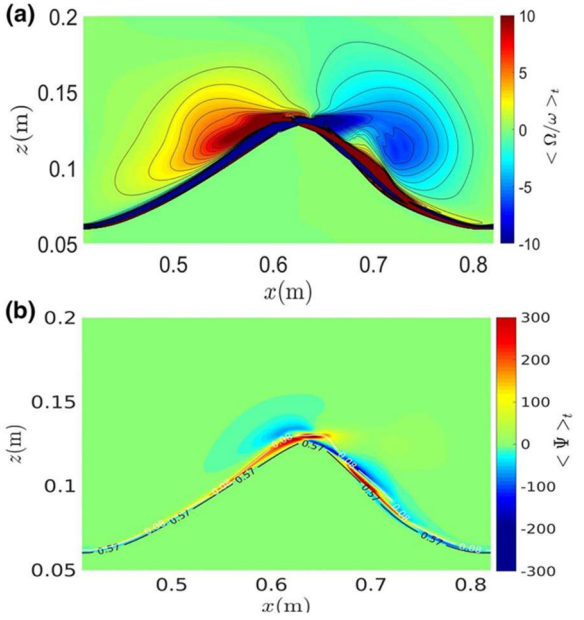

Figure 3: (a) Wave-period-averaged normalized vorticity (color-bar) for Case 1. Panel (b) shows the corresponding wave-period-averaged normalized sediment horizontal flux.

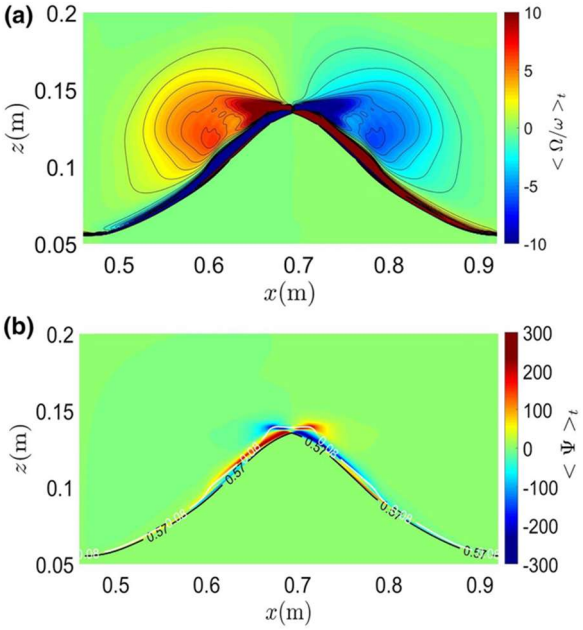

Figure 4: idem as figure 3 for case 2.

While the vorticity field and the sediment flux are symmetric in case 2 (figure 4, sinusoidal wave) a slight asymmetry is observed in case 1 (figure 3, 2nd order Stokes wave) which shows a larger primary vortex at the onshore side of the ripple (negative/clockwise vorticity), reflecting the stronger onshore flow driven by onshore velocity-skewed wave motion. This asymmetry generates an intense, offshore directed flow close to the onshore side of the ripple's surface and ripple crest which lead to a larger onshore transport via near-bed load. This the key mechanism by which the ripple migrates.

In figure 5, the space-time diagram of the bed elevation for case 3 and 4 are shown. This figure illustrates the model's capability to simulate the reduction and increase of ripple length and height due to two scenarios. The simulation is initialized with three orbital ripples in the domain resulted from a 5 sec wave of orbital velocity 0.48 m/s (case 2). In the first scenario (Figure 5a), we reduce the period to 3 sec and hence the orbital length is also reduced. This causes three large ripples to first split and then merge into 6 smaller ripples. In the second scenario, we increase the orbital velocity to 0.8 m/s and three large orbital ripples evolve into four smaller sub-orbital ripples via merging and sliding (Figure 5b). The interested reader is referred to

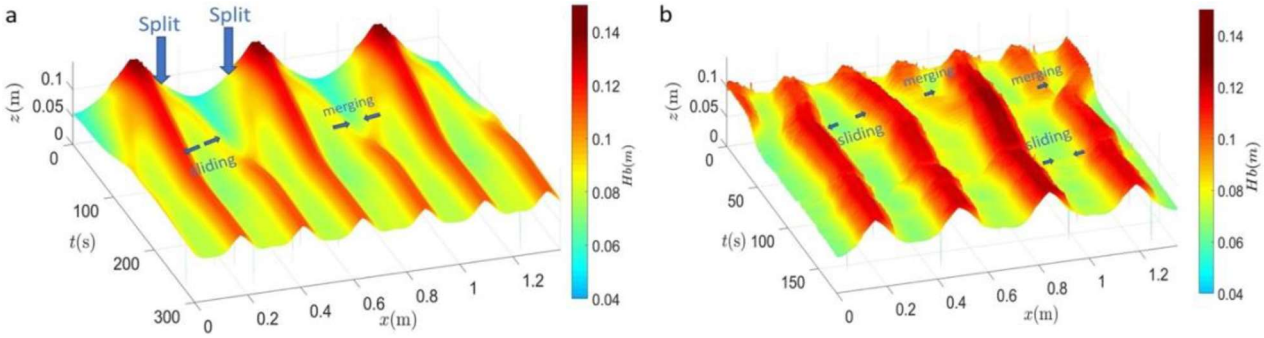

Figure 5: Time series of ripple bed evolution for case 3 (a) and case 4 (b)

Salimi-Tarazouj et al. (2021b) for more details about the effect of wave period on the ripple characteristics.

4 CONCLUSION

In this contribution we demonstrated the capabilities of the two-phase flow modeling approach to simulate the evolution and migration of ripples generated by an oscillatory flow. The model has been validated using experimental data and through a series of numerical experiments, the ripple's response to a step-change in the wave forcing has been studied. The model is capable of simulating "splitting", "sliding", "merging", and "protruding" as the ripples evolve to a new equilibrium state.

The model can also simulate the transition to sheet flow in energetic wave conditions and ripple reformation from a nearly flat bed condition. Simulation results reveal that the equilibrium state is such that the "primary" vortices reach half of the ripple length. Furthermore, an analysis of the suspended load and near-bed load ratio in the equilibrium state indicates that in the orbital ripple regime, the near-bed load is dominant while the suspended load is conducive to the ripple decaying regime (suborbital ripples) and sheet flow condition.

5 REFERENCES

Chauchat, J., Cheng, Z., Nagel, T., Bonamy, C., Hsu, T.-J., 2017. SedFoam-2.0: a 3-D two-phase flow numerical model for sediment transport 105194, 4367–4392. https://doi.org/10.5194/gmd-10-4367-2017

Ding, J., & Gidaspow, D. (1990). A bubbling fluidization model using kinetic theory of granular flow. AIChE Journal, 36(4), 523–538. https://doi.org/10.1002/aic.690360404

Johnson, P.C., Jackson, R., 1987. Frictional–collisional constitutive relations for granular materials, with application to plane shearing. Journal of Fluid Mechanics, 176, 67-93. doi:10.1017/S0022112087000570

Traykovski, P., Hay, A.E., Irish, J.D., Lynch, J.F., 1999. Geometry, migration, and evolution of wave orbital ripples at LEO-15. J. Geophys. Res. Ocean. 104, 1505–1524. https://doi.org/10.1029/1998JC900026

Salimi-Tarazouj, A., Hsu, T.-J., Traykovski, P., Cheng, Z., & Chauchat, J. (2021a). A numerical study of onshore ripple migration using a Eulerian two-phase model. Journal of Geophysical Research: Oceans, 126, e2020JC016773. https://doi.org/10.1029/2020JC016773

Salimi-Tarazouj, A., Hsu, T.-J., Traykovski, P., & Chauchat, J. (2021b). Eulerian two-phase model reveals the importance of wave period in ripple evolution and equilibrium geometry. Journal of Geophysical Research: Earth Surface, 126, e2021JF006132. https://doi.org/10.1029/2021JF006132

van der Werf, J. J., Doucette, J. S., O'Donoghue, T., & Ribberink, J. S. (2007). Detailed measurements of velocities and suspended sand concentrations over full-scale ripples in regular oscillatory flow. Journal of Geophysical Research, 112(2), 1–18. https://doi.org/10.1029/2006JF000614

Hydrodynamical regimes in turbulent flows over a wavy surface and dissolution instability

P. Claudin *Physique et Mécanique des Milieux Hétérogènes, PMMH UMR 7636 CNRS, ESPCI Paris, PSL Research University, Université Paris Cité, Sorbonne Université, Paris, France – philippe.claudin@espci.fr*
B. Andreotti *Laboratoire de Physique de L'Ecole Normale Supérieure, UMR 8550 CNRS, PSL Research University, Université Paris Cité, Sorbonne Université, Paris, France*

ABSTRACT: We theoretically investigate the pattern formation observed when a fluid flows over a solid substrate that can dissolve, melt or sublimate. We use a turbulent mixing description that includes the effect of the bed roughness. We show that the dissolution instability at the origin of the pattern that emerges is associated with an anomaly at the transition from a laminar to a turbulent hydrodynamic response with respect to the bed elevation. This anomaly, and therefore the instability, disappears when the bed becomes hydrodynamically rough.

1 INTRODUCTION

We are interested in pattern formation associated with a fluid flow over a solid bed, when mass transfer has a thermodynamic origin with melting, sublimation or dissolution of the bed. Figure 1 shows a typical example of scallops forming in limestone, in a river bed. The flow is influenced by the bed elevation and, in turn, erosion or transport induced by the flow makes the solid surface evolve. This feedback loop can lead to an unstable situation, where bed perturbations are amplified. Several linear stability analyses have been performed for these dissolution/melting problems, in order to compute the growth rate of a perturbation of given wavenumber k and determine the most unstable mode (Hanratty, 1981). In this presentation, we show that taking into account the bed roughness in the hydrodynamic description is of key importance as the dissolution instability is found to disappear when the bed becomes rough. Section 2 briefly summarizes the hydrodynamic model. Section 3 presents the stability analysis. Section 4 shows the main results and concludes. More details can be found in Claudin et al. (2017).

Figure 1. Centimeter-scale scallops in limestone on Ardèche river (France).

2 HYDRODYNAMIC MODEL

We consider a flow in the horizontal x-direction. The axis z is vertical. We use RANS equations to solve for the velocity u_i and pressure p fields. The stress tensor τ_{ij} is related to the strain rate $\dot{\gamma}_{ij} = \partial_i u_j + \partial_j u_i$ by means of a turbulent closure that involves a mixing length ℓ. In order to account for both smooth and rough regimes, we adopt here a van Driest-like expression for it:

$$\ell = \kappa(z + rd) \times \left[1 - \exp\left(-\frac{(z+sd)(\tau_{xz}/\rho)^{1/2}}{\nu \mathcal{R}_t}\right)\right]$$

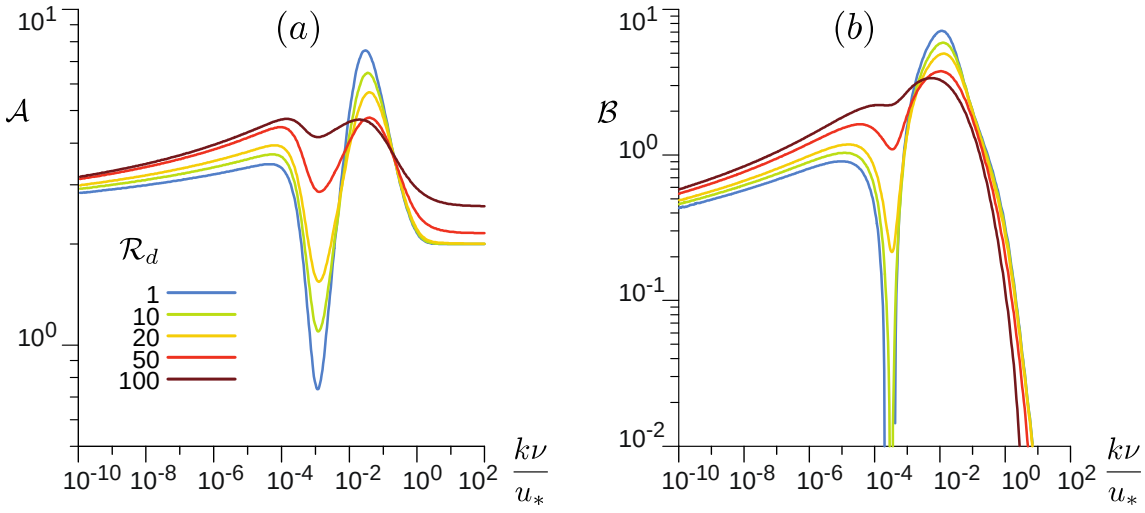

Figure 2. Basal shear stress coefficients $\mathcal{A}$ (a) and $\mathcal{B}$ (b) computed by the model as functions of $k\nu/u_*$. The different colors code for the value of the bed roughness Reynolds number $\mathcal{R}_d$ (legend). The laminar–turbulent transition (around $k\nu/u_* \simeq 10^{-3}$) gradually disappears when $\mathcal{R}_d$increases.

In this expression, $\kappa \simeq 0.4$ is the von Kármán constant, z is the distance to the bed, d is the sand equivalent bed roughness size, ν is the kinematic viscosity of the fluid, ρ is its mass density. $\mathcal{R}_t$ is the van Driest transitional Reynolds number, equal to $\mathcal{R}_t^0 \simeq 25$ in the homogeneous case of a flat bed. The exponential term suppresses turbulent mixing within the viscous sub-layer, close enough to the bed. The dimensionless numbers r and s are calibrated with measurements of velocity profiles over varied rough walls (see Claudin et al. (2017) and refs therein).

Following Hanratty (1981), $\mathcal{R}_t$ cannot be taken as a constant, but instead lags behind the pressure gradient by a space lag on the order of ν/u_* that is associated with a thickening of the boundary layer. We then write for $\mathcal{R}_t$ the spatial relaxation equation

$$a\frac{\nu}{u_*}\partial_x\mathcal{R}_t = b\frac{\nu\mathcal{R}_t^0}{\rho u_*^3}\partial_x(\tau_{xx}-p) - (\mathcal{R}_t - \mathcal{R}_t^0) \qquad (2)$$

where the constants a and b have been calibrated by Charru et al. (2013) on experimental data (Zilker et al., 1977; Frederick et al., 1988).

These data report measurements of the basal shear stress when the flow is perturbed by a sinusoidal bed $Z(x) = \zeta e^{ikx}$ (NB: we use complex notations for compactness, real parts are understood). At the linear order in $k\zeta$, the shear stress is also modulated and takes the generic form $\tau_{xz} = \rho u_*^2\left[1 + k\zeta e^{ikx}S_t\right]$. The mode function S_t depends on the dimensionless height kz. We define the two coefficients $\mathcal{A}$ and $\mathcal{B}$ by $S_t(0) = \mathcal{A} + i\mathcal{B}$. They encode the in-phase and in-quadrature stress linear response to the bed perturbation. They are computed by the hydrodynamic model, and their dependence on $k\nu/u_*$ if displayed in Fig. 2 for various values of $\mathcal{R}_d = du_*/\nu$. In the smooth limit (small $\mathcal{R}_d$), they show a marked transition between the turbulent regime associated with small wavenumbers $k\nu/u_* < 10^{-4}$ and the laminar regime, typically for $k\nu/u_* > 10^{-2}$. This `anomaly' at the laminar-turbulent transition, around $k\nu/u_* \simeq 10^{-3}$, experimentally evidenced by Hanratty and coworkers, plays as crucial role in the dissolution instability. It also shows up for the basal pressure response (Claudin et al., 2021), as well as for the effective topography -induced hydrodynamic roughness (Jia et al., 2023). Importantly, it disappears in the rough regime (Fourrière et al., 2010), for large enough $\mathcal{R}_d \gtrsim 100$.

3 LINEAR STABILITY ANALYSIS

We wish now to describe a passive scalar ϕ, e.g. the concentration of a chemical species or the temperature, which is transported by the flow. We model its dynamics by a simple advection–diffusion equation

$$\partial_t \phi + \vec{\nabla} \cdot \vec{q} = 0 \quad (3)$$

where the flux $\vec{q}$ is the sum of a convective and a diffusive term $\vec{q} = \phi \vec{u} - D\vec{\nabla}\phi$. Here, we take a diffusion coefficient D proportional to the turbulent viscosity and write

$$D = \frac{\upsilon}{\beta_\upsilon} + \frac{\ell^2 \dot{\gamma}}{\beta_t} \quad (4)$$

where $\dot{\gamma}$ is the modulus of the strain rate tensor. β_υ (resp. β_t) is the viscous (resp. turbulent) Schmidt number (or Prandtl numbers for temperature), here taken as constants.

To perform the linear stability analysis of these equations, we write the bed profile as

$$Z(x,t) = \zeta e^{(\sigma + i\omega)t + ikx} \quad (5)$$

where $\sigma(k)$ is the growth rate and $\omega(k)$ is the angular frequency of the bed pattern along x. The phase propagation speed is therefore $-\omega/k$. The equations of the model are linearized with respect to $k\zeta$ and can be solved with suitable boundary conditions. All components of their solution are written in the form of a correction to the base state (the flat case $k\zeta = 0$, homogeneous in x), proportional to kZ times a mode function. The evolution equation of the bed can be written as

$$\partial_t Z = q_0 - q_z(Z) \quad (6)$$

where $q_0 = \alpha(\phi_{sat} - \phi_0)$ is the scalar flux in the base state. The corresponding dispersion relation reads

$$\sigma + i\omega = q_0 k F(0) \quad (7)$$

where F is the mode function associated with the flux correction. This function is related to the hydrodynamic fields (see Claudin et al. 2017 for details).

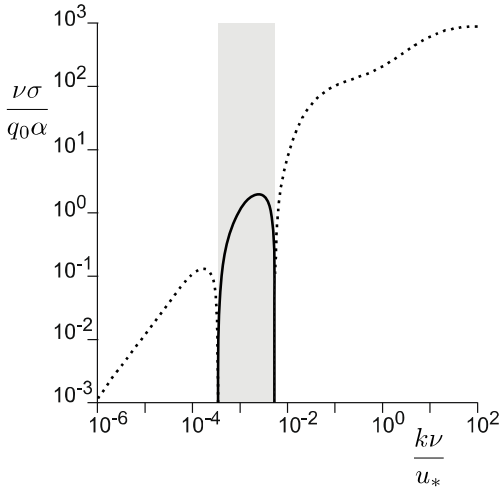

Figure 3. Dimensionless growth rate as a function of $k\nu/u_*$ in the limit of small α/u_* and for $\beta_\nu = 10^3$, $\mathcal{R}_d = 10$. Solid lines represent positive values. For negative values, $-\sigma$ is plotted (dotted lines). The grey region corresponds to the unstable ($\sigma > 0$) range of wavenumbers.

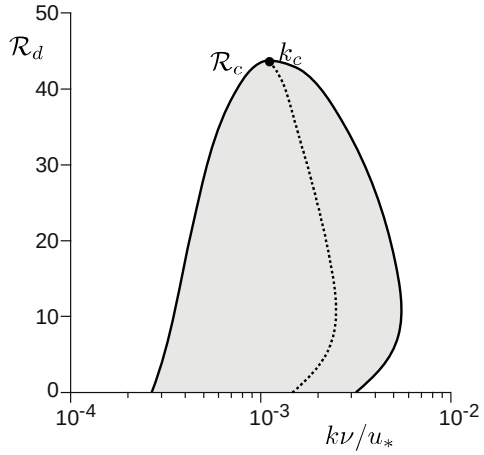

Figure 4. Stability diagram computed in the limit of small α/u_* and for $\beta_\nu = 10^3$. Solid line: marginal stability curve ($\sigma = 0$). Grey: unstable zone ($\sigma > 0$). Dotted line: location of the most unstable modes.

4 RESULTS AND CONCLUSIONS

The growth rate from (7) is displayed in Fig. 3, in the smooth case (small $\mathcal{R}_d$). We see a range of unstable wavenumbers with a positive growth rate, in which σ reaches a maximum value σ_m at k_m. As shown in Fig. 4, a key result is that the unstable band disappears above a critical value $\mathcal{R}_c$ of the roughness Reynolds number. This instability is governed by the laminar-turbulent transition, and is thus controlled by the

viscous length. An immediate robust result is that $k_m \propto u_*/\nu$ (with a prefactor on the order of 10^{-3}), a scaling law that is in good agreement with observations on various systems (Ashton & Kennedy, 1972; Blumberg & Curl, 1974; Curl, 1974; Thomas, 1979), including sublimation patterns on Mars (Bordiec et al., 2020).

One can understand the instability mechanism as follows. The erosion of the bed is driven by the mass flux itself controlled by the concentration gradient and the coefficient of diffusion. The concentration profile, enforced by the base state, is non-homogeneous, decreasing away from the surface. The crests of a modulated bed profile come closer to regions of lower concentration, enhancing the gradient with respect to the surface where ϕ is imposed. For a constant D, this peak effect increases the flux and thus the erosion at the crests, and this stabilising situation is what happens at large $k\nu/u_*$, when the wavelength is much smaller than the viscous sublayer. When turbulence is dominant, D is not constant any more, but is controlled by turbulent mixing. At small $k\nu/u_*$, turbulence is enhanced slightly upstream of the crests, and hence there is stabilizing erosion again. For wavenumbers in the intermediate range corresponding to the laminar–turbulent transition, however, turbulence is shifted downstream by means of the adverse pressure gradient (Eq. 2), enhancing mixing and thus erosion in the troughs, which is a destabilizing (amplifying) situation.

Further experimental studies, such as that of Bushuk et al. (2019), are needed to investigate the emergence and development of this instability in more detail, and in particular to follow the evolution of the bed roughness over time.

5 ACKNOWLEDGEMENT

We thank M. Bordiec, O. Bourgeois, S. Carpy, O. Durán and P. Jia for discussions.

6 REFERENCES

Ashton, G.D., Kennedy, J.F., 1972. Ripples on the underside of river ice covers. J. Hydraul. Div. ASCE 98, 1603. doi:10.1061/JYCEAJ.0003407

Blumberg, P.N., Curl, R.L., 1974. Experimental and theoretical studies of dissolution roughness. J. Fluid Mech. 65, 735. doi:10.1017/S0022112074001625

Bordiec, M., Carpy, S., Bourgeois, O., et al., 2020. Sublimation waves: Geomorphic markers of interactions between icy planetary surfaces and winds. Earth-Science Reviews 211, 103350. doi:10.1016/j.earscirev.2020.103350

Bushuk, M., Holland, D.M., Stanton, T.P., Stern, A., Gray, C., 2019. Ice scallops: a laboratory investigation of the ice–water interface. J. Fluid Mech. 873, 942. doi:10.1017/jfm.2019.398

Charru, F., Andreotti, B., Claudin, P., 2013. Sand ripples and dunes. Annu. Rev. Fluid Mech. 45, 469. doi:10.1146/annurev-fluid-011212-140806

Claudin, P., Durán, O. Andreotti, B., 2017. Dissolution instability and roughening transition. J. Fluid Mech. 832, R2. doi:10.1017/jfm.2017.711

Claudin, P., Louge, M., Andreotti, B., 2021. Basal pressure variations induced by a turbulent flow over a wavy surface. Front. Phys. 9, 682564. doi: 10.3389/fphy.2021.682564

Curl, R.L., 1974. Deducing flow velocity in cave conduits from scallops. NSS Bull. 36, 1.

Fourrière, A., Claudin, P., Andreotti, B., 2010. Bedforms in a turbulent stream: formation of ripples by primary linear instability and of dunes by nonlinear pattern coarsening. J. Fluid Mech. 649, 287. doi:10.1017/S0022112009993466

Frederick, K.A., Hanratty, T.J., 1988. Velocity measurements for a turbulent non-separated flow over solid waves. Exp. Fluids 6, 477. doi:10.1007/BF00196509

Hanratty, T.J., 1981. Stability of surfaces that are dissolving or being formed by convective diffusion. Annu. Rev. Fluid Mech. 13, 231. doi:10.1146/annurev.fl.13.010181.001311

Jia, P., Claudin, P., Andreotti, B., 2023. Topography-induced hydrodynamic roughness. Submitted.

Thomas, R.M., 1979. Size of scallops and ripples by flowing water. Nature 277, 281. doi:10.1038/277281a0

Zilker, D.P., Cook, G.W., Hanratty, T.J., 1977. Influence of the amplitude of a solid wavy wall on a turbulent flow. Part 1. Non-separated flows. J. Fluid Mech. 82, 29. doi:10.1017/S0022112077000524

Dunes morphodynamics superimposed on sand banks in a shallow macro-tidal environment: the example of the Haut Fond de Ouessant

P. Daguinos *UMR 6538 GEO-OCEAN, UBO, UBS, CNRS, Ifremer, 29280 Plouzane, France– paul.daguinos@univ-brest.fr*
N. Le Dantec *UAR 3113 IUEM et UMR 6538 GEO-OCEAN, UBO, UBS, CNRS, Ifremer, 29280 Plouzane, France– nicolas.ledantec@univ-brest.fr*
P. Le Roy *UMR 6538 GEO-OCEAN, UBO, UBS, CNRS, Ifremer, 29280 Plouzane, France– pascal.leroy@univ-brest.fr*
D. Menier *UMR 6538 GEO-OCEAN, UBO, UBS, CNRS, Ifremer, 56017 Vannes, France– david.menier@univ-ubs.fr*
G.Jouet *UMR 6538 GEO-OCEAN, UBO, UBS, CNRS, Ifremer, 29280 Plouzane, France– gwenael.jouet@ifremer.fr*
A.Ehrhold *UMR 6538 GEO-OCEAN, UBO, UBS, CNRS, Ifremer, 29280 Plouzane, France– axel.ehrhold@ifremer.fr*
M.Franzetti *UMR 6538 GEO-OCEAN, UBO, UBS, CNRS, Ifremer, 29280 Plouzane, France*
A.Trotot *UMR 6538 GEO-OCEAN, UBO, UBS, CNRS, Ifremer, 29280 Plouzane, France*

ABSTRACT: This study investigates the morphological parameters and migration rates of dune systems associated with a set of banner banks located at intermediate depths (50 m to 120 m) in the context of a highly dispersive shelf, offshore Brittany (Western France). The work mainly focuses on the Haut Fond d'Ouessant bank. New geophysical data (bathymetry, seismic, reflectivity) from Speedunes (2015) and Bankable (2019) cruises are analysed. We examine how the large range in basal surface depth over which the bank lies affect the dune morphodynamics. We also characterize sediment fluxes between these sediment structures, toward an overview map of sediment pathways across the Iroise shelf, in relation with the straits and the irregular shelf bottom.

1 INTRODUCTION

Submarine sand banks (or sand ridges) and dunes are the main bedforms of tide-dominated continental shelves. These structures are developed in response to variations hydrodynamic factors, but also sedimentary characteristics and long-term sea-level fluctuations (Allen 1968). The understanding of these morphodynamics variations and their roles on the sediment transport pathways is crucial for many applications such as marine resources exploitation, ecosystems protection, safety of marine infrastructures (Trentesaux 1993; Bajjouk et al. 2015). Nevertheless, assessing sediment fluxes in the context of submarine dunes and sand banks is still a scientific challenge due to the difficulty in collecting in-situ morphodynamic measurement. Some recent studies carried on marine dunes superimposed on banks allowed a better understanding of these systems (e.g., Franzetti et al. 2013; Homrani 2020 for submarine dune systems in Brittany). But surveys in intermediate bathymetric depth range (from 50 to 120 m) are still uncommon. Here we consider four sand banks located at intermediate depths on the Iroise Sea shelf in Western Brittany (France). The shelf is subject to large storms and under a macrotidal regime, with tidal range from 3 to 6 meters (Mariette et al. 1982). These banks consist mainly of biogenic sand and are associated with superimposed dunes. Here we focus on the *Haut Fond de Ouessant* Bank located at the south of Ouessant (Ushant)

Island, Southwest of the Fromveur channel. Dunes are located on the flanks of the bank while they are absent at the top. Two diachronic bathymetric datasets are used in this study to characterize the morphodynamics of these dunes superimposed on the bank, as well as to explore potential sedimentary pathways on the shelf.

2 STUDY ZONE

The study zone, named the Iroise Sea, is located in Western Brittany (France), between the Molene archipelago to the North, the Pointe du Raz and the Raz de Sein to the South and the Rade de Brest to the East (Fig. 1). The area is characterised as a highly dispersive shelf, at the confluence between the Atlantic Ocean and the English Channel, subject to strong tidal current and large swells. Due to this localisation, the Iroise Sea is also directly impacted by the English Channel's discharge (Kenyon and Stride 1970). Tidal currents are accelerated at straits (or "raz") and channels, generating alternating currents with maximum velocity exceeding 4m.s^{-1} (Hinschberger 1963; 'Service Hydrographique de La Marine (Ed.), 1957), and average current velocity slightly over 1m.s-1 during spring tides, especially at the proximity of the Fromveur and the Molene archipelago (Guillou and Chapalain 2018).

The sedimentary cover is very limited and heterogeneous, with the basement often at the seafloor. Sediments are principally characterised as biogenic sand. Sediment materials are organised in two main types of structures visible on the shelf: sandbanks with large dunes superimposed over them, and sediment draping. The shelf hosts 4 large sandbanks (10 to 50 sq. km): Four Bank, Armen Bank, Pierres Noires Bank, Haut Fond de Ouessant Bank), showing very contrasted morphologies but all having their base located at the same range of water depths (around 90 m). Except Pierres Noires

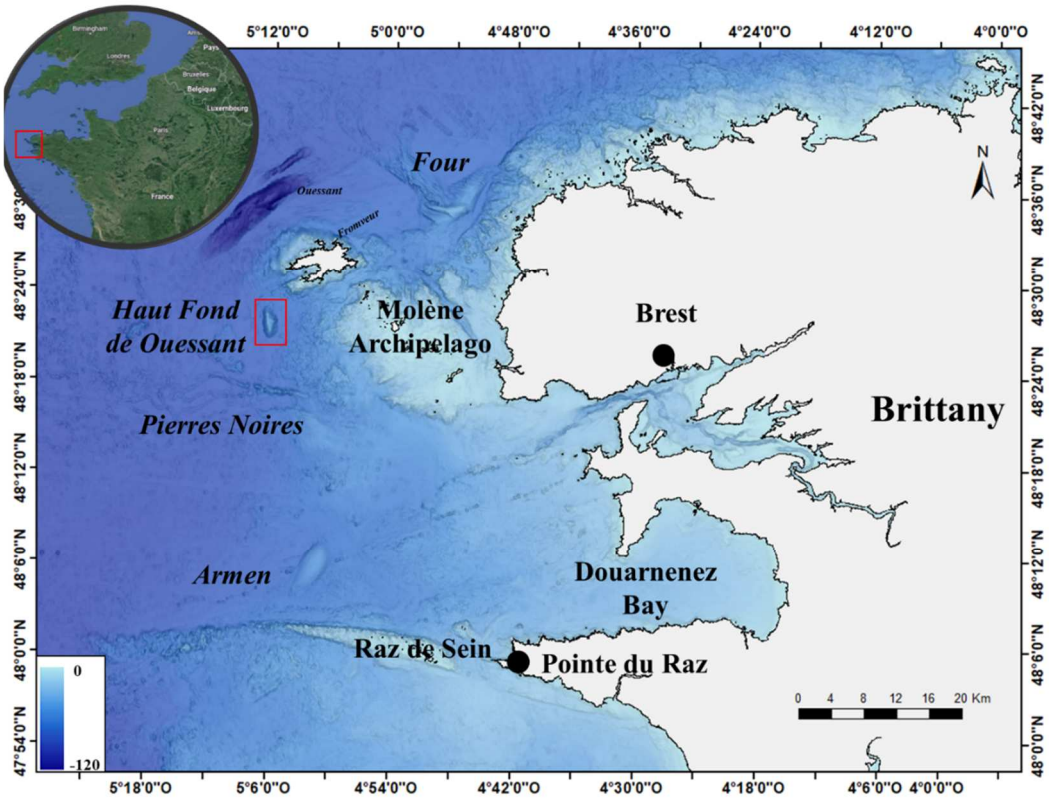

Figure 1: Localisation of the Iroise Sea, in red the Haut Fond de Ouessant Bank (insert: localisation of the Iroise Sea).

bank, they are considered as banner banks (Franzetti et al. 2013).The Haut Fond de Ouessant Bank, focus of this study, is an ellipsoidal bank with a length of 6 km and width of 2 km, and more than 45m high. It is associated with over 100 large dunes either superimposed on its flanks or in the dune field located directly north of the bank.

3 METHODS AND DATA

3.1 Dataset

The dataset used for this study consists of 2 Digital Elevation Models (DEM) obtained from research cruises in 2015 (Speedunes, RV Thalia) and 2019 (Bankable, RV Côtes de la Manche).

3.2 Methods

Data processing and analysis were realised on QPS (Qimera), ArcGIS and Matlab. Dunes crests were manually picked on GIS software, using the slope raster to identify them (Franzetti et al. 2013; Homrani 2020). Bathymetric profiles extracted from the DEM were analysed to estimate the morphological parameters of the dunes: height H, stoss side length a, lee side length b, dune length a+b, stoss side angle α, lee side angle β, aspect ratio H/L and asymmetry A=(L-2b)/L (Berné et al. 1989; Le Bot 2001; Knaapen 2005). Migration distances of dunes between the two datasets were calculated using an ArcGis algorithm with the function Model Builder tool. Here the application was to measure the distance between crests on two diachronic rasters using the measuring tools of ArcGIS. First a raster with the Euclidian distance to the crest for each pixel was created for the first dataset. The intersect with the crest of the second dataset gave directly the distance covered by each dune during the time between the two surveys. Volume variation, erosion or accretion, was also defined by computing the difference between the two rasters. These morphodynamics analyses were linked to the migration of the sedimentary stock.

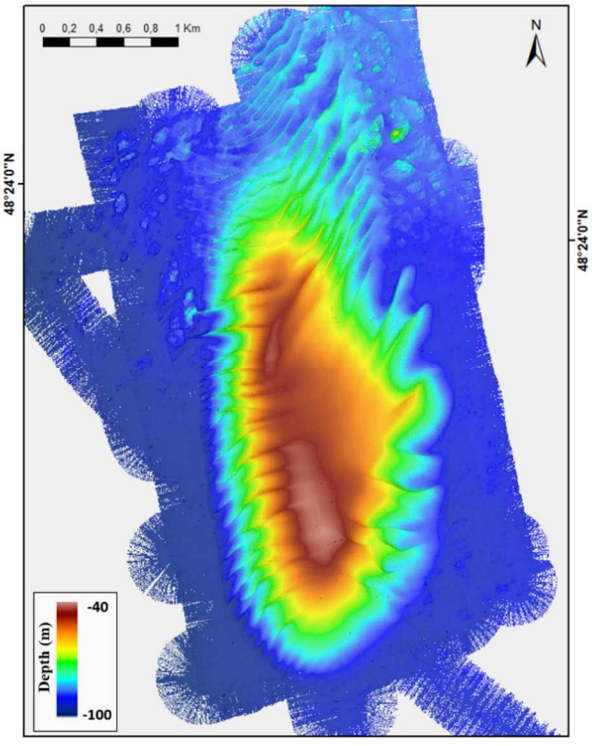

Figure 2: Bathymetric map of the Haut Fond de Ouessant Bank

4 FIRST RESULTS AND DISCUSSION

The surface of the Ouessant bank area is composed of 137 sedimentary structures on the bathymetrics datas from the bankable survey (2019), define as dunes. The North part of the bank is characterised by a dune field directly on the basement, whereas the other dunes are on the flanks of the bank. From the morphodynamics analyses, the Bank was divided into six parts. Three of them are localised on the East flank (labelled from 1 to 3 for the South East, East, and North East parts), 2 on the West flank (North West and South West), and the last one is the dune field at the north of the bank. There are no dunes on the top of the bank, which is likely related to the large Atlantic storms.

4.1 Morphological parameters

Dunes heights on the Haut Fond d'Ouessant range between 1 and 14 meters and wavelength from 0 to 250 meters. The sector number 2, corresponding to the middle eastern part of the bank is composed of the 3 dunes with the maximal height. No correlation was observed between the size

and the depth of the dunes. Except in sector 2 where the mean asymmetry is 0.16, the dunes are globally not very asymmetric, with an overall mean asymmetry of 0.4. The highest dunes are the most symmetric on this bank.

4.2 Dunes morphodynamics

Between 2015 and 2019, the migration speed ranges from 0.9 to 26.15 $m.y^{-1}$ with a mean of 6.8 $m.y^{-1}$, and 90% of the dunes have a migration rate lower than 10$m.y^{-1}$. The Table 1 gives the migration rate and the direction of each sector. These dunes exhibit an anti-clockwise rotation around the banks, except for the North-Eastern part where they migrate in clockwise direction. The western flank evolved faster than the eastern one, where the large, rather symmetric dunes may in fact not be migrating presently.

Table 1: Migration rate by sectors

Sectors	Migration ($m.y^{-1}$)	Migration orientation
1	5.9	North
2	3.4	North-West
3	7.4	North-West/South-West
4	10.2	South
5	6.4	South
6	5.5	South

With a small volume, only 5.5%, of sediment in movement relative to the overall bank volume, he volume analysis highlights that the sediment remobilization is mainly superficial, corresponding to the morphodynamics of the superimposed dunes.

Tidal current analysis reveals the presence of a tidal gyre over the area (Guillou et al. 2018), characterized by anticlockwise currents. Moreover, Ehrhold and al. 2017 reported a circular sedimentary system around the Molene archipelago. This system could also connect the Haut Fond de Ouessant Bank with the Bank du Four through the Fromveur Channel. The signatures of eastward sediment transport from the eastern side of the bank are consistent with an outgoing sediment flux from the Haut Fond d'Ouessant through the Fromveur channel. The top of the bank does not show any superimposed structures, which is likely to be explained by the existence of large storm waves occurring on the Iroise shelf. The flow velocity on the seafloor under these waves could reach 0.8 $m.s^{-1}$, which is enough to remobilize sediment. These storms limit the aggradation at the top of banks, as described in some bank genesis models (Huthnance 1982a; Huthnance 1982b).

5 CONCLUSION

This study is focused on the morphological evolution of a submarine dune bank at intermediate depth, subject to strong tidal current and large storms. In 2015, it was composed of 137 dunes, localized on their flank and on a dune field directly to the north. These dunes had a migration rate around 6.8$m.y^{-1}$ between 2015 and 2019. They migrated in anticlockwise direction for the Western and SouthEastern parts, and both in anti-clock and clockwise directions (depending on the dune under consideration) for the NorthEastern part. We suggest that the migration directions are linked to the tidal residual current. A recent (Guillou and Chapalain 2018) revealed the existence of a tidal gyre over the Bank, in accordance with local hydrodynamics. The absence of dunes on the top of the Bank could be explained by the sediment remobilization process due to large storm waves that limits aggradation on the top (Huthnance 1982a; Huthnance 1982b). At the scale of shelf, the sand accumulation at the Eastern termination of the Bank allows transfer through the nearby Fromveur strait, suggesting a large sandy sediment recycling loop that connects several sand banks across the Iroise Sea.

ACKNOWLEDGEMENT

This work is supported by the UBS and the ARED UBO. The authors would like to give a special thanks to the crew on the Thalia during the Speedunes survey and the crew of the Bankable survey on the Cote de la Manche, in particular to Michel Lounge and

Alexandre Valance who joined the team on the Bankable survey.

6 REFERENCES

Allen, J. R. L. 1968. 'The Nature and Origin of Bed-Form Hierarchies'. *Sedimentology* 10 (3): 161–82.

Bajjouk, T., J. Duchêne, B. Guillaumont, M. Bernard, M. Blanchard, S. Derrien-Courtel, P. Dion, S. Dubois, J. Grall, and D. Hamon. 2015. 'Les Fonds Marins de Bretagne, Un Patrimoine Remarquable: Connaître Pour Mieux Agir. Édition Ifremer-DREAL Bretagne, 152 p'.

Berné, Serge, G. Allen, JEAN-PAUL Auffret, H. Chamley, J. Durand, and O. Weber. 1989. 'Essai de Synthèse Sur Les Dunes Hydrauliques Géantes Tidales Actuelles'. *Bulletin de La Societe Gèologique de France* 6: 1145–60.

Franzetti, Marcaurelio, Pascal Le Roy, Christophe Delacourt, Thierry Garlan, Romain Cancouët, Alexey Sukhovich, and Anne Deschamps. 2013. 'Giant Dune Morphologies and Dynamics in a Deep Continental Shelf Environment: Example of the Banc Du Four (Western Brittany, France)'. *Marine Geology* 346: 17–30.

Guillou, Nicolas, and Georges Chapalain. 2018. 'Annual and Seasonal Variabilities in the Performances of Wave Energy Converters'. *Energy* 165: 812–23.

Hinschberger, F. 1963. 'Les Hauts-Fonds Sableux de l'Iroise et Leurs Rapports Avec Les Courants de Marée'. *Bull. Sect. Géogr. Com. Trav. Hist. Scient.* 75: 53–80.

Homrani, Sabrina. 2020. 'Morphodynamique Des Dunes En Eau Peu Profonde et Transport Sédimentaire: Le Banc Du Creïzic (Golfe Du Morbihan)'. PhD Thesis, Brest.

Huthnance, J. M. 1982. 'On the Formation of Sand Banks of Finite Extent'. *Estuarine, Coastal and Shelf Science* 15 (3): 277–99.

Huthnance, John M. 1982. 'On One Mechanism Forming Linear Sand Banks'. *Estuarine, Coastal and Shelf Science* 14 (1): 79–99.

Kenyon, N. H., and A. H. Stride. 1970. 'The Tide-Swept Continental Shelf Sediments between the Shetland Isles and France'. *Sedimentology* 14 (3–4): 159–73.

Knaapen, M. A. F. 2005. 'Sandwave Migration Predictor Based on Shape Information'. *Journal of Geophysical Research: Earth Surface* 110 (F4).

Le Bot, Sophie. 2001. 'Morphodynamique de Dunes Sous-Marines Sous Influence Des Marées et Des Tempêtes : Processus Hydro-Sédimentaires et Enregistrement : Exemple Du Pas-de-Calais'. *Http://Www.Theses.Fr*. Thesis, Lille 1. http://www.theses.fr/2001LIL10016.

Mariette, V., G. Rougier, Jean-Claude Salomon, and B. Simon. 1982. 'Courants de Marée En Mer d'Iroise'. *Oceanologica Acta* 5 (2): 149–59.

'Service Hydrographique de La Marine (Ed.), 1957. Instructions Nautiques. France, Côtes Nord et Ouest, Impression Nationnale. Ed, Instrucutions Nautiques. Paris, France -

Trentesaux, Alain. 1993. 'Structure et Dynamique Sédimentaire Du Middelkerke Bank, Mer Du Nord Méridionale'. PhD Thesis.

Morphological and internal variability of sand banks on a macro tidal dispersive shelf

P. Daguinos *UMR 6538 GEO-OCEAN, UBO, UBS, CNRS, Ifremer, 29280 Plouzane, France– paul.daguinos@univ-brest.fr*
P. Le Roy *UMR 6538 GEO-OCEAN, UBO, UBS, CNRS, Ifremer, 29280 Plouzane, France– pascal.leroy@univ-brest.fr*
D. Menier *UMR 6538 GEO-OCEAN, UBO, UBS, CNRS, Ifremer, 56017 Vannes, France– david.menier@univ-ubs.fr*
N. Le Dantec *UAR 3113 IUEM et UMR 6538 GEO-OCEAN, UBO, UBS, CNRS, Ifremer, 29280 Plouzane, France– nicolas.ledantec@univ-brest.fr*
A. Ehrhold *UMR 6538 GEO-OCEAN, UBO, UBS, CNRS, Ifremer, 29280 Plouzane, France– axel.ehrhold@ifremer.fr*
G. Jouet *UMR 6538 GEO-OCEAN, UBO, UBS, CNRS, Ifremer, 29280 Plouzane, France– gwenael.jouet@ifremer.fr*
M. Franzetti *UMR 6538 GEO-OCEAN,* UBO, UBS, *CNRS, Ifremer, 29280 Plouzane, France*

ABSTRACT: We investigated the morphological and architectural variability of four sandbanks, from the same area, at intermediate depths (from 50 to 120m) along the continental shelf of Western Brittany (France) in the Iroise Sea, a dispersive shelf exposed to large storms. In order to identify the parameters controlling the variability of sandbanks morphologies and architectures, we analyzed geophysical data (seismic, reflectivity and bathymetry) from several oceanographic cruises. Preliminary results reveal internal architectures composed of 4 to 5 seismic units for each bank. They are interpreted as controlled by the stepwise flooding of the Armorican basement shelf during the last transgression. This igneous basement that outcrops on the seafloor up to 100m deep has constrained local tidal circulation and swell exposure during the progressive flooding of the shelf, which explains the very contrasting morphologies and internal architectures of these coeval banks on the Iroise Sea shelf.

INTRODUCTION

Sandbanks are the main sedimentary bedforms on the median continental platforms. Understanding their formation, their evolution and their role as shelf sedimentary pathway is crucial for many applications such as the control and the exploitation of marine resources or the protection of marine species (Trentesaux 1993; Bajjouk et al. 2015). Numerous studies performed on these structures have brought a solid knowledge base on the sedimentary processes at play in their genesis and morphodynamics (Berné et al. 1989; Berne 1999; Trentesaux 1993; Mhammdi 1994; Lericolais 1997; Marsset et al. 1999; Le Bot 2001; Bastos, Collins, and Kenyon 2003; Ferret 2011; Vecchi et al. 2013; Franzetti 2014; Traoré et al. 2021). But most of these studies were conducted in areas either deeper or shallower than the intermediate depth area due to the difficulty to collect accurate morphodynamic data at this 50 to 120m depth range. The objective here is to highlight the parameters controlling the morphological and internal variations between four banks located on a dispersive shelf with a low sediment rate subject to large storms. To this end, we analysed geophysical data (seismic, reflectivity and bathymetry) from several oceanographic cruises (Geobrest, Sisplateau, SpeedDunes, Bankable and Sabaseti). This study also presents the first detailed description of the Pierres Noires Bank since it was identified (Hinschberger and Pauvret 1968).

1 STUDY ZONE

The Iroise Sea shelf (fFig. 1) is located in the Western Brittany (France). This highly dispersive platform is delimited by the Pointe du Raz and the Raz de Sein at the South, the Molene archipelago at the North and the Rade de Brest at the East. The tide is semi-diurnal with tidal range variation from 3 to 6 meters (macrotidal) between flood and ebb (Mariette et al. 1982). The hydrodynamic conditions are directly impacted by the English Channel's discharge (Kenyon and Stride 1970) due to the position of the shelf at the confluence of the Atlantic Ocean and English Channel. The Iroise Sea is also particularly exposed to large storms. The shelf presents a very limited sediment cover mainly composed of biogenic sediments. Between -50 and -120m, the shelf hosts 4 large sandbanks considered as banner banks (10 to 50 sq. km, *Four* Bank, *Armen* Bank, *Pierres Noires* Bank, *Haut Fond de Ouessant* Bank), all having their base at the same depth around 90 meters, and showing very contrasted morphologies.

The *Four* Bank is located between the coast and the Ouessant Island, in the north part of the shelf, with a size of 12 by 10 km for 45 meters high. This is the most studied of the four banks, with more than 10 years of bathymetric monitoring. The *Haut Fond de Ouessant* Bank is located at the south of the Ouessant Island and at the south-western end of the Fromveur channel. This bank has a size of 5 by 2 km and is more than 45 meters high.

The *Pierres Noires* Bank, located at the south of the *Haut Fond de Ouessant* Bank

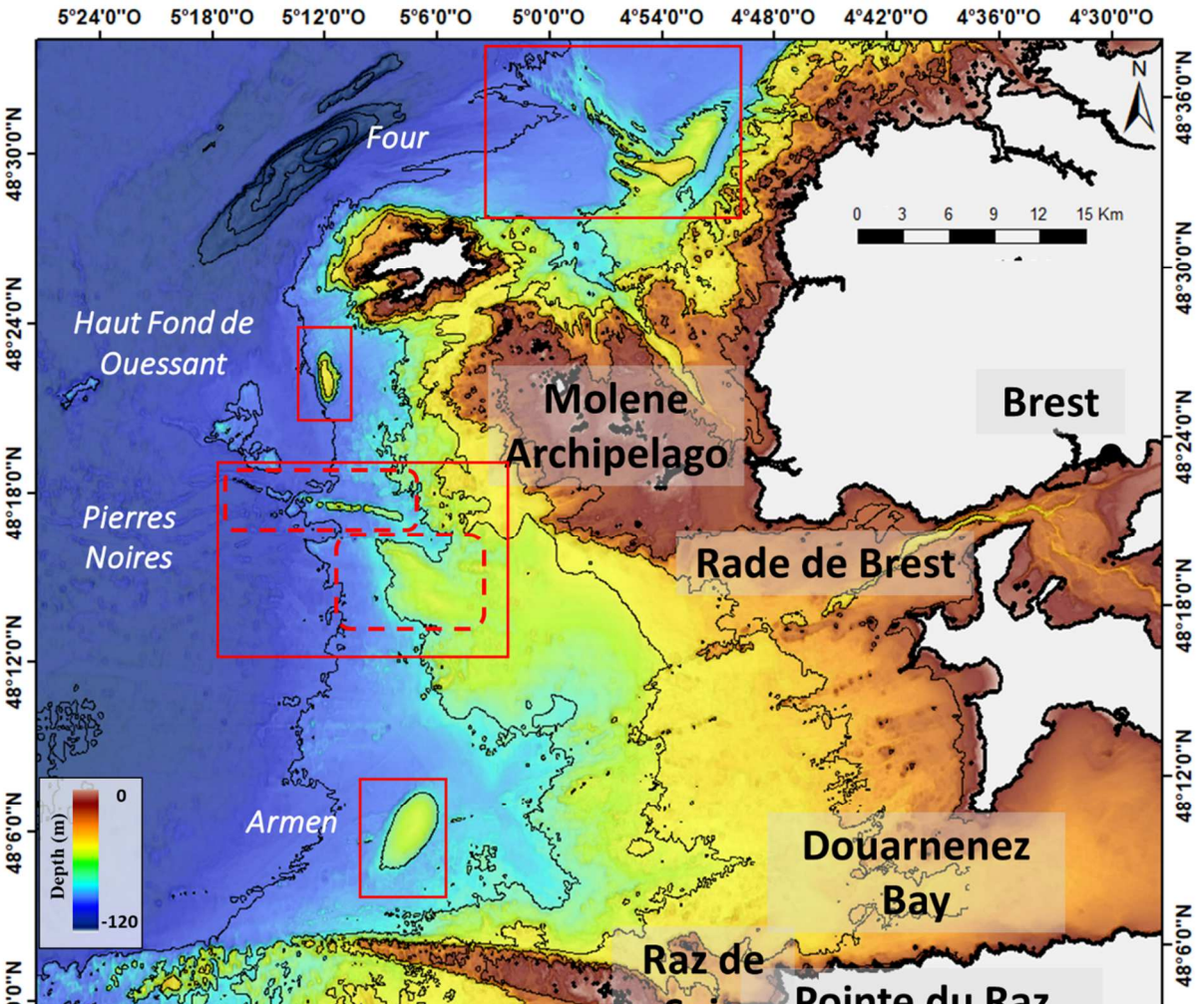

Figure 1: Localisation of the Banks (red squares) on the Iroise Sea shelf, showing the bathymetry, (insert: localisation of the Iroise Sea).

and at the South west of the Molene archipelago is a composite system comprising two contrasted parts. The first one to the north exhibits a quite spectacular elongated shape (13 by less than 1 kilometer). The second component was discovered recently and is reported for the first time in this study. It is larger than the first one and reveals a diffuse, non-ellipsoidal morphology (6 by 6 km, elevation 30m), with edges that are not so well-marked, especially on the eastern side that lies over a slightly steeper seafloor area.

Table 1: Marine seismic acquisitions

Missions	Years	Materials
GEOBREST	2011	Sparker monotrace
GEOBREST	2012	Sparker monotrace
GEOBREST	2013	Sparker monotrace
GEOBREST	2014	Sparker monotrace
GEOBREST	2019	Sparker monotrace
SISPLATEAU	2015	Sparker monotrace
SPEEDUNE	2015	Sparker multitrace HR
BANKABLE	2019	Sparker monotrace / multitrace HR
SABASETI	2023	Sparker monotrace

Armen Bank, located at the north of the Raz de Sein and the south of the Banc des *Pierres Noires* measures 8 km long for 5 km large and 20 m high.

3 MATERIALS AND METHODS

The dataset used for this study consists of a large panel of seismic lines acquired during research cruises (Table 1).

The dataset was corrected manually for tide, wave, and offset depending of the parameters of acquisition. The lines were interpreted on IHS Kingdom Suite software.

4 RESULTS AND DISCUSSIONS

4.1 Bathymetric observations

The bathymetric dataset analysis shows significative variations of basement morphologies over the intermediate depth range (50 to 120 m) where the banks are located. Four domains are distinguished. For water depths larger than 110m, the shelf is relatively flat with a slope gradient below 0.1%. From 90 to 110m depth, the slope gradient rises up to 2% and delineates a morphological step corresponding to the edge of the Cenozoic and Mesozoic basement cover. The four Banks are located on the inflexion point at the top of this domain. The step, from 60 or 70 to 90 meters is a domain with rough seafloor where no sediment seems to be accumulated. It is bounded to the top by another flat domain at about 60m (slope gradient << 1%) where large bedforms are absent. The four banks are surrounded by rocky reefs, and have been anchored essentially along this internal shelf break.

The morphology of the platform suggests the existence of a paleo embayment at about -90 m below present sea-level. It could have featured an initial stage where the four banks (*Armen, Ouessant and Pierres Noires*) may have been connected into a large coastal sand system. A residual continuous sandy belt is still identified at this depth range. Fluvial incisions connected to the inner shelf and terminating at the base of the banks are also identified, and could have contributed to sediment preservation during the nucleation phase of the banks.

4.2 Seismic observations

Seismic lines recorded along the banks reveal an internal architecture composed of 5 seismic units identified for each bank. The first unit is described with a strong amplitude seismic response, a thickness around 8m and a polarity toward the coast. The tops of these basal units of the four banks are at the same depths, about 85 meters.

The second units also have a comparable size between the banks, with the same erosive top discontinuity at a depth around 75 meters.

The top of units 3 and 4 are less visible than for units 1 and 2. Unit 5 highlights a currently active dune system on the banks.

4.3 First interpretations

The evolution of the bank is analyzed using the changes in polarity of the seismic units over time. The aggradation of Armen bank is associated with progradation from SouthWest to NorthEast. The basal unit of Haut Fond de Ouessant unit is located at the South West of the Bank, and the overall polarity of the Bank is in West SouthWest direction. The elongated shape of Pierres Noires Bank is first oriented in eastern direction for the basal unit, then in South western direction for unit 2, whereas the other units are oriented in South direction.

The basal units 1 and 2 are interpreted as residual estuarine or fluviatile deposits, maybe paleoshoals, and we suggest a non-bioclastic sediments composition, as the bank du Four (Franzetti 2014).

All these morphological variations seem to be controlled by two major factors: the shelf morphology and the flooding of the continental shelf, which are closely linked and are thought to have led to major local hydrodynamic variations on the Iroise shelf. Today, the tidal gyres that are present over the Haut Fond de Ouessant and Armen Banks explain the current morphodynamics on these banks. Pierres Noires Bank, at the confluence of the two gyres, also seems to be also controlled by these tidal gyres. They provide both sediment supply and oblique directions of the hydrodynamic currents, the later favoring the steep and elongated morphology of the bank, comparable to morphology of a linear dune.

5 CONCLUSIONS

Two main factors affect the formation of the banks and explain the visible and synchronous morphological and internal variations in the banks: the basement morphology and the flooding of the platform. These factors are linked and have given rise to changes from a local to a regional scale the shelf hydrodynamics.

-Sand Banks are localised at the same depth around 95 meters. This depth corresponds to a morphological step in the basement, which is thought to have stopped the progradation of the banks toward the coast in their early stages. The analysis of the bathymetry suggests the existence of a paleo embayment where the banks South of Ouessant were connected. Fluvial incisions on the inner shelf could be also a control factor.

-The flooding of the shelf affected the banks directly through the modification of regional hydrodynamic conditions, both in tidal currents and in the impact of storms. Local changes in hydrodynamic conditions most likely also occurred as indirect effects of the flooding of the shelf, in relation to the flooding of rocky reefs and inner shelf incisions.

6 ACKNOWLEDGEMENT

This work is supported by the UBS and the ARED UBO. The authors would like to give a special thanks to the crews of each marine survey who participated to the acquisitions of the dataset, in particular to Michel Lounge and Alexandre Valance who joined the team on the Bankable survey (2019).

7 REFERENCES

Bajjouk, T., J. Duchêne, B. Guillaumont, M. Bernard, M. Blanchard, S. Derrien-Courtel, P. Dion, S. Dubois, J. Grall, and D. Hamon. 2015. ‘Les Fonds Marins de Bretagne, Un Patrimoine Remarquable: Connaître Pour Mieux Agir. Édition Ifremer-DREAL Bretagne, 152 p’.

Bastos, Alex C., Michael Collins, and Neil H. Kenyon. 2003. ‘Morphology and Internal Structure of Sand Shoals and Sandbanks off the Dorset Coast, English Channel’. *Sedimentology* 50 (6): 1105–22.

Berne, Serge. 1999. 'Dynamique, Architecture et Préservation Des Corps Sableux de Plate-Forme'.

Berné, Serge, G. Allen, JEAN-PAUL Auffret, H. Chamley, J. Durand, and O. Weber. 1989. 'Essai de Synthèse Sur Les Dunes Hydrauliques Géantes Tidales Actuelles'. *Bulletin de La Societe Gèologique de France* 6: 1145–60.

Ferret, Y. 2011. 'Morphodynamique de dunes sous-marines en contexte de plate-forme mégatidale (Manche orientale). Approche multi-échelles spatio-temporelles'. Phdthesis, Université de Rouen. https://tel.archives-ouvertes.fr/tel-00687085.

Franzetti, Marcaurelio. 2014. 'Dynamique Des Bancs et Dunes Sableuses de Plateforme En Contexte Macrotidal : L'exemple Du Banc Du Four (Ouest Bretagne)'.

Hinschberger, Félix, and Rose-Blanche Pauvret. 1968. 'Les Fonds Sous-Marins de l'Iroise et de La Baie de Douarnenez (Finistère). Reconstitution d'un Réseau Hydrographique Immergé'. *Norois* 58 (1): 213–25.

Kenyon, N. H., and A. H. Stride. 1970. 'The Tide-Swept Continental Shelf Sediments between the Shetland Isles and France'. *Sedimentology* 14 (3–4): 159–73.

Le Bot, Sophie. 2001. 'Morphodynamique de Dunes Sous-Marines Sous Influence Des Marées et Des Tempêtes : Processus Hydro-Sédimentaires et Enregistrement : Exemple Du Pas-de-Calais'. *Http://Www.Theses.Fr*. Thesis, Lille 1. http://www.theses.fr/2001LIL10016.

Lericolais, Gilles. 1997. 'Evolution Plio-Quaternaire Du Fleuve Manche : Stratigraphie et Géomorphologie d'une Plateforme Continentale En Régime Périglaciaire'. These de doctorat, Bordeaux 1. https://www.theses.fr/1997BOR10672.

Mariette, V., G. Rougier, Jean-Claude Salomon, and B. Simon. 1982. 'Courants de Marée En Mer d'Iroise'. *Oceanologica Acta* 5 (2): 149–59.

Marsset, Tania, Bernadette Tessier, J.-Y. Reynaud, Marc De Batist, and Clara Plagnol. 1999. 'The Celtic Sea Banks: An Example of Sand Body Analysis from Very High-Resolution Seismic Data'. *Marine Geology* 158 (1–4): 89–109.

Mhammdi, Nadia. 1994. 'Architecture du banc sableux tidal de Sercq (Iles Anglo-Normandes)'. Université des sciences et technologies de Lille. https://archimer.ifremer.fr/doc/00034/14501/.

Traoré, Kalil, David Menier, Erwan Gensac, Pascal Le Roy, Clément Lambert, Paul Bessin, Kevin Pedoja, Anne Duperret, and Romain Le Gall. 2021. 'Evolution of a Holocene Banner Bank Controlled by Morphodynamics and Structural Setting of a Macrotidal Coast: Saint-Brieuc Bay (NW-Europe)'. *Geoscience Frontiers* 12 (5): 101183.

Trentesaux, Alain. 1993. 'Structure et Dynamique Sédimentaire Du Middelkerke Bank, Mer Du Nord Méridionale'. PhD Thesis.

Vecchi, Laura G., Salvador Aliotta, Silvia Susana Ginsberg, and Darío A. Giagante. 2013. 'Morphodynamic Behavior and Seismostratigraphy of a Sandbank: Bahía Blanca Estuary, Argentina'. *Geomorphology* 189 (May): 1–11. https://doi.org/10.1016/j.geomorph.2013.01.003.

Episodical sand wave migration: analysis of high temporal resolution bathymetry

J.H. Damveld *University of Twente, Enschede, Netherlands – j.h.damveld@utwente.nl*
R. van der Meijden *University of Twente, Enschede, Netherlands*
B.W. Borsje *University of Twente, Enschede, Netherlands*
S.J.M.H. Hulscher *University of Twente, Enschede, Netherlands*

ABSTRACT: In this work we present the analysis of a dataset containing high temporal and spatial bathymetric data. The data consists of several survey lines, of which a spatial overlap of around 30 meters can be used the determine sand wave migration. The interval between the survey lines varies between days and months. A lowpass filter is applied to the raw data to separate the superimposed megaripples from the sand waves, and subsequently the peaks have been determined by calculating the peak prominence. Overall the data shows a low average migration rate, but locally high variations are observed. Moreover, bidirectional migration is visible on the slopes of sand banks. The high spatial resolution also reveals the presence of megaripples on practically all stoss slopes of the sand waves, in contrast to the smooth lee slopes. Altogether, this dataset shows the unique potential for analysing the episodical nature sand wave migration.

1 INTRODUCTION

The seabed of coastal shelf seas, such as the North Sea, consist of various rhythmic bed patterns (Figure 1). Sand banks, oriented parallel to the main tidal current, have spacings of kilometres and heights of tens of metres. Sand waves, oriented perpendicular to the tidal current, are smaller with spacings of hundreds of meters and heights up to 10 metres. In particular these sand waves are relevant for offshore engineering as, on average, they migrate several metres per year (van der Meijden et al, 2023), thereby exposing cables/pipelines and other objects on the seafloor. It is therefore essential to understand their dynamic behaviour in order to realistically predict the dimensions and migration rates of sand waves.

The migration of sand waves is usually determined by measuring the horizontal displacement taken from seabed surveys. However, as these surveys generally have intervals of several years, short-term variability, triggered by e.g. storm events, is not captured in the data. In the scarcely available data that have a high temporal

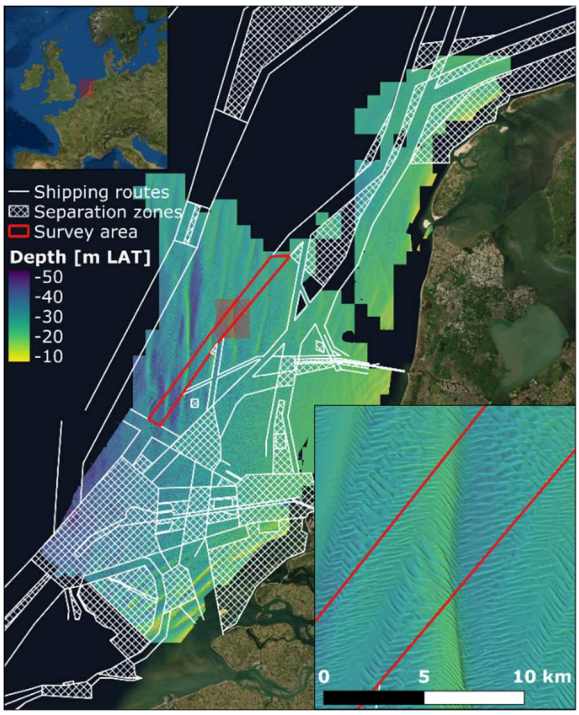

Figure 1. Bathymetric chart showing sand waves and sand banks of the Netherlands Continental Shelf. Data from the Dutch Hydrographic Service.

resolution (e.g. van Dijk et al, 2005), striking nonlinear effects (negative migration, shape changes, flattening) are observed after storms. In an effort to quantify the role of wind and wave processes on sand wave migration, Campmans et al (2018) developed a nonlinear sand wave model containing many important wave-related processes. They found that wind and waves may enhance sand wave migration and its temporal variability. However, they focussed on the long-term (annual – decadal) effects on sand wave migration. Hence, the effect of episodical events on the short-term variability of the seabed remains unclear.

In order to quantify this effect, there is a need for high quality bathymetric data, with a temporal resolution on the order of weeks to match the timescale of these episodical events. At the same time, the spatial resolution must be sufficiently high to allow for migration to be measured, as this can be expected to be on the order of meters between surveys. For practical reasons, seabed surveys (see e.g. the surveyed shipping lane in Figure 1) usually span over a long period of time. It is common practise to average the collected data (survey lines) to a single bathymetric map with a single timestamp, such that seabed changes within that period of time are lost. Analysis of this raw, non-averaged, data can thus reveal the seabed dynamics we are interested in.

Recently, the Dutch Hydrographic Service completed a survey of a shipping lane in the North Sea. As the total survey spans over more than half a year with varying intervals, this dataset is perfectly suited to analyse the episodical nature of sand wave migration. In this work, we aim to highlight the unique potential of this dataset. To this end, we will use the first and last survey lines as they can be expected to show the highest variations in migration. In our analysis we will further relate the dynamics of sand waves to bed forms of both larger (sand banks) and smaller (megaripples) spatial scale.

2 DATA AND METHODS

2.1 Location and survey data

The analysis in this work focusses on a shipping lane in the southern North Sea, roughly 75 km off the coast of the Netherlands (Figure 1). The total survey area is 90 km long and 4 km wide. The average depth in the area in 30 metres, but large variations are observed due to the presence of several sand banks, such as the Brown Bank.

The data has been collected by the Dutch Hydrographic Service using the vessel HNLMS *Luymes*, equipped with multibeam echosounder (MBES), measuring with a resolution of 1 m. The total time span of the survey is around 9 months (09/04/2021 – 16/01/2022), divided into 24 different survey days. Each day represents a single survey line within the dataset. In particular the spatial overlap between the survey lines is of interest as they can be used to reveal the seabed dynamics. Of the potential areas of overlap, 12 lines have an overlap of only a few days, 7 lines have an overlap of a few weeks and 9 lines have an overlap of at least 2 months.

For this work we focus on the overlap of day 4 (01/06-2021) and day 23 (15/01-2022), representing an interval of 7.5 months. Figure 2 shows a zoom the two survey lines, including the overlap, and the profile (red line) along which the data has been extracted. The overlap is around 20 to 30 metres wide, such that there is only a small part of the data left for the analysis, and , hence, only a 2D analysis can be performed.

2.2 Postprocessing of profile data

Several postprocessing steps have been taken before the data was ready for the analysis. Below these steps are explained.

2.2.1 Regridding

The data has been regridded twice. The first is to a resolution of 10 m (as in Figure 2), merely for supporting the operation of the heavy dataset (25 GB per survey line). This subset was used to determine the overlap and

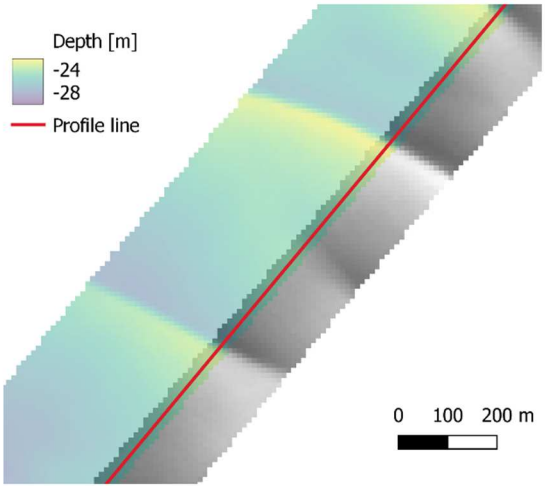

Figure 2. Two survey lines, with one survey line depicted using a grey colour scale. The overlap is visible from the transparency of both layers.

to acquire the coordinates of the profile line. The second is to a resolution of 1 m, since the data along the profile line had a varying resolution due to the slightly varying orientation of the survey area. The constant resolution was needed for the correct application of the lowpass filter. Moreover, some datapoints were missing as at some locations the profile line did not fully overlap with the survey lines.

2.2.2 Separating megaripples

Analogous to van Dijk et al (2008), we applied a lowpass filter to separate superimposed megaripples from the sand waves. Hereto, the sand wave signal is described as a Fourier series, where the resulting (groups of) frequencies (i.e. wavenumbers) can be attributed to a different bed form type. We have used a cut-off frequency of 40 metres to separate the signal, meaning that only bedforms of higher wavelength are used in the analysis of sand wave migration.

2.2.3 Determination of peaks

For the current analysis, we have chosen to apply the tracking of sand wave crests for the determination of sand wave migration. To determine the peaks in the dataset, we applied the *findpeaks* function from the Matlab 2023 Signal Processing Toolbox. It uses the concept of peak prominence, which measures the intrinsic height and location relative to the surrounding peaks. This method yielded a slightly different number of peaks for both survey lines due to some peaks not meeting the minimum prominence value of 1 m. Hence, subsequently all peaks in both survey lines were matched to their counterpart, and orphan peaks were deleted.

3 RESULTS

Both profiles are shown in Figure 3a, including their selected peaks. A zoom of the area is given in Figure 4, clearly displaying the dynamics of the seabed profile. The migration (horizontal displacement) of the peaks is shown in Figure 3b. It appears that locally relatively high migration rates are visible, and that there is no clear trend in direction visible along the survey area. The average migration for the whole area is 0.5 m/year, with a standard deviation of 9 m/year, which is again a clear indication of the high variation in migration over the area.

Compared to literature, the absolute migration rates at some locations are high. This is supported by the shape of the sand waves (see Figure 4), which are highly asymmetrical, indicating migration in the direction of the steep slope. However, the high migration rates may also arise from the presence of lower frequencies that are not fully filtered out, which can be attributed to superimposed megaripples. As can be see from the first peak in Figure 4, the peak detection suggests migration in negative x-direction, whereas the remainder of the profile indicates the opposite. This clearly shows that the migration detection for this particular sand wave is subject to the method and should be treated carefully. This will be further discussed in Section 4.

Although no overall trend in migration direction is visible from the data in Figure 3b, there is a relation visible with larger-scale bathymetry. Here, the black line denotes the smoothed bed profile of the area, of which the local slope is calculated for the peak locations. To highlight this relation, these

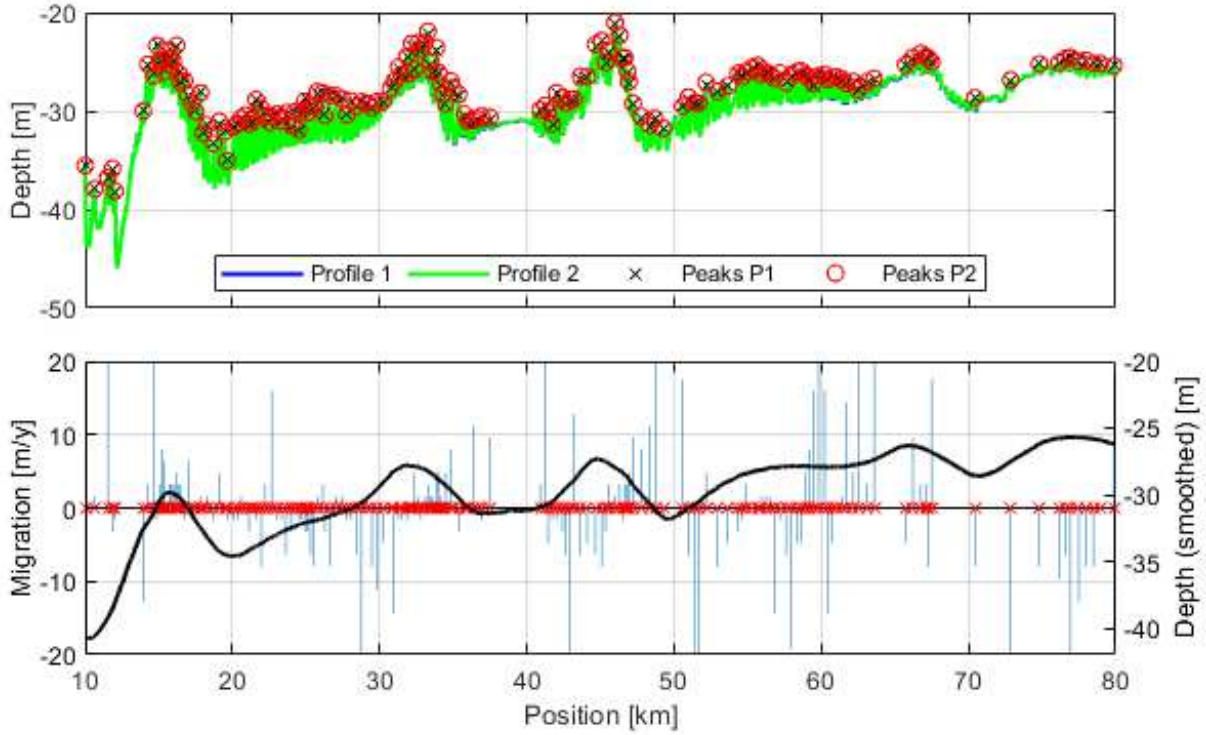

Figure 3. Top: Analysed profile line with their selected peaks. Bottom: the bars denote the migration (horizontal displacement) of the peaks. The red crosses denote all peaks, as some of the peaks did not display any migration. The black line is the smoothed profile used to isolate the underlying topography.

slopes are plotted as a function of the migration rates of the peaks. Although there is a large scatter present in the data, a negative relation is visible between background slope and migration. This observation is related to the bidirectional migration over sand waves (e.g. Zhou et al, 2021, van der Meijden et al, 2023). Note that in this 2D analysis this appears to be migration towards the sand bank crest, whereas from 3D analysis this is known to be more oblique to the sand bank crest.

4 DISCUSSION

We have presented a unique dataset containing bathymetric data of high resolution in both time and space. Such a dataset allows for analysis of the episodical nature of sand wave migration, caused by e.g.

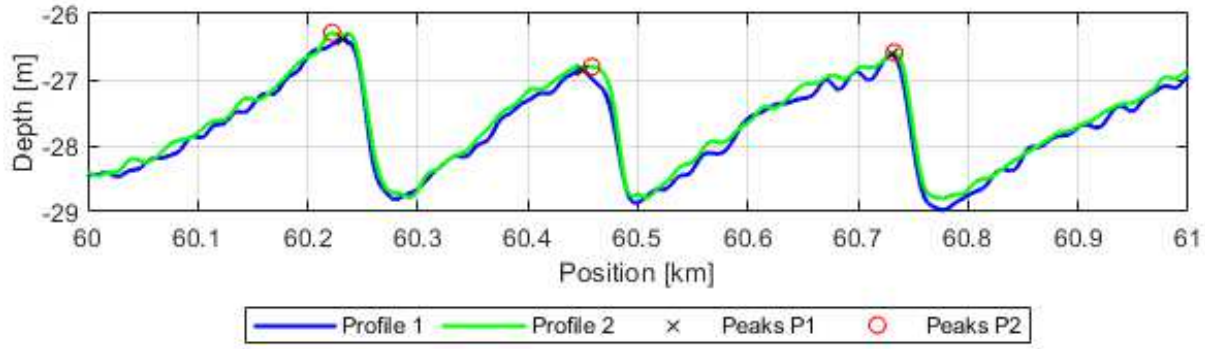

Figure 4. Zoom of figure 3a, clearly showing sand wave both profiles and their peaks.

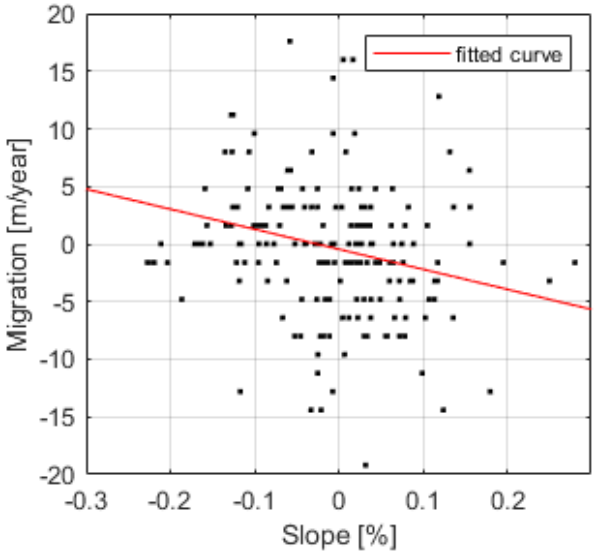

Figure 5. Slope of background topography versus sand wave migration.

storm events. In this work the two surveys lines with the largest temporal overlap have been used, and they clearly show the dynamics of the seabed. Even on such a short interval the migration rates are significant, highlighting the need for high temporal analysis.

No clear trend in migration direction and rate could be determined along the profile. However, the high variation of these indicators suggests that the migration is (partly) caused by an infrequent (strength, location, duration) forcing mechanism. Further analysis of data with smaller temporal overlap, and correlating these results to local wave data should reveal the actual cause for these dynamics. Another indicator which should also be analysed is the shape of the sand wave, which is know to be influenced by storms (van Dijk et al, 2005). For this at least the troughs locations should be determined as well, although a combination with a spatial cross correlation method (e.g. Duffy and Hughes-Clarke (2005)) may yield even better results, as the whole profile is used in the analysis.

Another advantage of using spatial cross correlation, is that the effects of noise from smaller scale bed forms, such as megaripples, may be suppressed. As shown in Figure 4, the presence of smaller features on top of the sand wave may influence the detection of the crest in a negative manner. Using a higher cut-off frequency in the Fourier analysis does not lead to improved results, and may even affect the frequency on which sand waves appear. Other methods that have been tested are a Butterworth filter (see also van Dijk et al, 2008) and fitting a higher order polyline through the data. All these methods did not lead to improved results. Another potential improvement could be to apply these filters on subsets of the data, where the subsets would be selected based on sand waves of comparable morphometric properties, similar to the procedure in van der Meijden et al (2023). Especially in case of analysing the survey lines with shorter time intervals, it is required to decrease the error margin in the methodology as much as possible, as the expected migration rates will also decrease.

The potential presence of superimposed ripples on sand waves is something which is widely known, and has been discussed in literature on multiple occasions (e.g. van Dijk et al, 2005, Damveld et al, 2018). The latter even highlighted the spatial dependence of these megaripples over sand waves, although this was only for a single sand wave and they focussed only on crest versus trough. In the data presented in this work these megaripples are shown to be present on a much wider scale, i.e. on nearly all sand waves in the 280 km^2 survey area. In particular, they consistently occur on the stoss slope, whereas the lee slope is much smoother. As pointed out by Damveld et al (2018), it is important to include such insights in morphodynamic models predicting sand wave dynamics, as these imply a strong spatially varying form roughness, which, in turn, will significantly affect sediment transport predictions. Supporting this statement on a much wider spatial scale, this work once again highlights the need for including spatially varying roughness elements in sand wave modelling studies.

5 CONCLUSIONS

In this work we have shown the potential of high temporal and spatial bathymetric data to be used for the detection of sand wave migration on short timescales. Overall the data reveals a low average migration and no clear trend in direction, but locally high variations are observed. Moreover, bidirectional migration is visible on all sand banks.

The high spatial resolution also reveals the presence of megaripples on practically all stoss slopes of the sand waves, in contrast to the smooth lee slopes. This emphasize the importance of resolving spatially varying roughness elements in morphodynamic sand wave models.

6 ACKNOWLEDGEMENTS

This work is part of the Footprint project, funded by the Dutch Research Council Science (NWO). We would also like to thank Noortje ten Broeke of the Dutch Hydrographic Service, who prepared and provided the raw data.

7 REFERENCES

Campmans, G. H. P., Roos, P. C., de Vriend, H. J., & Hulscher, S. J. M. H. (2018). The influence of storms on sand wave evolution: a nonlinear idealized modeling approach. Journal of Geophysical Research: Earth Surface. doi:10.1029/2018JF004616

Damveld, J. H., van der Reijden, K. J., Cheng, C., Koop, L., Haaksma, L. R., Walsh, C. A. J., Soetaert, K., Borsje, B. W., Govers, L. L., Roos, P. C., Olff, H., & Hulscher, S. J. M. H. (2018). Video Transects Reveal That Tidal Sand Waves Affect the Spatial Distribution of Benthic Organisms and Sand Ripples. Geophysical Research Letters, 45(21), 11837-11846. doi:10.1029/2018gl079858

van Dijk, T. A. G. P., & Kleinhans, M. G. (2005). Processes controlling the dynamics of compound sand waves in the North Sea, Netherlands. Journal of Geophysical Research: Earth Surface. doi:10.1029/2004JF000173

van Dijk, T. A. G. P., Lindenbergh, R. C., & Egberts, P. J. P. (2008). Separating bathymetric data representing multiscale rhythmic bed forms: A geostatistical and spectral method compared. Journal of Geophysical Research: Earth Surface, 113(F4). doi:10.1029/2007JF000950

Duffy, G. P., & Hughes-Clarke, J. E. (2005). Application of spatial cross correlation to detection of migration of submarine sand dunes. Journal of Geophysical Research: Earth Surface, 110(F4). doi:10.1029/2004JF000192

Van der Meijden, R., Damveld, J. H., Ecclestone, D. W., Van der Werf, J. J., & Roos, P. C. (2023). Shelf-wide analyses of sand wave migration using GIS: A case study on the Netherlands Continental Shelf. Geomorphology, 424, 108559. doi:10.1016/j.geomorph.2022.108559

Zhou, J., Wu, Z., Zhao, D., Guan, W., Cao, Z., & Wang, M. (2022). Effect of topographic background on sand wave migration on the eastern Taiwan Banks. Geomorphology, 398, 108030. doi:10.1016/j.geomorph.2021.108030

Deep Learning: A new tool for mapping and analysis dunes (e.g. Rub'Al Khali sand sea)

J. Daynac *UMR 6112 LPG, Le Mans, France – jimmy.daynac@univ-lemans.fr*
P. Bessin *UMR 6112 LPG, Le Mans, France – paul.bessin@univ-lemans.fr*
S. Pochat *UMR 6112 LPG, Nantes, France – stephane.pochat@univ-nantes.fr*
R. Mourgues *UMR 6112 LPG, Le Mans, France – regis.mourgues@univ-lemans.fr*

ABSTRACT: Aeolian dunes are bedforms of great scientific interest because their morphological characteristics (e.g. shape, size, spatial organization) depend on the physical characteristics of i) the moving fluid (e.g. velocity, direction of movement, viscosity), ii) the available sedimentary stock (e.g. density, shape, grain size). Mapping and morphometric analysis of these bedforms can provide elements to understand their formation processes. We developed a mapping protocol based on a Deep Learning approach and automatic tools to digitize their outline and mean crestline. The protocol shows the ability to produce a large numerical database of a dune field (e.g. Rub'Al Khali) that can be used to analyse several form parameters.

1 INTRODUCTION

The surface of some planet's present abundant periodic topographic forms at different scales (mm- km) in different environments called bedforms. These bedforms develop at the interface between the moving fluid and a deformable and/or erodible material. The aeolian bedforms result from wind action mainly in deserts, coastal areas (Pye and Tsoar, 2009; Zheng et al., 2022). Sand dunes correspond to a major bedforms type in aeolian systems and play an important role in understanding how aeolian environments evolve. They are described as aeolian sand mounds or ridges that exist independently of surrounding topography whether slipfaces are visible or not (Bagnold, 1974).

Generally, the dunes are grouped in field and sand seas. Their morphological characteristics (e.g. shape, size, spatial organization) play a critical role in understanding how aeolian environments evolve and interact with global changes (Thomas and Wiggs, 2008; Zheng et al., 2022).

The wide spatio-temporal coverage of satellite imagery and high-resolution digital terrain models are used to estimate and map the evolution of dunes on large-scale investigations. A large-scale dune mapping would provide a digital atlas to characterize variable sand dune morphologies that are crucial indicators of complex and evolving wind processes. In this work, we propose an automatic method of aeolian dunes mapping from DEM based on a Deep Learning approach which allows an instantaneous, massive and integrated extraction of several geometrical properties of each dune - from metric to regional scale.

The prevailing strategy is to extract the Residual Relief (RR, Hillier and Smith, 2008) in order to delete the regional topographic trend and map the different dune generations. Secondly, an unsupervised pixel-based classificator (Deep Learning – U-Net (Shumack et al., 2020)) trained with RR samples of different dune forms is used to detect and map dunes independently of the bedrock. Finally, the crestline of the sand dunes is skeletonized from the identification of high inflection point of the dunes with a Volumetric Obscurance approach (Rolland et al., 2022). The complex morphologies with

various forms are individualized according to the neighborhood relationships of the dune forms and crest.

To illustrate the method performance, the protocol is applied on a part of the Rub'Al Khali (660,000 km²) sand sea to map the various dune forms and extracts their crestlines. Then, we use this large digital database to illustrate an example of morphometric application by calculating basic geometrical properties (length, width, height of dunes and crestlines orientation).

2 NUMERICAL DUNE DEFINITION

Sand seas are the fullest expression of aeolians landscapes, being defined by a variety of shapes in which sand grains have accumulated by wind to make sand mounds called "dunes" (Livingstone and Warren, 2019; Lorenz and Zimbelman, 2014). The overall forms of dunes depends on the wind speed in the area, the duration of sand-transporting winds, the direction of the wind speed, the duration of sand-transporting winds, the direction of the winds and their variability (Blumberg, 2006; McKee, 1979).

Many freely available land surface remote sensing data provide a large dataset of high-resolution imagery and digital elevation models (DEMs). These latter are widely used for aeolian systems investigation because of : i) their large spatial coverage (covering all major dune fields in the world) and ii) their always increasing spatial resolution (Hugenholtz and Barchyn, 2010). Dunes can be interpreted on DEMs as three-dimensional bedforms characterized by high inflection points (dune crests) and low inflection points (dune base – dune shape) whether their slipfaces are visible or not (Fig.1).

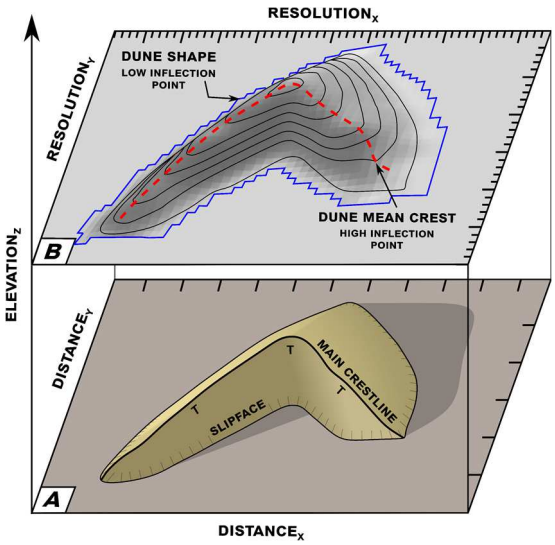

Figure 1. Dune definition. A. Naturalist representation of dune based on Bagnold (1974) descriptions. B. Numerical representation of a dune on a DEM as a 3D bedforms defined as high (dune crest) and low (dune shape) inflection points.

3 MAPPING PROTOCOL

3.1 Extracting and sampling Residual Relief

Dune fields and sand seas show superimposed generations of dunes (m to km-scale) producing complex topographic signal on DEMs (Fig.2). Each dune scale patterns can be examined independently if the topographic signal is disentangled (Hugenholtz and Barchyn, 2010).

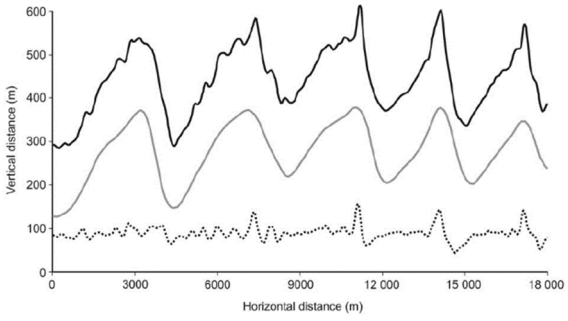

Figure 2. An example of Residual Relief separation showing discrimination of different dune generations. The original surface (black line), the Residual Relief of the medium-scale dunes (dotted black line), and the Residual Relief of small-scale dunes (grey line) (Hugenholtz and Barchyn, 2010).

Our strategy is to separate and isolate the different dune scales in order to highlight the aeolian dune patterns in dune field. For this, we calculated the Residual Relief (Hiller and Smith, 2008) on 100 training samples that are then used as learning data to map the dune shapes. Each sample represent a DEM on which dunes are identified (Fig.3A). These samples are selected from four arid regions and cover a large range of dune types (barchanoid, star, dome, linear and complex dunes). For this first development, we have avoided dune classifications to simplify mapping and interpretation. Dunes outlines were digitized manually on a GIS software and labelled as "ground truth" for the next step (Fig.3B).

3.2 Forms dunes recognition with Deep Learning

In this step, we used a Deep Learning algorithm as an unsupervised pixel-based classificator to form a mapping model of the aeolian dunes shape (Shumack et al., 2020).

All 100 residual relief samples from the DEMs were used by the algorithm as training data. First, the pixels DEM are convolved. At each convolution, for each DEM pixel that is located in a sliding matrix or kernel, the pixel values are multiplied by the kernel values. The sum of the matrices products generates an image of smaller dimension for which the maximum pixel values contained in the ground truth mask labelled are considered as "dune".

After the convolution, a max-pooling operation is used to retain the maximum values associated with the pixel labeled as "dune". All max pooling operations are subsequently reversed by a series of transposed convolutions, ending with an image matching the original input size (Ronneberger et al., 2015; Shumack et al., 2020). Lastly, the different convolutional steps are concatened and subject to more convolutions. The last step consists to use an activation function allowing to create a mapping model in which, each pixel corresponding to the dunes on an analyzed DEM is predicted and assigned by a "dune" class (Fig.3C).

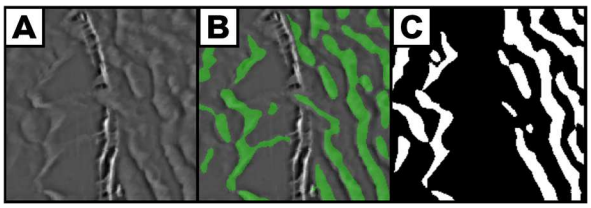

Figure 3. An example of mapping after the unsupervised classificator training on a DEM sample. A. Residual Relief. B. "Dune" ground truth mask manually digitised and used for the unsupervised classificator training. C. Output map after model calculation. The white area corresponds to automatically mapped dunes.

The accuracy assessment of our mapping model is performed on 20% of the training samples randomly selected as a validation subset. After the learning, the mapping model is evaluated with the classical metric: precision, recall and quality (Bianchi et al., 2021; Lewington et al., 2019; Telfer et al., 2015). These metric equations are based on the overlap prediction of the validation subset compared to the training manual map used like "ground truth".

3.3 Crest dunes skeletonization

The crestlines extraction is based on the Volumetric Obscurance algorithm (Rolland et al., 2022). The tool calculates for each pixel on a DEM the ratio between the volume below and above the topography in a sphere of a given radius centred at a given point of the topographic surface (Rolland et al., 2022). This process amplifies the pixel values on a DEM. Thus, the high inflection point pixels as being associated at the crestlines are accentuated favoring their recognition.

The output raster is reduced to a branched skeleton from the identification and digitization of high inflection points corresponding at the crests. The main crestline of the dunes is obtained from an automated analysis of branches connectivity of each bedforms crestlines. The algorithm assigns a connection type and length class to

the segments and by iteration, removes the loops and keeps the longest segment to digitize the longest crestline pathway, here considered as the main crestline.

Finally, we used the mapped crestlines to refine dune contours where dunes are adjacent to one another. First, we consider each main crestline as belonging to a morphology. Then, we used a seed region growing algorithm which from the dune crestlines, generates borders and individualizes the dunes.

4 RUB'AL KHALI APPLICATION

The unsupervised classificator is trained on a set of 100 DEM samples with dunes. After the training, the mapping model is assessed from 20% of the samples and reaches 92% of precision, 87% of recall and 70% of mapping quality. The mapping model of the dunes outline reveals a good performance and allows us to apply the protocol on eastern part of the Rub'Al Khali desert. This area is chosen because of its sand dunes diversity whose distribution and spatial variability (Fig.4A, B) at different scales of observation (Fig.4C) illustrate a variation of the wind regimes and the sand availability.

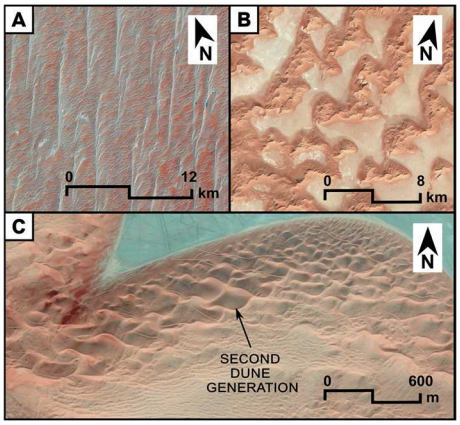

Figure 4. The spatial variability and the different dune scales on the Rub'Al Khali desert (Abdallah and Kumar, 2011; McKee, 1979). A. Linear dunes defined as a "compound dunes". B. Barchanoid dunes. C. An example of the second dune generation superimposed on the larger dunes.

The different automated steps are applied on the DEM of the Rub'Al Khali and a map of the different dune forms and generation is produced (Fig.5A). More than 78,000 dunes and crestlines are mapped in 6 hours of processing. The aeolian morphologies automatically mapped represents a covered sand surface of 58,000 km² (Fig.5B).

To demonstrate the model performance and applicability of the protocol in the analysis of the pattern's geometry at a field scale, we calculated for each dune their length, width, height and the median orientation of their main crestline (Fig.5C).

The morphometric analysis reveals a spatial variability of these parameters that quantify the diversity of the shapes at the field scale. This tool also provides an orientation estimate of the main crestlines which is related to the degree of dune organization.

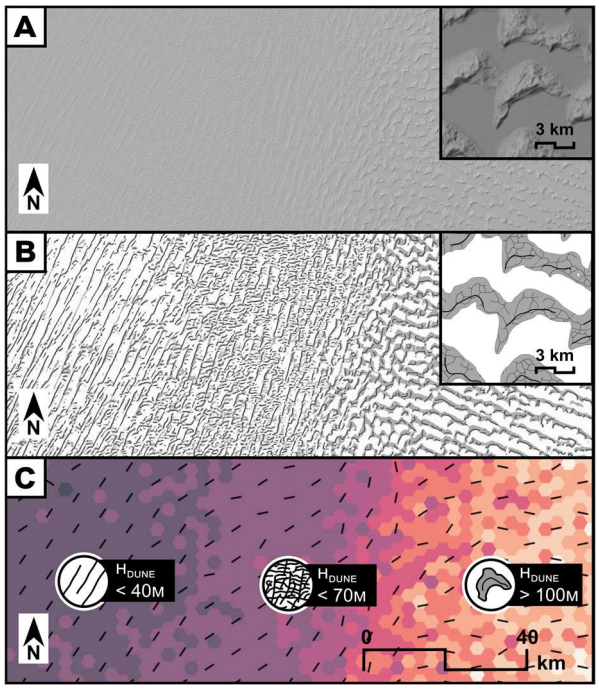

Figure 5. Part of the Rub'Al Khali dunes map produced by the automated protocol. A. Rub'Al Khali DEM and a barchan dune focus (on the right). B. Example of the automated mapping. The grey shapes are individualized dunes. The black lines are their mean crest. C. Spatial variability of the dune height (color gradient) and the crest orientation (black line).

5 CONCLUSION

This work presents a semi-automatic protocol to extract the aeolian dunes and their morphological characteristics from a DEM. The different numerical steps allow to separate the dune scales, digitize the dunes shape and skeletonize the mean crestline by using the Residual Relief extraction, the training and using of an unsupervised classificator (Deep Learning – U-Net) and the Volumetric Obscurance approach respectively.

This protocol reveals good performance to map various and complex dune forms. This work is an original production that completes atlases of this region present in the literature which illustrate the morphological boundaries defined by the aerial and satellite images interpretation (Abdallah and Kumar, 2011; Barth, 2001; Glennie, 1970; McKee, 1979).

Finally, this work demonstrates the ability to produce quickly and accurately a large numerical database that can be used to study the dune geometry on a field scale that reflects spatial variations in wind dynamics and sediment routing.

6 ACKNOWLEDGEMENT

Thanks to Samuel Shumack for our collaboration. This work was supported by the French National program PNP (Programme National de Planétologie).

7 REFERENCES

Abdallah, M., Kumar, A., 2011. An overview of Origin, Morphology and Distribution of Desert Forms, Sabkhas and Playas of the Rub' al Khali Desert of the Southern Arabian Peninsula. Earth Sci India 4.

Bagnold, R.A., 1974. The Physics of Blown Sand and Desert Dunes. Courier Corporation.

Barth, H.-J., 2001. Characteristics of the wind regime north of Jubail, Saudi Arabia, based on high resolution wind data. J. Arid Environ. 47, 387–402. https://doi.org/10.1006/jare.2000.0668

Bianchi, F.M., Grahn, J., Eckerstorfer, M., Malnes, E., Vickers, H., 2021. Snow Avalanche Segmentation in SAR Images With Fully Convolutional Neural Networks. IEEE J. Sel. Top. Appl. Earth Obs. Remote Sens. 14, 75–82. https://doi.org/10.1109/JSTARS.2020.3036914

Blumberg, D.G., 2006. Analysis of large aeolian (wind-blown) bedforms using the Shuttle Radar Topography Mission (SRTM) digital elevation data. Remote Sens. Environ. 100, 179–189. https://doi.org/10.1016/j.rse.2005.10.011

Glennie, K.W., 1970. Desert Sedimentary Environments. Elsevier Publishing Company.

Hiller, J.K., Smith, M., 2008. Residual relief separation: digital elevation model enhancement for geomorphological mapping. Earth Surf. Process. Landf. 33, 2266–2276. https://doi.org/10.1002/esp.1659

Hugenholtz, C.H., Barchyn, T.E., 2010. Spatial analysis of sand dunes with a new global topographic dataset: new approaches and opportunities. Earth Surf. Process. Landf. 35, 986–992. https://doi.org/10.1002/esp.2013

Lewington, E.L.M., Livingstone, S.J., Sole, A.J., Clark, C.D., Ng, F.S.L., 2019. An automated method for mapping geomorphological expressions of former subglacial meltwater pathways (hummock corridors) from high resolution digital elevation data. Geomorphology 339, 70–86. https://doi.org/10.1016/j.geomorph.2019.04.013

Livingstone, I., Warren, A., 2019. Aeolian Geomorphology: A New Introduction. John Wiley & Sons.

Lorenz, R.D., Zimbelman, J.R., 2014. Dune Worlds, Springer Berlin, Heidelberg. ed. Springer Praxis Books.

McKee, E.D., 1979. A Study of Global Sand Seas. U.S. Government Printing Office.

Pye, K., Tsoar, H., 2009. Aeolian Sand and Sand Dunes, Springer. ed. Springer Science & Business Media.

Rolland, T., Monna, F., Buoncristiani, J.F., Magail, J., Esin, Y., Bohard, B., Chateau-Smith, C., 2022. Volumetric Obscurance as a New Tool to Better Visualize Relief from Digital Elevation Models. Remote Sens. 14, 941. https://doi.org/10.3390/rs14040941

Ronneberger, O., Fischer, P., Brox, T., 2015. U-Net: Convolutional Networks for Biomedical Image Segmentation, in: Navab, N., Hornegger, J., Wells, W.M., Frangi, A.F. (Eds.), Medical Image Computing and Computer-Assisted Intervention – MICCAI 2015, Lecture Notes in Computer Science. Springer International Publishing, Cham, pp. 234–241. https://doi.org/10.1007/978-3-319-24574-4_28

Shumack, S., Hesse, P., Farebrother, W., 2020. Deep learning for dune pattern mapping with the AW3D30 global surface model. Earth Surf. Process. Landf. 45, 2417–2431. https://doi.org/10.1002/esp.4888

Telfer, M.W., Fyfe, R.M., Lewin, S., 2015. Automated mapping of linear dunefield morphometric parameters from remotely-sensed data. Aeolian Res., Eighth International Conference on Aeolian Research – ICAR 8 19, 215–224. https://doi.org/10.1016/j.aeolia.2015.03.001

Thomas, D.S.G., Wiggs, G.F.S., 2008. Aeolian system responses to global change: challenges of scale, process and temporal integration. Earth Surf. Process. Landf. 33, 1396–1418. https://doi.org/10.1002/esp.1719

Zheng, Z., Du, S., Taubenböck, H., Zhang, X., 2022. Remote sensing techniques in the investigation of aeolian sand dunes: A review of recent advances. Remote Sens. Environ. 271, 112913. https://doi.org/10.1016/j.rse.2022.112913

Bedform response to mean shear stress in the fluvial to tidal transition zone

S. de Lange, *Hydrology and Quantitative Water Management, ESG, Wageningen University, Wageningen, Netherlands – sjoukje.delange@wur.nl*

D. Murphy, *Department of Geography, Simon Fraser University, Burnaby, British Columbia, Canada - Dan Murphy daniel_murphy@sfu.ca*

R. Bradley, *Department of Geography, Simon Fraser University, Burnaby, British Columbia, Canada & Northwest Hydraulic Consultants Ltd., North Vancouver, British Columbia, Canada - ryan_bradley@sfu.ca*

R. Schrijvershof, *Hydrology and Quantitative Water Management, ESG, Wageningen University, Wageningen, Netherlands – reinier.schrijvershof@wur.nl*

K. Waldschläger, *Hydrology and Quantitative Water Management, ESG, Wageningen University, Wageningen, Netherlands – kryss.waldschlager @wur.nl*

R. Kostaschuk, *Department of Geography, Simon Fraser University, Burnaby, British Columbia, Canada - ray_kostaschuk@sfu.ca*

J. Venditti, *Department of Geography, Simon Fraser University, Burnaby, British Columbia, Canada - jeremy_venditti@sfu.ca*

T. Hoitink, *Hydrology and Quantitative Water Management, ESG, Wageningen University, Wageningen, Netherlands – ton.hoitink@wur.nl*

ABSTRACT: Bedform geometry in sand-bedded rivers is traditionally predicted with empirical equations, using reach-scale river characteristics as input parameters. Especially in the fluvial-to-tidal transition zone (FTTZ), where river discharge and tidal currents drive the flow, this is an inappropriate simplification. To understand variability in bedform geometry in the FTTZ, we assess the spatial variability of dunes in the Fraser River (Canada) and their relation to modelled flow characteristics.

Dune symmetry and aspect ratio increase in downstream direction, which is correlated with the increasing time and strength of flow reversal. However, predicting dune height in the FTTZ using tidally-averaged shear stresses resulted in an underestimation of dune height upstream (>40km from the river mouth), and an overestimation downstream. Using maximum shear stresses, only slightly overpredicted the dune height. Nevertheless, local variability could not be captured with any of these methods, which highlights the need for a new bedform predictor in tidal rivers.

1 INTRODUCTION

An estimation of bedform geometry is important for hydraulic roughness determination, navigable channel depth and sedimentary record interpretation. Bedform geometry and occurrence in sand-bedded rivers is traditionally predicted with phase diagrams and empirical equations, using reach-scale river characteristic (e.g., bed slope, water depth, grain size) as input parameters. Field observations supporting these equations are often made in regions where bedform fields are known to be present and are spatially uniform. Furthermore, in flow and sediment transport models, bedforms are often assumed to be spatially homogeneous and the resulting hydraulic roughness is therefore assumed to be quasi steady and uniform across the river, such that these empirical relations can be employed. However recent research has shown significant local spatiotemporal variation in dune height (Bradley et al., 2017) and geometry (Murphy et al., in progress),

limiting the validity of this assumption. To enable the prediction of dune geometry, its spatial variability needs to be better understood.

Especially in the fluvial-to-tidal transition zone (FTTZ), variation in flow velocity occur in shorter time frames than in rivers. The FTTZ can be defined as the part of the river that is upstream fully dominated by fluvial processes, to the downstream estuary fully dominated by tidal and coastal processes (Phillips et al., 2022). Dunes in the FTTZ are often believed to decrease in size in downstream direction, which is then related to the downstream fining and shallowing of the channel. However, Lefebvre et al. (2021) and Prokocki et al. (2022) recognize various bedform geometries, shapes and 3D planforms across the FTTZ. Neither of those researchers included cross-sectional

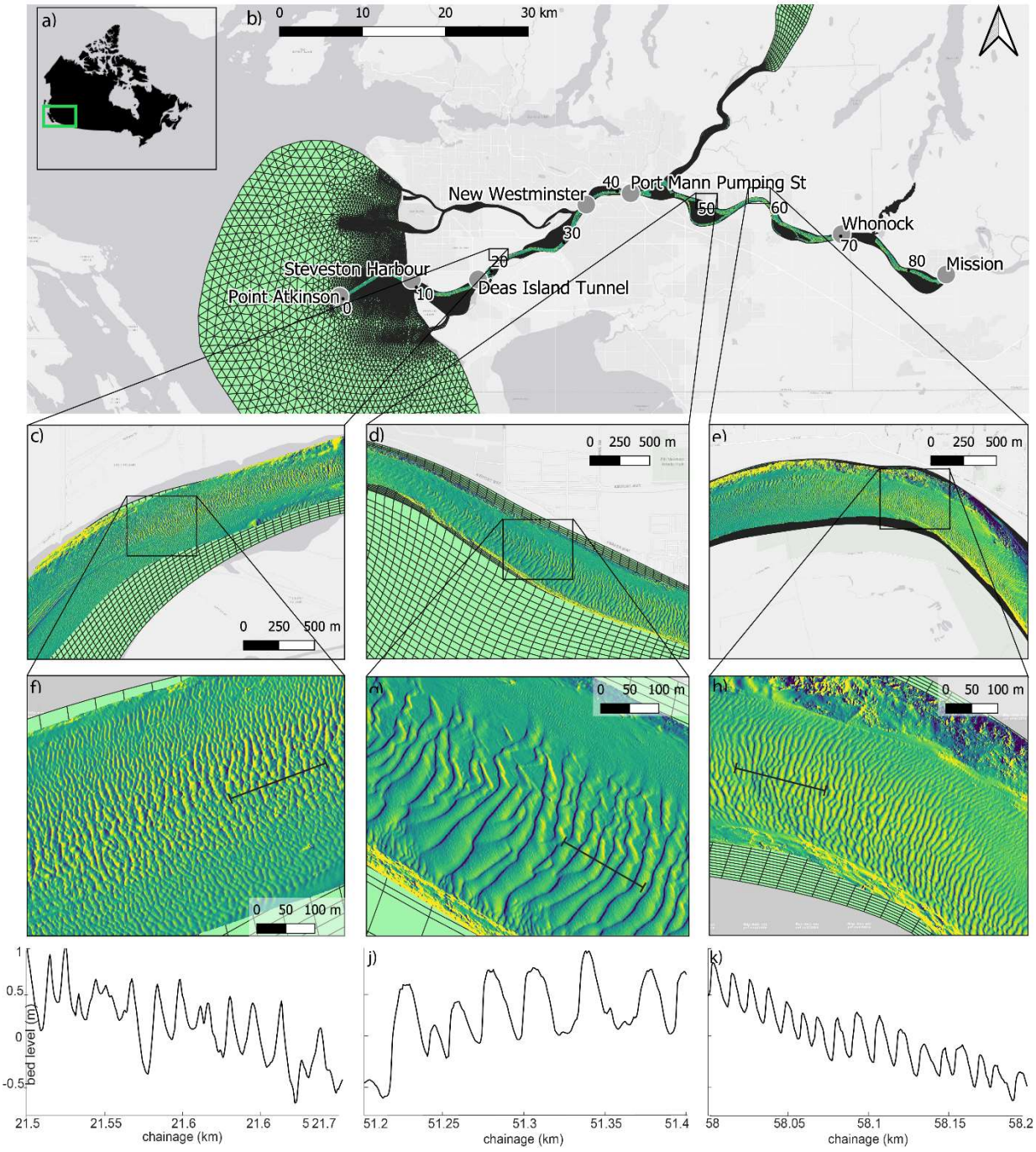

Figure 1. Study area. b) model domain. C-e) close ups of the focus areas. F-g) examples of dune fields.

variability in their work, and did not link their findings to the local hydrodynamical conditions. Therefore, to understand bedform geometry and variability in the FTTZ, we assess the spatial variability of dunes from multibeam bathymetric surveys and their relation to flow characteristics, using a 2D hydrodynamic model of a sand-bedded lowland river (Fraser River, Canada).

2 METHODS

Field data

Bathymetric field data was collected in the fluvial to tidal transition zone of the Fraser river (Figure 1) which was used to determine river and dune geometry. A Multibeam echosounder (MBES) was employed to collect riverbed data, and this data is provided by the Public Works and Government Services, Canada. The measured bathymetry comprises of data of the main channel between river kilometer -1 to 85 and covers the fairway of the river, but does not provide full bank-to-bank spatial coverage. Data were collected during base flow conditions in January, February and March 2021. MBES data is gridded onto a 1x1 m^2 grid.

Hydraulic model

A 2DH hydraulic model was set up in Delft3D Flexible Mesh (FM) model suite (Kernkamp et al., 2011). It calculates depth-averaged quantities based on the two-dimensional shallow water equation. The numerical domain covers the Fraser river from 81 km upstream, to the part where the offshore region of the strait of Georgia reaches a significant depth (>200 m). Bathymetry for the main channel is interpolated on an unstructured curvilinear grid system. The imposed upstream boundary conditions include measured discharge of 2018 at Mission (RK 81), and discharge at the confluences of Pitt River (RK 45) and Stave river (RK 74). At the downstream boundary, tidally-influenced water levels are imposed. Eight primary tidal constituents, the most important overtide (M4) and compound tides are determined via the Delft Dashboard toolbox (van Ormondt et al., 2020) using the TPXO8.0 database (Egbert & Erofeeva, 2002). The model was calibrated for low discharge by applying different Manning roughness coefficients and evaluating the resulting water levels and tidal amplitudes of the M2, M4 and K1 tide at 7 gauging stations. The best performing model had a uniform Manning's coefficient (roughness) of 0.026 m.

Data analysis

Bathymetry was analyzed to derive dune characteristics. Three longitudinal profiles were taken, along the center line and at approximately 80 m from the north and south bank. Additionally, in three focus areas (Figure 1), a longitudinal profile was taken every 10 meters. Bedform characteristics were determined by using a Bedform Tracking Tool (van der Mark et al., 2008).

River geometry was parametrized by river width, curvature (de Ruijsscher et al., 2020), transverse bed slope (de Lange et al., 2021) and excess depth (Vermeulen et al., 2014).

To get insight in the flow conditions, flow magnitude, direction, water depth and bed shear stress per grid cell was saved every ten minutes. A Godin filter (Godin, 1972) was used to calculate the tidally averaged values of flow velocity and shear stress during low discharge. The Godin filter removes the tidal and higher frequency signals to obtain a residual signal caused by the river flow.

Based on the modelled flow data, dune height was predicted using the widely accepted dune geometry predictor of van Rijn (1984):

$$\Delta = 0.11\, h \left(\frac{D_{50}}{h}\right)^{0.1} (1 - e^{-0.5T})(25 - T)$$

In which h = water depth (m), D_{50} = median grain size (m) and transport stage T. See van Rijn (1984) for details on calculation of T.

3 RESULTS AND DISCUSSION

Characteristics of FTTZ

The study reach is located fully in the FTTZ, where both the river discharge and the tidal current influence the water levels. In upstream direction, water levels are decreasingly influenced by tidal motion. Figure 2 indicates the decreasing amount of upstream directed shear stress when in upstream direction. This is tightly connected to decrease in the amount of time that the flow is reversed (decreasing from 40% to 10% of the time in 80 km).

Geometrically, the river does not show trends in longitudinal direction in width, curvature, transverse-bed slope or depth excess. The water depth increases in downstream direction.

The main channel of the Fraser riverbed consists of sand (D_{50} = 351 µm) and is well sorted. There is a minor trend of downstream fining in the lower 50 km of the river, (1.14 µm/km), resulting in a decrease in D_{50} approximately 100 µm over this reach. Additionally, gravel and clay patches are present in the outer banks of the river.

Dune geometry

Dune geometry along the river Fraser varies largely (Figure 3) and the dune covered part of the bed is characterized by dunes with heights up to 2.4 m (mean: 0.46, median: 0.39 m, std: 0.28 m) and lengths up to 194 m (mean: 24 m, median: 16, std: 22 m). Patterns in dune geometry can be observed, where certain areas contain relatively low and short dunes, while others show increasing or decreasing dune heights and lengths. Those patterns are not consistent over the whole river width, and where relatively large dunes prevail on one part of the river (e.g. north side), dunes can be small on the other parts (see for example around RK 68). The cross-sectional variation (expressed as the standard deviation) in dune height and length is about twice as high as the variation along the longitudinal direction.

Dune shape

The gradual decrease in tidal amplitude is not reflected in the primary geometrical components dune height and dune length, but the tidal currents do influence dune shape. We observe the dune crests become sharper,

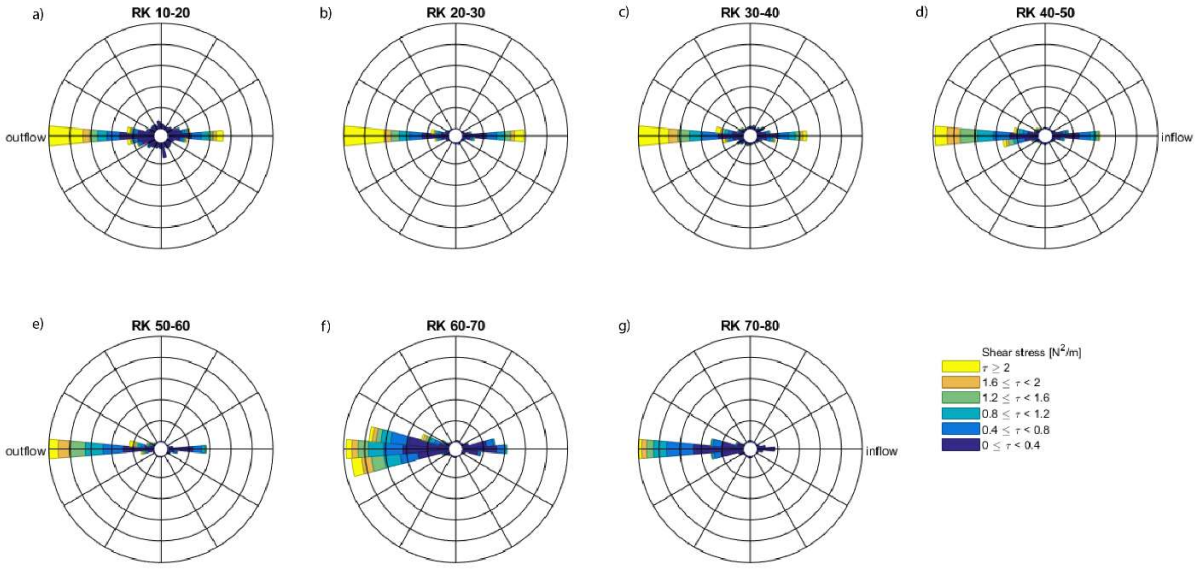

Figure 2. 'flow' roses, indicating the amount of shear stress that is directed either land outwards (left) or inwards (right). The amount of inward directed shear stress decreases in upstream direction. RK = river kilometer.

which is also observed in Lefebvre et al. (2021). Additionally, the aspect ratio (L/ H) of dunes increases in downstream direction, indicating dunes becoming flatter (lower and longer) (Figure 4A). Finally, dunes become more symmetrical indicated by the decrease in the ratio between leeside angle and stoss side angle (Figure 4C). Both the aspect ratio and the LSA/SSA-ratio can be linearly related to flow-reversal time (Figure 4B, D).

Dune geometry prediction

To be able to apply the predictor of van Rijn (1984) to the Fraser river, the input values need to be parameterized by either taking tidally-averaged or maximum values. Doing so, we are able to apply this predictor using more localized, modelled, values instead of reach-averaged estimations.

Using tidally-averaged shear stresses to predict dune height in the FTTZ, the predictor performs relatively well when all data is reached-averaged. However spatially, the predictor underestimates the dune height upstream (>40 km from the river mouth), and overestimates this downstream (<40 km) (Figure 5A). The underestimation of dune height upstream could be attributed to the

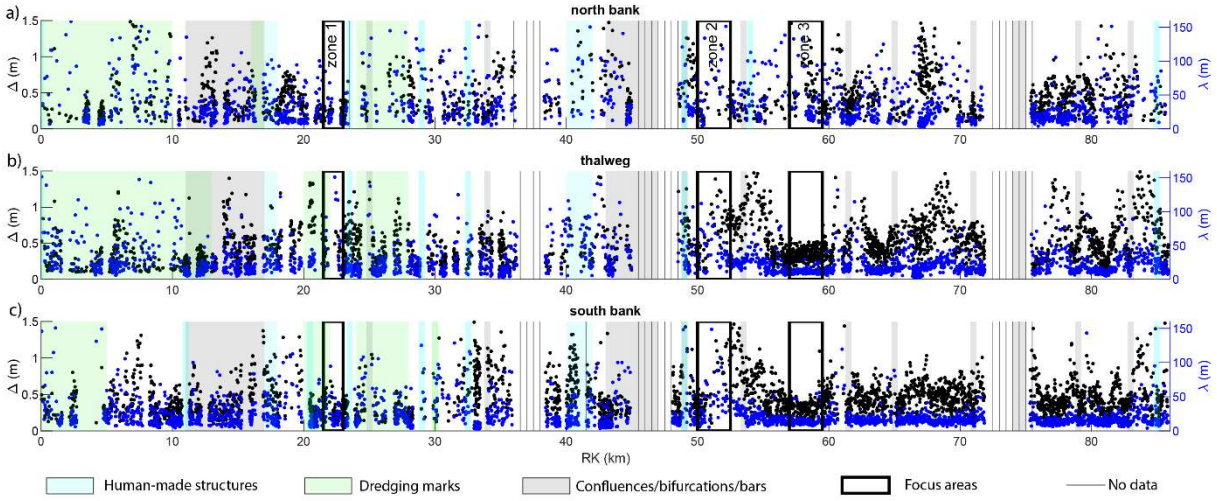

Figure 4. Dune geometry. a, b, c) Dune height Δ (black) and dune length λ (blue) through-out the research area. Human-made structures, dredging marks, confluences, bifurcations and bars, focus areas, and zones with no data are indicated (see legend).

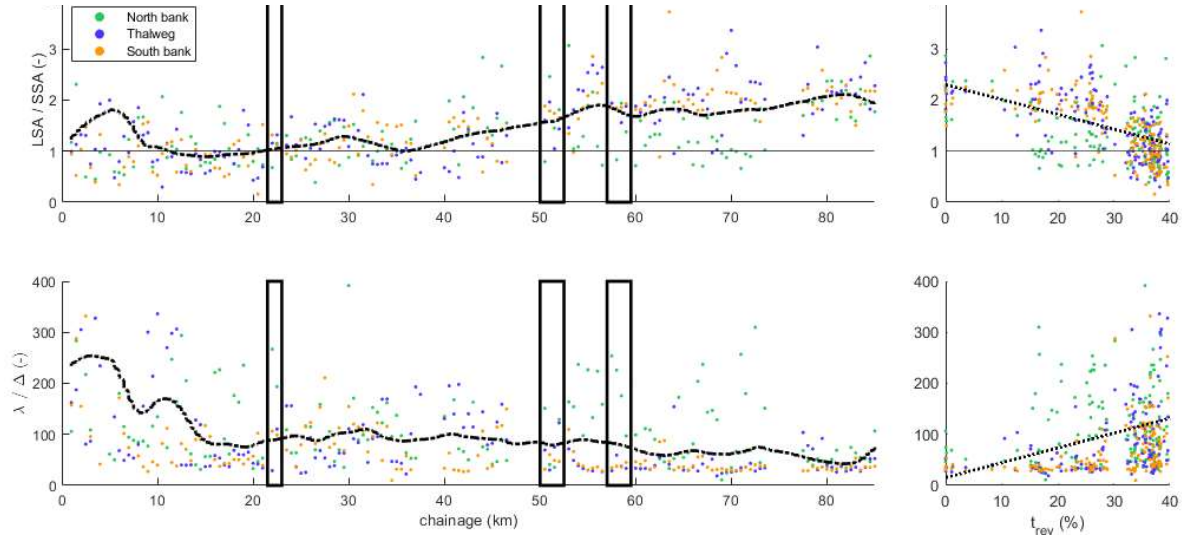

Figure 3. Dune shape. a) dune symmetry (leeside angle / stoss side angle) throughout the research area. c) aspect ratio (dune length / dune height) throughout the research area. b and d) symmetry and aspect ratio against percentage of time that the flow is reversed.

dune still adjusting to the previous high-water wave. The overestimation of dune height downstream, in the more tidally-dominated regime, is caused by the increase in water level downstream. The increase in water level is reflected by an increase in predicted dune height, but this response is not observed in our data. Most likely this can be attributed to the increase in tidal influence. T be able to apply current bedform predictors to tidal rivers, they should be adapted for tidal influence. Additionally, applying the predictor of van Rijn (1984) using the maximum values as parameterization for the shear stress, improves the spatial predictive capacity significantly, and mean dune height is slightly overpredicted with 0.16 m (~30%) along the whole reach (Figure 5B). Local variability cannot be captured in any of these methods, indicated by high RMSE values of 0.41 m for both methods. This stresses the need for more studies on localized bedform variability in the FTTZ.

4 CONCLUSIONS

Based on multibeam bathymetric data and a 2D hydrodynamic model of the FTTZ of the lowland, sand-bedded reach of the Fraser River, Canada, we can conclude that:

- Opposing the common assumption that dunes fade out towards the sea, dunes persist throughout the whole FTTZ.
- Downstream fining exists, but is irrelevant for dune height and length.
- There is a systematic change in dune shape, but not in dune height or length.
- Cross-sectional variability in dune geometry is twice as large as longitudinal variability.
- Dune geometry predictors based on tidally-averaged shear stress, overestimate dune height in the seaward part of the FTTZ.
- Intrinsic variability of dune height prevents dune predictors to function well on local scale.

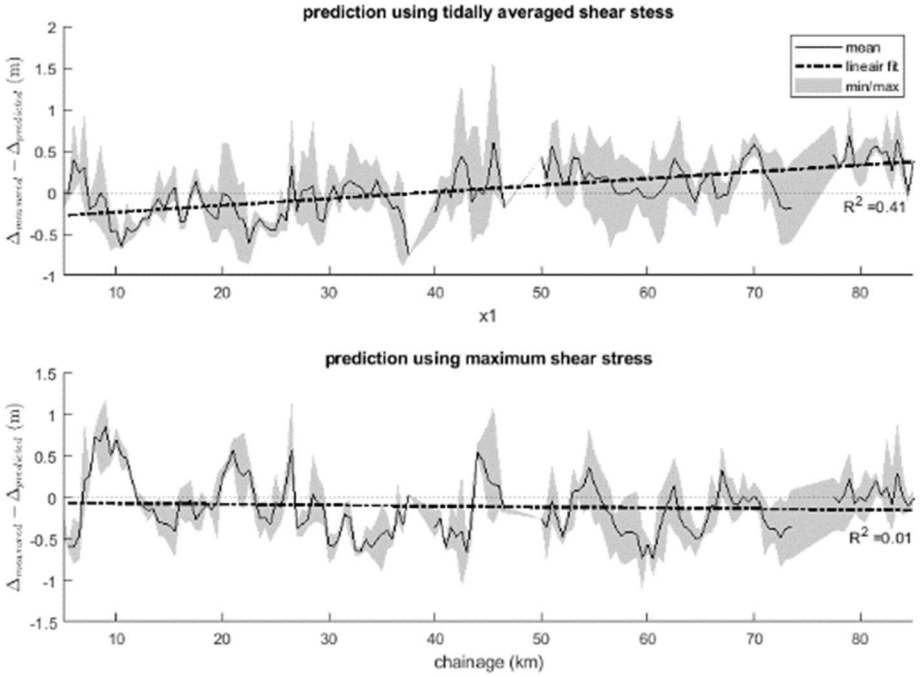

Figure 5. Measured minus predicted dune height, parametrized by a) tidally-averaged shear stress and b) maximum shear stress.

5 ACKNOWLEDGEMENT

The research was funded by the Netherlands Organisation for Scientific Research (NWO), within Vici project "Deltas out of shape: regime changes of sediment dynamics in tide-influenced deltas" (Grant NWO-TTW 17062).

6 REFERENCES

de Lange, S. I., Naqshband, S., & Hoitink, A. J. F. (2021). Quantifying Hydraulic Roughness From Field Data: Can Dune Morphology Tell the Whole Story? *Water Resources Research*, *57*(12), 1–22. https://doi.org/10.1029/2021WR030329

de Ruijsscher, T. v., Naqshband, S., & Hoitink, A. J. F. (2020). Effect of non-migrating bars on dune dynamics in a lowland river. *Earth Surface Processes and Landforms*, *45*(6), 1361–1375. https://doi.org/10.1002/esp.4807

Egbert, G. D., & Erofeeva, S. Y. (2002). Efficient inverse modeling of barotropic ocean tides. *Journal of Atmospheric and Oceanic Technology*, *19*(2), 183–204. https://doi.org/10.1175/1520-0426(2002)019<0183:EIMOBO>2.0.CO;2

Godin, G. (1972). *The analysis of tides*. University of Toronto Press.

Kernkamp, H. W. J., van Dam, A., Stelling, G. S., & de Goede, E. D. (2011). Efficient scheme for the shallow water equations on unstructured grids with application to the Continental Shelf. *Ocean Dynamics*, *61*(8), 1175–1188. https://doi.org/10.1007/s10236-011-0423-6

Lefebvre, A., Herrling, G., Becker, M., Zorndt, A., Krämer, K., & Winter, C. (2021). Morphology of estuarine bedforms, Weser Estuary, Germany. *Earth Surface Processes and Landforms*, *47*(1), 242–256. https://doi.org/10.1002/esp.5243

Prokocki, E. W., Best, J. L., Perillo, M. M., Ashworth, P. J., Parsons, D. R., Sambrook Smith, G. H., Nicholas, A. P., & Simpson, C. J. (2022). The morphology of fluvial-tidal dunes: Lower Columbia River, Oregon/Washington, USA. *Earth Surface Processes and Landforms*, *47*(8), 2079–2106. https://doi.org/10.1002/esp.5364

van der Mark, C. F., Blom, A., & Hulscher, S. M. J. H. (2008). Quantification of variability in bedform geometry. *Journal of Geophysical Research: Earth Surface*, *113*(3), 1–11. https://doi.org/10.1029/2007JF000940

van Ormondt, M., Nederhoff, K., & van Dongeren, A. (2020). Delft Dashboard: A quick set-up tool for hydrodynamic models. *Journal of Hydroinformatics*, *22*(3), 510–527. https://doi.org/10.2166/hydro.2020.092

van Rijn, L. C. (1984). Sediment transport, part III: Bedforms. *Journal of Hydraulic Engineering*, *110*(12), 1733–1754.

Vermeulen, B., Hoitink, A. J. F., van Berkum, S. W., & Hidayat, H. (2014). Sharp bends associated with deep scours in a tropical river: The river Mahakam (East Kalimantan, Indonesia). *Journal of Geophysical Research: Earth Surface*, *119*(7), 1441–1454. https://doi.org/10.1002/2013JF002923

Influence of silt in sand-silt mixtures on dynamic near-equilibrium bedform geometry

S. de Lange *Hydrology and Quantitative Water Management, ESG, Wageningen University, Wageningen, Netherlands – sjoukje.delange@wur.nl*

S. van de Veen *Hydrology and Quantitative Water Management, ESG, Wageningen University, Wageningen, Netherlands – sanne.vandeveen@wur.nl*

I. Niesten *Hydrology and Quantitative Water Management, ESG, Wageningen University, Wageningen, Netherlands – iris.niesten@wur.nl*

D. Boelee *Hydrology and Quantitative Water Management, ESG, Wageningen University, Wageningen, Netherlands – david.boelee@wur.nl*

K. Waldschläger *Hydrology and Quantitative Water Management, ESG, Wageningen University, Wageningen, Netherlands – kryss.waldschlager@wur.nl*

T. Hoitink *Hydrology and Quantitative Water Management, ESG, Wageningen University, Wageningen, Netherlands – ton.hoitink@wur.nl*

ABSTRACT: Subaqueous geometric bedform properties such as height, length and leeside angle are crucial in determining hydraulic form roughness and interpreting sedimentary records. Traditionally, bedform existence and geometry are predicted with phase diagrams and empirical equations, which are mostly based on uniform, cohesionless sediments. However, mixtures of sand, silt and clay are common in deltas, estuaries, and lowland rivers where bedforms are ubiquitous. Here, we test the influence of silt in sand-silt mixtures on bedform geometry, based on laboratory experiments conducted in a recirculating flume. Sand and silt content were systematically varied for various discharges. The results indicate that both fine (17 μm) and coarse silt (40 μm) do not stabilize the bed. Primary bedform height increases with decreasing sediment size of sandy mixtures, while the bedform height decreases with decreasing sediment size of silty mixtures, but both trends are minor. Additionally, a gradual transition from ripples to dunes is observed, and both scales can co-exist.

1 INTRODUCTION

Estimating bedform geometry is important for hydraulic roughness determination, fairway depth maintenance and sedimentary record interpretation. Bedform geometry and existence in sand-bedded rivers is traditionally predicted with phase diagrams and empirical equations. However, most phase diagrams and empirical equations are based on uniform, cohesionless sediments (Yalin, 1964; van Rijn, 1984; Parsons et al., 2016; Wu et al., 2021), while mixtures of cohesionless sand, physically cohesive mud, and benthic organisms are common in many coastal, deltas, estuaries, and lowland rivers

(Manning et al., 2010; Parsons et al., 2016; Schindler et al., 2015). Bedform dimensions may decrease when clay (<4μm) is present (Schindler et al. 2015), and when high suspended sediment concentrations (SSCs) suppress bedform growth (Ma et al., 2020). Non-cohesive silt (~30 - 63μm) is mainly transported in suspension and is therefore expected to limit bedform height and length. Additionally, the experiments of Bartzke et al. (2013) and Yao et al. (2022) demonstrate that silt could stabilize the bed because it fills the space in between the coarse sand particles. Consequently, the silt particles block the flow through the sediment bed and thus decrease the permeability. Weakly-cohesive silt (4-~30μm) is expected to limit bedform development similar to clay. Evidently, it is unknown what the exact influence of silt on bedform dimensions is.

Here, we test the influence of silt in sand-silt mixtures on bedform geometry, based on laboratory experiments conducted in a recirculating, tilted flume, in the Kraijenhoff van de Leur Laboratory for Water and Sediment Dynamics at Wageningen University & Research. We seek a relation between bedform geometry and silt content in the riverbed, bed shear stress and suspended sediment concentration (SSC). We hypothesize that with increasing silt concentration, SSC increases and the hydraulic roughness decreases, resulting in a decrease in bedform height and length. With this analysis we aim to quantify the influence of fine-grained bed sediment on bedform geometry.

2 METHODS

2.1 Experimental setup

The experiments were conducted in a tilting flume with recirculation facilities for both water and sediment in the Kraijenhoff van de Leur Laboratory for Water and Sediment Dynamics from Wageningen University and Research (Figure 1 and 2). The flume has an internal width of 1.20 m, length of 14.4 m, and height of 0.5 m. A diffuser at the upstream part made sure that the inflow was distributed over the entire width of the flume. The diffuser was followed by a stacked pile of PVC tubes that serve as a laminator, suppressing turbulence. At the end of the flume, a funnel was connected to the reservoir to make sure that bed transport was recirculated and did not deposit in front of the weir.

A sediment bed of 10 cm was applied, which consisted of a manually mixed combination of two grain sizes: a base sediment of medium sand (270 µm), mixed with fine sand (180 µm), coarse silt (40 µm) or fine silt (17 µm) (Table 1). Experimental runs were performed for different discharges (45, 80 and 100 L/s), to be able to distinguish the effect of transport stages, corresponding with an average flow velocity of 0.38, 0.67 and 0.83 m/s respectively. The flow depth was set to 15 cm measured from the initial flat sediment bed, and the water depth was kept the same for the different discharges by adjusting the weir height. The slope was set to 0.01 m/m.

Figure 1. Picture of the inflow of the flume.

To ensure equilibrium bedform conditions, experiments were ran for 10, 5 and 3 hours

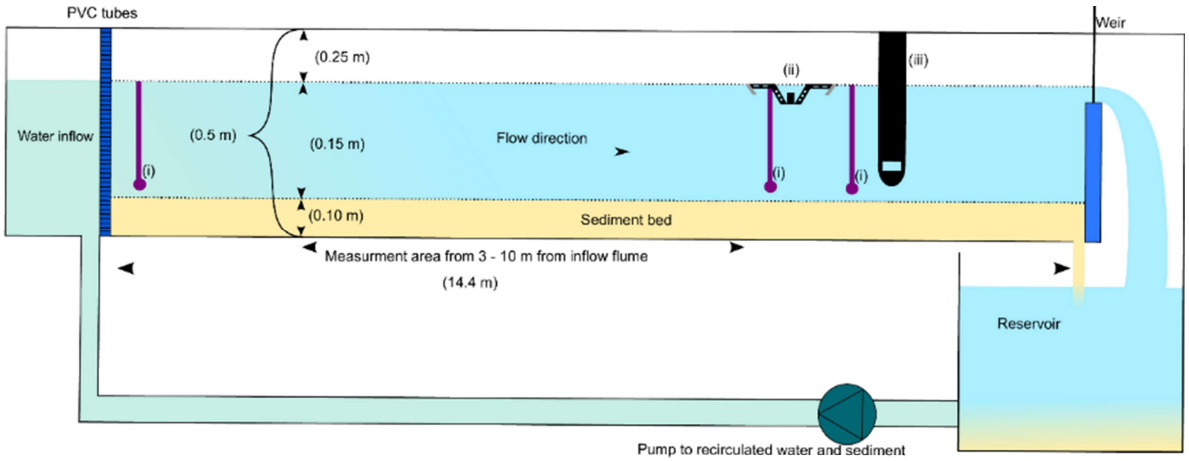

Figure 2. Schematic overview of the experimental set-up indicating with the following measurement instruments i) stilling wells at 2, 11, 12.5 meters from the inflow of the flume, ii) UB-Lab-2C, iii) LISST-200X.

for the discharges of 45, 80 and 100 L/s, respectively.

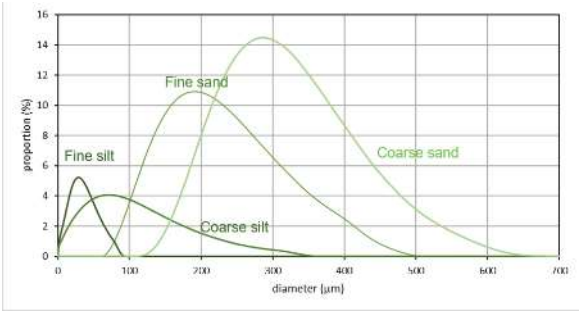

Figure 3. Sediment distribution of the used sediments, measured with a Mastersizer 2000.

2.2 Instrumentation

Table 1: Bed composition (%) of the experimental runs.

Experiment	Medium sand	Fine sand	Coarse silt	Fine silt
Sand_1	0	100	0	0
Sand_2	18	82	0	0
Sand_3	35	65	0	0
Sand_4	49	51	0	0
Sand_5	65	35	0	0
Sand_6	100	0	0	0
CoarseSilt_1	98	0	2	0
CoarseSilt_2	95	0	5	0
CoarseSilt_3	90	0	10	0
CoarseSilt_4	80	0	20	0
CoarseSilt_5	70	0	30	0
CoarseSilt_6	50	0	50	0
FineSilt_1	98	0	0	2
FineSilt_2	96	0	0	4
FineSilt_3	91	0	0	9
FineSilt_4	77	0	0	23
FineSilt_5	70	0	0	30

During the first and last 30 minutes of a run, a LISST-200X measured suspended sediment concentration and grain size, and an UB-Lab-2C measured acoustic velocity profiles. After each experimental run, the flume was drained slowly and a line laser scanner measured the bed topography.

2.3 Data analysis

Based on the topographical data, five transects were constructed with an interval of 200 mm in the crosswise direction through the bed elevation profiles. These profiles served as input for the bedform tracking tool from van der Mark & Blom (2007), which gives bedform height, length and leeside angles based on specific span values used to differentiate between different bedform scales. Three bedform lengths of interest were defined: 150 mm ± 100 (hereafter referred to as secondary bedforms), 500 mm ± 150 (referred to as small primary bedforms) and 1800 mm ± 350 (referred to as large primary bedforms).

3 RESULTS AND DISCUSSION

3.1 General bedform geometry

The general bedform pattern observed during the experiments, could be described as ripples during the 45 L/s experiments, mixed or transitional bedforms during the 80 L/s experiments, and dunes (with ripples super imposed) or upper stage plane bed (USPB) for experiments with 100 L/s (Figure 4).

Those three bedforms scales (ripples, small dunes, and large dunes) can co-exists, and can transition into each other. Traditional bedform stage diagrams do not account for this, and should be adjusted. Furthermore, this observation opposes the theory of Duran Vincent et al. (2019), who's research showed a scale break between ripples and dune.

Additionally, the definition of the scales differs depending on the chosen type of distinguishing characteristic. Scales can be differentiated on dimension (Schindler & Robert, 2004; Lapotre et al., 2017), steepness (Schindler & Robert, 2004; Robert & Uhlman, 2001), Yalin number (Lapotre et al., 2017) and by comparison with equations predicting bedform dimensions (Soulsby et al., 2012). A comprehensive and all-embracing definition is needed to differentiate bedform scales in different environments.

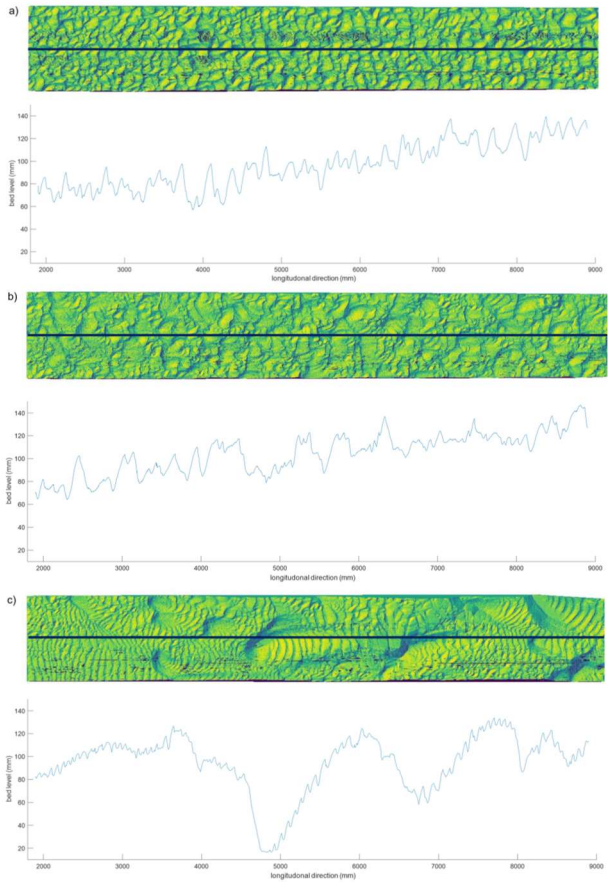

Figure 4. Topography of the bed of the runs with only coarse sand with the corresponding cross-section through the middle of the profile. a) indicates the bed geometry after the run with a discharge of 45 L/s, b) 80 L/s and c) 100 L/s. The dark blue lines indicate the location of the cross-section.

3.2 Influence of sediment composition

3.1.1 Bedform height (H)

Below, we focus on the 80 L/s case. With increasing fine sand content, the bedform height of the secondary (ripples) and small primary bedforms (dunes) decrease, but only minimally. The same observation is made for an increasing coarse silt and fine silt concentration. (Figure 5 A-C). The trend in decreasing ripple height with fining of the bed, can be explained by the fact that ripples are supposed to scale with grainsize. The decrease in height of small dunes cannot be directly explained, and with the current data we can only speculate that this is due to a transition to USPB. Additionally, the observed bedforms seem to be clean sand bedforms (Wu et al., 2021), in which the silt has been washed out. The largest dune scale was observed in the experiments with fine sand and coarse silt, but was absent in the fine silt experiments. We expect that the cohesivity of the fine silt suppresses the growth of larger bedforms. The presence of larger dunes at runs with a high concentration of fine sand, could be due to the higher mobility of the sediment, enabling more transport and therefore larger bedforms to occur. However, during runs with coarse silts, the larger bedforms seem to disappear if the material fines. Either the high suspended sediment concentration, or the increasing stability of the bed due to silt addition, could suppress the development of larger dunes. These hypotheses should be verified by studying the measured suspended sediment and flow velocity data.

3.1.2 Bedform length (L)

In the experiments with fine sand and coarse silt, the bedform length of all bedform scales increases when the bed gets finer. Only during the experiments with fine silt, the bedform length decreases. (Figure 5 D-F). These observations can be contributed due to the higher mobility of the sediment during the fine sand and coarse silt runs, moving the bedforms towards UPSB, and the higher cohesivity of the fine-silt bed, suppressing this transition.

3.1.3 Bedform steepness (H/L) and leeside angle

This increase in bedform length, in combination with decreasing bedform height, results in flatter bedforms (Figure G-I). This corresponds with observations in high SSC environments, suppressing bedform steepness (Ma et al., 2017). Bedforms in the fine silt environment are steeper than in the coarse silt and fine sand experiment, and the steepness remains constant when the bed fines. The same trends are observed for the mean leeside angle of the bedforms (Figure J-L). The increased cohesion could result in less transport, and higher angle of repose.

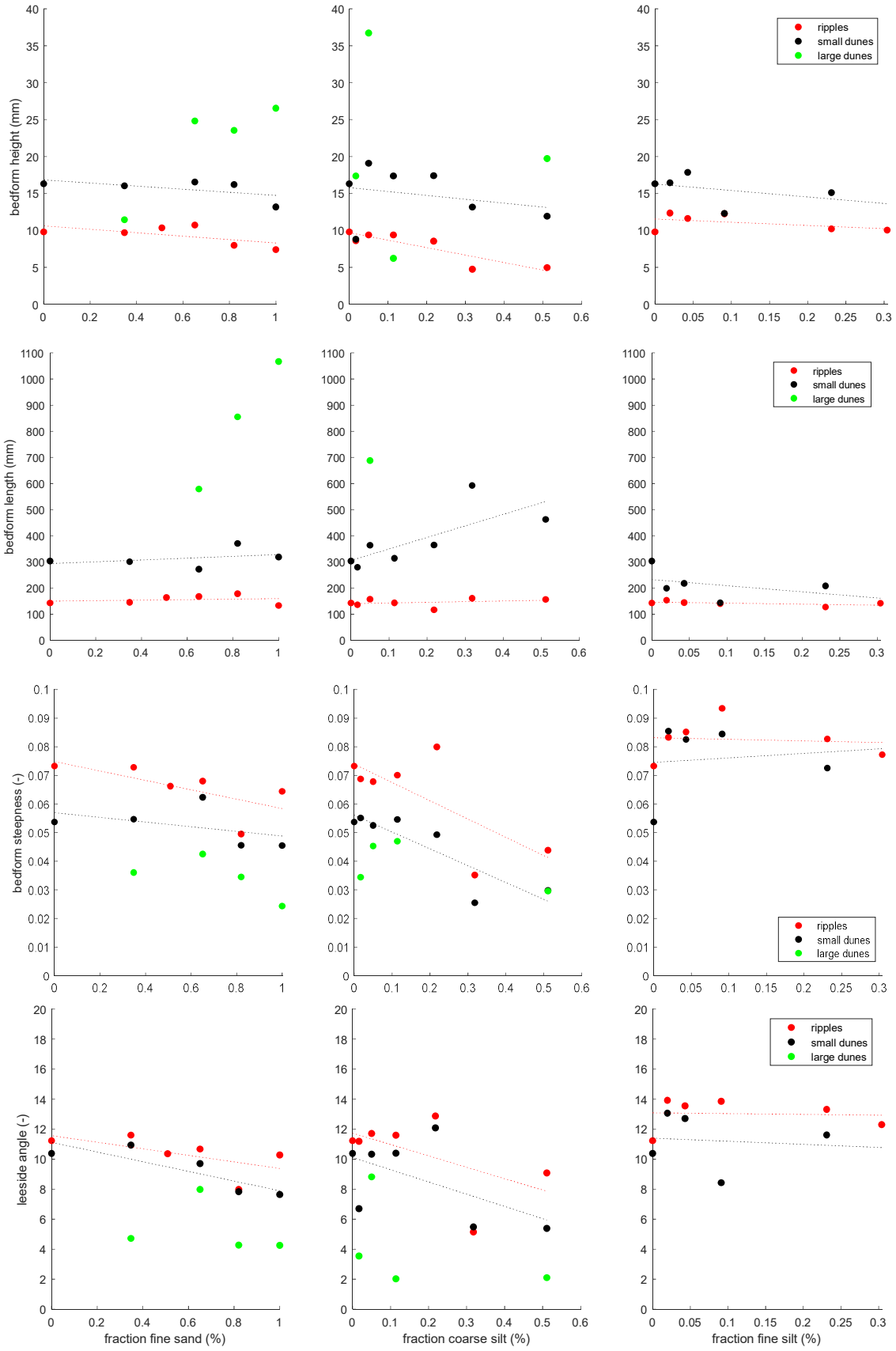

Figure 5. The relation between percentage fine sand (A, D, G), percentage coarse silt (B, E, H) and fine silt (C, F, I) in a medium sand mixture, and bedform height (A-C), length (D-F), steepness (height / length) (G-I) and leeside angle (J-L) of the experiments performed at 80L/s.

4 CONCLUSIONS

17 experiments were analysed with varying percentages of fine sand or coarse silt in the bed sediment for a discharge of 45, 80, and 100 L/s. Next, bedform height and length of the dunes and ripples were determined.

The addition of coarse silt effects the bedform geometry in the same way as the addition of fine sand does. An increase in transport capacity leads to a decrease in dune height and steepness, while the dune length increases. The addition of coarse silt does therefore not stabilize the bed, since the grains are too large to fill up the pores of the base material. The addition of fine silt results in shorter, steeper dunes, possibly due to the added cohesion of the material.

Finally, multiple scales of bedforms can co-exist and transition into each other, which should be implemented in bedform phase diagrams.

5 ACKNOWLEDGEMENT

This research is based on the MSc thesis of Sanne van de Veen. The research was funded by the Netherlands Organisation for Scientific Research (NWO), within Vici project “Deltas out of shape: regime changes of sediment dynamics in tide-influenced deltas” (Grant NWO-TTW 17062).

6 REFERENCES

Bartzke, G., Bryan, K., Pilditch, C., and Huhn, K. (2013). On the stabilizing influence of silt on sand beds. *Journal of Sedimentary Research*, 83, pp. 691–703.

Lapotre, M. G., Lamb, M. P., and McElroy, B. (2017). What sets the size of current ripples? *Geology*, 45(3), pp. 243–246.

Ma, H., Nittrouer, J. A., Naito, K., Fu, X., Zhang, Y., Moodie, A. J., Wang, Y., Wu, B., and Parker, G. (2017). The exceptional sediment load of fine-grained dispersal systems: Example of the yellow river, china. *Science Advances*, 3(5), pp. e1603114.

Ma, H., Nittrouer, J. A., Wu, B., Lamb, M. P., Zhang, Y., Mohrig, D., ... & Parker, G. (2020). Universal relation with regime transition for sediment transport in fine-grained rivers. *Proceedings of the National Academy of Sciences*, *117*(1), 171-176.

Manning, A., Baugh, J., Spearman, J., and Whitehouse, R. (2010). Flocculation settling characteristics of mud: Sand mixtures. *Ocean Dynamics*, 60, pp. 237–253, 2010.

Parsons, D. R., Schindler, R. J., Hope, J. A., Malarkey, J., Baas, J. H., Peakall, J., Manning, A. J., ... and Thorne, P. D. (2016). The role of biophysical cohesion on subaqueous bed form size. *Geophysical Research Letters*, 43(4), pp. 1566–1573.

Robert, A. and Uhlman, W. (2001). An experimental study on the ripple–dune transition. *Earth Surface Processes and Landforms*, 26(6), pp. 615–629.

Schindler, R. J. and Robert, A (2004). Suspended sediment concentration and the ripple–dune transition. *Hydrological Processes*, 18(17), pp. 3215–3227.

Schindler, R. J., Parsons, D. R., Ye, L., Hope, J. A., Baas, J. H., Peakall, J., Manning, A. J., ... and Bass, S. J. (2015). Sticky stuff: Redefining bedform prediction in modern and ancient environments. *Geology*, 43(5), pp. 399–402.

Soulsby, R., Whitehouse, R., and Marten, K. (2012). Prediction of time-evolving sand ripples in shelf seas. *Continental Shelf Research*, 38, pp. 47–62.

van der Mark, R. and Blom, A. (2007). A new and widely applicable tool for determining the geometric properties of bedforms.

van Rijn, L. C. (1984). Sediment transport, part iii: Bed forms and alluvial roughness. *Journal of Hydraulic Engineering*, 110(12), pp. 1733–1754.

Wu, X., Fernández, R., Baas, J. H., Malarkey, J., and Parsons, D. (2021). Discontinuity in equilibrium wave-current ripple size and shape caused by a winnowing threshold in cohesive sand-clay beds. *Earth and Space Science Open Archive*, pp. 40.

Yalin, M. S. (1964). Geometrical properties of sand wave. *Journal of the Hydraulics Division*, 90(5), pp. 105–119.

Yao, P., Su, M., Wang, Z., van Rijn, L. C., Stive, M. J. F., Xu, C., and Chen, Y. (2022). Erosion behavior of sand-silt mixtures: Revisiting the erosion threshold. *Water Resources Research*, 58(9).

Dune preservation and microplastics distribution over time, River Waal, Netherlands

T.A.G.P. van Dijk *Department of Applied Geology and Geophysics, Deltares, Utrecht, Netherlands; and Department of Geology, University of Illinois at Urbana Champaign, IL, USA – thaienne.vandijk@deltares.nl*
J. Best *Department of Geology; and Departments of Geography & GIS, Mechanical Science and Engineering and Ven Te Chow Hydrosystems Laboratory, University of Illinois at Urbana Champaign, IL, USA – jimbest@illinois.edu*
S. Krause *School of Geography, Earth and Environmental Sciences, University of Birmingham, Edgbaston, Birmingham, UK; and LEHNA–Laboratoire d'ecologie des hydrosystemes naturels et anthropises, Villeurbanne, France – s.krause@bham.ac.uk*
U. Schneidewind *School of Geography, Earth and Environmental Sciences, University of Birmingham, Edgbaston, Birmingham, UK – u.schneidewind@bham.ac.uk*
E. van Onselen *Department of Applied Geology and Geophysics, Deltares, Utrecht, Netherlands – erik.vanonselen@deltares.nl*
P. van Rijnsoever *Van den Herik, Sliedrecht, Netherlands – paul.vanrijnsoever@herik.nl*
M. Karaoulis *Department of Applied Geology and Geophysics, Deltares, Utrecht, Netherlands – marios.karaoulis@deltares.nl*
L. Haverson *School of Geography, Earth and Environmental Sciences, University of Birmingham, Edgbaston, Birmingham, UK – l.haverson@bham.ac.uk*
M.G. Kleinhans *Department of Physical Geography, Utrecht University, Utrecht, Netherlands – m.g.kleinhans@uu.nl*
J. Stam *Van den Herik, Sliedrecht, Netherlands – jaap.stam@herik.nl*

ABSTRACT: River valleys are major stores of sediments and plastics, providing archives of their accumulation. However, the temporal storage of sediments in river beds and the mechanisms of deposition and accumulation of microplastics within subsurface sediments remain poorly understood. This study aims to understand the links between dune dynamics, spatio-temporal sediment preservation and the patterns of microplastic accumulation in the subsurface. We collected short time series of bathymetric and sub-bottom profiler data in combination with 18 vibracores in the River Waal, Netherlands. Here, we explore linking the internal sedimentary structures to their formative bedforms, with the aim of establishing the date of formation with bathymetric records collected over the past two decades. Preliminary quantification of microplastics in one core reveals highest concentrations in the active dune, but also an occurrence of microplastics in underlying dune sets. These data will permit unprecedented insight into the development of the sedimentary architecture and its influence on the distribution of microplastics in riverine sediments.

1 INTRODUCTION

The sustainable management of lowland rivers requires a better understanding of spatio-temporal patterns of deposition and erosion of river beds. River dunes are ubiquitous features in sand- and gravel-bed rivers and are key elements in bedload transport (Best, 2005; Zomer et al., 2021). Understanding the links between dune dynamics and the spatio-temporal patterns of sediment preservation (or reactivation) in

river beds is important to both system knowledge and the sustainable use of rivers.

Furthermore, river valleys are not only the conduits through which sediments and plastics are transported to the ocean, but also are major stores for plastics. Macroplastics have been found to accumulate in tidal river zones, rather than flowing out to sea (Van Emmerik, 2021) and pollute river banks, beds and water. For microplastics, recent modelling (Drummond et al., 2022) has indicated long residence times of microplastics in river beds (av. 2.5 hrs km^{-1} to max av. 0.15 year km^{-1} for microplastics <100 μm in the main stems of rivers). Through hyporheic exchange (i.e., surface water enters the river bed upstream and re-emerges at some point downstream, while potentially mixing with upwelling groundwater along its flow path, in which dunes also play an important role; e.g. Packman and Brooks, 2001; Frei et al., 2019), microplastics may be incorporated into the bed, re-entered into the water or transported into deeper layers (long-term burial) and into the surrounding floodplains, thereby affecting both riverine ecology and that in the surroundings.

To date, dune dynamics have often been analysed using multibeam echo sounder (MBES) time series, but the spatio-temporal sediment preservation of dune sediments in the subsurface remains poorly understood. Moreover, the mechanisms of deposition and accumulation of microplastics within river sediments are still largely unknown, since present empirical studies merely include water samples and bed (surface) sediments. Vitally, observations must cover the spatial patterns and temporal dynamics of microplastics as related to sedimentary heterogeneity.

This paper presents a preliminary analysis (around selected cores) of dune preservation and microplastics distribution in the bed of the River Waal, a branch of the River Rhine in the Netherlands. The near-3-D dataset that we acquired provides a comprehensive archive of accumulation, in which times of deposition can be dated using bathymetric records. Future quantification and characterisation of microplastics within the preserved sediments will offer a unique opportunity to derive and explain the presence, type and abundance of microplastics in the sedimentary record. These data will permit unprecedented insight into the development of the sedimentary architecture and its influence on the distribution of microplastics in riverine sediments.

2 METHODS AND DATA

In three areas of the River Waal, Netherlands (Figure 1), with varying longer-term bed dynamics (Van Dijk et al., 2015) and varying grain size (Ten Brinke, 1997), we collected simultaneous MBES and sub-bottom profiling data in time series (Table 1). These data were combined with 18 vibracores down to depths of ca. 5 m.

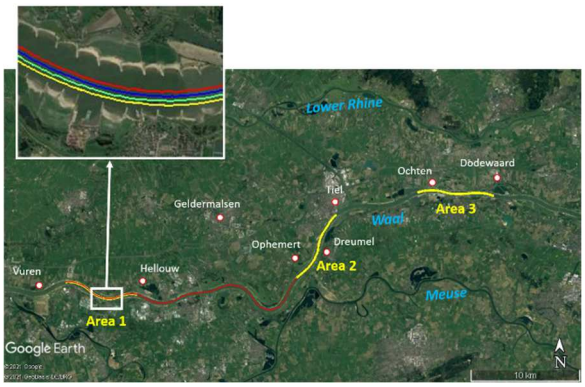

Figure 1: Locations of the three survey areas in the River Waal, Netherlands (yellow). The enlarged inset map of Area 1 shows the four survey lines. In addition, one track line (red in main figure) was surveyed to connect the most western Areas 1 and 2. Flow is from east to west.

2.1 Geophysical surveys

High-resolution MBES (for both bathymetry and backscatter) and sub-bottom profiler data (parametric echo sounder, PES) were recorded simultaneously, as to guarantee their ultimate correspondence in space and time. In each area, four 7 km-long lines were surveyed in the navigation channel (Figure 1), thus creating a near-3-D dataset, sailing in the upstream direction in order to limit the sailing speed to 5 km h^{-1} and provide excellent spatial data resolution.

Surveys were conducted by Van den Herik aboard the 'Sprinter', a small survey boat equipped with RTK, GPS and motion sensor. MBES data were recorded using a Teledyne RESON SeaBat T20-P at full swath (512 beams, -70/70°), 400 kHz and 50 pings s^{-1}, resulting in 50-200 observations m^{-2}. Sub-bottom profiling data were recorded with an Innomar Standard SES2000 Parametric Echo Sounder (PES), which was linked to the on-board GPS and motion sensor (Applanix) for optimal processing. The advantages of PES are that the echo sounder emits two primary frequencies, thereby creating two new secondary frequencies (a sum [high] and difference [low] frequency; Sambrook Smith et al., 2013), which results in a good return of the bed whilst preserving a good penetration at ca. 0.10 m vertical resolution. After testing for optimal settings, we used a low and high frequency of 8 and 100 kHz, respectively, ca. 43 pings s^{-1} (system-controlled) and we manually varied the start depth during surveying in order to obtain the optimal subsurface results.

Bathymetric data were gridded into 0.25 m resolution DEMs. PES data were processed to correct for vertical offsets, to convert to horizontal coordinates (i.s.o. $ping^{-1}$) and to suppress noise/to bring out reflectors, using auto-gain, and cleaning the water column.

2.1.1 Data in time series

Repeat surveys were near-exactly overlapping with the navigation lines of the first survey (S1). One repeat survey was conducted after 4 days in Area 1 (S1-R), and 3 weeks after the first survey in all three areas (S2; Table 1). The time in between the surveys was based on previous analyses of dune migration rates (Wilbers & Ten Brinke, 2003; Van Dijk et al., unpublished), so that dune migration between S1 and S2 would have resulted in dune displacement of half a wavelength of a large dune. The period of 4 days was just to be sure, in case dynamics were higher.

2.2 Vibracores

To link PES data to sediment characteristics, 18 vibracores were taken by Marine Sampling Holland (MSH) during survey S2, one day after the MBES and PES data for each of the three areas (Table 1). Core locations were based initially on the PES data from S1, to include clear internal active dune cross-stratification as well as sedimentary structures in the subsurface. Where dune migration dictated, based on inspection of the PES data of S2 (on the same day), core locations were refined. All vibracores penetrated to 5.9 m into the bed (often down into the multiple), but recovery was between 3.9 and 5.5 m, due to rodding.

Table 1: Survey overview

	Area 1	Area 2	Area 3
MBES & PES			
S1	31 May	1 Jun	2 Jun 2021
S1-R	3 Jun	.	.
S2	21 Jun	22 Jun	23 Jun 2021
VCs (S2)	22 Jun	23 Jun	24 Jun 2021

Sediment cores were split in the laboratory and described (according to NEN 5104 guidelines), whereby grain size was estimated using a comparative microscope. In addition, we made lacquer peels from the cores in order to bring out sedimentary structures, such as fine lamination.

2.3 Microplastics analyses

Cores were subsampled in the laboratory (using the 100 Plastic Rivers project laboratory protocol; UoB, 2019) throughout the depth of the cores and samples were analysed for microplastics (< 5 mm) at the University of Birmingham, using established methods (Nel et al., 2020). First, organic matter was digested (using H_2O_2, below 55°C) and density separation (using $ZnCl_2$ at 1.5 g cm^{-3}) was done to separate

microplastics from the sediment and to reduce false positive inclusion. Staining samples with Nile Red enabled fluorescent microscopy (lower size limit here is 64 µm) to count and measure putative plastic particles. µFTIR (micro-Fourier Transform Infrared Spectroscopy) will be performed on select samples (lower size limit is 20 µm) to identify polymer types. Herein, only plastic particles were counted in one core, but future analyses will be extended over the whole area and include particle size and polymer type data. Organic matter content was determined by loss on ignition (LOI).

2.4 Sediment grain-size analyses

Samples were analysed for grain-size distributions, using laser diffraction (Malvern Mastersizer) for the finer sediments and dry-sieving for the coarser sediments.

3 RESULTS

3.1 Morphology and sedimentary structures

Both the bathymetric and PES data show large dunes with superimposed small dunes. The PES data reveal internal sedimentary structures of the active dunes, exhibiting foresets of large dunes and smaller structures where superimposed small dunes descended along the lee slope of large dunes (Figure 2; Galeazzi et al., 2018). In nearly all data, the active large dunes have distinct horizontal reflectors at their base.

As revealed by the PES data, the sedimentary structures immediately below the active dunes and in the deeper subsurface, exhibit foresets of older dune sets (especially Area 1) or display larger-scale horizontal or concave reflectors.

The sediment cores showed large variations, comprising recent dune sediments to Pleistocene deposits. For example, core 2 (Area 1; west) comprised stacked sets of cross-bedded sand and gravel beds, whereas some cores in Area 3 (east) contained an organic clay layer and Pleistocene aeolian sands. In most sediment cores, the recent deposits of the active dunes were clearly distinct units with sharp basal boundaries.

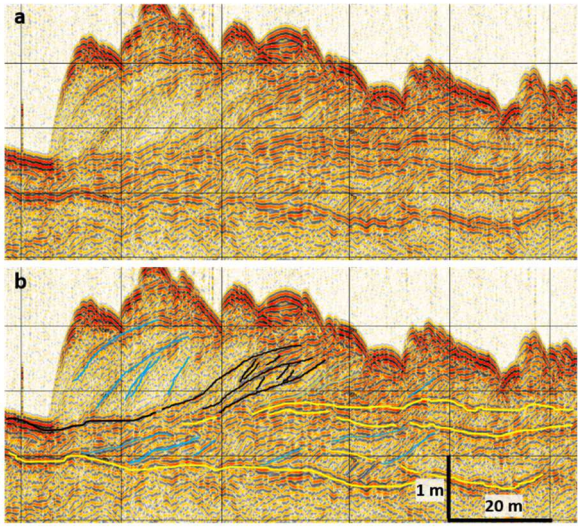

Figure 2: Example of sub-bottom profiler data (parametric echo sounding, PES), showing dune morphology, internal structures of the active dunes and reflections of older dune sets below. **a.** raw data. **b.** preliminary interpretation plotted on raw data.

3.2 Dune dynamics

Both the bathymetric and parametric echo sounding in time series, acquired during these surveys, record dune morphology and dune dynamics. The high-resolution bathymetry data is best used for quantitative morphometric and morphodynamic analyses, such as dune migration celerity. Quantitative analyses still have to be completed, but an initial estimate of average dune celerity based on one dune is 3.6 m day^{-1} in June 2021. Note that the PES data in time series are not only useful for determining sediment reactivation in the subsurface by dune movement, but also for identifying sedimentary structures to larger depths (i.e., where reflectors were within the signal multiple during one survey, they appeared in the other survey, by dune migration).

3.3 Dating of the sedimentary structures

By linking the bathymetry to the PES data, the more recent sedimentary structures can be dated accurately, thereby allowing for the reconstruction of depositional and erosional episodes. Dating the sediments is not only essential for future quantification of the spatio-temporal preservation of sediments in

the river bed, but also for the historic record of microplastics within these sediments and understanding the depositional processes and potential distribution of microplastics by hyporheic flow. In addition, a 2-weekly bathymetric time series over the past 16 years (2005-present) and a half-yearly time series (1999-2011) are available from Rijkswaterstaat, which provide a unique opportunity to date the dune structures. However, initial analyses of a selection of bathymetric profiles show a 'spaghetti'-plot, where dune migration causes a rapid and repeated replacement of dune deposits (active dune level). Moreover, a preliminary analysis of dune preservation, (i.e., exploring the riverbed built-up using bathymetric profiles – i.e., 1D – over time; Figure 4), revealed that dune migration has not only caused little preservation since 1999, but in some places the river bed has eroded into the 1999 bed. This implies that at these locations, recent dune deposits will directly overly pre-1999 sediments. This has also led to the finding that older pre-1999 bathymetric datasets (e.g. single-beam data) will be needed to date the sedimentary structures below the active dunes in the PES data.

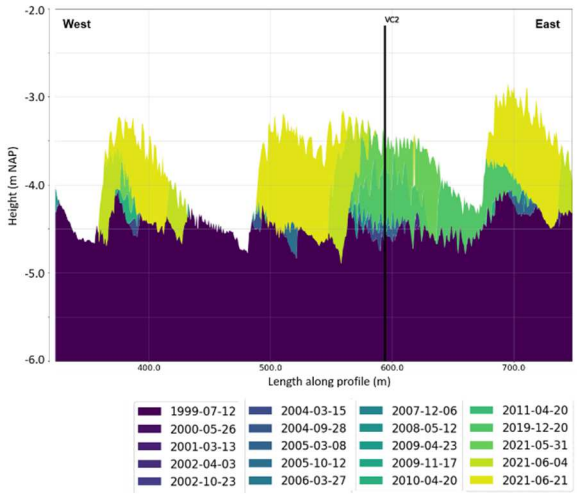

Figure 4: Exploring the analysis of dune preservation (example around core 2) for a small selection of bathymetric profiles between 1999 (purple) and the surveys in this study in 2021 (yellow and yellowish-green).

Additional indicators of the ages of the sediments are the occurrence of *Corbicula fluminea*, an invasive species of freshwater clam that was first recorded in the Rhine system in the Netherlands in 1987 (Den Hartog et al., 2007), and the geological model GeoTop of TNO Geological Survey of the Netherlands.

3.4 Microplastics (core 2)

The concentration of microplastics in core 2 was highest in the top 1 m of the core (see Figure 3, chart on the right). Nevertheless, small amounts of microplastic particles were found down to a depth of 3 m.

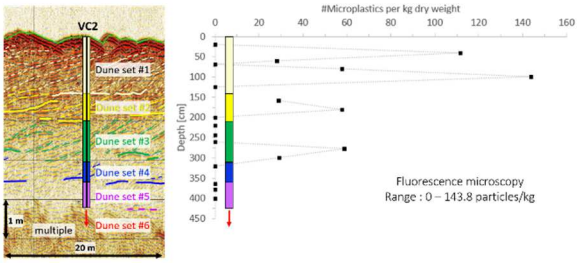

Figure 3: PES raw data with interpreted sedimentary structures around core 2, interpreted dune sets in core 2 and number of microplastics kg^{-1} per sample. The PES data are plotted on a vertically exaggerated scale, so the angles of lee slopes are steeper than in reality.

3.5 Interpretation around core 2

Core 2 is in the western part (lower reach) of the River Waal, where aggradation rates were expected to be largest. On the PES data, six dune sets were identified down to a depth of 5 m. The recovery depth of core 2 of 4.20 m captures five of these dune sets (Figure 3). The high content of microplastics in the top 1 m of the core corresponds to the active dunes (dune set #1). The occurrence of microplastics in the two older dune sets below (yellow and green in Figure 3) suggest active accumulation in older dunes or possible injection within hyporheic exchange.

4 DISCUSSION & FUTURE RESEARCH

The highest abundance of microplastics in the active dune set may confirm their recent deposition, simultaneously with the dune deposits. However, the occurrence of microplastics in the two older dune sets below suggests accumulation during deposition from older dunes (pre-1999) and/or inflow through hyporheic flow.

Although those older dune sets still need to be dated, these may potentially be pre-plastic era in age: if this is the case, hyporheic flow becomes the only mechanism for microplastic introduction into these lower dune sets. For the interpretation of microplastics within the sediments, it is thus crucial to assess the age of the sediments.

Using older (pre-1999) bathymetric data may help in determining the age of the dune sets below the active dune set. However, single-beam echo soundings may not go back in time far enough. In this case, linking the PES data to the Dutch geological model will provide crude depositional epochs of the Late Pleistocene and Early Holocene deposits.

At present, we have analysed the concentration of microplastics in core 2. Although this concentration was small, it is in the order of concentrations found in other rivers (i.e., to date, literature merely reports surface samples of the top 5 cm). Future analyses of all cores will provide the spatial distribution of microplastics (concentration, size and polymer type from FTIR) from surface samples and their vertical distribution in the subsurface of the River Waal.

For the geological context, future interpretation of the full MBES and PES datasets will present a near-3-D record of the sedimentary architecture. In combination with the 2-D bathymetric time series (surfaces rather than profiles) and vibracores, this is a unique 3-D dataset, which will allow quantification of dune dynamics and sediment preservation over time, identifying potential time gaps in the sediment cores and providing insight into the depositional processes of microplastics and hyporheic transport within these sediments. We can then start to link the spatio-temporal sediment storage to depositional events (e.g. floods). To date, creating such a dataset was only possible in flumes, whereas the field record presented herein may contribute to future data-driven morphodynamic modelling.

5 CONCLUSIONS

Dune stratification of active dunes, as revealed on the sub-bottom profiles in the River Waal, Netherlands, comprise foresets of large dunes and occasionally of superimposed small dunes. The combination of high-resolution bathymetry and simultaneously recorded PES data in time series allows for the quantification of spatio-temporal sediment preservation in the last two decades. The dune sets below the active layer may be dated using older bathymetric data.

Microplastics were more abundant in the active dune layer, but were present to a depth of 3 m, corresponding to two older dune sets. Future analyses of microplastics in all cores will provide the 3-D spatial distribution of microplastics in the subsurface. Combining these data with quantification of the sedimentary architecture leads to insights that permit explanation of processes that deposit and redistribute microplastics in river beds.

6 ACKNOWLEDGEMENT

This research was funded by the Dutch Topconsortia Knowledge and Innovation (TKI) base funding through Deltares (DEL107), and co-funded by Van den Herik Sliedrecht, Rijkswaterstaat (Rivers2Morrow programme) and Deltares's Strategic Research programme. Bram van der Kooy and Erik Roos (Van den Herik Sliedrecht) are thanked for their skilled help in linking the PES to on-board systems and with survey logistics.

7 REFERENCES

Best, J.L., 2005. The fluid dynamics of river dunes: A review and some future research directions. Journal of Geophysical Research 110, F04S02. doi:10.1029/2004JF000218

Den Hartog, C., van den Brink, F.W.B., van der Velde, G., 1992. Why was the invasion of the river Rhine by *Corophium curvispinum* and *Corbicula* species so successful? (opinion article) Journal of Natural History 26, 1121−1129. doi: 10.1080/00222939200770651

Drummond, J.D., Schneidewind, U., Li, A., Hoellein, T.J., Krause, S., Packman, A.I., 2022. Microplastic accumulation in riverbed sediment via hyporheic

exchange from headwaters to mainstems. Science Advances 8. doi:10.1126/sciadv.abi9305

Frei, S., Azizian, M., Grant, S.B., Zlotnikc, V.A., Toundykovd, D., 2019. Analytical modeling of hyporheic flow for in-stream bedforms: Perturbation method and implementation. Environmental Modelling and Software 111, 375-385. doi:10.1016/j.envsoft.2018.09.015

Galeazzi, C.P., Almeida, R.P., Mazoca, C.E., Best, J.L., Freitas, B.T., Ianniruberto, M., Cisneros, J., Tamura, L.N., 2018. The significance of superimposed dunes in the Amazon River: Implications for how large rivers are identified in the rock record. Sedimentology 65, 2388–2403. doi: 10.1111/sed.12471

Nel, H.A., Sambrook Smith, G.H., Harmer, R., Sykes, R., Schneidewind, U., Lynch, I., Krause, S., 2020. Citizen science reveals microplastic hotspots within tidal estuaries and the remote Scilly Islands, United Kingdom. Marine Pollution Bulletin 161, doi:10.1016/j.marpolbul.2020.111776

Packman, A.I., Brooks, N.H., 2001. Hyporheic exchange of solutes and colloids with moving bedforms. Water Resources Research 37, 2591-2605. doi:10.1029/2001WR000477

Sambrook Smith, G.H., Best, J.L., Orfeo, O., Bardy, M.E. and Zinger, J.A., 2013. Decimeter-scale in situ mapping of modern cross-bedded dune deposits using parametric echo sounding: A new method for linking river processes and their deposits. Geophysical Research Letters 40, 3883-3887. doi:10.1002/grl.50703

Ten Brinke, W.B.M., 1997. De bodemsamenstelling van Waal en IJssel in de jaren 1966, 1976, 1984 en 1995. Rijkswaterstaat RIZA, ISBN 9036950562

University of Birmingham, 2019. 100 Plastic Rivers – a global investigation. Unpublished, 8 pp.

Van Dijk, T.A.G.P., Van der Mark, C.F., Doornenbal, P.J., Menninga, P.J., Keppel, J.F., Rodriguez Aguilera, D., Hopman, V., Erkens, G., 2012. Onderzoek Meetstrategie en Bodemdynamiek. Deltares report, 1203749-000-BGS-0006.

Van Emmerik, T., 2021. Macroplastic research in an era of microplastic (editorial). Microplastics and Nanoplastics 1, doi:10.1186/s43591-021-00003-1

Zomer, J.Y., Naqshband, S., Vermeulen, B., Hoitink, A.J.F., 2021. Rapidly migrating secondary bedforms can persist on the lee of slowly migrating primary river dunes. Journal of Geophysical Research: Earth Surface 126. doi:10.1029/2020JF005918

Understanding marine dune dynamics in a shallow shelf sea using sediment mobility indices

N. Durand *France Energies Marines, Plouzané, France – noemie.durand@ite-fem.org*
P. Tassi *EDF Recherche & Développement, Chatou, France – pablo.tassi@edf.fr*
O. Blanpain *France Energies Marines, Plouzané, France – olivier.blanpain@ite-fem.org*
A. Lefebvre *MARUM, University of Bremen, Germany – alefebvre@marum.de*

ABSTRACT: Tides, winds, and waves shape the seabed of shallow shelf seas. In sandy, energetic environments, marine dunes can develop. The scale and dynamic behaviour of these bed forms warrant some interest, for example related to the interactions with human activities (mining, renewable energies). Yet, the morphology and dynamics of dunes are still poorly understood in open marine environments. A complex process-based model (http://www.opentelemac.org) is being developed for an application in the southern North Sea, offshore of Dunkirk in France, with the objective to improve our comprehension of the processes at play.

1 INTRODUCTION

Marine dunes are large, flow-transverse bed forms with height of 1 m to 5 m and wavelength of the order of hundreds of metres (Ashley 1990). They develop almost exclusively on sandy seabeds, in settings where bedload is the predominant mechanism of sediment transport. They are very dynamic sedimentary structures that grow, evolve and migrate in space and time, at rates of up to tens of metres per year.

A complex process-based numerical model (accounting for the interactions between currents, waves and sediment transport processes) is being developed for an application offshore of Dunkirk, on the northern coast of France, close to the Belgium border. Marine dunes coexist there with sand banks. The site is subjected to relatively strong tidal flows, and waves originating from the Atlantic Ocean and the North Sea.

The combined influence of waves and currents is expected to mobilise the sediments on the seabed. As a first step, outputs from the calibrated hydrodynamic and wave models are used to construct sediment mobility maps that highlight some of the processes at play in this complex and highly dynamic environment.

2 STUDY AREA

This study focuses on the southern North Sea, offshore of Dunkirk (Figure 1). Seabed levels in the area are generally between 7 and 30 m below mean sea level (MSL), noting the presence of offshore sand banks with crests as high as -6 m MSL. The seabed sediment consists of well sorted medium sands with d_{50} grain sizes between 240 and 450 µm based on recent samples. It is not expected that sediments exhibit cohesive properties.

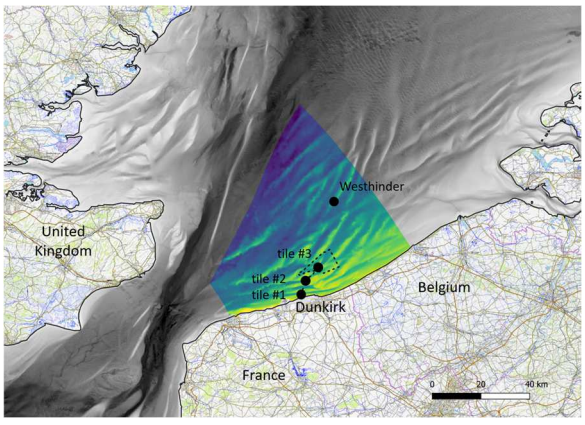

Figure 1. Location map showing the full model extent (in colour), the proposed offshore wind farm footprint (dashed line) and the survey tiles (filled circles) (Source of the background data: Shom 2015 and https://opentopomap.org/).

The region is characterised by a macro-tidal regime (ca. 5.5 m spring tidal range, 3.3 m neap tidal range). The tide is asymmetric: it rises faster than it falls. This asymmetry is also observed in the tidal currents and the flood, trending North-East, is generally stronger than the ebb, trending South-West (ca. 1.25 m/s compared to 0.75 m/s).

While the offshore wave climate (at Westhinder, Figure 1) is dominated by south-westerly waves, some significant events from the North-West to the North-East are noted. 56% of the waves are under 1 m. The wave condition with a 1-year return period is estimated at H_s = 4.4 m, with associated mean period, T_z, around 7 s.

3 METHODS

3.1 Metocean and bathymetric surveys

A large metocean and bathymetric data set has been collected in support of Dunkirk offshore wind farm project and for research purposes. Site-specific meteorological and hydrodynamic campaigns have been carried out for periods of up to six months. Long-term metocean observations are also available from the Flanders Marine Institute (VLIZ) at Westhinder measurement pile / buoy. All these records inform the wind velocity, atmospheric pressure, water level, current velocity (at various elevations in the water column), and wave conditions. They provide a valuable in-situ data set against which to calibrate the hydrodynamic and wave models.

Recurrent and detailed bathymetric surveys have been carried out. Two large-area surveys covering the wind farm footprint (dashed outline in Figure 1) were conducted in 2016-2017 (Shom) and in June 2021 (EMD). Separately, eight surveys were performed between 2019 and 2021 (FEM), in three pre-defined tiles (filled circles in Figure 1) selected to include a variety of bed forms. These local-area surveys will serve to calibrate the morphodynamic model. A special emphasis is placed on tile #1 (in the navigation approach channel) going forward. Bed levels surveyed in November 2019 are reproduced in Figure 2.

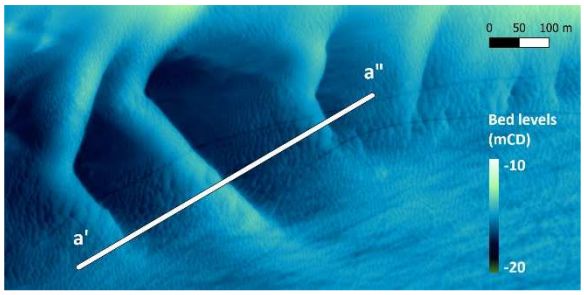

Figure 2. Bed levels in tile #1 in November 2019 (FEM) showing section a'-a" where dune profiles have been extracted.

3.2 Coastal area model

Both 2D and 3D coastal area models are being developed based on the open source TELEMAC system (www.opentelemac.org). These models consider interactions between tidal flows, winds, waves and sediment transport processes. The same computational domain and spatial discretisation are used throughout.

The domain extends from Calais to Ostend in Belgium, for approximately 80 km. Its offshore extent varies between 15 km in the Dover Strait and 75 km in the East (Figure 1). An unstructured finite element mesh with spatially varying resolution is used. The size of the triangular elements varies gradually from 10 m in the areas of interest to a maximum of 3000 m away from them. Overall, the computational domain comprises approximately 64 k nodes.

Digital elevation models of the seabed throughout the model area have been constructed that are relevant to different time periods.

3.3 Hydrodynamic model

The open source TELEMAC system has both 2-dimensional (2D) and 3-dimensional (3D) hydrodynamic modules. While TELEMAC-2D solves the depth-integrated shallow water equations, TELEMAC-3D solves the 3D Navier-Stokes equations with, or without, the hydrostatic pressure assumption (Hervouet 2007). Both modules were used in this study, and if the model validation is presented for the 3D module in section 3.5, subsequent mobility maps and analysis are largely based on depth-averaged results. In

the 2D model, the bottom roughness is parameterised with the Chézy formulation, spatially constant coefficient of 65 $m^{½}/s$. This value is appropriate for sandy seabeds. In the 3D model, a Nikuradse roughness of 862.5 µm is used, corresponding to 2.5 times the grain size representative of the study area.

Time-varying sea levels are applied along the open water boundaries of the hydrodynamic model. These time histories are computed from the 34 constituents available from the FES2014 database produced by Noveltis, Legos and CLS (https://www.aviso.altimetry.fr) at a spatial resolution of 1/16°. In addition to tidal forcing, time- and space-varying wind and pressure fields are applied over the model area to account for the effect of a wind blowing on the water surface and causing set-up and wind-induced currents, as well as the "inverted barometer" effect, caused by atmospheric pressure variations. These fields were extracted from the Météo-France short-term operational forecast AROME (Boutier 2007) at a spatial resolution of 1/40° and hourly intervals, after it was demonstrated that its higher resolution outweighed the reputedly lower accuracy of forecast models in the study area (Durand et al. 2022b).

3.4 Wave model

The wave generation and transformation module, TOMAWAC, solves the spectral action density balance equation with sources and sinks, and no a priori restrictions on the spectral shape or evolution (Benoit et al. 1996).

Time-varying wave spectra were obtained from the ANEMOC-3 sea state hindcast database (Raoult et al. 2018 and Teles et al. 2022) at 56 locations along the open boundaries of the wave model. The use of spectral data is preferred over integrated sea states, in that it reduces the loss of information between the global database and the local model. The spectra are discretised with 32 frequencies and 36 directions and output at half-hourly intervals. AROME time- and space-varying wind fields are applied over the model area to account for local wave generation due to winds. In shallow shelf seas, tidal effects also play a role on wave propagation and transformation. These effects are considered by using time- and space-varying maps of water depths and currents obtained from the validated hydrodynamic model of the same area.

3.5 Model calibration and validation

Durand et al. (2022a) details the procedure for the calibration and validation of the hydrodynamic model against in-situ free surface elevation and depth-averaged flow velocity data. Table 1 and Figure 3 present updated results.

Table 1: Performance of the hydrodynamic model against observed data for a complete spring-neap cycle. Root Mean Square Error (RMSE) values and Relative Mean Absolute Error (RMAE) in brackets

	tidal levels	current speeds
Site 1	--	0.13 m/s (19%)
Site 2	--	0.09 m/s (15%)
Site 3	0.26 m (5%)	0.11 m/s (17%)
Site 5	0.15 m (3%)	0.12 m/s (14%)
Site 7	--	0.09 m/s (13%)
Westhinder '16	0.18 m (3%)	--
Westhinder '21	0.15 m (3%)	--

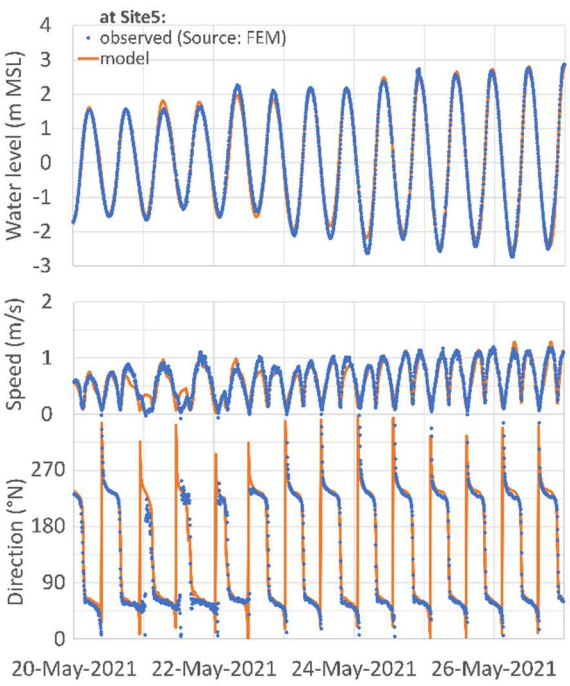

Figure 3. Comparison of model predictions against observed tidal levels (top), current magnitude (centre) and direction (bottom) for a 7-day period in 2021.

Durand et al. (2022b) presents the calibration and validation of the wave model against in-situ wave conditions (significant height, mean period and mean direction). These results are reproduced in Table 2 and Figure 4.

Table 2: Performance of the wave model against observed data (40 days in 2016, 16 days in 2021). RMSE values and RMAE in brackets

	Hm_0	Tm_{02}
Site 1	0.13 m (18%)	0.5 s (16%)
Site 2	0.15 m (15%)	0.4 s (10%)
Site 7	0.16 m (20%)	0.6 s (13%)
Westhinder '16	0.18 m (15%)	0.6 s (14%)
Westhinder '21	0.18 m (18%)	0.6 s (12%)
Gravelines	0.16 m (22%)	0.8 s (16%)

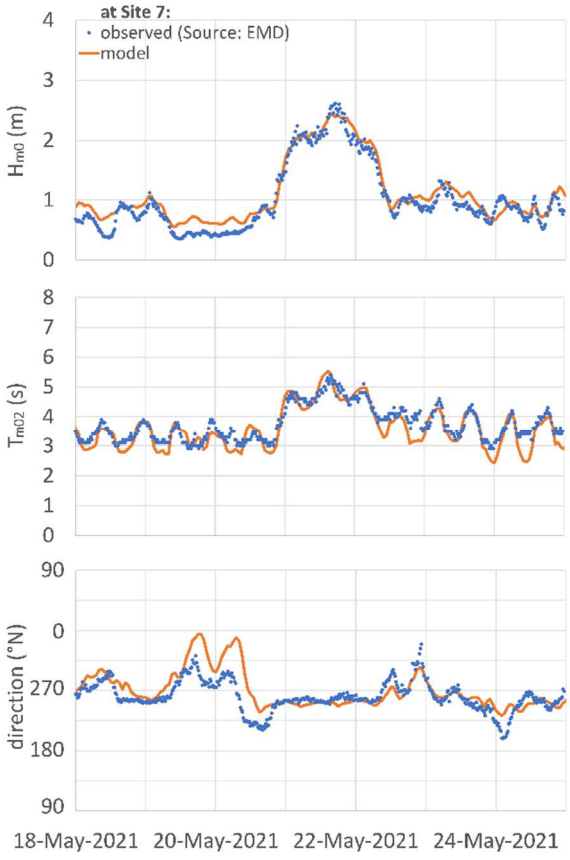

Figure 4. Comparison of model predictions against observed wave height Hm_0 (top), mean wave period Tm_{02} (centre), and mean wave direction (bottom) for a 7-day period in 2021.

Sutherland et al. (2004) propose a statistical approach based on RMAE, and associated classification, to evaluate the performance of numerical models. It follows that the hydrodynamic model results (tidal level and current magnitude) fall in the "excellent" category (RMAE < 20%) at all six validation sites. A similar conclusion is drawn for the wave model results at all but two sites where the performance is qualified as "good" (RMAE < 40%).

Calibrated numerical models can be used to overcome spatial and temporal limitations in field observations. And so a two-year period (January 2020 to December 2021) was run in the validated hydrodynamic and wave models to perform some preliminary analysis of sediment mobility in the study area, based on oceanographic considerations.

3.6 Bed shear-stress

Grain shear-stresses induced by currents and those induced by waves are computed independently by the coupled hydrodynamic and wave models. The shear-stresses generated by currents alone, τ_C, are computed from the water density ρ = 1027 kg/m^3, the dimensionless drag coefficient C_D (a function of the friction coefficient) and the depth-averaged current velocity U as a first approximation:

$$\tau_C = \rho C_D U^2 \quad (1)$$

The shear-stresses generated by waves alone, τ_W, are computed from the water density, the rms orbital velocity near the seabed U_{rms} (small-amplitude linear wave theory, in the absence of a current), and the dimensionless wave friction factor f_w defined in Swart (1976):

$$\tau_W = \rho f_w U_{rms}^2 \quad (2)$$

The mean and maximum bed shear-stresses during a wave cycle, due to the combined action of waves and currents, are computed from Soulsby (1997):

$$\tau_m = \tau_C \left[1 + 1.2 \left(\frac{\tau_W}{\tau_C + \tau_W}\right)^{3.2}\right] \quad (3)$$

$$\tau_{max} = \sqrt{(\tau_m + \tau_W \cos\phi)^2 + (\tau_W \sin\phi)^2} \quad (4)$$

where ϕ = angle between the current and wave directions.

3.7 Sediment mobilisation

To estimate sediment mobilisation, the threshold bed shear-stress for the onset of motion is computed for a sediment with median grain diameter d_{50} of 345 µm (corresponding to the average sample):

$$\tau_{cr} = \theta_{cr} \left[g \left(\rho_s - \rho \right) d_{50} \right] \quad (5)$$

where g = 9.81 m/s^2 is the acceleration due to gravity; ρ_S = 2650 kg/m^3 is the sediment density; and θ_{cr} is the threshold Shields parameter estimated from Soulsby (1997).

Seabed sediment is mobilised by either current, wave, or the combined wave and current action. The dominant processes will vary in space and in time. Their relative importance can be estimated from the percentage of time when the threshold bed shear-stress, τ_{cr} (Eq. 5), is exceeded by the tide-induced bed shear-stress, τ_C (Eq. 1), and by the wave-induced bed shear-stress, τ_W (Eq. 2), considered separately. Porter-Smith et al. (2004), Li et al. (2015), Coughlan et al. (2021) have used this type of representation to regionalise the prevailing processes. The classification scheme used in Porter-Smith et al. (2004) for the Australian Shelf was adapted in this work and a region is categorised as:

- "tide-dominated" when the percentage of time of tidal mobilisation is greater than three times that of wave mobilisation,
- "wave-dominated" when the percentage of time of wave mobilisation is greater than three times that of tidal mobilisation,
- "mixed" in between.

Another useful indicator of sediment mobility is the Mobilisation Frequency Index (MFI), defined as the percentage of time the threshold bed shear-stress for the chosen grain size, τ_{cr} , is exceeded by the maximum bed shear-stress under combined wave and current action, τ_{max} (Eq. 4). MFI therefore gives some indication on how often the seabed sediment is mobilised at a given location.

This is complemented by the Sediment Mobilisation Index (SMI) that integrates both the magnitude and frequency of sediment mobilisation. SMI is calculated as the mean ratio of the maximum combined bed shear-stress, τ_{max}, by the threshold bed shear-stress, τ_{cr} (only for those times when the threshold of motion is exceeded) times the percentage time exceedance (Li et al. 2009).

The spatial distribution of these indices over the study area was computed from the validated numerical model output for 2020-2021. Considering complete years removes any seasonal bias, although it is recognised that a more robust approach would consist in using a longer period (computational time constraints).

3.8 Sediment transport mechanism

The Rouse number, P, is a non-dimensional parameter that defines the shape of the suspended sediment concentration profile. By extension it is often used as an indicator for the mechanism of sediment transport. Bedload transport is prevailing when P values are greater than 2.5, and suspended transport is prevailing when P values are under 1.2 (Fredsøe & Deigaard 1992).

The Rouse number is expressed as the ratio between the sediment settling velocity w_s and the upwards velocity acting on the grain:

$$P = w_s / (\kappa \, u_*) \quad (6)$$

with κ the von Kármán constant = 0.40 (Soulsby 1997), and u_* the friction velocity. In these calculations, w_s. is estimated from Soulsby (1997) in the absence of in-situ measurements, and u_* was replaced by $\sqrt{\tau_m / \rho}$ since wave action will contribute to seabed sediment mobilisation in the study area.

4 RESULTS AND DISCUSSIONS

4.1 Maps of sediment mobility

By computing the percentage time of exceedance of the threshold shear-stress, a spatial assessment of the relative importance of current and wave processes in mobilising seabed sediment was carried out. The result of this analysis is shown in Figure 5. It follows that sediment in the study area is

predominantly mobilised by the strong tidal current (at least three times more than by waves) in relatively deep waters. Over the sand banks (an area broadly delineated by the -15 m MSL contour) the role of waves in stirring the sediments is enhanced and these areas are designated as "mixed" in accordance with Porter-Smith et al. (2004) classification. This corroborates our working hypothesis that wave action should not be discarded as a mechanism for sediment mobilisation (Durand et al. 2022b). Wave-dominated disturbance occurs in very localised areas, only close to the shore, where tidal currents are weakened, and wave orbital velocities stronger owing to reduced water depths. With this scheme, tile #1 is classified as "tide-dominated".

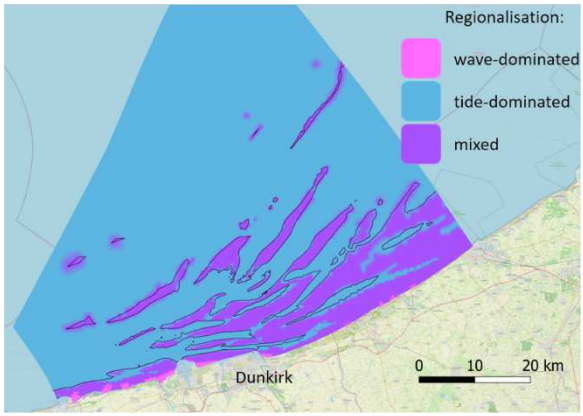

Figure 5. Regionalisation of seabed mobilisation by different dominant processes, also showing the -15 m MSL isobath. (Source of the background data: https://www.openstreetmap.org/).

It is recognised that this regionalisation is the result of an average over a two-year period and does not mean to say that wave contribution to sediment mobilisation is minimal in "tide-dominated" areas. Indeed, during storms for example, the wave action can be stronger than that of the currents in stirring the seabed sediment as illustrated in Durand et al. (2022b).

Figure 6 presents a map of the percentage time exceedance of the threshold bed shear-stress. MFI values range from 0 to 96%. High levels of exceedance (> 70%) are largely correlated to sand bank crests (water depths shallower than 15 m) and the "mixed" disturbance areas highlighted in Figure 5. Within tile #1, the seabed sediment is mobilised 60% of the time on average, with higher rates (up to 67%) on top of the dune crests, in the navigation channel.

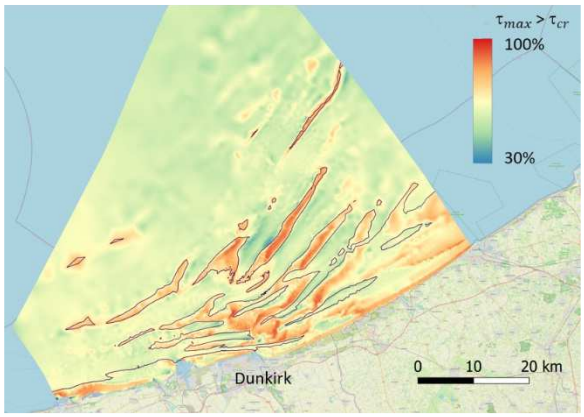

Figure 6. Mobilisation Frequency Index (MFI) computed from two years of model results, also showing the -15 m MSL isobath. (Source of the background data: https://www.openstreetmap.org/).

Figure 7 presents the spatial distribution of the Sediment Mobilisation Index. SMI values typically range between 0 and 2.5 in 'tide-dominated" areas. These values are comparable to those reported by Coughlan et al. (2021) in the Irish Sea, and generally higher than those reported by Li et al. (2015) in the Bay of Fundy. Higher SMI values (typically reaching 5.0) are computed in "mixed" areas, in particular along the coast and atop the sand banks (associated reduced water depths). These values are indicative of intense sediment mobilisation due to the combined wave and current action.

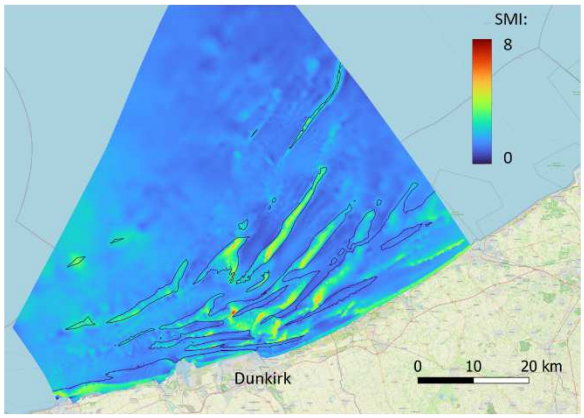

Figure 7. Sediment Mobilisation Index (SMI) computed from two years of model results, also showing the -15 m MSL isobath. (Source of the background data: https://www.openstreetmap.org/).

Within tile #1, SMI values range between 1.2 and 2.0. Remembering that the seabed sediment there is mobilised ca. 60% of the time, the threshold of motion is exceeded between 2 and 3 times, on average over a two-year period. It can be expected that tile #1 be more active during storms.

4.2 Map of sediment transport mechanism

The Rouse number, computed from Equation 6 over the whole model area, and averaged over the two-year period between 2020 and 2021, was estimated in excess of 2.5. This gives some indication that bedload is the dominant sediment transport mechanism in the study area (Fredsøe & Deigaard 1992) and is in line with Borsje et al. (2014) findings on the Dutch continental shelf that marine dunes could only form when Rouse numbers were greater than 2.0.

4.3 Dune profiles in tile #1

The evolution in time of the dune profile along section a'-a" (Figure 2), extracted from the local survey data, is depicted in Figure 8. For clarity, the time intervals between the successive bathymetric surveys will be referred to as periods A to G in the following.

It is clear from Figure 8 that the dunes evolution is not constant in time and is rather dependent on external factors. The dunes are very mobile during period A (compare to C and F with similar durations). In that period, the shape of the dunes remains mostly unchanged, and they migrate ca. 15 m to the East. Interestingly, lee slopes of the dunes become gentler during periods B and G, resulting in an apparent migration of the crest towards the West.

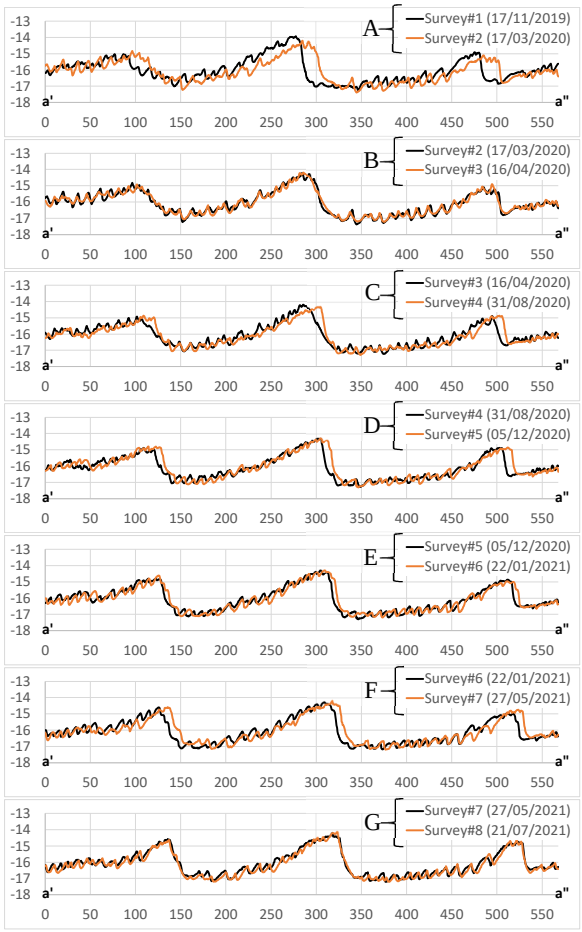

Figure 8. Dune profiles in tile #1, along section a'-a", showing the evolution in time.

5 CONCLUDING REMARKS

A coastal area model is being developed based on the complex process-based open source TELEMAC system. Overall, the comparisons presented in this and earlier work indicate a good performance of the hydrodynamic and wave models in the study area under a range of tidal currents and offshore wave and wind conditions.

Sediment mobility maps have been produced for the study area from validated model (hydrodynamic and wave) data for 2020-2021. The maps indicate that tidal as well as wave action plays a role in mobilising the seabed sediment, the predominant mode of transport being then bedload transport, in line with the presence of marine dunes in the area. The seabed sediment is more frequently set in motion, and bed shear-stresses more largely exceeded, in shallow areas (notably over the sand banks) than in waters deeper than ca. 15 m MSL, in line with expectations.

Focusing on tile #1, the next step will be to quantify how the oceanographic parameters vary between bathymetric surveys to explain the different dynamics illustrated in Figure 8. This task will be performed by including the sediment transport module GAIA (Tassi et al. 2023) into the coastal area model. Preliminary analysis indicates that the wave climate was markedly

different between period A (unusually high proportion of wave heights exceeding 1 m and maybe importantly a high proportion of south-westerly waves) and periods B and G (unusually large proportion of northerly waves) for example.

6 ACKNOWLEDGEMENTS

This work was initiated by France Energies Marines, with financial support from the French National Research Agency ANR (Grant no ANR-10-IEED-0006-34). The authors would like to thank the partners of the MODULLES project for providing site-specific data and giving permission to publish this work.

7 REFERENCES

Ashley, G.M., 1990. Classification of large-scale subaqueous bedforms: A new look at an old problem. Journal of Sedimentary Research 60, 160-172. doi:10.2110/JSR.60.160

Benoit, M., Marcos, F., and Becq, F., 1996. Development of a third-generation shallow water wave model with unstructured spatial meshing. Proceedings 25th Int. Conf. on Coastal Eng. 465-478. doi:10.9753/icce.v25.%25p

Borsje, B., Kranenburg, W., Roos, P., Matthieu, J., and Hulscher, S., 2014. The role of suspended load transport in the occurrence of tidal sand waves. Journal of geophysical research. Earth surface, 119(4), 701-716. doi:10.1002/2013JF002828

Boutier, F., 2007. Arome, avenir de la prévision régionale. La Météorologie, 58, 12-20. doi:10.4267/2042/18203

Coughlan, M., Guerrini, M., Creane, S., O'Shea, M., Ward, S. L., Van Landeghem, K. J., Murphy, J., and Doherty, P., 2021. A new seabed mobility index for the irish sea: Modelling seabed shear stress and classifying sediment mobilisation to help predict erosion, deposition, and sediment distribution. Continental Shelf Research, 229. doi:10.1016/j.csr.2021.104574

Durand, N., Tassi, P., Blanpain, O., and Lefebvre, A., 2022a. Towards numerical modelling of marine dunes in a shallow shelf sea. Actes des XVIIèmes Journées Nationales Génie Côtier-Génie Civil, Chatou, France. in press

Durand, N., Tassi, P., Blanpain, O., and Lefebvre, A., 2022b. Hydrodynamic modelling as a first step to assess marine dune dynamics: influence of waves. XVIIIth Telemac-Mascaret User conference. October 18-19, 2022. Paris-Saclay, France. in press

Fredsøe, J., and Deigaard, R., 1992. Mechanics of Coastal Sediment Transport. World Scientific. doi:10.1142/1546

Hervouet, J.-M., 2007. Hydrodynamics of Free Surface Flows: Modelling with the Finite Element Method. Wiley

Li, M.Z., Zou, Q., Hannah, C., Perrie, W., Prescott, R., and Toulany, B., 2009. Numerical Modelling of Seabed Disturbance and Sediment Mobility with applications to Morphodynamics on the Storm-dominated Sable Island Bank, Scotian Shelf. Geological Survey of Canada, Open File 6155

Li, M.Z., Hannah, C.G., Perrie, W.A., Tang, C.C.L., Prescott, R.H., and Greenberg, D.A., 2015. Modelling seabed shear stress, sediment mobility, and sediment transport in the Bay of Fundy. Can. J. Earth Sci. 52, 757-775. doi:10.1139/cjes-2014-0211

Porter-Smith, R., Harris, P., Andersen, O., Coleman, R., Greenslade, D., and Jenkins, C., 2004. Classification of the australian continental shelf based on predicted sediment threshold exceedance from tidal currents and swell waves. Marine Geology, 211(1), 1-20. doi:10.1016/ j.margeo.2004.05.031

Raoult, C., Joly, A., Andreevsky, M., and Joly-Laugel A., 2018. ANEMOC-3: Improving the ANEMOC-2 Sea state database by adding tide effects. Actes des 16èmes Journées de l'Hydrodynamique, 27-29 Novembre 2018, Marseille, France

Shom, 2015. MNT bathymétrique de façade atlantique. doi:10.17183/MNT_ATL100m_ HOMONIM_WGS84

Soulsby, R., 1997. Dynamics of marine sands. Thomas Telford Publishing

Sutherland, J., Walstra, D.J.R., Chesher, T.J., van Rijn, L.C., and Southgate, H.N., 2004. Evaluation of coastal area modelling systems at an estuary mouth. Coastal Engineering, 51, 119-142. doi:10.1016/j.coastaleng.2003.12.003

Swart, D. H., 1976. Predictive equations regarding coastal transports. Proceedings 15th Int. Conf. on Coastal Eng. 1113–1132. doi:10.9753/icce.v15.65

Tassi, P., Benson, T., Delinares, M., Fontaine, J., Huybrechts, N., Kopmann, R., Pavan, S., Pham, C.T., Taccone, F., and Walther, R., 2023. GAIA - a unified framework for sediment transport and bed evolution in rivers, coastal seas and transitional waters in the TELEMAC-MASCARET modelling system. Environmental Modelling and Software. 159(5). doi:10.1016/j.envsoft.2022.105544

Teles, M., Weiss, M, .and Benoit, M., 2022. Assessment of the ANEMOC-3 sea state hindcast database for modelling a series of energetic winter storms along the French coast. Actes des XVIIèmes Journées Nationales Génie Côtier-Génie Civil, Chatou, France. in press

Vortex trapping of sand grains over ripples under oscillatory flow

D. Frank-Gilchrist *U.S. Geological Survey - St. Petersburg Coastal and Marine Science Center, St. Petersburg, Florida, USA - dfrank-gilchrist@usgs.gov*
A. Penko *U.S. Naval Research Laboratory, Stennis Space Center, Mississippi, USA - allison.penko@nrlssc.navy.mil*
M. Palmsten *U.S. Geological Survey - St. Petersburg Coastal and Marine Science Center, St. Petersburg, Florida, USA - mpalmsten@usgs.gov*
J. Calantoni *U.S. Naval Research Laboratory, Stennis Space Center, Mississippi, USA- joe.calantoni@nrlssc.navy.mil*

ABSTRACT: Sand ripples significantly impact morphodynamics in the nearshore by generating coherent vortices, which can transport suspended sediment to greater heights in the water column than above flat beds. Coherent vortices can trap sediment grains if the settling velocity of the grain is smaller than the maximum vertical fluid velocity in the vortex (Nielsen 1992). Particle image and tracking velocimetry were used to measure small-scale fluid-sediment interactions over sand ripples in a small oscillatory flow tunnel. Here we present some of the first measurements of vortex-trapped sediment grains under oscillatory flows. Results showed that the vortex-trapped sand grain traversed an orbit off-center of the vortex near the ripple slope. Some grains then spiralled outward and settled to the bed; others were transported by the flow as the vortex was shed from the crest. Vortex trapping can delay settling and increase settling times, potentially causing inaccurate sediment transport predictions by large-scale numerical models, which do not typically account for this non-linear small-scale process.

1 INTRODUCTION

Sand ripples impact hydrodynamics and morphodynamics in the nearshore. For example, fluid velocities above ripple crests may be up to two times faster than the freestream (Van der Werf et al., 2007; Frank-Gilchrist et al., 2018). The hydrodynamics of the flow up to twice the ripple height above the ripple crest are dominated by coherent vortices, formed on the ripple slopes and ejected into the water column at flow reversal (Davies and Villaret, 1997; Rodríguez-Abudo et al., 2013).

The coherent vortices, shed from ripples, transport sediment as suspended load to greater heights in the water column than above flat beds (Van der Werf et al., 2006; Nichols and Foster, 2007; Frank-Gilchrist et al., 2018). Coherent vortices also trap sediment grains when the settling velocity of the sediment grain is smaller than the maximum upward fluid velocity in the vortex (Nielsen 1992). Under these conditions, the grain would traverse an orbit off-center of the vortex before spiraling outward and eventually settling to the bed or being transported by the flow. This can cause increased settling time, making vortex trapping an important mechanism that may affect sediment transport in coastal regions. The lack of delayed settling in models may lead to inaccurate predictions of bedform evolution, estimates of bed shear stresses, and consequently large-scale sediment transport processes impacting coastal regions.

In this study, one of the first observations of vortex trapping of sediment grains under oscillatory flows is presented. Measurements of small-scale fluid-sediment interactions by Frank-Gilchrist et al. (2018) were further analyzed for oscillatory flow conditions under which vortex trapping was observed. Qualitative comparisons with the vortex trapping hypothesis of Nielsen (1992) are also described.

2 EXPERIMENTAL METHODS

High-resolution experiments were conducted in the Small Oscillatory Flow Tunnel (S-OFT) at the U.S. Naval Research Laboratory at Stennis Space Center, Mississippi, USA. The test section is 2 m long with a flow cross-section of 0.25×0.25 m (Calantoni et. al, 2013). Oscillatory flow was generated with a piston and flywheel assembly to drive sediment transport and ripple formation (Frank-Gilchrist et al., 2018). The rippled bedforms were comprised of well-sorted, coarse quartz sand with a median grain diameter of 0.7 mm and density of 2,650 kgm^{-3}.

Phase-separated particle image velocimetry (PIV) and particle tracking velocimetry (PTV) were used to measure three-dimensional fluid velocities and two-dimensional sediment velocities in the oscillatory bottom boundary layer in a two-dimensional vertical plane of the water column. A downward-looking Nd: YAG laser was mounted above the test section to produce the 2 mm light sheet. Optical filters were installed on two high-speed cameras, set up in stereographic mode, to capture the light re-emitted at a higher wavelength by the fluorescent tracer particles (Figure 1). A neutral density filter was installed on the third camera, centered in the test section, to capture the light scattered by the sediment grains. The overlapping, simultaneously recorded images provided sediment particle and fluid velocities at high temporal (100 Hz) and spatial (≤ 1 mm) resolution. Further details of the experimental setup are described in Frank-Gilchrist et al. (2018).

The PIV images captured by the two outer cameras were processed with the LaVision software, DaVis (LaVision 2014) to calculate the three components of fluid velocity. The images captured by the center camera were used to calculated the mean image to represent the background intensity. The particle finder algorithm determined areas of contrast that had higher intensity than the background, given a threshold intensity (Ouellette, 2010). Contiguous areas of laser light intensity scattered by the grains that were higher than the threshold intensity count and larger than the minimum area of pixels representing the imaged sediment grain, were compared with the raw camera images to verify that sediment grains were detected. The centroid for each contiguous area of light was calculated to determine the location coordinates for each sediment grain (Ouellette, 2010). The grain location

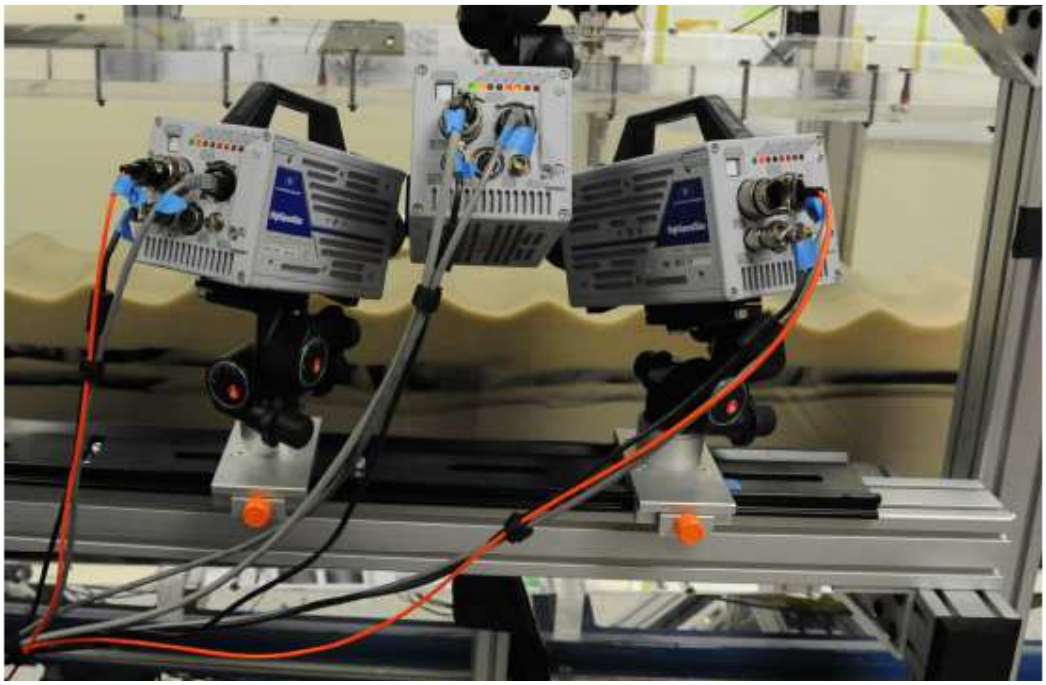

Figure 1. Experimental setup of particle image and tracking velocimetry system in the Small-Oscillatory Flow Tunnel at the U.S. Naval Research Laboratory, MS.

coordinates and estimated maximum displacement of the sediment grains between time steps were used by a particle tracking algorithm (Ouellette et al., 2006) to distinguish the sediment grains and determine the associated trajectories. The sediment grain trajectories were then compared with the vortex trapping hypothesis of Nielsen (1992).

3 RESULTS & DISCUSSION

Two-dimensional ripples were generated in the oscillatory flow tunnel, and high-resolution measurements of fluid-sediment interactions were made to assess sediment transport mechanisms over the sand ripples. The two-dimensional ripples generated in the oscillatory flow tunnel had a wavelength of 0.13 m and a ripple height of 0.025 m (Frank-Gilchrist et al., 2018). Here, we present preliminary results of one instance in which vortex trapping was observed during the experiment. The oscillatory flow period, T, was 2.35 s and the orbital velocity amplitude, U_o, was 0.26 ms^{-1}. The raw flow velocities were smoothed temporally and spatially to reduce noise and improve data quality. The velocities were then used to calculate the flow vorticity to better illustrate the location of the vortex relative to the vortex-trapped grain.

Figure 2 illustrates smoothed fluid velocities throughout the first half of the flow cycle. After flow reversal, the flow velocities were very small across the domain except for the extreme right side where a region of higher negative velocities was captured on the opposite side of the adjacent ripple (Figure 2(b)). As the freestream velocity accelerated, the nearbed velocity along the

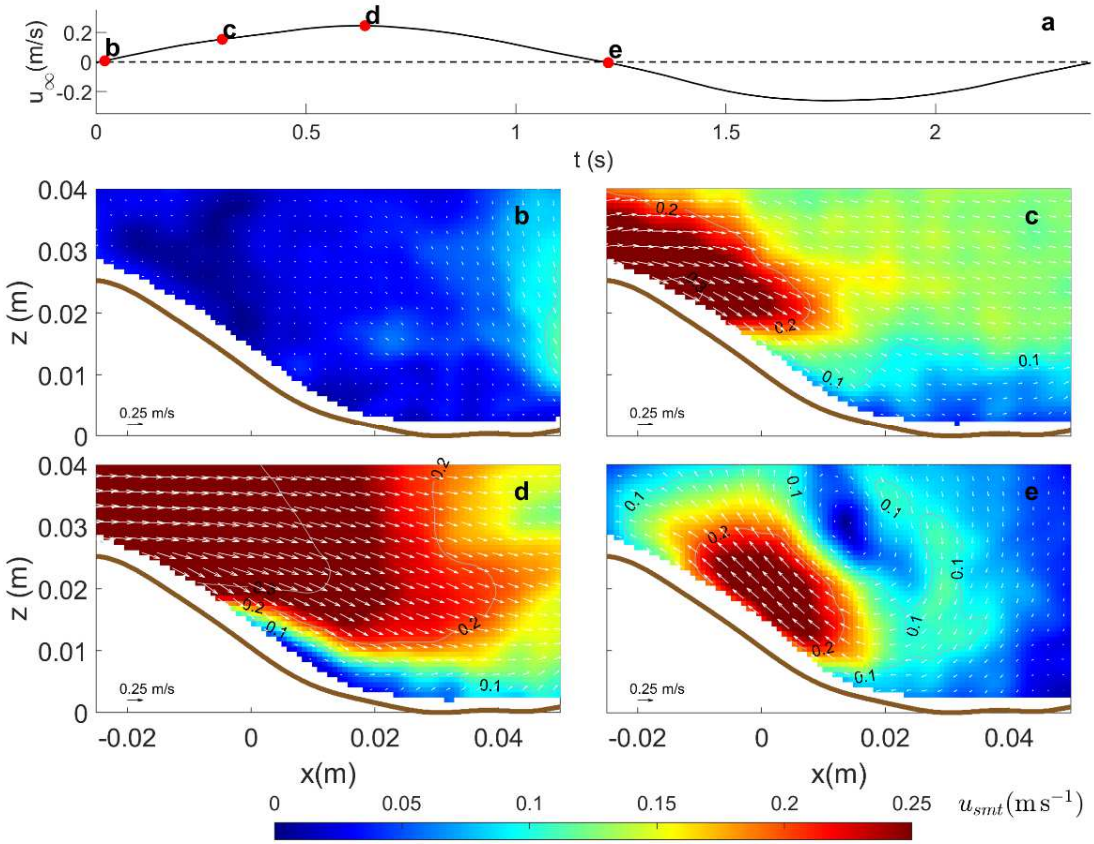

Figure 2: Time series of free-stream velocity is shown in panel (a). Fluid velocities are overlaid on color plots of velocity magnitude for the right half of the ripple, shown as white arrows in panels (b) – (e), at corresponding time steps indicated in panel (a). A scale vector is indicated in the bottom left corner of panels (b) – (e). The brown line delineates the average ripple shape for this trial.

ripple slope increased to a similar magnitude as the peak freestream velocity (Figure 2(c)). By the time of maximum freestream velocity, the flow across the domain had also increased significantly (Figure 2(d)). During the decelerating phase of the flow, the fluid velocities indicate a circular region of low velocity surrounded by fluid of higher velocity, suggesting the formation of a vortex just prior to flow reversal. (Figure 2(e)). The observed flow dynamics are in agreement with measurements by Van der Werf et. al (2007) of flow velocities over sand ripples, among others.

The panels shown in Figure 3(b) – (d) were taken just before the flow reversed from positive to negative when the cameras captured vortex generation on the ripple slope. For the time steps shown, the vortex diameter, estimated with a circle fit algorithm (Chernov, 2017), ranged from 0.024 – 0.03 m, of similar magnitude to the height of the vortex ripple. Some sediment grains were observed to prescribe semi-circular trajectories. The semi-circular path was off-center of the vortex core in the quadrants closer to the ripple slope, as hypothesized by Nielsen (1992) for vortex-trapped grains.

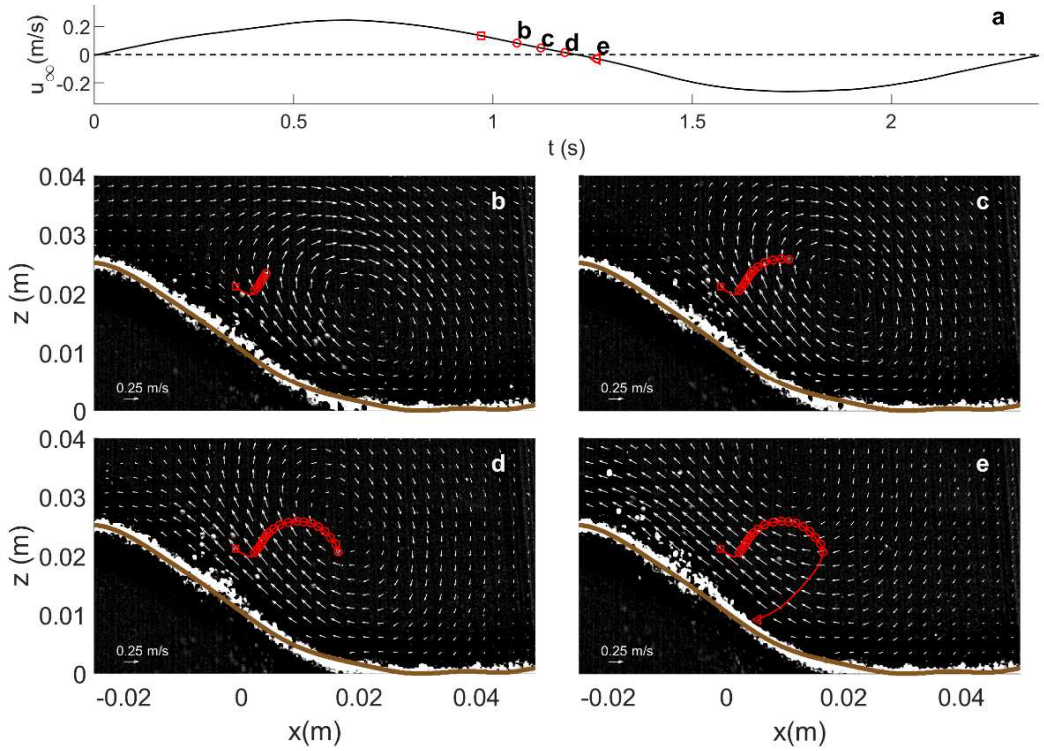

Figure 3: Time series of freestream velocity is shown in panel (a). Instantaneous velocities vectors are overlaid on PIV images of the right side of the ripple, shown as white arrows in panels (b) – (e) at corresponding time steps indicated in panel (a). A scale vector is indicated in the bottom left corner of panels (b) – (e), and the brown line delineates the average shape of the ripple bed for this trial. Shown in panels (b) – (e) is the trajectory of a vortex-trapped sand grain that traversed a semicircular path. The start and end times of the entire trajectory are indicated by red square and triangle symbols in panel (a), respectively. The time steps for the snapshot are indicated with sold circles in panel (a). The semi-circular portion of the trajectory is also indicated with circular markers in panels (b) – (e).

The grain highlighted in red was first mobilized and advected with the flow before being trapped in the vortex, illustrated by the initial straighter portion of the sediment grain trajectory (Figure 3(b)). As the grain began to settle, it interacted with the upward velocities of the vortex and was temporarily trapped in the vortex resulting in a change of direction, illustrated by the circular portion of the trajectory indicated with the circle markers (Figure 3(b-d)). The initial and final straight portions of the grain trajectory differ from the purely circular path hypothesized by Nielsen (1992) because the grain was being advected during these times rather than being trapped in the vortex. In addition, the vortices observed in these experiments were not stationary but were generated, advected then dissipated with each oscillatory flow cycle.

Next, the vorticity of the flow was calculated to determine the strength of the vortex. The smoothed and temporally averaged fluid velocities were used to calculate the vorticity to reduce the effects of small-scale turbulence and noise in the data. The time-varying vorticity, ω_v, was

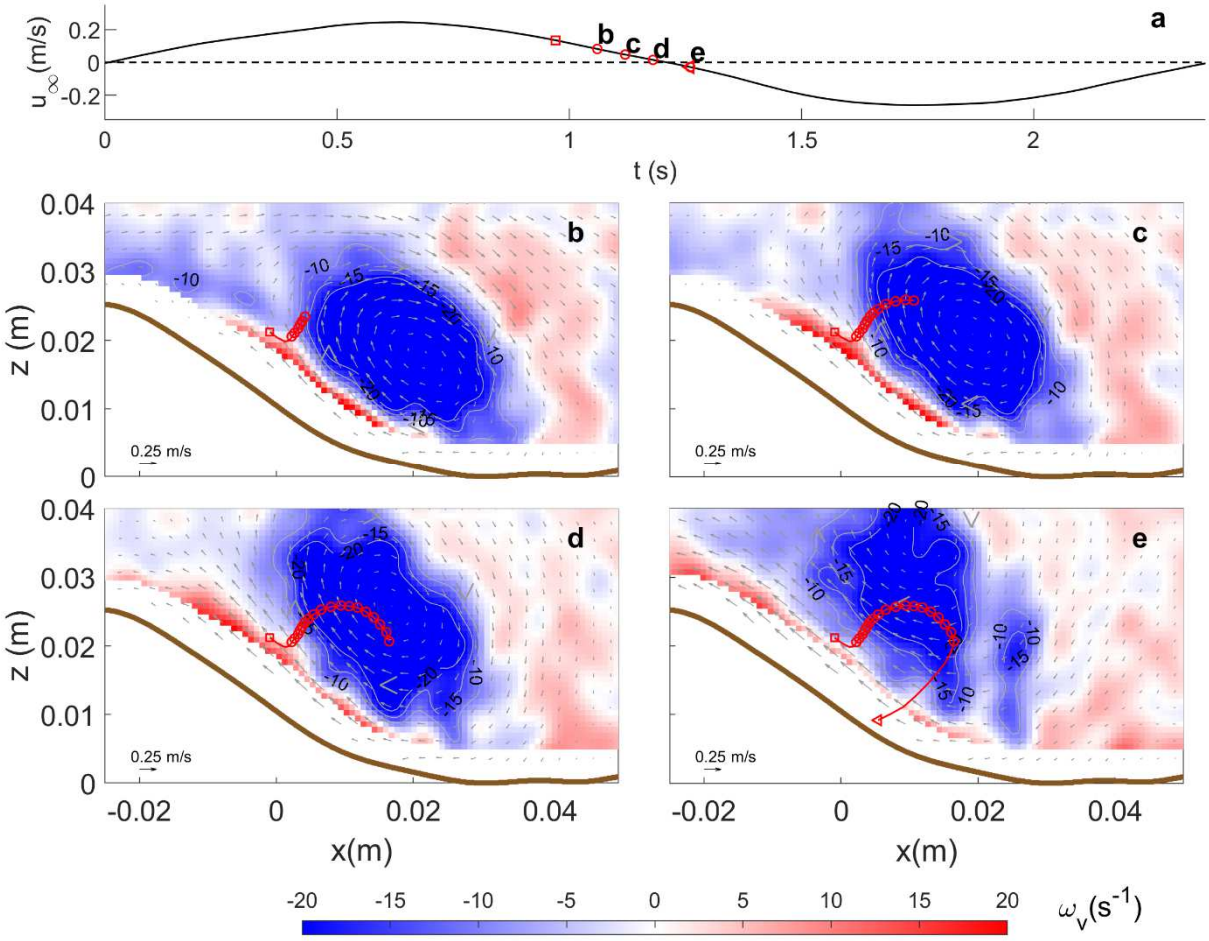

Figure 4: Time series of freestream velocity is shown in panel (a). Instantaneous velocities are overlaid on contour plots of vorticity for the right side of the ripple, shown as gray arrows in panels (b) – (e) at corresponding time steps indicated in panel (a). A scale vector is indicated in the bottom left corner of panels (b) – (e), and the brown line delineates the average shape of the ripple bed for this trial. Shown in panels (b) – (e) is the trajectory of a vortex-trapped sand grain that traversed a semicircular path. The start and end times of the entire trajectory are indicated by red square and triangle symbols in panel (a), respectively. The time steps for the snapshot are indicated with sold circles in panel (a). The semi-circular portion of the trajectory is also indicated with circular markers in panels (b) – (e).

calculated as the curl of the smoothed velocity field (Sveen, 2004; Nichols and Foster, 2007) (Figure 4). The observed vortex was asymmetric with the strongest vorticity in the upper left quadrant near the bed compared with the quadrants of the vortex that were closer to the freestream. The asymmetry of the vortex may be due to the flattened trough of the sand ripples that were generated in the oscillatory flow tunnel as opposed to the rounded concave shape that is more typical of sand ripples in the nearshore. This may have been due to a slight asymmetry in the forcing of the piston-flywheel assembly driving the oscillatory flow.

Figure (4) illustrates that the sediment grain was trapped near the region of higher vorticity. During the decelerating phase of the flow just after the maximum freestream velocity, the vortex was being generated and was still attached to the ripple slope (Figure 4b). Later in the flow cycle prior to flow reversal, the vortex had fully developed and was being advected with the flow before being shed from the ripple crest (Figure 4 (c-e). Although no measurements were made on the other side of the ripple during the opposite flow reversals for this trial, similar vortex development and flow dynamics were observed, as expected for the symmetric oscillatory flow.

This effort is ongoing and further analyses will be performed for this rich dataset. The trajectories will be determined for other sediment grains that were observed to prescribe semi-circular paths, as expected for vortex-trapped grains. In addition, the sediment grain velocities will be compared with the fluid velocities to perform quantitative comparisons with the vortex-trapping hypothesis of Nielsen (1992).

4 CONCLUSIONS

High-resolution measurements of fluid-sediment interactions over natural sand ripples under oscillatory flows were analyzed to assess an observation of a vortex-trapped sediment grain. Coherent structures were identified and determined to be a significant mechanism for mobilizing and transporting suspended sediments. The vortex-trapped grain was observed to move in a counterclockwise motion within the quadrants of the vortex closest to the ripple slope, in agreement with Nielsen (1992).

These results represent one of the first observations of vortex trapping of coarse sand grains over sand ripples under oscillatory flows. Vortex trapping is an important mechanism for sediment transport under these hydrodynamic conditions. Including vortex trapping in settling velocity calculations could improve sediment transport predictions in larger-scale numerical models.

5 ACKNOWLEDGEMENT

Donya Frank-Gilchrist was supported by the National Research Council Research Associateship Program at the Naval Research Laboratory Stennis Space Center when the experiments were conducted. Subsequent analyses were performed while Donya Frank-Gilchrist and Margaret Palmsten were affiliated with the U.S. Geological Survey St. Petersburg Coastal and Marine Science Center. Allison Penko and Joseph Calantoni were supported under base funding to the United States Naval Research Laboratory from the Office of Naval Research. The authors would like to acknowledge technical staff members at the United States Naval Research Laboratory for their assistance with experimental setup and data collection. This information is preliminary and is subject to revision. It is being provided to meet the need for timely best science. The information is provided on the condition that neither the U.S. Geological Survey nor the U.S. Government shall be held liable for any damages resulting from the authorized or unauthorized use of the information. Any use of trade, firm, or product names is for descriptive purposes only and does not imply endorsement by the U.S. Government.

6 REFERENCES

Calantoni, J., B. J. Landry, and A. M. Penko, 2013, Laboratory observations of sand ripple evolution using bimodal grain size distributions under asymmetric oscillatory flows. Journal of Coastal Research, 65, 1497–1502. https://doi.org/10.2112/SI65-253.1

Chernov, N., 2017, Circle Fit (Taubin method). (https://www.mathworks.com/matlabcentral/fileexchange/22678-circle-fit-taubin-method) MATLAB Central File Exchange. Retrieved September 2017.

Davies, A. G., and C. Villaret (1997), Oscillatory flow over rippled beds: Boundary layer structure and wave-induced Eulerian drift. International Series On Advances in Fluid Mechanics, 10 pp. 215-254.

Frank-Gilchrist, D., A. Penko, and J. Calantoni (2018), Investigation of sand ripple dynamics with combined particle image and tracking velocimetry. Journal of Atmospheric and Oceanic Technology, 35 (10), 2019–2036. https://doi.org/10.1175/JTECH-D-18-0054.1

LaVision, 2014: FlowMaster Product-Manual for DaVis 8.2. LaVision Rep., 188 pp.

Nichols, C. S., and D. L. Foster, 2007: Full-scale observations of wave-induced vortex generation over a rippled bed. Journal of Geophysical Research, 112. https://doi.org/10.1029/2006JC003841

Nielsen, P. (1992). Coastal bottom boundary layers and sediment transport. World Scientific, Singapore, 324pp.

Ouellette, N. T., Xu, H., and Bodenschatz, E. (2006), A quantitative study of three-dimensional Lagrangian particle tracking algorithms. Experiments in Fluids, 40 (2), 301–313.

Ouellette, N. T. (2010), Particle Tracking. Ouellette Lab. https://web.stanford.edu/nto/software tracking.shtml,. Accessed 12 September 2017.

Rodríguez-Abudo, S., D. Foster, and M. Henriquez, 2013, Spatial variability of the wave bottom boundary layer over movable rippled beds. Journal of Geophysical Research: Oceans, 118 (7), 3490–3506. https://doi.org/10.1002/jgrc.20256

Sveen, J.K. (2004), An introduction to MatPIV 1.6.1, 2nd ed., report. Department of Mathematics, University of Oslo, Oslo. pp. 1-27.

Van der Werf, J.J., Ribberink, J.S., O'Donoghue, T., and Doucette, J.S. (2006), Modelling and measurement of sand transport processes over full-scale ripples in oscillatory flows. Coastal Engineering, 53, 657–673. https://doi.org/10.1016/j.coastaleng.2006.02.002

Van der Werf, J.J., Doucette, J.S., O'Donoghue, T., and Ribberink, J.S. (2007), Detailed measurements of velocities and suspended sand concentrations over full-scale ripples in regular oscillatory flow. Journal of Geophysical Research: Earth Surface,112 (F2). https://doi.org/10.1029/2006JF000614

Hydrodynamic simulations of flow around a pile using turbulence-resolving models

A. Gilletta de Saint Joseph *FEM, Plouzané, France – alban.gilletta@france-energies-marines.org*
J. Chauchat *LEGI, Univ. Grenoble Alpes, Grenoble, France – julien.chauchat@univ-grenoble-alpes.fr*
C. Bonamy *LEGI, Univ. Grenoble Alpes, Grenoble, France – cyrille.bonamy@univ-grenoble-alpes.fr*
M. Robert *FEM, Plouzané, France – marie.robert@france-energies-marines.org*

ABSTRACT: With the increase of OWF in France, the question of sediment – flow – structure interactions has become essential. The interactions lead to the so-called scour process which is controlled by the flow vortices around the structure. To address this question, it is essential to have a reliable flow model. The aim of this contribution is to evaluate three turbulence modelling approaches: RANS, LES, hybrid RANS-LES and inlet boundary conditions to accurately predict the flow around the structure.

1 INTRODUCTION

With future objective of carbon neutrality by 2050, France is invested in the development of new renewable source of energy on its territory. As it is ranked second in terms of maritime space, the French bottom-fixed Offshore Wind Farms (OWF) the technical potential is estimated at 80 Giga Watts (GW), enough to provide about half of the national consumption. The English Channel is an important potential area benefiting from strong and steady wind over time and a moderate water depth to implement grounded structure. MOdelling of marine DUnes: Local and Large-scales EvolutionS in an OWF context (MODULLES) French project led by France Énergies Marines (FEM) focuses on the interactions between high and mobile submarine dunes and the future OWF off Dunkirk. This study is dedicated to small scale modelling of scour process around foundations of a single wind turbine facing turbulent current. The ability to predict how the scour process occurs around a wall-mounted circular cylinder is a major stake in order to size structures to protect them from damages. This phenomenon is driven by two hydrodynamical vortical structures namely the horseshoe vortex upstream the pile and the vortex-shedding downstream the pile. As these vortical structures are rather small, the required resolution for numerical simulation induces important computational cost. When the flow is highly turbulent, a way to capture the main eddies is to model turbulence. Different approaches exist, the most common model used in the engineering field is Reynolds Averaged Navier-Stokes (RANS). Advanced models, such as Large Eddy Simulations (LES) provide more accurate results by increasing the resolution part of turbulent structures while Hybrid RANS-LES models combine the two approaches. In this contribution, we analyze the accuracy of three turbulence modelling approaches, namely RANS, LES and hybrid RANS-LES to simulate the flow around a wall-mounted cylinder. An important technical question is the influence of the inlet boundary conditions especially for turbulence resolving

simulations (LES, hybrid RANS-LES). These two points are investigated using pimpleFOAM on two configurations: the plane channel flow and the wall-mounted cylinder case.

2 GOVERNING EQUATIONS

2.1 Navier-Stokes equations

When dealing with turbulence modelling, the Navier-Stokes equations are introducing the turbulent eddy viscosity, a fundamental parameter in turbulence modelling. Therefore these equations are presented by the coupled mass conservation equation (1) and momentum equation (2).

$$\frac{\partial \tilde{u}_i}{\partial x_i} = 0 \tag{1}$$

$$\frac{\partial \tilde{u}_i}{\partial t} + \frac{\partial}{\partial x_j}(\tilde{u}_i \tilde{u}_j) = \frac{-1}{\rho}\frac{\partial \tilde{p}}{\partial x_i} + \frac{\partial}{\partial x_j}\left[(\nu + \nu_t)\left(\frac{\partial \tilde{u}_i}{\partial x_j} + \frac{\partial \tilde{u}_j}{\partial x_i}\right)\right] \tag{2}$$

where u_i = velocity i^{th} component, p = modified pressure, ρ = fluid density, ν = kinematic viscosity, ν_t = turbulent eddy viscosity and ~ = time-averaging or filtering operator.

2.2 Turbulent eddy viscosity

RANS equations use time-averaging operator. The most widely used model is the k-ω SST model (Menter et al. 2003a) in which the turbulent eddy viscosity is defined as follows :

$$\nu_t = \frac{a_1 k}{max(a_1 \omega, S F_2)} \tag{3}$$

where a_1 = 0.31, k = Turbulent Kinetic Energy (TKE), ω = turbulent specific dissipation rate, S = invariant strain rate and F_2 = blending function.

Two transport equations for k and ω are added to close the system. This model behaves as a standard k-ω model in the viscous sublayer and as a k-ε model in the outer layer.

LES equations are obtained by applying a filtering operator to equations (1) and (2). In the Dynamic Lagrangian LES model (Meneveau et al. 1996), the turbulent eddy viscosity is defined in equation (4).

$$\nu_t = C(\mathbf{x}, t)\Delta^2|\bar{S}| \tag{4}$$

where C = function of **x** and t and Δ = integral scale of the subgrid-scale.

This model is part of the dynamic Smagorinsky group model in which C is no longer associated to classical Smagorinsky constant (Smagorinsky 1963) but varies over time and space. It enables more realistic turbulent features such as backscattering effect.

Hybrid RANS-LES combines both approaches. The switch between the two depends on the model used. This study focuses on the k-ω SST Scale Adaptative Simulation hybrid RANS-LES model (Menter & Egorov 2010b). By introducing a new term in the turbulent specific dissipation rate, based on a turbulent length scale defined as the velocity gradient over the velocity laplacian, the turbulent viscosity takes the value of the classical k-ω SST model when the flow is homogeneous and follows a classical Smagorinsky LES model when it is "disturbed".

2.3 Inlet boundary condition

One key issue to represent these vortical structures is to reproduce a well-developped turbulent flow at the inlet for turbulence-resolving model (Kirkil & Constantinescu 2015). While periodic boundary conditions are used as a reference for the plane channel flow configuration, two other approaches are tested for the wall-mounted cylinder: Divergence Free Synthetic Eddy Method (Poletto et al. 2013) and non-uniform boundary conditions implemented in OpenFOAM as turbulentDFSEM and GroovyBC respectively. DFSEM generates synthetic eddies based on random locations

and intensities while GroovyBC imposes a steady profile at the inlet. This study is mainly focusing on an influence of the inlet boundary conditions on the flow dynamic.

2.4 Configurations

Two configurations are studied in the present article. First, the plane channel flow configuration in order to assess best turbulent inlet boundary conditions. A first simulation using periodic boundary conditions succeeds in reproducing a converged fully developed turbulent flow, this simulation will be used as a reference. The computational domain is 20πH long, πH large and 1H high with H the water depth set to 0.06 m similarly to Fuhrman and co-workers experiment (Furman et al. 2010). The friction Reynolds number is often used to describe this configuration and is defined as follows:

$$Re_\tau = \frac{u_\tau H}{\nu} \quad (5)$$

Here $Re_\tau \approx 1000$. The wall-mounted cylinder configuration is similar to Roulund and co-workers experiment over a rigid bed (Roulund et al. 2005). The computational domain is 12D long, 8D wide and 1D high with D the cylinder diameter equal to 0.536 m. The friction Reynolds number is higher in this configuration, $Re_\tau \approx 7000$. Both configurations are shown in Figures 1-2.

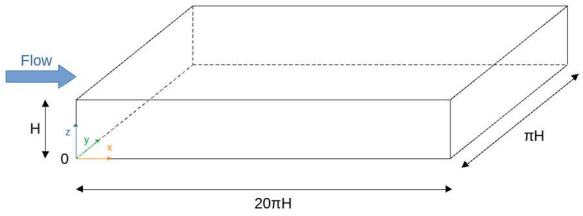

Figure 1. Plane channel configuration

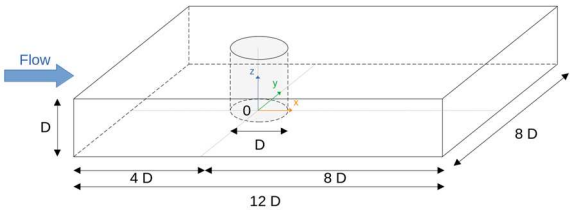

Figure 2. Wall-mounted cylinder configuration

3 RESULTS

This section is dedicated to simulations results of the two configurations performed with OpenFOAM.

3.1 Plane channel case

Figure 3 represents the streamwise profile of the friction velocity u_τ in the symmetry axis of the plane channel calculates as follows:

$$u_\tau = \sqrt{|\tau_{xy}|} \quad (6)$$

where τ_{xy} = bottom shear stress in the streamwise direction.

We introduce the notion of wall units defined as follows:

$$y^+ = \frac{y u_\tau}{\nu} \quad (7)$$

where y = distance to the wall or other length.

Three simulations are plotted using Dynamic Lagrangian LES model and same computational grid having a $z^+ = 6$, $y^+ = 30$ and $x^+ = 130$ respectively in the vertical, spanwise and streamwise directions in agreement with the resolution required for LES simulations (Métais 2018). The blue line corresponds to simulation using periodic boundary conditions and indicates an averaged friction velocity of 0.014 $m.s^{-1}$, slightly under the experimental value of 0.016 $m.s^{-1}$. Result from a RANS k-ω SST model using an imposed RANS profile boundary conditions with same mesh has

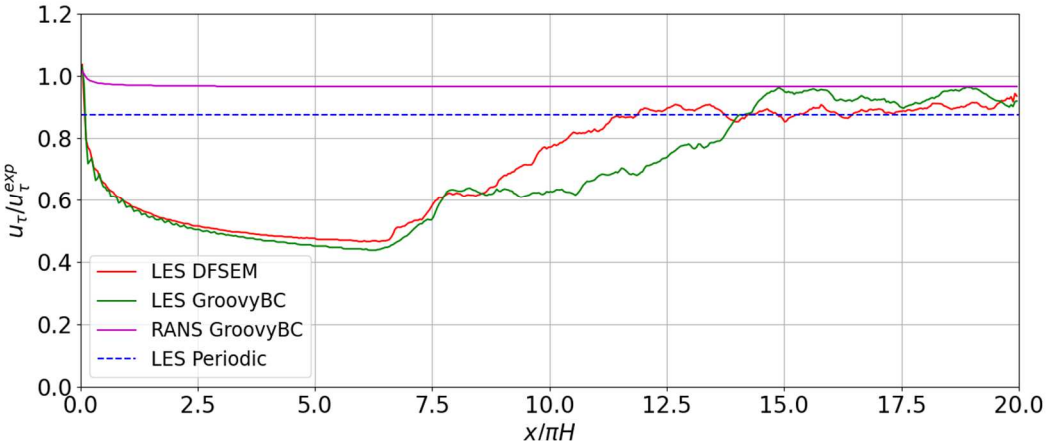

Figure 3. Time-averaged friction velocity profile in the symmetry axis

been added and shows a constant value close to the experimental friction velocity. LES simulations using imposed RANS profile and DFSEM inlet boundary conditions are quite similar since the friction value starts from the desired value due to the input parameter wished and drastically decays of about 50% until $x/\pi H \approx 6$. Then, they both increase until reaching the same value as the periodic boundary condition simulation. DFSEM reaches it sooner than the imposed RANS profile by about $2\pi H$.

Figure 4 represents three vertical profiles of the velocity, Reynolds stress and TKE scaled with experimental friction velocity. The average value for the periodic boundary condition simulation is taken over the entire computational domain while at least 25% of the channel length is taken for the three other simulations.

For all simulations, the velocity profiles are quite in fair agreement with the measurements represented by the blue crosses. Concerning the Reynolds stress, periodic boundary conditions has a linear expected shape likewise the RANS simulation but underestimates the maximum compared with the theory, that is to say $u_\tau^2 = 2.56 \times 10\text{-}4\ m^2.s^{-2}$. Without periodic boundary conditions, DFSEM results are

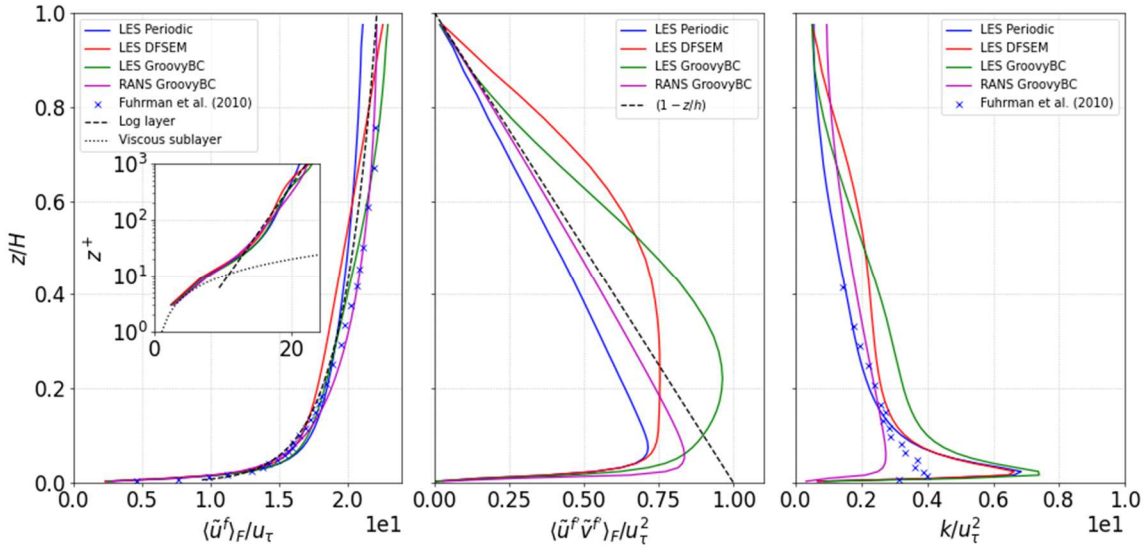

Figure 4. Time and space averaged velocity profile (left), Reynolds stress x-y component (centre) and TKE (right) with different inlet boundary conditions

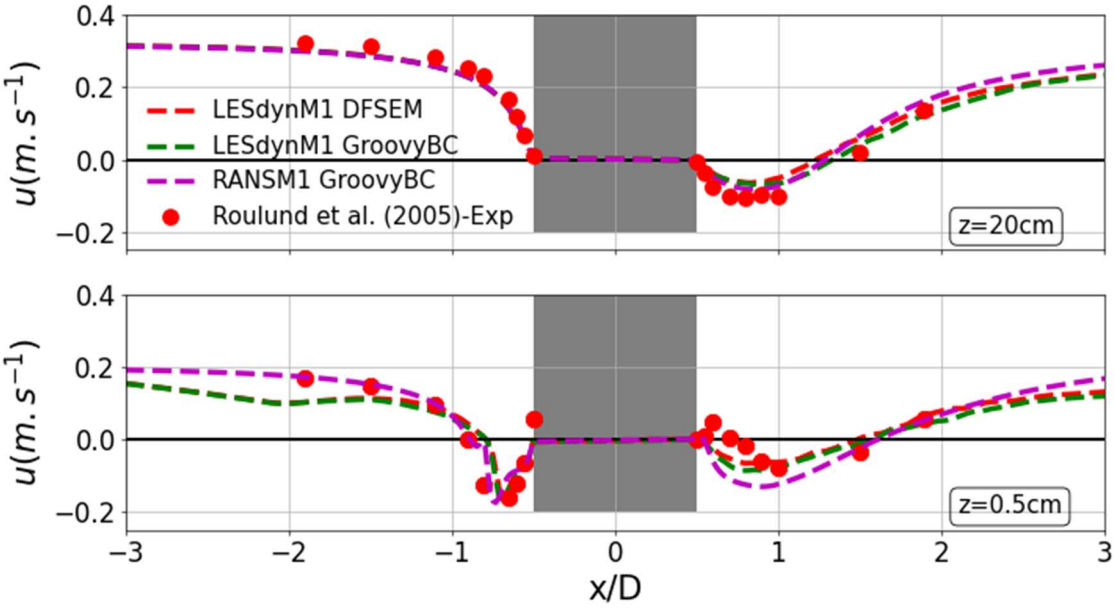

Figure 5. Time-averaged velocity profile of streamwise component in the symmetry plane at two elevations for Dynamic Lagrangian LES model.

quite good as the curve fits relatively well with the viscous sublayer profile but remains constant in the first part of the log layer and is overestimated. The linear expected profile is not retrieved with DFSEM, however it works better than imposed RANS profile where the Reynolds shear stress is overestimated in the log layer. Concerning the TKE vertical profile, the periodic boundary conditions simulation is in good agreement apart in the sublayer region where a peak is observed that is not present in the measurements and in RANS result. Complementary tests (not shown here) concluded that a finer mesh resolution reduces this peak. As the objective of this test is to evaluate inlet boundary condition, it clearly shows the superiority of DFSEM over the imposed RANS profile as the peak is intensified with the latter.

3.2 Wall-mounted cylinder case

3.2.1 Dynamic Lagrangian LES model

Figure 5 shows the streamwise velocity profile averaged in the symmetry axis in the vicinity of the cylinder over about 70 bulk time defined as follows :

$$T_b = \frac{H}{U} \quad (8)$$

Where U = 0.326 m.s^{-1} the average velocity.

The mesh used for all simulations is quite coarse with $z^+ = 4$, $y^+ = x^+ = 100$ for cells in the vicinity of the cylinder. The results are compared with Roulund and co-workers experiments (Roulund et al. 2005) and show overall good agreement. No important differences are observed between the two inlet boundary conditions. The main discrepancies are observed at the upstream and downstream side, on the near bed velocity that is underestimated. Whatever boundary conditions used, Dynamic Lagrangian LES model succeeds in representing the average streamwise velocity profile especially in the horseshoe vortex area where the velocity reaches a minimum value. The result from RANS k-ω SST, very similar, confirms the ability for LES model to reproduce mean velocity.

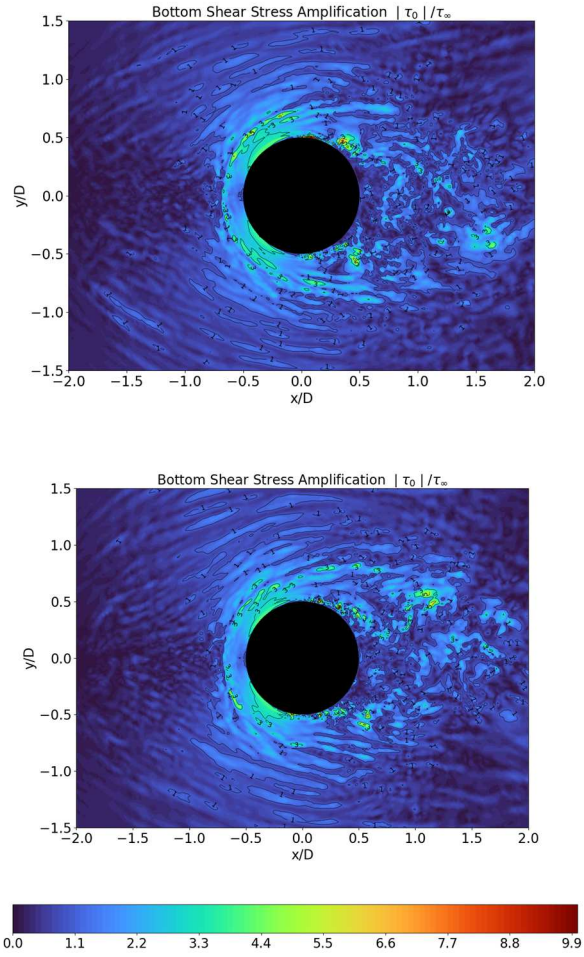

Figure 6. Averaged bed shear stress amplification with DFSEM boundary conditions (top) and GroovyBC boundary condition (bottom) for Dynamic Lagrangian LES model.

Figure 6 shows the time-averaged bed shear stress amplification map over 60 outputs for LES simulations using DFSEM boundary conditions in the top figure and imposed RANS profile in the bottom figure. The results are clearly not converged. When the average is taken over all time step, both simulations contain noises that represent extreme negative values far outside the expected range. This issue emphasizes the unstable behavior of Dynamic Lagrangian LES model for bed shear stress. Numerical schemes are probably the main reason of such instabilities. Therefore, Dynamic Lagrangian LES model fails in reproducing bed shear stress. As LES requires fine resolution and high computational cost, Hybrid RANS-LES models have been designed in order to reproduce more accurately the physical processes compared with RANS model, at an affordable cost. Results for k-ω SST-SAS Hybrid RANS-LES model are presented next.

3.2.2 k-ω SST-SAS Hybrid RANS-LES model

As mentioned previously, this model switches from RANS to LES mode if a perturbation of the flow is generated or detected such that the turbulent length scale defined is smaller than the length scale

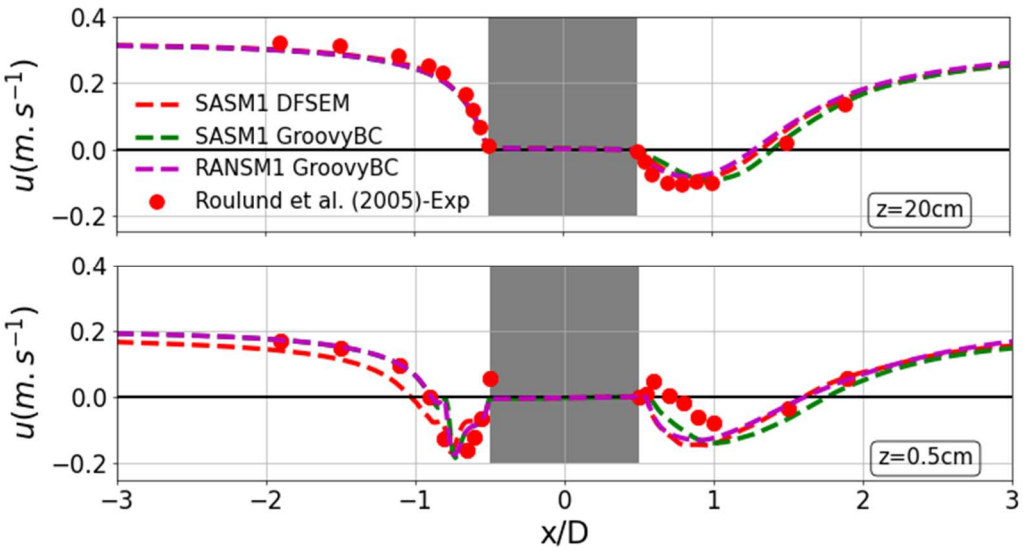

Figure 7. Time-averaged velocity profile of streamwise component in the symmetry plane at two elevations for k-ω SST-SAS Hybrid RANS-LES model.

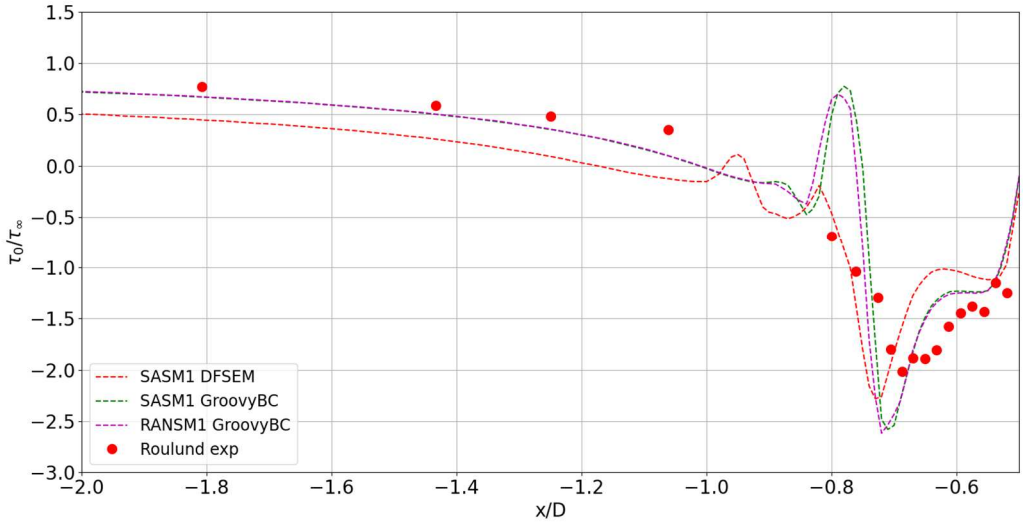

Figure 8. Time-averaged bottom shear stress amplification profile in the symmetry plane for k-ω SST-SAS Hybrid RANS-LES model.

modeled by the RANS model. In the plane channel case, there is no perturbation of the flow and the model behaves as a k-ω SST RANS model. In the wall-mounted cylinder case, the obstacle generates separated flow and disturbs the velocity so that the turbulence model is switched to the LES mode.

Figure 7 shows the velocity validation with the same mesh as the one used for the Dynamic Lagrangian LES model. Both boundary conditions give similar result except at the upstream side of the cylinder near the bed where DFSEM simulation slightly underestimates the velocity. Compared with LES simulations, the downstream near bed velocity is also underestimated by the Hybrid model. Despite this discrepancy, it can be infered that k-ω SST-SAS Hybrid RANS-LES model gives reasonable result. Adding to that, RANS result is closer to the imposed RANS profile hybrid simulation.

Figure 8 shows the time-averaged amplification of the bed shear stress profile upstream the obstacle over all time steps. Experimental results from Roulund and co-workers are shown as red dots. First, likewise Figure 7, RANS and hybrid simulations using imposed RANS profile give very similar result. It suggests that an imposed RANS profile boundary conditions prevents hybrid SAS model to switch from RANS to LES mode. Secondly, the two hybrid simulations give also similar results, which was not the case for LES results (not shown here). Both inlet boundary conditions reproduce the same patterns as the experiments with a minimum value representing the horseshoe vortex around -0.7D corresponding to an amplification of about 2. This minimum value is negative meaning that a reversing flow is taking place in this area, namely a clockwise rotating vortex. The main difference between the two simulations is the local maxima observed at -0.8D with imposed RANS profile simulation whereas two smaller ones are seen with DFSEM simulation at -0.8D and -0.9D.

The explanation of such a difference can be understood in Figure 9 representing snapshots of the simulations at two different times in the horseshoe vortex area. The results are colored by the spanwise vorticity. Experiments show that the horseshoe vortex

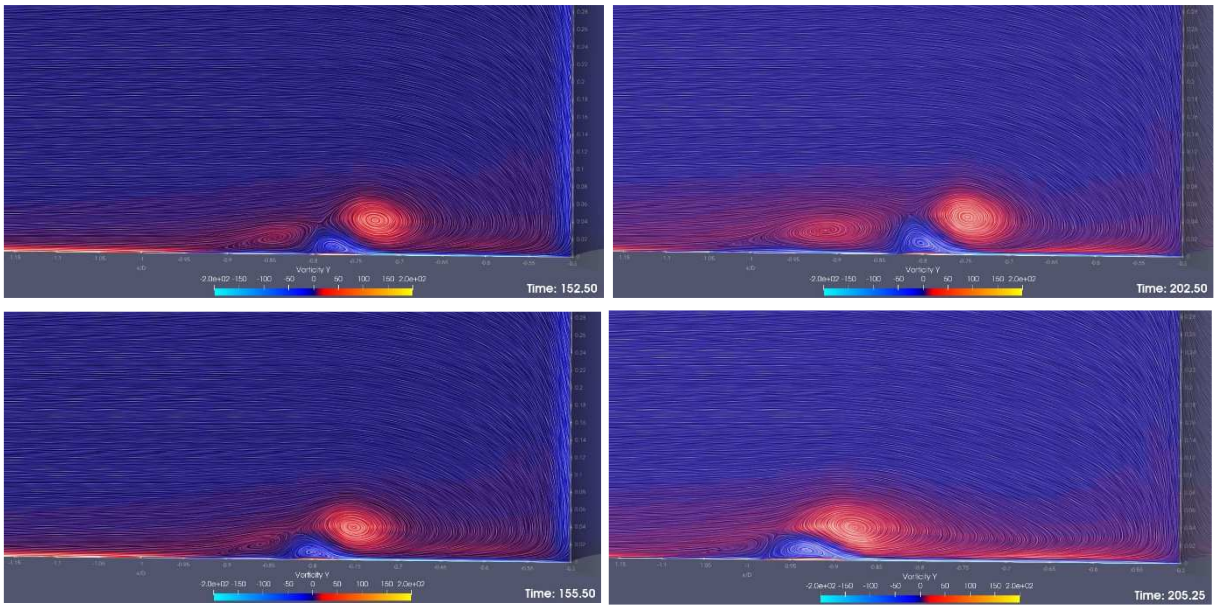

Figure 9. Instantaneous snapshots of spanwise vorticity with streamlines current for Groovy BC (left) and DFSEM (right) at the zero-flow mode (top) and the backflow mode (bottom).

is composed of several dynamic vortices (Baker 1980). In this figure, for both simulations, it is clearly observed, from downstream to upstream: one large primary clockwise vortex, one bottom-attached triangular counter clockwise vortex and one secondary clockwise vortex. Both simulations are able to reproduce vortex system. What is also seen from these snapshots is the dynamics of the system, evolving in a bimodal oscillation. The first mode takes place where all vortices move close to the cylinder, it is called the zero flow mode. The second mode takes place where all vortices move away from the cylinder and it is called the backflow mode (Kirkil & Constantinescu 2015). Snapshots from the two simulations represent these two modes. While the imposed RANS profile simulation shows a relatively short amplitude of about 0.02D between the two modes, DFSEM predicts a larger amplitude of 0.13D in better agreement with existing high Reynolds number simulations (Kirkil & Constantinescu 2015).

4 CONCLUSIONS

In this contribution, we demonstrate for the plane channel flow configuration that in order to establish a fully developed turbulent flow without periodic boundary conditions for LES simulations, either DFSEM or imposed RANS profile at the inlet boundary conditions can be used. However, the turbulence is establishing quite far away from the inlet, namely 13πH.

Implementing such a computational domain length in the LES simulations of wall-mounted cylinder case is difficult as it would increase drastically the computational cost. However because of the obstacle presence, no periodic boundary conditions can be used. No matter what inlet boundary conditions is used, both give unstable result in terms of wall shear stress using Dynamic Lagrangian LES model. k-ω SST−SAS Hybrid model gives almost as good result as LES model used in terms of velocity profile but is also much more stable for wall shear stress. With deeper analysis in the prediction of the horseshoe vortex, DFSEM can reproduce a more realistic vortices system than an imposed RANS profile that tends to prevent hybrid model to switch to LES mode and should be preferred.

5 ACKNOWLEDGEMENT

The authors gratefully acknowledge the support of the French project MODULLES partially funded by the ANR. We would like

to thank the Shom for its financial support and management. Most of the computations presented in this study were performed using LEGI laboratory cluster. We are thankful to the developers involved in OpenFOAM.

6 REFERENCES

Baker, C.J., 1980. The turbulent horseshoe vortex, Journal of Fluid Mechanics, 95, 347-367, doi:10.1017/S0022112079001506

Fuhrman, D.R., Dixen, M., Jacobsen, N.G., 2010. Physically-consistent wall boundary conditions for the k-ω turbulence model. Journal oh Hydraulic Researh, 48, 793-800, doi:10.1080/00221686.531100

Kirkil, G., Constantinescu, G., 2015. Effects of cylinder Reynolds number on the turbulent horseshoe vortex system and near wake of a surface-mounted circular cylinder. Physics of Fluids, 27, 075-102, doi:10.1063/1.4923063

Meneveau, C., Lund, T., Cabot, W., 1996. A Lagrangian dynamic subgrid-scale model of turbulence. Journal of Fluid Mechanics, 319, 353-385, doi:10.1017/S0022112096007379

Menter, F.R., Kuntz, M., Langtry, R., 2003a. Ten years of industrial experience with the SST turbulence model. Proceedings of the fourth international symposium on turbulence, heat and mass transfer, 625-632

Menter, F.R., Egorov, Y., 2010b. A scale-adaptative simulation method for unsteady turbulent flow predictions - Part 1: Theory and model description. Flow Turbulence Combust, 85, 113-138, doi:10.1007/s10494-010-9264-5

Métais, O., 2018. Large Eddy Simulation of Turbulence : Fundamentals and Applications – Lectures notes. Grenoble

Poletto, R., Craft, T., Revell, A., 2013. A New Divergence Free Synthetic Eddy Method of the Reproduction of Inlet Flow Condition for LES. Flow Turbulence and Combustion, 91, 519-539, doi:10.1007/s10494-013-9488-2

Roulund, A., Sumer, B.M., Fredøe, J., Michelsen, J., 2005. Numerical and experimental investigation of flow and scour around a circular pile. Journal of Fluid Mechanics, 534, 351-401, doi:10.1017/S0022112005004507

Smagorinsky, J., 1963. General circulation experiments with the primitive equations. Monthly Weather Review, 91, 99-164, doi:10.1175/1520-0493(1963)091<0099:GCEWTP>2.3CO;2

Soulsby, R.L., 1983. The Bottom Boundary Layer of Shelf Seas, in Elsevier Oceanography Series. Elsevier, 189-266

Dissertation

Roden, J.E., 1998. The sedimentology and dynamics of mega-dunes, Jamuna River, Bangladesh. PhD Thesis. University of Leeds, UK, 310pp

The Naval Seafloor Evolution Architecture: a platform for predicting dynamic seafloor roughness

W. S. Kearney *American Society for Engineering Education Postdoctoral Fellow (Former) - wkearn@gmail.com*
A. M. Penko *U.S. Naval Research Laboratory, Stennis Space Center, Mississippi, USA - allison.penko@nrlssc.navy.mil*

ABSTRACT: Predictions of waves, currents, sediment transport, and the acoustic response of the seafloor depend on reliable estimates of seafloor roughness due to bedform geometry. To predict the spatial and temporal dynamics of seafloor roughness under changing wave conditions, we have developed a modular modelling system, the Naval Seafloor Evolution Architecture (NSEA). NSEA is included in a repository of bottom boundary layer models within a larger modelling framework (Sediment Mobility Regime Estimator – SeaMoRE) developed to ingest regionally simulated wave and current conditions and output near bed hydrodynamics to drive smaller scale models. The near bed wave and current velocity output from SeaMoRE is used to drive a nonequilibrium spectral ripple model within NSEA to estimate the time-dependent power spectrum of the seabed elevation. From the timeseries of the amplitude power spectra, statistical characteristics of the seafloor, such as roughness lengths, can be derived. We illustrate the applicability of this model framework by using it to estimate seafloor ripple evolution during a field experiment off the coast of Panama City, Florida, USA and its potential to forecast seabed roughness variability at other locations using web accessible global models.

1 INTRODUCTION

Seafloor roughness can enhance bottom boundary layer turbulence, is evolved by sediment transported at the seafloor interface, and can have a dynamic feedback between the waves/currents that generate bedforms by also attenuating wave and current energy after formation.

Seafloor roughness is defined here as the unresolved variations in bathymetry at higher resolutions than gridded bathymetric data and/or unresolved in a numerical model. High-resolution models O(1mm-1cm) can directly simulate the interactions between fluid and sediment on the seafloor [Salimi-Tarazouj et al. (2021); Penko et al. (2013)], but are too computationally expensive to couple with regional nearshore wave and current models. Modules to predict roughness within hydrodynamic models are typically empirical in nature and based on the roughness being in equilibrium with the instantaneous forcing, which is not wholly realistic. Coupling (either one- or two-way) a seafloor spectral model to a hydrodynamic model allows for the generation of time-dependent seafloor elevation realizations correlated to the shear stress on the seabed caused by the propagation of surface waves and bottom currents. This method takes into account the time history of the forcing, allowing time for the roughness to adjust to the changing forcing conditions.

Presented here is a modelling framework for estimating seabed boundary conditions given user chosen wave and current models and a one-way coupled spectral seabed model to produce time-dependent realizations of seafloor roughness. The Seabed Mobility Regime Estimator (SeaMoRE) [Penko and Phillip, in review] ingests hydrodynamic information and outputs seafloor boundary layer forcing for input to the Naval Seafloor Evolution Architecture (NSEA) [Kearney and Penko, 2022], which characterizes the

spatial and temporal evolution of seafloor roughness.

2 MODEL DESCRIPTIONS

Seabed Mobility Regime Estimator

SeaMoRE is designed to extract and reformat a variety of publicly available meteorological and oceanographic (METOC) data from webservers. Current models (e.g., Navy Global Hybrid Coordinate Ocean Model (HYCOM), Navy Coastal Ocean Model (NCOM)) data are available via NOAA's National Centers for Environmental Information (NCEI) Environmental Research Division's Data Access Program (ERRDAP) server. Python code has been developed to automate the extraction of data needed for calculating the current bottom boundary layer forcing information by SeaMoRE [Penko et al., 2022]. Additionally, NOAA's WaveWatch III (WW3) Production Hindcast multi-grid spectral wave model provides historical and recent global and regional wave data. The WW3 Production Hindcast model can be used to provide the data for SeaMoRE's wave bottom boundary layer calculations. SeaMoRE ingests the wave and current model data along with sediment information (mean grain size and sediment density) and outputs gridded estimations of seabed sediment mobility (based on the critical threshold for sediment incipient motion and sheet flow) and near bed hydrodynamics (bottom current magnitude and direction, wave orbital velocity, wave bottom orbital excursion, and wave direction) (Figure 1).

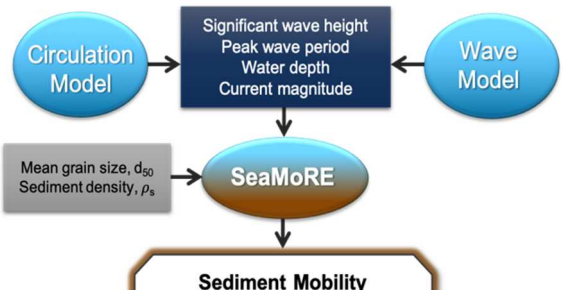

Figure 1: Flow chart depicting SeaMoRE's inputs and outputs.

Data is written in both NetCDF and CSV formats for reading into one-way coupled bottom boundary layer models (e.g., NSEA). For validation purposes, observational data can also be input to SeaMoRE, and the output from the sediment mobilization estimations can be compared to local observations of sediment transport as presented here.

Naval Seafloor Evolution Architecture

NSEA consists of four modules: forcing, seafloor evolution, seafloor synthesis, and observations. Information naturally flows from one module to the next (i.e., the seafloor evolution module uses the forcing information and its outputs are used by the seafloor synthesis module). The forcing information is directly provided by SeaMoRE at the location of interest. The seafloor evolution model [Penko et al., 2017, Kearney and Penko, 2022], approximates the evolution of the amplitude spectrum of the seafloor elevation by modelling the relaxation of the amplitude spectrum toward its equilibrium value calculated from an equilibrium ripple predictor method [e.g., Nielsen, 1981; Nelson et al., 2013] with a time scale based on the instantaneous ripple geometry and sediment transport rate [Traykovski, 2007]. Under strong forcing conditions, sheet flow conditions are expected to exist, in which case the entire bed is mobilized and any ripples present are washed out. In the absence of hydrodynamic forcing, bioturbation will slowly modify the roughness, leading to a decay of ripple amplitude and is modelled as a diffusive process [Jackson et al., 2009]. The output of the seafloor evolution model is the amplitude spectrum, which characterizes the statistical properties of the random seafloor elevation field. statistics of seafloor roughness such as the root-mean-square elevation or the peak ripple wavelength can be computed from the spectrum. Random realizations of seafloor elevations can then be generated from the output spectrum through a Fourier synthesis approach. Finally, the seafloor realization

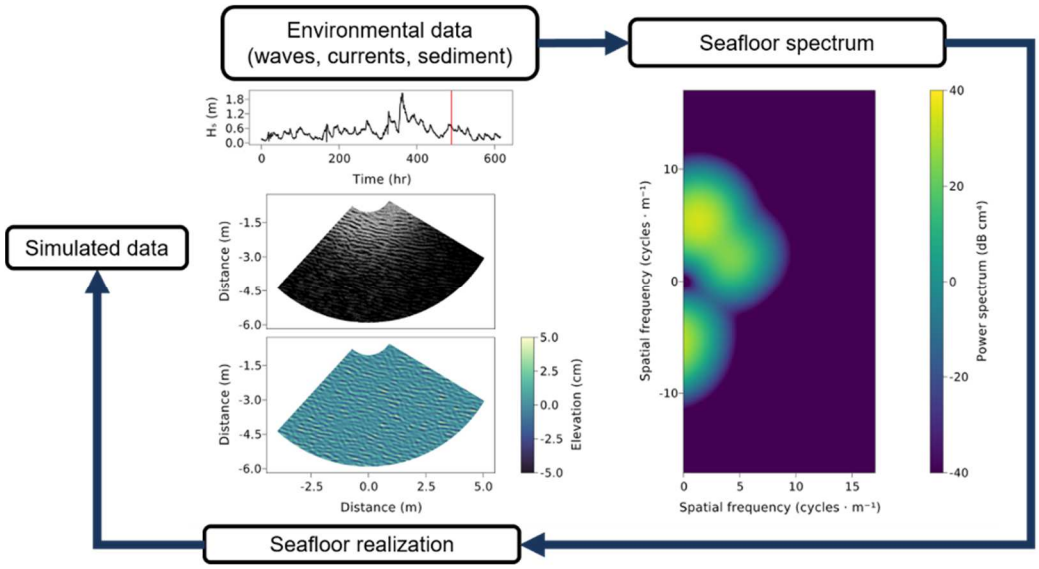

Figure 2: Flow chart of the input and output of the modules in NSEA.

elevations can be used to simulate a timeseries of acoustic data A flow chart depicting the inputs and outputs of the NSEA modules is shown in Figure 2. For complete model description see Kearney and Penko [2022].

3 RESULTS & DISCUSSION

The applicability and validation of this model architecture is presented by estimating seafloor roughness during the Target and Reverberation Experiment (TREX13) deployed off the coast of Panama City, FL, USA in 2013. Instrumentation on a quadpod in 8m water depth collected data for 34 days.

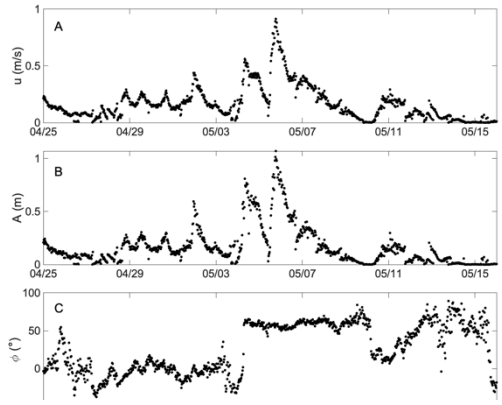

Figure 3: (A) Bottom orbital velocity, (B) bottom semiorbital excursion and (C) wave direction (0° North) from the TREX13 field experiment.

Wave height, period, and direction were recorded by a Nortek AWAC-AST at 2 Hz for 1,024 s every 30 minutes. Linear wave theory was used to estimate the bottom orbital velocity and the semiorbital excursion from the observed significant wave height. The forcing data input to NSEA included the bottom orbital velocity (u), wave semiorbital excursion (A), and the wave direction (ϕ) (Figure 3). A 2.25 MHz rotary sonar (Imagenex 881b) installed at a height of 1.05 m above the seafloor imaged approximately a 6 m × 6 m area under the quadpods every 12 minutes. A fast Fourier transform of a 3 m × 3 m patch of the backscatter image was computed and the wavenumber corresponding to the maximum Fourier amplitude was extracted and converted into an estimate of the ripple wavelength.

The SeaMoRE-NSEA coupled framework was validated with observations of the ripples generated on the seafloor recorded with the rotary sonar (Figure 4). SeaMoRE ingested the wave observations and estimated whether the seafloor was in a stable state (the estimated bottom shear stress was below the critical shear stress for sediment incipient motion), an active ripple state (the estimated bottom shear stress was between the critical threshold for sediment incipient motion and the critical threshold for sheet flow), or

turbulent (the estimated bottom shear stress was above the critical threshold for sheet flow). The contours in the top panel of Figure 4 shows the times when SeaMoRE predicts the stable (white), rippled (blue), and turbulent (red) regimes for the entire TREX experiment. The observed ripple wavelengths extracted from the rotary sonar backscatter image are plotted with black dots also in the top panel. The middle panels (a-d) are 3 m x 3 m images of the rotary sonar backscatter at four different times of the experiment showing the variability of the ripples.

At time (a), the seafloor is stable; however, ripples are present due to being generated by a previous forcing condition. NSEA predictions of a random seafloor realization at the same time as the sonar image is plotted in the bottom panels. The ripple geometry predicted in the seafloor realization in (a) is qualitatively similar to the sonar image. The ripple wavelengths and orientations are in good agreement with the observations. Note that the white color blocks in the top panel generally correspond to times when the ripple wavelengths are constant, indicating that SeaMoRE is in good agreement with the observations for the stable regime.

The blue shading indicates that sediment is predicted as being mobilized and/or ripples are actively evolving. At times (b) and (d), SeaMoRE predicts that the seafloor roughness is evolving, which is also observed in the sonar images. Note that the blue shading generally corresponds to times when the ripple wavelengths are observed as changing, showing that SeaMoRE is in good agreement with the observations for the ripple regime. At both times (b) and (d), NSEA predicts that the ripples are actively evolving and the wavelengths are increasing; however, it doesn't quite capture the three-dimensionality or the orientation of the ripple fields. The complex and three-dimensional ripple field could be a result of interacting waves and currents of varying directions which is presently not resolved in the model.

The red shading indicates that the bottom boundary layer is in a sheet flow regime, and

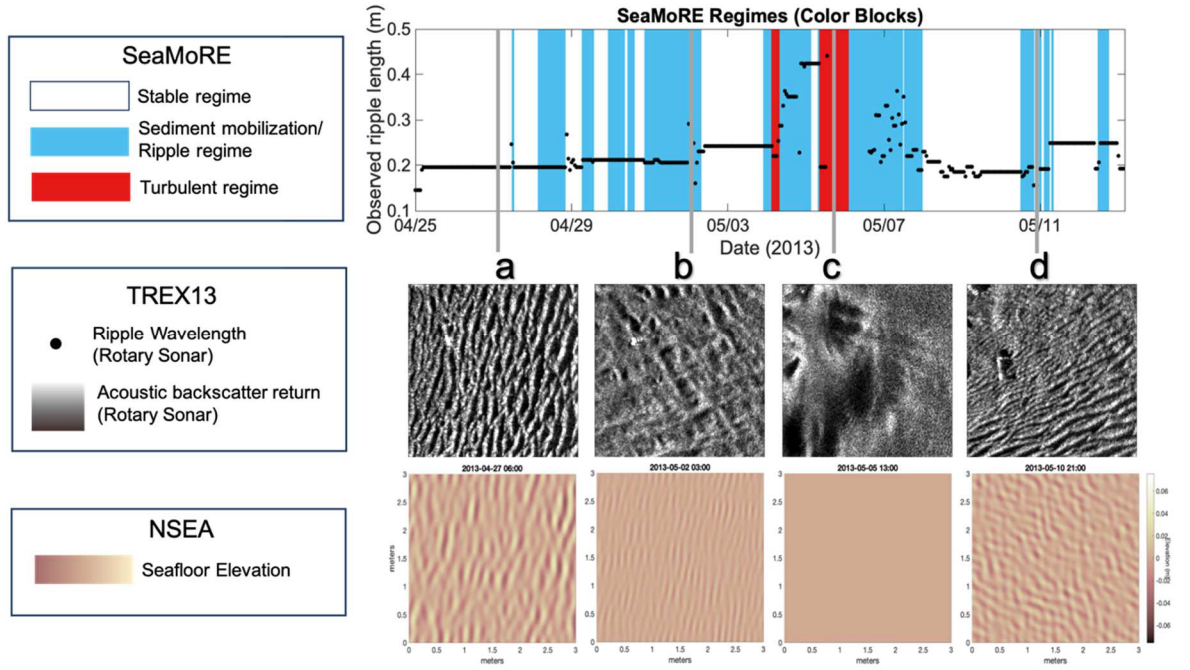

Figure 1: Output from SeaMoRE (color blocks in top panel) indicating the instantaneous seafloor regime and random seafloor elevation realizations output from NSEA (bottom panels) plotted with the rotary scanning sonar images (middle panels) and the peak ripple wavelength extracted using Fourier analysis on the sonar images (black dots in top panel). The grey lines in the top panel indicate the times of the four sonar images and NSEA model realizations.

the ripples are being washed out. SeaMoRE accurately predicts the two times in the time series that the ripples are sheared off completely by the flow and a smooth, flat bed results. NSEA also accurately predicts this result at time (c) as shown as no variations in seabed elevations in the bottom panel.

In general, both SeaMoRE and NSEA are in good agreement with observations of ripple fields as observed from rotary sonar backscatter images in 8 m of water depth. While both models compare well qualitatively, a more quantitative analysis and sensitivity testing is needed before the models can be applied at other locations.

4 CONCLUSIONS

A near bed hydrodynamic and sediment mobility model (SeaMoRE) was coupled with a seafloor roughness architecture (NSEA) to provide predictions of seabed regime (stable/evolving/turbulent) and random realizations of seabed elevations generated by local wave and current conditions. The models agreed well with observations made at the Target and Reverberation Experiment off the coast of Panama City, FL, USA, in 2013. Future work will include a sensitivity analysis on the models and validation at other field sites to determine the applicability of the models to other locations and conditions.

5 ACKNOWLEDGEMENTS

William Kearney was supported by the American Society for Engineering Education Postdoctoral Fellowship Program at the US Naval Research Laboratory at Stennis Space Center when the work was performed. Allison Penko was supported under base funding to the US Naval Research Laboratory from the Office of Naval Research. The authors would like to acknowledge Ryan Phillip for his contribution to SeaMoRE as presented in this paper. This information is preliminary and is subject to revision. It is being provided to meet the need for timely best science. The information is provided on the condition that neither the U.S. Geological Survey nor the U.S. Government shall be held liable for any damages resulting from the authorized or unauthorized use of the information. Any use of trade, firm, or product names is for descriptive purposes only and does not imply endorsement by the U.S. Government.

6 REFERENCES

Jackson, D. R., Richardson, M. D., Williams, K. L., Lyons, A. P., Jones, C. D., Briggs, K. B., & Tang, D. (2009). Acoustic observation of the time dependence of the roughness of sandy seafloors. IEEE Journal of Oceanic Engineering, 34(4), 407–422. https://doi.org/10.1109/joe.2009.2021287.

Kearney, W. S., & Penko, A. M. (2022). The Naval Seafloor Evolution Architecture: A Platform for Predicting Dynamic Seafloor Roughness. https://doi.org/10.48550/arXiv.2211.09092.

Nelson, T. R., Voulgaris, G., & Traykovski, P. (2013). Predicting wave-induced ripple equilibrium geometry. Journal of Geophysical Research: Oceans, 118(6), 3202-3220

Nielsen, P. (1981). Dynamics and geometry of wave-generated ripples. Journal of Geophysical Research: Oceans, 86(C7), 6467-6472.

Penko, A. M., Calantoni, J., Rodriguez-Abudo, S., Foster, D. L., & Slinn, D. N. (2013). Three-dimensional mixture simulations of flow over dynamic rippled beds. Journal of Geophysical Research: Oceans, 118(3), 1543-1555.

Penko, A., Calantoni, J., & Hefner, B. T. (2017). Modeling and observations of sand ripple formation and evolution during TREX13. IEEE Journal of Oceanic Engineering, 42(2), 260-267.

Penko, A.M., Schoenauer, S., and K. Hall (2022). Automated Method to Extract Oceanographic and Atmospheric Data from Online Sources, NRL Memorandum Report, NRL/7350/MR-2022/1, US Naval Research Laboratory, 1–24.

Penko, A. M. and R. Phillip (in review). Seabed Mobility Regime Estimator: Simplified prediction of seabed dynamics.

Salimi-Tarazouj, A., Hsu, T.-J., Traykovski, P., Cheng, Z., & Chauchat, J. (2021). A numerical study of onshore ripple migration using a eulerian two-phase model. Journal of Geophysical Research. Oceans, 126(2). https://doi.org/10.1029/2020jc016773.

Traykovski, P. (2007). Observations of wave orbital scale ripples and a nonequilibrium time-dependent model. Journal of Geophysical Research: Oceans, 112(C6).

Bedform transition in a sediment starved environment (SW Baltic Sea)

K. Krämer *Institute of Geosciences, CAU Kiel, Germany – knut.kraemer@ifg.uni-kiel.de*
M. Becker *Institute of Geosciences, CAU Kiel, Germany – marius.becker@ifg.uni-kiel.de*
C. Winter *Institute of Geosciences, CAU Kiel, Germany – christian.winter@ifg.uni-kiel.de*

ABSTRACT: The shallow nearshore waters of the southwestern Baltic Sea are a sediment starved environment. Between the wide outer Bay of Kiel and the narrow Fehmarn Belt, a transition from flow parallel sand ribbons through starved dunes into fully developed dunes can be observed. While their general orientation aligns with residual flow pattern, individual dunes exhibit a complex 3D structure. Having been described as dormant, give an estimate of long- and short term migration rates. We also present an approach for measuring starved dune lengths preserving global self-similarity and aspect ratio. The transition from sand ribbons to dunes is linked to the thickness of the mobile sand layer on top of rigid glacial till deposits.

1 INTRODUCTION

Lacking sediment input from major rivers, many shallow parts of the western Baltic Sea are considered sediment starved environments (Niedermeyer at al., 2011). The substratum is dominated by till deposits from the last glaciation. This heterogeneous material spanning grain sizes from clay to boulders is reworked and sorted by wave and current action. Mobile sands are available from the erosion of active cliffs (Averes et al., 2021) and abrasion on submarine platforms (Healy, 1980). Larger sand bodies are often confined to the littoral regions and form wave-dominated shore-parallel bars or shore-oblique ridges.
The hydrodynamics of the microtidal western Baltic are governed by fetch-limited waves and wind-induced seiching. Flows generated by basin scale oscillations are channeled through narrow straits, belts and over shallow sills. The Fehmarn Belt is considerably stratified due to the water mass exchange between the North Sea and the Baltic Proper. However, significant inflow of cold, saline and oxygen rich water from the North Sea occurs only during Major Baltic Inflow (MBI) events, which play an important role in hydrodynamics and ecology of the Baltic Sea (Mohrholz et al., 2015).

These limitations in both sediment availability and transport capacity make large flow transverse bedforms a rare phenomenon in this region. Nevertheless, in parts of the narrow straits where both sufficient sediment availability and higher current velocities come together, high energy bedforms such as giant ripples and dunes can be found (Werner & Newton, 1975; Kuijpers et al., 1993) amongst the abundance of other bedforms (Winter et al., this volume).

1.1 The bedform field in the southwestern Fehmarn Belt

In the southwestern Fehmarn Belt (FB), a large bedform field extends ca. 8000 m in the main flow direction and ca. 1700 m laterally (Fig. 1a). The bedforms have first been described as asymmetric giant ripples with length of around 60–70 m and heights of around 1.8–2.0 m on the basis of single-?beam echosounder recordings (Werner & Newton, 1970). Adapting more recent definitions we use the term dunes to describe the bedforms. Sidescan sonar surveys over larger areas of the Bay of Kiel towards the West show a series of flow parallel sand ribbons which have been proposed exist on lag deposits and serve as conduits feeding sediment into the dune field (Feldens et al., 2015). Investigations including detailed diver observations of individual dune

morphology and fauna distribution found adult specimen of sessile species in the surface layers interpreted as to that the bedforms had been immobile for several years (Werner et al., 1974), leading to the field being described as dormant. Although later studies showed an eastward progression of the eastern boundary, migration rates could not be determined with certainty due to lacking positioning accuracy of the positioning systems used (Feldens et al., 2009, 2015). Advances in GNSS technology and the use of online correction services (RTK) available in nearshore areas now allow for centimeter accuracy in horizontal and vertical domain (Lycourghiotis & Kariotou, 2022). For this study multibeam echosouder (MBES) surveys from recent expeditions were used for the generation of high resolution maps of bedform topography. Precisely positioned grab samples allow for an investigation of sedimentological properties across individual dune geometry and across the transition from sand ribbons to dunes.

2 METHODS

2.1 Seafloor morphology

Bathymetry and backscatter data were recorded with a MBES (Norbit WBMS STX, 550 kHz, 512 beams at 0.9° width) onboard RV ALKOR during cruises AL536 (05/2020), AL552 (03/2021) and AL574 (06/2022) with typical survey speed of 5 kn, 12 Hz ping frequency and a swath of 120° which in the range of water depths between 15 and 25 m resulted in an beam spacing of roughly 0.2 by 0.15 m across/along-swath. For positioning, a differential GNSS system with online real time kinematic (RTK) corrections was used which allowed a horizontal and vertical position accuracy < 0.02 m. Attitude (heave, pitch and roll) was provided by the build-in motion sensor (Applanix WaveMaster).

The raw MBES data were processed in MB-System (V5.7.9beta26) with corrections for attitude and raytracing using sound velocity profiles from CTD casts. The point cloud data was gridded in 0.5 m resolution to obtain a digital elevation models (DEM) of bathymetry and beam backscatter intensity.

2.2 Sub-bottom profiles

Shallow sub-bottom profiles were recorded in combination with the MBES data with an hull-mounted parametric sub-bottom profiler (Innomar SES-2000® medium, 8/100 kHz).

2.3 Sediment samples

Seafloor surface samples were taken by van Veen grab sampler. The position of the samples were recorded using an USBL transponder on the device combined with an RTK GNSS (AL552, 2021) and an RTK GNSS antenna positioned on the A-frame above the wire (AL574, 2022). The position accuracy is estimated as O(1 m) for the USBL and O(0.1 m) for the RTK antenna. In combination with the RTK positioned MBES surveys, this allows for a resolution of elements of the dune morphology (stoss/lee slope, trough) in contrast to the previously used differential GPS positioning which did not allow to differentiate between dune and lag sediments (Feldens et al., 2015). At the time of writing, the samples are being analyzed by dry sieving to obtain grain size distributions.

2.4 Hydrodynamics

Flow velocities in the dune field were estimated from a numerical model of the North and Baltic sea (modelling system GETM) available from the COSYNA data web portal (https://codm.hzg.de/codm/). Averaged over a representative wind year 09/2016 – 08/2017, the main residual current direction was 99° (Fig. 1b).

2.5 Bedform morphology

The dimensions height and length (H, L) of the bedforms were calculated using the 2020 bathymetry. Bed elevation profiles (BEPs) were extracted from the DEM in the main flow direction (99° E) with an along-profile spacing of 0.5 m and a lateral spacing of 10 m between the individual profiles using the Generic Mapping Tools software (GMT V6.0.0, Wessel et al. 2019). The resulting profiles were further

analyzed in GNU Octave (V5.9.0). First, the BEPs were filtered using an (5, 100) m bandpass filter to remove high frequency noise and secondary bedforms as well as the background bathymetry. The resulting zero-mean profiles were evaluated between zero-crossings to find crests as local maxima. As – in the starved state – the space between two dunes can be composed of boulder clay or lag deposits a seemingly random topography unrelated to the dunes and no well-defined troughs may occur (Fig. 2). This environment is challenging for the established methods of separating individual bedforms from BEPs developed for tidal or river dunes (Gutierrez et al., 2018; Cisneros et al., 2020; Wang et al., 2020). Especially the actual lengths of starved bedforms are difficult to obtain. Using crest-to-crest spacing would result in an overestimation of bedform lengths, due to the wide, additional space between individual starved bedforms. Therefore, the first and second maxima in the five-point averaging smoothed curvature were extracted as lee slope end (first peak) and stoss slope onset (second peak). For fully developed dunes, this closely corresponds with the trough location (Fig. 2). Stoss and lee slope lengths and heights were taken as differences in along-profile distance and vertical elevation between those three points. The total dune length was computed as the sum of stoss and lee length and total height as the average of stoss and lee height. Asymmetry was computed from the ratio of stoss and lee length. The resulting bedform dimension parameters were stored and exported for the position of the crest.

Slope angle and direction of the gradient of the bathymetry were calculated from the DEM using GMT grdgradient. To identify slipfaces, the resulting DEM was masked with a 10° cutoff. The profiles used for the calculation of the bedform dimensions described above were extracted from the masked DEM. Slipfaces were identified where at least three successive points at the grid spacing of 0.5 m had slopes >10°. The slipface direction was averaged over the respective segments and exported as vector components towards East and North (Fig. 1a).

2.6 Bedform migration rates

To evaluate migration rates a MBES bathymetry from 2007 was compared to data from surveys in 2020, 2021 and 2022. Lacking positioning accuracy, the 2007 was geo-referenced with the help of ground control points taken from immobile morphological features in the western part of the survey area. The remaining positioning error is estimated at ±2 m. The latest surveys were carried out with RTK GNSS with positioning accuracy below 0.02 m. In a first step, migration rates were estimated manually from the comparison of individual profiles over a few dunes.

3 RESULTS

3.1 Bedform morphology

Generally, the dune field is separated into an upper terrace in around 14 m water depth and a lower terrace at 21 m (Fig. 1a). The lateral slope between the terraces steepens from West to East. The field is further grouped into at least six distinct trains of dunes. Their origin can be traced to flow parallel sand ribbons curving into Fehmarn Belt from the larger Bay of Kiel towards the East. The individual trains merge laterally but defects and bifurcations along in their merging flanks can be traced for a long distance, in some cases throughout the entire length of the dune field.

Individual dunes show complex 3D geometries with lengthening and increasing planform curvature of crests, bifurcations, and isolated barchanoid dunes. Dune trains traversing the bathymetry gradient at an oblique angle show a behaviour similar to the refraction of shallow water waves: Dune crestlines bend inward when located in greater depth.

The dunes are asymmetric with peaks of 3° and 13° in the distributions of stoss and lee slope angles respectively. The steeper leeward faces dip towards ESE (median 100°). However, local slipface directions differ across the individual trains from West to East and appear to follow the changing residual flow direction into the FB. Throughout all available surveys starting from SBES in the 70s to recent MBES surveys

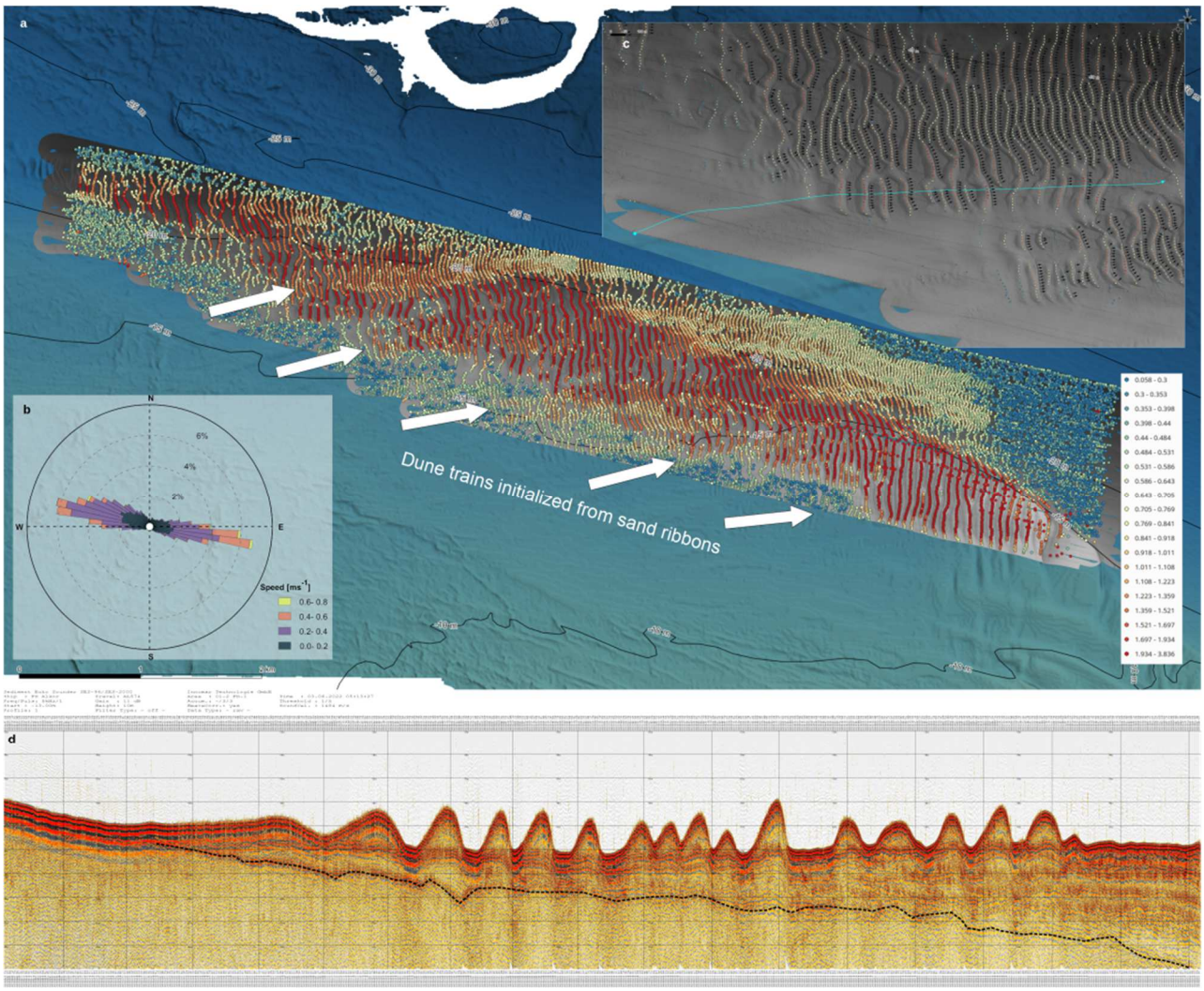

Figure 1. a) Overview map with detected dune crests. Colors indicate dune height. b) Current rose based on a representative wind year 2016/2017. Data: COSYNA. c) Detailed view showing dune topography, detected crests with height and slipface direction vectors for an exemplary transitions ob bedform states from flow-parrallel sand ribbons over barchanoid forms to starved dunes. The cyan line indicates the track of the SBP profile. d) SBP profile indicating increasing thickness of the mobile sandy bed layer above glacial till deposits (dashed black line).

(2022), a no reversal has not been observed, not even of individual dunes.

3.2 Bedform migration rates

Mean long term average migration rates (2007–2020) are estimated to 1.1 m/a. The comparison of the three successive surveys from 05/2020, 03/2021 and 06/2022 showed almost no migration between 2020 and 2021 and migration distances of about 2 m between 2021 and 2022 indicating intermittent dynamics.

3.3 Transport layer thickness

A SBP profile which follows the transition from sand ribbons through short-crested barchanoid dunes to starved long-crested dunes shows the increasing thickness of the overlying mobile sand on top of a downward dipping glacial till deposits (Fig. 1d). iI is seen that the thickness of the upper sand layer increases from West to East, in general. The highest, most regular and fully developed dunes are found in the shallow eastern part of the bedform field.

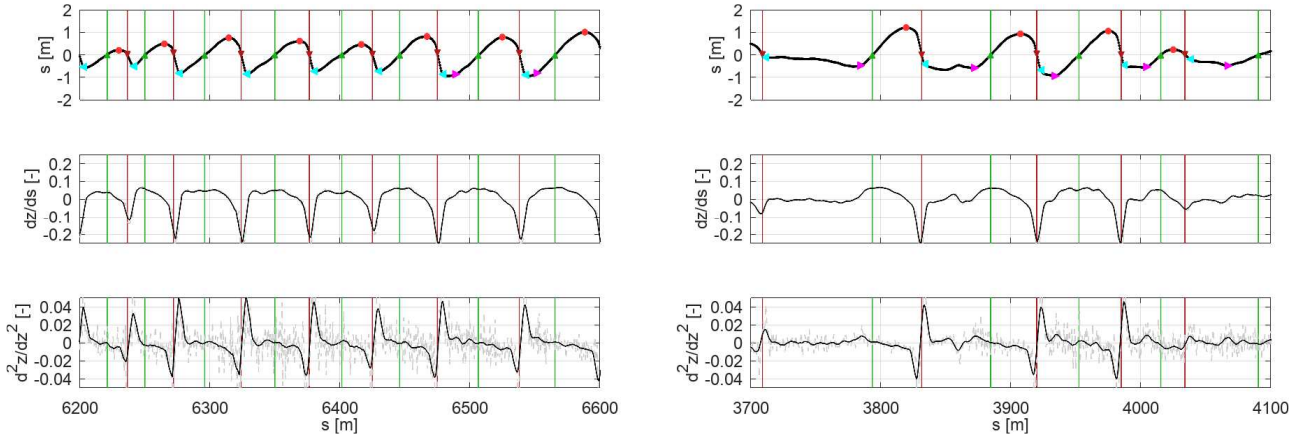

Figure 2. Separation of dunes and measurement of dimensions. Examples for bed elevation profiles z(s) (top row), slope dz/ds (middle row) and curvature d^2z/dz^2 (bottom row) for starved dunes (left panels) and fully developed dunes (right panels). Red (down) and green (up) lines mark zero-crossings of the BEPs, red dots mark crest positions, magenta rightward triangles mark stoss slope onset and cyan triangles mark lee slope end.

4 DISCUSSION

4.1 Determination of starved dune length

In this study a large number of dune shapes (16,372) were analyzed and show a large scatter in height (2^{nd} and 98^{th} percentiles: H_{02} = 0.25 m, H_{98} =2.14 m; L_{02} = 24.54 m, L_{98} = 109.36 m). Feldens et al. (2015) stated that the dune steepness "H/L plot beneath the global mean line" of Flemming (1988). This is true when crest to crest distances are used to measure dune length (Fig. 3). When length is measured between first and second curvature peaks as illustrated above and in Fig. 2, H/L ratios of individual dunes plot closer to the global mean given by Flemming (1988) as H = 0.0677 L0.8098 (Fig. 3). When the projected length in the direction of the slipface gradient is used in addition, the H/L ratios along individual dunes fit even better.

4.2 Planform structure of dunes in relation to local flow and transport pattern

The asymmetric shape of the dunes agrees with the direction of Baltic Sea inflow events, which are possibly the main driver for dune formation and migration. While average slipface directions agree with the main flow direction during inflow events, individual dune crests show a complex 3D structure with both inward focussing and outward fanning which may locally influence bedload transport directions leading to converging and diverging transport patterns. This potentially influences the sediment supply to the respective downstream dune. Further investigations have to be made into the relation between slipface direction, near-bed flow and bedload transport direction as the latter may be bound to the small scale downslope gradient direction.

4.3 Bedform transitions in relation to transport capacity and transport layer thickness

Bedform transitions from sand ribbons to (starved) dunes have to be re-evaluated based on bathymetry and sub-bottom profiles following the sand ribbon and dune train axes. By evaluating transport direction and capacity from high resolution numerical models and determining transport layer thickness of the available mobile sediment above a rigid base layer from SBP profiles the bedform types can be plottet against stability diagrams (e.g. Kleinhans, 2002).

5 CONCLUSIONS

In the microtidal southwestern Baltic Sea, a field of starved bedrforms is characterized by complex individual geometry and intermittent migration with a long-term average migration rate close to 1.1 m/a. Short term changes in migration rates obtained from annual surveys can help to understand the link between the

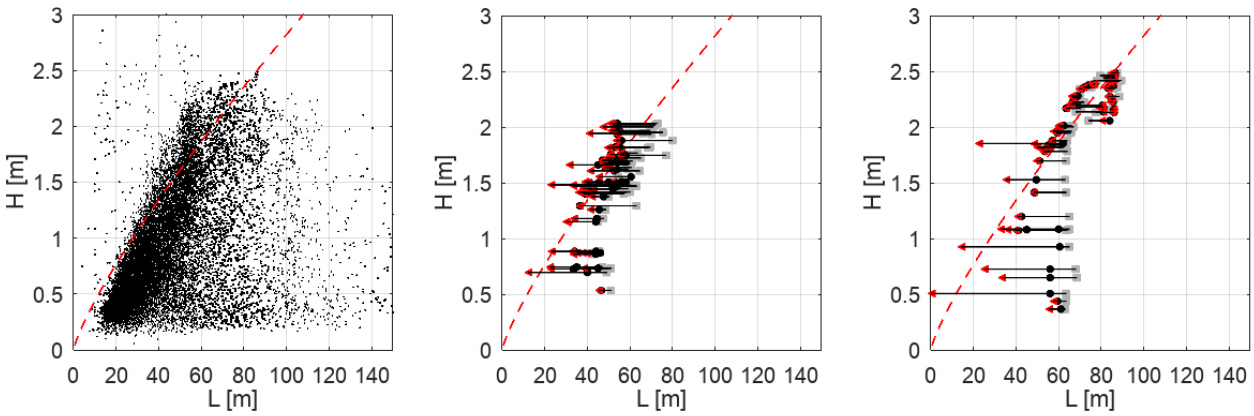

Figure 3. Dune dimensions H, L. The red dashed line indicates the global mean following Flemming (1988). Left: Entire dune field containing 16,372 dune geometries. Middle: Example for a starved dune. Right: Example for a fully developed dune. Grey squares indicate crest-to-crest lengths, black circles indicate adapted length based on first and second BEP curvature peaks and red triangles indicate the additional projection of the curvature-based lengths towards the direction of the corresponding slip faces.

history of forcing events and morphodynamic response of the dunes.

The mode of the bedforms changes from thin flow-parallel sand ribbons to flow-transverse (starved) dunes with the availability of sand from the substratum.

Starved dune lengths can be measured by evaluating local maxima of curvature between crests positions along BEPs. 3D dunes with large crestline curvature should be measured with respect to the direction of the slipface gradient to preserve global self-similarity and aspect ratio, e.g. by defining a curvilinear grid following streamlines for the extraction of the BEPs or by a two-step procedure which first extracts crestlines from parallel BEPs and in a second step follows the crestlines of individual dunes and extracts perpendicular profiles reaching the next upstream and downstream dune.

Porcile et al. (2022) already pointed out the need for further studies to understand the effect of sediment starvation on bedform migration rates. Here, the SW FB dune field could serve as an interesting field site other than spatially constrained river channels or laboratory flumes.

6 REFERENCES

Averes, T., Hofstede, J. L., Hinrichsen, A., Reimers, H. C., & Winter, C. (2021). Cliff retreat contribution to the littoral sediment budget along the baltic sea coastline of Schleswig-Holstein, Germany. Journal of Marine Science and Engineering, 9(8), 870.

Cisneros, J., Best, J., van Dijk, T., Almeida, R. P. D., Amsler, M., Boldt, J., ... & Zhang, Y. (2020). Dunes in the world's big rivers are characterized by low-angle lee-side slopes and a complex shape. Nature Geoscience, 13(2), 156-162.

Feldens, P., Diesing, M., Schwarzer, K., Heinrich, C., & Schlenz, B. (2015). Occurrence of flow parallel and flow transverse bedforms in Fehmarn Belt (SW Baltic Sea) related to the local palaeomorphology. Geomorphology, 231, 53-62, 10.1016/j.geomorph.2014.11.021.

Feldens, P., Schwarzer, K., & Diesing, C. H. M. (2009). Genesis and sediment dynamics of a subaqueous dune field in Fehmarn Belt (south-western Baltic Sea). Ergebnisse aktueller Küstenforschung, 80.

Flemming, B. W. (1988). Zur Klassifikation subaquatischer, strömungstransversaler Transportkörper. Bochumer geologische und geotechnische Arbeiten, 29(93-97), 44-47.

Gutierrez, R. R., Mallma, J. A., Núñez-González, F., Link, O., & Abad, J. D. (2018). Bedforms-ATM, an open source software to analyze the scale-based hierarchies and dimensionality of natural bed forms. SoftwareX, 7, 184-189.

Healy, T. (1980). The efficacy of submarine abrasion vs cliff retreat as a supplier of marine sediment in the Kieler Bucht, western Baltic.

Kleinhans, M. G., Wilbers, A. W. E., De Swaaf, A., & Van Den Berg, J. H. (2002). Sediment supply-limited bedforms in sand-gravel bed rivers. Journal of sedimentary research, 72(5), 629-640, 10.1306/030702720629.

Kuijpers, A., Werner, F., & Rumohr, J. (1993). Sandwaves and other large-scale bedforms as indicators of non-tidal surge currents in the Skagerrak off Northern Denmark. Marine Geology, 111(3-4), 209-221.

Lycourghiotis, S., & Kariotou, F. (2022). The "GPS/GNSS on Boat" Technique for the Determination of the Sea Surface Topography and Geoid: A Critical Review. Coasts, 2(4), 323-340.

Mohrholz, V., Naumann, M., Nausch, G., Krüger, S., & Gräwe, U. (2015). Fresh oxygen for the Baltic Sea—An exceptional saline inflow after a decade of stagnation. Journal of Marine Systems, 148, 152-166.

Niedermeyer, R. O., Lampe, R., Janke, W., Schwarzer, K., Duphorn, K., Kliewe, H., & Werner, F. (2011). Die deutsche Ostseeküste.

Porcile, G., Damveld, J. H., Roos, P. C., Blondeaux, P., & Colombini, M. (2022). Modelling the Genesis of Sand-Starved Dunes in Steady Currents. Journal of Geophysical Research: Earth Surface, e2022JF006796.

Wang, L., Yu, Q., Zhang, Y., Flemming, B. W., Wang, Y., & Gao, S. (2020). An automated procedure to calculate the morphological parameters of superimposed rhythmic bedforms. Earth Surface Processes and Landforms, 45(14), 3496-3509.

Werner, F., & Newton, R. S. (1970). Riesenrippeln im Fehmarnbelt (westliche Ostsee). Meyniana, 20, 83-90.

Werner, F., & Newton, R. S. (1975). High-energy bedforms in the nontidal great belt linking North Sea and Baltic Sea. In Geology and Engineering (pp. 381-389). Academic Press.

Werner, F., WE, A. & Tauchgruppe Kiel (1974). Sedimentologie und Ökologie eines ruhenden Riesenrippelfeldes. Meyniana 26, 39-62.

Wessel, P., Luis, J. F., Uieda, L., Scharroo, R., Wobbe, F., Smith, W. H., & Tian, D. (2019). The generic mapping tools version 6. Geochemistry, Geophysics, Geosystems, 20(11), 5556-5564.

ECOWind-ACCELERATE: accelerated seabed mobility around offshore windfarms.

K. Van Landeghem *School of Ocean Sciences, Bangor University, UK – k.v.landeghem@bangor.ac.uk*
C. McCarron *HR Wallingford, UK – c.mccarron@hrwallingford.com*
R. Whitehouse *HR Wallingford, UK – r.whitehouse@hrwallingford.com*
M. Clare *National Oceanography Centre, Southampton, UK – michael.clare@noc.ac.uk*
C. Unsworth *School of Ocean Sciences, Bangor University, UK – christopher.unsworth@bangor.ac.uk*

ABSTRACT: To identify opportunities for wider conservation with stackable benefits around offshore windfarms (OWF), we need to quantify existing changes and predict future changes to the marine environment from OWF expansion, with trophic interactions that start at the seabed. We are therefore building a calibrated and validated high-resolution local area coupled flow-sediment transport model to quantify the impact of OWF modified flows on seabed mobility (sediment transport, seabed composition and morphology). This will then be combined with impacts on the seabed from climate change. Here we focus on using various sizes of OWF and representing realistic seabed sediment composition, and preliminary results from flume laboratory experiments and TELEMAC 3D modelling will be presented at the MARID conference. This work is part of the new ECOWind-ACCELERATE project, where the team will quantify the impact of the seabed modifications on seabed habitats and the knock-on consequences for epi-benthic fish distribution and deep-diving seabirds.

1 INTRODUCTION

Offshore windfarms will be developed at an accelerated schedule under fast-track plans to switch away from fossil fuels. With ever larger offshore windfarms, and the cumulative effects of climate change, we thus urgently need to understand the way the seabed is modified in response and how such changes affect the wider marine ecosystem.

1.1 Seabed mobility around seabed infrastructure.

The seabed infrastructure associated with OWFs includes turbines, foundations and cables, plus the protective materials to keep it all safe. When natural currents in the water column deviate around such objects, the forces acting on the seabed enhance by up to a factor of four, with impacts stretching several kilometres beyond the object (Smyth and Quinn 2014, Whitehouse 1998, Vanhellemont & Ruddick 2014). These changes modify the properties and mobility regimes of the seabed, particularly at shallow cable corridor sites. It has been suggested that the effects that relate to the growing size of OWFs may be felt regionally, rather than just locally (van Berkel et al., 2020).

1.2 Seabed mobility driving habitats.

Habitat maps and models, which underpin local to regional marine spatial management via valuations of ecosystem services (ES), rarely consider dynamic changes to the seabed. Changes in substrate and suspended sediment load can define habitats, across a range of spatial scales, including: (i) changing extent and distribution of habitats (e.g. Fig. 1 – see end of this document); (ii) changing structure and function of habitats; and (iii) changes in supporting processes such as sediment suspension on which habitats rely. The close association of habitat type with the identity and diversity of benthic fauna mean such changes in habitat are likely to have significant impacts. For example, the

coarsening of habitat and introduction of hard substrates is likely to enhance species richness, abundance and productivity (Benoist et al 2019). On sand banks, even subtle changes in the proportion of silt drives changes in important high-calorie epi-benthic prey for deep-diving predators (Wright et al., 2000; Langton et al., 2021).

1.3 The mixed nature of seabed sediments in the Eastern Irish Sea.

To assess the impact of OWFs anywhere around the UK, an in-depth study is required across a range of depths, seabed habitats and OWF sizes. The Eastern Irish Sea is the ideal test bed for accelerated ecosystem impacts from OWF expansion. This area hosts several existing OWFs and four large planned OWFs (Fig. 1) lie within 10-20km of each other, and of other sites (incl. planned carbon storage). The variable seabed (Fig. 1-C1) defines habitat suitability (Fig. 1-C2), and the sand banks amid coarse sediments represent many environments also found in the S North Sea (Fig. 1-A).

1.4 Problems with predicting seabed mobility.

Uncertainty in sediment transport models is greater when the seabed is mixed, and with seabed composition as an important driver of habitat suitability (Fig. 1), benthic habitat maps are only relevant when the changing state of the seabed is considered. Mixed beds can experience energetic conditions just under the threshold of motion for the sand fraction, modified by the presence of gravel (McCarron et al., 2019). Any flow amplification could dislodge this sand and even form mobile sand waves. These could amplify the flow further and sand wave trains can extend many kilometres in the far-field of the original obstruction (see Section 2).

1.5 Physical modelling and field observations to validate/calibrate sediment transport.

Real-world observations (see Section 2) and scaled physical experiments (see Section 3) of flow modification can be used to calibrate and validate modelled predictions of local hydrodynamic modifications and seabed sediment transport. We recently validated TELEMAC-SISYPHE model outputs against observed flow deviations around individual objects, such as the SS Apapa shipwreck to the north of Anglesey, North Wales, UK (Fig. 2), with 18 repeat seafloor surveys since 2012. Larger scale effects will be assessed during the new ECOWind-ACCELERATE project.

1.6 Aims of this work.

No field-scale data exist yet from the much larger planned OWFs, to determine their cumulative impact from the increased “fetch”. We will thus use the world-class laboratory of HR Wallingford to run experiments to investigate the impacts of different OWF array scales on sediment transport, using existing length scale approaches (Frostick et al 2011) to ensure geometric similarity between experiments, offshore data and the hydro-morphodynamic model, with a best practice scaling approach (Whitehouse 1998). The main questions we focussed on:

- How well do the predicted hydrodynamics (using a sub-grid scale representation of a monopile or monopile array) represent actual effects on flow velocities?
- How does monopile diameter affect wake properties (i.e., downstream and cross-stream flow velocity anomalies)?
- How will increasing monopile diameter affect flows and bed morphodynamics?

2 OFFSHORE DATA AS INSPIRATION

2.1 Seabed mobility due to flow diversion around objects.

The team has been monitoring change in seabed mobility around seabed objects on mixed and coarse beds, as this is where many Offshore Wind Farms (OWF) around the UK will be built. Flow diversions around OWF objects and sedimentary bedforms are responsible for additional energy in the water column and for winnowing of the sand fraction with subsequent generation of migrating sand waves inducing further sand winnowing. This can result in mobile sands many kilometres beyond the initial flow diversion, even at depths of 50-80m (Fig. 2-A, B1), and these can host different benthic communities (Cheng et al., 2021). A small disintegration of the SS Apapa wreck resulted in a demonstrable shift in seabed mobility regime (Fig. 2-B2) with lateral changes in seabed composition over 100s of metres, new scour pits and a reversal in the migration direction by a 2.5m high sediment wave.

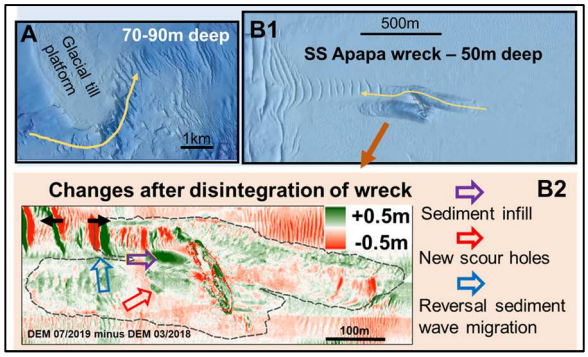

Figure 2. Seabed observations to capture impact of accelerated flow on bed mobility: Flow diversion causes sediment wave trains to form around glacial till platform (A) and a shipwreck (B).

2.2 Enhanced turbulent kinetic energy in the wake of a large sediment wave.

In the summer of 2021, our Bangor University team deployed an upward-facing ADCP on a frame near a 15m high sediment wave (Fig. 3). There is quadrupling of turbulent kinetic energy (TKE) 200m away from this large sediment wave (Fig. 3). The increase in TKE which persists up to 35m above the bed.

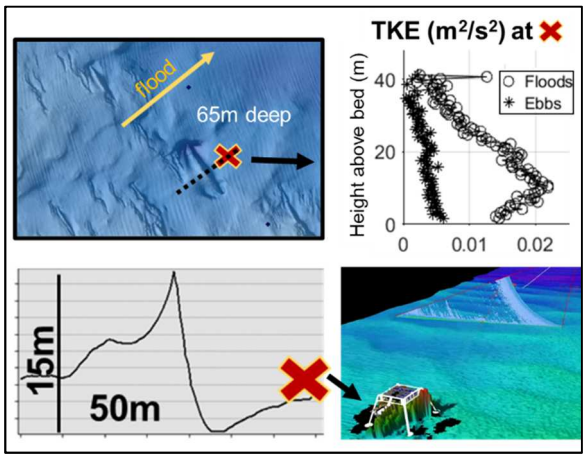

Figure 3. Seabed observations to capture impact of accelerated flow on bed mobility: Enhanced TKE in the wake of a 15m high sediment wave.

2.3 Seabed changes in the wake of a wind turbine.

From SEACAMS data around the scour-protected monopiles of the Rhyl Flats OWF, there are also signs of increased seabed mobility (Fig. 4) and changes to sedimentary bedform dimensions. The monopiles are nearly a third of the size of the monopiles we will see in future installations. The effect of flow diversion has altered the seabed from an exposed glacial bed of sand and gravel to a sandy bed with sediment waves in the wake of the turbine (Fig. 4 – bottom image). The reversed process can also happen, where the sediment waves already existed, but they have been washed away in the wake of the turbine (Fig. 4 – top image). These effects can extend for more than 100 times the diameter of the monopile, and where sediment waves are generated, they often set off a train of sandy bedforms for many more kilometres.

The way heterogeneous beds of glacial tills supports ecosystems will differ from the way a clean sandy bed does. So the impacts are profound and the impacts are variable, and the ECOWind-ACCELERATE project aims to predict this.

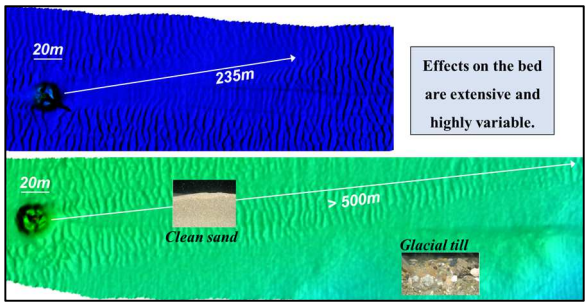

Figure 4: Increased seabed mobility by monopiles of the Rhyl Flats OWF in the Eastern Irish Sea. The seabed images are hypothetical.

2.4 Many different seabed substrates.

The Irish Sea was the scene of a massive ice stream draining the British-Irish Ice Sheet (Clark et al., 2022). This left behind sediments of all sizes and consolidation, and in the Irish Sea, there is great spatial variability in seabed sediment type (e.g. Fig 1 and example seabed images in Fig. 5). Having these gradients of different seabed substrates will allows us to use the spatial variability of today's relationships between bed and habitats to predict the future use of habitats.

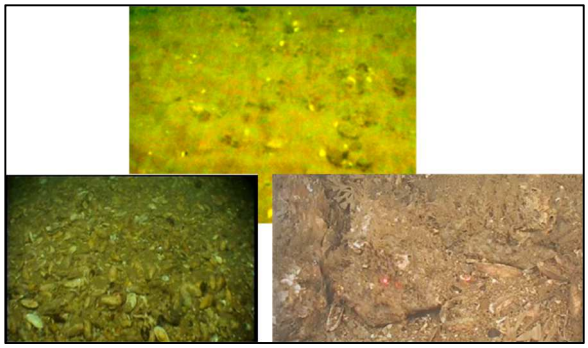

Figure 5: Images from the variable seabed in the Irish Sea (Van Landeghem, 2008).

3 EXPERIMENTAL FLUME LAB SETUP

3.1 Wave-current-sediment basin.

The UK Coastal Research Facility at HR Wallingford is a 27m wide by 54m long wave-current-sediment basin. Within the basin, a flume with working area of 3m wide by 30 m long was built. With an operational depth up to 0.8m, discharge is less than 1.2 m^3/s.

3.2 Instruments.

Hydrodynamics will be monitored using a vertical array of acoustic Doppler velocimeters (ADVs) and a Vectrino Profiler. These velocimeters will provide flow information at:

- 80% of flow depth (Top): Sideways looking ADV.
- 60% and 40% of flow depth: downwards looking ADV.
- 20% to bed: Vectrino Profiler.

Measurements will be taken across a 2D grid of points surrounding the monopile. Footage of the water surface will also be recorded using a high frame rate camera positioned directly above the monopile. Surface flow information will be obtained from PIV analysis of footage to support the vertical flow information.

Bed morphodynamics will be assessed using pre- and post-experiment bed scans collected using a 2D laser bed scanner.

3.3 Experimental design and integration with numerical models and offshore data.

The experimental setups includes cases with a single turbine, with a diameter that represents existing developments (e.g. monopiles of 5m in diameter) and a future Round 4 larger style monopile (12m diameter). Flow measurements and their morphodynamic extent will be measured offshore in the summer of 2023 in the wake of OWF. The TELEMAC-SISYPHE model will be configured to emulate the physical modelling setup, cross checked in both 3D and 2D mode.

Due to a slight delay in the work schedule, we cannot present preliminary results of the flume laboratory experiments in this extended abstract, but they will be presented at the MARID conference.

4 CONCLUSIONS

The forces acting on the seabed are guaranteed to change more rapidly over the next few decades due to accelerated effects of the climate crisis, interacting with the combined accelerated flows around new

large OWF infrastructure. These have the potential to change seabed mobility regimes, thus inducing changes to the integrity of the seabed, its habitats and associated benthic biodiversity and ecosystem services (both positive and negative).

Our outputs will provide valuable information not only for determining the rates and loci of seabed change for benthic habitat assessments, but also for the future design of resilient OWFs and inter-array and export cables that are vulnerable to the impacts of seabed currents, waves and human activities such as fishing. We thus aim to inform decision making by project partners on designing future climate change-adaptive and resilient structures.

5 ACKNOWLEDGEMENT

This work is funded by the ECOWind-ACCELERATE project (NE/X008886/1) Project, funded by the Natural Environment Research Council (NERC) and The Crown Estate. Additional support and data was provided by the SEACAMS projects and the Smart Efficient Energy Centre (SEEC) funded by the Welsh European Funding Office (WEFO) as part of the European Regional Development Fund (ERDF). The team thanks Ben Powell, Pete Hughes, Aled Owen and the crew of the RV Prince Madog for facilitating fieldwork under difficult working conditions due to COVID-19 restrictions.

6 REFERENCES

Benoist, N., Morris, K.J., Bett, B., Durden, J., Huvenne, V., Le Bas, T.P., Wynn, R.B., Ware, S.J. and Ruhl, H., 2019. Monitoring mosaic biotopes in a marine conservation zone by autonomous underwater vehicle. Conservation Biology 33(5), 1174-1186

Cheng, C.H., Borsje, B.W., Beauchard, O., O'flynn, S., Ysebaert, T. Soetaert, K.,2021. Small-scale macrobenthic community structure along asymmetrical sand waves in an underwater seascape Marine Ecology 42, e12657

Clark, C., Ely, J.C., Hindmarsh, R., Bradley, S.L., Ignéczi, A., Fabel, D., Ó Cofaigh, C., Chiverrell, R., Scourse, J., Benetti, S., Bradwell, T., Evans, D., Roberts, D., Burke, M., Callard, S.L., Medialdea, A., Saher, M., Small, D., Smedley, R., Gasson, E., Gregoire, L., Gandy, N., Hughes, A., Ballantyne, C., Bateman, M., Bigg, G., Doole, J., Dove, D., Duller, G., Jenkins, G., Livingstone, S., McCarron, S., Moreton, S., Pollard, D., Praeg, D., Sejrup, H.P., Van Landeghem, K. and Wilson, P., 2022. Growth and retreat of the last British–Irish Ice Sheet, 31 000 to 15 000 years ago: the BRITICE-CHRONO reconstruction. Boreas 51(4), 699-758

Frostick, L.E., McLelland, S.J. and Mercer, T.G. ed., 2011. Users guide to physical modelling and experimentation: Experience of the HYDRALAB network. CRC Press (IAHR Book Series)

Langton, R., Davies, I.M. and Scott, B.E., 2021. Seabird conservation and tidal stream and wave power generation: Information needs for predicting and managing potential impacts. Marine Policy 35, 623-630

McCarron, C.J., Van Landeghem, K.J.J., Baas, J.H., Amoudry, L.O., & Malarkey, J., 2019. The hiding-exposure effect revisited: A method to calculate the mobility of bimodal sediment mixtures. Marine Geology 410, 22-31

Smyth, T. and Quinn, R., 2014. The role of computational fluid dynamics in understanding shipwreck site formation processes. Journal of Archaeological Science 45, 220-225

van Berkel, J., Burchard, H., Christensen, A., Mortensen, L.O., Svenstrup Petersen, O. and Thomsen, F., 2020. The Effects of Offshore Wind Farms on Hydrodynamics and Implications for Fishes. Oceanography 33, 108-117

Vanhellemont, Q. and Ruddick, K., 2014. Turbid wakes associated with offshore wind turbines observed with Landsat 8. Remote Sensing of Environment 145, 105-115

Van Landeghem, 2008. High-resolution seafloor evidence for glacial and post-glacial environments in the tidally dominated Irish Sea. PhD Thesis, NUI, Department of Geology, University College Cork. http://library.ucc.ie/record=b1839572

Whitehouse, R., 1998. Scour at Marine Structures: A Manual for Practical Applications. ISBN 13: 9780727726551

Wright, P.J., Jensen, H. and Tuck, I., 2000. The influence of sediment type on the distribution of the lesser sandeel, Ammodytes marinus. Journal of Sea Research 44, 243-256

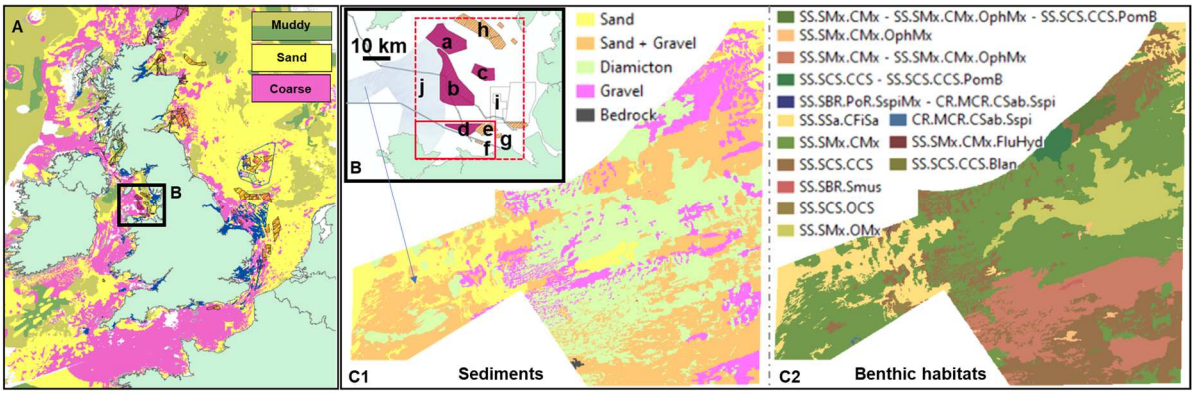

Fig. 1: A: About 24% of UK seabed has mixed and coarse sediments: many where windfarms are in place or planned (dashed polygons) and with sand banks (in blue) where sand is winnowed out. Data extracted from EMODnet – Sept 2021 version. B: Eastern Irish Sea, with OWFs Mona (a), Morgan (b) and Morecambe (c), within 10-20 km from the planned OWF Awel-y-Môr (d), the existing OWF Gwynt-y-Môr (e), Rhyl Flats (f), North Hoyle (g), Walney sites (h), and from a planned carbon storage site (i). Cable instalments for which we have data in grey, and two modelling domains of high-resolution bed stress modelling in red. C1-2: The Rhiannon dataset (j in (B)), has seabed sediment types (C1) defining benthic habitat distribution (C2).

Marine dune morphodynamics and sediment fluxes (off Dunkirk, France). Spatio-temporal variability and relations with hydrodynamic forcings.

S. Le Bot Univ Rouen Normandie, UNICAEN, CNRS, M2C UMR 6143, F-76000 Rouen, France – *sophie.lebot@univ-rouen.fr*
M. Bary France Energies Marines, Plouzané, France, *and,* Univ Rouen Normandie, CNRS, M2C UMR 6143, Rouen, France – *bary.mathilde@gmail.com*
M. Fournier Univ Rouen Normandie, CNRS, M2C UMR 6143, Rouen – *matthieu.fournier@univ-rouen.fr*
A. Husté Univ Rouen Normandie, ECODIV USC INRAE 1499, Rouen, France – *aurelie.huste@univ-rouen.fr*
N. Michelet France Energies Marines, Plouzané, France – *Nicolas.Michelet@france-energies-marines.org*
O. Blanpain France Energies Marines, Plouzané, France – *Olivier.Blanpain@france-energies-marines.org*
M. Nexer France Energies Marines, Plouzané, France – *Maelle.Nexer@france-energies-marines.org*
T. Garlan Shom, Département Géologie Marine, Brest, France – *thierry.garlan@shom.fr*

ABSTRACT: In the context of the future wind turbine project off Dunkirk (North of France), the morphodynamics of six medium to very large dunes (water depth around 14.5m LAT; heights around 1-3m; wavelengths around 84-232 m) is investigated. On the basis of eight bathymetric surveys realised between November 2019 and July 2021 (20 months), dune morphometric parameters, migration rates and associated sediment fluxes have been quantified. The spatial (intra- and inter-dune) and temporal variability in dune mophodynamics has been inspected through statistical analysis in relation with meteo-marine forcings. A strong intra-dune and weaker interdune variability is observed in dune morphology (e.g. wavelength, height, width), while dune migration and sediment fluxes display a similar response to forcing modifications. Some recommendations can be drawn up concerning the monitoring of dune fields in offshore wind farms.

1 INTRODUCTION

On the continental shelf, bedforms are mobile morphologies under the action of tides, winds and waves. The installation of offshore wind structures is concerned with major technical challenges, such as scouring around the pile foundations, burying and unearthing of cables (Carter et al., 2014), phenomena which are particularly exacerbated when the sedimentary dynamics is important and when submarine dunes are present (Couldrey et al., 2020). Marine dunes are located on sediment transfer pathways; they constitute essential functional areas for many biological species, and are such classified by the MFSD and Natura 2000 as a determinant habitat. The disturbance of these environments with the installation of seabed man-made structures can have significant consequences and needs to be anticipated and constrained.

Dunes morphodynamics is controlled by many factors such as sediment grain-size and hydrodynamics. It responds to variable meteo-marine forcings (tides, e.g. Tonnon et al., 2007 ; winds, waves, storms, e.g. Campmans et al., 2018) and sediment fluxes with modifications of their morphology and migration rates. However, the variability in dune morphodynamic response at the scale of the dune and the dune field is barely investigated (e.g. Salvatierra et al., 2015).

The objective of the present study is to get insights on dune morphodynamics in the area of the future wind turbine area off Dunkirk, with a special focus on the spatio-temporal variability of dune morphology, migration rates and associated sediment fluxes in response to various meteo-marine conditions.

2 STUDY AREA AND CONTEXT

A 50-km2 600 MW wind turbine project is planned in the southern North Sea, 10 km offshore Dunkirk (Fig. 1). This project aims to install a maximum of 46 wind turbines placed on the Binnen Ratel sandbank, connected to the land by cables passing in between the different coastal sandbanks up to Dunkirk. In order to better understand the burial and unburial of cables, the morphodynamic characteristics of the dunes and the associated sedimentary fluxes were studied within the framework of the DUNES project. The results presented here relate to a field of 6 dunes of around 0.5 km2 located along the cable corridor, in water depths between 14 and 17 m (Fig. 1).

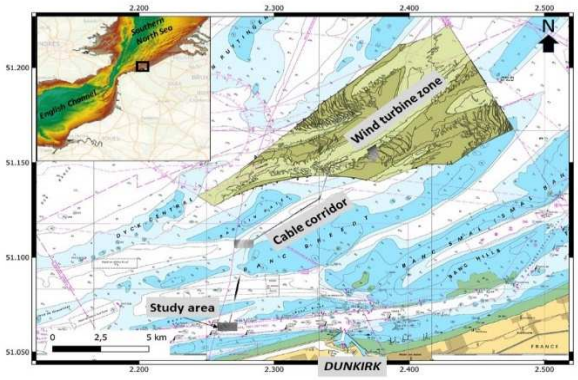

Figure 1. Localisation of the wind turbine project and the study area.

In the study area, the seabed is moulded with Holocene sandbanks, covered with large marine dunes, with heights about the meter and wavelength about the hundred of metres, and composed homogeneously of unimodal slightly gravelly sands with a mean median of 327.8 mm (Robert et al., 2021).

Tides are semi-diurnal with a macrotidal regime (3.5 and 5.5m in mean neap and spring conditions respectively; © SHOM). Flood and ebb currents flow towards the E-NE and W-SW respectively, with velocities mainly between 0.75-1 m/s and 0.5-0.75 m/s (© SHOM).

Residual flow is oriented towards the E-NE. Winds are mainly from SSW-WSW, with a secondary component from N-NE sector. Strong winds (>50 km/h) represent less than 1% of observations. Waves are mainly form SW and NE and attenuate on reaching the subtidal sandbanks with heights not exceeding 1.2 m for periods of 4 to 8 s in 80% of cases (Latapy et al., 2019).

3 MATERIAL AND METHODS

To characterize dune morphodynamics, sedimentary fluxes and their relation with hydrodynamics, bathymetric data as well as tide and wind data have been collected over a 21-month period.

3.1. Bathymetric data to morphodynamic parameters

Eight bathymetric surveys (namely S1 to S8) have been acquired between November 2019-July 2021 by GEOxyz using a Kongsberg EM2040C multibeam echosounder. Data resolution and accuracy are respectively 0.5 m and 0.05 m. A DEM has been produced at a 0.5-m resolution for each date.

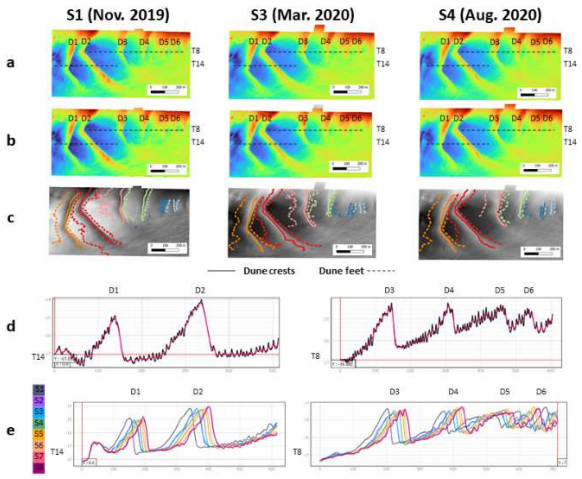

Figure 2. Bathymetric data processing. a: raw DEMs, b: filtered DEMs, c: DODs, d: vertical profiles (T8 and T14) in raw (black) and filtered (red) DEMs for S3, e: Vertical profiles (T8 and T14) in filtered DEMs for all surveys (S1 to S8).

Dunes are covered with smaller superimposed dunes (Fig. 2-a,d). In order to focus on the largest forms, DEMs have been filtered using a spatial low pass filter (Fig. 2-b). Dune crests and feet have been digitized (Fig. 2-c). Morphometric parameters (height, wavelength, width, sinuosity and asymmetry

indexes, crest depth) and migration distances of the dune crests have been measured from DEMs using QGIS along 20-m spaced profiles, perpendicular to dunes (West-East oriented) (Fig. 2-e).

3.2. Meteo-marine forcings

Data on meteo-marine forcings have been compiled. Coefficients indicative of tidal ranges (© SHOM) indirectly inform on tidal current strength and have been classified in 4 classes (neap, weak and strong spring, exceptional spring). The SW and NE events of strong winds (>50 km/h) were identified from the hourly data recorded at the Dunkirk meteorological station (infoclimat.fr). For each of the 7 periods in between bathymetric surveys, the meteo-marine have been resumed as follows : (i) percentages of occurrence of each tidal range class, and (ii) the duration and the number of strong wind events from SW and NE sectors.

3.3. Sediment fluxes

Sediment fluxes have been estimated over the 7 time-periods using the "dune tracking" formulation (Schmitt et Mitchell, 2014). This method considers that the sediment volume change of the dune form during the studied period can be related to sediment flux during this period, and is described by following formula:

$$Q_b = C \cdot H \cdot f \cdot (1 - \phi) \quad (1)$$

where C = dune migration rate; H = dune height; f = dune shape factor; and Φ = sediment porosity (0.4 classically used for sands).

The dune shape factor (f) is given by Equation 2:

$$f = \frac{V}{\lambda \cdot H} \quad (2)$$

where λ = dune wavelength; and V = dune surface (dune assimilated to a rectangular triangle) given by Equation 3:

$$V = (L \cdot H) \,/\, 2 \quad (3)$$

where L = dune width.

The volumic mass of silica (2650 kg/m^3) is used to express the fluxes in t/m/yr.

A code developed by Blanpain (2009) is used to estimate sediment fluxes with empirical formulas for the S2_S3 time-period where North-East have prevailed. The objective is to: (i) compare the sediment fluxes values obtained from "Dune tracking" method and empirical formulas, and (ii) better understand the reversal of dune migration direction observed during L2-L3 period. The formulas of van Rijn (1984) and Wu et al. (2000) are used in their classical form, and the formula of Yalin (1963) is adapted to include the wave influence:

$$Q_Y = \frac{0{,}5\,.\,U\,.(u_*^2 - u_{cri}^2)}{(s-1)g} \quad (4)$$

where U = $u_c + u_b$ describe the sum of the bottom current and orbital velocities; u_* = bottom friction, u_{cri} = critical velocity at which the sediment motion is initiated, s = the ratio between water and sediment volumic mass; and g = the gravity acceleration.

The fluxes are estimated at the center of the study area where the water depth is 15.6 m. Bottom current and free-surface elevation hourly timeseries were extracted from a MARS3D simulation while hourly wave conditions were extracted from a WaveWatch III (WWIII) simulation (Boudiere et al., 2013). Following the "Dune Tracking" method, sediment fluxes are expressed in t/m/yr and projected over the West-East axis (the transport direction is considered equal to the current direction).3.4. Statistical analysisStatistical analysis were performed to inspect the spatio-temporal variability of dune morphodynamics.

Statistical analysis was performed using R software (version 4.2.0; R Core Team, 2022) to analyse the spatio-temporal variability of dune morphodynamics. A linear mixed model was considered to investigate the effect of the dune, the survey (i.e. S1 to S8) and their interaction on dune wavelength, by considering a random effect of the transects. The model was fit using the R package lme4 (Bates et al., 2015).

For each dune, the maximum height, the maximum width and the maximum sinuosity among all transects were calculated for each survey. The difference between dunes was tested for these parameters using a non-parametric one-way analysis of variance, since assumptions of normality and homoscedasticity of data were not verified. A post hoc pairwise Wilcoxon rank sum test with Bonferroni correction was then performed to compare differences between pairs of dunes.

STATIS method is a multidimensional factorial analysis adapted for 3D datasets (variables*sites*dates) which cannot be explored by principal component analysis (PCA). It proceeds in three steps which allows us to focus the analysis at different temporal and spatial scales. The interstructure step realizes a classification of 2D tables (variables*samples). The compromise step performes a PCA to all 2D tables weighted by their contribution to the total variance. The intrastructure computes a PCA to every 2D table (variables*sites or dates) and plots the results in the compromise factorial plane to allow us the comparison of all factorial planes (Fournier et al., 2009).

4 RESULTS AND DISCUSSION

4.1. Meteo-marine scenarios

Over the entire study period, 174 wind events greater than 50 km/h and 145 days of cumulative duration of these events were recorded (Fig. 3).

During the 7 periods studied (S1_S2 to S7_S8), the wind conditions were variable (Fig. 3-a). Three scenarios can be distinguished according to the proportion of strong winds coming from the South-West and North-East sectors: 90% of the winds coming from the South-West sector (period S1_S2), 100% of North-East winds (S2_S3, S7_S8), and more variable winds, coming for 55-70% from the South-West and for 30% from the North-East (S3_S4, S4_S5, S5_S6, S6_S7). The periods S1_S2, followed by S4_S5, S6_S7 and S5_S6 periods, display high values of the wind index (number of events x cumulative duration of events) indicating a strong influence of wind conditions. Considering tidal conditions (Fig. 3-b), periods L1_L2, L2_L3, L4_L5 and L6_L7 are concerned with spring conditions for more than 10% of the time period duration (up to 18% for L2_L3).

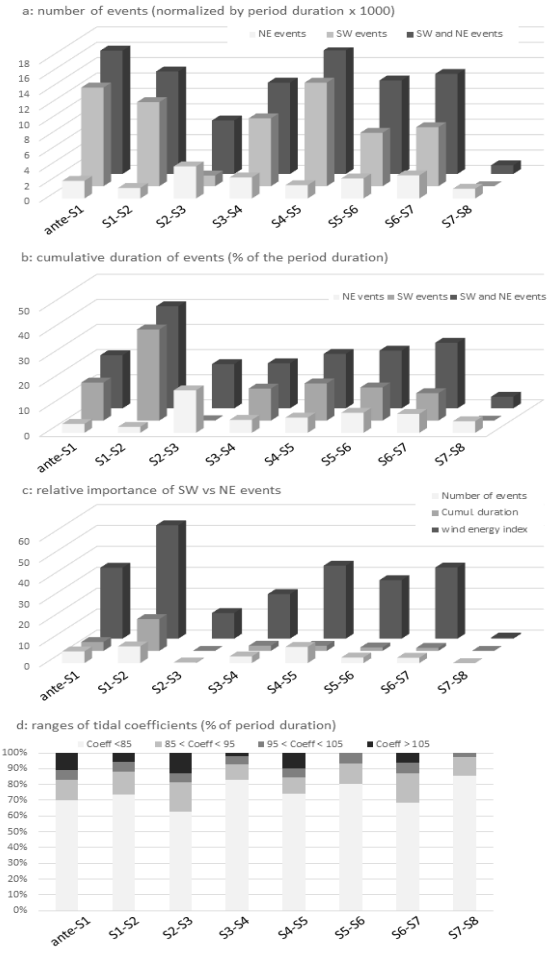

Figure 3. Tide and wind conditions during the 7 studied time-periods (S1_S1 to S7_S8). a: winds from SW and NE sectors per period: number of events, cumulative event duration and wind index (number of events x cumulative duration of events). b: tidal coefficient (>95 for spring tides).

In summary, the periods L1_L2, L4_L5 and L6_L7 display the most energetic hydrodynamic conditions, with preponderant SO winds for L1_L2 but variable wind directions for L4_L5 and L6_L7. The L2_L3 period is concerned with moderate energetic conditions, but winds come exclusively from NE sector.

4.2. Dune morphology

The bedforms observed on the seabed of the stud area are medium to very large dunes, named D1 to D6. They are oriented North-South, perpendicular to tidal currents, with crests around 14.1-14.5 m water depth. Their mean heights and wavelengths are between 1 and 3 m and 84 and 232 m respectively (Table 1). A significant relationship is found between dune height and wavelength (not observed with water depth) displaying a very low mean height/wavelength ratio of 0.012 (0.007 to 0.019) indicating dune equilibrium is not reached probably due to important wave effects and suspension increase (e.g. Ernsten et al., 2006; Tonnon et al., 2007):

$$H = 0{,}0137\lambda^{0{,}9088} \ (R^2=0{,}66) \qquad (5)$$

Table 1. Dune morphometric parameters, migration rates and associated sediment fluxes ("dune tracking" approach).

Parameters	Symbols	Mean or s.d.	D1	D2	D3	D4	D5	D6
Wavelength	λmean (m)	mean	164,61	216,1	232,92	164,32	120,77	84,65
		s.d.	8,02	6,04	5,76	4,34	4,62	10,16
Height	Hmax (m)	mean	2,96	2,93	2,32	1,45	1,19	1,03
		s.d.	0,08	0,16	0,11	0,13	0,16	0,19
Width	Lmax (m)	mean	241,83	275,96	187,61	169,49	145,16	73,67
		s.d.	80,07	23,18	26,64	9,66	8,06	8,97
Asymmmetry index	Ia	mean	0,32	0,52	0,26	0,22	0,31	0,58
		s.d.	0,03	0,02	0,02	0,04	0,16	0,07
Sinuosity index	Is	mean	0,82	0,77	0,87	0,87	0,88	0,86
		s.d.	0,06	0,05	0,05	0,08	0,05	0,1
Crest water depth	Zc (m)	mean	-14,52	-14,38	-14,39	-14,12	-14,45	-14,54
		s.d.	0,16	0,08	0,11	0,11	0,09	0,19
Migration rate	c (m/yr)	mean	25,94	37,2	31,99	20,57	23,69	31,63
		s.d.	18,59	11,69	12,75	34,68	33,65	22,7
Sediment flux	Q (t/m/yr)	mean	44,65	36,72	23,84	18,57	23,29	18,22
		s.d.	33,2	12,04	8,59	28,31	33,51	13,8

Smaller superimposed dunes are present with heights and wavelengths around 0.4-0.5 m and 10 m respectively, which have been retrieved from DEMs by pass-band filtering to focus on the primary bedforms. The primary dunes are slightly sinuous (sinuosity index values between 0.77 and 0.82), although D1 and D2 are clearly barkhan-type dunes with higher sinuosity indexes, indicative of stronger currents (e.g. Venditti et al., 2005). The dune asymmetry is important (asymmetry index between 0.22 and 0.58) with a permanent East polarity (Table 1).

A spatio-temporal variability of morphometric parameters was observed within and between dunes. The model showed a strong intra-dune variability, i.e. between sampled transects (Fig. 4-a). The mean wavelength varied significantly between dunes ($p < 0.05$) but not between surveys ($p > 0.05$). However, it did not vary significantly in the way between surveys on each dune ($p < 0.05$; Fig. 4-b). The smallest dunes (D4 to D6) seemed to show higher temporal variability in wavelength between surveys.

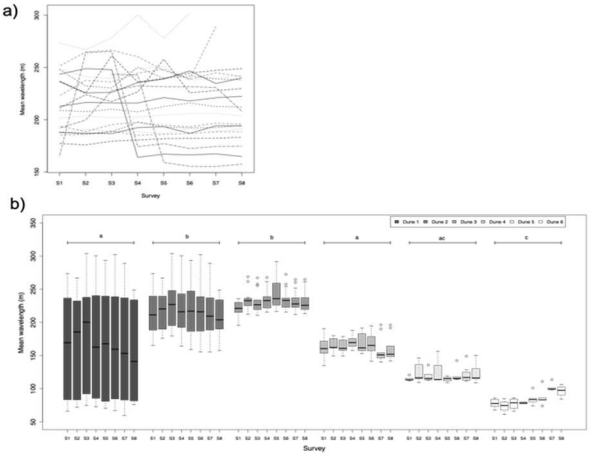

Figure 4. Spatio-temporal variability in dune wavelength highlighted by: a) an example of spatial variability measured along the 20-m spaced transects perpendicular to dune 2 (D2) during a survey, and b) the spatial and temporal variability between dunes and surveys together.

Over the study period, maximum height and maximum width varied significantly between dunes (Fig. 5-a,b respectively; Kruskal-Wallis tests: $\chi^2 = 42.60$, df = 5, $p = 4.46.10^{-8}$ and $\chi^2 = 35.82$, df = 5, $p = 1.03.10^{-6}$, respectively), as observed for height by Ernsten et al., 2006 over a semi-diurnal tidal cycle. Dunes are distributed according to a spatial West-East gradient, with the highest and largest dunes at the West (i.e. D1 to D3) and the smallest at the East (i.e. D4 to D6).

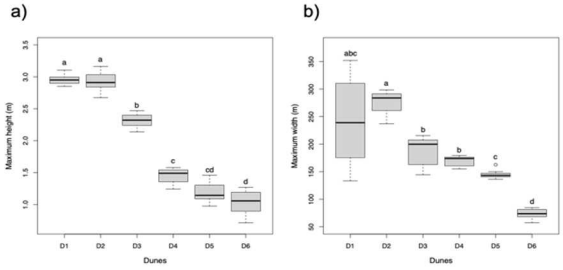

Figure 5. Comparison of maximum height (a) and maximum width (b) between dunes.

Only the dune D2 showed significantly a smaller maximum sinuosity index (Kruskal-Wallis tests: $\chi^2 = 13.47$, df = 5, p = 0.02).

4.3. Dune migration rates

At the scale of the whole studied time-period, the six dunes migrate toward the east with rates of the same order of magnitude, comprised between 20.57 m/yr (s.d. 34.68) and 37.20 m/yr (s.d. 11.69) (Table 1).These rates are similar to ones observed for dunes in the Dover Strait, some tens of kilometres away (Le Bot et al., 2000).

The six dunes display important migration rates towards the East during L1_L2, L4_L5 and L6_L7. During L2_L3 and L7_L8, migration decreases towards the East, even reverses towards the West (e.g. the smallest dunes D3, D4 and D5).

4.4. Dune associated sedimentary fluxes

- "Dune tracking" approach:

At the scale of the whole time-period, mean sediment fluxes are of the same order of magnitude for the 6 dunes, comprised between 18,22 ± 13,80 et 44,65 ± 33,20 t/m/yr and oriented towards the East (Table 1). The fluxes are higher for the largest dunes.

The 6 dunes display consistently the same time-evolution as the migration rates, in intensity and direction (see 4.3.2). This result was attended since the "Dune tracking" method is based on dune migration and morphology.

- Empirical approach:

First, the similar values obtained for sediment fluxes during L2_L3 (period with strong NE winds) with both methods ("Dune tracking", empirical formulas) attest the consistency of the values, and, as fact, allow a validation of the values of sediment fluxes obtained for the 6 other time-periods (Table 2). Second, the data extracted from MARS3D and WWIII models show that, in these strong NE wind conditions, the flood period is dominant with a ratio between ebb and flood peaks varying between 0.5 for strong tides (end of L2-L3 period) and 0.8 for weak tides (beginning of L2-L3 period) (Fig 6-a). The free-surface elevation data, also shows that the flood peak is synchronized with the high tide while the ebb peak is synchronized with the low tide. The waves extracted from the WWIII model are consistent with the strong wind conditions coming from the North-East.

Table 2. Synthesis of the sediment fluxes (t/m/yr) estimated using the « Dune Tracking »method and an empirical approach over L2-L3 period. +/–: East/West direction of the sediment fluxes, respectively. D1 to D6 correspond to the 6 dunes.

	« Dune tracking » approach						*Empirical approach*		
	D1	*D2*	*D3*	*D4*	*D5*	*D6*	*Yalin adapted (1963)*	*Van Rijn (1984)*	*Wu et al. (2000)*
Sediment fluxes	*-15,91*	*41,49*	*22,38*	*-29,77*	*-16,50*	*-2,73*	*-25.98*	*-21.85*	*-9.86*

The results show that the fluxes strongly depend on the waves (e.g. maximum fluxes over the 27/03-30/03 period and the 14/04 where significant wave height is respectively 2.0 and 1.5m; Fig. 6-b,c), even if the flux maximums are not synchronized with the significant wave height maximums but moreover with the low tide.

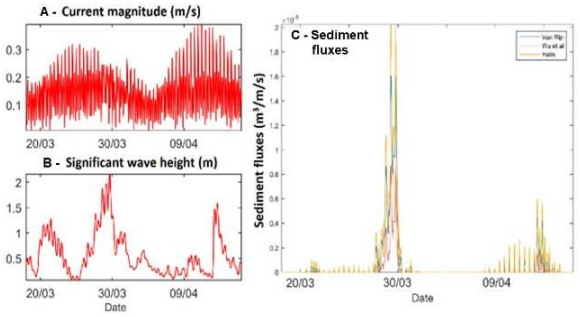

Figure 6. Realistic hydrodynamic conditions extracted from MARS3D and WW3 simulations over the L2-L3 period. Instantaneous sediment fluxes estimated using Yalin adapted (1963), Van Rijn (1984) and Wu et al. (2000) formulations.

In comparison, the current does not have a significant influence on these fluxes, except during the strong tides (and strong tidal current asymmetry) around the 11/04. Consequently, sediment flux is stronger during low tide and then more sediment is transported by currents on ebb period, bringing an explanation for the inversion of the migration direction.

4.5. Interrelations between dune morphodynamic parameters and forcings

The different parameters (dune morphology and migration rate, sediment fluxes, meteo-marine forcings) have been jointly analysed thanks to a STATIS analysis to inspect the correlations in-between in order to evaluate the spatio-temporal variability of dunes morphodynamics in relation with meteo-marine forcings.

The temporal analysis reveals a very strong interstructure since the 1st factorial plan gathers 93% of the variance with a strong correlation between 2D time tables defined by Rho Vectorial coefficients (a multivariate generalization for matrix of the squared Pearson correlation coefficient) [0.74-0.95], and is mainly carried by the D3 and D1 dunes. This F1 axis in compromise factorial plan accounts for the transverse morphology of the dunes (Fig. 7-a-1), with dunes of smaller dimensions and greater asymmetry for strong SW wind regimes and which present larger migration rates and associated sediment fluxes. The F2 axis indicates that the dunes are more sinuous for conditions of strong tidal currents and a regime of strong NE winds (Fig. 7-a-1).

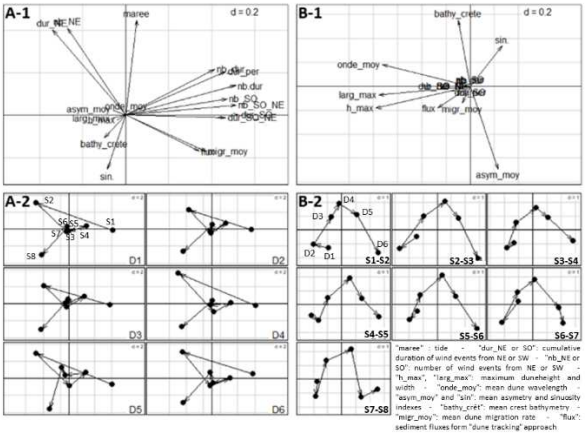

Figure 7. STATIS results in compromise (A1-B1) and intrastructure (A2-B2) factorial planes for temporal (A1-A2) and spatial (B1-B2) analyses.

Overall, the intrastructure still shows the same evolution trajectory of the characteristics of the dunes over time (Fig. 7-a-2). Distinct behaviors of all the dunes can be identified according to the periods, and confirm the 3 scenarios identified in 4.1.: the F1 axis distinguishes the period of strong and frequent SW winds (L1_L2; right part), the 2 periods of NE winds (L2_L3 and L7_L8; left part) and periods of more variable strong winds (L3_L4 to L6_L7; central position).

The spatial analysis reveals a strong, interstructure (but weaker than the temporal) with 85% of variance with lower correlations between 2D space tables defined by RV coefficients [0.56-0.92] carried by the 1st factorial axis, indicating that a large part of the variations in the morphodynamic characteristics of the dunes remains common. The rate of dune migration, sedimentary fluxes and meteo-marine forcings contribute very little to the inter-dune variability, which is mainly expressed at the level of morphology (Fig. 7-b-1). Overall, the infrastructure always shows the same trajectory whatever the period, with a passage from quadrant F1-/F2- to middle F1/F2+ then F1+/F2- from dune D1 to dune D6, supporting the existence of a West-East spatial morphological gradient (Fig. 7-b-2). We can distinguish 3 groups of dunes (D1 on one hand and D2, D4, D6 on the other hand) significantly different from a morphological point of view, while the dunes D3 and D5 present fluctuating similarities with one or another group.

5 CONCLUSION

In the framework of the wind turbine project off Dunkirk, a dune field has been monitored at a plurimonthly scale during 20 months to analyse dune morphology, migration and associated sediment fluxes in relation with meteo-marine forcings.

The main results indicate: (i) a West-East spatial morphological gradient within the dune field with, to the West, largest, more sinuous dunes with higher migration rates and sediment fluxes, suggesting an hydraulic attenuation along the dune field from West to East, in the direction of the main residual current, (ii) a similar dune response in terms of migration and sediment fluxes to meteo-marine scenarios, while the dune morphological parameters can evolve

according to various trends, suggesting reorganization of sedimentary volumes within the dunes, (iii) a strong intra-dune and an weak interdune variability for some morphological parameters (e.g. height, width, wavelength), and (iv) reversal of some dunes when strong NE winds oppose the tidal residual and induce strong sediment fluxes toward the West, due to a main wave action at low tide during ebb phase, inversing the sediment transport in the West direction.

Some recommendations can be drawn up concerning the monitoring of dune fields in offshore wind farms. The spatio-temporal variability of dune morphodynamics at a plurimonthly time-scale suggests to conduct bathymetric surveys on the whole dune field and also on the whole individual dune shapes. The relations with meteo-marine forcings indicate that surveys are required : (i) at a pluri-monthly time-scale, and (ii) in particular, after the winter stormy period and after periods whith strong SO and NE winds.

6 ACKNOWLEDGEMENT

This work was conducted in the framework of the DUNES project (France Energies Marines-French State, Agence Nationale de la Recherche, PIA, ANR 10 IEED 0006 33).

7 REFERENCES

Bates D., Mächler M., Bolker B., Walker S. 2015. Fitting Linear Mixed-Effects Models Using lme4. J. Stat. Soft. 67(1), 1–48

Blanpain, O. 2009. Dynamique sédimentaire multiclasse : de l'étude des processus à la modélisation en Manche. Thèse de doctorat, Université de Rouen, 315 pp

Boudière, E., Maisondieu, C., Harduin, F., Accensi, M., Pineau-Guillou, L., Lepesqueur, J. 2013. A suitable metocea hindcast database for the design of marine energy converters. Int. J. Mar. Energy 3-4, e40-e52

Campmans, G.H.P., Roos, P.C., Vriend, H.J., Hulscher, S.J.M.H. 2018. The Influence of Storms on Sand Wave Evolution: A Nonlinear Idealized Modeling Approach. J. Geophys. Res. Earth Surf. 123, 2070–2086

Carter, L., Gavey, R., Talling, P.J., Liu, J.T., 2014. Insights into Submarine Geohazards from Breaks in Subsea Telecommunication Cables. Oceanography 27 (2), 58-67

Couldrey, A.J., Benson, T., Knaapen, M.A.F., Marten, K.V., Whitehouse, R.J.S., 2020. Morphological evolution of a barchan dune migrating past an offshore wind farm foundation. Earth Surf. Proc. Landf. 54(12), 2745-3068

Ernstsen, V.B., Noormets, R., Winter, C., Hebbeln, D., Bartholomä, A., Flemming, B.W., Bartholdy, J. 2006. Quantification of dune dynamics during a tidal cycle in an inlet channel of the Danish Wadden Sea. Geo-Mar. Lett. 26, 151-163

Fournier, M., Motelay-Massei, A., Massei, N., Aubert, M., Bakalowicz, M., Dupont, J.P. 2009. Investigation of Transport Processes inside Karst Aquifer by Means of STATIS. Groundwater 47, 391-400

Latapy, A., Héquette, A., Pouvreau, N., Weber, N.Robin-Chanteloup, J.B. 2019. Mesoscale morphological changes of nearshore sand banks since the early 19th century, and their influence on coastal dynamics, Northern France. J. Mar. Sci. Eng. 7, 73.

Le Bot, S., Trentesaux, A., Garlan, T., Berné, S., Chamley, H. 2000. Influence des tempêtes sur la mobilité des dunes tidales dans le détroit du Pas-de-Calais. Ocean. Acta, 23, 129–141

R Core Team 2022. R: A language and environment for statistical computing. Version 4.2.0. R Foundation for Statistical Computing, Vienna, Austria. URL https://www.R-project.org/

Robert, A.E., Quillien, N., Bacha, M., Caulle, C., Nexer, M., Parent, B., Garlan, T., Desroy, N. 2021. Sediment migrations drive the dynamic of macrobenthic ecosystems in subtidal sandy bedforms. Mar. Poll. Bull. 171, 11269.

Schmitt, T., Mitchell, N.C. 2014. Dune-associated sand fluxes at the nearshore termination of a banner sand bank (Helwick Sands, Bristol Channel). Cont. Shelf Res. 76, 64-74

Tonnon, P.K., Van Rijn, L.C., Walstra, D.J.R., 2007. The morphodynamic modelling of tidal sand waves on the shoreface. Coastal Engineering, 54, 279-296.

van Rijn L.C., 1984. Sediment transport, part I: bed load transport. J. Hydraul. Eng., 110(10), 1431-1456.

Venditti, J., Church, M., Bennett, S., 2005. On the transition between 2D and 3D dunes. Sedimentology. 52. 1343 – 1359

Wu, W., Wang, S. S. Y., Jia, Y., 2000. Non uniform sediment transport in alluvial rivers. J. Hydr. Res., 38, 427 - 434.

Yalin, M. S., 1963. An expression for bedload transportation. J. Hydr. Division Am. Soc. Civ. Engi., 90, 105 - 119.

What is a dune?
Towards a homogenisation of the nomenclature of bedforms

A. Lefebvre *MARUM - University of Bremen, Bremen, Germany – alefebvre@marum.de*
R. Bernhard *MARUM & Faculty of Geosciences - University of Bremen, Bremen, Germany*
L. Scheiber *Ludwig-Franzius-Institute for Hydraulics, Estuarine and Coastal Engineering, Leibniz University Hannover, Hannover, Germany*
E. Miramontes *MARUM & Faculty of Geosciences - University of Bremen, Bremen, Germany*

ABSTRACT: Despite a workshop and recommendations published 30 years ago on the nomenclature and description of large flow-transverse bedforms, many terms are still in use. It is uncertain whether these names are used because of intrinsic differences between bedform types (e.g. river dunes, marine sand waves, sediment waves) or for other reasons. We would like to have an open discussion about this topic. We are conducting a literature survey to provide a comprehensive basis of the current terms used. We will invite MARID participants to share their thoughts and ideas about the subject and conduct an online survey to reach the wider community. To facilitate the discussion, we propose a preliminary classification.

1 INTRODUCTION

In 1990, Gail M. Ashley published a manuscript entitled “Classification of large-scale subaqueous bedforms: a new look at an old problem”. She reported on a symposium conducted in Texas three years earlier, during which the nomenclature of large-scale subaqueous flow-transverse bedforms was discussed by 27 researchers. The symposium panel (consisting of 19 participants) proposed to name all large-scale subaqueous bedforms “dunes” instead of the variety of terms used until then (e.g. megaripples, dunes, sand waves, etc.). They also provided a set of primary and secondary descriptors to describe dune properties (Table 1).

Despite the recommendations given in Ashley (1990), a plethora of terms continues to be used to describe large-scale flow-transverse bedforms, often without clear definition or distinction between the different nomenclature. For example, (marine) dunes and sand waves are used interchangeably in many contexts. Smaller bedforms superimposed on larger ones may be referred to as megaripples or secondary dunes. It is currently unclear if different terms are used due to intrinsic differences between bedform types, or if it is due to the different scientific communities. Ashley (1990) already noted that the “poor communication among scientists and engineers has perpetuated the multiplicity of terms”. Researchers from fluvial, coastal or deep marine environments, from industry or academia, from various disciplines, such as sedimentology, oceanography, coastal and offshore engineering or geomorphology may use a specific vocabulary. Furthermore, terminology may be different depending on the country or working group in which they work.

We therefore feel the need to bring together researchers working on as many environments and disciplines as possible to discuss and define the different types of flow-transverse bedforms. Everyone is invited to participate in the discussion and bring their own expertise and views. On this basis, we aim to produce an updated and extended classification scheme.

Table 1: Classification scheme recommended by the SEPM Bedforms and Bedding Structures Research Symposium (Ashley, 1990)

Subaqueous Dunes				
First Order Descriptions (necessary)				
Size: Spacing =	small 0.6-5 m	medium 5-10 m	large 10-100 m	very large > 100m
Height* =	0.075-0.4 m	0.4-0.75 m	0.75-5m	> 5 m
Shape: 2-Dimensionnal 3-Dimensionnal				
Second Order Descriptors (important) - Superposition: simple or compound (sizes and relative orientation) - Sediment characteristics (size, sorting)				
Third Order Descriptors (useful) - Bedform profile (stoss and lee slope lengths and angles) - Fullbeddedness (fraction of bed covered by bedforms) - Flow structure (time-velocity characteristics) - Relative strength of opposite flows - Dune behaviour-migration history (vertical and horizontal accretion)				

*Height calculated using the equation $H = 0.0677\ L^{0.8098}$ (Flemming, 1988)

2 METHODS

2.1 Literature survey

A survey of the scientific literature related to large-scale flow transverse bedform is done to identify some common definitions and specific names, possibly depending on the communities. Some of the characteristics which are identified for each paper include: bedform type (e.g. number of times the terms “dune”, “sand wave”, “megaripple”, “sediment wave”, “bedform”, etc. are used), author affiliation, environment in which the bedforms are found (e.g. flume, river, tidal inlet, continental shelf, continental slope, deep environment, etc.), the processes forming the bedforms (e.g. river flow, tidal currents, bottom currents, internal waves, etc.), bedform characteristics (height, length, migration rate, presence of secondary bedform, etc.) and other relevant information (e.g. water depth, sediment type, etc.).

The database will be analysed to assess if there is a nomenclature dominantly used depending on e.g., environment or affiliation. It can serve as a basis for the discussion by providing a comprehensive and detailed depiction of the many names still used for flow-transverse bedforms, and by whom they are used.

The database will be made publicly available for researchers to use and further develop it.

2.2 Discussion during MARID

During the conference, we would like to invite interested scientists to share with us their ideas and thoughts.

2.3 Community survey

A survey will be carried out after MARID VII in order to get some quantitative and qualitative information. This survey will be widely distributed in order to provide the opportunity for as many scientists as possible (also those who were not at MARID) to share their views on the subject.

3 DISCUSSION POINTS

In this section, we address the three topics which were raised by Ashley (1990). We provide an update about these topics in view of the recent literature and suggest discussion points. Preliminary results of the literature survey are given and a classification scheme is suggested in order to foster a lively conversation between the participants.

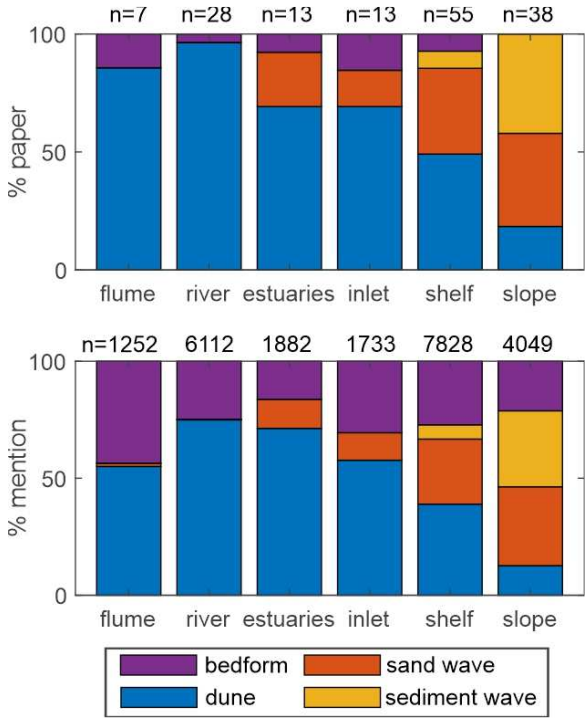

Figure 1. Preliminary results of the literature survey. Upper panel: percentage of papers depending on main bedform type and environment; lower panel: percentage of mention of bedform type for all the papers in each environment. n refers to the total number of papers or mention for the specific environment

3.1 Types of flow transverse bedforms

Ashley (1990) stated that "1) all large flow-transverse bedforms are a similar phenomena; the morphologic variety reflects the response to channelization, fluctuating water level, speed, and direction; 2) large bedforms occur as a continuum of sizes, not as discrete groups; and (3) large bedforms should be given one name rather than be split into classes."

The workshop participants managed to agree on the term "dune" and Ashley (1990) recommended using this term for future communication. However, until now, there is still a variety of terms used to describe large flow transverse bedforms, as our literature survey illustrates (Figure 1). In laboratory and fluvial environments, only the terms "dune" and "bedform" are used. However, in marine environments, "sand wave" and "sediment wave" are also used, more and more as the environment gets deeper.

The literature survey highlights some developments which happened since the publication of Ashley (1990). The use of multibeam echosounder surveys has made high-resolution mapping possible for large portions of the seabed. Bedforms have now been identified in many regions of the world which previously could not be mapped accurately, including on the continental shelf, slope and abyssal plain. These bedforms have been named dunes, cyclic steps, sediment waves, or more precisely mud waves, sand waves or gravel waves, if the sediment in which they form is known.

The main question which we need to answer as a community: is there a physical difference between bedform types from varied environments?

Ashley (1990) recognised three environments with different settings: rivers, sandy coastal embayments and continental shelves. For the literature review, we divided the environments into 6 categories: (1) flume with unidirectional flows, very low water depth (typically less than 50 cm) and relatively high Froude numbers (typically 0.3-0.6); (2) rivers with channelized unidirectional flow, and a wide range of grain sizes and hydrologic characteristics; (3) estuaries with channelized flow, tidally-varying currents (either with a full flow reversal, but sometimes with flow variations without reversal), seasonal river flow variations and possible influence of estuarine circulation; (4) tidal inlets, with channelized flow and tidally reversing currents; (5) continental shelf, with relatively deep, unchannelized flow, with the influence of tidal currents, wind and wave-generated currents and bottom currents; and (6) slope with the influence of internal tides and waves, along-slope bottom currents and turbidity flows.

Considering the wide variety of sediment types, water depths and hydrodynamics in these environments, we are questioning if

there is an intrinsic difference between river, tidal and marine shallow and deep-water bedforms. Is there a continuum of bedforms or can separate entities be defined since the driving hydrodynamic forcings creating them, their morphology, interaction with the flow and internal structure are different?

In order to determine the different bedform types and their properties, we suggest some points to discuss:

(1) **Origin.** Bedforms generally develop as the flow transports and deposits sediment. Research about the origin and growth of bedforms has been carried out in laboratory settings with unidirectional flow and waves, and with numerical simulations on unidirectional and reversing flows (tidal currents and waves). Against this background, the question can be asked: does bedform formation vary depending on the hydrodynamics (unidirectional currents, tidal currents, wind waves, internal waves, etc.) and sedimentological properties (e.g. muddy, sandy and gravelly sediment)?

(2) **Interaction with the water surface and link between water depth and bedform size.** In river environments, dunes are often opposed to ripples. River dunes are defined as bedforms which interact with the water surface and whose size is controlled by water depth (Bradley and Venditti, 2017). Ripples are small elements that do not interact with the water surface and with sizes controlled by sediment grain size and water depth (Venditti, 2013). Bedforms found on the continental shelf can be very large (up to > 30 m in height, (Franzetti et al., 2013)) but are often relatively small compared to the water depth and are therefore unlikely to interact with the water surface. Their height may also not be controlled by water depth but, at least some cases, depth controls their steepness (Damen et al., 2018). Therefore, we can wonder if river and marine bedforms are different bedform types based on their interaction with the water surface and depth.

(3) **Bedform morphology and influence on hydrodynamics.** Hulscher and Dohmen-Janssen (2005) made a distinction between river dunes and marine sand waves. They first noted their similarities, especially their large spatial scales compared to the water depth, which differentiate them from ripples and megaripples. They then highlighted their difference: marine sand waves were defined as sinusoidal-like bed features, quite symmetric with small temporal variations (migration speed and amplitude) compared to river dunes; and river dunes are described as asymmetric, often with flow separation, migrating fast, and being more pronounced during river floods than during low river discharge. Since then, however, it has been demonstrated that bedforms in large rivers have low to intermediate lee side angles (Cisneros et al., 2020). They are therefore not as steep as angle-of-repose bedforms which typically form in shallow water (e.g. flumes) and are unlikely to produce a permanent flow separation. Therefore, we can ask: is flow above marine bedforms significantly different from flow above river dunes? Obviously, flow in tidal environments reverses, so there will be noticeable differences. But, if we think about the time during which flow is going in one direction, is there some differences due to bedform morphology? Venditti (2013) noted that ripples are generally steeper than dunes, but with an overlap suggesting that larger aspect ratios (height / length) are not a mutually exclusive property of either ripples or dunes. Until now, there has not been a systematic study of the steepness of marine bedforms which would help in assessing the variability of their slopes and clarify if there is a notable difference between river and marine bedform slope/steepness.

(4) **Internal structure**. Bedform stratification and their deposits are important for interpreting past flow conditions and environments. Differences can be recognised between small-scale cross-laminations created by ripples and large-scale cross-bedded sequences created by dunes, but also between bedforms formed in rivers and tidal environments, as well as depending on

bedform morphology, notably three-dimensionality and bedform superposition (Dalrymple and Rhodes, 1995). Wynn and Masson (2008) described sediment waves as very large depositional features (length of several km, height up to 50 m) formed by bottom currents with poorly developed laminae and intense bioturbation resulting from steady quasi-continuous sedimentation. Cartigny et al. (2011) proposed a classification of sediment waves into dunes, antidunes and cyclic steps based on their morphology, stratigraphy and migration. Dunes develop at Froude number < 1, migrate downslope, and have an internal structure showing some lee-side cross-bedding. Anti-dunes form at Froude number between 1 and 2, can be migrating down or upslope, and their internal structure is not well known. Cyclic steps, created by turbidity currents, form at very high Froude numbers (>2), are migrating upslope, and their internal structure shows parallel or cross bedding from their stoss sides. Based on this description of bedforms, it seems that their internal structure could help in differentiating some bedform types.

(5) **Continuum in environments.** Until now, we treated the different environments, and especially river and marine, as separate and distinct environments. However, there are transition zones between rivers and oceans, namely estuaries, in which numerous bedforms are found. The hydrodynamics, sedimentological inventory and water depth characteristics are intermediary between fluvial and marine settings. Furthermore, the marine environment also presents a variety of hydrodynamic forcings and sedimentary properties. Therefore, there is not just one type of "marine bedforms" but a variety of them, such as for example, the large fields of bedforms controlled by tidal influence on the Dutch continental shelf (Damen et al., 2018), coarse-grained bedforms in the tidally-dominated Irish Sea (Van Landeghem et al., 2009), deep-water bedforms formed by bottom currents on drowned isolated carbonate terraces (Miramontes et al., 2019) or very large bedforms on the upper continental slope generated by episodic internal waves (Reeder et al., 2011).

We repeat here the first questions asked by Ashley (1990) "do all large-scale bedforms relate to the same hydrodynamic phenomenon, and do they occur in a continuum of sizes or as discrete groups? If they are all related, is there a single acceptable term?" We propose a tentative classification (Figure 2) which we are happy to discuss. This classification defines "dunes" following Ashley (1990) as all the large-flow transverse bedforms found in fluvial, estuarine and marine environments, with the precision that they show cross-bedded stratigraphy. This distinguishes them from ripples, which are small in size, from sediment waves, which are much larger, form in muddy sediment and show laminar stratigraphy, and anti-dunes or cyclic steps, which form at very high Froude numbers. We also recognise a number of different types of dunes (Figure 2, not all are represented here).

3.2 Bedform superimposition

Ashley (1990) asked "what is the significance of bedform superposition?". First, we note that since 1990, the word 'superimposed' has been used more frequently than 'superposed'. The definitions given by Oxford Languages are as follow: (1) Superposed: placed on or above something else, especially so that both things coincide; (2) Superimposed: placed or laid over something else, typically so that both things are still evident. Since both definitions are roughly equivalent and superimposed is the term predominantly used in recent publications, we will keep on using it here.

The question that was discussed in 1987 and can still be discussed is: are superimposed bedforms inherently different from large primary bedforms in terms of flow and sediment transport? The panel concluded that superimposition "appears to be a function of available space and time for growth and migration and reflects complexity of conditions rather than fundamental

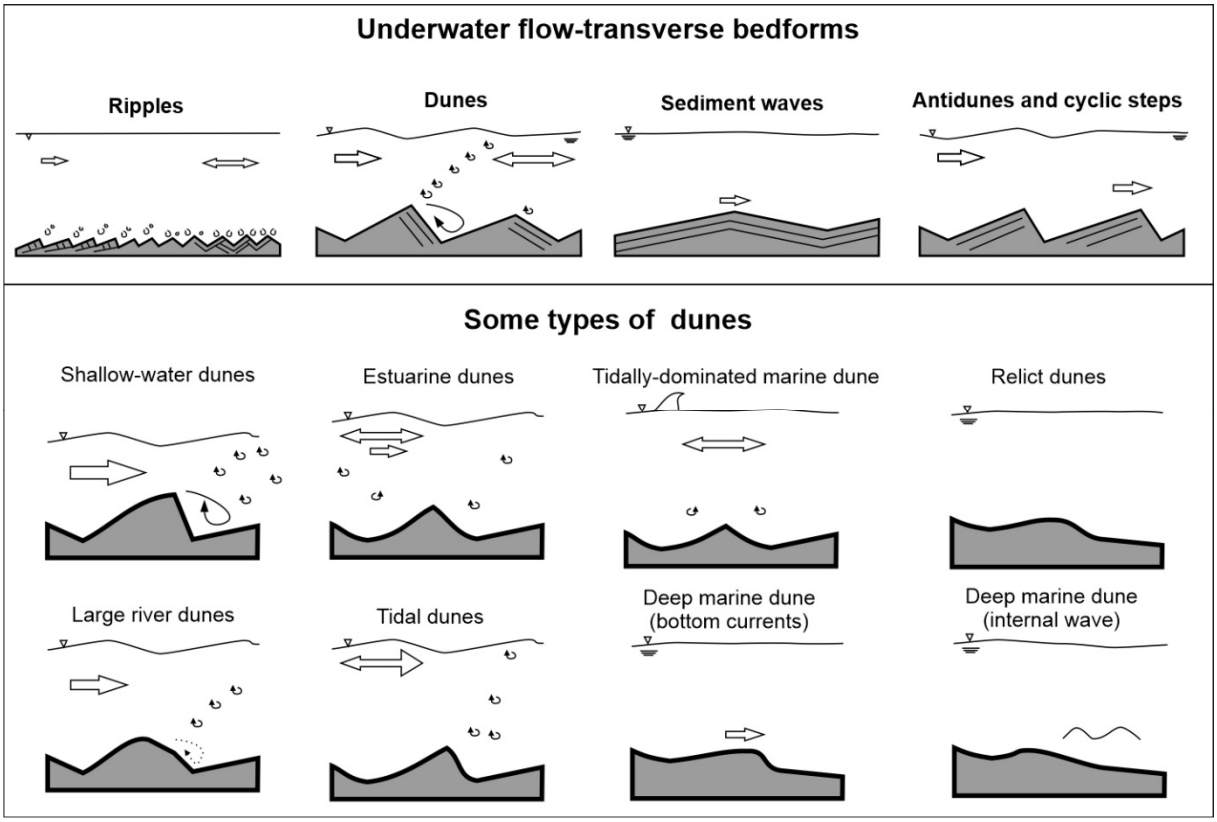

Figure 2. Top: at least 4 types of flow-transverse bedforms are recognised and differentiated based on their origin, interaction with the flow, their morphology and their stratigraphy. Bottom: examples of dune types

processes of bedform genesis". They suggested that bedform superimposition should be kept as second-order descriptor (simple or compound bedforms) rather than a classification term.

However, superimposed bedforms are still called by a variety of terms, such as "sand waves" (Venditti et al., 2005), "superimposed dunes" (Ernstsen et al., 2006), megaripples (Bellec et al., 2019) or simply "secondary bedforms" (Zomer et al., 2021). Using superimposition or bedform size as a classifying parameter implies that there is a fundamental difference between large simple bedforms and superimposed or compound forms.

3.3 Descriptors

The third discussion point of Ashley (1990) concerned the descriptors of bedform morphology and behaviour. These descriptors were chosen to be hydraulically significant in order to provide a link between internal structure, morphology and the flow that created the bedforms. They should improve communication amongst scientists working on bedforms or their deposits.

Following the progress of bedform research during the last 30 years, we believe that the descriptors given by Ashley (1990) (Table 1) can be updated to better consider the relevant bedform parameters. For example, the definition of "bedform profile" can be made more precise by including some information such as the mean and maximum lee side angles, as well as the position of the maximum angle. The anthropogenic activities (e.g. dredging) should also be detailed, as they may have a strong impact on dune characteristics.

Table 2: Some descriptive parameters of underwater dunes

Morphology	
Size[1]	Small: L=0.6-5 m Medium: L= 5-10 m Large: L= 10-100 m Very large L= > 100m
3D organisation[2] and fullbeddedness[1]	Isolated, field, on a bank; fraction of bed covered by bedforms
Three-dimensionality	Non-dimensional span, bifurcation index, morphological type[2] (barchans, rhomboidal, trochoidal, transverse)
2D shape[3,4]	Asymmetry, stoss and lee slope lengths and mean angles, value and position of maximum angle
Hierarchy	Simple or compound, primary or secondary
Environment	
Water depth	Total water depth and relative bedform height
Anthropogenic impact	Dredging activities, offshore construction
Sedimentology	
Sediment characteristics	Size, sorting, skewness
Stratigraphy	Internal structure
Hydrodynamics	
Main hydrodynamics	River discharge, tidal flow, waves, internal waves
Flow structure	Velocity and turbulence characteristics
Flow variation	In time and/or space
If tidal flow	Relative strength of opposite flows
Biological activity	
Biota and fish	Distribution
Dynamics	
Dune behaviour	Migration history and rates

[1] Ashley (1990)
[2] Garlan et al. (2016)
[3] Cisneros et al (2021)
[4] Lefebvre et al. (2021)

We also question the structure of the descriptive parameters (first, second and third order parameters). It seems to us that the descriptors, and especially their ranking, was done from a sedimentological point of view, with the descriptor orders reflecting the important parameters which are going to influence bedform deposit. Considering the range of scientists studying bedforms and the variety of applications, the focus on bedform deposit can be questioned. Therefore, we think there might not be a need for classification between different order descriptors, but with other parameters such as morphology, environment, sedimentology, hydrodynamics, biological activity and dynamics (Table 2).

4 CONCLUSIONS

Despite the recommendation on the nomenclature of large flow-transverse bedforms given over 30 years ago, a variety of terms are currently in use. We propose to discuss and clarify the classification of large flow-transverse bedforms.

5 ACKNOWLEDGEMENT

Alice Lefebvre is funded through funded through the Cluster of Excellence ‘The Ocean Floor – Earth’s Uncharted Interface’.

6 REFERENCES

Ashley, G. M.: Classification of large-scale subaqueous bedforms: A new look at an old problem, J. Sediment. Res., 60, 160-172, https://doi.org/10.2110/JSR.60.160, 1990.

Bellec, V. K., Bøe, R., Bjarnadóttir, L. R., Albretsen, J., Dolan, M., Chand, S., Thorsnes, T., Jakobsen, F. W., Nixon, C., Plassen, L., Jensen, H., Baeten, N., Olsen, H., and Elvenes, S.: Sandbanks, sandwaves and megaripples on Spitsbergenbanken, Barents Sea, Mar. Geol., 416, 105998, https://doi.org/10.1016/j.margeo.2019.105998, 2019.

Bradley, R. W. and Venditti, J. G.: Reevaluating dune scaling relations, Earth-Science Reviews, 165, 356-376, https://doi.org/10.1016/j.earscirev.2016.11.004, 2017.

Cartigny, M. J. B., Postma, G., van den Berg, J. H., and Mastbergen, D. R.: A comparative study of sediment waves and cyclic steps based on geometries, internal structures and numerical modeling, Mar. Geol., 280, 40-56, https://doi.org/10.1016/j.margeo.2010.11.006, 2011.

Cisneros, J., Best, J., van Dijk, T., de Almeida, R. P., Amsler, M., Boldt, J., Freitas, B., Galeazzi, C., Huizinga, R., Ianniruberto, M., Ma, H. B., Nittrouer, J. A., Oberg, K., Orfeo, O., Parsons, D., Szupiany, R., Wang, P., and Zhang, Y. F.: Dunes in the world's big rivers are characterized by low-angle lee-side slopes and a complex shape, Nat. Geosci., 13, 156-+, https://doi.org/10.1038/s41561-019-0511-7, 2020.

Dalrymple, R. W. and Rhodes, R. N.: Chapter 13 Estuarine Dunes and Bars, in: Dev. Sedimentol., edited by: Perillo, G. M. E., Elsevier, 359-422, 1995.

Damen, J. M., van Dijk, T. A. G. P., and Hulscher, S. J. M. H.: Spatially Varying Environmental Properties Controlling Observed Sand Wave Morphology, Journal of Geophysical Research: Earth Surface, 123, https://doi.org/10.1002/2017JF004322, 2018.

Ernstsen, V. B., Noormets, R., Winter, C., Hebbeln, D., Bartholomä, A., Flemming, B. W., and Bartholdy, J.: Quantification of dune dynamics during a tidal cycle in an inlet channel of the Danish Wadden Sea, Geo-Mar. Lett., 26, 151-163, https://doi.org/10.1007/s00367-006-0026-2, 2006.

Franzetti, M., Le Roy, P., Delacourt, C., Garlan, T., Cancouët, R., Sukhovich, A., and Deschamps, A.: Giant dune morphologies and dynamics in a deep continental shelf environment: Example of the banc du four (Western Brittany, France), Mar. Geol., 346, 17-30, https://doi.org/10.1016/j.margeo.2013.07.014, 2013.

Garlan, T., Brenon, E., Marchès, E., and Blanpain, O.: From regional variability of the morphology of dunes to a new method of their classification, MARID 2016. Fifth International Conference on Marine and River Dune Dynamics, Caernarfon, United Kingdom, 4– 6 April 2016,

Hulscher, S. J. M. H. and Dohmen-Janssen, C. M.: Introduction to special section on Marine Sand Wave and River Dune Dynamics, Journal of Geophysical Research: Earth Surface, 110, https://doi.org/10.1029/2005JF000404, 2005.

Lefebvre, A., Herrling, G., Becker, M., Zorndt, A., Krämer, K., and Winter, C.: Morphology of estuarine bedforms, Weser Estuary, Germany, Earth Surf. Processes Landforms, https://doi.org/10.1002/esp.5243, 2021.

Miramontes, E., Jorry, S. J., Jouet, G., Counts, J. W., Courgeon, S., Le Roy, P., Guerin, C., and Hernández-Molina, F. J.: Deep-water dunes on drowned isolated carbonate terraces (Mozambique Channel, south-west Indian Ocean), Sedimentology, 66, 1222-1242, https://doi.org/https://doi.org/10.1111/sed.12572, 2019.

Reeder, D. B., Ma, B. B., and Yang, Y. J.: Very large subaqueous sand dunes on the upper continental slope in the South China Sea generated by episodic, shoaling deep-water internal solitary waves, Mar. Geol., 279, 12-18, https://doi.org/10.1016/j.margeo.2010.10.009, 2011.

Van Landeghem, K. J. J., Wheeler, A. J., Mitchell, N. C., and Sutton, G.: Variations in sediment wave dimensions across the tidally dominated Irish Sea, NW Europe, Mar. Geol., 263, 108-119, https://doi.org/10.1016/j.margeo.2009.04.003, 2009.

Venditti, J. G.: Bedforms in sand-bedded rivers, in: Treatise on Geomorphology, edited by: Shroder, J., and Wohl, E., Academic Press, San Diego, CA, 137-162, 10.1016/B978-0-12-374739-6.00235-9, 2013.

Venditti, J. G., Church, M., and Bennett, S. J.: Morphodynamics of small-scale superimposed sand waves over migrating dune bed forms, Water Resour. Res., 41, https://doi.org/10.1029/2004WR003461, 2005.

Wynn, R. B. and Masson, D. G.: Chapter 15 Sediment Waves and Bedforms, in: Dev. Sedimentol., edited by: Rebesco, M., and Camerlenghi, A., Elsevier, 289-300, 10.1016/S0070-4571(08)10015-2, 2008.

Zomer, J. Y., Naqshband, S., Vermeulen, B., and Hoitink, A. J. F.: Rapidly Migrating Secondary Bedforms Can Persist on the Lee of Slowly Migrating Primary River Dunes, Journal of Geophysical Research: Earth Surface, 126, e2020JF005918, https://doi.org/doi.org/10.1029/2020JF005918, 2021.

The influence of lee side shape on flow above bedforms

A. Lefebvre *MARUM - University of Bremen, Bremen, Germany – alefebvre@marum.de*
J. Cisneros *the University of Texas at Austin, Austin, USA – jcisneros1024@gmail.com*

ABSTRACT: Underwater dunes have a diversity of morphology, ranging from low to high-angle lee sides, and sharp or rounded crests. We carried out a large number of numerical simulations of flow over dunes with a variety of morphologies to investigate the influence of lee side morphology on flow properties. Our results show that the value of the mean lee side angle and the value and position of the maximum lee side angle have an influence on the flow properties investigated. We propose a classification with 3 types of dunes: (1) low-angle dunes (mean lee side < 10°), over which there is generally no permanent flow separation; (2) intermediate-angle dunes (mean lee side 10-20°) over which there is likely an intermittent flow separation; and (3) high-angle dunes (mean lee side >20°) over which the flow separates at the brink point and reattaches shortly after the trough, and over which turbulence is high.

1 INTRODUCTION

Until recently, most studies focussed on so-called “high-angle dunes” which possess a steep lee side with slopes of around 30°. These dunes commonly form in small rivers and in flumes (Van der Mark et al., 2008). Over such dunes, flow separation and recirculation over the lee side produces a turbulent wake and induces bedform roughness. However, many dunes have recently been observed to be “low-angle dunes” with lee side angles much lower than the angle-of-repose. Over low-angle dunes, flow separation is absent or intermittent, and turbulence and roughness are lower than over high-angle dunes (Kwoll et al., 2016, Lefebvre and Winter, 2016). In large rivers, mean lee side angles are commonly between 5° and 20° (Cisneros et al., 2020) as illustrated in Figure 1 by data from the Mississippi and Waal Rivers. Bedform lee sides in tidal environments are also often low, with, for example in the Weser Estuary, typical values of 5 to 20° (Lefebvre et al., 2021, Figure 1).

In addition, contrary to previous simplifications of lee side shape, the lee side is rarely a straight line but rather made of several steeply and gently sloping portions. Typically, a comparatively steep slope is observed somewhere along the lee side with gentler slopes towards the crest and/or the trough. In large rivers, the maximum lee side angle is on average 20.5° (Cisneros et al., 2020). In constrained tidal environments (e.g. estuaries and tidal inlets), maximum lee side angles are usually less than 20° (Dalrymple and Rhodes, 1995, Lefebvre et al., 2021, Prokocki et al., 2022) (Figure 1c). It is likely that marine dunes (i.e. dunes found in open marine environments such as continental shelves) have a variety of mean and maximum lee side angles. In any case, it should be noted that in tidal environments, flow reverses from one tidal phase to the next. However large dunes usually stay oriented in one direction during the whole tidal cycle. Therefore, lee sides may be steep during one tidal phase but gentle during the following tidal phase.

Interestingly, the shape of river and estuarine dunes differs. River dunes have their steepest slope close to the trough and a rounded crest (Cisneros et al., 2020), whereas estuarine dunes have their steepest slope close to the crest and a sharp crest (Dalrymple

and Rhodes, 1995; Lefebvre et al., 2021). In open marine environments, various morphologies are found, from sharp to round crests (Van Landeghem et al., 2009, Zhang et al., 2019). Therefore, the difference in dune shape is not strictly reflecting differences between river and tidal environments, but rather the complex interaction between dune morphology, sediment properties and hydrodynamics.

The influence of the lee side morphology and how it fits within the coupling of feedbacks in the morphodynamic triad has not yet been systematically studied. The aim of this work is therefore to characterise flow properties (velocities and turbulence) over low and high-angle dunes with their steepest slope close to the crest and close to the trough using numerical experiments.

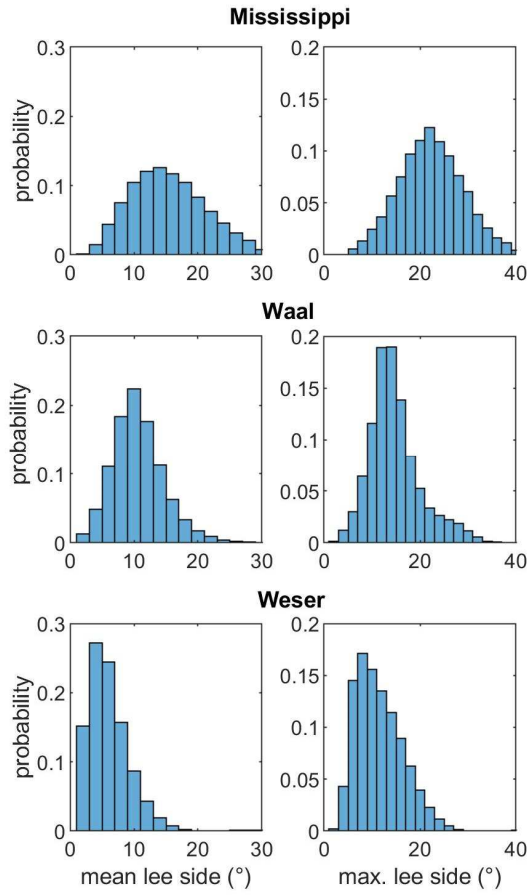

Figure 1. Mean and maximum lee side angles from dunes found in the Mississippi and Waal Rivers (data from Cisneros et al., 2020) and the Weser Estuary (Data from Lefebvre et al., 2021).

2 METHODS

2.1 Model description

Numerical experiments were carried out using Delft3D (Deltares, 2014), a process-based open-source integrated flow and transport modelling system. In order to capture non-hydrostatic flow phenomena such as flow separation and recirculation on the lee of dunes, the non-hydrostatic pressure can be computed.

The Delft3D modelling system has been used to setup a two-dimensional vertical (2DV) numerical model using the non-hydrostatic pressure correction technique to simulate horizontal and vertical velocities and turbulent kinetic energy (TKE) above fixed bedforms. The model has been previously calibrated, validated and verified (Lefebvre et al., 2014a, Lefebvre et al., 2014b). The simulations were performed on a 2DV plane Cartesian model grid over a fixed bed (i.e. no sediment transport) composed of 10 similar bedforms. The following conditions were prescribed constant in time at the lateral open boundaries of the model domain: a logarithmic velocity profile at the upstream boundary, and a water surface elevation of 0 m at the downstream boundary. The bed roughness was set as a uniform roughness length z_0 = 0.0001 m. The dune height and length, the water depth and the vertical and horizontal grid size were kept similar for all simulations. The horizontal grid size was set as dx = 0.09 m (271 grid point per dune). A non-uniform vertical grid size, stretched in the vertical direction with fine spacing near the bed and coarser spacing in the water column, was used.

2.2 Model experiments

A total of 88 simulations were carried out to test the influence of lee side morphology on flow velocities and turbulent kinetic energy. For all simulations, bedform height (H_b = 0.89 m) and length (L_b = 24.4 m), water depth (h = 8 m) and mean flow velocity (0.8 m/s) were kept similar. The stoss side followed a cosine shape and the lee side was made of either a line (straight lee side) or three lines (complex lee side). The straight

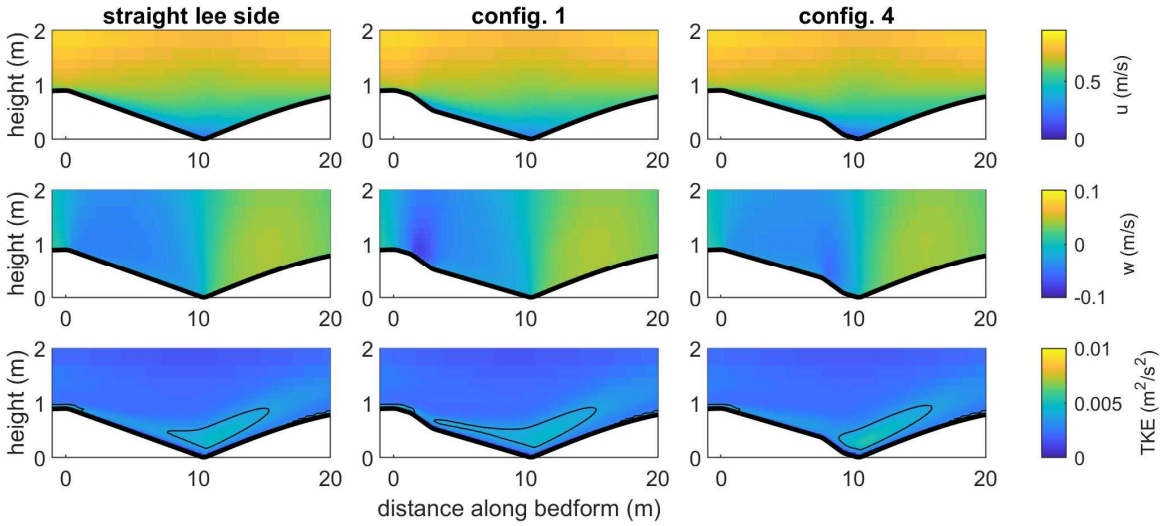

Figure 2. Horizontal streamwise velocity (u), vertical velocity (w) and turbulent kinetic energy (TKE) over dunes with mean lee side of 5°, a straight lee side (left panel), a max lee side angle of 10° situated close to the crest (config. 1, middle panel) and close to the trough (config. 4 right panel)

lee side experiments were made with lee side angles varying from 5° to 30°, in increments of 5°. For each mean lee side angle, simulations were done with the lee side composed of three segments: a steep portion where the maximum angle was fixed and upper and lower lee sides which had angles adjusted so that the mean angle would be between 5 and 30°, in increments of 5°. The steep portion height was one third of the bedform height. For each maximum lee side angle, four configurations were tested, with the position of the steep portion varying from close to the crest to close to the trough.

2.3 Model output analysis

From the simulation results, the horizontal and vertical velocities and the TKE above the 7th bedform (from a total of 10 bedforms) were investigated. The position and size of the flow separation zone, when present, was calculated as the region in which the flow going upstream (i.e. negative horizontal velocity) is compensated by flow going downstream. Because Delft3D uses the Reynolds-averaged Navier–Stokes equations, it was not possible to model intermittent flow separation zone; only permanent flow separation can be simulated and was considered here. The mean and maximum TKE over the 7th bedform were computed as indicators of the overall turbulence produced and dissipated over each dune shape. The turbulent wake was defined as the region where TKE is more than twice the average TKE above a flat bed with similar hydrodynamic conditions.

3 RESULTS

Based on our results, it is useful to make a distinction between low-angle, intermediate-angle and high-angle dunes.

3.1 Low-angle dunes

Flow and turbulence patterns over low-angle dunes (mean lee side < 10°) are illustrated by Figure 2, which shows dunes with a mean lee side of around 5° and a maximum angle of 10°, the most common configuration in the Weser Estuary. As typically observed over dunes, the horizontal velocity is highest above the crest and lowest above the trough. Vertical velocity shows flow going downwards above the lee side, with the strongest downward flow observed above the steep portion, and flow going upwards above the stoss side. There is generally no flow separation except if the

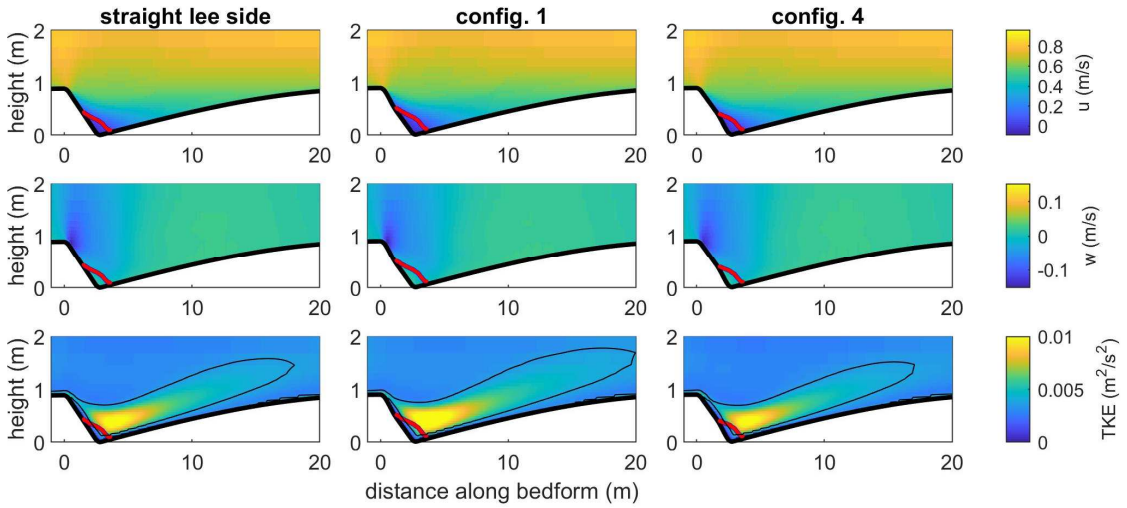

Figure 3. Horizontal streamwise velocity (u), vertical velocity (w) and turbulent kinetic energy (TKE) over dunes with mean lee side of 20°, a straight lee side (left panel), a max lee side angle of 25° situated close to the crest (config. 1, middle panel) and close to the trough (config. 4 right panel)

steep portion is at least 20° and situated close to the trough. However, it should be noted that this type of dunes (with a mean lee side angle < 10° and maximum angle > 20°) is not commonly observed. The turbulent wake generally starts over the steep portion and extends downstream down to a distance of ca. 5 m after the trough. Therefore, although the mean and maximum TKE are strongest for steep portions closest to the trough, the turbulent wake is longest for steep portions close to the crest (Figure 2).

3.2 Intermediate-angle dunes

Flow over intermediate-angle dunes (defined here as mean lee side angles between 10° and 20°) is difficult to correctly characterise from the results of our simulations. No systematic variations in flow separation zone and turbulent wake properties with mean and maximum angles could be established. This is likely because over intermediate-angle dunes, these properties are time-dependant. For example, flow separation is likely to be intermittent. As time-dependency is not resolved in the model we used, it is difficult to draw conclusions from our results. We suggest that these dunes should be investigated with laboratory experiments, field measurements and Reynolds-resolving models in order to precisely characterise time-dependant flow properties.

3.3 High-angle dunes

Over high-angle dunes (defined here as mean lee side angles over 20°), a flow separation is always observed. The flow generally separates over the steep portion and reattaches shortly after the trough (Figure 3). As a result, flow separation is longer for maximum angles situated close to the crest than for those situated close to the trough. The highest downward velocity is always situated just after the crest, independently of the maximum angle position. Significant differences are observed for the turbulent wake: it is especially strong (i.e. high TKE intensity) and spatially developed for steep portions close to the crest. As the position of the steep portion is getting closer to the trough, the turbulent wake decreases in size and intensity.

4 DISCUSSION

Our results show that the mean lee side angle has the strongest control over flow

separation and turbulence over dunes, with a secondary influence of the position and value of the maximum lee side angle. We propose a distinction between three types of dune: low-angle dunes, intermediate-angle dunes and high-angle dunes. This differs from most classifications which recognise only high and low-angle dunes but not intermediate (Best, 2005, Kostaschuk and Venditti, 2019, Venditti, 2013). We base our classification between low, intermediate and high-angle dunes on flow properties investigated in the present study, but also on flow properties and sediment dynamics from previous research. Properties of each dune category can be identified. Over low-angle dunes (mean lee side < 10°), there is no flow separation, except if a very steep portion (slope > 20°) is found. Low-angle dunes generate little turbulence and are likely to induce little bedform roughness (Lefebvre and Winter, 2016; Kwoll et al., 2016). Over intermediate dunes (mean lee side angles between 10° and 20°), flow separation is intermittent (Kwoll et al., 2016). Turbulence and roughness are intermediate between low and high-angle dunes. No pattern can be found between the position of the maximum angle and flow properties. Our results show the limitations of studying intermediate dunes with Reynolds-averaged models such as Delft3D. Over high-angle dunes (mean lee side > 20°), a developing to fully-developed flow separation is present, a strong turbulent flow is observed and a high bedform roughness is created. If the maximum angle is close to the crest, flow separation is longer and the turbulent wake is stronger than if the maximum angle is close to the trough.

This distinction between low, intermediate and high-angle dunes is important for a range of processes such as the evaluation of bed roughness, understanding the relation between hydrodynamics, sediment transport and dune morphology, how dunes are identified in the depositional record, and unravelling the controlling processes leading to different lee side angle slopes and shapes.

5 CONCLUSIONS

Numerical simulations were carried out in order to estimate the influence of the value and position of the maximum lee side angle on flow above dunes with varied mean lee side slopes. Based on our results and previous literature, we propose a distinction between three types of dunes:

- Low-angle dunes, with mean lee side lower than 10°. Over such dunes, there is generally no permanent flow separation. The turbulent wake is weak, but strongest and most contained (limited spatial extent) for steep maximum angles situated close to the trough.
- Intermediate-angle dunes, with mean lee side of 10 to 20°. Over such dunes, there is rarely a permanent flow separation but it is likely that an intermittent flow separation forms. When present, flow separation is observed over the trough, independently of the maximum lee side angle position.
- High-angle dunes, with mean lee side of more than 20°. Over such dunes, the flow separates at the brink point and therefore, flow separation is longest if the maximum angle is close to the crest. The turbulent wake is strong, strongest and most extended for steep maximum slopes situated close to the crest.

This classification is more specific than previous classification, which only introduced low and high-angle dunes, and describes the specifics of flow properties depending on lee side morphology. It allows for a precise consideration of the interaction between dune morphology and flow. To correctly take this interaction and its consequences into account, detailed reports of dune morphology from varied environments are needed.

6 ACKNOWLEDGEMENT

Alice Lefebvre is funded through the Cluster of Excellence ‘The Ocean Floor – Earth’s Uncharted Interface’.

7 REFERENCES

Best, J., 2005. The fluid dynamics of river dunes: A review and some future research directions. Journal of Geophysical Research 110, 21. https://doi.org/10.1029/2004JF000218

Cisneros, J., Best, J., van Dijk, T., de Almeida, R.P., Amsler, M., Boldt, J., Freitas, B., Galeazzi, C., Huizinga, R., Iannirubertо, M., Ma, H.B., Nittrouer, J.A., Oberg, K., Orfeo, O., Parsons, D., Szupiany, R., Wang, P., Zhang, Y.F., 2020. Dunes in the world's big rivers are characterized by low-angle lee-side slopes and a complex shape. Nature Geoscience 13, 156-+. https://doi.org/10.1038/s41561-019-0511-7

Dalrymple, R.W., Rhodes, R.N., 1995. Chapter 13 Estuarine Dunes and Bars, in Developments in Sedimentology. Elsevier, 359-422

Deltares, 2014. User Manual Delft3D-FLOW. Deltares,

Kostaschuk, R.A., Venditti, J.G., 2019. Why do large, deep rivers have low-angle dune beds? Geology 47, 919-922. https://doi.org/10.1130/g46460.1

Kwoll, E., Venditti, J.G., Bradley, R.W., Winter, C., 2016. Flow structure and resistance over subaquaeous high- and low-angle dunes. Journal of Geophysical Research: Earth Surface 121, 545-564. https://doi.org/10.1002/2015JF003637

Lefebvre, A., Herrling, G., Becker, M., Zorndt, A., Krämer, K., Winter, C., 2021. Morphology of estuarine bedforms, Weser Estuary, Germany. Earth Surface Processes and Landforms https://doi.org/10.1002/esp.5243

Lefebvre, A., Paarlberg, A.J., Ernstsen, V.B., Winter, C., 2014a. Flow separation and roughness lengths over large bedforms in a tidal environment: a numerical investigation. Continental Shelf Research 91, 57-69. https://doi.org/10.1016/j.csr.2014.09.001

Lefebvre, A., Paarlberg, A.J., Winter, C., 2014b. Flow separation and shear stress over angle of repose bedforms: a numerical investigation. Water Resources Research 50, 986-1005. https://doi.org/10.1002/2013WR014587

Lefebvre, A., Winter, C., 2016. Predicting bed form roughness: the influence of lee side angle. Geo-Marine Letters 36, 121-133. https://doi.org/10.1007/s00367-016-0436-8

Prokocki, E.W., Best, J.L., Perillo, M.M., Ashworth, P.J., Parsons, D.R., Sambrook Smith, G.H., Nicholas, A.P., Simpson, C.J., 2022. The morphology of fluvial-tidal dunes: Lower Columbia River, Oregon/Washington, USA. Earth Surface Processes and Landforms 47, 2079-2106. https://doi.org/10.1002/esp.5364

Van der Mark, C.F., Blom, A., Hulsher, S.J.M.H., 2008. Quantification of variability in bedform geometry. Journal of Geophysical Research 113, F03020. https://doi.org/10.1029/2007JF000940

Van Landeghem, K.J.J., Wheeler, A.J., Mitchell, N.C., Sutton, G., 2009. Variations in sediment wave dimensions across the tidally dominated Irish Sea, NW Europe. Marine Geology 263, 108-119. https://doi.org/10.1016/j.margeo.2009.04.003

Venditti, J.G., 2013. Bedforms in sand-bedded rivers, in Treatise on Geomorphology. Academic Press, 137-162

Zhang, H., Ma, X., Zhuang, L., Yan, J., 2019. Sand waves near the shelf break of the northern South China Sea: morphology and recent mobility. Geo-Marine Letters 39, 19-36. https://doi.org/10.1007/s00367-018-0557-3

The influence of sediment transport formulae on modelling river dune development

L. R. Lokin *University of Twente, Enschede, The Netherlands and HKV, Lelystad, The Netherlands – l.r.lokin@utwente.nl*
J. J. Warmink *University of Twente, Enschede, The Netherlands – j.j.warmink@utwente.nl*
S. J. M. H. Hulscher *University of Twente, Enschede, The Netherlands – s.j.m.h.hulscher@utwente.nl*

ABSTRACT: Simulating river dunes, with the eventual goal to predict dune dimensions and propagation speed in the field, offers many challenges. In this study we simulated river dunes in a 2DV numerical dune development model and evaluated the effect of different processes in bed load transport on the dune. This is done based on the Meyer-Peter & Müller transport formula, with two different adjustments. First an increased critical shear stress was used and secondly spatial relaxation was implemented. The results of this study show that the balance between the bed shear stress and the critical shear stress, is more important to obtain correct trends for dune height for low flow than for high flows. Parameterizing these processes needs to be done with care.

1 INTRODUCTION

In heavily navigated rivers, such as the Rhine, dredging to maintain a prescribed navigable depth is of utmost economic relevance. This fairway maintenance focusses on reducing bottle necks caused by local shoals. One of the sources of these shoals are river dunes, often propagating over already shallow areas in the river.

Predictions of river dune propagation and height can support efficient planning of maintenance dredging, or estimations of the shallowest points in the fairway. To determine both dune height and propagation for such predictions, numerical dune development models can be used. These types of models vary from models based on the 2D Saint-Venant equations in the vertical plane (Giri & Shimizu, 2006; Paarlberg et al., 2009; Nelson et al., 2011) to fully 3D models using direct numerical simulation (Nabi et al., 2013). The main constraint for predictions is that the calculation times of the predicted variables should be shorter than real time, preferably by at least 1 to 2 orders of magnitude smaller.

A model that has been validated for dune development with small calculation times is the dune development model by Paarlberg et al. (2009). While this model has been validated on flume studies representing high flow regimes (Paarlberg et al., 2009) and has been applied for the transition to upper stage plane bed (van Duin et al., 2017, 2021), it still needs validation for low flow regimes. As during low flows shoals caused by dunes may hamper shipping most.

Sediment transport during low flows is assumed to be bed load dominant. In the Waal River, dunes during low flows decrease in height but increase in length (Lokin et al., 2022). A similar pattern is visible for dunes during extreme high flow in the transition towards upper stage plane bed (Naqshband et al., 2017). However, during these low flows the underlying mechanism is different.

Therefore, the objective of this study was to investigate the influence of different bed load dominant sediment transport mechanisms, included in the Meyer-Peter & Müller (1948) transport equation. on dune development during low to median flow.

2 MODEL DESCRIPTION

The dune development model used in this study, is the model developed by (Paarlberg et al., 2009). This model was built on work for marine sand waves (Hulscher, 1996; Németh et al., 2006; van den Berg et al., 2012). Further model development has been focussing on (extreme) high flows and the

transition to upper stage plane bed (Van Duin & Hulscher, 2014; van Duin et al., 2021) and dune splitting (Warmink et al., 2014). In this section, the model set-up as used in this study is shortly introduced.

2.1 Flow

The flow is described by the 2D Saint-Venant equations in the vertical plane. The most important assumption within the flow module is the turbulence closure, which is solved through a constant eddy viscosity. The vertical boundary conditions are periodic. This simulates a virtually infinite row of identical dunes, by only one dune in the model domain.

For a full description of the equations and the numerical implementation we refer to the work by Paarlberg et al. (2009) and van den Berg et al. (2012).

2.2 Sediment transport and bed update

Sediment transport is based on the Meyer-Peter & Müller (1948) formula (Eq. 1). This formula is based on bed load transport and through the critical shear stress incipient motion is taken into account. Because of the relatively steep slopes found in dunes, the shear stresses are corrected for the slope (e.g. Sekine & Parker, 1992). The total bed load transport is determined by the following set of equations:

$$q_b = \begin{cases} \beta[\tau - \tau_c]^n [1 + \eta \frac{\partial z_b}{\partial x}] & \text{if } \tau - \tau_c \geq 0 \\ 0 & \text{if } \tau - \tau_c < 0 \end{cases} \quad (1)$$

$$\tau_c = \tau_{c,0} \frac{1+\eta\frac{\partial z_b}{\partial x}}{\sqrt{1+\left(\frac{\partial z_b}{\partial x}\right)^2}} \quad (2)$$

$$\tau_{c,0} = \tau_c^* g \Delta D_{50} \quad (3)$$

where β is the calibration factor determined by $\beta = \frac{m}{\Delta g}$ with m is 4 and Δ the relative density of sand normalised by the density of the water, τ is the local shear stress, τ_c the critical shear stress, and n is the non-linearity factor set to 3. The term $\left[1 + \eta \frac{\partial z_b}{\partial x}\right]$ is related to the bed slope correction, with η is th bes slope parameter which is inversely related to the angle of repose ϕ and $\frac{\partial z_b}{\partial x}$ the local bed slope. Equation 2 shows the bed slope correction on the critical shear stress, whith $\tau_{c,0}$ as the non-corrected critical shear stress, which is dependent on the critical Shields parameter (τ_c^*) and the median grain size (D_{50}) (Eq. 3).

Optionally, the Meyer-Peter & Müller formula can be extended by a spatial relaxation formula (Equation 4). This extension was proposed by Tsujimoto et al., (1990) and is based on the assumption that sediment transport needs some distance to adapt to spatially changing flow conditions.

$$\frac{\partial q_b}{\partial x} = \frac{q_{b,e} - q_b}{\Lambda} \quad (4)$$

where $q_{b,e}$ is the equilibrium transport determined by Equation 1, q_b is the actual transport, and Λ is the step length (Einstein, 1950)and is defined by:

$$\Lambda = \alpha D_{50} \quad (5)$$

with α is the non-dimensional step length, determined following (van Duin et al., 2021)

The sediment tranport as determined based on the flow field is translated into a bed update using the Exner equation, with a correction for the bed porosity (ε):

$$(1 - \varepsilon)\frac{\partial z_b}{\partial t} = -\frac{\partial q_s}{\partial x} \quad (6)$$

3 RESEARCH METHOD

3.1 Validation data

To validate the model results, the dune height and propagation speed are compared to these parameters as found in the Waal River (Netherlands). The derivation and the exact values of these parameters can be found in Lokin et al. (2022). While the aim of this study is to assess the influence of the

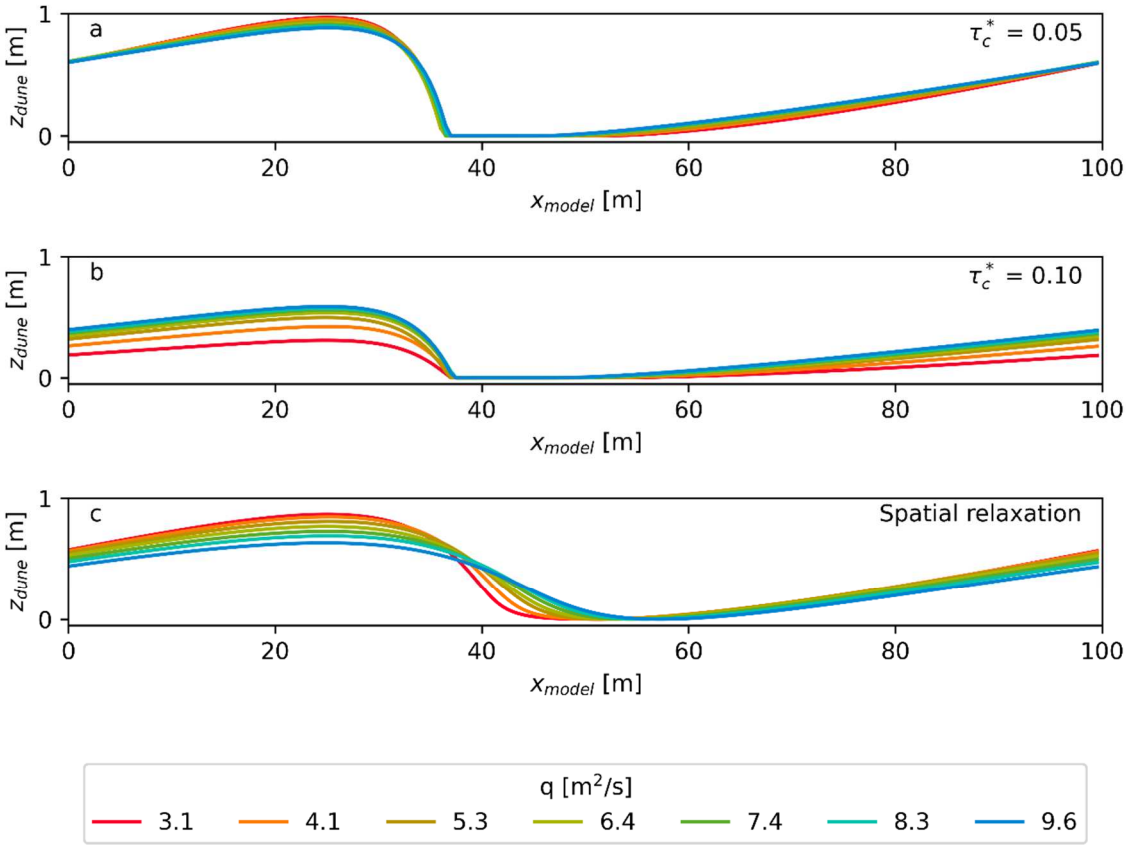

Figure 1. Simulated dune shapes for the different sediment transport conditions. The vertical axis represents z_{dune}, which is the bed level with respect to the trough. a) Normal Shields stress conditions b) Increased Shields stress conditions and c) normal shields stress with spatial relaxation conditions.

sediment transport equation, the trends in these data are more important than the exact values. Therefore, the model is not calibrated to fit perfectly to the data.

3.2 Simulations and model settings

Flow conditions and sediment sizes are in line with the conditions in the Waal river (Lokin et al. submitted.). With these conditions three different variants of the Meyer-Peter & Müller equation are tested. The first condition is the "basic" formula with the bed slope correction and a critical Shield stress of $\tau_c^* = 0.05$. This is a value representative for the median grain size. The second condition has an increased critical shields stress, $\tau_c^* = 0.1$, which can be seen as the effect of a lower flow velocity due to (partial) flow separation at the lee slope. The third condition has the normal critical Shield stress combined with the spatial relaxation process.

Table 1: General simulation settings

Parameter	Value	
Domain length (L)	100	m
Specific discharge (q)	3.1 – 9.6	m^2/s
Bed slope (i)	$5e^{-5}$	m/m
Median grain size (D_{50})	1.0	mm

The hydraulic conditions mimic the flow conditions varying from low to median conditions in the Waal River, while for all conditions the domain length is kept constant. The model settings are shown in Table 1. All simulations are run for 100 days, which ensures that dunes have reached their equilibrium shape.

4 RESULTS

4.1 Dune shape and height

Each individual simulation, with the different transport conditions, results in plausible dune shapes (Fig. 1); the simulated shapes can be found in rivers and for each simulation the lee slope angles are smaller than the angle of repose. However, the trends with regard to the specific discharge and

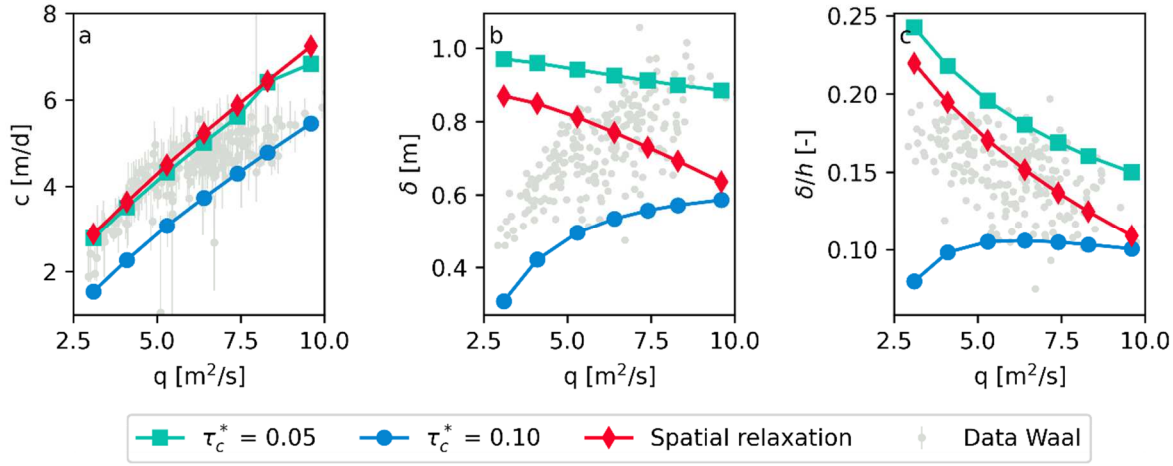

Figure 2. Propagation speed (a), dune height (b) and dune height over water depth (c) as function of the discharge for the three sediment transport variants. The light grey dots in the background are the observed values from the Waal River (Lokin et al. 2022)

therefore the flow conditions show distinctive differences between the three transport conditions.

The dunes simulated with the "normal" critical shear stress all have the same shape (Fig. 1a) and the dune height decreases by 10 cm between the lowest and highest discharges (Fig. 2b). While an increase of dune height is expected, since the water depth increases as well.

The increase of dune height from low to high discharge is found in the simulations with the increased critical Shields stress (Fig. 1b). While the rate of increase in height decreases with the increasing discharge (Fig. 2b). For the low discharges the transport capacity, mainly depending on $\tau - \tau_c$, determines the dune height. While at higher discharges this parameter appears to be of less importance.

For the dune height over water depth (Fig. 2c), the trend in the field data is best represented by the normal shields stress and linear relaxation simulations. Combined with the trend of the dune height only, it can be deducted that the simulated water depth is not corresponding to the water depth found in the Waal. Calibration of this water depth may improve these trends and therefore predictive power of the model.

4.2 Propagation speed

The propagation speed of all dunes are fairly similar to the propagation speed found in the field data (Fig. 2a). Decreasing the critical Shields stress, decreases the propagation speed accordingly.

Adding spatial relaxation barely influences the propagation speed. Because the dune height is smaller than without spatial relaxation and the total sediment transport is the same in both cases, not all sediment transport in the spatial relaxation case contributes to dune propagation. This is an artefact of the processes which are parameterized by adding this spatial relaxation; suspended sediment.

5 DISCUSSION

5.1 The effect of the critical shear stress

The results show that realistic dunes can be simulated with different variants of the Meyer-Peter & Müller sediment transport formula. However, the effect of increasing the shear stress on the dune is height opposite to the effect of adding spatial relaxation.

Increasing the critical shear stress can mimic or correct for several processes that influence the total sediment transport, which are not explicitly included in the dune development model. A first processes is linked to the turbulence closure model. Because of the sudden flow expansion at the lee side of the dune, partial flow separation occurs. This results in energy losses which are not resolved by the constant eddy viscosity. A second process is linked to hiding and exposure. The model only uses the median grain size to calculate sediment transport, while the Waal river is bi-modal (Ylla Arbós et al., 2021). Hiding and

exposure increases the shear stress needed to bring sediment in motion.

Both these processes result in a smaller transport capacity, ensuing a smaller dune height and smaller propagation speeds. For the case with $q = 3.1$ m2/s, this is most significant as here the dune height is limited by the transport capacity. The dune crest can only move due to a fairly small transport capacity, where most sediment is then deposited in the dune crest. A small transport capacity can only maintain small dunes.

Increasing the discharge, thus flow velocity will lead to higher transport capacity on the stoss slope and the dune crest, while also the dune trough deepens. Eventually the dune height will reach a balance where the dune troughs will have no transport and the crest enough to maintain the equilibrium dune height and to propagate steadily.

5.2 The effect of spatial relaxation

De dune height decreases with increasing discharge for the simulations with spatial relaxation is opposite to what is expected from the field data. While spatial relaxation mimics the effect of bed material that is brought in suspension and settles further downstream, for example, on the stoss slope of the downstream dune. This is a process that is linked to the transition to upper stage plane bed (Naqshband et al., 2017). And considering the trends in dune height it may not be relevant for dune formation during low flows.

Whilst spatial relaxation is necessary to simulate the transition to upper stage plane bed, it does not contribute to low dunes during low flows. Therefore, when trying to simulate dunes over the entire discharge domain, the parameterization of this spatial relaxation needs to be revisited. Such that for both low and extreme high flow the processes that are dominant in dune formation, are also dominant in the simulation.

When simulating dunes during flood waves and extreme low flows, the parameterization of all processes that are dominant in the development in the dunes need to be revisited. Such that during low flows dune heights increase with the discharge, to decrease again at the discharge that where upper stage plane bed may be expected.

6 CONCLUSIONS

In this study we compared the effect of an increased critical shear stress and spatial relaxation implemented in the Meyer-Peter & Müller transport formula on simulated dune shapes. Processes mimicked by the increased critical shear stress, decreased flow velocities due to flow separation and hiding and exposure, result in a realistic trend for the relation dune height to discharge, for low flow cases. Spatial relaxation parameterizes the processes important for the transition to upper stage plane bed. To further improve the dune development model for forecasting, these processes need to be parameterized with great care, to ensure the correct processes are dominant in the dune development.

7 ACKNOWLEDGEMENTS

This research is part of the research program Rivers2Morrow (2018-2023). Rivers2Morrow is financed by the Dutch Ministry of Infrastructure and Water Management. All measurement data were made available by Rijkswaterstaat. Our words of gratitude for collecting and sharing these data go out to technical staff of Rijkswaterstaat. We thank ir. J.W.C.A. Lokin for his help with updating the model code.

8 REFERENCES

Einstein, H. A. (1950). The bed load function for sediment transport in open-channel flows. In *Technical Bulletin No. 1026, U.S. Dept. of Agriculture, Soil Conservation Service.* (p. 71).

Giri, S., & Shimizu, Y. (2006). Numerical computation of sand dune migration with free surface flow. *Water Resources Research*, *42*(10). https://doi.org/10.1029/2005WR004588

Hulscher, S. J. M. H. (1996). Tidal-induced large-scale regular bed form patterns in a three-dimensional shallow water model. *Journal of Geophysical Research: Oceans*, *101*(C9), 20727–20744. https://doi.org/10.1029/96JC01662

Lokin, L. R., Warmink, J. J., Bomers, A., & Hulscher, S. J. M. H. (2022). River Dune Dynamics During

Low Flows. *Geophysical Research Letters*, *49*(8), e2021GL097127. https://doi.org/10.1029/2021GL097127

Lokin L. R., Warmink, J.J., & Hulscher S. J. M. H. (submitted). The effect of sediment transport models on simulating river dune dynamics. Submitted for publication.

Meyer-Peter, E., & Müller, R. (1948). Fromulas for Bed-Load Transport. *IAHSR, 2nd Meeting, Stockholm 7-9 April, 1948*, 39–64.

Nabi, M., De Vriend, H. J., Mosselman, E., Sloff, C. J., & Shimizu, Y. (2013). Detailed simulation of morphodynamics: 3. Ripples and dunes. *Water Resources Research*, *49*(9), 5930–5943. https://doi.org/10.1002/wrcr.20457

Naqshband, S., Hoitink, A. J. F., McElroy, B., Hurther, D., & Hulscher, S. J. M. H. (2017). A Sharp View on River Dune Transition to Upper Stage Plane Bed. *Geophysical Research Letters*, *44*(22), 11,437-11,444. https://doi.org/10.1002/2017GL075906

Nelson, J. M., Logan, B. L., Kinzel, P. J., Shimizu, Y., Giri, S., Shreve, R. L., & Mclean, S. R. (2011). Bedform response to flow variability. *Earth Surface Processes and Landforms*, *36*(14), 1938–1947. https://doi.org/10.1002/esp.2212

Németh, A. A., Hulscher, S. J. M. H., & Van Damme, R. M. J. (2006). Simulating offshore sand waves. *Coastal Engineering*, *53*(2–3), 265–275. https://doi.org/10.1016/J.COASTALENG.2005.10.014

Paarlberg, A. J., Dohmen-Janssen, C. M., Hulscher, S. J. M. H., & Termes, P. (2009). Modeling river dune evolution using a parameterization of flow separation. *Journal of Geophysical Research: Earth Surface*, *114*(1). https://doi.org/10.1029/2007JF000910

Sekine, M., & Parker, G. (1992). BedLoad Transport on Transverse Slope. I. *Journal of Hydraulic Engineering*, *118*(4), 513–535. https://doi.org/10.1061/(ASCE)0733-9429(1992)118:4(513)

Tsujimoto, T., Mori, A., Okabe, T., & Ohomoto, T. (1990). Non-equilibrium sediment transport: a generalized model. *Journal of Hydroscience and Hydraulic Engineering*, *7*(2), 1–25.

van den Berg, J., Sterlini, F., Hulscher, S. J. M. H., & van Damme, R. (2012). Non-linear process based modelling of offshore sand waves. *Continental Shelf Research*, *37*, 26–35. https://doi.org/10.1016/J.CSR.2012.01.012

Van Duin, O. J. M., & Hulscher, S. J. M. H. (2014). Modelling the transition from dunes to the upper-stage plane bed. *Proceedings of the International Conference on Fluvial Hydraulics, RIVER FLOW 2014*, 1067–1074. https://doi.org/10.1201/b17133-144

van Duin, O. J. M., Hulscher, S. J. M. H., & Ribberink, J. S. (2021). Modelling Regime Changes of Dunes to Upper-Stage Plane Bed in Flumes and in Rivers. *Applied Sciences 2021, Vol. 11, Page 11212*, *11*(23), 11212. https://doi.org/10.3390/APP112311212

van Duin, O. J. M., Hulscher, S. J. M. H., Ribberink, J. S., & Dohmen-Janssen, C. M. (2017). Modeling of spatial lag in bed-load transport processes and its effect on dune morphology. *Journal of Hydraulic Engineering*, *143*(2), 04016084. https://doi.org/10.1061/(ASCE)HY.1943-7900.0001254

Warmink, J. J., Dohmen-Janssen, C. M., Lansink, J., Naqshband, S., van Duin, O. J. M., Paarlberg, A. J., Termes, P., & Hulscher, S. J. M. H. (2014). Understanding river dune splitting through flume experiments and analysis of a dune evolution model. *Earth Surface Processes and Landforms*, *39*(9), 1208–1220. https://doi.org/10.1002/esp.3529

Ylla Arbós, C., Blom, A., Viparelli, E., Reneerkens, M., Frings, R. M., & Schielen, R. M. J. (2021). River Response to Anthropogenic Modification: Channel Steepening and Gravel Front Fading in an Incising River. *Geophysical Research Letters*, *48*(4), e2020GL091338. https://doi.org/10.1029/2020GL091338

Anomalous evolution of aerodynamic roughness and shear velocity on large flows

M.Y. Louge, *Mechanical Engineering, Cornell University, Ithaca, NY, USA – MYL3@cornell.edu*
A. Valance, *Institut de Physique de Rennes, Université de Rennes, Rennes, France*
J. Fang, *Ecole Polytechnique Fédérale de Lausanne, Lausanne, Switzerland*
S. Harnett, *Mechanical Engineering, Cornell University, Ithaca, NY, USA*
F. Porté-Angel, *Ecole Polytechnique Fédérale de Lausanne, Lausanne, Switzerland*
P. Chasle, *Institut de Physique de Rennes, Université de Rennes, Rennes, France*

ABSTRACT: We recorded aerodynamic roughness and shear velocity along transects on and around crescent-shaped barchan dunes of 4.5 m and 27 m height in the Qatar desert. The data revealed unexpected evolution of aerodynamic roughness from very large on the desert floor to much lower than the prescription of Nikuradse (1933) for a smooth surface. While qualitatively conforming to the predictions of Jackson and Hunt (1975), the shear velocity also exhibited an anomalously high value at the slope discontinuity between the upwind and avalanche faces. These measurements call into question the formulation of boundary conditions in numerical simulations over evolving bedforms, whether they are designed for aeolian or marine experiments.

1 INTRODUCTION

Turbulent flows over large bedforms are difficult to compute with fidelity (Smyth 2016). Most efforts have focused on improving the size and resolution of numerical simulations, by scaling-up the domain of methods such as Large-Eddy-Simulations (LES) (Stoll & Porté-Agel 2006, Omidyeganeh & Piomelli 2013, Fang & Porté-Agel 2016, Liu et al. 2019, Hardy et al. 2021, Zheng et al. 2021, Jin et al. 2021), Reynolds-Averaged Navier-Stokes (RANS) (Jin et al. 2021, Lane et al. 2004, Lefebvre et al. 2014, Michelsen et al. 2015), or methods coupling morphodynamics with a fluid mechanics solver such as Lattice methods (Narteau et al. 2019, Lü et al. 2018, Zhang et al. 2022), LES or RANS (Sotiropoulos & Khosronejad 2016).

However, less attention has been paid to verifying boundary conditions at the surface on the geophysical scale. As suggested by Launder and Spalding (1974), most models adopt a condition that relates shear stress $\tau_0 = \rho\, u^{*2}$ on the surface to velocity in the next grid cell aloft, as prescribed by the profile in the core of the turbulent boundary layer,

$$u(z) = \frac{u^*}{\kappa} \ln\left(\frac{z}{z_0}\right) \quad (1)$$

where u* is the shear velocity, z is elevation above the surface, ρ is the fluid density, κ=0.41 is von Kármán's constant, and z_0 is an effective aerodynamic roughness. In fluvial environments, the Chézy condition (Lefebvre et al. 2004, D'Ippolito et al. 2021) amounts to a similar prescription. If the domain is small enough that the solver can resolve the viscous sublayer explicitly, for example on sand ripples (Jin et al. 2022) or in laboratory-scale bedforms in flumes (Omidyeganeh & Piomelli 2013), then a no-slip condition u = 0 may instead be imposed at z = 0. However, the required space discretization is, for the capabilities of current machines, too fine to handle large objects such as desert or submarine dunes.

Meanwhile, Eq. 1 alone does not account for the role of the inertial inner layer that Jackson and Hunt (1975) discovered. These authors showed that, over a low hill, gas

inertia compels the maximum shear stress to arise upstream of the maximum speed at the hill crest. Unfortunately, because numerical simulations rarely resolve the thickness of this inner layer, they cannot capture this important effect, which contributes to dune inception (Kroy et al. 2002).

Another common situation is to find dunes surrounded by a flat desert floor covered with stones. For instance, in our field of barchans, sands of 351 μm mean diameter were surrounded by rocks of decimetric size (Louge et al. 2013), thereby creating a sharp discontinuity in geometrical surface roughness. While it is possible to simulate a complicated rugged bedform topography on the size of flume experiments (Hardy et al. 2021), such endeavor is not feasible in the field. Instead, to handle geophysical scales in such meteorological situations as wind transitioning from the ocean to a coastal forest, Walmsley et al (1986) incorporated an evolution of geometrical roughness within the framework of Jackson and Hunt (1975).

In general, one implicitly assumes that aerodynamic roughness z_0 is related to its geometrical counterpart. For turbulent flows in *smooth* pipes, reconciling Eq. 1 with the universal turbulent core profile in wall units yields an effective aerodynamic 'roughness' satisfying

$$\ln\left(\frac{u^* z_0}{\nu}\right) = -a_u \kappa \quad (2)$$

where a_u=5.1 and ν is the kinematic fluid viscosity. However, as u* rises with pipe Reynolds number, Nikuradse (1933) showed that the Darcy friction factor reaches an asymptote that becomes invariant with u*, but that now depends on the geometrical size of wall roughness. By integrating the velocity profile in Eq. 1 for internal turbulent flows in pipes, one can recover the measured Darcy friction coefficient and, reconciling it with the asymptotic data of Nikuradse (1933) for internal pipe wall roughened with sand of diameter d, extract the classical effective aerodynamic roughness at high u*,

$$z_0 \simeq \frac{d}{\omega} \quad (3)$$

where ω≃33. This expression, which captures the limit of large roughness or large Reynolds number, now explicitly involves a geometrical characterization of surface bumps. Assuming a universal character of wall-bound turbulence, it is commonly adopted even for external flows that do not resemble Nikuradse's pipes, for example on the surface of sand dunes at sufficiently large u∗ (Andreotti et al. 2002). However, as the next section shows, we found instances where aerodynamic roughness is considerably smaller than what Eqs. 2 or 3 suggest.

2 FIELD EXPERIMENTS

We measured shear velocity and aerodynamic roughness by positioning triads of ultrasonic anemometers to penetrate the inertial inner layer described by Jackson and Hunt (1975). All measured profiles closely conformed to the log-law for the core of turbulent boundary layers. As Fig. 1 illustrates, shear velocity first decreased, then recovered as air climbed on the small dune along a centerline transect, with a local maximum ahead of the crest as Jackson and Hunt (1975) predicted.

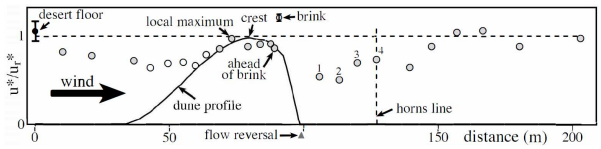

Figure 1: Shear velocity relative u* to its value at the crest u_r* along the transect on the centerline of a barchan dune of 4.5 m height.

At odds with existing models of the downstream dune wake (Kroy et al. 2002), an anomalous peak of shear velocity arose on the dune centerline at the brink. By forsaking descriptions of the wake as a bubble bound by a solidified streamline (Kroy et al. 2002), our direct application of the theory of Jackson and Hunt (1975) to the actual dune shape, including its discontinuous slope at the brink, suggested the origin of such anomaly (Louge et al. 2023).

We also recorded the evolution of aerodynamic roughness along the same transect, from its high value on the rough desert floor to lower ones on the dune and its wake. To question whether the Nikuradse (1993) formulation remained valid, we referred aerodynamic roughness to its asymptotic geometrically-rough limit in Eq. 3 and defined $\ln z_0\dagger = \ln(z_0\,\omega/d)$. If, as is often expected, $\ln z_0$ cannot fall below its asymptotic value $\ln(d/\omega)$ at large shear velocity, then one should always observe $\ln z_0\dagger>0$. However, as Fig. 2 shows, there are locations near the dune's upstream toe where this inequality is not met.

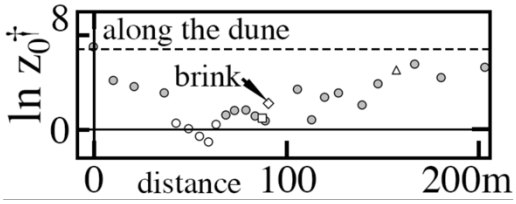

Figure 2: Log of the aerodynamic roughness relative to its value at high u*, $\ln z_0\dagger= \ln(z_0\,\omega/d)$, vs distance along the transect of Fig. 1.

Figure 3 confirms these observations along a similar transect on the larger dune of 27 m height. There, we also observed a peak of shear velocity at the brink, as well as sharply negative $\ln z_0\dagger$. More remarkably, values of $\ln z_0$ recorded near the upwind toe were even smaller than those prescribed by Eq. 2 for a smooth surface (dotted line).

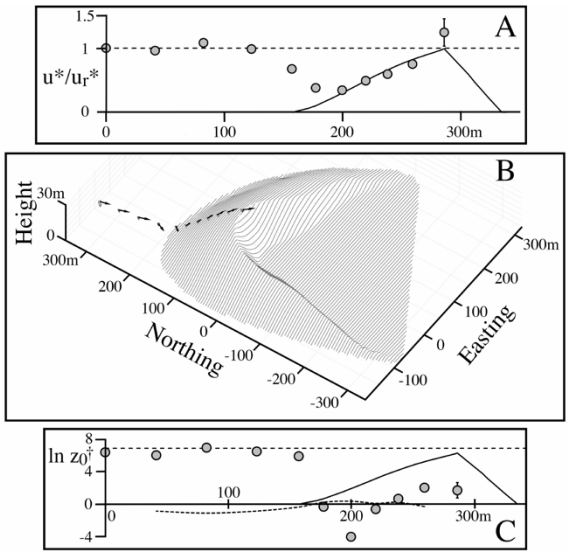

Figure 3: Observations on the larger dune of 27.2 m height. (A) Profile of u^*/u_r^* along the transect shown in (B). The horizontal dashed line marks $u^*=u_r^*$, where u_r^* is the reference shear velocity that we simultaneously recorded with a fixed anemometer triad upstream of the dune, on the origin of distances plotted. (B) Dune topography with superimposed roving anemometer positions and arrows proportional to u^*/u_r^* and aligned with the wind velocity. (C) Profile of $\ln z_0\dagger$ along the transect. The dashed horizontal straight line is $\ln z_0\dagger=6.9$ from Louge, et al. (2023). The dotted line is aerodynamic roughness for a smooth surface (Eq. 2). In (A) and (C), the solid line shows dune altitude along the transect with an arbitrary scale.

3 CONCLUSIONS

Turbulent boundary conditions on the surface of large isolated barchan dunes standing on a rough, nearly horizontal desert floor are not as straightforward to specify as what numerical simulations typically prescribe. First, we found that it is important to resolve the relatively thin inner layer described by Jackson and Hunt (1975). Without such precaution, a simulation is unlikely to capture the peaking of surface shear stress ahead of the dune crest, or the existence of a sharp maximum of shear velocity at the brink, both of which are associated with the inner layer.

Second, we observed that, as the log of aerodynamic roughness evolves from a relatively large value on the stone-covered desert floor to the smoother dune, this quantity can descend well below the classical model derived from data for internal flows in rough pipes (Nikuradse 1933). Therefore, sadly, it appears that numerical simulations of large, field-size bedforms must resolve the turbulent boundary layer closely, at least through the inner layer – and possibly closer to the surface –, so the evolution of aerodynamic roughness can be properly captured.

These observations should also be relevant to marine and fluvial bedforms, which are subject to similar variations in detailed topography between sea floor and dunes, and which also possess slope discontinuities where gravity currents first arise.

In this context, dune fields with steady, nearly unidirectional winds constitute a natural laboratory where turbulent surface boundary conditions may be measured at scale.

We are currently writing an article (Louge et al. 2023) that presents our desert data in greater detail, including their interpretation within the Jackson and Hunt framework (Jackson & Hunt 1975, Kroy et al. 2002), the existence of multiple thresholds of sand entrainment, and variations of shear velocity and aerodynamic roughness during aeolian transport through the lens of Bagnold's focal point in the turbulent boundary layer (Bagnold 1941, Jenkins & Valance 2014).

4 ACKNOWLEDGMENT

This work was made possible by the support of NPRP grants 09-546-2-206 and 6-059-2-023 from the Qatar National Research Fund, and a Qatar Foundation Research Excellence Award. This research was supported in part by the National Science Foundation under Grant No. NSF PHY-1748958.

5 REFERENCES

Andreotti, B., Claudin, P., and Douady, S. (2002). Selection of dune shapes and velocities. Part 1: Dynamics of sand, wind and barchans. The European Physical Journal B-Condensed Matter and Complex Systems 28, 321-339. doi:10.1140/epjb/e2002-00236-4.

Bagnold, R. A. (1941). The physics of blown sand and desert dunes. Chapman and Hall, Methuen, London.

D'Ippolito, A., Calomino, F., Alfonsi, G. and Lauria, A. (2021). Flow resistance in open channel due to vegetation at reach scale: a review. Water 13, 116:1-27. doi:10.3390/w13020116.

Fang, J. and Porté-Agel, F. (2016). Intercomparison of terrain-following coordinate transformation and immersed boundary methods in large-eddy simulation of wind fields over complex terrain. J. Phys. Conf. Ser. 753:082008. doi:10.1088/1742-6596/753/8/082008.

Hardy, R. J., Best, J. L., Marjoribanks, T. I., Parsons, D. R., and Ashworth, P. J. (2021). The influence of three-dimensional topography on turbulent flow structures over dunes in unidirectional flows. Journal of Geophysical Research: Earth Surface 126, e2021JF006121. doi:10.1029/2021JF006121.

Jackson, P. S. and Hunt, J. C. R. (1975). Turbulent wind flow over a low hill. Quart. J. R. Met. Soc. 101:929–955. doi:10.1002/qj.49710143015.

Jenkins, J.T., and Valance, A (2014): Periodic trajectories in aeolian sand transport. Physics of Fluids 26, 073301. doi:10.1063/1.4885576.

Jin, T., Wang, P., and Zheng, X. (2021). Characterization of wind-blown sand with near-wall motions and turbulence: From Grain-scale distributions to sediment transport. Journal of Geophysical Research: Earth Surface 126, e2021JF006234. doi:10.1029/2021JF006234.

Jin, C., Coco, G., Tinoco, R. O., Ranjan, P., Gong, Z., Dutta, S., San Juan, J. E., and Friedrich, H. (2022). High resolution Large Eddy Simulations of vortex dynamics over ripple defects under oscillatory flow. Journal of Geophysical Research: Earth Surface 127, e2021JF006328. doi:10.1029/2021JF006328.

Kroy, K., Sauermann, G. and Herrmann, H. J. (2002). Minimal model for sand dunes. Phys. Rev. Lett. 88:054301, doi:10.1103/PhysRevLett.88.054301.

Lane, S. N., R. J. Hardy, L. Elliott, and D. B. Ingham (2004). Numerical modeling of flow processes over gravelly surfaces using structured grids and a numerical porosity treatment. Water Resources Research 40, W01302. doi:10.1029/2002WR001934.

Launder, B.E., and Spalding, D.B. (1974). The numerical computation of turbulent flows. Computer Methods in Applied Mechanics and Engineering 3, 269-289. doi:10.1016/0045-7825(74)90029-2.

Lefebvre, A., A. J. Paarlberg, and C. Winter (2014). Flow separation and shear stress over angle-of-repose bed forms: A numerical investigation. Water Resources Research 50, 986-1005. doi:10.1002/2013WR014587.

Liu, Y., Fang, H., Huang, L. and He, G. (2019). Numerical simulation of the production of three-dimensional sediment dunes. Physics of Fluids 31, 096603. doi:10.1063/1.5108741.

Louge, M.Y., Valance, A., Ould el-Moctar, A., Xu, J., Hay, A.G., and Richer, R. (2013). Temperature and humidity within a mobile barchan sand dune, implications for microbial survival. J. Geophys. Res. Earth Surf. 118, 1-14. doi:10.1002/2013JF002839.

Louge, M.Y., Valance, A., Fang, J., Harnett, S., Porté-Agel, F., and Chasle, P. (2023). Evolution of turbulent boundary conditions on the surface of large barchan dunes: anomalies in aerodynamic roughness and shear velocity, aeolian thresholds and the role of dune skewness. J. Geophys. Res. Earth Surf., in preparation.

Lü, P., Dong, Z., and Rozier, O. (2018). The combined effect of sediment availability and wind regime on the morphology of aeolian sand dunes. Journal of Geophysical Research: Earth Surface 123, 1-9. doi:10.1029/2017JF004361.

Michelsen, B., Strobl, S., Parteli, E.J. and Pöschel, T (2015). Two-dimensional airflow modeling underpredicts the wind velocity over dunes. Scientific reports 5, 1-8. doi:10.1038/srep16572.

Narteau, C., Zhang, D., Rozier, O., and Claudin, P. (2009). Setting the length and time scales of a cellular automaton dune model from the analysis of superimposed bed forms. Journal of Geophysical

Research: Earth Surface 114, 1-18. doi:10.1029/2008JF001127.

Nikuradse J. (1933). Strömungsgesetze in rauhen Rohren (Laws of Flow in Rough Pipes). Forschung auf dem Gebiete des Ingenieurwesens, Ausgabe B Band 4:1-62, NACA Technical Memorandum 1292, Washington, D.C.

Omidyeganeh, M. and Piomelli, U. (2013). Large-eddy simulation of three-dimensional dunes in a steady, unidirectional flow. Part 1. Turbulence statistics. Journal of Fluid Mechanics 721, 454-483. doi:10.1017/jfm.2013

Sotiropoulos, F. and Khosronejad, A. (2016). Sand waves in environmental flows: Insights gained by coupling large-eddy simulation with morphodynamics. Physics of Fluids 28, 021301. doi:10.1063/1.4939987.

Smyth, T.A. (2016). A review of Computational Fluid Dynamics (CFD) airflow modelling over aeolian landforms. Aeolian research 22:153-164. doi:10.1016/j.aeolia.2016.07.003.

Stoll, R. and Porté-Agel, F. (2006). Dynamic subgrid-scale models for momentum and scalar fluxes in large-eddy simulations of neutrally stratified atmospheric boundary layers over heterogeneous terrain. Water Resources Research 42, W01409:1-18. doi:10.1029/2005WR003989.

Walmsley, J.L., Taylor, P.A. and Keith, T. (1986). A simple model of neutrally stratified boundary-layer flow over complex terrain with surface roughness modulations (MS3DJH/3R). Boundary-Layer Meteorology 36, 157-186. doi:10.1007/BF00117466.

Zhang, Q., Deal, E., Perron, J. T., Venditti, J. G., Benavides, S. J., Rushlow, M., and Kamrin, K. (2022). Fluid-driven transport of round sediment particles. From discrete simulations to continuum modeling. Journal of Geophysical Research: Earth Surface 127, e2021JF006504. doi:10.1029/2021JF006504.

Zheng, X., Jin, T., and Wang P. (2020). The influence of surface stress fluctuation on saltation sand transport around threshold. Journal of Geophysical Research: Earth Surface 125, e2019JF005246. doi:10.1029/2019JF005246.

Simulation of bedform formation using an Eulerian two-phase flow model.

A. Mathieu *CACR, University of Delaware, Newark, DE, USA – amathieu@udel.edu*
A. Salimi-Tarazouj *NWS/NCEP/EMC, NOAA, University of Maryland, College Park MD, USA*
T.-J. Hsu *CACR, University of Delaware, Newark, DE, USA*
C. Bonamy *LEGI, University of Grenoble Alpes, G-INP, CNRS, 38000 Grenoble, France*
J. Chauchat *LEGI, University of Grenoble Alpes, G-INP, CNRS, 38000 Grenoble, France*

ABSTRACT: A full understanding of the mechanisms responsible for bedform formation is not yet achieved. In this work, we apply a new tool, an Eulerian turbulence-resolving two-phase model. to investigate the formation of ripples starting from an initially flat bed. An experimental configuration is reproduced numerically and numerical experiments are performed to assess the predictive capabilities of the two-phase model. Although the results show a grid-size dependency, the main features of ripple formation are reproduced by the model. Results show the important role played by turbulent coherent structures in the early stage of ripple formation. We hypothesize that the grid-size dependency is related to timescale of ripple evolution and closure models.

1 INTRODUCTION

The evolution of bedforms in the fluvial and coastal environment has been investigated for more than a century (Bucher 1919, Engelund & Fredsoe 1982, Best 2005, Charru et al. 2013). Yet, no consensus on the mechanisms responsible for the generation of bedforms has been reached. Significant insight on the initiation of bedforms has been revealed by both linear stability analysis and experimental observations (Kennedy 1963, Kuru et al. 1995, Fourrière et al. 2010, Perillo et al. 2014). However, from the numerical point of view, the large spectrum of spatial and temporal scales involved in bedform formation makes simulation of the phenomenon extremely challenging, especially for the investigation of the role played by small scale turbulent coherent structures on the subsequent morphological evolution into larger bethymetric features. Recent developments in turbulence-resolving Eulerian two-phase flow modelling represent a good opportunity to tackle this challenge (Mathieu et al. 2021, Mathieu et al. 2022). In the Eulerian two-phase flow model, both the carrier and the dispersed phase composed of sediment particles are seen as a continuum. Using the Eulerian two-phase flow model is a good compromise between computationally expensive Lagrangian two-phase flow methodologies for which individual particle dynamics have to be computed and single phase flow models for which sediment transport is assumed as empirical bedload and suspended load and bed morphology relies on the Exner equation.

In this study, we apply for the first time the turbulence-resolving Eulerian two-phase flow methodology to investigate bedform formation from a flat bed in a unidirectional flow. The model and numerical configurations are presented in section 2, results are shown and discussed in section 3, then, conclusions are drawn in section 4.

2 MATERIAL AND METHODS

2.1 Eulerian two-phase flow model

The turbulence-resolving two-phase model sedFoam (Chauchat et al. 2017, Mathieu et al. 2021) (https://github.com/SedFoam/sedfoam) is used to simulate the formation of bedforms in unidirectional flows using the Large-Eddy Simulation (LES) methodology.

2.1.1 Governing equations

In the Eulerian two-phase flow formalism, coupled mass and momentum conservation equations for the fluid and the solid phases are solved. The mass conservation for the fluid and the solid phase are given by

$$\frac{\partial(1-\phi)}{\partial t}+\frac{\partial(1-\phi)u_i^f}{\partial x_i}=0 \quad (1)$$

$$\frac{\partial\phi}{\partial t}+\frac{\partial\phi u_i^s}{\partial x_i}=0 \quad (2)$$

respectively with x the position vector, i=1,2,3 representing the streamwise, vertical and spanwise components, ϕ the filtered sediment concentration andu^f, andu^s the fluid and solid Favre filtered velocities.

The fluid and solid momentum conservation equation are written as

$$\frac{\partial\rho^f(1-\phi)u_i^f}{\partial t}+\frac{\partial\rho^f(1-\phi)u_i^f u_j^f}{\partial x_j}= -(1-\phi)\frac{\partial P^f}{\partial x_i}+\frac{\partial}{\partial x_i}\left[T_{ij}^f+\sigma_{ij}^f\right] -I_i+\rho^f(1-\phi)g_i+(1-\phi)f_i^v \quad (3)$$

$$\frac{\partial\rho^s\phi u_i^f}{\partial t}+\frac{\partial\rho^s\phi u_i^s u_j^s}{\partial x_j}=-\phi\frac{\partial P^f}{\partial x_i}-\frac{\partial P^s}{\partial x_i} +\frac{+\partial}{\partial x_i}\left[T_{ij}^s+\sigma_{ij}^s\right]+I_i+\rho^s\phi g_i+\phi f_i^v \quad (4)$$

With ρ^f and ρ^s the fluid and solid densities and P^f and P^s the fluid and solid phase pressures. The effective fluid and solid stress tensors T^f and T^s are given by

$$T_{ij}^f=\rho^f(1-\phi)\nu^f\left(\frac{\partial u_j^f}{\partial x_i}+\frac{\partial u_i^f}{\partial x_j}-\frac{2}{3}\frac{\partial u_k^f}{\partial x_k}\delta_{ij}\right) \quad (5)$$

$$T_{ij}^s=\rho^s\phi\nu^s\left(\frac{\partial u_j^s}{\partial x_i}+\frac{\partial u_i^s}{\partial x_j}-\frac{2}{3}\frac{\partial u_k^s}{\partial x_k}\delta_{ij}\right) \quad (6)$$

Where ν^f and ν^s are the fluid and solid phases viscosities, gis the acceleration of gravity and f^v a volume force driving the flow. Coming from the filtering of the non-linear advection term, σ^f and σ^s are the sub-grid scale stress tensors. The momentum exchange term between the two phases I is modelled using a drag law.

Table 1: Flow, particle and numerical parameters

Configurations	$h(m)$	$u_\tau(m/s)$	$d_p(mm)$	Re_τ	L_x/h	L_z/h	Δx^+	Δz^+	Δy^+ (interface)
Venditti - coarse	0.150	0.028	0.5	4,200	6.3	3.1	114	57	20.0
Venditti - fine	0.150	0.028	0.5	4,200	6.3	3.1	75	38	14.0
Num. Exp. 1 - coarse	0.075	0.020	0.5	1,500	6.3	3.1	25	13	3.0
Num. Exp. 2 - coarse	0.050	0.020	0.5	1000	9.4	4.7	25	13	3.0
Num. Exp. 3 - coarse	0.025	0.020	0.5	500	18.8	9.4	25	13	3.0
Num. Exp. 3 - fine	0.025	0.020	0.5	500	18.8	9.4	20	9	2.4

2.1.2 Closure models

In the LES framework, the effect of the unresolved turbulent scales are taken into account by modelling the sub-grid scale stress tensors. In our study, σ^f and σ^s are modelled using the dynamic Lagrangian methodology derived for the two-phase model by Mathieu et al. (2021).

To represent to complex behaviour of the dispersed solid phase, the solid phase pressure and viscosities are modelled using the kinetic theory for granular flows from Chassagne et al. (submitted) coupled with a frictional model at high volume fraction (Johnson & Jackson 1997, Schaeffer 1987).

2.2 Numerical set-up

In this study, we present six different configurations to assess the predictive capabilities of the two-phase flow model. Two configurations reproduce the experimental configuration from Venditti et al. (2005) designed to investigate the mechanisms of bedform formation. This configuration consists of an unidirectional flow having a depth h=0.15m developing over a flat sediment bed composed of particles having a median diameter d_p= 0.5mm. The Reynolds number Re_τ based on the friction velocity u_τ=0.028m.s^{-1} is equal to 4,200. The two configurations investigated differ by the numerical resolution in order to investigate the grid size dependency. Information on the grid size in wall units for all the configurations are presented in Table 1 together with flow and particle parameters.

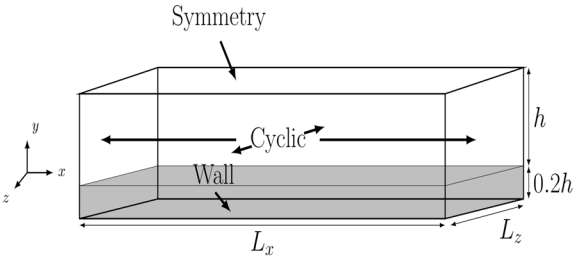

Figure 1: Sketch of the numerical domain and boundary conditions

Four other configurations are preformed as numerical experiments for which there is no experimental data for comparison to investigate the effect of the water depth and grid resolution on the bedform development. Compared with the experimental configuration of Venditti et al. (2005), these numerical experiments have a smaller water depth (h=0.075, 0.05 and 0.025m) and a lower friction velocity u_τ=0.02m.s^{-1} resulting in a lower Reynolds number Re_τ=1500, 1000 and 500. Consequently, we can significantly increase mesh resolution and better resolve the interactions between the fluid turbulence and the sediment bed.

The numerical domain for all six configurations consists of a periodic box with cyclic boundary conditions in the streamwise and spanwise directions, a symmetry plane at the top and a deposited sediment bed having a depth 0.2 h at the bottom (see Figure 1). It differs between the configurations in the water depth, the mesh resolution and dimensions in the streamwise and spanwise directions (L_x and L_z respectively).

3 RESULTS

For all the configurations presented in this study, bedforms develop spontaneously at the top of the sediment bed everywhere in the numerical domain consistently with the observations of Venditti et al. (2005).

Table 2: Quasi-2D ripple length predicted by the two-phase model compared with experimental results

Configurations	λ_{2D}(Num)	λ_{2D}(Exp)
Venditti - coarse	0.103 m	0.110 m
Venditti - fine	0.059 m	0.110 m
Num. Exp. 1 - coarse	0.028 m	-
Num. Exp. 2 - coarse	0.029 m	-
Num. Exp. 3 - coarse	0.030 m	-
Num. Exp. 3 - fine	0.026 m	-

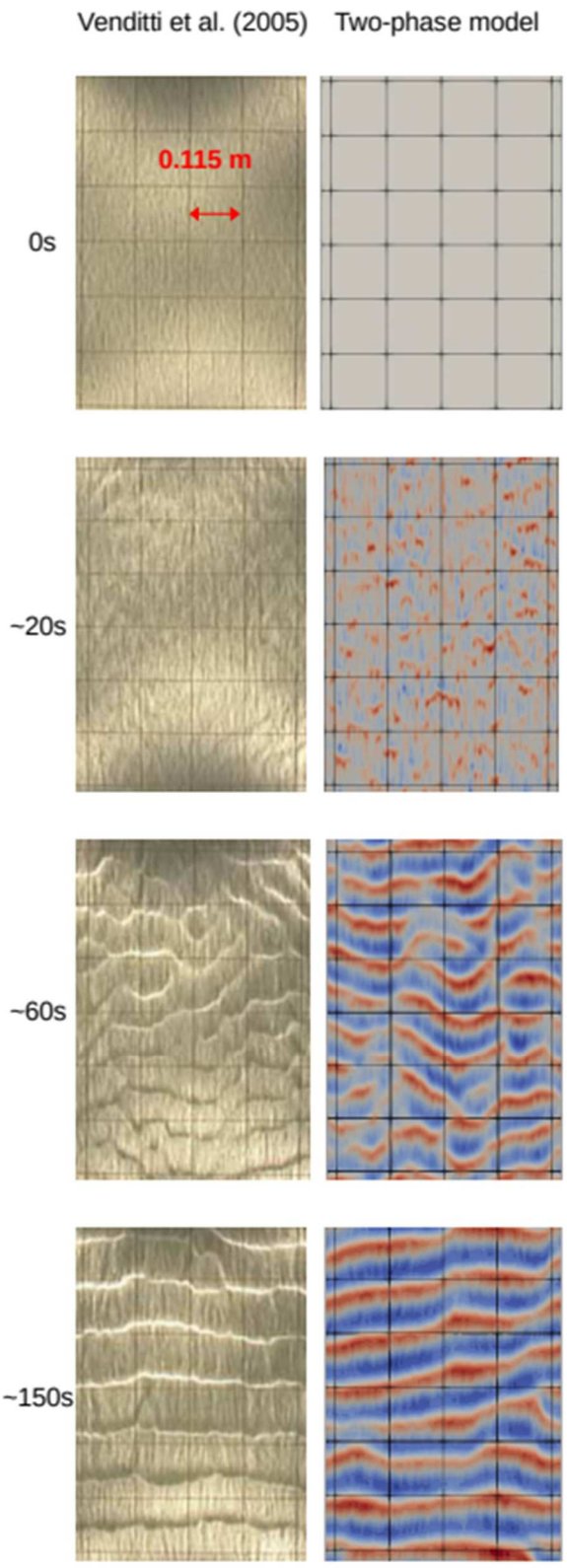

Figure 2: Snapshots of the bed from experimental configuration of Venditti et al. (2005) (left) and numerical simulation with coarse mesh (right) at different times.

Highly unstable in the first few seconds, initial bed defects taking the form of streamwise sediment ridges generated by turbulent coherent structures rapidly transition to more stable quasi 2D ripples having an identifiable length-scale λ_{2D}. This length-scale is presented in Table 2 for all the configurations.

It appears that for the two configurations aiming at reproducing the experiment from Venditti et al. (2005), there is a difference in the lenght-scale λ_{2D} predicted by the two-phase model for a different resolution. Using a coarser mesh gives a larger λ_{2D} ripple length closer to measured data.

Snapshots of the bed taken from the experimental configuration of Venditti et al. (2005) and the numerical simulation using the coarser mesh are presented in Figure 2. The comparison between experiments and the simulation show that the spatio-temporal development of bedforms is qualitatively reproduced by the two-phase model. Starting from a flat bed, turbulent coherent structures drives the generation of small flow parallel sediment ridges which then rapidly evolve into cross-hatch pattern which eventually transition to quasi 2D ripples.

The qualitative prediction of the temporal evolution of bedform formation shows that the turbulence-resolving Eulerian two-phase flow model can potentially be a great tool to investigate the role of the flow hydrodynamics and the fluid turbulence on the mechanisms driving in the initial stage of bedform development. However, it seems that simulation results are significantly affected by the mesh resolution. Grid size dependency needs before the model can be used to predict ripple evolution, which is known to strongly depend on grain size and flow intensity.

For the numerical experiments, the predicted λ_{2D} slightly increases for decreasing water depth. However, this increase can not be considered significant considering that λ_{2D} only increases by 7% for a water depth smaller by a factor 3. This confirms that our numerical experiments lie in the ripple regime for which the length-

scale associated with the bedform is independent of the water depth.

Snapshots of the bed elevation for the three numerical experiments using a coarse resolution are shown on Figure 3.

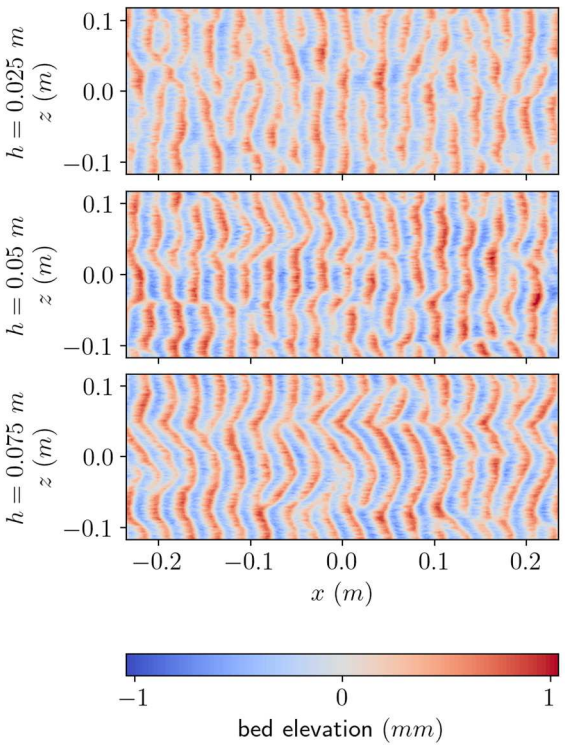

Figure 3: Colormaps of bed elevation for numerical experiments 1, 2 and 3 using the coarser mesh at the quasi-2D stage of ripple development

Even if the streamwise length-scale associated with the ripples is similar for the three numerical experiments, it appears from Figure 3 that the spanwise morphological evolution of the bed is more affected by the water depth with more sinuous ripples for increasing water depth. This can be attributed to the interaction between the ripples and the large-scale turbulent structures scaling with the water depth.

Similarly to the configurations reproducing the experimental configuration of Venditti et al. (2005), the ripple length predicted for the numerical experiment 3 is sensitive to the mesh resolution.

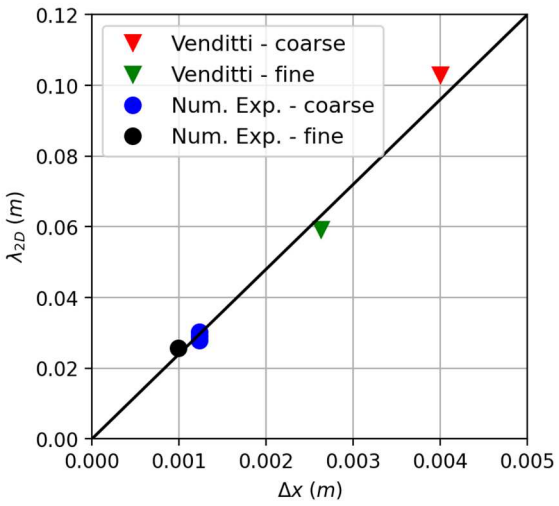

Figure 4: Predicted ripple length by the Eulerian two-phase flow model as a function of the grid size in the streamwise direction

Figure 4 confirms that there is a clear dependency between the predicted ripple length and the grid size in the streamwise direction. This issue needs to be addressed in the future by more comprehensive grid convergence test and comparison with linear stability analysis to determine its origin and to be able to quantitatively predict the spatio-temporal evolution of the ripple formation process.

4 CONCLUSIONS

In this study, numerical simulations of bedform formation in an unidirectional flow starting from a flat bed using a turbulence-resolving Eulerian two-phase flow model are presented. It is the first attempt to apply this modelling methodology to bedform formation configurations. Using turbulence-resolving two-phase flow model can significantly improve our understanding of the mechanisms at the origin of bedform formation, especially the interactions between the turbulent coherent structures and the sediment bed.

Two configurations reproducing an experiment if Venditti et al. (2005) and four additional numerical experiments allowed to investigate the effect of the water depth and the numerical resolution on the predicted ripple length. Comparison between snapshots of the resolved bathymetry from the

experiment and the simulation showed that the main features of the spatio-temporal evolution of bedform are reproduced by the two-phase model. The numerical experiments showed that the dependency between the predicted quasi-2D ripple length and the water depth is not significant as should be expected in the ripple regime. However, numerical results show a grid-size dependency. This issue needs to be addressed in the future.

5 REFERENCES

Best, J., 2005. The fluid dynamics of river dunes: A review and some future research directions. Journal of Geophysical Research – Earth Surface, 110, F04S02, doi:10.1029/2004JF000218

Bucher, W.H., 1919. On ripples and related sedimentary surface forms and their paleogeographic interpretation. American Journal of Science, s4-47 (279), 149-210, doi:10.2475/ajs.s4-47.279.149

Charru, F., Andreotti, B., Claudin, P., 2013. Sand Ripples and Dunes. Annual Review of Fluid Mechanics, 45, 469-493, doi:10.1146/annurev-fluid-011212-140806

Chassagne, R., Chauchat, J., Bonamy, C., (submitted). Journal of Fluid Mechanics

Chauchat, J., Cheng, Z., Nagel, T., Bonamy, C., Hsu, T.-J., 2017. SedFoam-2.0: a 3-D two-phase flow numerical model for sediment transport. Geoscientific Model Development, 10, 4367-4392, doi:10.5194/gmd-10-4367-2017

Engelund, F., Fredsoe, J., 1982. Sediment Ripples and Dunes. Annual Review of Fluid Mechanics, 14, 13-37, doi:10.1146/annurev.fl.14.010182.000305

Fourrière, A., Claudin, P., Andreotti, B., 2010. Bedforms in a turbulent stream: formation of ripples by primary linear instability and of dunes by nonlinear pattern coarsening. Journal of Fluid Mechanics, 649, 287-328, doi:10.1017/S0022112009993466

Johnson, P.C., Jackson, R., 1987. Frictional–collisional constitutive relations for granular materials, with application to plane shearing. Journal of Fluid Mechanics, 176, 67-93. doi:10.1017/S0022112087000570

Kennedy, J.F., 1963. The mechanics of dunes and antidunes in erodible-bed channels. Journal of Fluid Mechanics, 16(4), 521-544. doi:10.1017/S0022112063000975

Kuru, W.C., Leighton, D.T., McCready, M.J., 1995. Formation of waves on a horizontal erodible bed of particles. International Journal of multiphase Flow, 6, 1123-1140, doi:10.1016/0301-9322(95)00035-V

Mathieu, A., Chauchat, J., Bonamy, C., Balarac, G., Hsu, T.-J. (2021). A finite-size correction model for two-fluid large-eddy simulation of particle-laden boundary layer flow. Journal of Fluid Mechanics, 913, A26. doi:10.1017/jfm.2021.4

Mathieu, A., Cheng, Z., Chauchat, J., Bonamy, C., Hsu, T.-J. (2022). Numerical investigation of unsteady effects in oscillatory sheet flows. Journal of Fluid Mechanics, 943, A7. doi:10.1017/jfm.2022.405

Perillo, M., Best, J., Yokokawa, M., Sekiguchi, T., Takagawa, T., Garcia, M., 2014. A unified model for bedform development and equilibrium under unidirectional, oscillatory and combined-flows. Sedimentology, 61(7), 2063-2085, doi:10.1111/sed.12129

Schaeffer, D., 1987. Instability in the evolution equations describing incompressible granular flow. Journal of Differential Equations, 66(1), 19-50, doi:10.1016/0022-0396(87)90038-6

Venditti, J., Church, M., Bennett, S., 2005. Bed form initiation from a flat sand bed. Journal of Geophysical Research – Earth Surface, 110, F01009, doi:10.1029/2004JF000149.

Estimation of marine dune migration using a three-dimensional numerical modelling

N. Michelet *France Energies Marines, Brest, France – nicolas.michelet@france-energies-marines.org*
M. Bary Univ Rouen Normandie, UNICAEN, CNRS, M2C UMR 6143, F-76000 Rouen, France – *bary.mathilde@gmail.com*
O. Blanpain *France Energies Marines, Brest, France*
S. Le Bot Univ Rouen Normandie, UNICAEN, CNRS, M2C UMR 6143, F-76000 Rouen, France – *sophie.lebot@univ-rouen.fr – sophie.lebot@univ-rouen.fr*
M. Nexer *France Energies Marines, Brest, France*
A. Lefebvre *Marum – Center for Marine environment Sciences, University of Bremen, Bremen, Germany*

ABSTRACT: A study using the dune Tracking method and based on bathymetric surveys performed over the Dunkirk future windfarm cable corridor area, show that dune migration is mostly eastward. However, during a month between March and April 2020, on the study area which comprise 6 dunes, 4 of the dunes move toward the west while two others follow the general eastward tendency. An estimation of the sediment fluxes using empirical formulation identify the influence of the current, waves and free-surface evolution and brings a first explanation on this inversion of migration direction. However, this study is made in 0D (calculations are made at a single point) and do not allow to understand the intra- or inter-dune variability as shown by the measured migration speeds. To overcome this limitation and start to investigate the dune migration, a fully non-linear three-dimensional numerical model was implemented using the CROCO modelling system, which included the sediment transport module developed by USGS. An idealized case was setup on a numerical domain covering the dune field (1000m x 500m) using bathymetric and sediment grain-size data as ground boundary and forced with idealized current and waves.

1 INTRODUCTION

In the next few years, an offshore wind farm (OWF) will be installed off the coast of Dunkirk on a large marine dune field. To ensure the safety criterium for the windfarm structures and to evaluate their impact on the seabed it is necessary to understand the dynamics of the underwater dunes. Eight bathymetric surveys were performed between November 2019 and July 2021 on a box located along the export cable corridor (Table 1). Morphometric parameters and migration rates was measured from the bathymetric data and the dynamic of these dunes was estimated through the associated sediment fluxes calculated using the Dune Tracking method (Bary et al., 2021). Results showed that the dunes migration is generally eastward and reaches up to several meters per month. However, between March and April 2020, based on the crest movements, most of them seem to have a westward propagation due to the presence of strong winds coming from the East-North-East. An estimation of sediment fluxes associated to the dune mobility was performed using a zero-dimensional (0D) model (Michelet et al., 2022). It brings a first explanation on this migration direction inversion by highlighting the major influence of the wave forcing. When there is no storm, the stronger flood currents than ebb currents result in an eastward dune migration. However, the synchronization of the low tide with the ebb current peak during some storm can generate a stronger current-wave bottom stress during the ebb period than during the flood. More sediment are thus mobilized and the bedload

flux increases during the ebb compared to the flood, and results in an overall westward propagation. This calculation was however made in 0D and cannot explain the fact that during the same survey period, some dunes migrate eastwards and other westwards.

Table 1: Bathymetric surveys dates.

Survey name	Date
S1	16/11/2019
S2	17/03/2020
S3	16/04/2020
S4	31/08/2020
S5	05/12/2020
S6	22/01/2021
S7	27/05/2021
S8	03/07/2021

Using the second bathymetric survey (named S2) as the initial state of the bed, a three-dimensional simulation was setup with idealized forcing. The aim of the study is to understand the relative influence of the current and waves on the morphological changes and bring insight to understand the observed migration patterns.

2 DATA & METHOD

2.1 Study site

The numerical domain is based on an area (named B1) located off the Dunkirk coast along the windfarm export cable corridor (Figure 1). On this area, the bathymetric surveys show a dune field with, from west to east, two barchans, a sinuous one and three rectilinear dunes.

The area is macrotidal with a stronger maximum flood than ebb velocities (1.25 m/s against 0.75 m/s, Latapy, 2020). In term of wave forcing, the major part comes from the English Channel, from the west, while the other comes from the inside of the North Sea. Bonnefille et al. (1971) collected data and showed that the wave period is comprised between 5 and 12 s while the significant wave height is generally lower than 1.2 m and could reach 3 m during storm events (Latapy, 2020).

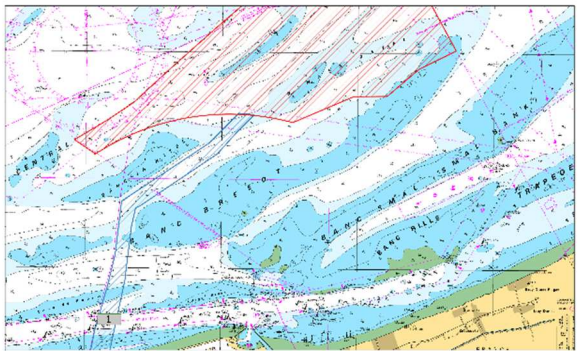

Figure 1. Location of Dunkirk windfarm area (red area) and the area of interest where bathymetric surveys were performed noted 1 on the figure.

2.2 CROCO model description

CROCO is a three-dimensional, free-surface numerical model that solves finite-difference approximation of the Reynolds-Averaged Navier Stokes (RANS) equation using the hydrostatic and Boussinesq approximations. The flow is assumed to be turbulent over a rough bottom allowing the existence of a logarithmic profile. The computation is performed using a C-Arakawa

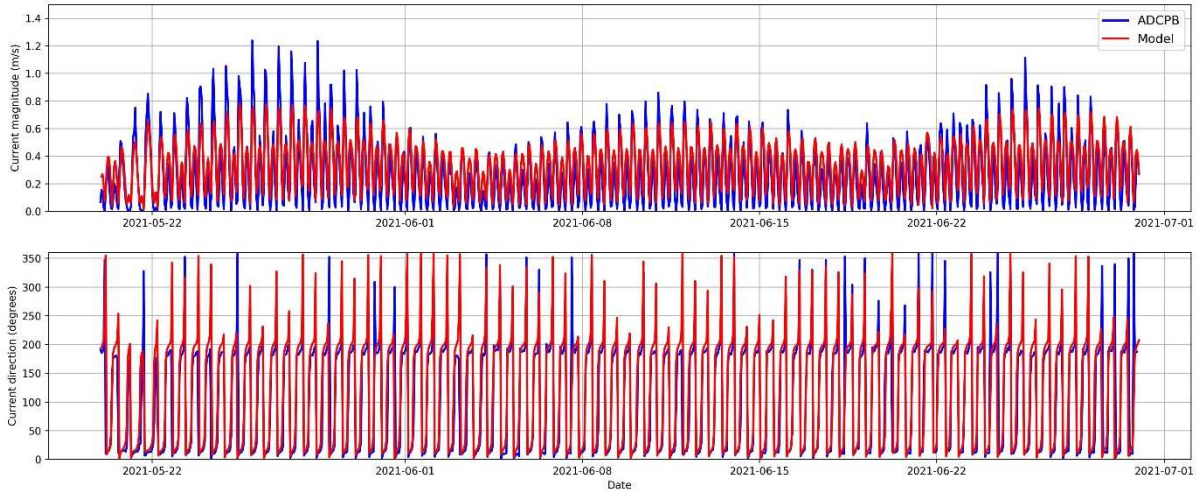

Figure 2. Current magnitude and direction comparison between regional simulation and Acoustic Doppler Current Profiler (ADCP) on B1 area.

grid over horizontal dimensions and a terrain following σ coordinate along the vertical dimension.

2.3 Sediment module

Like the water column, the sediment is represented as a constant number of layers that extend under the horizontal water cells (Warner et al., 2005). Each layer is initialized with a thickness, sediment-class distribution, porosity and age. The in-situ analysis showed that the sediment is homogeneous over the area so that a medium sand with d_{50} = 328 µm is considered in the class distribution. The porosity is also set constant (0.41). Since no suspended sediment is considered, the sediment age is left to 0 the default value. To initiate the morphodynamic study, only the bedload transport was considered. The formulation of Meyer-Peter Muller (1948) is used. Therefore, the bedload flux depends on the skin-friction component of bottom stress which is calculated with the maximum wave-current combined stress. The bed evolution is calculated using the Exner equation. Since the suspended sediment transport is not considered, no erosion or sedimentation is included in the equation which is then written as follow:

$$\frac{\partial z_b}{\partial t} = -\frac{f_{mor}}{1-p}\left(\frac{\partial q_b}{\partial x}\right) \quad (1)$$

The height of the bed z_b is then function of the bedload flux q_b, the sediment porosity p and the morphological acceleration factor f_{mor}, here set to 10.

2.4 Model setup

Current and free-surface elevation were defined following the results of a preliminary regional simulation performed on an area covering the Eastern part of the English Channel and the southern part of the Northern Sea. This simulation was validated against tidal gauge (not shown here) and Acoustic Doppler Current Profilers data (ADCP). The mean averaged error for the barotropic current magnitude is 0.11 m/s (Figure 2).

Based on these results, an idealized mean spring tidal cycle were created accounting for the asymmetrical features regime in this area. The current direction was extracted at each peak and are respectively N70° and N250° during flood and ebb periods. In the same way, an idealised free-surface elevation was created which accounts for the synchronisation of the low tide with the ebb peak and the high tide with the flood peak (Figure 3).

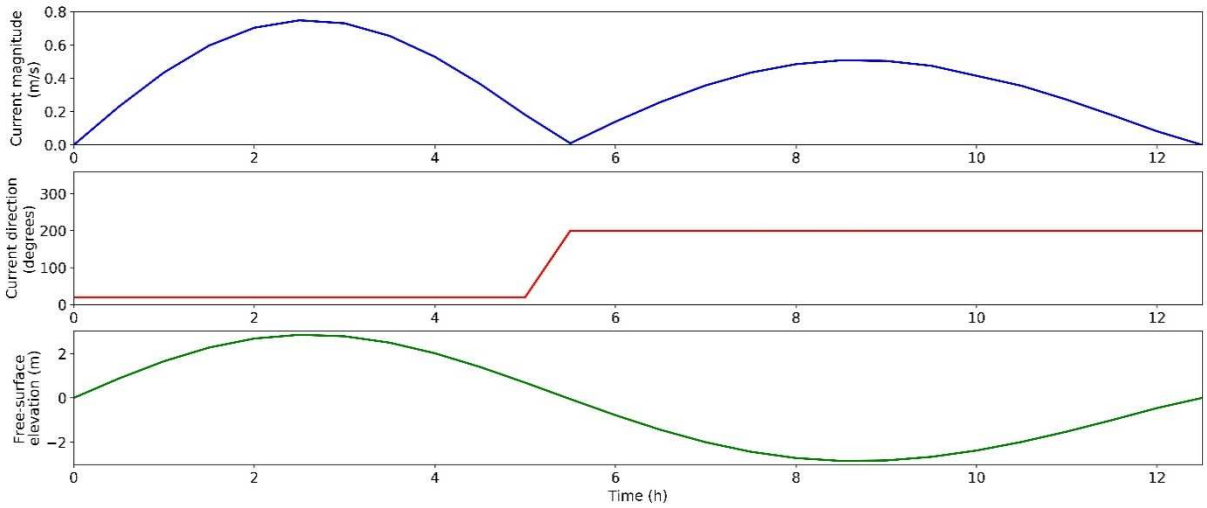

Figure 3. Current magnitude, current direction and free-surface elevation idealized forcing.

Two cases were setup and run over 4 days with a morphological acceleration factor of 10. In both cases current and free-surface elevation conditions described above are repeated in loop. On the Case 1, no wave forcing is accounting while on Case 2, constant wave conditions were considered and fixed to the maximum significant wave height observed during the period between S2 and S3 (Table 1). It is then fixed to Hs = 2 m with a peak period of Tp = 6 s. Wave direction is also set this way to come from the East-North-East (N33.75°).

3 RESULTS AND DISCUSSION

3.1 Effect of tidal currents

The following figure 4 represents the difference between the initial and final bathymetry after a simulation without waves. The current induces an important sediment transport over the dunes with the stronger bathymetric difference on the two barchans varying between 0.5 and 1 m depending on the position on the dune. This difference indicates that the stronger sediment transport is located over the higher dunes. Since the current forcing is the same over the entire area, these higher values are due to the dune morphology and especially to the shallow depth of their crests. The shallower the dune crest, the stronger the bathymetric variations. Indeed, the barchans have a mean height of 2.04 m and 1.95 m while the third dune is 1.61 m height. The variation of this last one is lower than those of the barchans with values comprised between 0.25 and 0.75 m. Variations are strongly reduced for the three rectilinear dunes located to the east in accordance with their mean heights of 1.08 m, 0.85 m and 0.69 m, from west to east respectively.

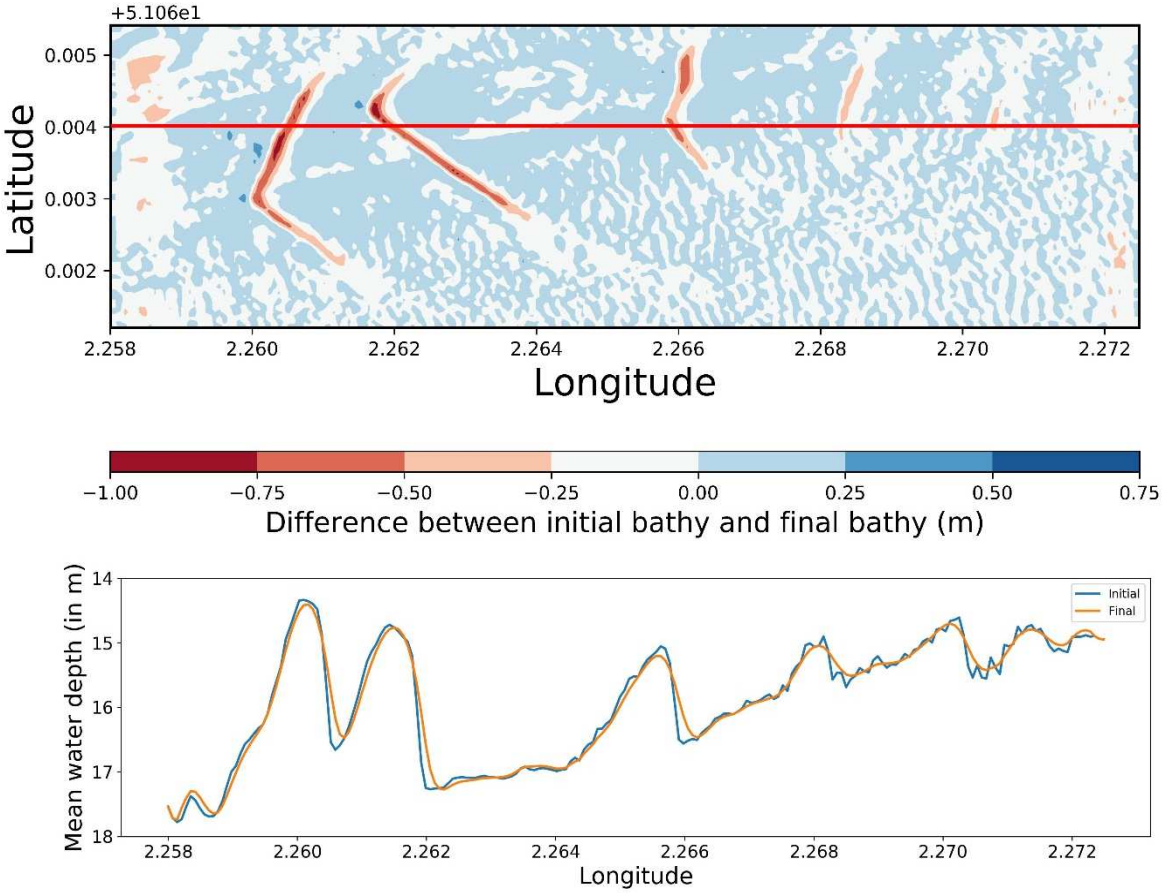

Figure 4: Top Difference between initial and final bathymetry for the case without wave forcing. The red line shows the location of the longitudinal profile displayed on the lower panel. Bottom. Initial (blue) and final (orange) longitudinal profiles from the case without wave forcing.

The lower panel of figure 4 represents the longitudinal profile of the initial and final bathymetry for the simulation without waves. The initial profile show that the six primary dunes are superimposed with smaller secondary dunes and ripples. These structures are smoothed by the model which does not consider their migration. It thus estimates a stronger erosion over the four dunes on the east compared to the 2 barchans on the west. This model does not consider the migration of these smaller structures and since their presence should favour the migration of the primary dunes (Idier et al., 2002), the influence of the current here might be underestimated.

The migration of the primary dunes is however in accordance with the forcing. The difference between the two profiles, shows that the highest bathymetric variations are located on the troughs and the crestal parts of the dunes. This movement is in accordance with the flood dominant current which then induce a sediments transport from the crests to the eastern troughs.

3.2 Effect of the waves

On Case 2, the forcings were tidal current and wave. This wave climate is homogeneous and constant over the whole period which means that its influence on the sediment transport is then related to the bathymetric differences. The combination of current-wave bed shear stress is naturally higher and then induce stronger sediment transport than in Case 1 with current alone. Le Bot & Trenteseaux (2004) have noted that the influence of strong waves formed by a storm can reduce, cancel, or even inverse dune

migration direction. Here, the results are in accordance with their observation. The stress induced by the wave is stronger during the ebb period due to the synchronization with the low water level. The difference of bed shear stress between flood and ebb period is then weakened. Over the tidal cycle, the residual transport is then lower which could result in a migration reduction.

This influence is well represented over the second dune with an increase of its height. Indeed, as described by Tonnon et al. (2007), as long as the bedload transport is dominant, a symmetrical tidal current will result in the increase of the dune height. Here, the difference between the bed shear stress at ebb and flood current peaks is reduced but still slightly stronger during flood period. Therefore, the influence of this forcing is closer to a symmetrical tidal current. In could then explain that in Case 2 (contrary to Case 1) the second dune crest depth is reduced while at the same time its trough is moving eastward.

Over the two barchans on the west, the forcing induces either an increase of the dune height for the second dune or only a weak change of the crest for the first dune. However, on the following dunes, the most notable changes concern their morphology. In the case of the third dune, the difference between the initial and final bathymetry shows a reduction of the horizontal asymmetry of this dune. Its morphology adapts to the forcing and its crest is then moving toward the west while the eastern trough is following the general tendency.

This difference of migration direction between crests and troughs brings more insight on the migration inversion observed between surveys S2 and S3. Indeed, the Dune Tracking method was applied on a short period of 30 days (March – April 2020). The dune migration speed and direction were estimated following the difference of the crest's positions between these two surveys. However, during this period, the influence of a storm and the waves coming from the East-North-East could then induce a temporary reduction of its asymmetry or the movement of a secondary dune (at the crest) to the west. It could then let think that it is moving toward the west. Figure 5 also displays the migration direction of the crests and troughs. As we can see, all troughs are moving toward the east in accordance with what is expected. However, the crests of the dunes 3, 4 and 5 show an opposite movement. Here on the dune 4, the smoothing of the secondary dunes artificially moves the crest to the west but for dune 3 and 5, the westward movement of the sediment induce a clear reduction of the asymmetry.

By estimating the migration with the crest positions difference for the Dune Tracking, the results would then show an inter-dune variability with multiple dunes moving

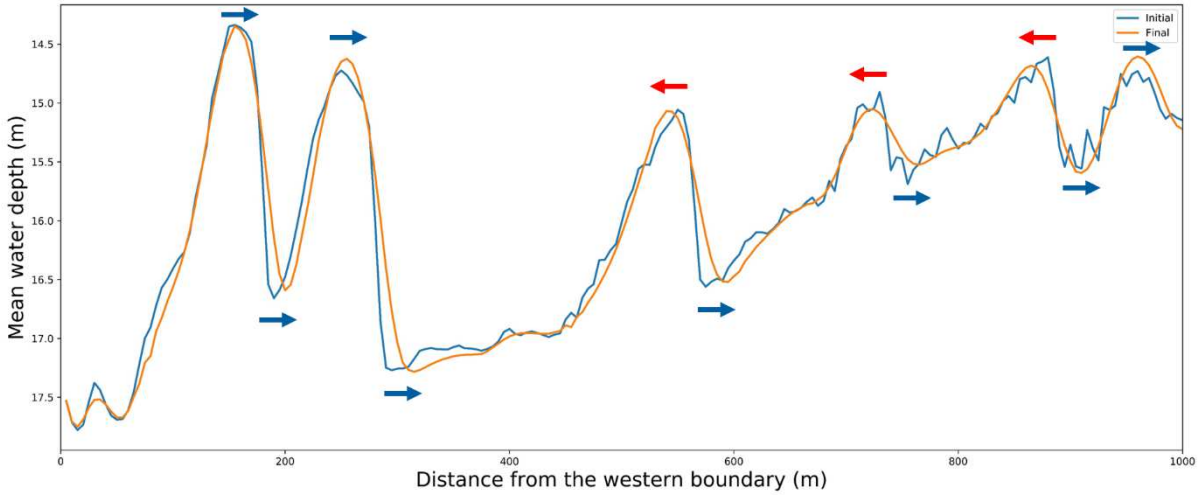

Figure 5. Initial and final longitudinal profiles from the case accounting the wave forcing along the red line displayed on the top panel of Figure 4. Blue and red arrows respectively show the eastern and western migration of the crests and troughs.

toward the west and some towards the east. However, over this short period, by only considering the crest position, it is difficult to assess if we are looking at the crest movement or the entire dune movement. In order to avoid this potential bias creating by dune crest movement, Ernstsen et al. (2006), recommend applying this method by considering the troughs positions. They also suggest to perform it on surveys conducted at similar times during the tidal period. That is because they saw some strong variations of the crest position during a tidal period. Our results show a modification of some dunes morphology which are created by wave activity. In this case, the influence of the waves is much stronger than in reality since it is considered constant during 4 days. However, it illustrates some modifications that could appears during a short period of time and should be considered when analysing bathymetric surveys.

This limitation on the estimation of the migrations parameters is however limited to small migration distances. For the other surveys that have shown movement of tens of meters for each dune, the movement of the crest or the change of its horizontal asymmetry would not induce any difference on the migration direction. Therefore, to make sure that the dune migration was affected between surveys S2 and S3, the migration speed and direction estimation used in the Dune Tracking method should also be performed on the trough. Moreover, it could be interesting to apply the method proposed by Knaapen (2005) which used either the movement of the crests and troughs to determine the dune migration. A comparison of the results of both methods would then give more information on the dune movement during this short period.

4 CONCLUSION

An idealized three-dimensional model including the morphodynamics was implemented to understand the migration direction observed between two bathymetric surveys performed off the Dunkirk coast. The bathymetry initialized in the model come from an in-situ survey (March 2020) while idealized hydrodynamic forcings were setup with and without waves. Two simulations were run with idealised boundary conditions, the first with the influence of the tides only, the second with tides and waves. On both simulations, the model smoothed the secondary dunes, and results can only be used to consider the primary dune morphodynamic.

Submitted to a (eastward) flood dominant current, all dunes follow an eastern migration. An erosion is predicted on the crest and deposition is observed at the foot of the dune steep side, in the trough, inducing its movement to the east. Sediment transport is stronger over the shallower crests than over the deeper ones. Including the influence of idealised waves (representing a storm impact) change this migration and equilibrate the bottom shear stress between flood and ebb periods. Some dune movement is then closer to morphodynamic observed in a symmetrical tidal environment. The height of the symmetrical dunes is increasing while the horizontal asymmetry is reduced for others.

These results show that the movement of a dune is then not homogeneous. The movement of the crest may not represent the migration of the whole dune. Indeed, beside its migration, a dune morphology could also change. In particular cases like between S2 and S3, the migration might then be misunderstood if only the displacement of the dune and not its morphological evolution is considered. A combination of the modification of the crests and troughs positions should then be applied to avoid accounting for short-term processes and/or morphology evolution in the study of the global migration of these forms. A perspective of this study would be then to estimate the migration speed and direction using this combination and a classical method and compare the different information that could be extracted using both.

5 ACKNOWLEDGEMENT

This work has received support from France Energies Marines and the State, managed by the National Research Agency under the Investments for the Future program, bearing the reference ANR-10-IEED-0006-34.

6 REFERENCES

Bary, M., Le Bot, S., Nexer, M., Garlan, T., Blanpain, O., Kervella, Y., Horrani, S., Turki, I., 2021. Morphodynamique de dunes sous-marines et flux sédimentaires associés à l'échelle mensuelle à saisonnière. Cas du futur parc éolien au large de Dunkerque. 27ème Réunion des Sciences de la Terre, Lyon, 01-05 Novembre 2021.

Bonnefille, R., Lepetit, J.P., Graff, M., Leroy, J., 1971. Nouvel avant-port de Dunkerque, Mesures en nature. Laboratoire National d'Hydraulique. Report HC042/05.

Ernstsen, V.B., Noormets, R., Winter, C., Hebbeln, D., Bartholomä, A., Flemming, B.W., Bartholdy, J., 2006. Quantification of dune dynamics during a tidal cycle in an inlet channel of the Danish Wadden Sea. Geo-Marine Letters, 26, 151-163.

Idier, D., Ehrhold, A., Garlan, T., 2002. Morphodynamique d'une dune sous-marine du détroit du Pas de Calais. Comptes Rendus Geoscience, 334, 1079-1085.

Knaapen, M.A.F., 2005. Sandwave migration predictor based on shape. Journal of Geophysical research, 110.

Latapy, A., 2020. Influence des modifications morphologiques de l'avant-côte sur l'hydrodynamisme et l'évolution du littoral des Hauts-de-France depuis le XIXe siècle. Thèse de Doctorat, université du Littoral Côte d'Opale.

Le Bot, S., Trentesaux, A., 2004. Types of internal structure and external morphology of submarine dunes under the influence of tide- and wind-driven processes (Dover Strait, northern France). Marine Geology, 211, 143-168..Michelet, N., Bary, M., Blanpain, O., Le Bot, S., Nexer, M., 2022. Estimation de l'influence des conditions hydrodynamiques sur les flux sédimentaires associés à la migration des dunes au large de Dunkerque. Journée Nationales Génie Côtier – Génie Civil, Chatou, 2022.

Peter-Meyer, E., Muller, R., 1948. Formulas for bed load transport. Proceedings of 2nd meeting of the international association for hydraulic structures research, Delft, 39-64.

Tonnon, P.K., Van Rijn, L.C., Walstra, D.J.R., 2007. The morphodynamic modelling of tidal sand waves on the shoreface. Coastal Engineering, 54, 279-296.

Warner, J.C., Sherwood, C.R., Arango, H.G., Signell, R.P., 2005. Performance of four turbulence closure models implemented using a generic length scale method. Ocean Modelling, 8, 81-113.

Coexistence of two dune growth mechanisms

C. Narteau *Université Paris Cité, Institut de Physique du Globe de Paris, CNRS, France – narteau@ipgp.fr*
S. Courrech du Pont *MSC, Université Paris Cité, CNRS, France – sylvain.courrech@u-paris.fr*

ABSTRACT: We review field measurements, subaqueous laboratory experiments and numerical simulations documenting dune growth, shape and alignment under multidirectional flow conditions. In zones of infinite sand supply, dune patterns select the orientation for which the sand flux perpendicular to the crest is maximum. In zones of low sand availability, dunes tend to align with the direction of the resultant sand flux at the crest. In the first case, periodic dunes grow in height from the available sedimentary resource in the interdune area. In the second case, dunes elongate by developing a finger-like structure on the non-erodible ground. These two dune growth mechanisms are modelled and quantified from the dynamic interactions between topography, flow and sediment transport to predict dune orientation, wavelength, migration speed and growth rate. This framework can provide new information about flow conditions and sediment properties in remote places where dunes exhibit different orientations, especially in marine environments.

1 INTRODUCTION

In all environments in which they occur, in arid deserts, underwater, or on other planets, dune fields often exhibit complex shapes combined with ridges of variable orientation. According to local sediment transport and flow properties, it is therefore essential to understand the origin of such diversity by documenting the mechanisms of dune growth based on elementary physical processes.

Dunes have been primarily classified according to their shape considering both sand availability and flow directional variability (Wasson & Hyde, 1983). In aeolian research, the wind directional variability is usually measured by the RDP/DP dimensionless parameter (Fig. 1). It is the ratio between the resultant drift potential (RDP, the norm of the mean sand flux vector) and the drift potential, DP (the mean of the norms of the individual sand flux vectors). In zones of low sand availability under nearly unidirectional winds (i.e., for high, close to one, RDP/DP-values), crescentic barchan dunes propagate on a non-erodible ground (Fig. 1). Under the same wind conditions, barchanoid and transverse linear dunes form where sand availability increases. They all exhibit a strong asymmetry between a gentle upstream slope and a slip face in the lee. On the other hand, network dunes and star dunes are observed in major depositional centers exposed to wide multidirectional wind regime (i.e., where the RDP/DP-value tends to zero). For intermediate wind directional variability, linear dunes develop. Given the seasonal changes in wind direction on Earth, these linear dunes are widespread in terrestrial sand seas, but their alignments, symmetry and slopes vary greatly depending on the sand availability and the wind regime.

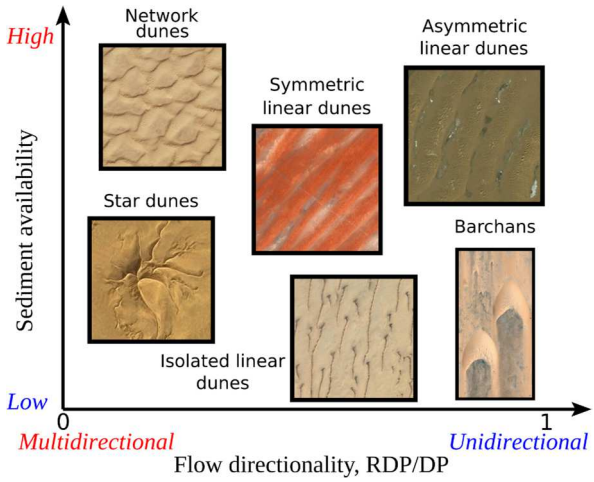

Figure 1. Classification of dune shape according to wind directionality and sediment availability (modified from Wasson & Hyde, 1983).

Dunes have also been classified according to their orientation. The crest lines of barchan dunes are approximately perpendicular to the resultant transport direction, whereas, by definition, the interlaced arms of star dunes have no unique orientation (Zhang et al., 2012). For linear dunes, Hunter et al. (1983) used the angle Φ between their crestlines and the resultant transport direction on a flat sand bed to describe them as longitudinal (Φ≤15°), oblique (15°<Φ<75°) or transverse (Φ≥75°).

A significant breakthrough in understanding the relationships between bedform orientation and flow regime was the work of Rubin & Hunter (1987). When considering a bidirectional flow regime, they experimentally showed that subaqueous bedforms select the orientation for which the sum of the normal to crest components of the two transport vectors reaches its maximum value. Thus, they introduced the gross bedform-normal transport rule (from now the GBNR), which can be generalized to multidirectional flows in natural environment (Ping et al., 2014). Using this rule together with the dune shape classification, a given wind regime should therefore be associated with a specific dune type and a single orientation. This unique line of reasoning has been recently challenged on the basis of experimental, numerical and field observations. Here, we review these observations and present a set of evidences that demonstrate that two dune growth mechanisms can be at work and coexist. According to sand availability and flow properties, we develop a formalism for dune pattern recognition, including qualitative and quantitative variables such as dune shape, orientation, wavelength and growth rate.

2 TWO DUNE GROWTH MECHANISMS

Comparing the dune orientations in arid desert on Earth with the alignment predicted by the GBNR, Lancaster (1991) observed a clear mismatch for linear dunes. In addition, dunes with different orientations are locally observed in many planetary environments, and asymmetric barchans clearly exhibit two crest orientations, one associated with the main crescentic body, the other associated with the alignment of the longer arm. All these observations indicate that there was a hidden controversy about dune orientation and that current models were not sufficient to explain the observed diversity of dune patterns.

Using underwater laboratory experiments, Reffet et al. (2010) showed that under symmetric bidirectional flow with a divergence angle θ_d>90°, a sand pile located on a non-erodible bed slowly transforms into a longitudinal linear dune. Its crest is aligned with the mean flow and advection directions, causing the growth of a finger-like structure at the downstream end of the crest. By numerically exploring different multidirectional flow regimes with no resultant transport on a flat sand bed (RDP=0), Zhang et al. (2012) reproduced for the first time the formation of star dunes with arms elongating in multiple direction. Overall, we demonstrated that the finger-like structures associated with star-dunes arms were in fact not aligned according to predictions of the GBNR (Fig. 2a). Instead, this specific type of dunes elongate in the direction of the sediment flux at the crest, which may significantly differ from the direction of the sand flux on a flat sand bed because of the speed-up effect (i.e., the acceleration of the flow over a positive topography). It then became clear that this essential ingredient had to be taken into account to predict dune orientation and that it was necessary to evaluate the impact of sediment availability, not only on dune shape, but also on dune growth and orientation.

On the basis of this evaluation, a new set of underwater laboratory experiments with asymmetric bidirectional flow regimes, and different conditions of sediment availability have been developed. According to the bedform dynamics observed in these experiments, Courrech du Pont et al. (2014) demonstrated that there are indeed two dune growth mechanisms and that sediment availability selects the overriding mechanism for dune formation or evolution (Fig. 2b):

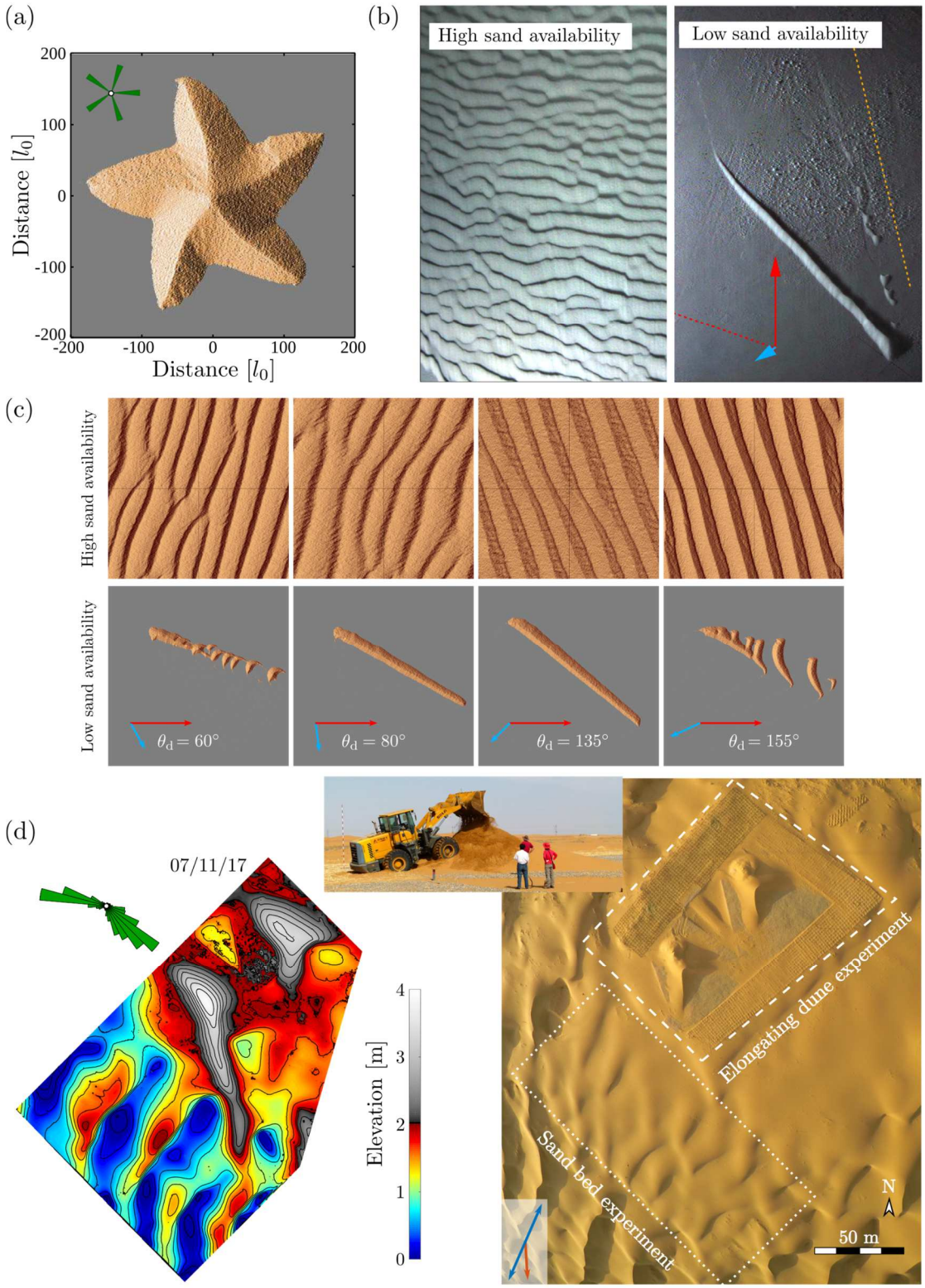

Figure 2. Two dune growth mechanisms: (a) Numerical simulations of star dunes (Zhang et al., 2012). Crest alignments switch from the bed instability to the elongating mode where sediment is no longer available. (b) Subaqueous laboratory experiments with the same wind regime (see arrows) but different condition of sediment availability (Courrech du Pont et al., 2014). Dashed and dotted lines show the bisector and the resultant sediment flux on a flat surface, respectively. (c) Same as (b) using numerical simulations (Gao et al., 2015) for different angles of divergence θ_d. (d) Landscape scale experiment showing the coexistence of the two dune growth mechanism under natural wind conditions (Lü et al., 2021; Lü et al., 2022).

1- On an erodible sand bed, dunes grow in height and migrate selecting the orientation αI for which the normal-to-crest components of transport are maximum, a result consistent with the GBNR when considering the speed-up effect. This is the bed instability mode, which refers to the ability for a sand bed to organize in periodic bedforms as soon as there is transport

2- On a non-erodible ground, dunes grow by elongation away from the source of sediment in the direction αF of the resultant sand flux at the crest. This is the fingering or the elongating mode. Classical geomorphological sand sources are depositional areas related to coastal or river systems, topographic obstacles or pre-existing dunes (Gadal et al., 2020b).

Hence, the same multidirectional wind regime is associated with two modes of dune orientations according to the sand availability. These two modes may locally coexist as a result of changes in sediment availability or due to the development of superimposed bedforms.

In addition to the model described below (Sec. 3), the spatial and temporal development of incipient dunes in the bed instability mode can also be theoretically analyzed through a linear stability analysis (Elbelrhiti et al., 2005; Narteau et al., 2009, Lü et al., 2021). In multidirectional flow regimes, it predicts not only dune orientation but also the selected pattern wavelength, the associated initial growth rate, and propagation velocity (Gadal et al., 2019; Gadal et al., 2020a; Lü et al., 2021). While the elongating mode of dune growth is not associated with a specific size-selection mechanism, the observed periodicity in fields of elongating dunes reflects the interdependence of dune patterns over the course of their evolution, when they develop from periodic dunes in the bed instability mode or interact through collisions or flow perturbations (Gadal et al., 2020b).

3 A MODEL FOR DUNE ORIENTATIONS

Let us consider an infinite linear dune of orientation α of height H, and width 2W. To account for the wind speed-up, the shear velocity vector $\boldsymbol{u}_{\mathbf{flat}}$ and the flow orientation θ can be used to determine the shear velocity at the crest

$$\boldsymbol{u}_{\mathbf{crest}} = \boldsymbol{u}_{\mathbf{flat}} \left(1+\beta \left(H/W\right) \left|\sin(\theta- \alpha)\right|\right) \quad (1)$$

where (H/W)|sin(θ- α)| is the aspect-ratio of the dune experienced by the flow and β a dimensionless coefficient that takes into account other physical ingredients (e.g., roughness) affecting surface wind speed (Jackson and Hunt, 1975). Then, a transport law adapted to the studied environment can be used to determine the flux vectors $\boldsymbol{Q}_{\mathbf{flat}}$ and $\boldsymbol{Q}_{\mathbf{crest}}$ on a flat sand bed and at the crest, respectively. The parallel- and normal-to-crest components of transport at the crest are

$$\begin{aligned} Q_{/\!/} &= ||\boldsymbol{Q}_{\mathbf{crest}}|| \cos(\theta- \alpha) \\ Q_{\perp} &= ||\boldsymbol{Q}_{\mathbf{crest}}|| \sin(\theta- \alpha) \end{aligned} \quad (2)$$

The growth rate of dunes is taken proportional to the overall normal-transport at the crest averaged over the entire time period under consideration,

$$\sigma = \langle|Q_{\perp}|\rangle/(HW) \quad (3)$$

According to the GBNR, but taking into account the speed-up effect, dunes in the bed instability align in the direction for which the growth rate is maximum:

$$\left(\frac{d\sigma}{d\alpha}\right)_{\alpha_I} = 0 \quad (4)$$

Dunes in the fingering modes elongates in the direction of the sand flux at the crest, the orientation for which ⟨Q⊥⟩=0 and ⟨Q//⟩>0, i.e.,

$$\arccos\left(\frac{Q_{crest}\left(\alpha_F\right)\cdot u_{\alpha_F}}{\left\|Q_{crest}\left(\alpha_F\right)\right\|}\right) = 1 \quad (5)$$

where $u_{\alpha F}$ is the unit vector in the direction α_F. The orientations $\{\alpha_I, \alpha_F\}$ of the dunes in the bed instability and the elongating modes being determined, all the parameters characterizing their dynamics can be estimated. For example, Eqs. 2 and 3 give the

sand flux vectors at their crest $\{\boldsymbol{Q}_I, \boldsymbol{Q}_F\}=\{\boldsymbol{Q}_{crest}(\alpha_I), \boldsymbol{Q}_{crest}(\alpha_F)\}$ and their growth rate $\{\sigma_I, \sigma_F\}=\{\sigma(\alpha_I), \sigma(\alpha_F)\}$, respectively. The growth-rate ratio σ_F/σ_I can be used to estimate the predominant mode of dune orientation in zones of low sand availability.

4 VALIDATIONS AND APPLICATIONS

4.1 Validation of the elongation mechanism

Using the wind data of climate reanalyses over the past 30 yr, Courrech du Pont et al. (2014) verified that the predicted orientations $\{\alpha_I, \alpha_F\}$ agree within 5° with the alignment of aeolian dune patterns in terrestrial sand seas, not only for small dunes (~30 m wide) but also for larger and older dunes (~1 km wide). Interestingly, most of the linear dune patterns are oriented according to the elongating mode of dune growth, suggesting that most of them develop along aeolian transport routes from source areas (Chanteloube et al. 2022).

Gao et al. (2015) numerically investigated the development of bedforms for two different conditions of sand availability to provide evidence for the expression of the two dune growth mechanisms across the entire parameter space of bidirectional flow regimes (i.e., divergence angle, transport ratio). The complete phase diagrams of dune shape and orientation in both the bed instability and the elongating modes are used to quantitatively validate the prediction of the model (see Sec. 3). In the simulations, different dune patterns emerge in zones of low sand availability (Fig. 2c), and there are systematic transitions from trains of barchans to isolated linear elongating dunes. These transitions are well captured by the growth-rate ratio σ_F/σ_I, which compares the ability of the flow to build the dune topography in the two modes of dune growth.

Based on 50 yr of aerial and satellite imagery of aeolian landforms in Niger, Lucas et al. (2015) demonstrate for the first time in the field that dunes can elongate in the direction of the resultant sand flux at the crest, with no lateral migration. As they develop downwind of residual hills in a zone of low sediment availability submitted to bimodal wind regime, these longitudinal dunes are ideal bedforms to isolate and quantify the elongation mechanism. From the elongation rate of individual dunes, we then derived the sand flux parallel to the crests to show that this specific dune type can also be studied for assessing transport and wind conditions, comparably to the more traditional methods using the migration of transverse and barchan dunes in the bed instability mode.

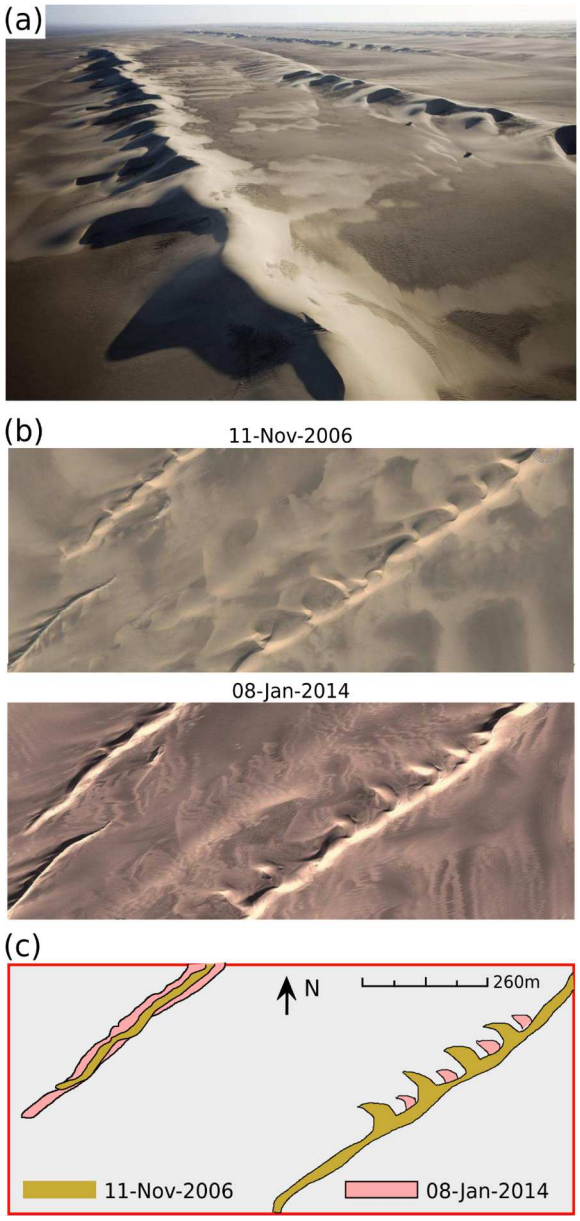

Figure 3. (a) Raked linear dunes in the Kumtagh desert in China. (b) Evolution of dune shape from 2006 to 2014 showing (c) elongation of the linear pattern and the oblique migration of the superimposed dune pattern in the bed instability mode of dune growth.

4.2 Coexistence of the two growth mechanisms

A landscape-scale experiment at the edge of the Gobi desert is a unique site to study dune morphodynamics under natural wind conditions and controlled boundary conditions (Ping et al., 2014). After flattening a dune field in 2013, and based on 4 yr of high-resolution topographic data, Lü et al. (2022) showed how, depending on sand availability, the same wind regime can lead to two different dune orientations, which reflect the two dune growth mechanisms (Fig. 2d). As periodic oblique dunes emerge from a sand bed and develop to 2 meters in height, we analysed the initial linear phase of the bed instability (Lü et al., 2021) and then the defect dynamics that drive the non-linear phase of pattern coarsening. Starting from conical sand heaps deposited on gravels, we observed the transition from dome to barchan and asymmetric barchan shapes (Lü et al., 2022). We identified a minimum size for arm elongation and evaluate the contribution of wind reversals to its longitudinal alignment. These experimental field observations support the model and the numerical simulations (Gao et al., 2015; Rozier et al., 2019), providing practical solutions for quantitative analysis of dune evolution under various wind regimes and bed conditions.

Raked linear dunes keep a constant orientation for considerable distances with a marked asymmetry between a periodic pattern of semi-crescentic structures on one side and a continuous slope on the other (Fig. 3). Lü et al. (2017) showed that this shape is associated with a steady-state dune type arising from the coexistence of the two dune growth mechanisms. Primary ridges elongate in the direction of the resultant sand flux. Semi-crescentic structures result from the development of superimposed dunes growing in the bed instability mode. In the particular case of raked linear dunes, these two mechanisms produces primary and secondary ridges with similar height but with different orientations, which are oblique to each other. The raked pattern develops preferentially on the leeward side of the primary ridges according to the direction of propagation of the superimposed bedforms. As shown by numerical modelling, raked linear dunes occur where both these oblique orientations and dynamics are met.

4.3 Planetary dunes and the inverse problem

On Titan, a moon of Saturn, dune fields cover more than 17% of the surface. Their confinement to the equatorial belt, shape, and eastward direction of propagation offer crucial information regarding both the wind regime and sediment supply. Lucas et al. (2014) presented a comprehensive analysis of Titan's dune orientations using automated detection techniques on radar images. By investigating the two dune growth mechanisms using wind fields generated by climate modelling, we found that the giant dunes on Titan grow by elongation on a non-mobile substratum. To be fully consistent with both the local crestline orientations and the eastward propagation of Titan's dunes, the sediment should be predominantly transported by strong eastward winds, most likely generated by equinoctial storms or occasional fast westerly gusts (Charnay et al., 2015; Rodriguez et al., 2018). Additionally, the meridional transport predicted in models can explain why Titan's dunes are confined within ±30° latitudes, where sediment fluxes converge.

Dunes on Mars also show clear evidence of the coexistence of the two dune growth mechanisms. Using the high contrast between the dune material and substrate, Fernandez-Cascales et al. (2018) provided the first quantification of relationship between sediment availability and dune orientation. Abrupt and smooth dune reorientations are associated with inward and outward dynamics of dunes approaching and ejecting from major sedimentary bodies, respectively. These reorientation patterns along sediment transport pathways are interpreted as discontinuous and continuous transitions from the elongating to the bed instability modes of dune growth and vice-versa. In

addition, assuming bidirectional wind regimes, the intersections between model predictions for the two modes permitted solving of the inverse problem of predicting the wind regime from dune orientation. The relationships between sediment cover and dune orientation can therefore be used to constrain the flow regime in environments where direct measurements are impossible.

5. CONCLUSION

The two dune growth mechanisms have now been observed in many planetary environments and documented in the field through a dedicated set of landscape-scale experiments. For both mechanisms and their interactions, the results of various laboratory experiments and a large number of numerical simulations support comprehensive theoretical models, boosting confidence in their applicability for quantitative predictions of dune morphodynamics (shape, orientation, growth and migration rates) under various flow regimes and bed conditions.

Opposite flow directions are ubiquitous over subaqueous bedforms in tidal environments. In addition, there are many possible sources of tidal asymmetry and the complexity of specific bathymetry and geometry in estuaries can produce multidirectional flow regimes. Hence, the dune growth mechanisms discussed here may also coexist in river and oceanic settings. In this case, marine and river dunes may offer new opportunities for better characterization of the flow regimes, sediment resources and transport properties.

6 REFERENCES

Magnolia, R.A., 1941, The physics of wind blown sand and desert dunes, Methuen.

Chanteloube C., Barrier, L., Derakshani, R., Gadal, C., Braucher, R., Payet, V., Léanni, L., Narteau, C., 2022, Source-to-sink aeolian fluxes from arid landscape dynamics in the Lut Desert, Geophysical Research Letters, 49, e2020GL097342, 2022.

Charnay B., Barth, E., Rafkin, S., Narteau C. et al., 2015, Methane storms as a driver of Titan's dune orientation, Nature Geoscience, 8, 362-366.

Courrech du Pont S., C. Narteau, X. Gao, 2014, Two modes for dune orientation, Geology, 42, 743-746.

Elbelrhiti, H., Claudin, P., Andreotti B., 2005, Field evidence for surface-wave-induced instability of sand dunes. Nature 437, 720–723.

Fernandez-Cascales L., Lucas, A., Rodriguez, S., Gao, X., Spiga, A., Narteau, C., 2018, First quantification of relationship between dune orientation and sediment availability, Olympia Undae, Mars, Earth and Planetary Science Letters, 489, 241-250.

Gadal, C., Narteau, C, Courrech du Pont, S., Rozier, O., Claudin, P., 2019, Incipient bedforms in a bidirectional wind regime, J. Fluid Mech., 862, 490–516.

Gadal C., C. Narteau, S. Courrech du Pont, O. Rozier, P. Claudin, 2020a, Spatial and Temporal Development of Incipient Dunes, Geophysical Research Letters, 47, e2020GL088919.

Gadal C., C. Narteau, S. Courrech du Pont, O. Rozier, P. Claudin, 2020b, Periodicity in fields of elongating dunes, Geology, 48.

Gao X., C. Narteau, O. Rozier, S. Courrech du Pont, 2015, Phase diagrams of dune shape and orientation depending on sand availability, Scientific Reports, 5, 14677.

Gao X., Narteau, C., Gadal, C., Migration of reversing dunes against the sand flow path as a singular expres-sion of the speed-up effect, Journal of Geophysical Research, 126, doi:10.1029/2021JF006492.

Hunter, R. E., Richmond, B. M., Alpha, T. R., 1983, Storm-controlled oblique dunes of the Oregon coast. Geol. Soc. Am. Bull. 94, 1450–1465.

Jackson, P. & Hunt, J., 1975, Turbulent wind flow over a low hill. Q. J. Roy. Meteorol. Soc. 101, 929–955.

Lancaster N., 1991, The orientation of dunes with respect to sand-transporting winds: a test of Rubin and Hunter's gross bedform-normal rule, NATO advanced workshop on sand dust, and soil and their relation to aeolian and littoral processes, University of Aarhus, 47-49.

Lü P., C. Narteau, Z. Dong, O. Rozier, S. Courrech du Pont, Unravelling raked linear dunes to explain the coexistence of bedforms in complex dunefields, Nature Communications, 8, 14239, 2017.

Lü, P., Narteau, C., Dong, Z., Claudin, P., Rodriguez, S., An, Z., Fernandez-Cascales, L., Gadal, C., Courrech du Pont, S., 2021, Direct validation of the dune instability theory, Proceedings of the National Academy of Sciences, 18, e2024105118.

Lü, P., Narteau, C. , Dong, Z., Claudin, P., Rodriguez, S., An, Z., Gadal, C., Courrech du Pont, S., 2022, Coexistence of two dune growth mechanisms in a landscape-scale experiment, Geophysical Research Letters, 49, e2021GL097636.

Lucas A., Rodriguez, S., Narteau, C., Charnay, B., Courrech du Pont, S., 2014, Growth mechanisms

and dune orientation on Titan, Geophysical Research Letters, 41, 6093-6100.

Lucas A., C. Narteau, S. Rodriguez, O. Rozier, Y, Callot, A. Garcia, S. Courrech du Pont, 2015, Sediment flux from the morphodynamics of elongating linear dunes, Geology, 43, 1027-1030.

Narteau, C., Zhang, D., Rozier, O., Claudin, P., 2009, Setting the length and time scales of a cellular automaton dune model from the analysis of superimposed bed forms, J. Geophys. Res. Earth Surf, 114, 1–18.

Ping, L., Narteau, C., Dong, Z., Zhang, Z., Courrech du Pont, S., 2014, Emergence of oblique dunes in a landscape-scale experiment, Nat. Geosci., 7, 99–103.

Reffet, E., Courrech du Pont, S., Hersen, P., Douady, S., 2010, Formation and stability of transverse and longitudinal sand dunes, Geology, 38, 491–494.

Rodriguez S. et al., 2014, Global mapping and characterization of Titan's dune fields with Cassini: Correlation between RADAR and VIMS observations, Icarus, 230, 168-179.

Rodriguez S. et al., 2018, Gobservational evidence for active dust storms on Titan at equinox, Nature Geosci., 11, doi:10.1038/s41561-018-0233-2.

Rozier O., Narteau, C., Gadal, C., Claudin, P., Courrech du Pont, S., 2019, Elongation and stability of a linear dune, Geophysical Research Letters, 46, 14521-14530.

Wasson, R. & Hyde, R., 1983, Factors determining desert dune types. Nature, 304, 337–339.

Direct validation of the dune instability theory

C. Narteau *Université Paris Cité, Institut de Physique du Globe de Paris, CNRS, France – narteau@ipgp.fr*
P. Lü *School of Geography and Tourism, Shaanxi Normal University, China – lvping@lzb.ac.cn*
P. Claudin *ESPCI, PSL Univ, Sorbonne Univ, Univ Paris Cité, CNRS, France – claudin@pmmh.espci.fr*
Z. Dong *School of Geography and Tourism, Shaanxi Normal University, China – dongzb@lzb.ac.cn*
S. Rodriguez *Université Paris Cité, Institut de Physique du Globe de Paris, CNRS, France – rodriguez@ipgp.fr*
C. Gadal *Université Paris Cité, Institut de Physique du Globe de Paris, CNRS, France – gadal@ipgp.fr*
S. Courrech du Pont *MSC, Université Paris Cité, CNRS, France – sylvain.courrech@u-paris.fr*

ABSTRACT: We designed a landscape-scale experiment at the edge of the Gobi desert, China, to quantify the development of incipient dunes under the natural action of winds. We identified two successive phases, from the initial flat sand bed to a meter-high periodic pattern. During the initial phase, we measure the growth rate of dunes of different wavelengths. We identify the existence of a maximum growth rate, which readily explains the mechanism by which dunes select their size, leading to the prevalence of a 15 m wavelength pattern. We quantitatively compare our experimental results to the prediction of the dune instability theory using transport and flow parameters independently measured in the field. The remarkable agreement between theory and observations demonstrates that the linear regime of dune growth is permanently expressed on low-amplitude bed topography, before larger regular patterns and slip faces eventually emerge.

1 INTRODUCTION

Dune research has always been stimulated by the question of the origin of periodic bedforms that are ubiquitous in rivers, oceans and planetary sand seas. However, the size-selection mechanism leading to the emergence of periodic dunes have never been observed and quantified in a natural environment .

Underwater experiments have shown that, as soon as the flow is strong enough to transport grains, a flat sand bed destabilizes into periodic bedforms migrating at a constant speed (Kennedy 1963). Wind tunnel experiments and Ralph Bagnold's attempts in the field to create artificial dunes have failed because the initial sand piles were not large enough (Bagnold 1941). There is indeed a minimum length-scale for the formation of dunes, which has been estimated to be of the order of 10 m in aeolian systems on Earth based on the smallest wavelength of the superimposed bedforms observed on the flanks of large dunes (Elbelrhiti 2005). After 20 years of intensive research, this characteristic length-scale is assumed to be regulated by the balance between a destabilizing process associated with the turbulent flow response to the topography and a stabilizing process due to transport inertia.

Linear stability analysis of flat sand beds sheared by a fluid flow provide the so-called dispersion relation (Andreotti et al. 2002, Narteau et al. 2009, Gadal et al. 2019, Charru et al. 2013), i.e., the growth rates $\sigma(k)$ of sinusoidal bed perturbations over the whole range of possible wave numbers k (wavelength $\lambda=2\pi/k$). These stability analysis are by definition restricted to the linear regime of incipient dune growth, the period during which the amplitude of each mode (wavelength) grows exponentially and independently from one another. The theoretical relation writes

$$\sigma(k)=Qk^2(B-Akl_{\mathrm{sat}})/(1+(kl_{\mathrm{sat}})^2) \qquad (1)$$

where Q is the mean sand flux and l_{sat} the distance downwind required for the sand flux to reach saturation (i.e., transport inertia). The perturbation of wind streamlines near the bed, in the so-called inner layer, is described with the aerodynamic parameters A and B, so that the upwind shift between the wind speed and the bed topography can be expressed as $\arctan(B/A)/k$.

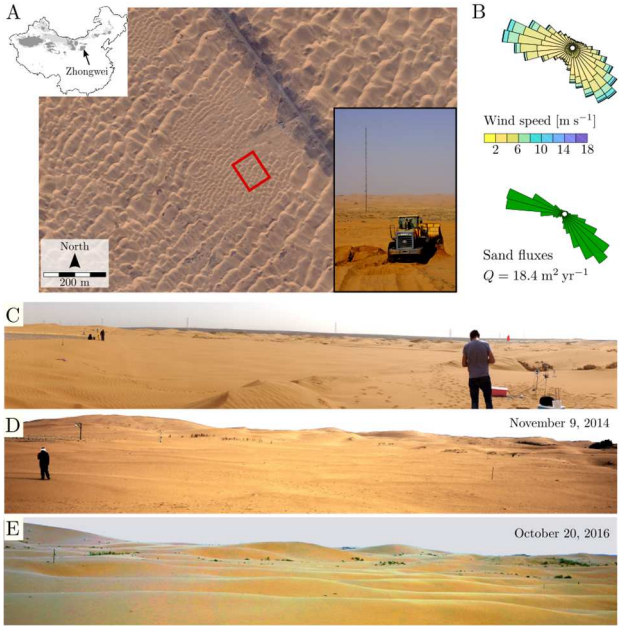

Figure 1. (A) The landscape-scale experiment site in the Tengger desert (37°33’38’’N, 105°2’0.8’’E). The red square shows the location of the flat sand bed experiment. (B) Wind and sand flux roses. (C) The sand bed after flattening. (D) Incipient dunes at the end of the linear phase of dune growth. (E) Mature dunes during the non-linear phase.

Here we present the results of a long-term field experiment in which we have been able to measure in the same desertic area all these parameters. Thus, we obtain a comprehensive description of incipient dune growth under the natural action of wind, which is directly confronted to the dune instability theory (Lü et al. 2021).

2 A LANDSCAPE-SCALE EXPERIMENT

Landscape-scale experiments started in 2009 in the Tengger desert at the southeastern edge of the Gobi basin in China (Fig. 1A, Ping et al. 2014). The experiment dedicated to incipient dune growth has been conducted from April 2014 to November 2017. Preexisting dunes were leveled on 9 April 2014 to form a flat rectangular bed 100 m long and 75 m wide (Fig. 1C). We monitored dune growth over the following 42 mo (Fig. 1D,E) through a series of 20 topographic surveys using a ground-based laser scanner (Lü et al. 2021; Lü et al. 2022). To get a better resolution on the early stage of dune growth and to account for windy periods, these topographic data are not regularly distributed in time and are more frequent in 2014 as well as in the spring and fall of each year. To compare datasets from different scans, we installed a reference system of concrete posts over the entire experimental dune field.

3 RESULTS

3.1 Sand transport properties

As in most of the Tengger desert, the mean grain size in the experimental area is of about 190 μm. Using an impact sensor placed above a flat sand bed, we monitored saltation activity under winds of varying strength. As shown in Fig. 2, the empirical relation between wind speed and the impact rate yields an estimated threshold wind speed for aerodynamic entrainment of sand grains, u_{th}=0.23±0.04 m s^{-1}. Combining this threshold value with local wind data, we calculate the saturated sand flux on a flat sand bed using the eolian transport law of Ungar and Haff (1987). From January 2014 to November 2017, the mean flux is Q=18.4±4.2 m^2 y^{-1}.

To estimate the saturation length, l_{sat}, we constructed a flat bed armored with coarse gravels and cobbles, which acted as a sand trap. At a time without active transport, we build a 12-m-long, 3-m-wide, and 20-cm-high flat sand berm immediately downwind of the coarse bed, as determined from the direction of the prevailing wind. We measure the surface elevation of this sand berm using the terrestrial laser scanner before and after a wind event. The difference in topography along the wind direction gives the mean transport rate profile for this time interval. There is a net erosion on the whole sand slab, with an amplitude that dampens with respect to the downwind distance from the nonerodible bed. These observations indicate an increasing sand flux converging toward its saturated value. Assuming an exponential relaxation of the sand flux (Andreotti et al., 2010), we obtain l_{sat}=0.95±0.2 m (Lü et al. 2021).

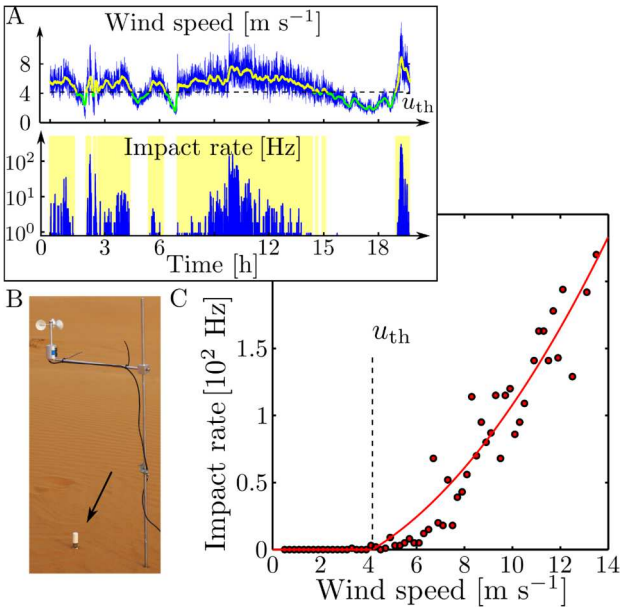

Figure 2. (A) Grain impact rate and wind speed with respect to time. (B) Picture of the impact sensor placed above a flat sand and below a cup anemometer. (C) Relationship between grain impact rate and wind speed u. The solid line is the best fit of $(u^2-u_{th}^2)$ to the data with a critical entrainment threshold u_{th}=4.16 m s^{-1}. Periods above the transport threshold are highlighted in yellow in (A).

3.2 The upwind shift in wind speed

To estimate the values of the aerodynamic parameters A and B used in Eq. 1, we measured the flow properties on dunes of small amplitude. We recorded wind speed at heights of 4, 12, 50, and 100 cm above the bed by moving an anemometer mast upwind of a known elevation dune profile (Fig. 3A). The wind speeds measured at different heights were synchronized and normalized by the wind speed measured at 1 m high by a reference cup anemometer located at the top of a larger dune in the vicinity, which allowed us to reconstruct the perturbation in wind speed on low dunes at different stages of dune growth. As predicted in the limit of low sinusoidal bedforms, Fig. 3B shows that the wind perturbation at all heights reflects the topography of the underlying incipient dunes, both in amplitude and wavelength. The amplitude of perturbation in wind speed decreases with height above the bed. More importantly, there is always an upwind shift in wind speed for the two bottom anemometers at heights of 4 and 12 cm but not for the two top anemometers at heights of 50 and 100 cm. This indicates that, on incipient dunes in our experimental area, the thickness l of the inner layer is between 12 and 50 cm. Within this inner layer, using the upwind shift (≈1 m) and the amplitude of the perturbation in wind speed recorded by the two bottom anemometers, we get A=3±1 and B=1.5±0.5 for dune aspect ratios varying from 0.012 to 0.025 (Fig 3C).

3.3 Emergence of a periodic dune pattern

Within the experimental plot, we select a central rectangular area with a width of 48 m and a length of 82 m (red square in Fig. 1A). The long side of this rectangle is oriented northwest–southeast to align with the prevailing transport direction. We remove the mean slope of this rectangular area by fitting a plane to the elevation data. Throughout the experiment, this plane maintained a gentle southwest-facing slope as observed after the flattening of the dune field. The residual topography is shown for different times in Fig. 4. Within the observation area, we chose to follow the time evolution of elevation along 34 parallel transects with a constant spacing of 1.4 m. These transects are oriented perpendicularly to the final dune orientation observed in November 2017. Fig. 4 shows the elevation profiles with respect to time for a given transect. Over the 42 mo of the experiment, the amplitude of the dunes increases by two orders of magnitude from a few centimeters to a few meters. Whereas no periodic pattern is discernible after flattening, a characteristic wavelength of 15 m emerges over the first few months of the experiment (Fig. 1D,E). The variation of the mean amplitude of the dune pattern, defined as the rms of the topography, is not homogeneous over time and displays a sudden change in rate at the end of 2014 (Fig. 4). Before, from April to October 2014, this amplitude stays almost constant. During this time period, despite a smoother topography, there is nothing to suggest that dunes will appear at a specific wavelength. Starting in November 2014, the surface elevation exhibits a periodic dune pattern with marked crestlines and a northeast-southwest orientation.

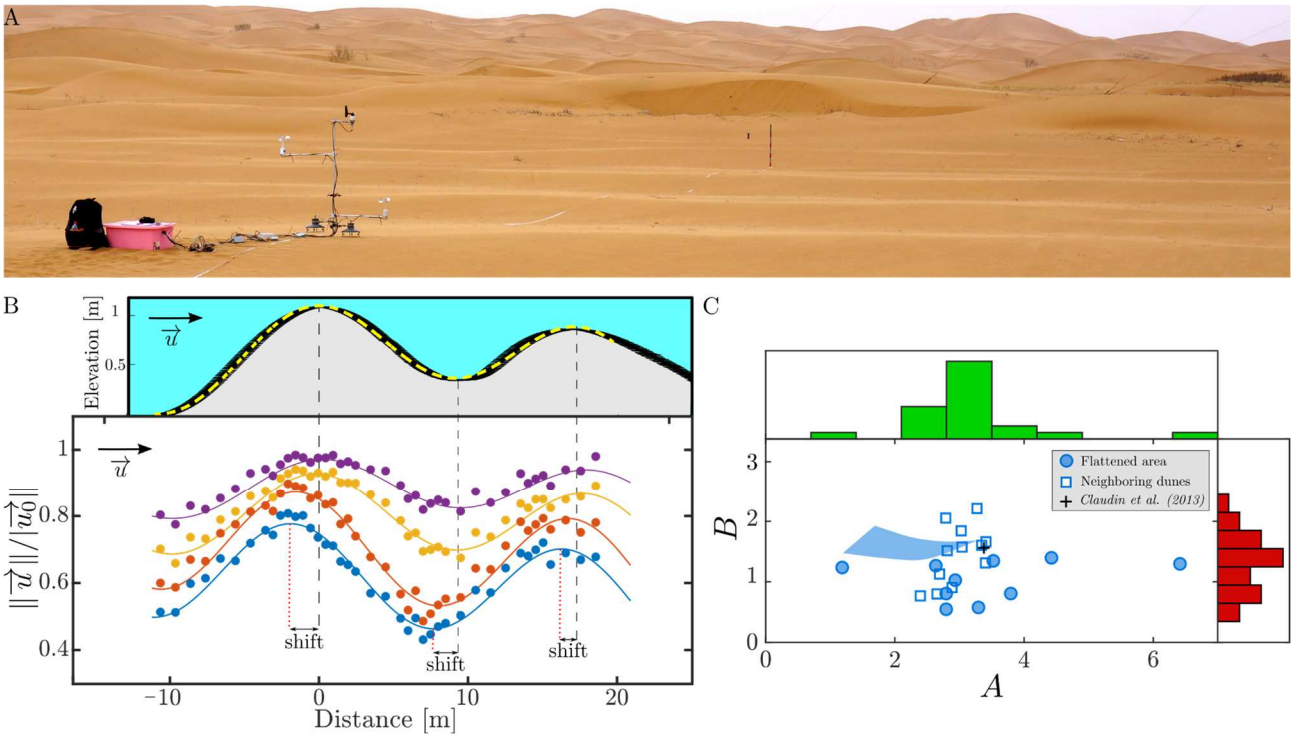

Figure 4. The upwind velocity shift on low sinusoidal bedforms. (A) The mobile anemometer mast, with anemometers located at heights of 4 and 12 cm inthe inner layer and at heights of 50 and 100 cm in the outer layer. The decameter aligned with the mean wind direction gives the direction followed during the successive measurements on sinusoidal incipient dunes. (B) Elevation and normalized wind speed according to distance along the dune profile (blue, red, yellow, and purple for anemometers at 4, 12, 50, and 100 cm, respectively). The normalized wind speed is the wind speed measured along the profile divided by the one recorded by the reference anemometer. Note the upwind shift in wind speed in the inner layer near the bed but not in the outer layer above. Dashed lines show the two dune crests and the trough along the elevation profile. Dotted lines show the maximum and minimum wind speeds in the inner layer. (C) Aerodynamic parameters *A* and *B* measured during dune growth (circles) and on neighboring dunes (squares). The blue area shows the best-fit values of *A* and *B* to the experimental dispersion relation shown in Fig. 5B for $0.6< l_{sat}<1.2$. The distributions of *A* and *B* are illustrated by green and red histograms, respectively.

Then, the mean amplitude increases significantly at a constant rate of 0.5 m y^{-1} for 3 y (Fig. 4). We found that the transition between these two different stages of dune growth occurs for a mean slope of the order of 0.03, when dune crests and slip faces emerge and begin to spatially organize throughout the experimental plot. Steeper slopes highlight the increase in dune aspect ratio (Gadal et al., 2020; Phillips et al., 2019), which is the main control parameter for aerodynamic nonlinearities. Hence, we ascribe the two different stages to the linear and the nonlinear phases of the dune growth instability.

3.4 Experimental dispersion diagram

For each topographic survey, we performed a spectral decomposition of the elevation data to isolate the contribution of individual modes (wavelengths) to the overall topography. The variation of the amplitude of these surface waves is not homogeneous over time and displays a sudden change in rate at the end of 2014 (Fig. 5A) for a mean slope of the order of 0.03. We ascribe it to the transition from the linear to the nonlinear phases of the dune growth instability. During the linear phase, we obtain the experimental dispersion relation of the dune instability by plotting the growth rate of the different modes as a function of their wave number *k* (Fig. 5B). It provides eolian experimental evidence of the difference in growth rates of nascent dunes of various wavelengths when they are not large enough to generate flow recirculations. These results are consistent with the theoretical

prediction of the linear stability analysis with a clear maximum and a continuous trend from unstable (growing waves, σ>0) to stable regimes (decaying waves, σ<0). The most unstable mode corresponds to the wavelength of the emerging dune pattern in the field (≈15 m); the neutral mode (σ=0) is about 9 m (Richards, 1980).

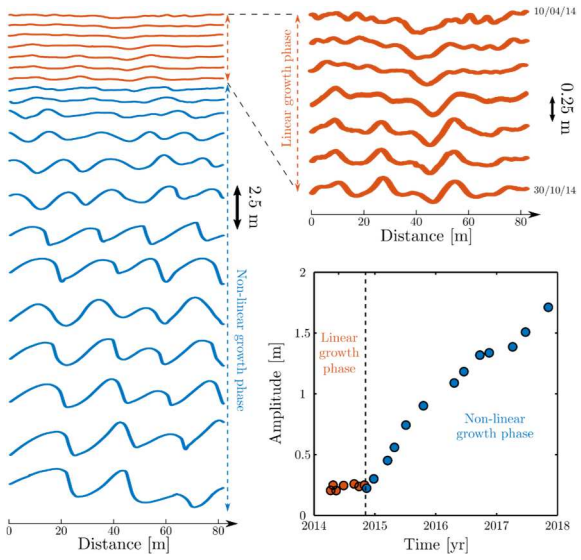

Figure 4. Dune growth in the flat sand bed experiment. Detrended elevation profiles along the same transect from 10 April 2014 to 7 November 2017 (left). Zoomed-in view of the elevation profiles from 10 April 2014 to 30 October 2014 shows the evolution of topography during the linear phase of dune growth (top right). The mean amplitude of bedforms with respect to time. Colors and dashed lines are used to separate the linear (orange) and the nonlinear (blue) phases of dune growth.

4 DISCUSSION

In order to meet the challenge of comparing and evaluating theoretical models of dune growth with observational data, the landscape-scale experiment conducted in an active dune field under the natural action of wind yields a unique set of quantitative relationships. By removing uncertainties about boundary and initial conditions, we verify that dunes can emerge from a flat sand bed and validate the theory behind this dune growth mechanism. We elucidate the origin of periodic bedforms, showing the wavelength selection as dunes increase in height. Meanwhile, we highlight the inherent benefits of combining field observations with theory to derive information about the sediment transport and flow properties from the morphodynamics of incipient dunes.

We provide an original dataset for an in-depth understanding of the linear phase of the dune instability, when the growth rates of the different modes evolve independently from each other (Lü et al. 2021). We find that this linear phase is at work from the earliest stage of dune growth, as soon as sand transport starts even when, at first glance, no regular structure seems to be in place. It takes time for the most unstable wavelength to prevail over all of the other modes that contribute to the sand bed topography. When periodic dunes are observed, the nonlinear phase has already taken over, aerodynamic nonlinearities have developed, and the different modes interact with each other to lead to pattern coarsening (Gao et al., 2015, Lü et al. 2022; Valance et al., 2010). We show here that the continuous transition from the linear to the nonlinear regimes is controlled by the dune aspect ratio for remarkably low values (≈0.03), consistent with laboratory measurements on sinusoidal beds (Charru et al. 2013). This transition coincides with the spatial organization of bedforms according to the alignment of mature dunes. For mean slope values of 0.07 (4°, typical of the flattest dune slopes), the transition is completed, and it is no longer possible to differentiate between the growth rates of the different modes. Nevertheless, the most unstable mode can still be observed to provide relevant length and timescales of the dune instability.

Our experiments bridge the gap between theoretical physics and geophysical surveys and can translate into concrete research avenues across scientific domains, in particular for river and marine dunes. Instability theory applies to many natural systems, especially to examine the relationships between flow and surface properties on subaqueous bedforms in rivers or oceans. For all these natural systems, we show here that, when the technological step in data acquisition is taken, field studies can

be carried out to test theoretical outputs against observations and to develop better forecasts of landscape morphogenesis.

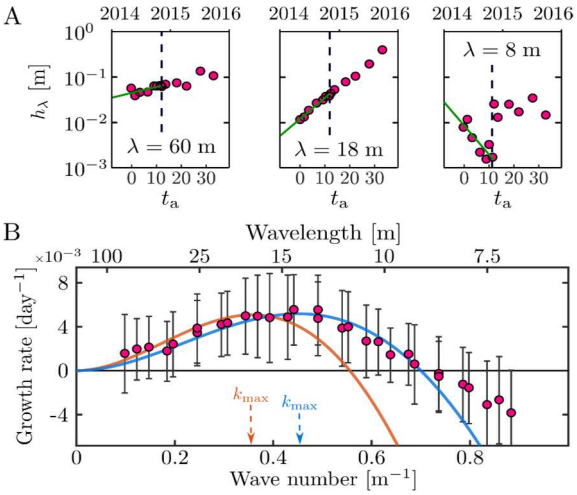

Figure 5. (A) Amplitudes of 60-, 18-, and 8-m wavelengths with respect to the dimensionless transport timescale t_a; t_a is set to zero on 10 April 2014. Two different regimes are observed before and after t_a=10.7, the 30 October 2014 (dashed lines). They are associated with the linear and nonlinear phases of dune growth. The growth rate of each wavelength (green lines) is determined by an exponential fit performed during the linear phase ($0 \leq t_a \leq 10.7$). (B) The experimental dispersion relation for the linear regime of the dune instability (i.e., the growth rate with respect to the wave number during the linear phase). Error bars show mean and standard deviation derived from 34 independent transects. Solid lines are dispersion relations using Eq. 1 and the best fit to the data $\{l_{sat}, A, B\}$={0.7, 1.96, 0.96} (blue) or the same parameters measured independently in the field $\{l_{sat}, A, B\}$={0.95, 3, 1.5} (orange). The most unstable wavelengths $\lambda_{max}=2\pi/k_{max}$ are equal to 14.6 and 18.5 m, respectively.

5 REFERENCES

Andreotti, B., Claudin, P., Pouliquen, O., 2010, Measurements of the aeolian sand transport saturation length. Geomorphology 123, 343–348.

Bagnold, R.A., 1941. The physics of wind blown sand and desert dunes. Methuen.

Charru, F., Andreotti, B., Claudin, P., 2013. Sand ripples and dunes. Annu. Rev. Fluid Mech., 45, 469–493.

Claudin, P., Wiggs, G. Andreotti, B., 2013. Field evidence for the upwind velocity shift at thecrest of low dunes. Boundary Layer Meteorol. 148, 195–206.

Elbelrhiti, H., Claudin, P., Andreotti B., 2005. Field evidence for surface-wave-induced instability of sand dunes. Nature 437, 720–723.

Gadal, C., Narteau, C, Courrech du Pont, S., Rozier, O., Claudin, P., 2019. Incipient bedforms in a bidirectional wind regime. J. Fluid Mech., 862, 490–516.

Gao, X., Narteau, C., Rozier, O., 2015, Development and steady states of transverse dunes: A numerical analysis of dune pattern coarsening and giant dunes. J. Geophys. Res., 120, 2200–2219.

Kennedy, J., 1963. The mechanics of dunes and antidunes in erodible bed channels. Journal of Fluid Mechanics, 16, 521–544.

Lü, P., Narteau, C., Dong, Z., Claudin, P., Rodriguez, S., An, Z., Fernandez-Cascales, L., Gadal, C., Courrech du Pont, S., 2021. Direct validation of the dune instability theory. Proceedings of the National Academy of Sciences, 18, e2024105118.

Lü, P., Narteau, C. , Dong, Z., Claudin, P., Rodriguez, S., An, Z., Gadal, C., Courrech du Pont, S., 2022. Coexistence of two dune growth mechanisms in a landscape-scale experiment. Geophysical Research Letters, 49, e2021GL097636.

Narteau, C., Zhang, D., Rozier, O., Claudin, P., 2009. Setting the length and time scales of a cellular automaton dune model from the analysis of superimposed bed forms. J. Geophys. Res. Earth Surf, 114, 1–18.

Phillips, J., et al., 2019. Low-angle eolian deposits formed by protodune migration, and insights into slipface development at white sands dune field, New Mexico. Aeolian Research, 36, 9–26.

Ping, L., Narteau, C., Dong, Z., Zhang, Z., Courrech du Pont, S., 2014, Emergence of oblique dunes in a landscape-scale experi-ment, Nat. Geosci., 7, 99–103.

Richards, K. J., 1980. The formation of ripples and dunes on an erodible bed. J. Fluid Mech., 99, 597–618.

Ungar, J., Haff, P., 1987. Steady state saltation in air. Sedimentology, 34, 289–299.

Valance, A., 2011. Nonlinear sand bedform dynamics in a viscous flow. Phys. Rev. E, 83, 036304.

Study marine dunes in an offshore windfarm context

M. Nexer *France Energies Marines, Plouzané, France – maelle.nexer@ite-fem.org*
T. Garlan *Shom, Département Géologie Marine, 29200 Brest, France*
A. Lefebvre *MARUM, University of Bremen, Leobener Str. 8, 28359 Bremen, Germany*
N. Quillien, *France Energies Marines, Plouzané, France*
A. Gangloff *Shom, Département Géologie Marine, 29200 Brest, France*
O. Blanpain *France Energies Marines, Plouzané, France*
S. Le Bot, *Univ Rouen Normandie, CNRS, M2C UMR 6143, F-76000 Rouen, France*
M. Bacha, *France Energies Marines, Plouzané, France & Laboratoire d'Océanologie et de Géosciences, UMR 8187 CNRS, Université du Littoral Côte d'Opale, 32 Avenue Foch, 62930 Wimereux, France*
M. Bary, *France Energies Marines, Plouzané, France & Univ Rouen Normandie, CNRS, M2C UMR 6143, F-76000 Rouen, France*
N. Durand, *France Energies Marines, Plouzané, France*
A. Gilletta de Saint Joseph, *France Energies Marines, Plouzané, France*
N. Michelet, *France Energies Marines, Plouzané, France*
A. Robert, *France Energies Marines, Plouzané, France & Ifremer Unité Littoral, Laboratoire Environnement et Ressources de Bretagne Nord, CRESCO, 38 rue du Port-Blanc, Dinard, 35800, France*

ABSTRACT:

Mobility of the sedimentary substrate, both through the flow of sedimentary particles and through the migration and evolution of sedimentary structures, has direct implications on the design, implementation, longevity, and safety of ORE (ocean renewable energy) devices. Marine dunes are very present on the English Channel and North Sea coast where most of the future Europeans offshore windfarms (OWF) are located and planned to be constructed. Cable installation and foundations for OWF in this environment is a challenge due to the seabed mobility. This mobility can bring risks of cable over-burying or un-burying and uncertainties about foundations scouring conditions. Consequently, there is a need to anticipate variations in sediment thickness to limit damage to infrastructure and to design anti-scouring protection and better anticipate OWF costs. Furthermore, marine dunes are areas of high ecological importance. It is therefore important to understand the effect that the installation of MRE infrastructure can have on dune morphodynamics to limit the impacts on the ecosystem. To address all these issues for OWF industry, two research and development collaborative projects have been set up: DUNES & MODULLES. The first project (DUNES) aimed at collecting *in situ* data on seabed, hydrodynamics and ecosystem via bathymetric surveys, current measurements and biological sampling. The second one (MODULLES) aims to model the influence of these dunes on offshore wind farms at different spatio-temporal scales from a few seconds and centimeters to several years and kilometers *via* numerical and physical modeling. During MARID, marine dunes issues for ORE sector will be depicted. An overview of the DUNES and MODULES projects will be given to present how we address these issues with research and development project.

1 MARINE DUNES AND OFFSHORE WINDFARM

Marine dunes are among the most dynamic sedimentary bodies and are very present on the English Channel and North Sea. At the end of 2021, offshore wind turbines represented 28.3 GW of installed capacity in Europe, almost all of it in the North Sea. The European Commission aims to have 300 GW of installed capacity by 2050 (Figure *1*).

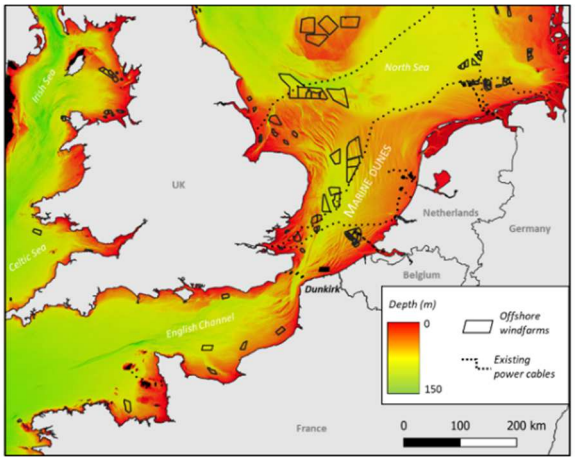

Figure 1 : Bathymetry of the North Seas (North Sea, English Channel, Irish Sea, Celtic Sea), planned and in operation Offshore Wind Farms (OWF) and power cables (data from EMODNET)

Cable installation and foundations of OWF in this environment is a challenge due to the high seabed mobility. This mobility can bring risks of cable over-burying or un-burying and uncertainties about foundations scouring conditions (Figure *2*). It is therefore important to anticipate variations in sediment thickness to limit damage to infrastructure (heat transfer diffusion, exposition to fishing) and to design anti-scouring protection.

Marine dunes are essential functional areas as feeding and breeding grounds for many species. They are classified by the Marine Strategy Framework Directive (MSFD) and by Natura 2000 as key habitats. The French Ministry in charge of the environment therefore asks developers to assess particularly the impact of offshore wind farms on the habitat of marine dunes and their ecosystem.

In this context, it is important to address the following question: how to study marine dunes in an offshore windfarm context.

To answer this question, France Energies Marines initiated two collaborative projects: DUNES (2019-2022) and MODULLES (2021-2024). These projects aim to deepen our knowledge of the marine dunes field off Dunkirk where an OWF is planned in 2027 *via:*

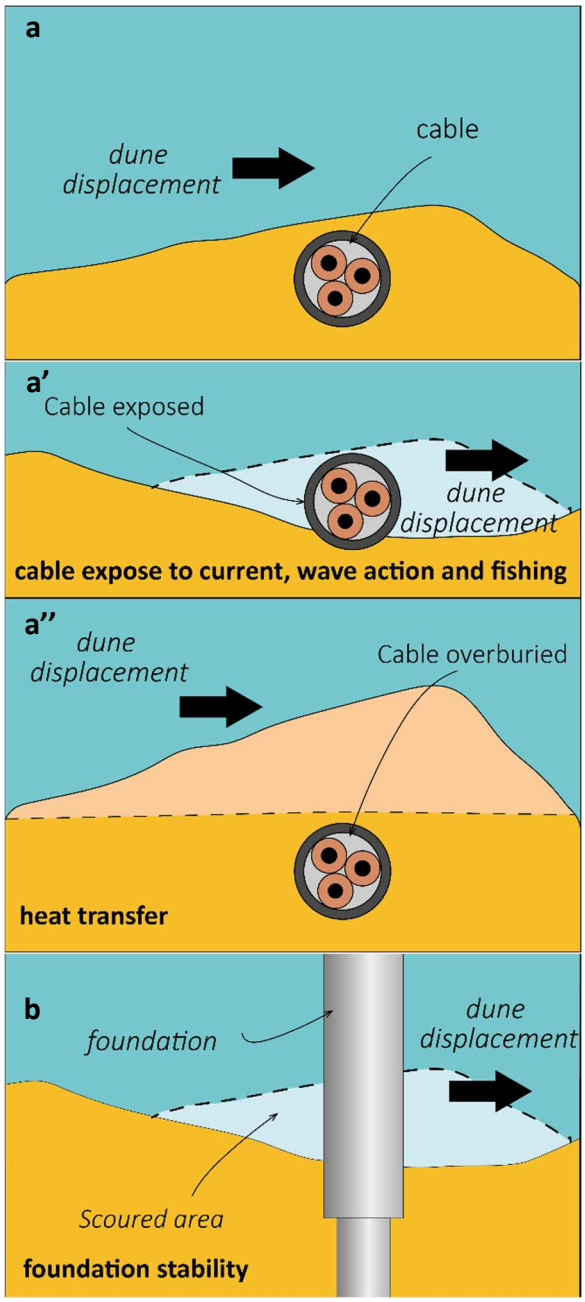

Figure 2 : Effect of marine dunes on OWF component: a) cable under marine dunes; a') unburied cable after a marine dunes displacement, a'') overburied cable under a marine dune experiencing heat issue, b) OWF foundation experiencing stability issue due to scouring.

- *in situ* morphodynamic observation and analysis,
- Marine dunes numerical and physical modelling,
- Thermal modelling,
- Ecosystem characterisation.

2 IN SITU MORPHODYNAMICS OF MARINE DUNES

2.1 Data acquisition

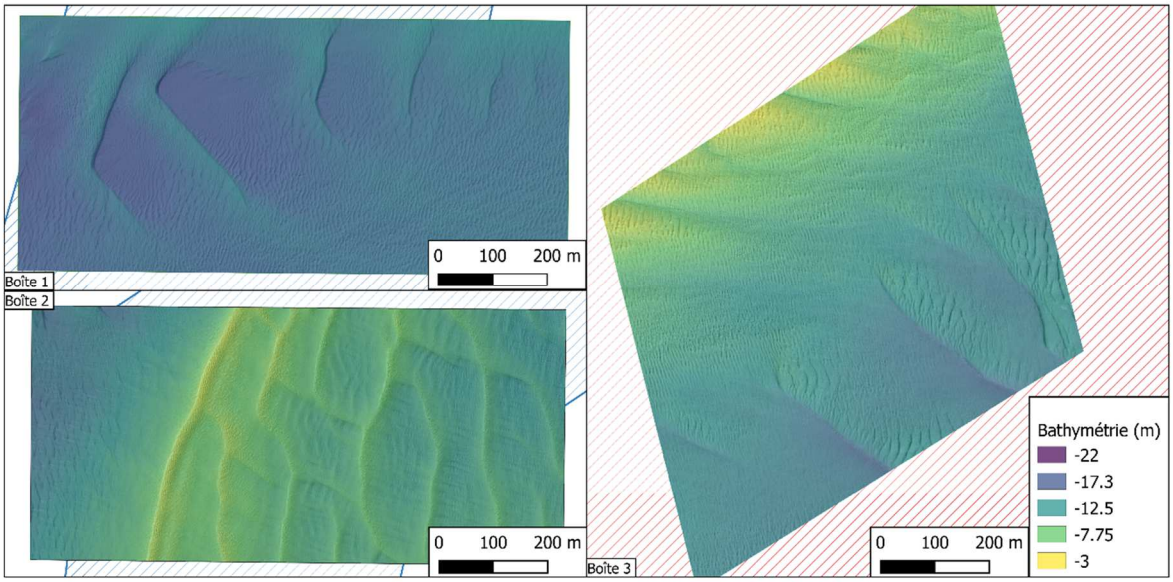

Figure 3 : Dunes morphologies off Dunkirk, bathymetric surveys realized in march 2020.

A protocol was implemented to acquire high spatial and temporal resolution data. To study the impact of forcing (wind, waves and current) on the marine dunes, it was necessary to perform numerous bathymetric surveys with a short time step. To allow this type of measurement and limit costs, three boxes were defined with an area of about 1 x 0.5 km (Figure 3). The boxes are located on the corridor of the connection cables and in the future OWF. They include different types of dunes: barchans, straight and three-dimensional dunes. Eight bathymetric surveys of these three boxes were carried out over a period of 21 months between November 2019 and July 2021.

The bathymetric surveys were complemented by an Acoustic Doppler Current Profiler (ADCP) campaign. Three ADCPs were deployed for 1.5 months in spring 2021 to measure the hydrodynamic. Two of them were positioned at the entrance and exit of box 1 near the buoys of the access channel of Dunkirk's harbour. The third ADCP was positioned north of box 3 in an area between two banks free of dune. The ADCPs were positioned on weighted cages that were launched and recovered by diver. The length of deployment was chosen to limit risks of silting while offering a relatively long timeframe.

2.2 Morphometric analysis

The acquired bathymetric data were processed to obtain a DTM (Digital Terrain Model) with a resolution of 0.5 m, which was used for a morphometric study and numerical modelling (Figure 3). The morphometric analysis has been performed for boxes 1 and 3 because dunes morphology of box 2 was judged too complex. DTM has been analysed as follow:

1) DTM filtering to smooth the roughness and limit the influence of secondary sedimentary figures (ripples and small dunes) in morphologies identification

2) Digitization of crest and troughs along transects perpendicular to the crest at 20 m intervals.

3) Measurement and calculation of morphometric parameters (bathymetry, height, wavelength, width, sinuosity) along these same transects.

4) Calculation of the migration speed (in m/year) of the crest along the same transects between two successive surveys.

Estimation of the associated sediment fluxes (in t/m/yr) has been done with the "Dune Tracking" method and three empirical equations (Hoekstra et al., 2004). “Dune tracking” uses morphometric indices of marine dune (height, wavelength, and width), sediment parameters (porosity and density) and migration velocities to approximate the volume of dune sediments that moves over time. All the figures obtained were compared to meteocean data (wind data at Dunkirk meteorological station and tidal data) to evaluate the influence of meteorological and oceanic forcing on the morphodynamic (see Le bot et al. 2023 in these proceedings for more details on the results).

Flux calculations were performed using realistic forcings and compared to the results of the "Dune Tracking" method. Then, the calculations were performed on an idealized case to refine the study of the influence of hydrodynamic processes (Michelet et al., 2022).

3 MARINE DUNES MODELLING

To better understand the dynamics of marine dunes and their interaction with OWF at different space and time scales (from days to years), marine dunes are modelled at different scales numerically and physically using bathymetric and current data acquired from 2019 to 2021.

3.1 Mesoscale numerical modelling

At mesoscale (from a dune to a dune field), two different numerical models are implemented using CROCO and TELEMAC-MASCARET modelling systems.

CROCO is a free-surface modelling system that solves the finite-difference approximations of the Reynolds-averaged Navier–Stokes equations. Space discretisation is performed with structured squares element. Waves are considered by coupling the spectral model Wave Watch 3 (WW3). The sediment dynamics is solved thanks to USGS sediment model (Blaas et al., 2007) (see Michelet et al. 2023, in these proceedings for results).

The open-source TELEMAC-MASCARET modelling system (TMS) is an integrated modelling tool for use in the field of free surface flows. The space discretisation is performed with unstructured triangular elements, which means that it can be locally refined in the area of interest. The three-dimensional (3D) discretisation is performed by extruding each triangle along the vertical direction into linear prismatic columns, spanning the water column from the bottom to the free surface. In TMS, simulation modules can be internally coupled to simulate sediment transport and morphodynamics. Modules Telemac-3d and Tomawac solve respectively the current and wave fields to the sediment transport and bed evolution module Gaia (see Durand et al. 2023, in these proceedings for results).

The two models will test different scenarios in term of waves, current and anthropogenic structures (cables, foundations…).

Numerical results from both numerical tools will be compared with each other and with field and laboratory observations. A particular focus will be put on the strengths and limitations of each numerical approach and modelling strategy.

3.2 Fine scale numerical modelling

The aim here is to carry out small-scale modelling of the scouring phenomena around a ground-based structure (e.g., wind turbine foundation) lying over a sandy seabed, subject to wave and current actions at intermediate depths.

The two major scientific barriers identified in the simulations of small-scale modelling of scour around structures are: i) turbulence modelling and accurate simulation of flow hydrodynamics including vortices dynamics and ii) sediment flux modelling. To address the first point, hydrodynamic simulations are performed using different turbulence modelling approach ranging from LES (Large Eddy

Simulation) to RANS (Reynolds Averaged Navier Stokes) and Hybrid to accurately reproduce the Horse-Shoe-Vortex dynamics and the lee-wake shed vortices. Sediment flux modelling is performed *via* various two-phase flow simulations of scour around a cylinder using sedFOAM with the best turbulence modelling approach deduced from the hydrodynamic simulations. (see Gilletta et al. 2023, in these proceedings for results).

3.3 Flume modelling of marine dunes

Marine dunes are modelled in two different flumes: In one of them, the hydrodynamics will focus on the interaction between unidirectional currents and a complex wave spectrum, whereas in the other, tidal currents will be reproduced. These experiments will permit to: (i) extend the range of explored dimensionless quantities (such as Reynolds number or Shields parameter) to derive general formulation and deepen our knowledge of dune morphodynamics under complex forcings, (ii) investigate the influence of superimposed bedforms generated by combined flows on the overall bed roughness, and subsequently on flow properties and dune dynamics.

In a second set of experiments, a cylinder will be added to the experiment to better understand scouring in a marine dune's context (see Vah et al. 2023 and Abroug et al. 2023 in these proceedings for more details).

3.4 Modelling thermal diffusion in marine dunes

Dense grid of power cables is part of each OWF, connecting individual turbines to the substation. Export power cables are then used to reach the mainland. These cables are sensitive to heat as they are designed to work below a specific internal temperature, above which materials (specifically, the insulation) can be damaged. The thermal models for power cable sizing is well established for cables in open water or in air, or buried on land. The thermal boundary conditions of a subsea cable buried in the marine sediment are not so well controlled. Indeed, marine sediment is porous and contains a variable part of water that may influence heat transfers. Therefore, a set of numerical experiments is planned to simulate the impact of dune migration on the distribution between advective and conductive heat fluxes. Several models of varying complexity will be used and compared: 1D analytical model provided by IEC, 1D model not considering advection, 1D model considering advection, and 2D Finite Element Model taking all phenomena into account (see Morvan et al. 2023 in these proceedings for more details).

4 CARACTERISATION OF MARINE DUNES ECOSYSTEMS

The installation of the offshore wind turbines will change the local environment depending on the phase of the OWF project; the resulting pressures/changes will then influence dune ecosystems depending on the pressures/changes intensity and the resistance/resilience of dune systems. From a geomorphological point of view, the changes potentially induced in the shape of dunes, in grain size, in time of refilling after perturbation, all have effects on living communities; indeed, the communities living in sediment are strongly related to sediment characteristics (Robert et al., 2021), some are adapted to muddy environment and others to clean coarse sand.

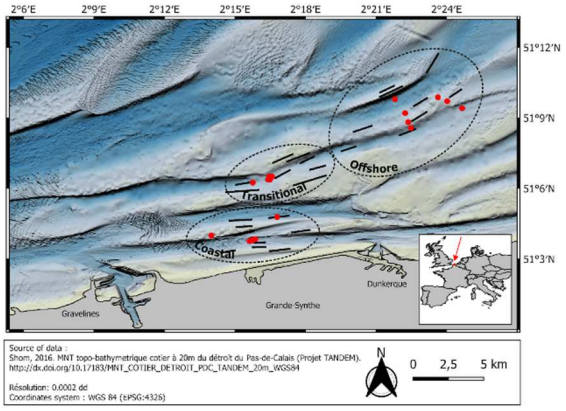

Figure 4 : Marine dunes sampling performed to study their ecosystem (Robert et al., submitted)

Marine dunes affect benthic species distribution (Robert et al., 2021). As we see above, OWF installation create marine dunes morphodynamic disturbance, which can cause effect on benthic habitat.

To study marine dune ecosystem and prevent effect of OWF construction, a sampling of all organisms from the water column to the sediment was performed (Figure 4).

Macrobenthic organisms (>1 mm) were collected with a Van Veen grab (0.1 m^2) whereas megabenthic organisms (> 10 mm) as well as fish species were collected with a commercial bottom-trawl. The latter was equipped with a reduced cod-end mesh of 20 mm stretched to improve the catch of juveniles and small fish. A total of twenty-three stations were sampled with grabs and twenty-six trawl hauls were performed. Stations were distributed in three boxes, according to a gradient of distance from the coast (coastal area, transitional area, and offshore area). This sampling strategy was performed both in Autumn 2019 (October) and Spring 2020 (May) to assess the seasonal variability of the benthic food web.

Organisms (meiofauna, macrobenthic organism and ichtyofauna) were then identified in the lab to establish a list of species for each compartment (Figure 5).

Then, stable isotope signatures of potential sources of carbon and nitrogen in the benthic ecosystem were gathered from an aliquot of sediment, extracted from grab samples (Sedimentary Organic Matter; SOM) and by filtering water on a GFF filter with a Niskin bottle (Particulate Organic Matter, POM). This isotopic analysis has permitted to understand the relation of each compartment of marine dunes ecosystem and decipher spatio-temporal variations in the food web structure (see Robert et al. 2023 in these proceedings for more details).

Figure 5 : binocular photographs of some characteristic invertebrates of the dunes off Dunkirk

5 CONCLUSION

Marine dunes are common in the North Sea where many OWF are planned. As they are very dynamic structures, OWF developers are closely interested in these sedimentary features to prevent their effect on components (cables, foundations).

To better our knowledge on relation between marine dunes and OWF off Dunkirk, we build an innovative multi-disciplinary approach including:

- In situ observation and analysis of morphodynamic and ecosystem of marine dunes
- Numerical modelling of marine dunes at two different scales (meso and finescale)
- Physical modelling of marine dunes in flumes
- Thermal diffusion modelling of heat produced by an export cable in marine dunes.

All these results will permit to help developers to better anticipate cost related to

marine dunes and prevent effect of OWF on marine dunes and their ecosystem.

6 ACKNOWLEDGMENT

This work has received support from France Energies Marines and the State, managed by the National Research Agency under the Investments for the Future program, bearing the reference ANR-10-IEED-0006-33 and ANR-10-IEED-0006-34.

7 REFERENCES

Abroug I., Weill P., Abcha N., (2023) Morphology and dynamics of subaqueous dunes generated under unidirectional flow, MARID VII, Rennes, 2023

Durand N., Tassi P., Blanpain O., Lefebvre A., (2023) Understanding marine dune dynamics in a shallow shelf sea using sediment mobility indices; MARID VII, Rennes, 2023

Gilletta de St Joseph A., Chauchat J., Bonnamy C., Robert M., (2023), hydrodynamic simulations of flow around a pile using turbulence-resolving models, MARID VII, Rennes, 2023

Hoekstra, P., Bell, P., van Santen, P., Roode, N., Levoy, F., & Whitehouse, R. (2004). Bedform migration and bedload transport on an intertidal shoal. Continental Shelf Research, 24(11), 1249-1269.

Le Bot, S., Bary, M., Fournier, M., Husté, A., Michelet, N., Blanpain, O., Nexer, M., Garlan, T., (2023). Marine dune morphodynamics and sediment fluxes (off Dunkirk, France). Spatio-temporal variability and relations with hydrodynamic forcings. MARID VII, Rennes, 2023

Michelet, N., Bary, M., Blanpain, O., Le Bot, S., Nexer, M., (2022). Estimation de l'influence des conditions hydrodynamiques sur les flux sédimentaires associés à la migration des dunes au large de Dunkerque. Journée Nationales Génie Côtier – Génie Civil, Chatou, 2022.

Michelet N., Bary M., Blanpain O., Le Bot S., Nexer M. (2023), Estimation of marine dune migration through three-dimensional numerical modelling and sediment flux calculation., MARID VII, Rennes, 2023

Morvan A., Rivière A., Maison A., (2023), Potential thermal impact of wind farms within a dynamic seabed, MARID VII, Rennes, 2023

Robert, A. E., Quillien, N., Bacha, M., Caulle, C., Nexer, M., Parent, B., ... & Desroy, N. (2021). Sediment migrations drive the dynamic of macrobenthic ecosystems in subtidal sandy bedforms. Marine Pollution Bulletin, 171, 112695.

Robert A. E., Quillien N., Bacha M., Caulle C., Nexer M, Parent B., Garlan T., Amara R., Desroy N., (2023) How it works: benthic ecosystem functioning of submarine sand dunes, from traits-based diversity to isotopic diversity, MARID VII, Rennes, 2023

Vah, M., Ouzaouit M., Besnard H., Jarno A., Morvan B., Marin F., (2023) Bedload quantification by passive acoustic measurement: case of an isolated dune, MARID VII, Rennes, 2023

Modelling effects of shoreface-connected sand ridges on the shoreline evolution: Application to the Belgium coast

A. Nnafie *IMAU, Utrecht University, Utrecht, the Netherlands – a.nnafie@uu.nl*
H.E. de Swart *IMAU, Utrecht University, Utrecht, the Netherlands*
T. Verwaest *Flanders Hydraulics Research, Antwerp, Belgium*

ABSTRACT: This study explores potential impacts of observed onshore migration of shoreface-connected sand ridges (sfcr) on the Belgium shelf on the evolution of the adjacent shoreline using a coupled shelf-shoreline model. Results suggest that the closer sfcr are located to the coast, the stronger are the undulations along the shoreline. These changes in the shoreline are explained in terms of topographically-induced changes in wave characteristics. Key topics of future research will also be discussed.

1 INTRODUCTION

An analysis of historical bathymetric data of the Belgium shelf reveals that a field of shoreface-connected sand ridges (hereafter referred to as sfcr, see Figure 1) migrate landward, at rates in the order of meters per year (R. Houthuys, personal communication). As previous studies (Xu et al., 2015, Safak et al., 2017, Nnafie et al., 2021) have demonstrated that these ridges affect the onshore wave propagation and thereby the patterns of wave breaking and refraction in the nearshore zone, the observed onshore migration of the sfcr on the Belgium shelf might have significant impacts on the evolution of the adjacent shoreline.

The aim of this study is to investigate the impacts of onshore migrating sfcr on the evolution of the Belgium shoreline at timescales of decades. To this end, the shelf

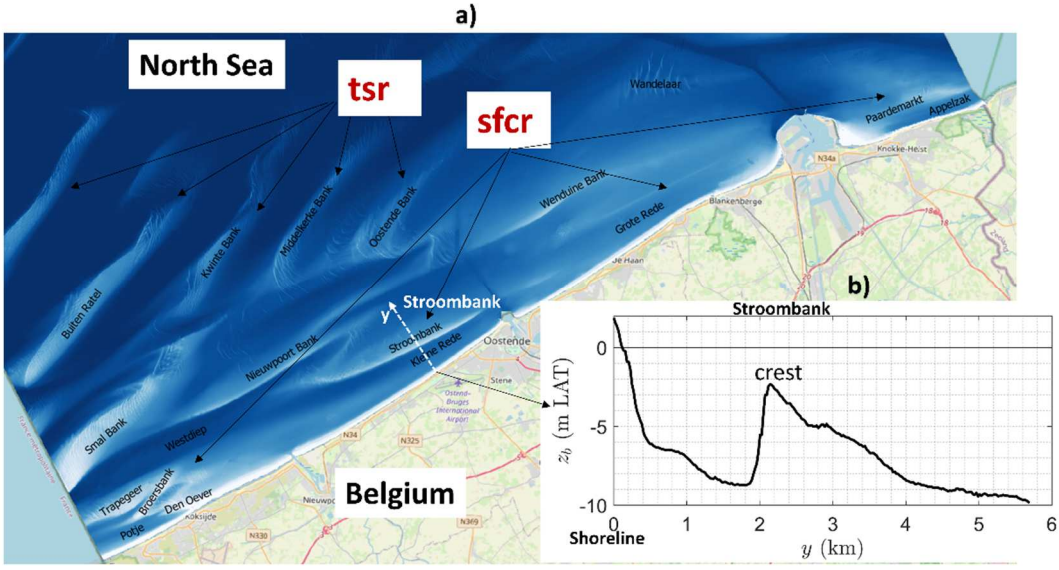

Figure 1. a) Bathymetric map (LAT, m) of observed fields of shoreface-connected sand ridges (sfcr) and the more offshore located tidal sand ridges (tsr) on the Belgium shelf. b) Bathymetric profile along a transect over the ridge "Stroombank".

and shoreline areas will be studied in conjunction with each other. This will be done by using an existing coupled shelf-shoreline numerical model (Nnafie et al., 2021). The model and experiments are described in Section 2, followed by results (Section 3) and conclusions (Section 4).

2 MATERIAL AND METHODS

2.1.1 Model

The model is similar to that in Nnafie et al. (2021), but it has been modified such that it is representative for the Belgium shelf and nearshore coastal zone. This model distinguishes between processes on the shelf ($x_1 \leq x \leq x_L$, $0 \leq y \leq y_L$), in the nearshore zone ($0 \leq x \leq x_2$, $0 \leq y \leq y_L$) and in a coupling zone ($x_1 \leq x \leq x_2$) between the shelf and nearshore zones (Figure 2). On the shelf, the depth-averaged currents, waves and their interactions are computed with Delft3D-SWAN (Lesser et al., 2004, Booij et al., 1996). The water motion is forced by an M_2 tide and constant waves at the seaward boundary, having a significant wave height H_{s0}, peak period T_{p0} and wave direction θ_0 (relative to the shore-normal, positive counter-clockwise). In the nearshore zone, waves, sediment transport, as well as changes in bed level and position of the shoreline are calculated with Q2Dmorfo (Arriaga et al.,

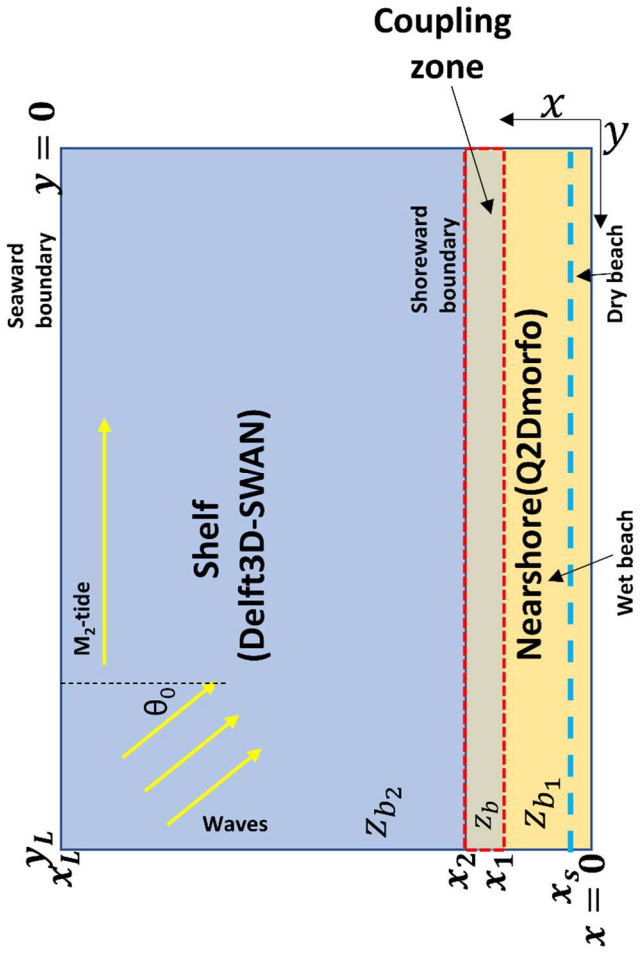

Figure 2. Domains of the shelf ($x_1 \leq x \leq x_L$, $0 \leq y \leq y_L$) and shoreline models ($0 \leq x \leq x_2$, $0 \leq y \leq y_L$), with $x - y$ pointing in, respectively, the cross-shore and alongshore directions. The red rectangle denotes the coupling zone ($x_1 \leq x \leq x_2$). Bed levels $z = z_{b1}$, $z = z_b$ and $z = z_{b2}$ denote the bottom levels of the nearshore, coupling zone and the shelf, respectively. Shoreline position $x_s(y,t)$ marks the border between the dry ($z_b > 0$) and wet beaches ($z_b \leq 0$). Tidal forcing is imposed at the seaward boundary of the shelf (x_L) as an M_2 tidal wave. Furthermore, only mean wave conditions are considered, having a significant wave height H_{s0}, peak period T_{p0} and wave direction θ_0 (relative to the shore-normal, positive counter-clockwise).

2017). Bed levels $z = z_{b1}$, $z = z_b$ and $z = z_{b2}$ denote the bottom levels of the nearshore, coupling zone and the shelf, respectively. Shoreline position $x_s(y,t)$ marks the border between the dry ($z_{b1} > 0$) and wet beaches ($z_{b1} \leq 0$). Initially, the beach has a width x_{s0}. Note that the shelf model is morphostatic, i.e., the bathymetry is kept fixed, whereas the nearshore model is morphodynamic.

2.1.2 Model parameters

Dimensions of the coupled model domain, bathymetry, tides and waves were based on observations on the Belgian coast. Other parameter values were adopted from the work by Nnafie et al. (2021) and Arriaga et al. (2017). The dimensions of the coupled model domain are $x_L \times y_L = 55 \times 75$ km. The coupling zone stretches between $x_1 = 2.5$ km and $x_2 = 5$ km. The dry beach has an initial width of 500 m (i.e., $x_{s0} = 500$ m) and its height is 1 m. Depth increases from 0 m at the shoreline (x_s) to 43 m at the seaward end. The imposed M_2 tidal wave at the seaward boundary ($x = x_L$) has an amplitude $\hat{\zeta}_2 = 1.8$ m. Regarding the waves, S-SW wave conditions were prescribed at the offshore boundaries (with parameters $H_{s0} = 1$ m, $T_{p0} = 5.7$ s, $\theta_0 = 50^o$), which is a crude simplification of observed wave climate in the Belgian coastal region. The computational grid of the morphostatic shelf model has sizes of about 750 m in the cross- and alongshore directions, respectively, while the hydrodynamic time step is 1 minute. The alongshore grid size of the shoreline model is the same as that of the shelf model. However, to resolve the surf zone processes, the cross-shore grid size is much smaller (20 m) and its time step is set to 0.01 days.

2.1.3 Experiments

Three experiments ("Couple-Exp$i$", $i = 1,2,3$) were carried out with the coupled model. An artificial field of sfcr was superimposed on the sloping bed of the shelf (Figure 3). An increasing i means that sfcr are located more onshore. The shoreline is initially straight and is situated at $x_s = 500$ m. As a reference case, a fourth experiment ("Couple-Exp0") was carried out in the absence of sfcr on the shelf (top panel in Figure 3). With this experiment, the relative impact of the presence of sfcr on the adjacent shoreline can be obtained by comparing the situations with and without their presence with each other. The experiments were run for 50 years.

3 RESULTS AND DISCUSSION

Results of the experiments with the coupled model are presented in Figure 4a. Shown are snapshots of the shelf and nearshore bed-levels after 50 years of morphodynamic evolution for different offshore locations of the sfcr ("Couple-Exp$i$", $i = 1,2,3$'). The reference situation (i.e., no sfcr on the shelf) is depicted in the top left panel. The simulated longshore profiles of shoreline positions x_s at $t = 50$ years are presented in Figure 4b. The initial positions of the shoreline (x_{s0}) is situated at 500 m. These figures clearly demonstrate that the presence of sfcr on the shelf causes the formation of shoreline undulations along the adjacent shoreline, which are absent when there are no sfcr. The more onshore the bedforms are located, the stronger these undulations become. As was explained by Nnafie et al. (2021), topographic wave refraction due to the presence of the sfcr leads to the focussing of wave energy density over the crests of the ridges and defocussing of energy in their

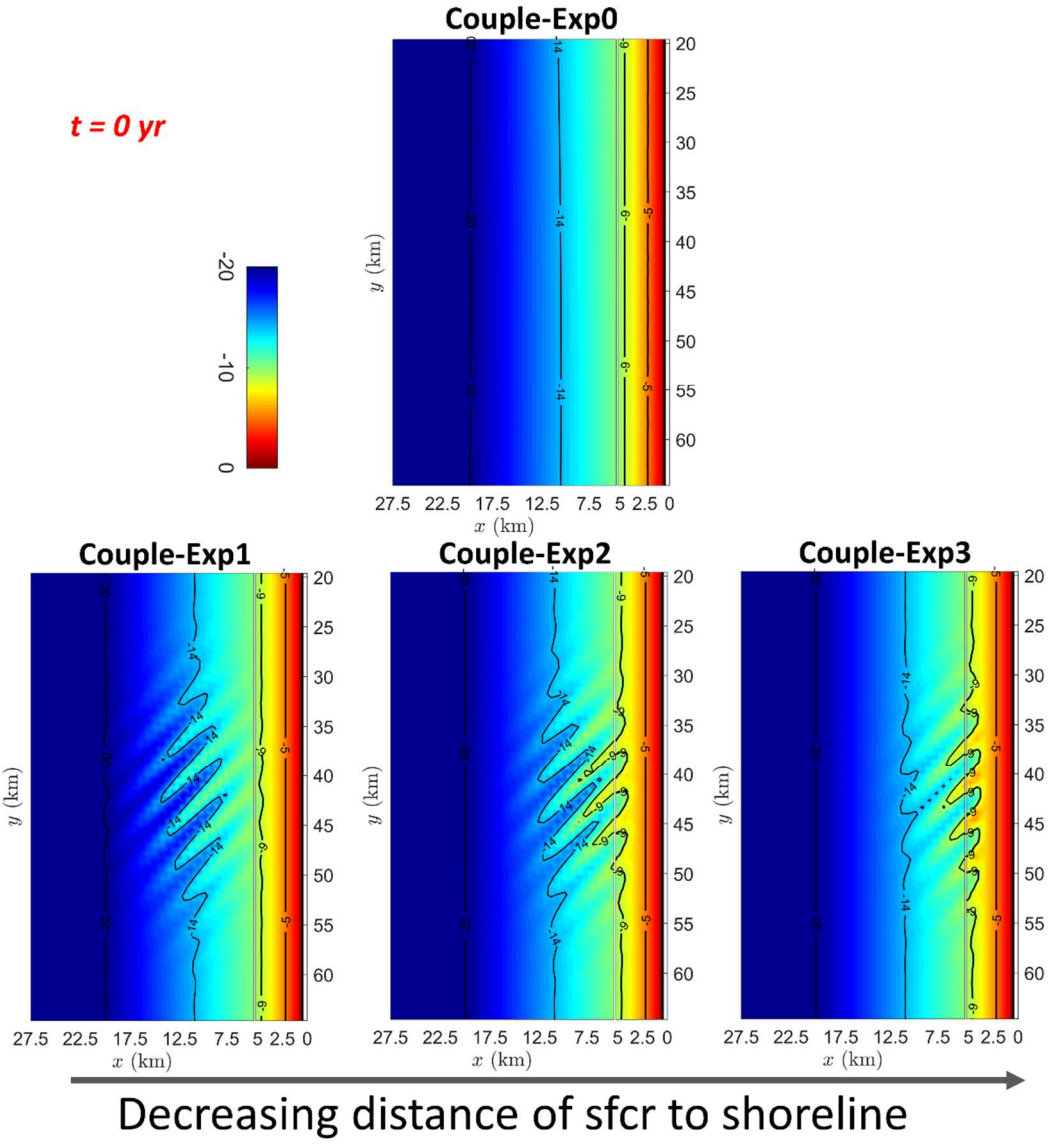

Figure 3. Initial bathymetries in run series "Couple-Exp$i$", $i = 0,1,2,3$'. In the lower panels artificial sfcr were superimposed on the sloping bathymetry, while no sfcr were present on the shelf in the top panel (reference case, "Couple-Exp0"). In each panel, the coast is located on the right. The thick black lines denote the initial shoreline position (x_s).

troughs. Consequently, areas of alternating high and low wave energy occur along the shoreline, which are associated with strong and weak longshore sediment transport. As a result, large alongshore gradients in the alongshore sediment transport occur, thereby creating hotspot areas of erosion and accretion along the shoreline. The more onshore the sfcr are located, the stronger are the alongshore gradients and thus the more distinct are these erosion/accretion areas.

These results suggest that an onshore movement of sfcr is expected to induce stronger shoreline undulations along the shoreline. However, as this model is still under development, these results cannot be translated into projections of the impact of onshore migrating sfcr on the Belgium shoreline. The used wave forcing is crudely simplified. Also, the geometry (offshore extent, orientation with respect to coastline, alongshore spacing) of the artificial sfcr used in the model do not reflect that of observed sfcr on the Belgium shelf. These two issues are key topics of future research.

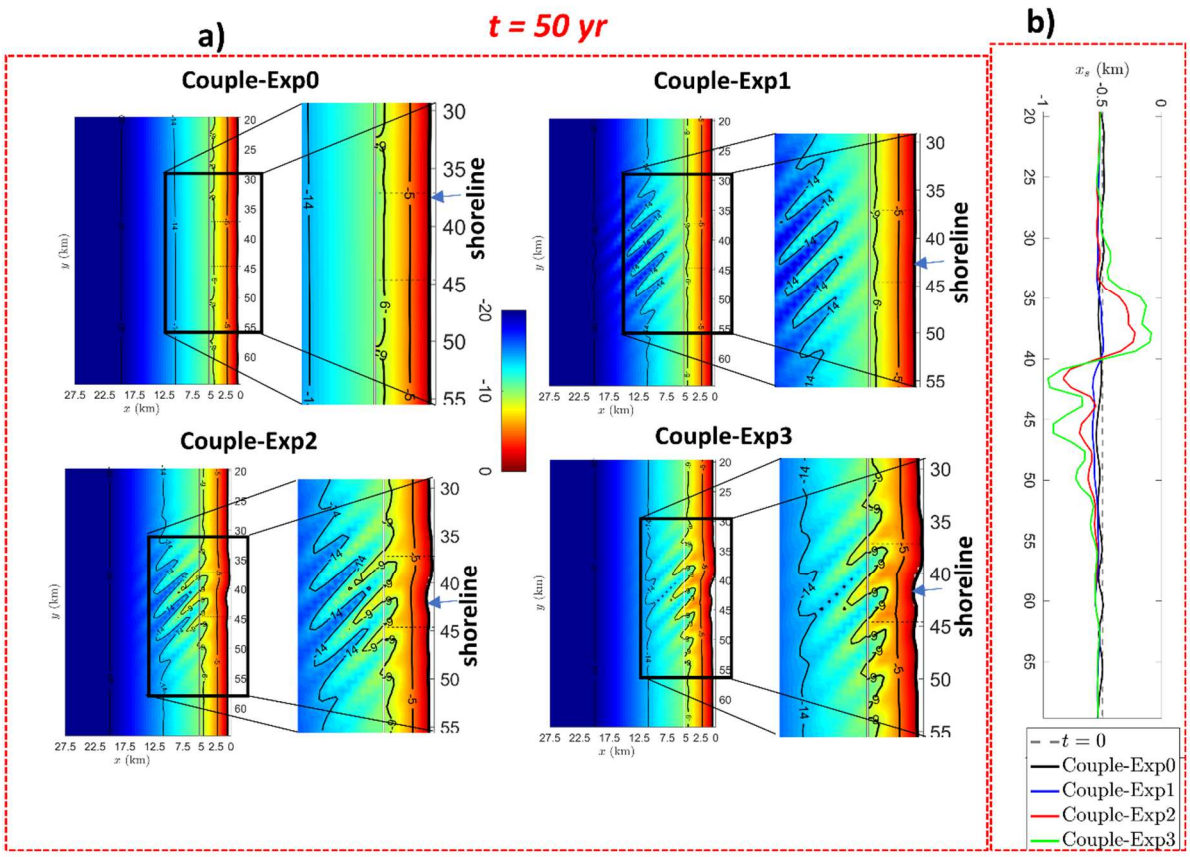

Figure 4. Results of run series "Couple-Exp$i$", $i = 0,1,2,3$' (bathymetry). a) Snapshots (with zoom-ins) of the shelf and nearshore bed-levels at $t = 50$ yr. In each panel, the coast is located on the right. The thick black lines denote shoreline position x_s at $t = 50$ yr. Alongshore profiles x_s after 50 years for the different cases are shown in b). Here, the initial shoreline position ($t = 0$) is denoted by the dashed grey line.

4 CONCLUSIONS AND OUTLOOK

Model results suggest that an onshore movement of sfcr is expected to induce stronger undulations along the shoreline. These undulations develop along the segment of the shoreline where areas of alternating high and wave energy density form as a result of wave refraction over the ridges. Interesting aspects that will be investigated in the near future include sea-level rise, a more realistic wave climate and a more realistic geometry of the sfcr on the Belgium shelf.

5 REFERENCES

Arriaga, J., Rutten, J., Ribas, F., Falqués, A., Ruessink, G., 2017. Modeling the Long-Term Diffusion and Feeding Capability of a Mega-Nourishment. Coastal Engineering 121: 1–13. doi:10.1016/j.coastaleng.2016.11.011

Booij, N., Holthuijsen, L. H., Ris, R. C., 1996. The "SWAN" wave model for shallow water. Coastal Engineering Proceedings, (25). doi:10.9753/icce.v25.%25p

Lesser, G. R., Roelvink, J. A., Van Kester, J. A. T. M., Stelling, G. S., 2004. Development and validation of a three-dimensional morphological model. Coastal Engineering, 51(8), 883–915. doi:10.1016/j.coastaleng.2004.07.014

Nnafie, A., de Swart; H. E., Falqués, A., Calvete, D., 2021. Long-Term Morphodynamics of a Coupled Shelf-Shoreline System Forced by Waves and Tides, a Model Approach. Journal of Geophysical Research: Earth Surface 126 (12). doi:10.1029/2021JF006315

Safak, I., List, J. H., Warner, J. C., & Schwab, W. C., 2017. Persistent shoreline shape induced from offshore geologic framework: Effects of shoreface connected ridges. Journal of Geophysical Research: Oceans, 122(11), 8721–8738. doi:10.1002/2017JC012808

Xu, T. 2015. Wave transformation and alongshore sediment transport due to obliquely oriented shoreface-connected ridges. PhD Thesis. Georgia Institute of Technology, USA, 108pp

Exploring the main drivers of sand wave dynamics

P.H.P. Overes *University of Twente, Twente, Deltares, Delft, Netherlands – p.h.p.overes@utwente.nl*
B.W. Borsje *University of Twente, Twente, Netherlands – b.w.borsje@utwente.nl*
A.P. Luijendijk *Deltares, Delft, Netherlands – arjen.luijendijk@deltares.nl*
S.J.M.H. Hulscher *University of Twente, Twente, Netherlands – s.j.m.h.hulscher@utwente.nl*

ABSTRACT: Offshore developments, such as the construction wind farms, require detailed predictions of sand wave dynamics. State-of-the-art process-based models have not been able to satisfy this need due to several model limitations and gaps in our understanding of sand wave dynamics. In this study, the influence of tidal and non-tidal currents on sand wave dynamics is investigated. Using the newly developed, highly efficient Delft3D Flexible Mesh model, the local hydrodynamics can be reproduced very well, as shown by a validation using field measurements. Moreover, its efficiency allows for computing multi-year hydrodynamics and bed level changes in reasonable computational efforts, which is unprecedented in sand wave modelling. The results show a significant influence of the non-tidal currents on the sand wave morphology, including periods of sand wave migration opposing the long-term migration direction. Improved understanding of these tidal and non-tidal processes and their effect on the delicate balance of sand wave dynamics is vital for modelling in-situ sand wave dynamics for engineering purposes.

1 INTRODUCTION

All over the world offshore activities have been on a rise over the last decades. With an ever-growing population, the offshore area can fulfil various functions, such as green energy production, for which space on land is lacking. Moreover, with a growing connectedness, through goods, energy and data, a well-maintained infrastructure is needed. However, many sandy, shallow seas around the world, such as the North Sea, are covered with active bed forms (Damen et al., 2018). As a result of their size and dynamic character, tidal sand waves may pose a threat to offshore constructions and navigation channels. Through deformation and migration of these bedforms, cables and pipelines can become exposed and navigational depths can be reduces (Nemeth et al., 2003).

Tidal sand waves are found on shallow seabeds throughout the world. These sand waves have lengths of hundreds of meters, can grow up to 25% of the water depth (Damen et al., 2018) and migrate with speeds up to tens of meters per year (Van der Meijden et al., 2023). Hulscher (1996) used stability analysis to explain their occurrence. She found a delicate system of tide-averaged residual circulation cells, which causes sand wave growth through bed load transport.

To enable construction in sand wave areas, data-driven analyses has been used to provide predictions of future bed levels. In these types of analysis measured sand wave bathymetries are extrapolated into the future, using migration rates from historic data (e.g. Deltares, 2016). However, these extrapolated bathymetries are subject to significant uncertainties. Process-based models could assist in increasing our understanding of the sand wave system and reducing these uncertainties. Furthermore, these types of models could offer solutions for data-scarce areas and give insight into the effect of human interventions and extreme conditions.

Past efforts to numerically simulate the sand waves have resulted in increased understanding of the sand wave system. It was found that residual currents (Nemeth et al., 2002) and superposition of the M4 tidal component (Besio et al., 2003) can cause migration of sand waves. Moreover, Leenders et al. (2021) found a significant influence of underlying tidal sand banks on sand waves, causing upslope migration.

Campmans et al. (2018) studied the influence of wind waves combined with (steady) wind driven currents on sand waves. They found an increased migration rate and a reduced sand wave height due to surface waves.

However, in all long-term modelling studies the equilibrium sand wave height is largely overestimated (e.g. Van den Berg et al., 2012, Van Gerwen et al. 2018), although comparison with the field is complicated due to numerous model simplifications. Krabbendam et al. (2022) were the first to apply a sand wave bathymetry based on measurements in their Delft3D-4 model. Although the migration rates seemed to be well represented, the results showed growing sand waves, while, in reality, they were stable in height. Moreover, the shapes of the sand wave deformed during the simulation, leading to reduced steepness of the lee-side slopes.

These differences between the model results and reality indicate that there are still processes missing in our simulations. A common factor between these and other studies are the simplifications made in the hydrodynamic forcing of the model. In all cases it is assumed that sand wave dynamics are purely caused by the main tidal components (M2 and M4), possibly combined with a constant residual current. However, in the field we often see shape deformations and changes in migration rate over time (see for example Figure 1). This cannot be explained through purely periodic forcing. Moreover, at the Taiwan shoal a substantial influence of a passing tropical storm was found by Bao et al. (2020). They discovered height reductions of over a meter (for sand waves with a height of ~15m) and momentarily increased migration rates of the sand waves.

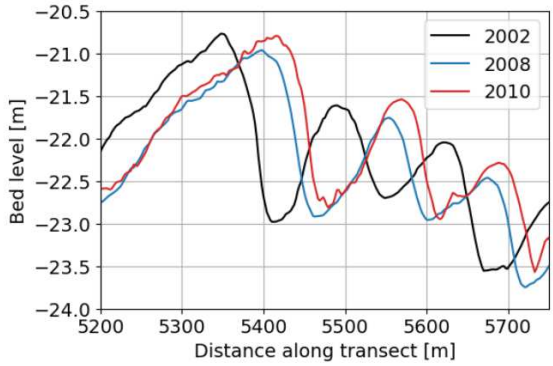

Figure 1. Observed changes in sand wave height and migration rate over time. From MBES data of a transect close to Texel, The Netherlands

The aim of this paper is to determine the influence of irregular time-varying currents on sand wave dynamics. It is hypothesized that non-tidal currents from hydrodynamic events, such as storms, have a significant influence on the temporal sedimentation and erosion rates, and thereby on sand wave migration and shape.

2 METHODS

To study the influence of time-varying hydrodynamic influences on sand wave dynamics, a Delft3D Flexible Mesh (FM) sand wave model is set up. To allow for validation of the hydrodynamics within the model a location is chosen where Acoustic Doppler Current Profiler (ADCP) measurements are available.

2.1 Study site

The chosen location lies within the Hollandse Kust Zuid (HKZ) offshore wind farm area. In relation to the development of the wind farm, two ADCP buoys were deployed here for a period of two years. At the site location (shown in Figure 2), sand waves are present with a height of around 3 meters and a wavelength between 300 and 700 meters. The mean water depth is 23 meters. The sand waves migrate with 1-2 meters per year towards the north-east.

2.1.1 Measurement data

An ADCP measurement buoy was deployed at the model site from June 2016 until June 2018. The buoy measured among others the current profile over depth and the water level. The current was measured at intervals of 2 meters, between 4 and 20 meters below the surface. Measurements are available at intervals of 10 minutes and are publicly available via RVO (2018)

The current data has high coverage (94%) and showed excellent correlation with a neighbouring buoy (deployed for robustness), see Deltares and Fugro (2018).

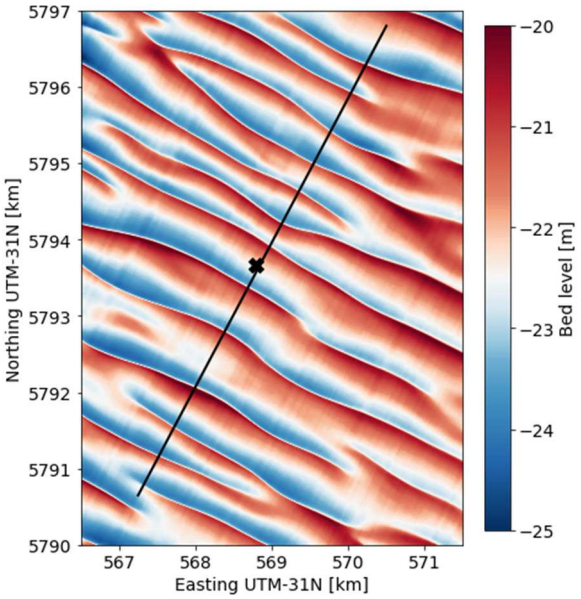

Figure 2. Measured sand wave bathymetry at model location (2016), including sand wave transect in the model indicated by line and the location of the ADCP buoy indicated by the cross.

This data is thus judged to be highly trustworthy.

The measurement device for the water level measurements showed more problems. The device was frequently out of order and thus only has a coverage of 26% of the period. Moreover, significant offsets were observed between the data of the two buoys. The data was corrected for the offset using the large scale DCSM model (see Deltares and Fugro, 2018).

In relation to wind farm development also high resolution Multibeam Echosounder (MBES) bathymetry data was collected. The survey took place in the spring of 2016, which perfectly aligns with the available hydrodynamic data.

2.2 Delft3D Flexible Mesh model

To simulate hydrodynamics, sediment transport and morphology the newly developed Delft3D FM modelling software is used. This model is the successor of the Delft3D-4 model (Lesser et al., 2004), which is established in sand wave modelling (see a.o. Borsje et al., 2014; van Gerwen et al., 2018 and Leenders et al., 2021). The Delft3D FM model offers the possibility to use unstructured grids (flexible meshes) and can run models in parallel (on multiple nodes), contrary to its predecessor. Combined with a time-varying timestep, automatically defined based on the Courant number, the efficiency is increased significantly. For the numerical scheme refence is made to the user manual (Deltares, 2023)

2.3 Sand wave model set-up

The model set-up used in this study is based on the Delft3D-4 model by Borsje et al. (2014). Some alterations had to be made, to make the model suitable for simulating realistic, time-varying hydrodynamics in this study site. In this section the main focus will be on the differences in the set-up.

2.3.1 Model lay-out

To reduce computational effort a 2DV model is set up, limiting the domain to the direction perpendicular to the crest and the vertical (see Figure 2). Since the sand waves are quite regular and long crested in this domain, this simplification is expected to have limited effect on the results. The original domain length from Borsje et al. (2014) is reduced from 50 to 17 km. By bringing the boundaries closer to the area of interest, the hydrodynamics at the boundary are more alike what is present in the sand wave domain. In the middle of the domain a sand wave area of 7 km is present, where the sand waves are dampened over the outermost kilometre. This sand wave bathymetry, composed from measurements, is superimposed on the static bathymetry. At the location of the sand waves, horizontal grid cells of 2 meters are used, which increase in size towards the boundaries, outside of the area of interest. In the vertical 40 sigma layers are used, with increasing size from 0.05% at the bed to 14% at the surface.

2.3.2 Hydrodynamic set-up

The Riemann boundaries in the original model set-up (Borsje et al., 2014, which are developed to simulate tidal conditions, are replaced by one velocity (SW) and one water level (NE) boundary. In this way non-tidal currents can be included, which is not

Table 1: Model cases. Positive velocities indicate flood direction (from left to right in the figures)

Case	I	II	III
Forcing type	M2, M4, Z0	M2, S2, M4, Z0	Complete timeseries
Residual current type	Constant	Constant	Time-varying
Residual current strength [m/s]	+0.026	+0.026	Between -0.40 and +0.74

possible using Riemann boundaries. The timeseries for the boundary conditions are derived from the large scale DCSM model (see Deltares, 2018), which includes tidal flows, meteorological influences and density driven flows. With this model a hindcast is done for the measurement period (June 2016 to June 2018). To allow for comparison of the results in- and excluding non-tidal currents, also purely tidal models are set up (see Table 1). For these models, specific tidal components are filtered out of the current and water level timeseries.

2.3.3 Morphodynamic set-up

For simplicity the morphodynamic parameters are not tuned and purely based on measurement or previous model studies. A single fraction sediment is used, with a log-uniformly distributed grainsize. The median grainsize is chosen as 350 μm based on Deltares (2016). The Chézy bed roughness (C) is taken as 70 $m^{1/2}s^{-1}$ and the bed slope parameter α_{bs} of 3 is applied, following Van Gerwen et al. (2018). Only bed load transport is included in the model, since this is expected to be the dominant transport mode. The bed load transport is calculated following the Van Rijn 2004 transport formula. No morphological scaling is applied, so that the hydrodynamic time equals the morphological time. The first 2 days of the simulation are used as hydrodynamic spin-up, excluding morphological change.

2.3.4 Model cases

To assess the impact of non-tidal currents, three model cases are defined. The cases are listed in Table 1. The Case I model most resembles the state-of-the-art model set-up. Here the M2 tidal component (which causes sand wave growth) is combined with the M4 tidal component and a constant residual current (leading to migration). In Case II the S2 tidal component is added, which generates a spring-neap tidal cycle. The Case III model is forced by a timeseries of the full hydrodynamics (including meteorological influences). All models are run for 2 years. For Case III this period spans June 2016 until June 2018 (coinciding with the ADCP measurements).

3 RESULTS

3.1 Hydrodynamic validation

To assess the quality of the model nesting and the ability of the model to reproduce non-tidal currents and water levels a validation is done between the sand wave model and the ADCP measurements. For this validation the current measurements at a depth of 12 meters below the surface are used, since here the best agreement between the two buoys was found (Fugro and Deltares, 2018). The modelled velocity at this depth is constructed through interpolation. As shown in Figure 3, a good agreement is found between the modelled and measured velocities. The model is well able to reproduce momentary high current velocities. Some outliers are visible, which can be attributed to measurement inaccuracies, and the velocity is slightly overestimated in the sand wave model. A similar comparison between the sand wave model and the large scale DCSM model shows a RMSE of 0.036 m/s, indicating that these errors cannot be reduced much further, while using the DCSM model as nesting host.

The modelled and measured water level show good agreement (see Figure 3). Since there were some technical issues with the water level measurements only the first 4.5 months of measurements at the end of 2016 are used for the comparison here. After a long

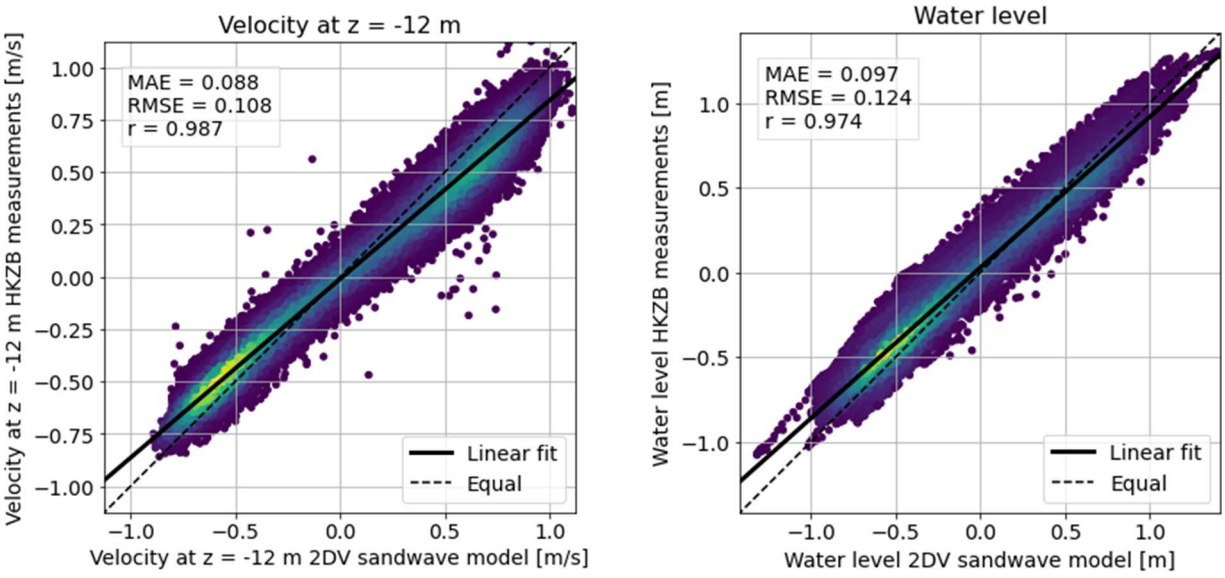

Figure 3. Validation of the modelled current velocities (left) and water levels (right), from the Case III sand wave model with the ADCP measurements.

interception, the last 1.5 months of measurements in 2018 showed a large absolute offset, probably caused by incorrect referencing. The model shows a slight overestimation of the water level variations, but otherwise a nice match is found. Again, with a 0.02 m RMSE between the sand wave model and the DCSM model, not much room for improvement is left.

3.2 Morphodynamic results

The morphodynamic development of the sand waves clearly shows the influence of time variations in the current velocities. In the more traditional model set-up in Case I we see a steady pattern of erosion at the crest of the sand wave and deposition at the steep lee slope. This indicates migration of the sand wave in flood direction. Since every tide is the same with this type of forcing (M2, M4 and Z0), the sedimentation and erosion patterns stay the same throughout the run.

When we add the S2 tidal component in Case II we see more variation in the sedimentation and erosion patterns due to the creation of a spring-neap tidal cycle. During neap tides the bed is quite stable, while during spring type significant migration is occurring.

Lastly the full forcing model shows a very scattered pattern, where spring-neap tidal cycle can still be distinguished in the results, but the rates differ significantly between consecutive days. Events can cause large instantaneous migration. At other times, a sedimentation-erosion pattern indicating migration opposite to the long-term migration direction can be distinguished. This can be recognized by the erosion of the lee-side slope. The tide averaged sedimentation and erosion rates during these events can easily be 4-8 times higher than what is found using a simple tidal forcing (Case I). The different periods in the model showed similar results, with a highly chaotic character.

4 DISCUSSION

In this research we have improved the model set-up of the state-of-the-art sand wave model and shown the importance of non-tidal current for sand wave dynamics. By applying a different kind of boundary conditions more realistic hydrodynamics could be included in the model and the accuracy of both tidal and non-tidal hydrodynamics was improved. The switch to the Delft3D FM modelling software increased the efficiency of the model significantly. This offers the possibility to run years of hydro- and morpho-dynamics in a 2DV sand wave model in just a few days (without using a morphological scale factor; i.e. morfac). The morphological results show a large influence of the time-varying hydrodynamics on sand wave migration.

Periods with sedimentation-erosion pattern indicating opposite migration are observed.

One limitation of this study is the exclusion of free surface waves. Waves can influence sand waves even at large water depths. Campmans et al. (2018) found that especially extreme waves have a significant influence on sand wave migration, even with a low probability of occurrence. The hydrodynamic events present in the Case III model would, in reality, largely coincide with the periods of intense wave action. In this way the sedimentation-erosion pattern leading to migration caused by these wind-driven currents are amplified and the patterns will be even more stochastic.

Due to the 2DV set-up of the model, currents with an angle of incidence with respect to the sand waves were only included with their component in the along transect direction. Although sediment transport along the crests will not directly lead to sand wave migration, these currents may well help in reaching the sediment transport threshold. Moreover, in sand wave fields with more variation in the bathymetry this along crest direction cannot be left out of consideration.

The morphological parameters used in this study were not calibrated. They are purely based on recent papers and field measurements. These parameters are not expected to have a significant effect on the qualitative results of this study, although the magnitude of the sedimentation and erosion could differ. The scattered pattern of sedimentation and erosion caused by the non-tidal currents will still be present and may even be amplified through different morphological parameters (e.g. when the threshold for sediment transport is changed).

In the model including full forcing, sedimentation-erosion pattern indicating migration in both ebb and flood direction were found. To a certain extent, these effects cancel out on longer time periods. In some areas, with storm events from both directions, with similar magnitudes, a constant residual current may thus be an acceptable approximation. However, especially when large events are present, such as the tropical storm in the study by Bao et al. (2021), these specific events may not be neglected. In these areas one storm can transport more sediment than an entire year of tidal forcing. These events thus lead to a certain stochasticity, which should be considered when predicting future bed levels in sand wave areas. The same holds for areas where tidal currents are close to the critical current for sediment transport. Here the ability of the tides to cause migration and deformation of sand waves is limited, increasing the importance of specific events.

5 CONCLUSIONS

This research shows the delicacy of the sand wave system. Relatively small changes in hydrodynamic forcing can have a large influence on sand wave dynamics. We should thus be careful when trying to predict the dynamics of sand wave fields using simplified models.

As a next step the morphodynamic results of the model can be validated using field measurements. Since there are no measurements available for the simulation period used in this study, this is not an option here. By running the simulation for the period between two bathymetry measurements, the need for calibration of the morphological parameters can be determined. With a calibrated model, more accurate predictions of sand wave migration and deformation can be realized using process-based models. Moreover, these models can give insight into uncertainties in predictions related to extreme events.

6 REFERENCES

Bao, J., Cai, F., Shi, F., Wu, C., Zheng, Y., Lu, H., & Sun, L. (2020). Morphodynamic response of sand waves in the Taiwan Shoal to a passing tropical storm. Marine Geology, 426, 106196. doi:10.1016/j.margeo.2020.106196

Van den Berg, J., Sterlini, F., Hulscher, S. J., Van Damme, R., 2012. Non-linear process based modelling of offshore sand waves. Continental Shelf Research, 37, 26-35. doi:10.1016/j.csr.2012.01.012

Besio, G., Blondeaux, P., Brocchini, M., Vittori, G., 2003. Migrating sand waves. Ocean Dynamics, 53(3), 232-238. doi:10.1007/s10236-003-0043-x

Borsje, B. W., Kranenburg, W. M., Roos, P. C., Matthieu, J., & Hulscher, S. J. M. H. (2014). The role of suspended load transport in the occurrence

of tidal sand waves. Journal of Geophysical Research: Earth Surface, 119(4), 701-716. doi:10.1002/2013JF002828

Campmans, G. H. P., Roos, P. C., De Vriend, H. J., Hulscher, S. J. M. H., 2018. The influence of storms on sand wave evolution: A nonlinear idealized modeling approach. Journal of Geophysical Research: Earth Surface, 123(9), 2070-2086. doi:10.1029/2018JF004616

Damen, J.M., van Dijk, T.A.G.P., Hulscher, S.J.M.H., 2018. Spatially varying environmental properties controlling observed sand wave morphology. Journal of Geophysical Research: Earth Surface, 123(2), 262-280. doi:10.1002/2017JF004322

Deltares, 2016. Morphodynamics of Hollandse Kust (zuid) Wind Farm Zone

Deltares, 2018. The 3D Dutch Continental Shelf Model – Flexible Mesh (3D DCSM-FM)

Deltares and Fugro, 2018. Hollandse Kust (zuid) Wind Farm Zone Campaign report – June 2016 to June 2018

Deltares, 2023 D-Flow Flexible Mesh – User Manual

Van Gerwen, W., Borsje, B. W., Damveld, J. H., Hulscher, S. J. 2018. Modelling the effect of suspended load transport and tidal asymmetry on the equilibrium tidal sand wave height. Coastal Engineering, 136, 56-64. doi:10.1016/j.coastaleng.2018.01.006

Hulscher, S. J., 1996. Tidal-induced large-scale regular bed form patterns in a three-dimensional shallow water model. Journal of geophysical research: Oceans, 101(C9), 20727-20744. doi:10.1029/96JC01662

Krabbendam, J., Nnafie, A., de Swart, H., Borsje, B., Perk, L., 2021. Modelling the past and future evolution of tidal sand waves. Journal of marine science and engineering, 9(10), 1071. doi:10.3390/jmse9101071

Leenders, S., Damveld, J. H., Schouten, J., Hoekstra, R., Roetert, T. J., Borsje, B. W., 2021. Numerical modelling of the migration direction of tidal sand waves over sand banks. Coastal engineering, 163, 103790. doi:10.1016/j.coastaleng.2020.103790

Lesser, G. R., Roelvink, J. V., van Kester, J. T. M., Stelling, G. S. (2004). Development and validation of a three-dimensional morphological model. Coastal engineering, 51(8-9), 883-915. doi:10.1016/j.coastaleng.2004.07.014

Van der Meijden, R., Damveld, J. H., Ecclestone, D. W., Van der Werf, J. J., Roos, P. C., 2023. Shelf-wide analyses of sand wave migration using GIS: A case study on the Netherlands Continental Shelf. Geomorphology, 424, 108559. doi:10.1016/j.geomorph.2022.108559

Németh, A. A., Hulscher, S. J., & de Vriend, H. J. 2002. Modelling sand wave migration in shallow shelf seas. Continental Shelf Research, 22(18-19), 2795-2806. doi:10.1016/S0278-4343(02)00127-9

Németh, A.A, Hulscher, S.J.M.H., De Vriend, H.J. 2003. Offsore Sand Wave Dynamics, Engineering Problems and Future Solutions. Pipeline & Gas Journal, April 2003

RVO, 2018. https://offshorewind.rvo.nl/

The residual sand and mud transport in the Schelde-estuary, based on the calculation of the sediment balance

Y. Plancke *Flanders Hydraulics Research & Port of Antwerp-Bruges, Antwerp, Belgium – Yves.Plancke@mow.vlaanderen.be*
G. Vos *Flanders Hydraulics Research & Antea Group, Antwerp, Belgium – Gwendy.Vos@mow.vlaanderen.be*
D. Meire *Flanders Hydraulics Research, Antwerp, Belgium – Dieter.Meire@mow.vlaanderen.be*

ABSTRACT: A sand and mud balance is calculated for the Schelde-estuary for 3 different periods since 2001. The balances are calculated over different segments of the estuary, each 5 to 10 km long, using topo-bathymetric surveys. The differences in volumes are explained by sediment transport at both the up-estuarine and down-estuary boundary, but also by human interventions (e.g. dredging, disposal, extractions). The distinction between sand and mud was made based on bottom samples, taken along estuary, covering all habitats. The sand transport shows an up-estuarine transport over the entire estuary. The mud transport has a different pattern, with a down-estuarine transport over most of the estuary.

1 INTRODUCTION

Sediment transport is important for several estuarine functions. The morphology determines both the tidal penetration in the estuary and the port accessibility (Smolders et al. 2015). Suspended sediment influences the light penetration in the water column and therefore it is crucial for ecology (Meire et al. 2005). The residual sediment transport is crucial for the future evolution of the estuary. To visualise this residual sediment transport on a longer time scale (years), a sediment balance was calculated for the Flemish part of the Schelde-estuary.

1.1 Schelde-estuary

The Schelde-estuary is a macro-tidal estuary with a length of 180 km in Flanders and the southern part of the Netherlands (Figure 1). The sediment balance is calculated for the Zeeschelde, the part up-estuary of the Dutch-Belgian border (KM 60 to KM 160). The morphology is characterised by single channel system with neighbouring tidal flats and salt marshes. The estuary is characterised by semi-diurnal tides, causing ebb and flood currents with important sediment transports of both cohesive as non-cohesive sediments (Baeyens et al. 1998). The Schelde-estuary serves different estuarine functions and therefore faces managers with multiple challenges: increasing tidal propagation vs. safety against flooding; sedimentation in the navigation channel vs. port accessibility; changing dynamics vs. ecology.

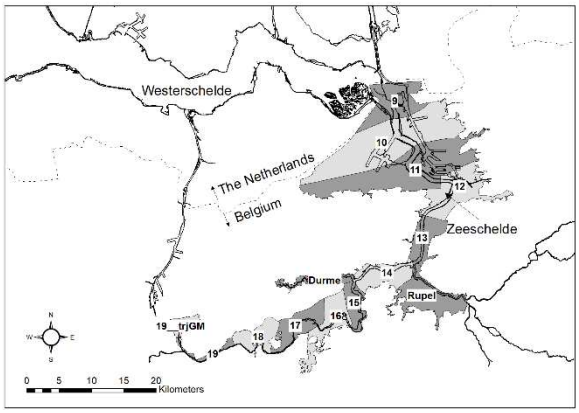

Figure 1. The Schelde-estuary and the schematisation in boxes

2 METHODOLOGY

2.1 Sediment balance concept

The sediment balance (Rosati 2005) is calculated starting from the principle of conservation of mass applied to a simplified schematisation (boxes) of the system (Figure

2). The boxes were defined as 5 to 10 km-long segments (Figure 1), which were previously defined within the OMES-project. Within a certain box, changes in sediment volume are explained by (1) an up-estuarine flux of sediment, (2) an down-estuarine flux of sediment and (3) external factors creating a flux of sediment (eg. sediment mining). The changes in volumes are derived from topo-bathymetries for different moments. At the most up-estuarine boundary, the sediment flux is derived from measurements. The external fluxes are derived from registrations. Starting from these known parameters the down-estuarine sediment flux is derived, which is also the up-estuarine flux for the neighbouring box.

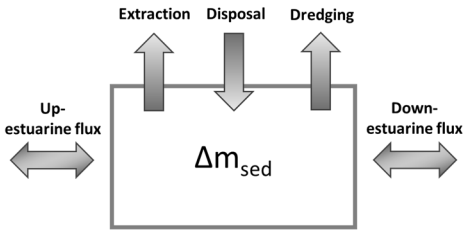

Figure 2. Concept of sediment balance

Where non-cohesive (sand) and cohesive (mud) sediment have a different influence on ecosystem services, it was decided to make a distinction between both sediment fractions. Therefore a sand balance and a mud balance was calculated.

2.2 Topo-bathymetry

For the Schelde-estuary topo-bathymetric information is available for several decades. However, the sediment balance requires a full coverage of the estuary, this was only available since 2001. Within the last 20 years, 4 topo-bathymetric datasets were available, allowing the calculation of the balances for 3 different time periods:

- 2001-2011
- 2011-2016
- 2016-2019

Bathymetric data was collected using singlebeam echo sounding (2001) and multibeam echo souding (2011, 2016, 2019). Topographic data (intra- and supratidal) was collected using LIDAR. Different datasets were merged to get a full coverage of the estuary.

2.3 Fluvial sediment influx

At the up-estuarine boundaries, fluvial sediment fluxes are available. These fluxes are calculated from daily values of discharge and sediment concentration measurements (Vandenbruwaene et al. 2022). For each period, the total fluvial influx can be calculated.

2.4 Human interventions

Within the Schelde-estuary sediment is extracted at several locations, both for commercial purposes, as for dike construction/improvement. Also dredging and disposal takes place to guarantee port-accessibility. With regard to this last aspect, detailed information is available containing the exact location and time of the dredging and disposal works. For the sediment extraction the information is aggregated at a larger spatial scale, however this information was converted at the required spatial scale of the boxes. In this way, the external sediment fluxes are taken into account in the calculation of the sediment balance.

2.5 Sand-mud distinction

The distinction between sand and mud was made based on the sand-mud-percentage for several 100’s of bottom samples. The samples were taken over different habitats [deep/moderate deep/undeep subtidal, intertidal, supratidal, anthropogenic subtidal, anthropogenic intertidal (Van Ryckegem et al. 2022)], and results showed important differences per habitat. The respective fraction of sand (>63 µm) and mud is determined on the samples. Subtidal habitats are dominated by a large (~ 80%) sand content, while inter- and supratidal habitats have a more muddy content. Therefore a specific sand-mud-percentage as applied per habitat-class.

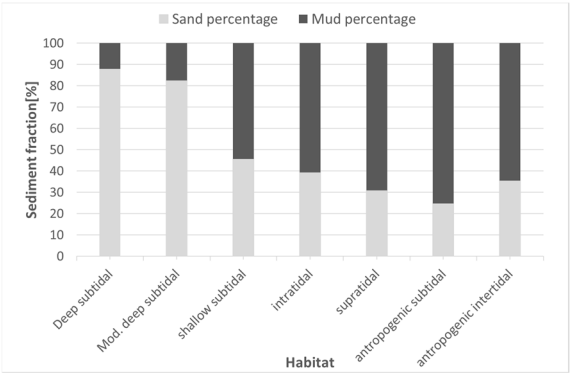

Figure 3. Sand-mud percentage for different habitats

2.6 Volumes to mass conversion

Some data were available as volumes (changes in topo-bathymetry, some dredging/disposal information) while other (fluvial influx, some dredging/disposal information) were available as masses. Therefore it was necessary to convert the values - and the choice was made to convert the volumes to masses, using both porosity and sediment density. Based on Koltermann et al. (1995) the porosity was derived depending on the sand-mud-percentage within the specific habitat:

If $\boldsymbol{\varphi_v < 0.4}$

$$\boldsymbol{\phi} = \phi_{Sd} - \frac{\boldsymbol{\varphi_v}}{\varphi_m} * (\phi_{Sd} - \boldsymbol{\phi_m}) \quad (1)$$

If $\boldsymbol{\varphi_v \geq 0.4}$

$$\boldsymbol{\phi} = \boldsymbol{\phi_m} + \frac{(\boldsymbol{\varphi_v} - \varphi_m)}{(\mathbf{1} - \varphi_m)} * (\phi_{Sh} - \boldsymbol{\phi_m}) \quad (2)$$

With: $\boldsymbol{\varphi_v}$: relative mud fraction [-]

$\boldsymbol{\phi_{Sd}}$: porosity of pure sand = 0.4 [-]

$\boldsymbol{\phi_{Sh}}$: porosity of pure mud = 0.8 [-]

$\boldsymbol{\phi_m}$: minimum porosity = 0.24 [-], occurring for mud fraction equal to 40%

From the porosity, the mass of a certain sediment volume can be calculated. A sensitivity analysis was performed on the importance of this conversion method (vs fixed porosity overall).

3 RESULTS

3.1 Sand balance

The sand balance for the period 2016-2019 (Figure 4) shows up-estuarine transport of sand over the entire estuary. For the previous periods 2011-2016 and 2001-2011 the most upstream parts of the estuary show down-estuarine transports (Figure 4). The location where the residual transport changes from down- to up-estuarine transport, moves progressively more down-estuary when going back in time. What causes this shift still has to be determined. The sensitivity analysis shows that differences in sand-mud percentages cannot account entirely for the differences in sediment transport, and human interventions haven't changed much through the years.

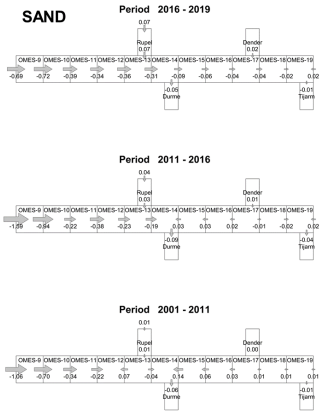

Figure 4. Sand balance for different periods (see figures 4 and 5 at the end of the paper)

3.2 Mud balance

The mud balance for all periods is shown in Figure 5. The residual transport is down-estuary throughout most of the estuary Only for the period 2016-2019 the transport at the downstream border of the Zeeschelde is directed upstream, while the Durme tributary is characterised by an influx of cohesive sediment (mud).

At the most down-estuarine part of the Zeeschelde, the residual mud transport is much larger than in the other parts of the estuary; This is related by the dredging and disposal of muddy sediments in the navigation channels and tidal docks of the

port of Antwerp-Bruges in this region. The disposal strategy in the shown periods, is characterised by disposal locations (OMES 11) up-estuary from the major dredging locations (OMES 9 and 10). The recirculation of this sediment comes clearly out of the calculated mud balance.

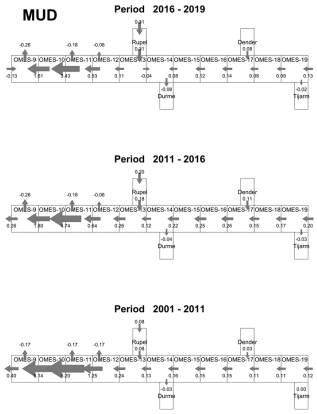

Figure 5. Mud balance for different periods (see figures 4 and 5 at the end of the paper)

4 CONCLUSIONS

Starting from different topo-bathymetric surveys, the sand and mud balance for the Flemish part of the Schelde-estuary was calculated. It was chosen to convert all data into masses in order to calculate a mass balance.

The sand balance shows an up-estuarine transport over the entire estuary. This can be explained by the importance of higher flow velocities in the sand transport, where the sand transport relates to velocity to the power 3 to 5 (eg. Engelund-Hansen formula). The Schelde-estuary is characterised by higher flood velocities, leading to a flood dominance in sand transport.

The mud transport has a different pattern, with a down-estuarine transport over most of the estuary. Only at the most downstream location, mud transport is up-estuarine. For mud transport the classic advection-diffusion equation is valid. The tidal asymmetry (increase of ebb period up-estuary) and the increasing importance of fresh water discharge up-estuary, will result in a more ebb-dominant transport.

Comparing different periods shows similar residual transport directions, although the magnitude varies between different periods. A possible explanation is the temporal variation of fresh water discharge in the Schelde-estuary. This will certainly have an effect on the mud transport, but seems to have an effect on the sand transport as well.

This analysis has shown the temporal and spatial variation in sand and mud transport is an instrument that can be used in future estuarine management.

5 REFERENCES

Baeyens, W., B. van Eck, C. Lambert, R. Wollast, and L. Goeyens, 1998. “General description of the Scheldt estuary.” In Trace metals in the Westerschelde Estuary: A case-study of a polluted, partially anoxic estuary, 1–14. Dordrecht, Netherlands: Springer.

Koltermann, C. E. and S.M. Gorelick, 1995. Fractional packing model for hydraulic conductivity derived from sediment mixtures, Water Resour. Res., 31 (12), 3283– 3297, doi:10.1029/95WR02020.

Meire, P., T. Ysebaert, S. Van Damme, E. Van Den Bergh, T. Maris, and E. Struyf, 2005. “The Scheldt estuary: A description of a changing ecosystem.” Hydrobiologia 540 (1–3): 1–11. https://doi.org/10.1007/s10750-005-0896-8.

Rosati, J.D., 2005. “Concepts in Sediment Budgets” Journal of Coastal Research, 21(2), 307–322. http://www.jstor.org/stable/4299417

Smolders, S., Y. Plancke, S. Ides, P. Meire, and S. Temmerman, 2015. “Role of intertidal wetlands for tidal and storm tide attenuation along a confined estuary: A model study.” Nat. Hazards Earth Syst. Sci. 15 (7): 1659–1675. https://doi.org/10.5194/nhess-15-1659-2015.

Vandenbruwaene, W.; Bertels, J.; Michielsen, S.; Thant, S.; van den Berg, M.; Brackx, M.; Hertoghs, R.; Claeys, S.; Plancke, Y.; Meire, D.; Vereecken, H.; Deschamps, M. (2022). Monitoring Effecten Ontwikkelingsschets (MONEOS) – Jaarboek monitoring 2021: Data rapportage monitoring waterbeweging en fysische parameters in Zeeschelde en bijrivieren. Versie 3.0. WL Rapporten, PA047_11. Waterbouwkundig Laboratorium: Antwerpen. (in Dutch)

Van Ryckegem, G., Vanoverbeke, J., Van de Meutter, F., Vandevoorde, B., Mertens, W., Mertens, A., Van Braeckel, A., Smeekens, V., Thibau, K., Bezdenjesnji, O., Buerms, D., De Regge, N., Hessel, K., Lefranc, C., Soors, J., & Van Lierop, F. (2022). MONEOS - Geïntegreerd datarapport INBO: Toestand Zeeschelde 2021. Monitoringsoverzicht en 1ste lijnsrapportage Geomorfologie, diversiteit Habitats en diversiteit Soorten. (Rapporten van het Instituut voor Natuur- en Bosonderzoek; Nr. 26). Instituut voor Natuur- en Bosonderzoek. (in Dutch) https://doi.org/10.21436/inbor.85928183

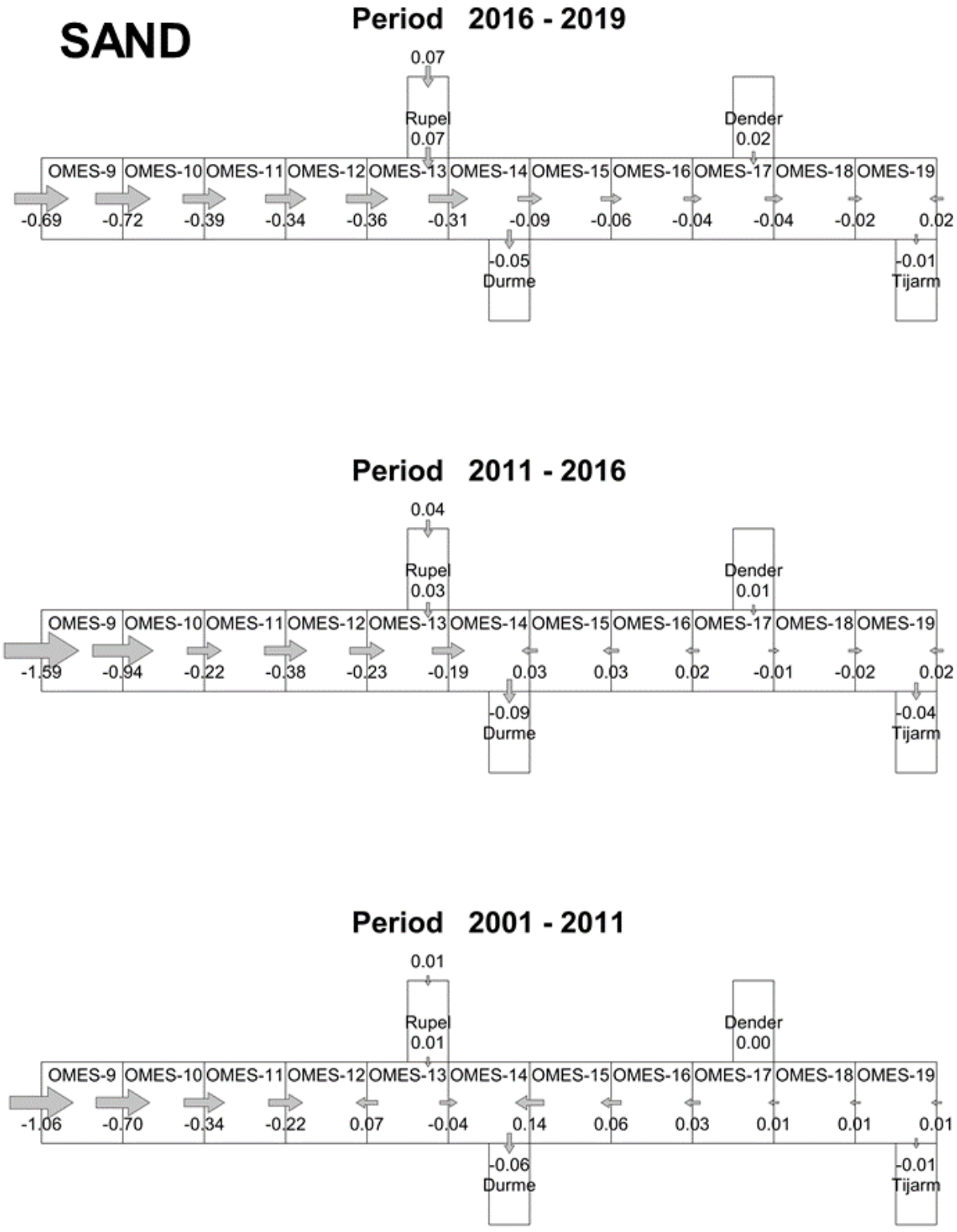

Figure 4. Sand balance for different periods

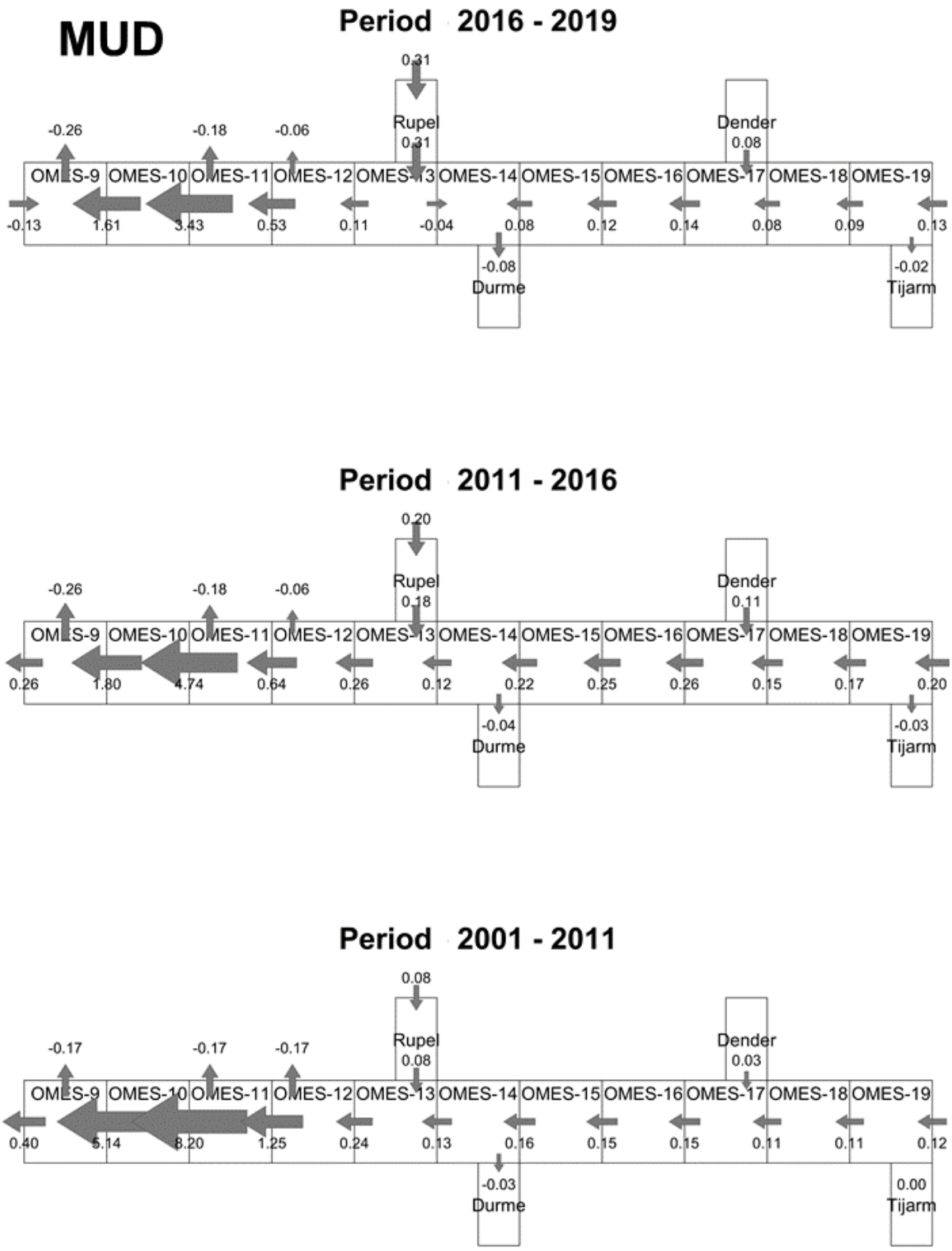

Figure 5. Mud balance for different periods

Tidal sand waves on the lower shoreface: effects on basin-scale hydrodynamics

L. Portos-Amill *University of Twente, Enschede, The Netherlands – l.portosamill@utwente.nl*
P.C. Roos *University of Twente, Enschede, The Netherlands – p.c.roos@utwente.nl*
J.H. Damveld *University of Twente, Enschede, The Netherlands – j.h.damveld@utwente.nl*
S.J.M.H. Hulscher *University of Twente, Enschede, The Netherlands – s.j.m.h.hulscher@utwente.nl*

ABSTRACT: Lower shoreface seabed dynamics are poorly understood. Tidal sand waves (as well as other bedforms) play an important role in the sediment transport and bed evolution of this region. Yet, they are usually overlooked in basin-scale modeling studies. The present work presents a novel method to parametrize bedform friction in order to include sand wave effects on the hydrodynamics of basin-scale domains (such as the North Sea, hundreds of km). Preliminary results show that, due to the presence of sand waves, the flow is deflected and modified in magnitude.

1 INTRODUCTION

The lower shoreface forms the transition between the inner shelf and the upper shoreface. It is usually covered by bedforms characterized by different spatial and temporal scales. We can find ripples (a few decimeters long), tidal sand waves (100 – 1000 m long), and ridges (5 – 10 km long). These bedforms are usually found to co-exist in the field, for example ripples on top of sand waves, and/or sand waves on top of ridges (van der Spek et al., 2022). Thus, they can interact and affect the flow through a modified bed roughness (Soulsby, 1983). As a result, they also affect sediment transport, and thus the morphodynamic evolution of the seabed, resulting in a closed hydro- and morphodynamic loop (Fig. 1).

However, sand waves as well as other bed patterns are mostly studied in isolation (e.g., Blondeaux, 1990; Hulscher, 1996; Roos et al., 2004). Little is known about the two-way

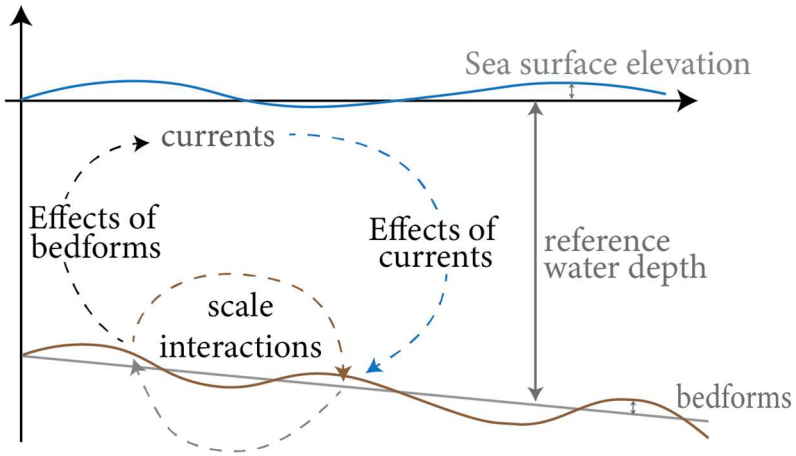

Figure 1. Sketch of the proposed research: We will investigate the effects of bedforms on the currents, but also the interactions between sand waves and larger-scale bedforms, which affect (and are affected by) the currents.

couplings between sand waves and other bedforms, and how these affect the flow. Consequently, the effects of bedforms on basin-scale flows (such as in the North Sea, see Fig. 2a) are usually not considered in modeling studies (see Brakenhoff et al., 2020, and references therein). Similarly, the effects of sand waves on the flow at a sand wave field scale (Fig. 2b) are poorly understood. The above mentioned knowledge gaps primarily concern the hydrodynamics of the lower shoreface. In addition, there is a lack of knowledge regarding the morphodynamics of sand waves on the lower shoreface. More specifically, the effects of a sloping background topography on sand wave evolution (Fig. 2c) and vice versa remain unclear. As part of the MELODY project (ModEling LOwer shoreface seabed DYnamics for a climate-proof coast), the proposed research will tackle these knowledge gaps in order to better understand the dynamics of sand waves on the lower shoreface. Since sand waves (as well as other bedforms) affect the flow and hence sediment transport, more insight on their dynamics will contribute to a better understanding and representation of the processes shaping the lower shoreface.

By addressing the above mentioned knowledge gaps, the proposed research aims to: (1) explain bedform effects on basin-scale hydrodynamics; (2) understand how sand waves affect the flow at sand wave field scales; and reveal sand wave morphodynamics superimposed on a sloping background topography (such as ridges or the lower shoreface) during (3) the sand wave formation stage, and (4) the subsequent evolution. Aims (1) and (2) will serve to better represent bedform-induced hydrodynamics on larger-scale domains (basin scale or sand wave field scale, respectively). Aims (3) and (4) will serve to gain system knowledge on sand wave dynamics on the lower shoreface.

This work focuses on the first aim, i.e., the effects of sand wave-induced friction on basin-scale hydrodynamics. An overview of the methodology used and preliminary results are presented and discussed in §2. Future research approaches are summarized in §3.

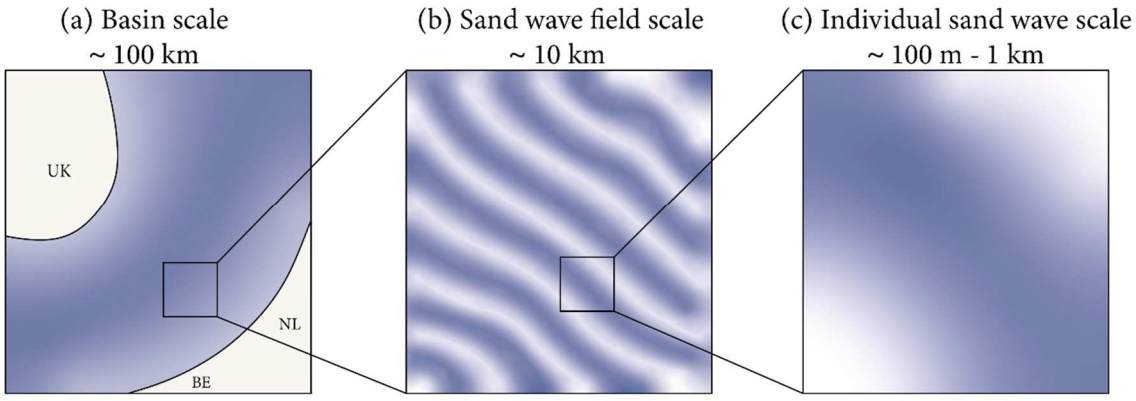

Figure 2. Sketch of the different spatial scales considered in the proposed research: (a) basin scale, such as the North Sea, corresponding to hundreds of km, (b) sand wave field scale, containing several sand waves within it, and corresponding to tens of km, and (c) individual sand wave scale, corresponding to hundreds of m. The proposed research aims to include sand wave effects on the hydrodynamics at basin (a) and sand wave field (b) scales, as well as understanding sand wave (c) morphodynamics superimposed on a sloping background topography.

2 BEDFORM-INDUCED FRICTION IN BASIN-SCALE FLOWS

2.1 Motivation

The effects of sand waves and/or ridges on hydrodynamics are usually overlooked in modeling studies considering basin-scale domains. In such cases, the friction coefficient is usually taken as an overall calibration parameter, thus taken constant in the entire domain (see Brakenhoff et al., 2020, and references therein). In order to better represent bedform-induced effects on basin-scale hydrodynamics, we hereby derive a parametrization of the bed shear stress, which incorporates local bedform field information. Therefore, by using the given parametrization on a basin-scale domain, the effects of bedforms can be accounted for, without actually resolving them.

2.2 Methodology

Consider a basin-scale domain (such as the North Sea, see Figure 3a), where different sand wave fields are present. Each sand wave field is characterized by the sand wave field profile $h(x,y)$, mean water depth H and orientation angle θ (defined as the angle of the crest-normal direction with respect to the x-coordinate). The momentum and continuity equations for a depth-averaged, shallow water flow on the f-plane read

$$\frac{\partial u}{\partial t} + u\frac{\partial u}{\partial x} + v\frac{\partial u}{\partial y} - fv + \frac{\tau_{b,x}}{H+h+\zeta} = -g\frac{\partial \zeta}{\partial x}\,, \tag{1a}$$

$$\frac{\partial v}{\partial t} + u\frac{\partial v}{\partial x} + v\frac{\partial v}{\partial y} + fu + \frac{\tau_{b,y}}{H+h+\zeta} = -g\frac{\partial \zeta}{\partial y}\,, \tag{1b}$$

$$\frac{\partial \zeta}{\partial t} + \frac{\partial}{\partial x}[(H+h+\zeta)u] + \frac{\partial}{\partial y}[(H+h+\zeta)v] = 0\,. \tag{1c}$$

Here, u and v are the depth-averaged velocities in the x and y directions, respectively. Furthermore, f is the Coriolis

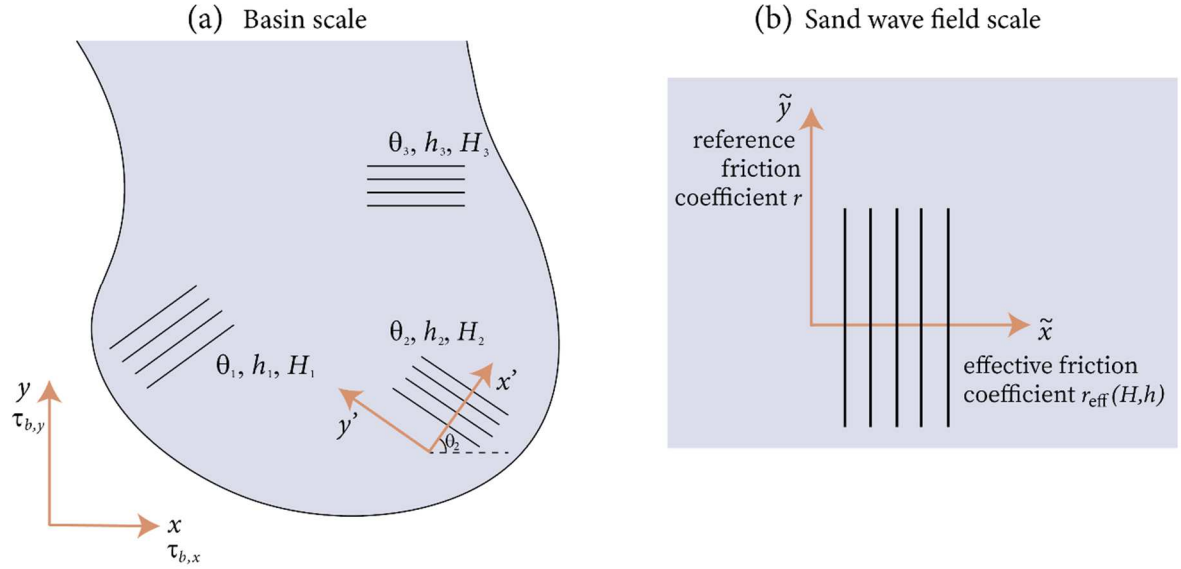

Figure 3. Sketch of the 2DH hydrodynamic model used: (a) basin-scale domain with several sand wave fields (each characterized by the bedform averaged orientation angle θ, sand wave field profile $h(x,y)$, and mean water depth H), and (b) sand wave field-scale domain with the $\tilde{x}$ axis pointing in the cross-crest direction. As a result of this choice of axis orientation, the friction experienced by the bedform-averaged flow is different in $\tilde{x}$ and $\tilde{y}$ directions. Note that two different reference systems are considered at basin scale, (x',y') being rotated with respect to (x,y).

parameter, g is the gravitational acceleration, and ζ is the vertical displacement of the sea surface with respect to the mean (defined at $z = 0$). The friction terms are written in terms of the bed shear stresses, $\tau_{b,x}$ and $\tau_{b,y}$. In the absence of bedforms ($h \equiv 0$), we adopt

$$\tau_{b,x} = ru, \quad \tau_{b,y} = rv, \tag{2}$$

where for convenience, as a first step, the bed shear stresses are parametrized to scale linearly with the flow velocities. Here, r is the *reference* friction coefficient, corresponding to a mean water depth H. The main motivation behind the following methodology is to obtain parametrizations for the bed shear stresses such that the dependence on bedforms is already accounted for in $\tau_{b,x}$ and $\tau_{b,y}$, and it is thus not explicitly included in the equations. We will see that due to the presence of sand waves, the expressions for the bed shear stresses will differ from those in Equation (2). As a result, $\tau_{b,x}$ and $\tau_{b,y}$ will depend on both flow velocity components u and v, and on sand wave field characteristics, such as bedform height, shape and angle of orientation.

We define three reference systems (Fig. 3): two basin-scale reference systems (x,y) and (x',y'), the latter being rotated by an angle θ with respect to the former. The third reference system, $(\tilde{x}, \tilde{y})$, is defined at sand wave field scale (also referred to as *local* reference system). The $\tilde{x}$-axis points in the cross-crest direction, and the $\tilde{y}$-axis int the along-crest direction.

By zooming in on the local reference system $(\tilde{x}, \tilde{y})$, we can assume periodicity in the $\tilde{x}$ direction and uniformity in $\tilde{y}$, because we consider regular bedforms (Fig. 3b). For simplicity, we assume steady flow and a low Froude number, such that the contribution of the free surface displacement to the local water depth can be neglected. We also decompose the forcing terms into two components,

$$-g\frac{\partial \zeta}{\partial \tilde{x}} = -\tilde{F} - g\frac{\partial \tilde{\zeta}}{\partial \tilde{x}}, \tag{3a}$$

$$-g\frac{\partial \zeta}{\partial \tilde{y}} = -\tilde{G}, \tag{3b}$$

where $\tilde{F}$ and $\tilde{G}$ are the components corresponding to the tidal wave, thus spatially uniform at sand wave field-scale. The corresponding momentum and continuity equations in the local reference system read

$$\tilde{u}\frac{\partial \tilde{u}}{\partial \tilde{x}} - f\tilde{v} + \frac{r\tilde{u}}{H+h} = -\tilde{F} - g\frac{\partial \tilde{\zeta}}{\partial \tilde{x}}, \tag{4a}$$

$$\tilde{u}\frac{\partial \tilde{v}}{\partial \tilde{x}} + f\tilde{u} + \frac{r\tilde{v}}{H+h} = -\tilde{G}, \tag{4b}$$

$$\frac{\partial}{\partial \tilde{x}}[(H+h)\tilde{u}] = 0. \tag{4c}$$

From Equation (4c), we infer a spatially uniform discharge $Q = (H+h)\tilde{u}$. Furthermore, we define the spatial averaging operator

$$\langle \cdot \rangle = \frac{1}{L}\int_0^L \cdot \, d\tilde{x}, \tag{5}$$

with L covering an integer number of bedforms. We also define sand wave field-averaged flows $\widetilde{U} = \langle \tilde{u} \rangle$ and $\tilde{V} = \langle \tilde{v} \rangle$, such that

$$\begin{aligned} \widetilde{U} = \langle \tilde{u} \rangle &= \left\langle \frac{Q}{H+h} \right\rangle = \frac{Q}{H}\left\langle \frac{1}{1+h/H} \right\rangle \\ &= \frac{Q}{H}\left\langle 1 - \frac{h}{H} + \frac{h^2}{H^2} - \cdots \right\rangle \\ &\approx \frac{Q}{H}\left(1 + \frac{\langle h^2 \rangle}{H^2}\right) = \frac{Q}{\alpha H}, \end{aligned} \tag{6}$$

thus $\tilde{u}$ can be written in terms of $\widetilde{U}$ as

$$\tilde{u} = \alpha \widetilde{U}\frac{H}{H+h}. \tag{7}$$

Here we have defined the factor α as

$$\alpha = \frac{H^2}{H^2 + \langle h^2 \rangle}. \tag{8}$$

Substituting Equation (7) into Equations (4a,b), and by taking the spatial average over the sand wave field, Equations (4a,b) reduce to

$$-f\tilde{V} + \frac{r_{\text{eff}}\widetilde{U}}{H} = -\tilde{F}, \tag{9a}$$

$$\alpha f \tilde{U} + \frac{r\tilde{V}}{H} = -\tilde{G}\,, \tag{9b}$$

respectively, where we have defined the *effective* friction coefficient r_{eff} as

$$r_{\text{eff}} = \alpha H^2 \left\langle \frac{1}{(H+h)^2} \right\rangle . \tag{10}$$

We thereby identify two different friction coefficients acting on the $\tilde{x}$ and $\tilde{y}$ directions (r_{eff} and r, respectively), with r_{eff} comprising sand wave-induced effects. Thus, sand wave-induced friction effects are experienced in the crest-normal direction.

By zooming out on the basin-scale and rotated reference system, (*x'*,*y'*) (Fig. 3a), we can include sand wave-induced effects on the basin-scale flow by considering the above obtained friction coefficient. Hence, sand wave information is already accounted for, and we do not need to explicitly include h in the momentum equations, yielding

$$\frac{\partial u'}{\partial t} + u'\frac{\partial u'}{\partial x'} + v'\frac{\partial u'}{\partial y'} - fv' + \alpha\frac{r_{\text{eff}}u'}{H+\zeta} = -g\frac{\partial \zeta}{\partial x'}\,, \tag{11a}$$

$$\frac{\partial v'}{\partial t} + u'\frac{\partial v'}{\partial x'} + v'\frac{\partial v'}{\partial y'} + \alpha f u' + \frac{rv'}{H+\zeta} = -g\frac{\partial \zeta}{\partial y'}\,. \tag{11b}$$

By transforming to the non-rotated basin-scale reference system, (*x*,*y*) (Fig. 3a), we obtain the depth-averaged, shallow water equations for a basin-scale, non-steady flow on the *f*-plane, in which the effects of bedforms are implicitly incorporated trough the bed shear stresses $\tau_{b,x}$ and $\tau_{b,y}$. As a result, the flow is not resolved at sand wave scale, yet the effects of bedforms on the flow are considered. The corresponding momentum equations read

$$\frac{\partial u}{\partial t} + u\frac{\partial u}{\partial x} + v\frac{\partial u}{\partial y} - fv + \frac{\tau_{b,x}}{H+\zeta} = -g\frac{\partial \zeta}{\partial x}\,, \tag{12a}$$

$$\frac{\partial v}{\partial t} + u\frac{\partial v}{\partial x} + v\frac{\partial v}{\partial y} + fu + \frac{\tau_{b,y}}{H+\zeta} = -g\frac{\partial \zeta}{\partial y}\,. \tag{12b}$$

Given that we are interested in the effects of bedform-induced friction, and for the sake of simplicity, α has been approximated to 1 in the Coriolis terms. Yet, it is included in the parametrization for r_{eff} (Eq. 10), on which $\tau_{b,x}$ and $\tau_{b,y}$ depend, i.e.,

$$\tau_{b,x} = u\frac{r_{\text{eff}}+r}{2} + \frac{r_{\text{eff}}-r}{2}(u\cos 2\theta + v\sin 2\theta) \tag{13a}$$

$$\tau_{b,y} = v\frac{r+r_{\text{eff}}}{2} + \frac{r_{\text{eff}}-r}{2}(u\,sin\,2\theta - v\,cos\,2\theta), \tag{13b}$$

which replaces Equation (2). Indeed, Equation (13) shows that both velocity components u and v affect both bed shear stress components. Note that the present analysis only considers hydrodynamics, so the bed is considered not to change over time.

2.3 Preliminary results

The described analysis has been applied in a local reference system with two different (synthetic) bedform patterns, both uniform in the $\tilde{y}$ direction, one purely sinusoidal and the other more sharply crested,

$$h_1(\tilde{x}) = \hat{h}\cos(k\tilde{x})\,, \tag{14a}$$

$$h_2(\tilde{x}) = \hat{h}\sum_{j=1}^{10}\frac{1}{j^2}\cos(jk\tilde{x}). \tag{14b}$$

Here k corresponds to the bedform wavenumber, $\hat{h}$ is the bedform amplitude, and we have taken a mean water depth of $H = 20$ m (Fig. 4a). Note that both bed profiles have the same mean water depth.

The respective values of r_{eff} increase with the bedform amplitude relative to the mean water depth (Fig. 4b), with r_{eff} being always larger than r. Furthermore, the sinusoidal sand wave

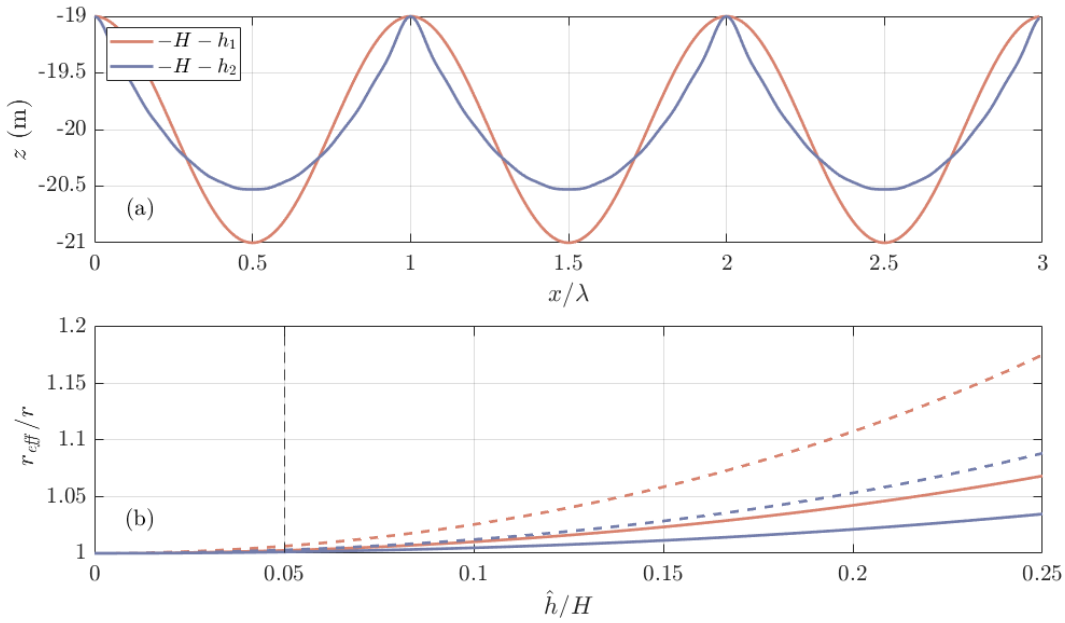

Figure 4. (a) Different sand wave profiles used in the present study, and (b) resulting effective friction coefficient r_{eff} relative to the reference friction coefficient r for different sand wave field amplitudes. Thick solid lines in panel (b) correspond to the situation in which the bed shear stress is parametrized linearly on the flow velocity, while thick dashed lines correspond to a bed shear stress scaling quadratically on the flow velocities (further discussed in §2.4.1). The vertical dashed line in panel (b) corresponds to the situation depicted in panel (a), where the sand wave field amplitude is 1 m. We have taken a Coriolis parameter representative for the North Sea ($f = 1.15 \cdot 10^{-4}$ s^{-1}), and a linear friction coefficient of $r = 2.5 \cdot 10^{-3}$ m/s.

field results in a higher friction coefficient (for equal sand wave field amplitudes). This is because the region over which the bedform is above mean water depth is larger in the sinusoidal bedform case, thus resulting in higher friction. Note that the results are independent on the chosen bedform wavelength.

2.4 Discussion

2.4.1 Flow deflection over a wavy bed

Starting from Equation (9) and further considering the situation in which the same forcing is present, but now on a flat bed, we can obtain the flow on a wavy bed (U,V) with respect to that on a flat bed (U_0,V_0),

$$U = \frac{r^2 H^{-2} + f^2}{r_{\text{eff}} r H^{-2} + \alpha f^2} U_0 \,, \qquad (15a)$$

$$V = V_0 + \frac{f}{H} \frac{r_{\text{eff}} - \alpha r}{r_{\text{eff}} r H^{-2} + \alpha f^2} U_0 \,. \qquad (15b)$$

This results in variations in flow magnitude and angle (Fig. 5). These effects depend, however, on the angle ϕ_0 of the flow with respect to the $\tilde{x}$ axis. When the flow is purely in the $\tilde{y}$ direction ($\phi_0 = \pm 90°$) the flow is not modified because the sand waves are straight-crested in this direction.

2.4.2 Simplifications

Several simplifications have been made in order to obtain the sand wave field-scale friction parametrizations. Most importantly, the bed shear stress has been taken to scale linearly on the flow velocities, whereas it is usually taken to scale quadratically (Soulsby, 1997). The effects of bedforms become more relevant if the bed shear stress is taken to scale quadratically on the flow velocity (dashed lines in Figure 4b). Future work will incorporate this formulation in order to better capture the effects of bedforms on friction.

Separately, for simplicity we have also assumed steady state and low Froude number when computing the parametrizations at sand

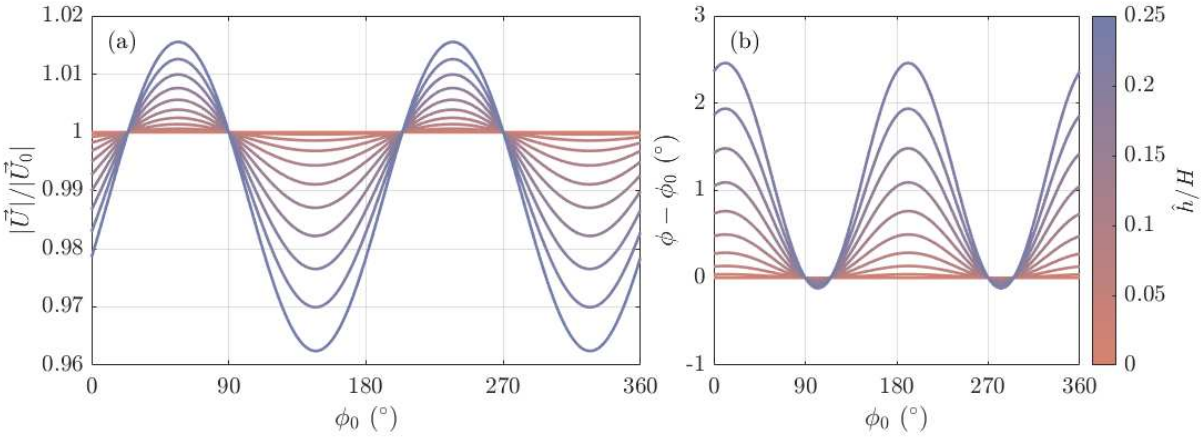

Figure 5. Effects of sand wave-induced friction on local flow (sand wave-scale) depending on the sand wave amplitude with respect to the mean water depth, and the flow angle with respect to the $\tilde{x}$ axis. There are variations in flow magnitude (a), and angle (b). The applied sand wave field is sinusoidal (Eq. 12a).

wave field scale (Eq. 4), but we aim to use them in non-steady models, which do not necessarily lie in the low Froude number regime (Eq. 10).

3 CONCLUSIONS AND FUTURE WORK

We have developed friction coefficient parametrizations that serve to include the effects of sand waves on basin-scale modeling studies. The presented results show variations in flow magnitude and angle due to the presence of bedforms. The magnitude of these effects depends on the bedform amplitude with respect to the mean water depth, and on the flow angle with respect to the sand wave field orientation.

The model presented will be further developed. Most importantly, the bed shear stresses should be taken quadratic on the flow velocities. Furthermore, the overall effect of different (and realistic) sand wave fields on a basin-scale flow will be tested in the future.

4 ACKNOWLEDGEMENTS

This work is part of the MELODY project, which is partly funded by NWO (Dutch Research Council).

5 REFERENCES

Blondeaux, P., 1990. Sand ripples under sea waves Part 1. Ripple formation. Journal of Fluid Mechanics, 218, 1-17. doi:10.1017/S0022112090000908

Brakenhoff, L., Schrijvershof, R., van der Werf, J., Grasmeijer, B., Ruessink, G., & van der Vegt, M., 2020. From ripples to large-scale sand transport: the effects of bedform-related roughness on hydrodynamics and sediment transport patterns in Delft3D. Journal of Marine Science and Engineering, 8(11), 892. doi:10.3390/jmse8110892

Hulscher, S.J.M.H., 1996. Tidal-induced large-scale regular bed form patterns in a three-dimensional shallow water model. Journal of Geophysical Research: Oceans, 101(C9), 20727-20744. doi:10.1029/96JC01662

Roos, P.C., Hulscher, S.J.M.H., Knaapen, M.A.F., & van Damme, R.M.J., 2004. The cross-sectional shape of tidal sandbanks: Modeling and observations. Journal of Geophysical Research: Earth Surface, 109(F2). doi:10.1029/2003JF000070

Soulsby, R.L., 1983. The Bottom Boundary Layer of Shelf Seas, in Elsevier Oceanography Series. Elsevier, 189-266

Soulsby, R.L., 1997. Dynamics of marine sands. T. Telford London, UK.

van der Spek, A., van der Werf, J., Oost, A., Vermaas, T., Grasmeijer, B., & Schrijvershof, R. 2022. The lower shoreface of the Dutch coast – An overview. Ocean & Coastal Management. doi:10.1016/j.ocecoaman.2022.106367

What is the representative elementary volume of preserved dune deposits?

A.J.H. Reesink *Lancing College, Lancing, BN15 0RW, UK and Energy and Environment Institute, University of Hull, Hull, UK – ajhr@lancing.org.uk*
L. Colombera *School of Earth and Environment, University of Leeds, Leeds, UK and Department of Earth and Environmental Sciences, University of Pavia, Pavia, Italy*
D. Das *Department of Geography, University of Santa Barbara, CA, USA*
R.A. Duller *School of Environmental Sciences, University of Liverpool, Liverpool, UK*
V. Ganti *Department of Geography, University of Santa Barbara, CA, USA*
N.P. Mountney *School of Earth and Environment, University of Leeds, Leeds, UK*
D.R. Parsons *Energy and Environment Institute, University of Hull, Hull, UK*

ABSTRACT: Sediment preservation is a selective process in which preserved dune strata present themselves as the equivalent of short TikTok videos of the rock record, capturing only partial and selective information. By recognising and accounting for this bias, we can unlock the potential of preserved dune strata as a source of information on formative flow and sediment transport conditions. This paper examines the state of knowledge from recent and current publications and highlights three areas that require further systematic research. First, research is needed that examines the links between flow, form, and preserved strata with explicit emphasis on bedform scour. Herein, specific attention is also needed to examine precisely how *process-to-product models* can be used in reverse (*product-to-process*) to interpret the multiplicity of controls that shaped the rock record. Second, *multiple lines of evidence* from, e.g., depositional units associated with, e.g., dunes, bars, and floods can be used to reduce uncertainty in palaeo-hydrological interpretations. Finally, a focus on the definition of *'representative samples for preserved dune deposits'* is needed to resolve the temporal and spatial variability in preservation potential within depositional systems. The broad concepts discussed herein apply widely to all sedimentary systems, and as such, dune preservation presents an exemplary case for the wider analysis of the long-term burial or re-mobilisation of carbon and microplastics in our sediment systems.

1 INTRODUCTION

Preserved dune deposits present a rich record of the past, yet one that is incomplete and inherently biased. Precisely what palaeo-hydrological information is contained in the sedimentary record can only be interpreted reliably after the preservation bias has been quantified. The analysis of dune deposits also has a wider significance for our understanding of sediment preservation. We need to know how to use and adapt process-based and quantitative models of sedimentary preservation if we are to understand, for example, the fate of *microplastics* or predict the rate at which *carbon is sequestered* through burial within sedimentary systems such as mudflats. Thus, there exist two central questions as to what precisely controls dune preservation, and how we can adapt and use the conceptual models accounting for dune preservation for different conditions.

Preserved dune deposits present themselves as the equivalent of short TikTok videos of the rock record, capturing only partial and selective information. The preservation bias that characterises the rock record and is a crux problem in geological investigations (Barrell, 1917; Sadler, 1981; Paola et al., 2018). Recurrence of erosion is a

mechanism in the 'shredding' of environmental signals (Jerolmack & Paola), and yet dune deposits themselves are used widely and with increasing nuance and success to reveal information on formative hydrological conditions (e.g. Wood et al., 2023; Lyster et al., 2022). These studies demonstrate, but do not constrain, the value of dune sets as palaeo-hydrological indicators.

To visualise how dune deposits are linked to the dynamic evolution of dunes, the morphodynamic feedback (Leeder, 1983) can be extended to include a unit for the sedimentary deposits (Fig. 1). This usefully highlights that the interpretation of dune deposits requires knowledge of hydraulics, and that dune deposits provide invaluable information that helps us constrain the natural form-flow dynamics of dunes. This paper examines this premise and summarises a number of gaps in our understanding of the links between 'live' dunes and their preserved deposits in order to define some focal points for future research.

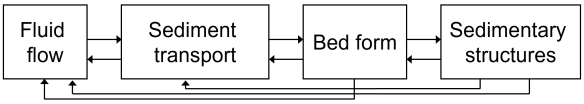

Figure 1. A simple diagram of the morphodynamic feedbacks that control the dynamic evolution of dunes and their deposits – 'bed form' includes scour depth.

2 PRESERVATION AS A FUNCTION OF A DUNE SCOUR DISTRIBUTION

To examine preservation, it is useful to first consider some fundamental principles. A preserved dune set, like any sedimentary bed, is defined by its lower and upper bounding surfaces: they are the deepest and second-deepest scour that occurred during the period of its formation. This observation indicates the overriding importance of *the 'extremes' in the distribution of scour depths*. However, this notion of extremes is contrasted against the strange ordinariness of the stratigraphic record, and in particular of river channel deposits (Paola et al., 2018).

Because of our ability to create dunes experimentally under a range of conditions, dunes have become quite possibly the most intensely studied case of sedimentary preservation (e.g. Paola and Borgman, 1991; Leclair and Bridge, 2001; Jerolmack & Mohrig, 2005). The analytical and mathematical models of sedimentary preservation (Kolmogorov, 1951; Paola and Borgman, 1991) are based on the premise that the recurrence of erosion ('random topography' cf. Paola and Borgman, 1991) can be linked to specific characteristics of the preserved dune-set distribution. This concept – referred to as *variability-dominated preservation* – is widely applicable to all sedimentary systems, and provides a crucial piece of knowledge for 'hot topics', such as the fate of microplastics in sediment systemsand carbon sequestration by means of the long-term burial of carbon-rich sediment. A flexible examination of the key premises that underpin this key model has the potential to unlock its application more widely, and a study of dunes has the potential to fulfil this important function.

The classic '*variability-dominated model'* of dune preservation (Paola and Borgman, 1991) describes the distribution of preserved sets as a function of the distribution of dune scour (central theory in Fig 2). The core concept of the variability-dominated model is its focus on the tail of the scour-depth distribution. Assumptions are made about the tail of the scour distribution in order to arrive at a quantitative analytical solution that links deposits back to their scour distribution. The procedure of quantitatively linking a scour distribution to the associated strata has been validated through flume-based research (Leclair and Bridge, 2001) and constrained though examination of exceptions to the rule (Reesink et al., 2015). The key weakness of this model appears to be its dependency on our understanding of relative importance of multiple co-operating controls on dune scour (Fig 1.).

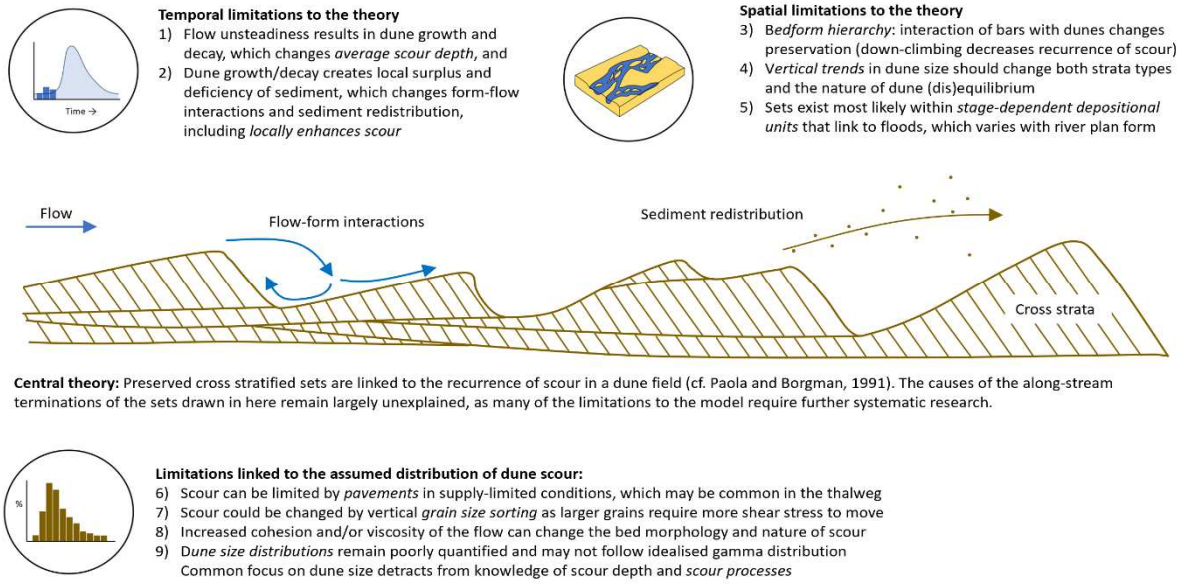

Figure 2. Review of the central theory on how a distribution of dynamically evolving dunes create selectively preserved cross-stratified sets, with a number of limitations.

3 CONSTRAINING THE VARIABILITY-DOMINATED MODEL

In research aimed at constraining the existing models, there have been three recent key advances on how dune morpho-dynamic processes affect preservation potential.

First, the '*unsteadiness hypothesis'* of Leary and Ganti (2020) examines how unsteady flow affects preservation. The greater potential for deep scour when dunes are out of equilibrium with the flow during waning flow stages (cf. Reesink et al, 2018) is likely to create a systematic bias in the preserved strata. The spread in the preserved dune set distribution (covariance) might be an indicator of the degree of disequilibrium between the flow and the dunes.

Second, the '*hierarchy hypothesis*' by Ganti et al. (2020) examines how interactions between dunes and larger-scale morphology such as bars affects preservation. It is well known that dunes decelerate and decrease in size as they deposit sediment on the low-angle lee slopes of unit bars (Reesink et al., 2015). Areas of significant net deposition are not captured properly by the variability-dominated model because the deposits are not the product of a 'distribution'. In decelerating flows, each dune deposits sediment as it *decreases in height downstream (Rubin and* Hunter, 1982). This observation highlights that dune scour, aggradation, and migration are not independent variables, which is problematic for the application of the variability-dominated model. The evidence of zones of net deposition by down-climbing dunes is common in the rock record (e.g. Haszeldine, 1983).

Third, the '*transport stage hypothesis*' by Das et al. (2022) examines how decreased scour at both low and high transport stages affects preservation. Any such change in scour depth affects the recurrence and distribution of dune scour. The conclusion herein is that set thickness may be more sensitive to transport stage than flow depth, and as such, that estimations of palaeo-flow depths based on cross stratified sets may be necessarily low in resolution. Simultaneously, dune sets may be useful as indicators of transport stage, which raises questions about what variables shape the

rocks record, and which ones may be interpreted from it.

To test the viability of models derived from such experimental studies, Colombera et al. (in review) examine a large dataset of measurements of preserved cross stratified set thicknesses from different river systems. Their findings indicate that only a quarter of the investigated cases matches expectations based on the idealised variability-dominated model. The majority of the results do not follow the idealised model, nor do they indicate another simple systematic correlation between set thickness statistics and hydrological parameters. Although the absence of a clear relation between cross stratified sets and formative hydrological parameters may be in part due to the nature of a meta-analysis (Colombera et al. in review), it also highlights interesting hypotheses for further research.

First, a multitude of factors act simultaneously to create preserved dune strata (Fig. 3). When there is a multiplicity of factors or processes leading to a single product, a simple inverse interpretation may not be possible (Fig. 3). Instead, multiple parallel lines of evidence may be needed to resolve the uncertainty. Fortunately, a range of options is available, including the use of covariance alongside the mean of set thickness (Leary and Ganti, 2020) and the addition of, among others, analyses of unit-bar sets (Alexander et al., 2020), unit-bar cross strata (Reesink, 2018), and co-sets and other coherent depositional units (e.g. Reesink et al., 2014).

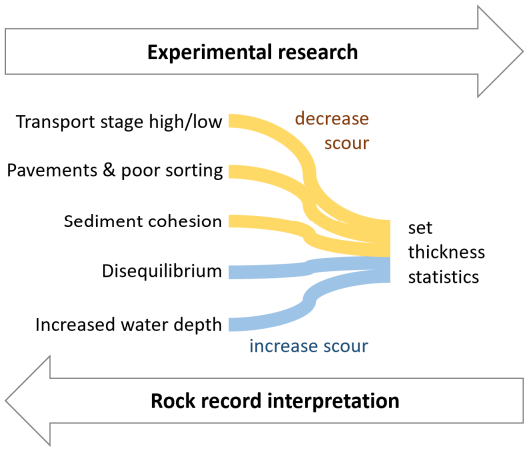

Figure 3. A multiplicity of formative factors complicates the interpretation of the rock record, necessitating the addition of further parallel lines of evidence in an interpretation.

Second, the lack of a clear correlation between preserved sets and hydrological parameters may be linked to the inherent variability within river systems. For example, river depth and width scale to discharge, and as such are perpetually re-adjusting to changes in river flow. Bridge (1993) highlighted that in addition to re-equilibration of the channel, the main zones of scour and deposition change over time and with stage. This notion has since been confirmed and expanded through field studies (e.g. Szupiany et al., 2012; Hackney et al., 2018). Furthermore, floods vary, and all perennial rivers have an ephemeral zone over the bar tops where changes in flow are much greater than those seen in the thalweg (Demyanov et al., 2019). Significant differences in dune development and scour may be expected within rivers.

4 A SIMPLE STOCHASTIC EXAMINATION

For the case of dunes, a major question appears from the recent research: *how much do dune distributions vary, and how are different scour distributions reflected in the sedimentary record?* This paper examines this question through some simple forward modelling. Figure 4 presents two contrasting distributions: 1) a gamma distribution with a

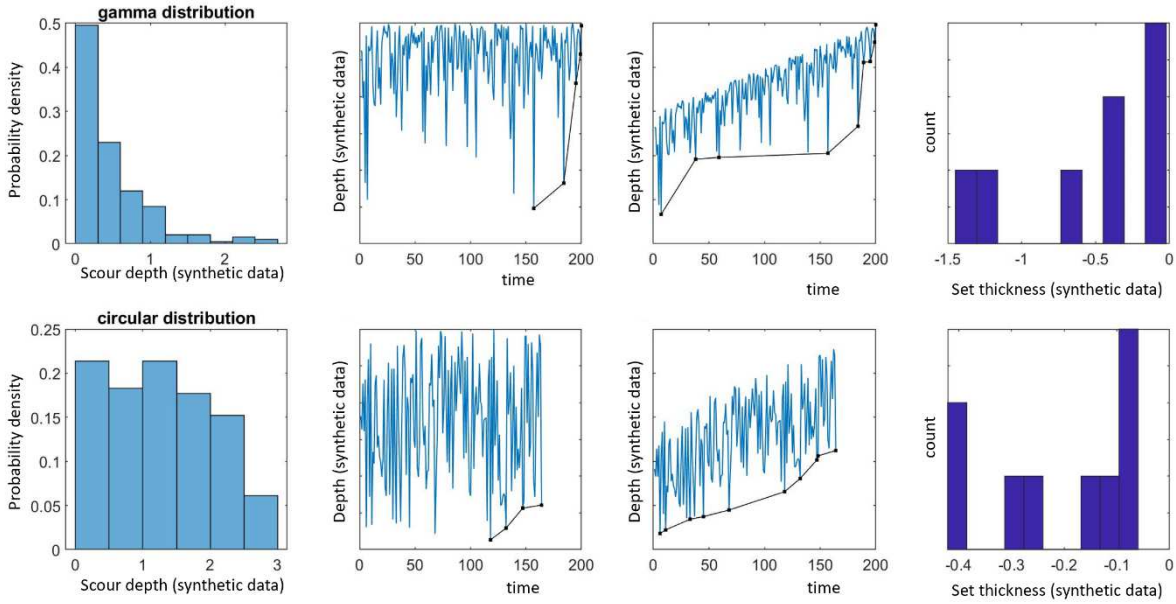

Figure 4. Two contrasting scour distributions (left), the stratigraphy they create under zero deposition and net deposition, and the thickness distribution they leave behind (right).

distinctive concave tail, and 2) a contrasting 'circular' distribution that has a finite, convex tail (a simple Monte-Carlo solution from random data with $x^2+y^2<1$). This simple stochastic modelling as makes it possible to examine how different scour distributions may be reflected within strata in the rock record.

Figure 4 shows that the contrast in the shape of the tail of the scour distribution leads to major differences in the preserved stratigraphy. A long and thin tail (Fig 4. top) is associated with fewer deep scours, and this creates greater gaps in the record, and thicker sets. The more abrupt end of a distribution's tail is associated with smaller gaps in the record, and thinner sets. The contrast between the two different tails of the scour distributions highlights the need to understand the controls on the distribution of dune scour. Dune scour distributions are known to be controlled by a number of contrasting factors, including transport stage, water depth, dune interactions, sediment cohesion, fluid viscosity, and grain-size sorting. Each factor has a different control on dune scour, thus changing the recurrence of scour and the ultimate distribution of associated strata.

The value of simple stochastic analyses is of course limited. The recurrence or erosion is not the same as a 'scour distribution' because dune sequences are not random. For example, scour depth varies with discharge. Furthermore, 'superimposed' aggradation does not account for the fact that sediment transport occurs through dune migration – aggradation and dune migration are not independent variables. Dune sequences are constrained in time and space. However, the analysis highlights that the shape of the tail and recurrence of the deepest scours are the key. The key focus in the analysis of preserved set needs to shift away from controls on dune scour towards what determines the formation of the deepest scours in a sequence.

One key process, dune interaction, presents itself as a reasonable candidate for a *dune-scour process-hypothesis for dune preservation.* Dunes that grow compete for space, and dunes that decay have to shed sediment and split (Reesink et al., 2018). This simple premise is a foundation for thinking about dune disequilibrium, with notable

implications for the nature of dune scour. If we accept that enhanced dunes scour is linked to the dynamic interaction between dunes, then it may follow that dune preservation is controlled by interactions between successive dunes. This has two major implications: 1) additional knowledge is needed on the nature of dune interactions in relation to scour; and 2) if correct, the tail of a dune scour distribution might be dominated by specific conditions – locally enhanced scours – which are hydrodynamically and geometrically constrained, and thus, can be captured as a specific adaptation of the dune scour distribution.

Additional understanding and advances are needed to constrain the temporal and spatial scales of the process to product relationships. We postulate a set of questions to the research community: (i) *at what temporal and spatial scales should we examine the recurrence of dune scour and preserved dune deposits*; (ii) *is there a representative elementary volume* for dune deposits?* Answering these questions requires a holistic flow-form-deposit approach with a focus on the evolution of dune scour, and a recognition that there is an unresolved heterogeneity in preservation potential within river deposits.

** the smallest volume of preserved dune deposits over which a measurement can be made that will yield a value representative of the whole.*

5 CONCLUSIONS

Knowledge of dune preservation is improving, and this yields increasingly nuanced understanding of rivers in the geological past. However, the current interpretative models remain subject to significant uncertainty. Three areas that require further systematic research are identified. First, our *process-to-product models* and their inverse interpretations (*product-to-process*) require more process-based understanding, which ought to focus on the precise controls on the deepest scours as opposed to scour in general. Second, *multiple lines of evidence* from, e.g., depositional units associated with, e.g., dunes, bars, and floods can be used to reduce uncertainty in palaeo-hydrological interpretations. Finally, a focus on the definition of *'representative samples for preserved dune deposits'* is needed to resolve the temporal and spatial variability in preservation potential within depositional systems.

6 REFERENCES

Alexander, J. S., McElroy, B. J., Huzurbazar, S., & Murr, M. L., 2020. Elevation gaps in fluvial sandbar deposition and their implications for paleodepth estimation. *Geology*, *48*(7), 718-722.

Barrell, J., 1917. Rhythms and the measurements of geologic time. *Bulletin of the Geological Society of America*, *28*(1), 745-904.

Bridge, J. S. (1993). Description and interpretation of fluvial deposits: a critical perspective. *Sedimentology*, *40*(4), 801-810.

Colombera L., Duller R., Reesink A., Mountney N.P., Jeavons V., in review. Records of dune disequilibrium in fluvial cross-stratified sands: a comparative analysis of recent channel deposits. *Sedimentology*

Das D., Ganti V., Bradley R., Venditti J., Reesink A.J.H. Parsons, D., 2022. The influence of transport stage on preserved fluvial strata. *Geophysical Research Letters.*

Demyanov, V., Reesink, A. J. H., & Arnold, D. P. (2019). Can machine learning reveal sedimentological patterns in river deposits? *Geological Society, London, Special Publications*, *488*(1), 221-235.

Ganti, V., Hajek, E. A., Leary, K., Straub, K. M., & Paola, C., 2020. Morphodynamic hierarchy and the fabric of the sedimentary record. *Geophysical Research Letters*, *47*(14), e2020GL087921.

Hackney, C. R., Darby, S. E., Parsons, D. R., Leyland, J., Aalto, R., Nicholas, A. P., & Best, J. L. (2018). The influence of flow discharge variations on the morphodynamics of a diffluence–confluence unit on a large river. *Earth Surface Processes and Landforms*, *43*(2), 349-362.

Haszeldine, R. S., 1983. Descending tabular cross-bed sets and bounding surfaces from a fluvial channel in the Upper Carboniferous coalfield of north-east England. *Modern and ancient fluvial systems*, 449-456.

Jerolmack, D. J., & Mohrig, D., 2005. Frozen dynamics of migrating bedforms. *Geology*, *33*(1), 57-60.

Kolmogorov, A. N. 1951. Solution of a problem in probability theory connected with the problem of

the mechanism of stratification. *Am. Math. Soc. Trans.*, *53*, 171-177.

Leary, K. C., & Ganti, V., 2020. Preserved fluvial cross strata record bedform disequilibrium dynamics. *Geophysical Research Letters*, *47*(2), e2019GL085910.

Leeder, M.R., 1983. On the interactions between turbulent flow, sediment transport and bedform mechanics in channelized flows. In: Collinson, J.D., and Lewin, J., eds., Modern and ancient fluvial systems: IAS Special Publications 6, 5-18. DOI: 10.1002/9781444303773.ch1

Lyster, S. J., Whittaker, A. C., Hajek, E. A., & Ganti, V., 2022. Field evidence for disequilibrium dynamics in preserved fluvial cross-strata: A record of discharge variability or morphodynamic hierarchy? *Earth and Planetary Science Letters*, *579*, 117355.

Paola, C., & Borgman, L., 1991. Reconstructing random topography from preserved stratification. *Sedimentology*, *38*(4), 553-565.

Paola, C., Ganti, V., Mohrig, D., Runkel, A. C., & Straub, K. M., 2018. Time not our time: physical controls on the preservation and measurement of geologic time. *Annual Review of Earth and Planetary Sciences*, *46*, 409-438.

Reesink, A. J. H., 2019. Interpretation of cross strata formed by unit bars. *Fluvial Meanders and Their Sedimentary Products in the Rock Record*, 173-200.

Reesink, A. J., Ashworth, P. J., Sambrook Smith, G. H., Best, J. L., Parsons, D. R., Amsler, M. L., Hardy, R.J., Lane, S.N., Nicholas, A.P., Orfeo, O., Sandbach, S.D., Simpson, C. J. and Szupiany, R. N., 2014. Scales and causes of heterogeneity in bars in a large multi-channel river: Río Paraná, Argentina. *Sedimentology*, 61, 1055-1085.

Reesink, A. J. H., Van den Berg, J. H., Parsons, D. R., Amsler, M. L., Best, J. L., Hardy, R. J., Orfeo, O. and Szupiany, R. N., 2015. Extremes in dune preservation: Controls on the completeness of fluvial deposits. *Earth-Science Reviews*, 150, 652-665.

Reesink, A. J. H., Parsons, D. R., Ashworth, P. J., Best, J. L., Hardy, R. J., Murphy, B. J., McLelland, S.J. and Unsworth, C., 2018. The adaptation of dunes to changes in river flow. *Earth-Science Reviews*, 185, 1065-1087.

Rubin, D. M., & Hunter, R. E. (1982). Bedform climbing in theory and nature. *Sedimentology*, *29*(1), 121-138.

Sadler, P. M. 1981. Sediment accumulation rates and the completeness of stratigraphic sections. *The Journal of Geology*, *89*(5), 569-584.

Szupiany, R. N., Amsler, M. L., Hernandez, J., Parsons, D. R., Best, J. L., Fornari, E., & Trento, A. (2012). Flow fields, bed shear stresses, and suspended bed sediment dynamics in bifurcations of a large river. *Water resources research*, *48*(11).

Wood, J., McLeod, J. S., Lyster, S. J., & Whittaker, A. C., 2023. Rivers of the Variscan Foreland: fluvial morphodynamics in the Pennant Formation of South Wales, UK. *Journal of the Geological Society*, *180*(1), jgs2022-048.

Potential thermal impact of wind farms within a dynamic seabed

A. Rivière *Mines Paris-PSL, UMR 6251, CNRS, Univ Rennes, 35042, France*
agnes.riviere@minesparis.psl.eu
A. Maison *France Energies Marines, Plouzané, France – antoine.maison@ite-fem.org*

ABSTRACT: Offshore wind farms (OWF) have an enormous potential of replacing conventional energy sources. These wind farms are connected to the shore by high-voltage power cables. The cables are usually buried in the seabed. Depending on the power transmission, the cables produce more or less dissipative heat, which is released into the sediments. Heat is carried through the sediments by conduction, and by advection and mechanical dispersion with flowing pore water. Marine dunes are among the most dynamic sedimentary bodies found in the English Channel and North Sea, where most of the future Europeans OWF are expected to be located. However, the heat flow pattern in dynamic marine dunes around such anomalously high heat sources are poorly described. The objective is to better understand the thermal regime of sand around a buried cable under a marine dune and to simulate the impact of dune migration on the thermal processes. This work is part of the MODULLES project: MOdelling of marine DUnes: Local and Large-scale EvolutionS in an OWF context, funded by France Energies Marines and the French government, under the "Investissements d'Avenir" program managed by the French National Research Agency ANR.

This study investigates the impact of the thermal regime of sandy sediments within and below dynamic dunes through coupled numerical simulations of heat transport inside the cable and Darcy-groundwater flow and heat transport in the sediments. This study provides a guidance on the choice of optimal models and procedures for numerical modeling of the thermal processes of buried cable.

Dynamic of the benthic ecosystem of bedform areas assessed via structural diversity, functional diversity and isotopic diversity

A. E. Robert *IFREMER, Unité Littoral, Laboratoire Environnement et Ressources de Bretagne Nord, CRESCO, 38 rue du Port-Blanc, Dinard, 35800,* France alexandre.robert@ifremer.fr
N. Quillien *France Energies Marines – Environmental Integration R&D Program - 525 Avenue Alexis de Rochon, 29280 Plouzané, France* nolwenn.quillien@france-energies-marines.org
M. Bacha *Laboratoire d'Océanologie et de Géosciences, UMR 8187 CNRS, Université du Littoral Côte d'Opale, 32 Avenue Foch, 62930 Wimereux, France mahbac@gmail.com*
C. Caulle *Ocean Zoom, 2 chemin de la Houssinière, 44300 Nantes, France clemence.caulle@oceanzoom.fr*
M. Nexer *France Energies Marines – Environmental Integration R&D Program - 525 Avenue Alexis de Rochon, 29280 Plouzané, France maelle.nexer@france-energies-marines.org*
B. Parent *Ocean Zoom, 2 chemin de la Houssinière, 44300 Nantes, France briz.parent@gmail.com*
T. Garlan *Shom, 29200 Brest, France thierry.garlan@shom.fr*
E. Feunteun *Muséum National d'Histoire Naturelle, Laboratoire Biologie des Organismes et Ecosystèmes Aquatiques, BOREA (MNHN, CNRS, Sorbonne Université, Université de Caen, IRD, Université de Guadeloupe Antilles), Station Marine de Dinard, CRESCO, 35800 Dinard, France eric.feunteun@mnhn.fr*
A. Carpentier *Université de Rennes 1, BOREA (Muséum National d'Histoire Naturelle, Sorbonne Université, Université de Caen Normandie, Université des Antilles), Campus de Beaulieu, 35000, Rennes, France alexandre.carpentier@univ-rennes1.fr*
R. Amara *Laboratoire d'Océanologie et de Géosciences, UMR 8187 CNRS, Université du Littoral Côte d'Opale, 32 Avenue Foch, 62930 rachid.amara@univ-littoral.fr*
N. Desroy *IFREMER, Unité Littoral, Laboratoire Environnement et Ressources de Bretagne Nord, CRESCO, 38 rue du Port-Blanc, Dinard, 35800, France nicolas.desroy@ifremer.fr*

ABSTRACT: Thanks to the combination of various measures of diversity (structural diversity, functional diversity and isotopic diversity) the present study investigates the spatio-temporal dynamic of the benthic ecosystem of bedform areas. Results suggest that the macro-scale distribution of species is mainly driven by the migration rate of bedforms (sandbank, barchan dune and transversal dune) which changes the sediment grain size and reduces macrobenthic diversity. Conversely, the high frequency of migration events homogenizes macrobenthic communities between the troughs to the crest of bedforms. The benthic community structure also changes between seasons due to the massive recruitment of juveniles. However, if species identity and structural diversity change it have little consequences on the general ecosystem functioning. Especially, the benthic food web of bedforms areas appears very stable with limited variations, both in space and time. It displays very simplistic trophic pathways, and the present study confirms the major role of Phytoplankton blooms (and especially *Phaeocystis*) in sustaining the benthic food web.

As bedform areas are targeted for the installation of offshore windfarms, this study will provide a sound scientific basis for future impact assessments.

1 INTRODUCTION

The French continental shelf and especially the Dover straight, the western English Channel, and the Iroise and Celtic Seas exhibit sandy bedforms such as sandbank, dunes and ripples (see the classification of subaqueous bedforms by Ashley, 1990). These structures differ in their morphology (Aernouts, 2005; Le Bot, 2001; Le Bot et al., 2005; Van Lancker et al., 2009) but also in their dynamic: whereas sandbanks are stable over hundreds of years, subtidal dunes are mobile, moving up to one hundred

meters per year in the southern bight of the North Sea (Le Bot, 2001). The morphology of sand ripples changes at short time scale (tidal cycle).

Knowledge on benthic communities inhabiting sandy bedforms stems from large-scale studies that did not specifically target these habitats (*e.g.* Desroy, 2002: 800 km^2; Van Hoey et al., 2004: 2600 km^2). They revealed the presence of two principal macrobenthic communities distributed according to the seabed substrate: a *Nephtys cirrosa/ Ophelia borealis* community found in medium to fine sand assemblage, and a *Magelona johnstoni/ Hesionura elongata* community on muddy heterogeneous sediments. In the French part of the North Sea, these communities exhibit a remarkably low diversity and density with respectively 4.7 and 11.7 species.0.5 m^{-2} as well as 19.2 and 113.4 ind.0.5 m^{-2} (Desroy, 2002).

At a smaller spatial scale, certain studies revealed a decrease in species richness, abundance and Shannon's diversity along the slope of bedforms, from the trough to the crest, in relation to grain size increase (Baptist et al., 2006; Damveld et al., 2018; Ferret, 2011; Mestdagh et al., 2020; van Dijk et al., 2012). These studies were based on taxonomic approaches and, *de facto*, did not consider the role played by species in the ecosystem. More generally, the benthic ecosystem functioning, and especially trophic relations, are poorly known on bedform areas.

Thanks to various measures of biodiversity (structural diversity, functional diversity, and isotopic diversity) the present study aims at improving the knowledge on the dynamic of the benthic ecosystem on bedforms areas.

2 MATERIAL & METHODS

2.1 Study area

The present study focused on an 80 km^2 area located within the French Flander bank, offshore the Dunkirk harbor (Figure 1). The study area was chosen because it exhibits a large variety of bedforms and is targeted for the future commissioning of an offshore wind farm.

2.2 Sampling strategy

Biological material was collected according to a stratified sampling design (Figure 1). Samples were perform (i) in a coastal area with barchan dunes (crescent-shaped dunes), (ii) a transitional area with transversal dunes (*i.e.* straight-lined dunes) and (iii) an offshore area with a sandbank.

Macrobenthic organisms were collected via 23 stations distributed between the trough, the slope and the crest of each bedform (and not only sandbanks). Three additional stations were positioned within a reference area, free from bedforms. Three replicates were collected at each sampling station using a Van Veen grab (0.1 m^2), approximately with a 5–10 m accuracy in the positioning (the vessel size was 20 m length overall). One sub-sample has also been extracted at each station for grain size analysis.

This sampling strategy has been reproduced in autumn 2019 and spring 2020 in order to assess the temporal dynamic of the ecosystem.

2.3 Material collection for stable isotopes analysis

At each sampling station, one additional grab sample has been collected in order to analyse the stable isotope signatures of macrobenthic organisms. In order to provide a larger insight about the benthic food web, 26 trawl hauls (commercial trawl with a “Grande Ouverture Verticale”) were also performed on the coastal, the transitional and the offshore area (Figure 1). The cod-end mesh was reduced to a 20 mm mesh-size (stretched) in order to improve the catch of juvenile fish and megabenthic species.

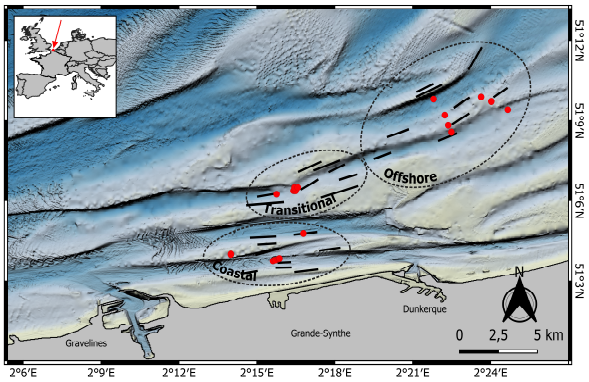

Figure 1 Map of the study area. Red dots represent the location of grab samples whereas black lines represent the location of trawl hauls. Source of data : Shom, 2016. MNT topo-bathymetrique côtier à 20m du détroit du Pas-de-Calais (Projet TANDEM).

A total of 37 species contributing to almost 90% of the biomass was selected for stable isotopes analysis. A maximum of 5 sub-samples per species and size class was dissected at each zone. Samples consisted of muscle tissue for fish and large organisms (bivalves, crustaceans) whereas the entire organism's body was used for the smallest species (small annelids).

Stable isotope signatures of potential sources of carbon and nitrogen were gathered from an aliquot of sediment, extracted from grab samples (Sedimentary Organic Matter; SOM) and by filtering 500mL of water on a GFF filter thanks to a Niskin bottle (Particulate Organic Matter, POM).

Samples processing for stable isotope analysis was similar to the method described in Quillien et al., (2016).

The $\delta^{13}C$ values as a proxy of food source (Bearhop et al., 2004; Post, 2002) and $\delta^{15}N$ values as proxy of the trophic position (Hussey et al., 2014; Post, 2002) were determined by weighting the ^{13}C:^{12}C or ^{15}N:^{14}N ratio of a sample relative to the ^{13}C:^{12}C ratio in a standard (Vienna Pee Dee Belemnite for carbon and N_2 in air for nitrogen) :

$$\delta^{13}C \text{ or } \delta^{15}N=[(R_{sample}/R_{standard}) - 1] \times 10^3$$

with R corresponding to the ratio $^{13}C/^{12}C$ or $^{15}N/^{14}N$.

2.4 Data analysis

Structural diversity, functional diversity as well as isotopic diversity were assessed thanks to a combination of multivariate analysis (non-metric MultiDimensional Scaling, fuzzy Principal Component Analysis and $\delta^{13}C$ vs. $\delta^{15}N$ biplot) and univariate indices (see Table 1).. Biological traits scores used to assess functional diversity have been published as open access database in the SEANOE portal (Robert et al., 2021. doi:10.17882/80785).

Table 1 Univariate indices used to assess structural diversity, the functional diversity as well as the isotopic diversity of bedform areas

Diversity	Univariate indices	References
Structural diversity	Species richness (S)	
	Shannon's diversity (H')	Shannon and Weaver (1949)
	Pielou's evenness (J')	Pielou (1966)
	Total abundance (Ab.)	
	Total biomass (Biom.)	
Functional diversity	Functional Richness (FRic)	
	Functional Evenness (FEve)	Villéger et al. (2008)
	Functional Divergence (FDiv)	
	Functional Redundancy (Fred)	van der Linden et al. (2012)
Isotopic diversity	$\delta^{13}C$ range (CR)	Layman et al. (2007)
	$\delta^{15}N$ range (NR)	
	Isotopic Richness (IRic)	
	Isotopic divergence (IDiv)	Cucherous set and Villéger (2015)
	Isotopic dispersion (IDis)	
	Isotopic evenness (IEve)	
	Isotopic uniqueness (IUni)	

3 RESULTS-DISCUSSION

3.1 Spatio-temporal variations of benthic communities

Benthic communities are shaped by sediment movements - It is well known that sediment movements represent a natural source of disruption for macrobenthic organisms by burying them, in the same way

as dredging deposition (Foster et al., 2010; Jones et al., 2016), or by disrupting their metabolism. The selectivity induced by such environmental constraints is reflected in the trait composition of species within the Dunkirk area. Most organisms are deposit feeders or mobile predator-scavengers. Several species have short life cycles and high productivity, in relation with their small size (Brey, 2001), which allow fast recolonization and the ability to sustain high mortality rates. Moreover, most of the organisms have pelagic eggs and larvae,

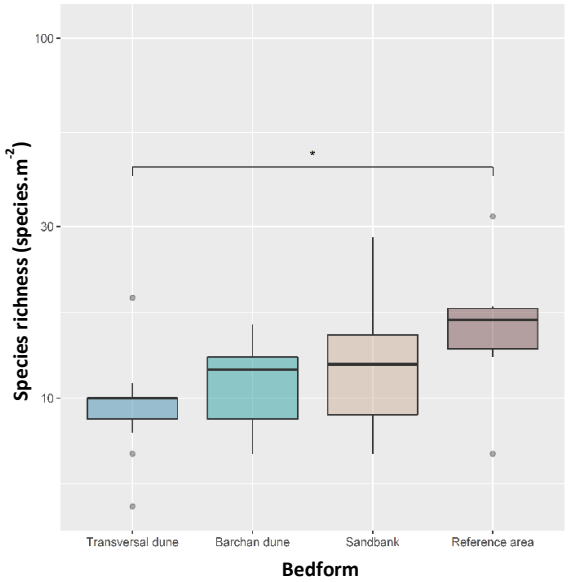

Figure 2 Distribution of the species richness between the different bedforms and within the reference area. Statistical differences have been assessed thanks to pairwise-Wilcoxon tests. Stars denote the p-value of the tests: "***": p-value <0.001; "**": p-value <0.01; "*": p-value <0.05.

which provide the capacity to avoid the disturbance by living out of the sediment during their first development stages. Some species were also emergent (*e.g. Gastrosaccus spinifer*) and/ or sufficiently mobile (*e.g. Bathyporeia pelagica, Bathyporeia elegans, Urothoe brevicornis*) to avoid burying. Finally, and as observed by (Breine et al., 2018) on Belgian dunes, sessile species and suspension-feeders were almost absent from the studied area.

Magnitude of the natural disruptions was uneven within the studied area. The transversal dune can be considered the most impacted with a cumulative rate of migration equivalent to 108 m in ten months (not shown). The impact was lower on the barchan dunes, with around 40 m of migration in ten months, and considered null on the sandbank and on the reference area. These differences were reflected in the species richness (Figure 2) and biomass that showed a gradient between bedforms. To our knowledge, no additional studies investigated how structural and functional diversity vary with the kind of bedform.

A classical pattern of seasonal variability - Structural diversity and to a less extent, functional diversity, were generally higher in spring, relative to autumn. For instance species richness increased by 1.7 and 2.1, and abundance by 8.7 and 2.1 on the transversal dunes and the sandbank, respectively. Spring settlement was reflected by very high densities of juveniles *Lanice conchilega* but also by higher abundance of small species such as *Magelona filiformis*, *Hesionura elongata*, *Crangon crangon*, *Spio martinensis*, *Bathyporeia gracilis*, *Eumida sanguinea* and *Salvatoria clavata*. This was consistent with several studies conducted in the North Sea where benthic communities exhibit a maximum at the end of summer and beginning of autumn due to settlement. They sho a a minima at the end of the winter and beginning of spring due to immigration and high mortality rates (Reiss and Kröncke, 2005; Van Hoey et al., 2007).

Sediment movements homogenize the benthic community within bedforms -- Sedimentary characteristics varied along the slope of the transversal dune and of the sandbank (Figure 3). The median grain size increased towards the crest of transversal dunes, which was consistent with previous studies (Carvalho et al., 2018; Damveld et al., 2018; Mestdagh et al., 2020), probably because transversal dunes are oriented perpendicular to the tidal current which induces a trap of fine sediment in inter-dunes depressions. Conversely, a very slight decrease of the median grain size (not significant) was observed between the trough

and the crest of the sandbank (Figure 3). This bedform is oriented parallel to the main tidal currents. Bed shear stress could be stronger in inter-banks depressions, which, in turn, may induces the advection of fine sedimentary particles.

Variations of sedimentary characteristics within bedforms did not alter the structural and functional diversity along the slope of the sandbank and dunes. This result differs from those obtained by a few rare studies performed on this topic, revealing a higher benthic diversity in the trough compared to the crest of bedforms (Damveld et al., 2018; Ellis et al., 2011; van Dijk et al., 2012). did not show any clear trend along the sandbank and the transversal dune profiles which differ from previous studies. It is hypothesized that natural sediment reworking induces a small-scale homogenization of macrobenthic communities within bedforms of the Dunkirk area.

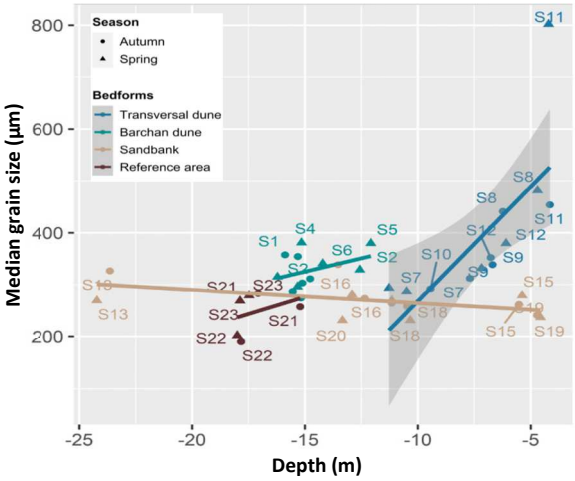

Figure 3 Relationship between the median grain size against the depth as proxy of the position of the sampling stations within each type of bedform. Significant relationships are represented by a regression line associated with a grey polygon which corresponds to the confidence interval of the regression. Non-significant trends are nonetheless represented but the confidence interval has not been drawn.

3.2 Dynamic of the benthic food web

A simple food web structure - Stable isotopes analysis revealed a very simplistic but particular food web, composed by four trophic guilds only: (i) deposit feeders, (ii) filter feeders/deposit feeders, (iii) small benthic predators and (iv) large predators. This simple structure is in accordance with the low diversity of bedform areas (14 ± 6 macrobenthic species per m^{-2} at Dunkirk).

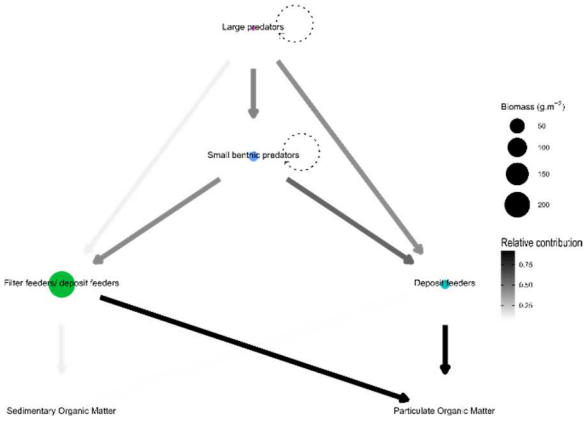

Figure 4 Schematic representation of the benthic food web of subtidal sand dunes. Width of arrows are proportional to the contribution of each food source in the diet of each consumer multiplied by the relative biomass of consumers to provide an idea about trophic fluxes.

Importance of the bentho-pelagic coupling - In the study area, the organic matter content in the sediment remains below 0.5% (not shown) so that the benthic organisms may have been adapted to feed on other source. Effectively, outputs of mixing models clearly suggest a strong bentho-pelagic coupling, with POM contributing to more than 80% in the diet of primary consumers (deposit feeders and filter feeders/deposit feeders). The southern North Sea is typified by major phytoplankton blooms where *Phaeocystis globosa* is often the dominant species (Karasiewicz et al., 2018; Karasiewicz and Lefebvre, 2022; Lefebvre and Dezécache, 2020). As *Phaeocystis* represents an important part of POM, it is thus very likely to sustain the benthic food web of sandbanks, as described by Franco et al. (2008) in the Southern Bight of the North Sea.

Temporal variations in the signature of the main food source – A decrease in the mean values of of $\delta^{13}C$ of POM has been observed between autumn and spring. It may result from the selective consumption of

Dissolved Inorganic Carbon by phytoplanctonik cells (the ^{12}C is primarily consumed while the ^{13}C accumulates) during the growth period, and/or a switch toward the utilization of HCO_3^- instead of CO_2 when the latter is depleted (France et al., 1997; Leggett et al., 2000, 1999). Conversely, the $\delta^{15}N$ decreased in spring due to a possible shift of dominant species in the plankton community with a larger proportion of heterotrophic organisms (Aberle et al., 2010; Agurto, 2007).

The structure of the food web remain relatively stable between seasons - A significant decrease in the range of $\delta^{13}C$ has been observed between autumn and spring but seasonal variations decreased as the trophic level of trophic guilds increased (Figure 5). This result suggests the utilization of a narrower spectrum of food sources (Layman et al., 2007). Here it may reflects a larger contribution of POM in the diet of primary consumers during *Phaeocystis* blooms, which, in turn may cascade in the rest of the food web. Despite this, the $\delta^{13}C$ vs. $\delta^{15}N$ biplot remained relatively similar between autumn and spring (not shown), which suggests that no particular shift in the diet of trophic guilds occurred and that the higher diversity found in spring (see paragraph 3.1) has little impact on trophic relationships. This result is probably due to the remarkably low diversity of bedforms areas (whatever the season), which limit the number of possible trophic pathway.

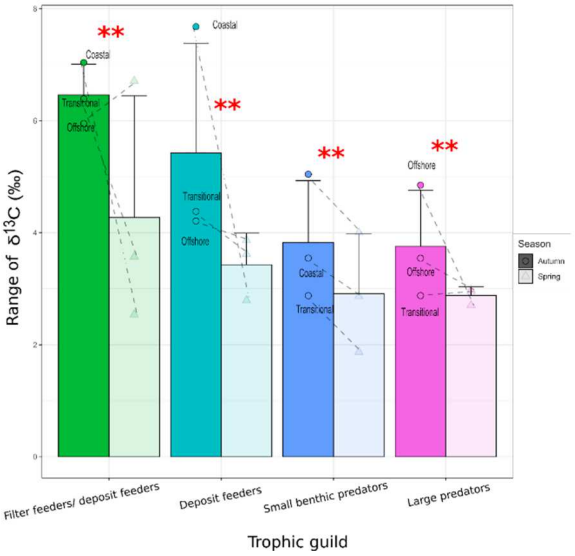

Figure 5 Spatio-temporal variations in the values of isotopic diversity indices for each trophic guild. Statistical differences have been assessed thanks to pairwise-Wilcoxon tests. Stars denote the p-value of the tests: "***": p-value <0.001; "**": p-value <0.01; "*": p-value <0.05.

4 CONCLUSIONS

The present study provides evidence that sediment movements associated with bedform migrations are responsible for the spatial (between bedforms) variations of benthic communities and to their homogenization over the slope of the bedform. However, if species identity vary to some extent in space and time, the ecosystem functioning, and especially trophic relationships, remains relatively stable with only with minor variations.

5 ACKNOWLEDGEMENTS

This work was funded by France Energies Marines and by the French National Agency of Research in the framework of the program "Investing for the Future" (reference ANR-10-IEED-0006-33).

6 REFERENCES

Aberle, N., Hansen, T., Boettger-Schnack, R., Burmeister, A., Post, A.F., Sommer, U., 2010. Differential routing of 'new'nitrogen toward higher trophic levels within the marine food web

of the Gulf of Aqaba, Northern Red Sea. Mar. Biol. 157, 157–169.

Aernouts, D., 2005. Le rôle des changements bathymétriques à l'avant-côte sur l'évolution des littoraux meubles du Cap Gris-Nez à Dunkerque, Côte d'Opale, Nord de la France. Littoral.

Agurto, C., 2007. Assessing mesozooplankton trophic levels in the Baltic Sea and North Sea: a stable isotope study (PhD Thesis). Christian-Albrechts-Universität.

Ashley, G.M., 1990. Classification of large-scale subaqueous bedforms; a new look at an old problem. J. Sediment. Res. 60, 160–172.

Baptist, M.J., van Dalfsen, J., Weber, A., Passchier, S., van Heteren, S., 2006. The distribution of macrozoobenthos in the southern North Sea in relation to meso-scale bedforms. Estuar. Coast. Shelf Sci. 68, 538–546.

Bearhop, S., Adams, C.E., Waldron, S., Fuller, R.A., MacLeod, H., 2004. Determining trophic niche width: a novel approach using stable isotope analysis. J. Anim. Ecol. 73, 1007–1012.

Breine, N.T., De Backer, A., Van Colen, C., Moens, T., Hostens, K., Van Hoey, G., 2018. Structural and functional diversity of soft-bottom macrobenthic communities in the Southern North Sea. Estuar. Coast. Shelf Sci. 214, 173–184. https://doi.org/10.1016/j.ecss.2018.09.012

Brey, T., 2001. Population dynamics in benthic invertebrates. A virtual handbook, http://www.awi-bremerhaven.de/Benthic/Ecosystem/FoodWeb/Handbook/main.html. Alfred Wegener Institute for Polar and Marine Research, Germany.

Carvalho, A.N., Pereira, F., Bosnic, I., Taborda, R., Drago, T., Gaspar, M.B., 2018. Sedimentary dynamics and benthic macrofauna distribution: Insights from the shoreface in southern Portugal. J. Sea Res. 137, 9–25.

Cucherousset, J., Villéger, S., 2015. Quantifying the multiple facets of isotopic diversity: new metrics for stable isotope ecology. Ecol. Indic. 56, 152–160.

Damveld, J.H., Van Der Reijden, K.J., Cheng, C., Koop, L., Haaksma, L.R., Walsh, C.A.J., Soetaert, K., Borsje, B.W., Govers, L.L., Roos, P.C., others, 2018. Video transects reveal that tidal sand waves affect the spatial distribution of benthic organisms and sand ripples. Geophys. Res. Lett. 45, 11–837.

Desroy, N., 2002. Macrobenthic resources of the shallow soft-bottom sediments in the eastern English Channel and southern North Sea. ICES J. Mar. Sci. 60, 120–131. https://doi.org/10.1006/jmsc.2002.1333

Ellis, J.R., Maxwell, T., Schratzberger, M., Rogers, S.I., 2011. The benthos and fish of offshore sandbank habitats in the southern North Sea. J. Mar. Biol. Assoc. U. K. 91, 1319–1335.

Ferret, Y., 2011. Morphodynamique de dunes sous-marines en contexte de plate-forme mégatidale (Manche orientale). Approche multi-échelles spatio-temporelles (PhD Thesis). Université de Rouen.

Foster, T., Corcoran, E., Erftemeijer, P., Fletcher, C., Peirs, K., Dolmans, C., Smith, A., Yamamoto, H., Jury, M., 2010. Dredging and port construction around coral reefs. PIANC Environmental Commission. Report.

France, R., Del Giorgio, P., Westcott, K., 1997. Productivity and heterotrophy influences on zooplankton delta13C in northern temperate lakes. Aquat. Microb. Ecol. 12, 85–93.

Franco, M., Soetaert, K., Costa, M., Vincx, M., Vanaverbeke, J., 2008. Uptake of phytodetritus by meiobenthos using 13C labelled diatoms and Phaeocystis in two contrasting sediments from the North Sea. J. Exp. Mar. Biol. Ecol. 362, 1–8.

Hussey, N.E., MacNeil, M.A., McMeans, B.C., Olin, J.A., Dudley, S.F., Cliff, G., Wintner, S.P., Fennessy, S.T., Fisk, A.T., 2014. Rescaling the trophic structure of marine food webs. Ecol. Lett. 17, 239–250.

Jones, R., Bessell-Browne, P., Fisher, R., Klonowski, W., Slivkoff, M., 2016. Assessing the impacts of sediments from dredging on corals. Mar. Pollut. Bull. 102, 9–29.

Karasiewicz, S., Breton, E., Lefebvre, A., Fariñas, T.H., Lefebvre, S., 2018. Realized niche analysis of phytoplankton communities involving HAB: Phaeocystis spp. as a case study. Harmful Algae 72, 1–13.

Karasiewicz, S., Lefebvre, A., 2022. Environmental Impact on Harmful Species Pseudo-nitzschia spp. and Phaeocystis globosa Phenology and Niche. J. Mar. Sci. Eng. 10, 174.

Layman, C.A., Arrington, D.A., Montaña, C.G., Post, D.M., 2007. Can stable isotope ratios provide for community-wide measures of trophic structure? Ecology 88, 42–48.

Le Bot, S., 2001. Morphodynamique de dunes sous-marines sous influence des marées et des tempêtes: processus hydro-sédimentaires et enregistrement: exemple du Pas-de-Calais (PhD Thesis). Lille 1.

Le Bot, S., Van Lancker, V., Deleu, S., De Batist, M., Henriet, J., Haegeman, W., 2005. Geological characteristics and geotechnical properties of Eocene and Quaternary deposits on the Belgian continental shelf: synthesis in the context of offshore wind farming. Neth. J. Geosci. 84, 147–160.

Lefebvre, A., Dezécache, C., 2020. Trajectories of changes in phytoplankton biomass, Phaeocystis globosa and diatom (incl. Pseudo-nitzschia sp.) abundances related to nutrient pressures in the eastern English channel, southern north sea. J. Mar. Sci. Eng. 8, 401.

Leggett, M., Johannsson, O., Hesslein, R., Dixon, D., Taylor, W., Servos, M., 2000. Influence of inorganic nitrogen cycling on the δ15N of Lake

Ontario biota. Can. J. Fish. Aquat. Sci. 57, 1489–1496.

Leggett, M., Servos, M., Hesslein, R., Johannsson, O., Millard, E., Dixon, D., 1999. Biogeochemical influences on the carbon isotope signatures of Lake Ontario biota. Can. J. Fish. Aquat. Sci. 56, 2211–2218.

Mestdagh, S., Amiri-Simkooei, A., van der Reijden, K.J., Koop, L., O'Flynn, S., Snellen, M., Van Sluis, C., Govers, L.L., Simons, D.G., Herman, P.M., others, 2020. Linking the morphology and ecology of subtidal soft-bottom marine benthic habitats: A novel multiscale approach. Estuar. Coast. Shelf Sci. 238, 106687.

Pielou, E.C., 1966. The measurement of diversity in different types of biological collections. J. Theor. Biol. 13, 131–144.

Post, D.M., 2002. Using stable isotopes to estimate trophic position: models, methods, and assumptions. Ecology 83, 703–718.

Quillien, N., Nordström, M.C., Schaal, G., Bonsdorff, E., Grall, J., 2016. Opportunistic basal resource simplifies food web structure and functioning of a highly dynamic marine environment. J. Exp. Mar. Biol. Ecol. 477, 92–102.

Reiss, H., Kröncke, I., 2005. Seasonal variability of benthic indices: an approach to test the applicability of different indices for ecosystem quality assessment. Mar. Pollut. Bull. 50, 1490–1499.

Robert, A.E., Quillien, N., Bacha, M., Caulle, C., Nexer, M., Parent, B., Garlan, T., Desroy, N., 2021. Biological traits of macroinvertebrates associated with subtidal sandy beforms.

Shannon, C.E., Weaver, W., 1949. The mathematical theory of information. Urbana Univ. Ill. Press 97, 128–164.

van der Linden, P., Patrício, J., Marchini, A., Cid, N., Neto, J.M., Marques, J.C., 2012. A biological trait approach to assess the functional composition of subtidal benthic communities in an estuarine ecosystem. Ecol. Indic. 20, 121–133.

van Dijk, T.A., van Dalfsen, J.A., Van Lancker, V., van Overmeeren, R.A., van Heteren, S., Doornenbal, P.J., 2012. Benthic habitat variations over tidal ridges, North Sea, the Netherlands, in: Seafloor Geomorphology as Benthic Habitat. Elsevier, pp. 241–249.

Van Hoey, G., Degraer, S., Vincx, M., 2004. Macrobenthic community structure of soft-bottom sediments at the Belgian Continental Shelf. Estuar. Coast. Shelf Sci. 59, 599–613.

Van Hoey, G., Vincx, M., Degraer, S., 2007. Temporal variability in the Abra alba community determined by global and local events. J. Sea Res. 58, 144–155.

Van Lancker, V., Du Four, I., Degraer, S., Fettweis, M., Francken, F., Van den Eynde, D., Devolder, M., Luyten, P., Monbaliu, J., Toorman, E., others, 2009. "QUANTIFICATION OF EROSION/SEDIMENTATION TO.

Villéger, S., Mason, N.W., Mouillot, D., 2008. New multidimensional functional diversity indices for a multifaceted framework in functional ecology. Ecology 89, 2290–2301.

Multibeam echosounder backscatter strength signature of dune fields in the Belgian part of the north Sea.

M. Roche *Federal Public Service Economy, Continental Shelf Service, 1000 Brussels*
F. Barette *Federal Public Service Economy, Continental Shelf Service, 1000 Brussels*
K. Degrendele *Federal Public Service Economy, Continental Shelf Service, 1000 Brussels*
A.-S. Piette *Federal Public Service Economy, Continental Shelf Service, 1000 Brussels*

ABSTRACT: The relationship between asymmetrical sand waves morphology, surface sediment and multibeam backscatter is investigated by analysing three sand waves fields located on different sandbanks in the Belgian part of the North Sea. High resolution multibeam bathymetric and backscatter data, Van Veen grab samples and sediment profile imaging data were acquired specifically for this study in October 2022. Special care was taken to ensure accurate positioning of sediment samples and seafloor images to allow reliable correlation with acoustic data and assignment of each sample to a sand wave morphological unit (stoss side, crest, lee side and trough). Grain size analysis of the fraction above 2 mm completes the data set. Overall, the variation in backscatter levels is in line with the dune morphology, but shifts are observed locally. The highest backscatter values are detected along the stoss sides and on the crests. A significant positive correlation is observed between backscatter and the percentage of gravel composed mainly of shell fragments. The highest correlations correspond to grain classes close to the wavelength of the acoustic signal. In the northern area, a particular multi-crests sand waves morphology is observed likely to be related to the antagonism of ebb and flow and the particular nature of the sediment, half of which consisting of shells and shell fragments ranging from 2 mm to 8 mm.

1 INTRODUCTION

The sorting of surface sediments across tidal sand waves shows that, in general, coarser grains tend to accumulate on the stoss sides and crests while finer sediments are concentrated on the lee sides and troughs (Van Lancker and Jacobs, 2000; Cheng et al., 2020; Gaida et al., 2020). Modeling studies largely confirm this pattern (Roos et al., 2007; Damveld at al., 2020). However, reverse trends are also mentioned (Wemmenhove, 2004; Anthony and Leth, 2002). These antagonisms could be related to differences in hydrodynamics and sediment composition (Van Oyen and Blondeaux, 2009).

Multibeam echosounder (MBES) technology, which simultaneously records bathymetry and backscatter (BS), is a particularly well suited tool for the mapping of sand waves with a high spatial resolution. The high resolution bathymetric data allows the calculation of appropriate angular and insonified area corrections to be applied to the raw BS measurements. Once corrected, the BS is an excellent proxy for the sediment, as well as, if calibrated, comparable from one MBES to another, as long as the measurements are taken in the same frequency range (Lurton and Lamarche, 2015).

This paper presents a series of MBES measurements controlled by Van Veen grab samples and Sediment Profile Imaging (SPI) on three areas locates on the Belgian part of the North Sea and shaped by sand waves. The aim is to analyse, compare and evaluate the relationships between surface sediments and sand wave morphology. Some critical methodological issues are also highlighted.

2 MATERIAL AND METHODS

2.1 Study areas

The three study areas are located on different sandbanks in the Belgian part of the North Sea (Figure 1).

The southernmost BR area is located north of the Buiten Ratel, on the northern edge of a depression that divides the bank into two sides in its northern central part. Deep from -14.8 to -20.7 m Lower Astronomical Tide (LAT), BR area covers 13.7 ha (670 m by 205 m) and is modelled by sand waves oriented NW-SE with wavelengths of 200-250 m and amplitudes of 3-4 m (Figure 2a). In BR area the sand waves show a rather pronounced asymmetry $\left(\frac{L\ stoss\ side - L\ lee\ side}{L\ stoss\ side + L\ lee\ side}\right)$ with a mean value of 0.6 (Figure 2b). Bathymetric time series collected from 2010 to 2022 indicate an average migration speed of the sand waves of 2.7 m/year to the north-east. This displacement is lower than the displacement values given for sand waves of similar asymmetry (Knaapen, 2005). A cumulative volume of 143 10^3 m^3 of sand was removed from this area mainly from 2003 to 2014. Since then, this part of the sandbank has been closed to sand extraction.

Located in the western part of the Thornton sandbank, TB area occupies a seabed surface of 9.5 ha (533 m by 179 m) with depths ranging from -20.3 to -25.5 m LAT. The sand waves modelling this area are oriented NW-SE with wavelengths around 150 m and amplitudes of 4 m (Figure 3a). These sand waves are substantially asymmetric with a mean value of 0.4 (Figure 3b). For these sand waves, an average migration speed of 2.6 m/year towards the NE has been estimated on time series of bathymetric measurements made from 2014 to 2022. As for BR area, this displacement is lower than the values published by Knaapen (2005) for sand waves of similar asymmetry. Overall, these sand waves are morphologically very similar to those of the BR area. TB area was subject to fairly intensive sand extraction between 2014 and 2020 with a cumulative extracted volume of 221 10^3 m^3. Since 2021, extraction is prohibited in this area.

The WH area is located at the northern extent of the Westhinder sand bank. This area covers 18.3 ha (870 m by 210 m) with depths ranging from -10.8 to -28.5 m LAT. Giant sand waves curving westwards at the northern end of the Westhinder bank are oriented NW-SE in the WH area. These sand waves have variable wavelengths ranging from 240 to 320 m and variable amplitudes from 5 to 11 m (Figure 4a). These sand waves show asymmetries with values of about 0.4 in opposite directions: eastward for the sand wave located at the west of WH and westward for the two sand waves located at the centre and east of WH. The comparison of the current morpho-bathymetric situation with those of 2009 and 2013 demonstrates an average migration rate of 0.6 m/yr in the two opposite directions in agreement with the asymmetry orientation.

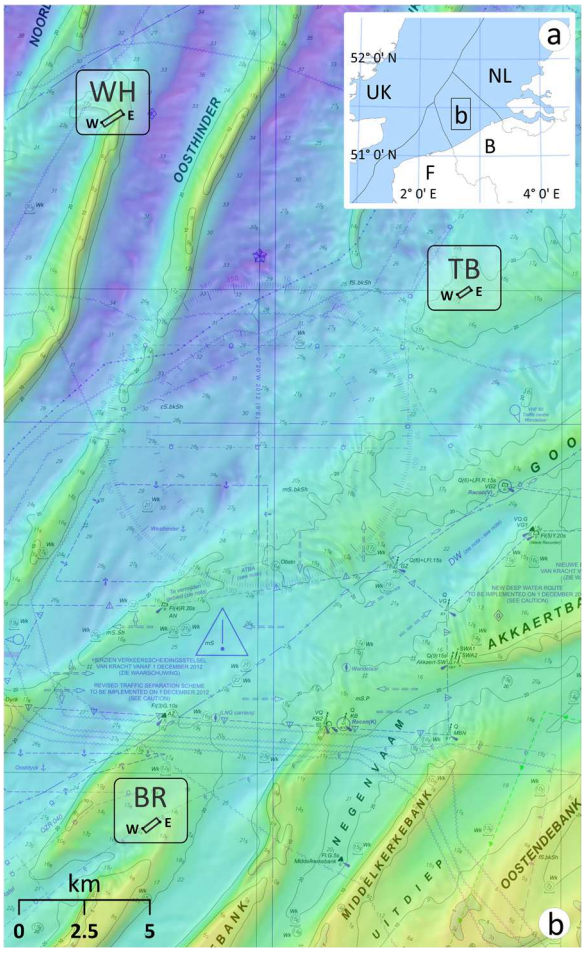

Figure 1. a: Regional location of the surveyed areas. b: Detailed location of the surveyed areas in the Belgian part of the North Sea. BR area, northern part of the Buiten Ratel sandbank (W: 51° 18.8550', 2°

36.2477'; E: 51° 18.9914', 2° 36.8075'); TB area, western part of the Thorntonbank (W: 51° 29.9222', 2° 46.5438'; E: 51° 30.0038', 2° 47. 0116'); WH area, northern end of the Westhinder bank (W: 51° 33.4358', 2° 34.7586'; E: 51° 33.5969', 2° 35.4870'); latitude and longitude in WGS84 degree decimal minutes; base map: Hydrographic map BNZ 2014 from Flemish Hydrographic Service combined with Bathymetric terrain model LAT from Flemish Hydrographic Service and FPS Economy.

2.2 MBES data

Bathymetric and backscatter (BS) data were collected using a Kongsberg EM2040 MKII 04 Dual Rx multibeam echosounder (MBES) installed on the RV Simon Stevin. This system is coupled with an IX Blue Octans motion sensor and an MGB-Tech RTK GPS positioning system, together ensuring decimetric XYZ accuracy of the data. A SBE 21 SeaCAT thermosalinograph provides continuous sound velocity measurements. To ensure inter-comparability of BS levels, all MBES data were recorded using the same acquisition settings (300 kHz, normal multi-sector transmission mode, medium pulse length of 108 µs).

The bathymetric data were processed following a standard workflow with QPS-Qimera® (2.5.1, 2022): integration of the RTK correction, reduction of the Z values in the LAT, fine-tuning of the roll, pitch and heading offsets and cleaning of the soundings. Finally, a bathymetric model with a resolution of 1x1 m was calculated for each of the study areas.

BS data were processed using QPS-FMGT® (7.10.2, 2022). The previously calculated bathymetric model has been incorporated to refine the estimation of incidence angles and insonified areas. The beam pattern has been corrected for. For cartographic purposes, a continuous BS mosaic with a resolution of 1x1 m is calculated with all the BS values.

However, only BS data acquired in the range of incidence angles ±[20°,60°] are considered to ensure a rigorous spatial inter-comparability of the BS values and analysis of the correlations with sand wave morphological units and sediment granulometry.

Limiting the use of BS to this angular range has a double advantage: within it, the BS values are stable regarding the incident angle and, as they are essentially controlled by the impedance contrast, the roughness and the volume scattering of the sediment, they are the ones that best discriminate sediment types. (Jackson et al., 1986; APL, 1994; Lamarche and Lurton, 2018).

2.3 Ground truthing

For each area, a series of Van Veen grab samples and Sediment Profile Imaging (SPI) images were taken along a transect perpendicular to the sand wave crests immediately after the acoustic measurements (17 for BR, 13 for TB and 4 for WH). The grab samples and SPI images are not strictly in the same position: the Van Veen was operated with the starboard winch of the RV Simon Stevin, the aft winch was used for the SPI. The raw positions of the grab samples and SPI images were carefully corrected for the respective distances of the two winches from the GPS antenna and for the ship's heading at the moment the instruments touched the seabed. These corrections are essential to ensure a correct spatial match between the sedimentological and acoustic data. The corrected positions of the grab samples and SPI images are shown by area on the bathymetric and BS maps in Figures 2, 3 and 4.

After drying the samples, a particle size analysis of the fraction larger than 2 mm was carried out by weighing, using 2, 4, 8, 16 and 32 mm sieves. Observation of the sediments shows that the gravelly fraction mainly consists of whole shells and shells fragments. The analysis of the sandy fraction of less than 2 mm in size is carried out using a Malvern Mastersizer 3000 laser particle analyser. Semi-quantitatively, 4 classes of shell density at the sediment surface were estimated from

the raw SPI images (0 = absent, 1 = present, 2 = abundant, 3 = very abundant).

3 ANALYSIS AND RESULTS

The analyses were carried out at two scales. Locally, in each of the areas, profiles combining bathymetry and BS in the incidence angle interval of ±[20°, 60°] make it possible to assess the spatial relationship between the morphology of the sand waves and the BS variations. Globally, in order to analyze the relationships between the level of BS, the morphology of the sand waves and the granulometry of the sediments, the descriptive statistics of BS (mean and std) in the angular interval ±[20°, 60°] were estimated in rectangles of 50x10 m around the samples. The orientation of the rectangles was defined by calculating the median value of the aspect (downward direction of the maximum rate of change in value from each cell to its neighbours) derived from the bathymetric model resampled to a 5x5 m resolution, within a buffer with a radius of 20 m around each sample location. This method ensures the calculation of BS statistics in homogeneous morphological units of sand waves surrounding the grab samples. Around the positions of the SPI images, BS statistics were extracted using the same principle. Depending on its position, each sample was assigned to a sand wave morphological unit (stoss side, crest, lee side and trough). Global correlations between all the variables considered were established using a summary table gathering all the data.

3.1 BR area

The data collected in the BR area are summarised in Fig. 2. The profile in fig. 2c shows a spatial correlation between the BS and the bathy-morphology. The highest BS values, around -14 dB, are observed on the stoss sides. In the lee troughs the BS values drop to -19 dB. Considering the ± 1 dB inherent transducer sensitivity reported for Kongsberg MBES systems (Hammerstad, 2000), the observed difference of 5 dB is definitely significant. The sediments on the stoss sides reflect three times more acoustic energy than those on the leeward troughs. However, the BS and bathymetric profiles show a phase shift for two of the three sand waves in the BR area. For these two sand waves, the BS level decreases progressively in the middle part of the stoss sides, so that their ridges have intermediate BS values around -17 dB. The third sand wave located in the eastern part of BR shows a perfect phasing between bathy-morphology and BS.

The grain size analysis of the grab samples demonstrates the predominantly sandy nature of the surface sediments in the BR area: the percentage of the sandy fraction ranges from 90% to practically 100% with an average of 97%. The gravelly fraction is composed mostly of shell fragments between 2 and 16 mm.

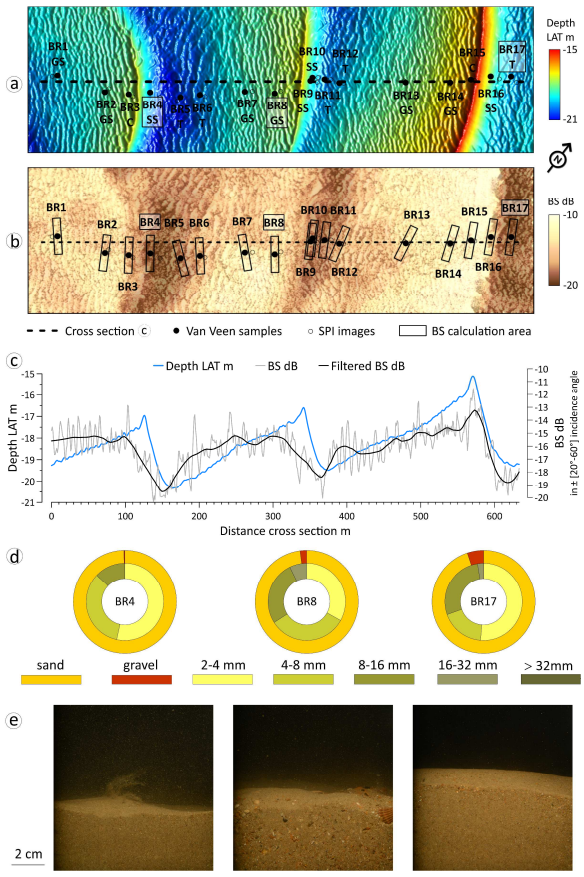

Figure 2. Summary of data collected over BR area. a: Bathy-morphological map (depth in LAT m) with positions of grab samples, SPI images and cross section presented in 2 c , XY scale is given by the cross section, assignment to a morphological unit is indicated below the sample ID (GS = stoss side - gentle slope, C = ridge - crest, SS = lee side - steep slope and T = trough); b: BS map (dB), positions of grab

samples, 50x10m buffers used for BS statistics calculation and c section; c: Bathymetry and BS cross-section (average of values over a 20 m corridor on either side of the line) (BS raw data and filtered data using a lowess Gaussian quadratic function); d: Granulometry of samples BR4, BR8 and BR9, outer ring gives the percentages of sand and gravel, inner ring gives the percentages of the gravel classes; e: SPI images of samples BR4, BR8 and BR9.

In agreement with the spatial correlation observed between the BS and the morphology of the sand waves, the highest percentages of gravel are observed in the gentle slope and ridge samples and, on the contrary, the lee side and through samples are overall very poor in gravel (fig. 2d). The observation of SPI images suggests a fairly homogeneous seafloor with few surface scatterers (fig. 2e).

3.2 TB area

Figure 3 summarises the data collected in TB area. The BS variations correlate very well with the bathymetric variations of the three sand waves (fig. 3c). The stoss and lee sides and the through show low BS quite stable values around -17 dB. On the stoss side, around -22.5 m LAT, the slope break marking a quick decrease in the bathymetry, is accompanied by an increase in the BS level up to the ridges, where the values reach -14 dB. Beyond the ridges, on the leeward side, the BS decreases in parallel with the bathymetry to return to values oscillating around -17 dB.

TB samples (fig. 3d) show a predominantly sandy grain size composition with the proportion of grains smaller than 2 mm ranging from 77 to 98% with an average of 89 %. The gravels are mainly composed of shell fragments between 2 and 16 mm. With the exception of one sample (TB03) situated on the leeward side, all samples with a gravel fraction greater than 10 % come from the sand wave crests. Here the relationship between the BS, the sediment and the morphology of the sand waves is clear.

The SPI images (fig. 3e) show a contrasting interface from sample to sample with a semi-quantitative estimate of the

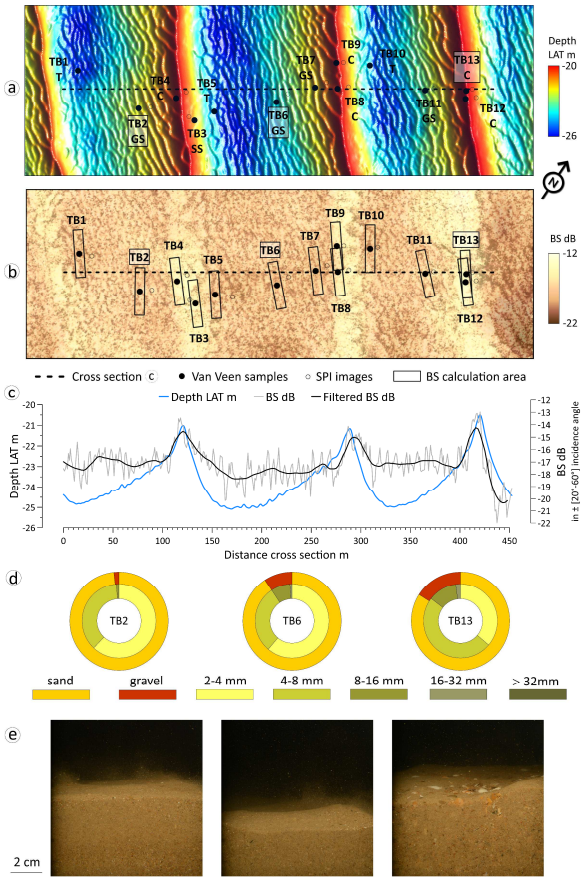

Figure 3. Summary of data collected over TB area. Refer to the legend of Figure 2 (only values, scales, grab samples labels and SPI images differ).

abundance of scatterers present on the sediment surface varying between absent and very abundant. However, no discernible relationship is observed between this semi-quantitative estimate of the abundance of scatterers present on the sediment surface with the BS and the particle size composition of the sediment.

3.3 WH area

Fig. 4 presents the data collected on the WH zone. In the WH area, due to the opposing asymmetry of the sand waves, their relationship with the BS has to be considered separately. The western sand wave, shows BS levels that follow the bathymetry with a phase shift, the BS level increasing from -14 to -10 dB from the middle part of the stoss side to the end of the lee side (fig. 4c). The BS-bathymetry phase shift is the opposite of that observed in the BR area.

In the eastern area, the BS fluctuates by 1 to 2 dB around -10 dB, which represents 4 to 5 times the acoustic energy reflected by the sands of BR and TB areas. These variations are not spatially related to the bathymetry. The particular type of sediment in this area explains the high BS values. The gravel fraction of the 3 samples taken in this part of WH ranged from 22% to 50%, with an average of 40% (fig. 4d). As can be seen from the composition of the grab samples and the SPI images, these gravels consist mainly of shells and shell fragments (fig. 4e). The sand waves in this area are made up of a sediment that consists of up to 50% of shell fragments with grain sizes between 2 and 8 mm.

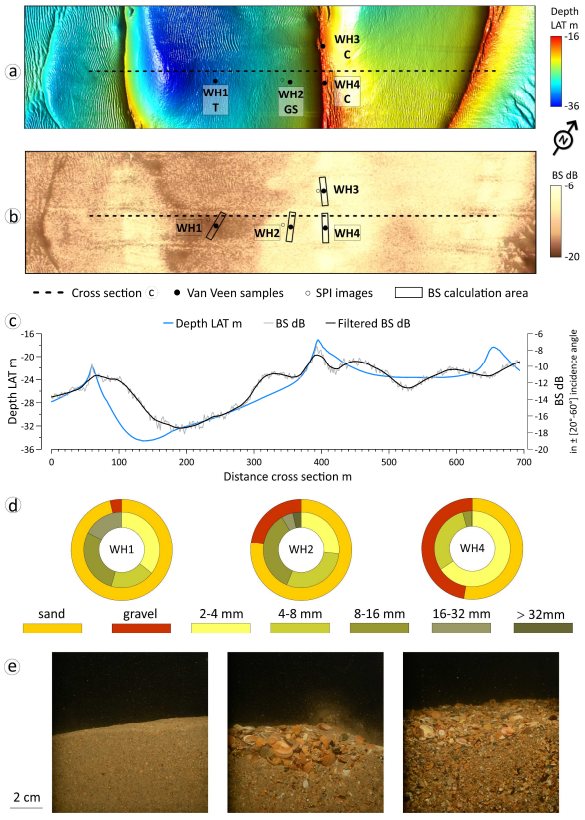

Figure 4. Summary of data collected over WH area. Refer to the legend of Figure 2 (only values, scales, grab samples labels and SPI images differ).

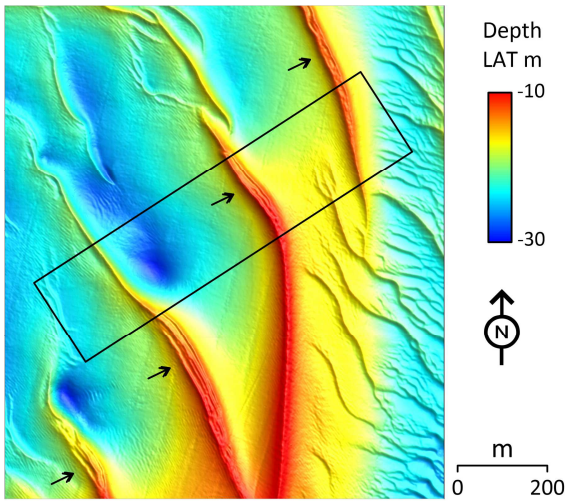

Figure 5. Complex sand wave pattern of the northern end of the Westhinder bank around the WH area. The arrows point to areas of sand waves with multiple ridges. FPS Economy data, RV Belgica survey 2009/03).

On a larger scale, in the northern region at the end of the Westhinder bank, the asymmetry of the sand waves indicates two directions of sediment transport in accordance with flow and the ebb similar to those observed in the central part of the bank. (Deleu et al., 2004).

The tide currents convergence combined with the shelly sediment, produces a complex pattern of sand waves (Fig. 5). Some sand waves locally show several parallel ridges modelling their tops in an undulating surface wide up to 30m locally.

3.1 Correlation analysis

The extraction of BS data in 50x10m buffers around the grab samples allows to quantify the correlations between the BS and the granulometric data. These correlation are presented in table 1.

Table 1: Correlation (Pearson's r) BS mean and std with gravel fractions. Significant value ($p < 0.01$) are in bold.

	mean BS dB in ± [20°-60°]	std BS dB in ± [20°-60°]
> 2mm	**0.86**	**-0.57**
2-4 mm	**0.83**	**-0.55**
4-8 mm	**0.82**	-0.46
8-16 mm	0.42	-0.41
16-32 mm	0.08	-0.14
> 32 mm	0.34	-0.45

The BS shows a significant positive correlation with the percentage of gravel. However, the 2-4 mm and 4-8 mm fractions contribute the most to this correlation. The acoustic wave interacts with the sediment on the scale of its wavelength and the grain sizes of these fractions are close to the wavelength of the acoustic signal used (5 mm at 300 kHz). Beyond 8 mm, the correlations are no longer significant, the BS seems not sensitive to an increase in the coarsest fractions. A similar relationship of BS with sediment grain size has been observed in the Belgian part of the North Sea (Montereale Gavazzi, 2019).

Only BR and TB data are considered to evaluate the trend of BS values with respect to the morphological units because these two areas have similar sand wave characteristics (wavelength, amplitude, asymmetry and migration speed) and comparable surface sediments.

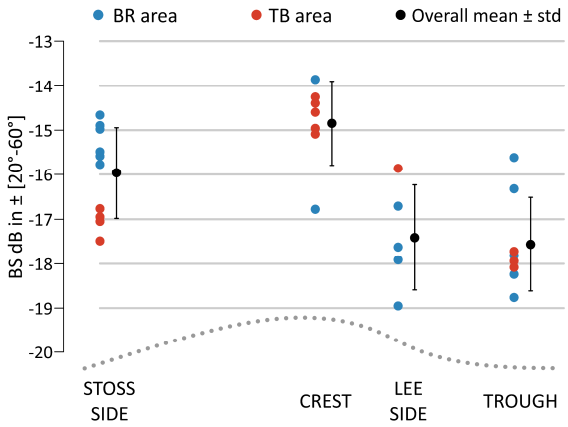

Figure 6. Relationship between BS level and morphological units of sand waves in the BR and TB areas.

The relationships between the mean BS levels estimated in the 50x10m buffers around the grab samples and the morphological units are presented in Fig. 6. Considering BR and TB together, by mean, the BS levels are higher on the stoss sides and the crests than on the lee sides and the troughs but the magnitude of this difference is only 1 to 2 dB.

Within each morphological unit, the range of individual measurements is in the order of 3 to 4 dB, exceeding the range of the overall means values which is 2.5 dB. The variance between the mean BS levels estimated in the buffers surrounding the samples leads to a mixed interpretation.

The pattern is clearer for TB than for BR due to a sharper grain size distribution between the morphological units. In particular, the accumulation of shells and shell fragments on the crests of the sand waves is clearly visible in the SPI images of TB. In BR area, BS levels are more variable within the crests, the lee sides and the troughs. Overall, the SPI images show a more homogeneous seafloor on BR than on TB.

4 CONCLUSION

Careful sample positioning and appropriate corrections to account for the angular dependence of BS are required when coupling MBES bathymetric and high resolution BS data with ground truth data (grab samples and SPI images) to analyse the relationships between surface sediment grain size and sand wave morphology. The use of BS values controlled by the same sediment interface characteristics is ensured by extracting values within a limited angle of incidence range of ±[20°, 60°].

The BS shows a significant positive correlation with the percentage of gravel which consists mainly of shells and shell fragments from 2-8mm close to the wavelength of the acoustic signal used (5 mm at 300 kHz). The spatial relationship between the bathymetry and the BS and the correlations between the BS and the granulometric data demonstrate a granulometric sorting in relation with the sand waves morphological units in line with published data and models.

The peculiar multi-crested shape of the sand waves in an area covered by sediments containing 50% of shells and shell fragments, suggests a sustained control of the sediment on the morphology and dynamics of these sand waves.

In the BR and TB zones, the integration of additional data is necessary to better define the causes of the BS variations in relation to

the morphological units of the sand waves: bathymetric and calibrated BS time series, local hydrodynamic data and granulometric analysis of the sandy fraction.

The dominant role of shells and shell fragments in the acoustic response of the sediment is largely confirmed. However, the field data remain sparse compared to the acoustic data. The addition of field data, including geotechnical ones, is necessary to better understand the sedimentological significance of the BS.

The approach remains surface based. Cores are needed to verify that, according to Walther's Law (Middleton, 1973), the lateral distribution of sediments at the surface of the sand waves is reflected in their vertical sedimentary sequence. However, offshore cores are expensive, so funding must be considered.

5 ACKNOWLEDGMENTS

The VLIZ and the crew of the RV Simon Stevin are acknowledged for providing the ship time, the organization and the good execution of the measurements and collection of samples and images during the campaign 22-600 in October 2022.

6 REFERENCES

APL, 1994. APL-UW High-Frequency Ocean Environmental Acoustic Models Handbook. Technical Report APL-UW TR9407, Applied Physics Laboratory, University of Washington, Seattle, WA, USA.

Anthony, D., Leth, J.O., 2002. Large-scale bedforms, sediment distribution and sand mobility in the eastern North Sea off the Danish west coast. Mar. Geol. 182 (3), 247–263.

Cheng, C. H., Soetaert, K., & Borsje, B.W. (2020). Sediment characteristics over asymmetrical tidal sand waves in the Dutch North Sea. Journal of Marine Science and Engineering, 8(6), 409.

Damveld, J. H., Borsje, B. W., Roos, P. C., & Hulscher, S. J. M. H., 2020. Horizontal and vertical sediment sorting in tidal sand waves: Modeling the finite-amplitude stage. Journal of Geophysical Research: Earth Surface, 125.

Deleu, S., Van Lancker, V., Van den Eynde, D., Moerkerke, G. 2004. Morphodynamic evolution of the kink of an offshore tidal sandbank: the Westhinder Bank (Southern North Sea), Continental Shelf Research, Volume 24, Issue 15, 1587-1610.

Hammerstad, E., 2000. EM Technical Note: Backscattering and Seabed Image Reflectivity. Horten, Norway: Kongsberg Maritime AS. Technical note.

Gaida, T. C., van Dijk, T., A.G.P., Snellen, M., Vermaas, T., Mesdag, C., Simons, D., G., 2020. Monitoring underwater nourishments using multibeam bathymetric and backscatter time series, Coastal Engineering, Volume 158, 103666.

Jackson, D.R., Baird, A.M., Crisp, J.J., Thomson, P.A.G., 1986. High-frequency bottom backscatter measurements in shallow water. J. Acoust. Soc. Am. 80, 1188–1199.

Knaapen, M. A. F. (2005), Sandwave migration predictor based on shape information, J. Geophys. Res., 110.

Lurton, X.; Lamarche, G. (Eds) (2015) Backscatter measurements by seafloor-mapping sonars. Guidelines and Recommendations. 200p.

Middleton, G., 1973. Johannes Walther's Law of Correlation of Facies: Geological Society of America Bulletin, 38: 979-988.

Montereale Gavazzi, G., O., A., 2019. Development of seafloor mapping strategies supporting integrated marine management: application of seafloor backscatter by multibeam echosounders. PhD Thesis, Ghent University, Ghent, Belgium.

Roos, P. C., Hulscher, S. J. M. H., Van der Meer, F. M., Van Dijk, T. A. G. P.,Wientjes, I. G. M., & Van den Berg, J. (2007). Grain size sorting over offshore sandwaves: Observations and modelling. In S. J. M. H. Hulscher & C. M. Dohmen-Janssen (Eds.), RCEM 2007, 5th IAHR symposium on river, coastal and estuarine morphodynamics (pp. 649–656). Enschede: University of Twente.

Van Lancker, V., Jacobs, P., 2000. The dynamical behaviour of shallow marine dunes. In: International Workshop on Marine Sandwave and River Dune Dynamics. University of Lille, France

Van Oyen, T., Blondeaux, P., 2009. Grain sorting effects on the formation of tidal sand waves. J. Fluid Mech. 629, 311–342.

Wemmenhove, T., 2004. Grain size sorting on tidal sandbanks. In: International Workshop on Marine Sandwave and River Dune Dynamics. University of Twente, Enschede, Netherlands.

Nonlinear modeling of estuarine sand dunes: first results with unidirectional flow

W.M. van der Sande *University of Twente, Enschede, the Netherlands – w.m.vandersande@utwente.nl*
P.C. Roos *University of Twente, Enschede, the Netherlands – p.c.roos@utwente.nl*
T. Gerkema *NIOZ Royal Netherlands Institute for Sea Research, Yerseke, the Netherlands – theo.gerkema@nioz.nl*
S.J.M.H. Hulscher *University of Twente, Enschede, the Netherlands – s.j.m.h.hulscher@utwente.nl*

ABSTRACT: Estuarine sand dunes can be seen as intermediate bedforms between river dunes and marine sand waves. Past research has focused on understanding their growth in the linear regime. Here, we present a new morphodynamic model with lateral periodic boundary conditions to investigate estuarine sand dune dynamics in the nonlinear regime. Being still under development, we use the model in a riverine setting (unidirectional flow) and show flow properties (velocity, turbulent kinetic energy and excess pressure) as well as morphodynamic development. The model is capable of capturing lee-side effects and nonlinear morphodynamic interactions between bedform modes. Future work will be directed to extend the forcing to bi-directional flow to represent estuarine conditions.

1 INTRODUCTION

Sand dunes occur in shelf seas (known as tidal sand waves), rivers (river dunes) and estuaries (estuarine sand dunes). Depending on the environment, they have lengths on the order of tens of meters (rivers) or hundreds of meters (seas). They have been explained as free instabilities of the sandy bed subject to flow (Engelund, 1970). Modeling efforts have been directed to hindcast sand dunes (Krabbendam et al., 2021), and to understand the mechanisms that determine their size, shape and dynamics (e.g., the effect of wind waves, Campmans, 2017 and turbulence, Blondeaux & Vittori, 2005).

Such modelling efforts can roughly be divided into two groups: linear stability models and nonlinear models. Linear stability models linearize the sand-water system around a basic state (i.e. flow and sediment transport over a flat bed) to investigate the initial growth of bedforms. The strength of these models is that they are computationally cheap, allowing for systematic sensitivity analyses, and that they enable to disentangle the effects of different physical processes (e.g., the effect of bed-load from suspended load transport, Campmans, 2017). However, they cannot give information on shape and height of sand dunes in the finite-amplitude regime.

Nonlinear models, on the other hand, can model finite height and shape (although modeling bedform lengths in the finite amplitude regime is an ongoing quest, see also discussion). When the forcing is asymmetric (such as in rivers or estuaries, and to a lesser extent also in seas), dunes become asymmetric as well, giving rise to wake effects which become important at lee slopes larger than about 10 degrees (Lefebvre & Winter, 2016). In the past, the morphodynamic implications of lee side effects have been parameterized (Paarlberg et al., 2009), and more recently efforts have been made to resolve the flow field – also in the separation zone – in a morphodynamic model of smaller-scale bedforms (order of a meter, Doré et al., 2016), and on a larger scale (Doré et al., 2018). The model used in these two studies is capable of capturing lee-side effects because it is non-hydrostatic and uses a k-ω turbulence closure. However, the simulation times used (order of days) were not long enough to capture growth of large-scale bedforms towards equilibrium.

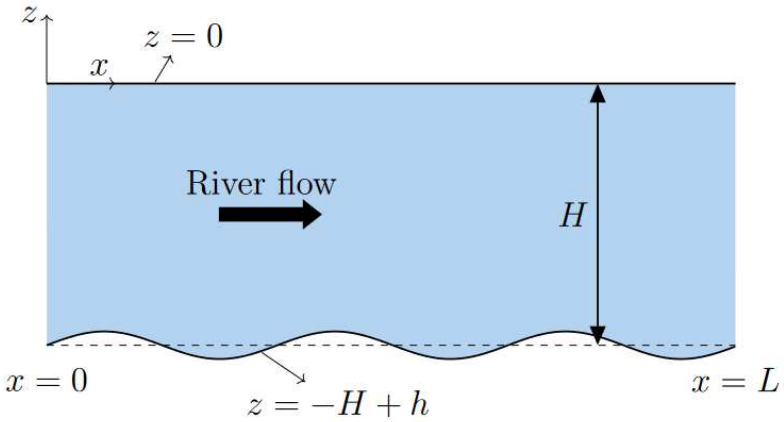

Figure 1. Overview of the 2DV model domain which represents a local portion of a river with domain length L, mean depth H and topography h, forced by river flow; the water surface is fixed (following from the rigid lid assumption).

Here, we will present a nonlinear morphodynamic sand dune model, which is capable of running long-term simulations to find (large-scale) sand dunes. Herein, we will focus (for now) on the riverine case by implementing unidirectional forcing. Results will show the equilibrium height and shape of these dunes, and the evolution thereto.

2 METHODS

2.1.1 Hydrodynamics

The model domain is outlined in Figure 1. The hydrodynamic module is solved with OpenFOAM, and solves the (non-hydrostatic) 2DV RANS equations with k-ω turbulence closure. At the surface we assume a rigid lid, and we impose a no-slip condition at the bed; the lateral boundaries are periodic. The model is forced by a constant barotropic pressure gradient, the magnitude of which is chosen such as to achieve a depth-averaged velocity of 1 m/s to the right at the beginning of the simulation, which aims to represent a riverine scenario.

2.2 Sediment transport and bed evolution

We use bed-load transport only (hence for now ignore suspended sediment transport). It is modelled as a power law of the bed shear stress τ (with coefficient α and power β), supplemented with a bed slope correction term (Bagnold, 1956; Lesser et al., 2004):

$$q = \alpha|\tau|^{\beta}\left(\frac{\tau}{|\tau|} - f_{\lambda}\right), \quad (1)$$

$$f_{\lambda} = 1 - \frac{\tan\Theta}{\cos\left(\arctan\left(\frac{\partial h}{\partial x}\right)\right)\left[\tan\Theta + \frac{\partial h}{\partial x}\frac{\tau}{|\tau|}\right]}. \quad (2)$$

Here, q is the bed-load sediment transport ($m^2\ s^{-1}$), and f_{λ} is the slope correction term, which acts stronger for larger bed slopes, with an asymptote at the angle of repose Θ. Furthermore, h is the bed level (superimposed on the mean bed level $z = -H$) and x the horizontal coordinate in our 2DV domain.

Lastly, the Exner equation links the divergence of sediment transport to the bed evolution:

$$(1-p)\frac{\partial h}{\partial t} = -\frac{\partial q}{\partial x}, \quad (3)$$

where p is the bed porosity.

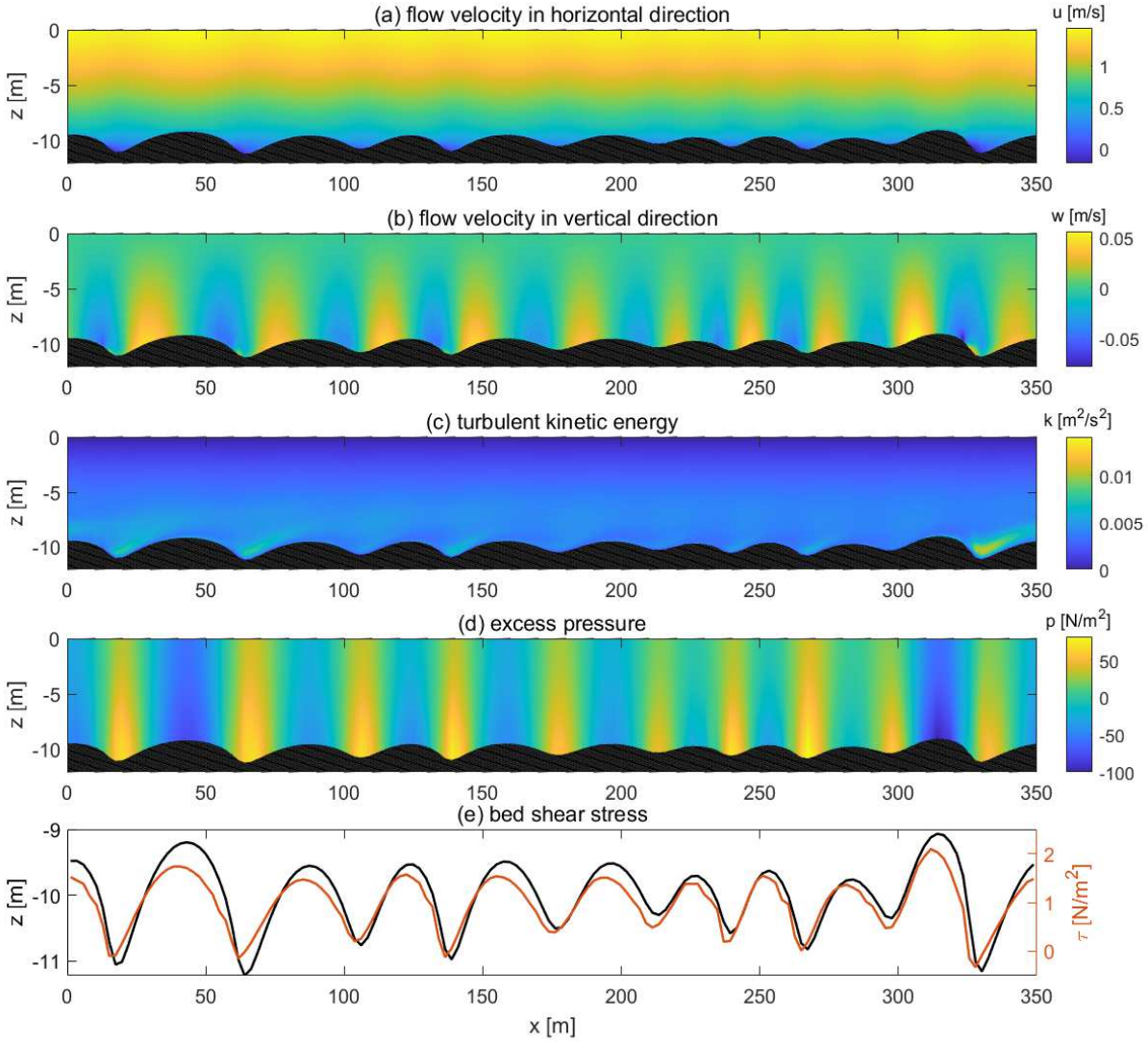

Figure 2. Flow properties over multiple dunes in a periodic domain. From top to bottom: (a) horizontal and (b) vertical flow, (c) turbulent kinetic energy, (d) excess pressure (difference between actual pressure and hydrostatic pressure), and (e) the bed level (left axis) and in orange the bed shear stress (right axis).

3 RESULTS

3.1 Hydrodynamics

We show flow properties over multiple bedforms in a periodic domain with a domain length of $L = 350$ m. The dunes shown have actually been generated by our morphodynamic model, which is further addressed in Section 3.2. Figure 2 shows the bed pattern in all subfigures, and contains the horizontal and vertical flow velocity, turbulent kinetic energy, (excess) pressure and bed shear stress. The excess pressure p is defined as the actual pressure minus the hydrostatic pressure.

The model is, by construction, capable of handling lee-side effects, which can be seen by the flow reversal in the wake around $x = 325$ m. Lee-side effects give rise to increased turbulent kinetic energy in the wake region. Excess pressure mainly varies in the horizontal direction, although it should be noted that smaller excess pressure variations in the vertical are responsible for wake effects.

Bed shear stress drops in the lee-side, supporting the parameterization used by Paarlberg et al. (2009) for bed shear stress in the flow separation zone.

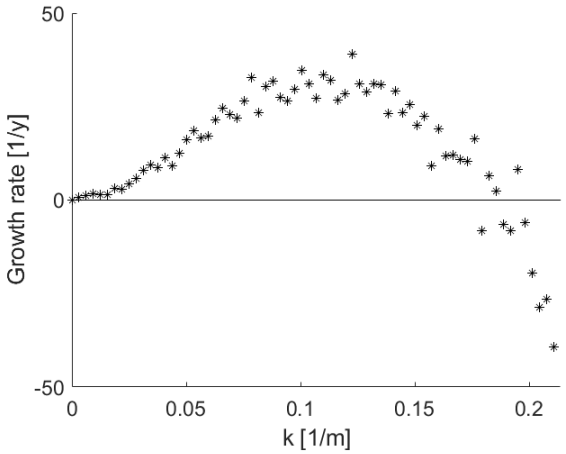

Figure 3. Growth curve as obtained by the morphodynamic model in the linear (initial) phase. Here, k is the topographic wavenumber.

3.2 Morphodynamics

Firstly, we use the initial morphodynamic evolution resulting from our model to find a growth curve which allows comparison to the outcome of linear stability models (Figure 3). It is obtained by starting with a random bed perturbation of small amplitude, the evolution of which reveals the growth rates of all topographic modes involved. The growth rates we find are of similar order of magnitude as those resulting from linear stability models (e.g. Van der Sande et al., 2021). The wavenumber of the fastest growing mode resembles those of river dunes (Lokin et al., 2022). The scatter in Figure 3 is similar as found in an earlier similar study (Campmans et al., 2018), and is likely due to numerical inaccuracies.

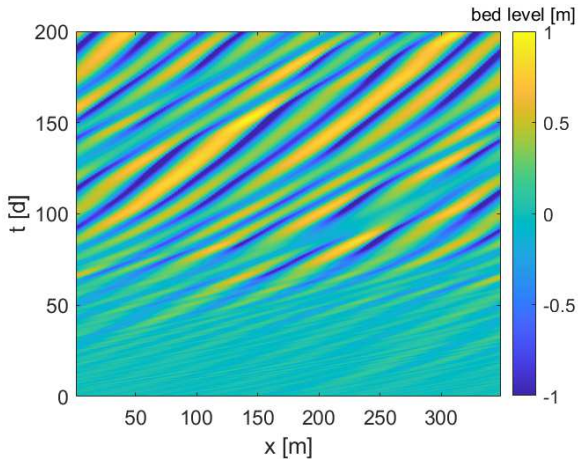

Figure 4. Time stack plot of morphodynamic development during 200 days. The bed profile at $t = 200$ d is the same as shown in Figure 2.

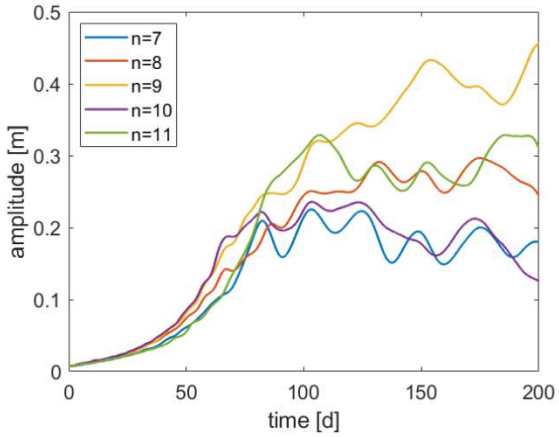

Figure 5. Development of the most dominant modes during the simulation. Herein, the amplitude in meters is defined as follows: $h_n = \hat{h}_n \cos(2n\pi x/L - \phi_n)$, with n the mode and L the domain length (350 meters).

Furthermore, we show a time stack plot of dune evolution from an initially perturbed bed, which also includes bed evolution in the nonlinear regime (Figure 4). From this plot, pattern formation as well as migration rates and merging behavior can be discerned.

The development of the most dominant bedform modes corresponding to Figure 4 is shown in Figure 5. Initially, the bedforms show exponential growth (as following from linear stability analyses). After roughly 50 to 100 days, the evolution of the modes starts to deviate from this.

3.3 Feedback of morphodynamics on hydrodynamics: roughness

Due to non-hydrostatic effects of dunes on the flow, the flow field experiences an increased roughness as dunes grow in our morphodynamic model. Figure 6 shows deceleration of the domain-averaged horizontal flow velocity as dunes develop from a flat bed, akin to found by Lefebvre (2013), although here we show the change in domain-averaged flow velocity as dunes develop.

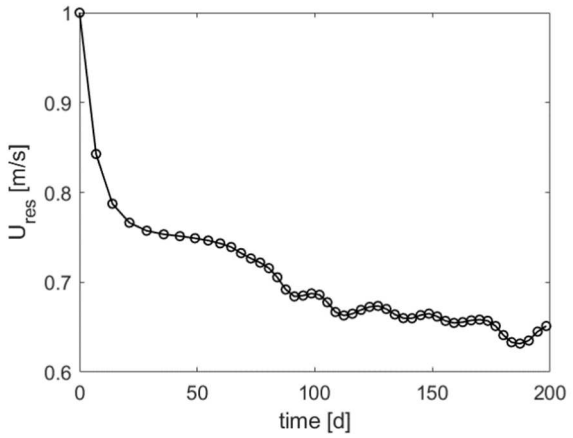

Figure 6. Domain-averaged horizontal flow velocity over time as dunes develop.

4 DISCUSSION

4.1 Dunes as linear instability

Some studies (e.g., Doré et al., 2016; Fourrière et al., 2010) contest that dunes are formed by a linear stability mechanism, and instead argue that dunes form because of amalgamation of smaller scale bedforms (i.e. ripples). The growth curve (Figure 3), nonlinear development of dunes resulting from our model (Figure 4) suggest that these two mechanisms are not mutually exclusive. Instead, the linear instability mechanism allows dunes to initiate and persist while they grow further through amalgamation.

4.2 Equilibrium dune length

From the preliminary runs carried out with our model, we could not find a stable equilibrium of more than one dune in our model domain. This is a defect encountered in many nonlinear bedform models with spatially periodic boundary conditions, which has been pragmatically dealt with in the past by setting the domain length equal to the expected wavelength (e.g. as resulting from linear stability analysis). Laboratory experiments (Bacik et al., 2021) suggest that a combination of suspended sediment transport and turbulence (in their words: "sand trapping efficiency" and "turbulence intensity") ensure the stable coexistence of two bedforms in a circular flume. An earlier linear study suggested that suspended sediment transport dampens long wavelengths (Borsje et al., 2014). Hence, the omission of suspended sediment transport in our model might be the cause that small wavenumbers continue growing throughout the simulation. This is also suggested by the results of Doré et al. (2016), who included suspended sediment transport and found multiple dunes on a periodic domain. However, their simulation time (order of hours) was not long enough to ensure an equilibrium condition.

Another hypothesis (instead of limited merging) is that dune length is limited through dune splitting. Warmink et al. (2014) showed instances of dune splitting in laboratory experiments, and presented a nonlinear model with a parameterization for dune splitting which yields realistic equilibrium bedform lengths.

4.3 Future research directions

Here, we used a unidirectional forcing, which represents a riverine scenario. In the future, we will also include time-periodic forcing to better represent a marine or estuarine setting, and will build upon past research on estuarine sand dunes (Van der Sande et al., 2021, Van der Sande et al., in press) to include the effects of salinity gradients (through for instance gravitational circulation).

Our model uses a k-ω turbulence closure, which has been shown to be more accurate for flows with adverse pressure gradients (e.g. flow separation) than the widely used k-ϵ closure (Bardina et al., 1997). Hence, our model setup enables accurate calculations of the flow field over asymmetric dunes. Regardless, our model would benefit from validation against data to improve on the chosen (Nikuradse) skin roughness length, and on the choice of the wall function for ω.

The presented model is based on the RANS-equations (i.e. averaged over a turbulent timescale), which, by construction, is not capable of simulating phenomena such as 'wake-flapping' (Kostaschuk, 2000; Kwoll et al., 2017; Omidyeganeh & Piomelli, 2011). This phenomenon has been shown to be important for suspended sediment

transport (Shugar et al., 2010; Yuill et al., 2020). To describe this effect in a morphodynamic model as presented here, one would need to resort to large-eddy simulations, or find parameterizations to represent it in RANS-based models.

5 CONCLUSIONS

We have presented a newly developed nonlinear morphodynamic model for estuarine sand dunes. Currently, it is capable of capturing river dune dynamics forced by a unidirectional current in the finite amplitude regime. Results show that the hydrodynamic module is capable of capturing lee-side effects as amply described in the literature.

Furthermore, the morphodynamic module shows initially linear growth of sand dunes from a slightly perturbed bed, and later nonlinear interactions between modes, reflecting behavior such as merging of dunes.

In the future, the model will be extended to include bi-directional flow and analysis will be extended to determine roughness coefficients over time as dunes develop.

6 REFERENCES

Bacik, K. A., Caulfield, C. C. P., & Vriend, N. M. (2021). Stability of the Interaction between Two Sand Dunes in an Idealized Laboratory Experiment. *Physical Review Letters*, *127*(15), 154501. https://doi.org/10.1103/PhysRevLett.127.154501

Bagnold, R. A. (1956). The flow of cohesionless grains in fluids. *Philosophical Transactions of the Royal Society of London. Series A, Mathematical and Physical Sciences*, *249*, 235–297. https://doi.org/10.1098/rsta.1956.0020

Bardina, J. E., Huang, P. G., & Coakley, T. J. (1997). *Turbulence Modeling Validation, Testing, and Development*. https://ntrs.nasa.gov/api/citations/19970017828/downloads/19970017828.pdf

Blondeaux, P., & Vittori, G. (2005). Flow and sediment transport induced by tide propagation: 2. The wavy bottom case. *Journal of Geophysical Research*, *110*(C08003). https://doi.org/10.1029/2004JC002545

Borsje, B. W., Kranenburg, W. M., Roos, P. C., Matthieu, J., & Hulscher, S. J. M. H. (2014). The role of suspended load transport in the occurrence of tidal sand waves. *Journal of Geophysical Research: Earth Surface*, *119*(4), 701–716. https://doi.org/10.1002/2013JF002828

Campmans, G. H. P., Roos, P. C., de Vriend, H. J., & Hulscher, S. J. M. H. (2017). Modeling the influence of storms on sand wave formation: A linear stability approach. *Continental Shelf Research*, *137*, 103–116. https://doi.org/10.1016/j.csr.2017.02.002

Campmans, G. H. P., Roos, P. C., de Vriend, H. J., & Hulscher, S. J. M. H. (2018). The Influence of Storms on Sand Wave Evolution: A Nonlinear Idealized Modeling Approach. Journal of Geophysical Research: Earth Surface, 123(9), 2070–2086. https://doi.org/10.1029/2018JF004616

Doré, A., Bonneton, P., Marieu, V., & Garlan, T. (2016). Numerical modeling of subaqueous sand dune morphodynamics. *Journal of Geophysical Research: Earth Surface*, *121*(3), 565–587. https://doi.org/10.1002/2015JF003689

Doré, A., Bonneton, P., Marieu, V., & Garlan, T. (2018). Observation and numerical modeling of tidal dune dynamics. *Ocean Dynamics*, *68*(4–5), 589–602. https://doi.org/10.1007/s10236-018-1141-0

Engelund, F. (1970). Instability of erodible beds. *Journal of Fluid Mechanics*, *42*(2), 225–244. https://doi.org/10.1017/S0022112070001210

Fourrière, A., Claudin, P., & Andreotti, B. (2010). Bedforms in a turbulent stream: Formation of ripples by primary linear instability and of dunes by nonlinear pattern coarsening. In *Journal of Fluid Mechanics* (Vol. 649). https://doi.org/10.1017/S0022112009993466

Kostaschuk, R. (2000). A field study of turbulence and sediment dynamics over subaqueous dunes with flow separation. *Sedimentology*, *47*(3), 519–531. https://doi.org/10.1046/j.1365-3091.2000.00303.x

Krabbendam, J., Nnafie, A., de Swart, H., Borsje, B., & Perk, L. (2021). Modelling the past and future evolution of tidal sand waves. *Journal of Marine Science and Engineering*, *9*(10). https://doi.org/10.3390/jmse9101071

Kwoll, E., Venditti, J. G., Bradley, R. W., & Winter, C. (2017). Observations of Coherent Flow Structures Over Subaqueous High- and Low-Angle Dunes. *Journal of Geophysical Research: Earth Surface*, *122*(11), 2244–2268. https://doi.org/10.1002/2017JF004356

Lefebvre, A., Ernstsen, V. B., & Winter, C. (2013). Estimation of roughness lengths and flow separation over compound bedforms in a natural-tidal inlet. *Continental Shelf Research*, *61–62*, 98–111. https://doi.org/10.1016/j.csr.2013.04.030

Lefebvre, A., & Winter, C. (2016). Predicting bed form roughness: the influence of lee side angle. *Geo-Marine Letters*, *36*(2), 121–133. https://doi.org/10.1007/s00367-016-0436-8

Lesser, G. R., Roelvink, J. A., van Kester, J. A. T. M., & Stelling, G. S. (2004). Development and validation of a three-dimensional morphological model. *Coastal Engineering*, *51*(8–9), 883–915. https://doi.org/10.1016/j.coastaleng.2004.07.014

Lokin, L. R., Warmink, J. J., Bomers, A., & Hulscher, S. J. M. H. (2022). River Dune Dynamics During Low Flows. Geophysical Research Letters, 49(8), 1–9. https://doi.org/10.1029/2021GL097127

Omidyeganeh, M., & Piomelli, U. (2011). Large-eddy simulation of two-dimensional dunes in a steady, unidirectional flow. *Journal of Turbulence*, *12*, 1–31. https://doi.org/10.1080/14685248.2011.609820

Paarlberg, A. J., Dohmen-Janssen, C. M., Hulscher, S. J. M. H., & Termes, P. (2009). Modeling river dune evolution using a parameterization of flow separation. *Journal of Geophysical Research: Earth Surface*, *114*(F1). https://doi.org/10.1029/2007JF000910

Shugar, D. H., Kostaschuk, R., Best, J. L., Parsons, D. R., Lane, S. N., Orfeo, O., & Hardy, R. J. (2010). On the relationship between flow and suspended sediment transport over the crest of a sand dune, Río Paraná, Argentina. *Sedimentology*, *57*(1), 252–272. https://doi.org/10.1111/j.1365-3091.2009.01110.x

Van der Sande, W. M., Roos, P. C., Gerkema, T., & Hulscher, S. J. M. H. (2021). Gravitational Circulation as Driver of Upstream Migration of Estuarine Sand Dunes. *Geophysical Research Letters*, *48*(14), 1–10.

Van der Sande, W. M., Roos, P. C., Gerkema, T., & Hulscher, S. J. M. H. (In press). Shorter estuarine dunes and upstream migration due to intratidal variations in stratification. Estuarine , Coastal and Shelf Science. https://doi.org/10.1016/j.ecss.2023.108216https://doi.org/10.1029/2021GL093337

Warmink, J. J., Dohmen-janssen, C. M., Lansink, J., Naqshband, S., Van Duin, O. J. M., Paarlberg, A. J., Termes, P., & Hulscher, S. J. M. H. (2014). Understanding river dune splitting through flume experiments and analysis of a dune evolution model. Earth Surface Processes and Landforms, 39, 1208–1220. https://doi.org/10.1002/esp.3529

Yuill, B., Wang, Y., Allison, M., Meselhe, E., & Esposito, C. (2020). Sand settling through bedform-generated turbulence in rivers. *Earth Surface Processes and Landforms*, *45*(13), 3231–3249. https://doi.org/10.1002/esp.4962

Dune scaling in the Tien River, Vietnamese Mekong Delta

L. Scheiber *Ludwig-Franzius-Institute of Hydraulic, Estuarine and Coastal Engineering, Leibniz University Hannover, Hannover, Germany – scheiber@lufi.uni-hannover.de*
C. Jordan *Leibniz University Hannover, Hannover, Germany – jordan@lufi.uni-hannover.de*
T. Schlurmann *Leibniz University Hannover, Hannover, Germany – schlurmann@lufi.uni-hannover.de*

ABSTRACT: The Vietnamese Mekong Delta has recently received increased media attention after reports revealed the morphological impacts of upstream dam constructions and unsustainable sand mining practices. Consequently, intensive bathymetric surveys were conducted in the dry and wet season of 2018 to map the conditions at the bed of the northern branch of the Mekong, the Tien River. The morphological features in this 20 km long focus area are analysed in this study. Our quantification of prevailing bedform characteristics and comparison with universal trend lines reveals bedforms of particularly small size. Therefore, we assess corresponding transport stages from a numerical model and discuss, which influence anthropogenic processes might have on the local geomorphology.

1 BACKGROUND

Subaqueous bedforms, such as dunes and ripples, can form under and are eventually controlled by various flow conditions, e.g. in the deep sea (Franzetti et al., 2013), tidal inlet channels (Lefebvre et al., 2022) and rivers (Cisneros et al., 2020). Their geometric extents can reach more than a thousand metres in length and tens of metres in height. These dimensions were long thought to be directly related to water depth (Yalin, 1964), but recent flume experiments suggest that bedforms ultimately scale with the transport stage (Bradley & Venditti, 2019). This indicator of potential sediment entrainment is based on the classical Shields diagram and considers local shear stress, grain size and flow velocity (Bradley & Venditti, 2017).

In this study, we scrutinize bathymetric data from two field campaigns in the Tien River in Southern Vietnam. Particularly, we quantify local bedform characteristics and compare them with universal trend lines. Furthermore, we assess prevailing flow conditions and discuss anthropogenic processes that are suspected to control the morphology in this part of the Mekong.

2 STUDY SITE

The Vietnamese Mekong Delta (VMD) is home to around 17 million inhabitants and provides food security across Southeast Asia (GSO, 2021). North of the delta, the Mekong splits into two main branches: the Tien River and the Hau River. On their way to the sea, the Tien River and Hau River are further split into eight distributary channels. The hydrological regime in the VMD is generally characterized by a dry season (November-May) and a wet season (June-October). The monthly discharges at Kratie (Cambodia) vary between 1,600 and 37,000 m^3/s (MRC, 2010). Furthermore, the VMD may be classified as a wave-influenced, tide-dominated delta (Wright, 1985). With an average tidal range of around 2.5 ± 0.1 m at its mouth (Gugliotta et al., 2017), the delta may be classified as mesotidal (Davies, 1964). Tidal variations can still be observed beyond the border to Cambodia, even though the tidal range diminishes in landward direction (Gugliotta et al., 2017).

The sediment inventory is highly variable in the lower 100 km of the distributary channels, whereas sand dominates in the upstream parts of both the Tien and Hau River (Gugliotta et al., 2017). Estimates for the yearly sediment load at Kratie vary

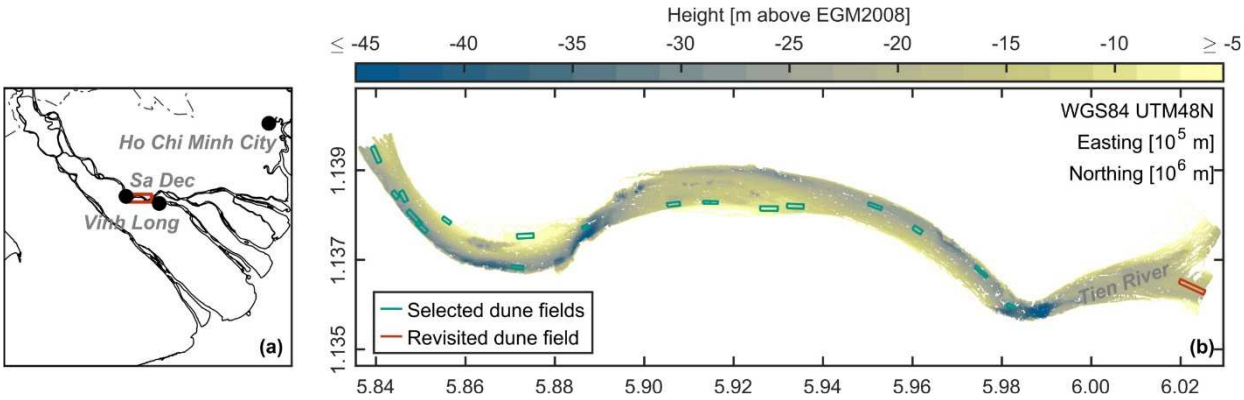

Figure 1. (a) The study site is located in the Tien River between the Vietnamese cities of Sa Dec and Vinh Long. (b) An extensive multibeam echo sounding (MBES) survey during the dry season of 2018 allowed us to produce a digital elevation model (DEM), which comprises multiple dune populations. The dune fields assessed during this study are depicted in green. A single field that was revisited during the wet season is highlighted in red colour.

between 40-160 Mt/yr (Milliman & Meade, 1983; Nowacki et al., 2015). Even though the sediment flux is dominated by cohesive sediments, the annual sand flux entering the delta is around 6.2 ± 2.0Mt/yr (Hackney et al., 2020). In the distributary channels, the sediment transport is directed seaward during periods of high discharge, whereas sediment is imported landward during periods of low discharge (Nowacki et al., 2015).

3 METHODOLOGY

Focusing on a 20 km stretch of the Tien River, which is located between the cities of Sa Dec and Vinh Long (cf. Fig. 1a), bathymetric surveys were conducted during the 2018 dry and wet seasons (Jordan et al., 2019b). During the first multibeam echo sounding (MBES) survey in the dry season, various kinds of bedforms covered extended areas of the riverbed at the surveyed section. After observing these bedforms in the bathymetric data (Jordan et al., 2019a), we selected 20 dune fields for further analysis. This was accomplished by assessing both hill shading plots of the digital elevation model (DEM) and its first spatial derivative, the slope layer. In a second step, we applied a validated, semi-automatic algorithm to systematically measure these bedform populations (Scheiber et al., 2021). Because this routine assesses two-dimensional bed elevation profiles (BEP), we defined multiple parallel transects to characterize each dune field. For all bedforms identified along these longitudinal sections, heights, lengths and average water depths were calculated. Assuming that conditions were nearly homogeneous across a dune field, we combined the transect results into statistical mean, median and maximum dimensions. Several dune fields were revisited during the wet season. While bedforms at some sites were seemingly washed-out, one particular area was evidently still populated by dunes. Figure 1b highlights this focus area in red colour. In addition, the hydrological situation during the measurements is depicted in Figure 2. River discharges during the two field campaigns fell into the 77 % and 15 % exceedance percentiles, respectively.

Aside from this geomorphological assessment, we used the hydro-numerical model presented by Jordan et al. (2020) to simulate flow velocities and shear stresses across the study site. The simulation also allowed insights into the distribution of sediments, which were considered in the form of median grain sizes. On this basis, we were able to estimate prevailing transport stages at each dune field. Specifically, we calculated the local Shields numbers τ_* according to Bradley and Venditti (2017). Critical shields numbers τ_{*c} were determined by the explicit formulation of the Shields diagram by Cao et al. (2006). The transport stage is given by the ratio of these two variables τ_*/τ_{*c}. In a final step, we related the prevailing dune dimensions and transport

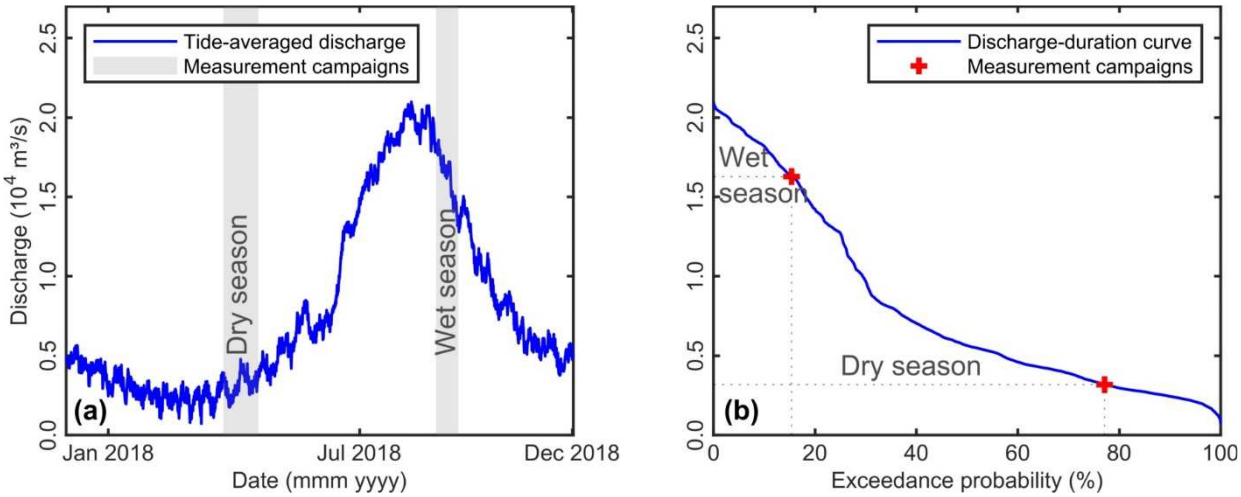

Figure 2. (a) Tide-averaged discharges at My Thuan station near the Tien River. (b) While the first survey was conducted during the dry season with relatively low river discharges that were exceeded on ca. 77 % of days in 2018, the second campaign took place during the wet season with discharges ranging near the 15 % exceedance percentiles.

stages in a scaling diagram similar to the one presented by Bradley and Venditti (2019).

4 PRELIMINARY RESULTS

The surveyed 20 km stretch of the Tien River comprises bedforms of various height and length scales. Figure 3 below summarizes the determined dimension pairs in a double-logarithmic scatter plot. As a reference to global observations, the illustration also contains two blue regression lines that correspond with the mean and maximum values of a large data set published by Flemming (1988). These lines are complemented by the results of an own regression depicted in red colour.

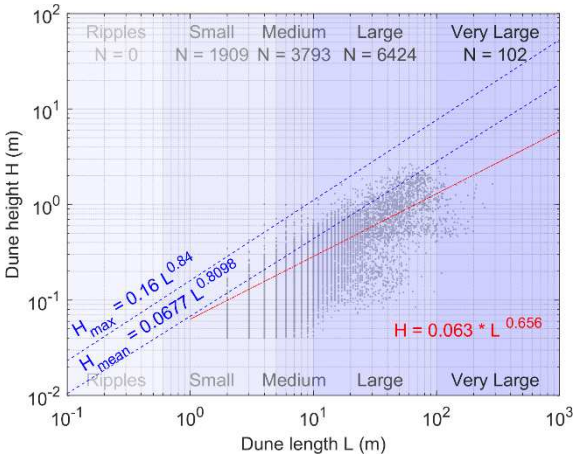

Figure 3. The double-logarithmic scatter plot illustrates the co-domain of identified dune height/ length pairs. While dashed blue lines represent the mean and maximum published for a comprehensive global data set by Flemming (1988), the red line describes the mean dimensions of the study site.

In total, we assessed 12,228 individual bedforms along 377 transects from 20 dune fields. The water depth at these focus areas was 20.1 m on average but ranged between 3.7 m and 38.1 m. While minimum dune dimensions were limited by the bathymetric resolution, maximum heights and lengths reached 2.7 m and 286.0 m, respectively. The corresponding median and mean values are summarized in Table 1.

Table 1: Arithmetic mean, median and maximum dune heights H and lengths L as well as corresponding water depths d in the Tien River, Southern Vietnam.

Statistical value	Median	Mean	Max.
Height H (m)	0.22	0.36	2.70
Length L (m)	10.00	16.39	286.00
Depth d (m)	21.67	20.13	38.06
Steepness H/L	0.02	0.03	0.25

Evident in consideration of the dune steepness is that bedforms in the study area do not reach the equilibrium conditions postulated by Flemming (1988). On the contrary, Figure 3 shows that our custom regression line lies well below the estimate for global mean and maximum dimensions. This can also be understood from the

regression function, which reads as follow for the presented analysis:

$$H_{mean} = 0.063 \times L^{0.656} \quad (1)$$

This suggests that local constraints prevent full bedform development. To understand, whether this is a result of the prevailing transport stages or something different, we juxtaposed our results with the scaling laws of Bradley and Venditti (2019).

Table 2: Minimum, mean and maximum values of normalized dune heights and lengths as well as transport stages across all dune fields during dry and wet seasons.

Statistical value	Min.	Median	Max.
Normalized height H/d	0.01	0.10	0.24
Normalized length L/d	0.05	0.44	41.42
Transport stage τ_*/τ_{*c} (dry season)	0.59	3.82	6.35
Transport stage τ_*/τ_{*c} (wet season)	5.82	15.64	24.48

In the three panels of Figure 4, we relate this crucial indicator of sediment entrainment with different dune characteristics. The statistical values pertaining to the constituents of this plot are summarized in Table 2.

Most prominently, the transport stages observed during dry season conditions ranged between 0.59 and 6.35. This is much lower than the turning point between growth and decline, which Bradley and Venditti (2019) postulate at approximately $\tau_*/\tau_{*c} = 18$ for dune heights. The wet season transport stages, however, ranged from 5.82 to 24.48, which suggests the beginning of upper-plane conditions. In addition, the comparison between these predictions and our field observations points in the same direction as Figure 3 before: dunes at the Tien River do not reach their fully developed dimensions.

5 DISCUSSION

The trend lines by Flemming (1988) suggest that dunes at the study site are either longer or less high than fully developed ones. The comparison with scaling functions by Bradley and Venditti (2019), in turn, indicates that both height and length are undersized in relation to water depths. A potential reason is the scarcity of medium and coarse sediments as a result of sand mining, which was the original motivation for these field campaigns. It may also result from the ongoing construction of upstream dams (Kondolf et al., 2014). Such underdeveloped dune heights have been reported for sediment-starved laboratory experiments by Tuijnder et al. (2009). On the other hand, no evidence pointed at crest shapes turning into barchan dunes as the field observations from Kleinhans et al. (2002) would suggest for sediment-scarce environments.

Also, concerning wet season observations, we can only speculate about the fate of bedforms at the revisited focus areas without dunes. Given that transport stages were consistently in the range of the outlined turning point or beyond, bedforms might

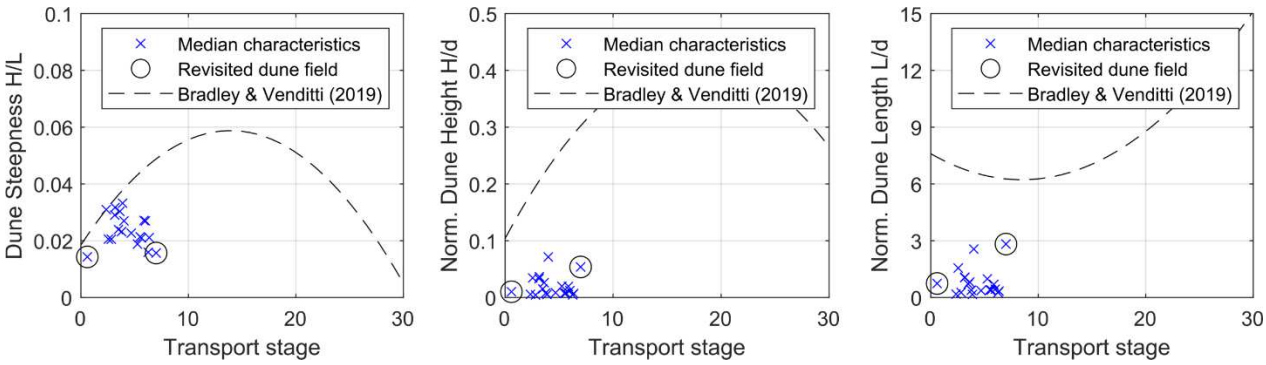

Figure 4. Relations between the dune characteristics (a) steepness, (b) normalized height and (c) normalized length and transport stage. Blue crosses depict the median values for all dune fields, whereat black circles highlight the focus area revisited during the wet season. The dashed black graphs represent the scaling laws from Bradley and Venditti (2019).

have been washed out due to upper plane conditions. Alternatively, dune heights may have declined until measurement accuracy made reasonable tracking impossible. Finally, it should be noted that not all 20 dune fields could be revisited during wet season.

6 CONCLUSIONS

Several natural constraints are known to influence the scaling of bedforms. Here, we analysed bathymetric data from two field campaigns and measured bedforms at twenty different dune fields in the Tien River in Southern Vietnam. We quantified prevalent dune dimensions and juxtaposed them with local flow conditions that were obtained from a validated hydro-numerical model.

At the study site, we observed dunes of up to 2.7 m in height and 286.0 m in length. However, these dimensions seem under-developed when compared to regressions for average dune steepness or normalized extents in consideration of the corresponding transport stage. We suspect that limited dune sizes during the dry season (with low discharge) are related to sediment starvation, which results from an anthropogenic sediment deficit in the form of sand mining or reservoir retention. High transport stages during the wet season, however, indicate the beginning of upper-plane conditions. This would explain washed-out bedforms or at least impediments to reliable measurements. In any case, further investigations are needed to better understand and elucidate the morphological processes that control the formation and scaling of bedforms in this part of the Mekong.

7 ACKNOWLEDGEMENT

This study was sparked in the context of a thesis at the Faculty of Civil Engineering and Geodesy at the Leibniz University Hannover. We would like to thank the examiner, Jan Visscher, for his abiding interest and fruitful discussions. Moreover, we thank Laura Hector for her contributions as a student assistant at the Ludwig-Franzius-Institute. The original field surveys, which allowed us the described insights into the Tien River morphology and which are the basis of this study, were performed as part of Catch-Mekong (https://catchmekong.eoc.dlr.de/), a research project with funding provided by the German Ministry of Education and Research (BMBF) (FKZ: 02WM1338D).

8 REFERENCES

Bradley, R. W., & Venditti, J. G. (2017). Reevaluating dune scaling relations. Earth-Science Reviews, 165,356–376. doi:10.1016/j.earscirev.2016.11.004

Bradley, R. W., & Venditti, J. G. (2019). Transport Scaling of Dune Dimensions in Shallow Flows. Journal of Geophysical Research: Earth Surface, 124(2), 526–547. doi:10.1029/2018JF004832

Cao, Z., Pender, G., & Meng, J. (2006). Explicit formulation of the Shields diagram for incipient motion of sediment. Journal of Hydraulic Engineering,1097–1099. doi:10.1061/(ASCE)0733-94292006

Cisneros, J., Best, J., van Dijk, T., Almeida, R. P. de, Amsler, M., & Boldt, J., et al. (2020). Dunes in the world's big rivers are characterized by low-angle lee-side slopes and a complex shape. Nature Geoscience, 13(2), 156–162. doi:10.1038/s41561-019-0511-7

Davies, J. L. (1964). A morphogenic approach to world shorelines. Zeitschrift für Geomorphologie, 127-142. doi:10.1127/zfg/mortensen/8/1964/127

Flemming, B. W. (1988). On the classification of subaquatic flow-transverse bedforms. Bochumer Geol. U. Geotech. Arb., 29, 44–47.

Franzetti, M., Le Roy, P., Delacourt, C., Garlan, T., Cancouët, R., Sukhovich, A., & Deschamps, A. (2013). Giant dune morphologies and dynamics in a deep continental shelf environment: Example of the banc du four (Western Brittany, France). Marine Geology, 346, 17–30. doi:10.1016/j.margeo.2013.07.014

GSO. (2021). Statistical Yearbook of Viet Nam 2020.

Gugliotta, M., Saito, Y., van Nguyen, L., Ta, T. K. O., Nakashima, R., & Tamura, T., et al. (2017). Process regime, salinity, morphological, and sedimentary trends along the fluvial to marine transition zone of the mixed-energy Mekong River delta, Vietnam. Continental Shelf Research, 147, 7–26. doi:10.1016/j.csr.2017.03.001

Hackney, C. R., Darby, S. E., Parsons, D. R., Leyland, J., Best, J. L., & Aalto, R., et al. (2020). River bank instability from unsustainable sand mining in the lower Mekong River. Nature Sustainability, 3(3), 217–225. doi:10.1038/s41893-019-0455-3

Jordan, C., Tiede, J., Lojek, O., Visscher, J., Apel, H., & Nguyen, H. Q., et al. (2019a). Digital elevation models showing sand mining activities within the Tien River branch, Vietnamese Mekong Delta. doi:10.1594/PANGAEA.909665

Jordan, C., Tiede, J., Lojek, O., Visscher, J., Apel, H., & Nguyen, H. Q., et al. (2019b). Sand mining in the Mekong Delta revisited - current scales of local sediment deficits. Scientific Reports, 9(1), 17823. doi:10.1038/s41598-019-53804-z

Jordan, C., Visscher, J., Viet Dung, N., Apel, H., & Schlurmann, T. (2020). Impacts of Human Activity and Global Changes on Future Morphodynamics within the Tien River, Vietnamese Mekong Delta. Water, 12(8), 2204. doi:10.3390/w12082204

Kleinhans, M. G., Wilbers, A., Swaaf, A. de, & van den Berg, J. H. (2002). Sediment Supply-Limited Bedforms in Sand-Gravel Bed Rivers. Journal of Sedimentary Research, 72(5), 629–640. doi:10.1306/030702720629

Kondolf, G. M., Rubin, Z. K., & Minear, J. T. (2014). Dams on the Mekong: Cumulative sediment starvation. Water Resources Research, 50(6), 5158–5169. https://doi.org/10.1002/2013WR014651

Lefebvre, A., Herrling, G., Becker, M., Zorndt, A., Krämer, K., & Winter, C. (2022). Morphology of estuarine bedforms, Weser Estuary, Germany. Earth Surface Processes and Landforms, 47(1), 242–256. doi:10.1002/esp.5243

Milliman, J. D., & Meade, R. H. (1983). World-Wide Delivery of River Sediment to the Oceans. The Journal of Geology, 91(1), 1–21. doi:10.1086/628741

MRC. (2010). State of the Basin Report 2010: Vientiane: Mekong River Commission (MRC).

Nowacki, D. J., Ogston, A. S., Nittrouer, C. A., Fricke, A. T., & Van, P. D. T. (2015). Sediment dynamics in the lower Mekong River: Transition from tidal river to estuary. Journal of Geophysical Research: Oceans, 120(9), 6363–6383. doi:10.1002/2015JC010754

Scheiber, L., Lojek, O., Götschenberg, A., Visscher, J., & Schlurmann, T. (2021). Robust methods for the decomposition and interpretation of compound dunes applied to a complex hydromorphological setting. Earth Surface Processes and Landforms, 46(2), 478–489. doi:10.1002/esp.5040

Tuijnder, A. P., Ribberink, J. S., & Hulscher, S. J. M. H. (2009). An experimental study into the geometry of supply-limited dunes. Sedimentology, 56(6), 1713–1727. doi:10.1111/j.1365-3091.2009.01054.x

Wright, L. D. (1985). River Deltas. In R. A. Davis (Ed.), Coastal Sedimentary Environments (pp. 1–76). New York, NY: Springer New York. doi:10.1007/978-1-4612-5078-4_1

Yalin, M. S. (1964). Geometrical Properties of Sand Wave. Journal of the Hydraulics Division, 90(5), 105–119. doi:10.1061/JYCEAJ.0001097

The influence of geometric definitions on dune characteristics

L. Scheiber *Ludwig-Franzius-Institute of Hydraulic, Estuarine and Coastal Engineering, Leibniz University Hannover, Hannover, Germany – scheiber@lufi.uni-hannover.de*
A. Lefebvre *MARUM – Center for Marine Environmental Sciences, University of Bremen, Bremen, Germany – alefebvre@marum.de*

ABSTRACT: Dune height and length are two widely used measures to characterize a bedform, but their geometric definitions are not consistent throughout the literature. In this sensitivity study, we investigate how different definitions can influence the dune dimensions of three benchmarking data sets. In particular, we quantify relative differences and interpret them against the background of dune inclination and asymmetry. Dividing the results into subsets of bathymetries and dune sizes allows us to attribute the causes for significant differences before discussing practical implications and recommendations.

1 BACKGROUND

Subaqueous bedforms have been the subject of scientific investigations for more than a century (Cornish, 1901). These geomorphological features, also known as sand waves, dunes or (mega-)ripples, can be observed in diverse flow environments including rivers (Cisneros et al., 2020; Zomer et al., 2021), tidal inlet channels (Lefebvre et al., 2022; Scheiber et al., 2021) and continental margins (Durán et al., 2020; Miramontes et al., 2020). With regard to their geometric extents, individual bedforms can reach tens of metres in height and hundreds of metres in length (Franzetti et al., 2013). When measuring these critical dune characteristics, however, various geometric definitions are used in scientific literature (cf. Fig. 1). For instance, dune length is measured as the horizontal distance (L_1)

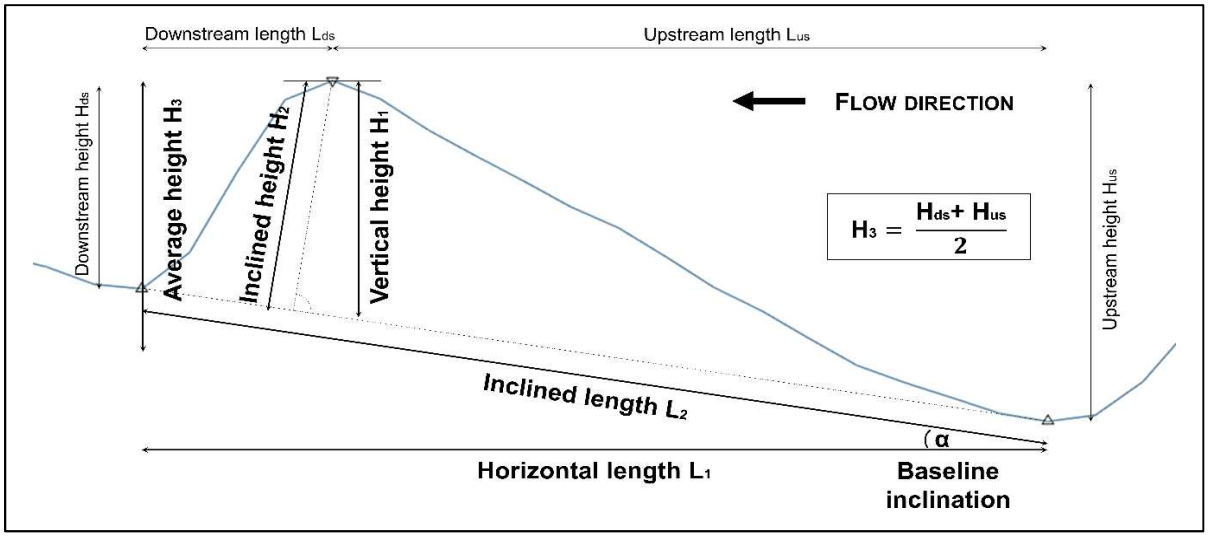

Figure 1. Common geometric definitions for calculating height and length of a dune, which is, in our case, defined by two troughs. If these are (nearly) on the same level, horizontal and inclined lengths can be assumed equal. The same applies for height, which can also be calculated from average up- and downstream heights.

between two troughs (or two crests) or as the inclined distance (L_2). In a similar way, dune height can either be calculated as the vertical height (H_1) or inclined height (H_2). A third option with regard to the calculation of height is averaging vertical distances between the crest and up- and downstream troughs (H_3).

Applying these different definitions will result in small deviations, if the troughs are roughly on the same level, but larger deviations can be expected over inclined bedforms. For instance, this can be the case at so-called compound dunes, where small secondary dunes are superimposed on the slopes of larger primary dunes. This poses the risk of inaccuracies, especially when dune characteristics are used as a proxy for more complex processes. In this study, we quantify the sensitivity of existing height and length definitions by systematically assessing three benchmarking data sets. On this basis, we discuss the available options and try to give a final recommendation.

2 METHODOLOGY

To allow for the full range of bedform types, we selected benchmarking data sets from three different flow environments: a flume, a river and a tidal inlet channel. In-depth descriptions of these bathymetries can be found at Bradley and Venditti (2019), Parsons et al. (2005) and Lefebvre et al. (2022), respectively. To avoid any bias from the natural constraints, all data sets were limited to 100 transects of 450 m length each. As an example, Figure 2 shows one of these transects from the Weser tidal inlet below the corresponding surface plot. After identifying prevailing bedforms with the semi-automated algorithm presented in Scheiber et al. (2021), we calculate corresponding dune dimensions based on the aforementioned definitions. The resulting arrays, three for dune heights H_1 / H_2 / H_3 and two for dune lengths L_1 / L_2, are then compared with each other.

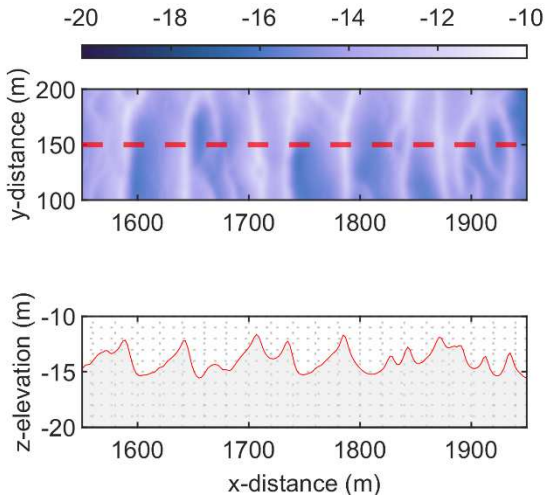

Figure 2. Bed elevation map (top) and exemplary transect (bottom) highlighting the tidally-constrained bedforms in the Weser inlet channel.

A helpful indicator for contrasting two results arrays is the relative difference d_r, which relates absolute differences to arithmetic mean values. For our specific case, this could read as follows:

$$d_r = \frac{H_1 - H_3}{\left(\frac{H_1 + H_3}{2}\right)} \quad (1)$$

where H_1 is the vertical and H_3 is the average dune height. This relative difference can be calculated for all identified bedforms. In a second step, its frequency of occurrence can be assessed and displayed in histograms. This gives us valuable information about how often and where specific differences can be expected. The repercussions of these differences are also present in the statistical parameters that describe the frequency of results, most prominently arithmetic mean and percentile values, which are often used to characterize the physical properties of a dune field. After assessing the complete results data set in the first instance, we repeated the described analyses for the subsets of (three) individual bathymetries and (five) dune size classes according to Ashley (1990) to better understand the reasons for particularly high sensitivities.

3 RESULTS AND DISCUSSION

Table 1 summarizes the arithmetic mean values for the most relevant parameters in this sensitivity study. The first line contains the results for all 21,939 assessed bedforms and already points at a crucial finding: the differences between vertical and inclined dune heights (H_1 vs. H_2) are remarkably small. The same applies for horizontal and inclined lengths (L_1 vs. L_2), which can also be seen in the distribution of their relative differences in Figure 3 below.

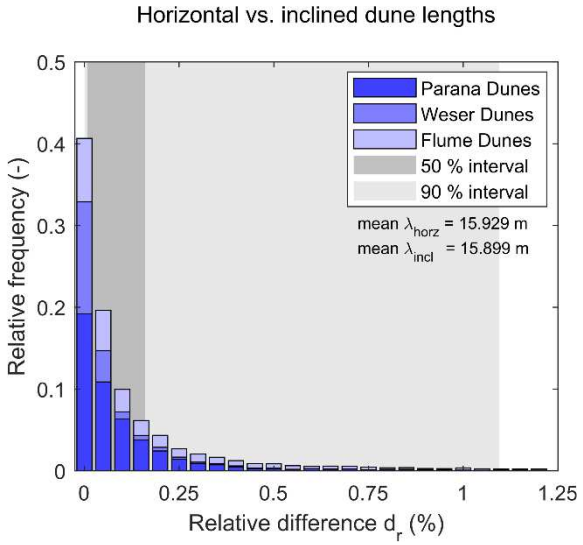

Figure 3. Relative frequency of occurrence for the relative differences between horizontal and inclined dune lengths. Blue shades relate to the three bathymetries and grey shades represent the 50 % and 90 % intervals, respectively.

In this illustration, dark and light grey patches illustrate the 50 % and 90 % intervals, respectively. The depicted intervals imply that 19 out of 20 assessed dunes show length deviations of less than 1.1 %. Related to the presented mean lengths, this translates into an absolute difference of 17.5 cm. However, the mean length itself only deviates by 3.0 cm. This similarity of results is corroborated by data about the dune baseline: an average inclination of $\alpha = 2.544°$ corresponds to a ratio between L_1 and L_2 of $\cos \alpha = 0.999$, which makes these approaches nearly equal.

Although this trend holds true for dune heights H_1 and H_2 as well, deviations of the average height H_3 are significantly larger. For instance, mean values for H_1 and H_2 are almost identical ($\Delta H \leq 0.3$ cm) throughout all bathymetric subsets, whereas H_3 mean values are between 9.0 and 32.7 cm higher than H_1 and H_2. This points at a systematic divergence, which can also be traced in the distribution of relative differences in Figure 4. One third of all dunes yields negligible differences of ± 5 % or less. However, the remainder of the frequency distribution shows a pronounced left tail. Overall, the average relative difference for the complete data set is -26.8 % with particularly high values in the subset of large dunes. Even though the average baseline angle reaches its maximum in this group, relative differences do not scale with dune inclination alone as the comparison with bathymetric subsets shows:

Table 1: Arithmetic mean values for three dune height (H) and two dune length (L) definitions. These values are complemented by the corresponding sampling sizes (N), information about the baseline inclination (α and cos α), the relative difference (d_r) between vertical and average dune heights as well as the ratio between left and right dune slopes (L_l/L_r) as a proxy for dune asymmetry. The total data set was further differentiated into subsets depending on bathymetry and dune size classes according to Ashley (1990), respectively.

Data Set	N (-)	H_1 (m)	H_2 (m)	H_3 (m)	L_1 (m)	L_2 (m)	α (deg)	cos α (-)	d_r (%)	L_l/L_r (-)
Total	21,939	0.481	0.480	0.648	15.899	15.929	2.544	0.999	-26.806	2.916
Paraná	10,926	0.264	0.264	0.354	9.438	9.451	2.251	0.999	-25.894	2.800
Weser	4436	0.779	0.779	0.903	33.909	33.920	1.117	1.000	-16.885	2.429
Flume	6577	0.641	0.638	0.965	14.484	14.558	3.993	0.995	-35.014	3.435
Small	7320	0.130	0.129	0.146	3.253	3.258	2.261	0.999	-10.839	1.460
Medium	6223	0.202	0.201	0.272	6.660	6.675	2.389	0.999	-25.479	2.259
Large	8263	0.977	0.975	1.353	32.491	32.557	2.946	0.999	-42.375	4.722
Very large	133	2.097	2.097	2.098	113.325	113.329	0.375	1.000	-0.501	1.593

the flume data contains dunes that are even more inclined, but relative differences are not as extreme as in the set of large dunes. This is because vertical and average heights are only identical in case of symmetrical dunes. Although such cases exist, bedforms under natural conditions are frequently asymmetric. In this study, the most symmetric bedforms are those from the tidally-constrained Weser bathymetry, which consequently coincide with minimal relative differences (cf. Tab. 1).

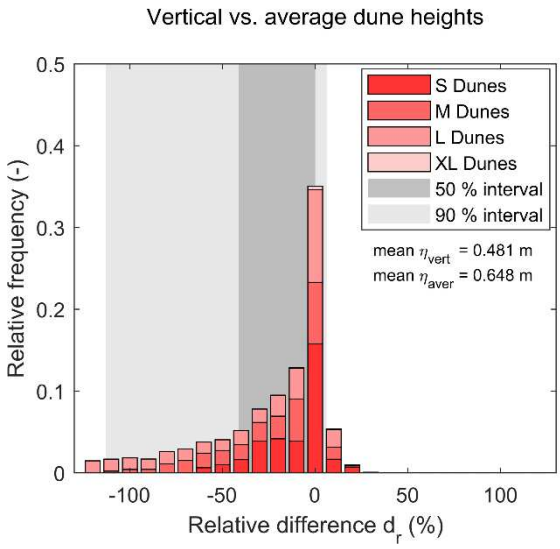

Figure 4. Relative frequency of occurrence for the relative differences between vertical and average dune heights. Red colours correspond with dune sizes according to Ashley (1990).

With regard to practical implications, we can draw two major conclusions from these findings: first, the inclination of a baseline can be neglected when calculating dune characteristics ($L_1 \approx L_2$ and $H_1 \approx H_2$), independent of the prevailing flow conditions or dune sizes. Secondly, using average dune heights yields significantly different results for the case of asymmetric dunes ($H_3 \neq H_1$). But nevertheless, both measures can be justified. H_1 and H_2, one the one hand, define dune height phenomenologically as the extent that a bedform crest can rise from the surrounding sediment. On the other hand, H_3 is used to describe dune height in terms of a vertical obstacle or roughness element that impedes horizontal flow. It is therefore not helpful to discard or propagate one definition in general. Rather than that, a suitable height definition should be chosen with care and applied consistently throughout connected analyses. The presented results can be seen as a sound basis for such decisions.

4 CONCLUSIONS

Dune height and length are widely applied to describe bedforms, but various definitions co-exist in academic literature. The presented sensitivity analysis scrutinizes, how the choice for a specific definition can impact results. According to our systematic analysis of three benchmarking bathymetries, the inclination of natural dunes is typically small enough to regard horizontal and direct trough-to-trough distances as equal. The same applies for vertical and orthogonal dune heights. However, the average dune height can yield significantly larger values than the aforementioned definitions with relative differences occasionally exceeding -100 %. In the present case, the average relative difference is -26.8 % at a sampling size of 21,939 bedforms in total. Although this finding illustrates the importance of a suitable height definition, it still leaves readers with an independent choice: while both vertical and orthogonal dune height reflect the physical constraints of dune growth, average dune height can be used to describe flow resistance. Hopefully, the findings of this study can support other bedform enthusiasts in choosing the most suitable geometric definitions for their research.

5 ACKNOWLEDGMENT

The topic of this study emerged from discussions between the two authors and was initiated as a thesis at the Faculty of Civil Engineering and Geodesy at the Leibniz University Hannover. We wish to thank the involved examiners, Torsten Schlurmann and Jan Visscher, as well as the supervisor, Christian Jordan, for their abiding interest and fruitful discussions. Moreover, we are indebted to the working groups who provided us with bathymetric data. The presented analyses would not have been possible without them.

6 REFERENCES

Ashley, G. M. (1990). Classification of large-scale subaqueous bedforms; a new look at an old problem. Journal of Sedimentary Research, 60(1), 160–172. doi:10.2110/jsr.60.160

Bradley, R. W., & Venditti, J. G. (2019). Transport Scaling of Dune Dimensions in Shallow Flows. Journal of Geophysical Research: Earth Surface, 124(2), 526–547. doi:10.1029/2018JF004832

Cisneros, J., Best, J., van Dijk, T., Almeida, R. P. de, Amsler, M., & Boldt, J., et al. (2020). Dunes in the world's big rivers are characterized by low-angle lee-side slopes and a complex shape. Nature Geoscience, 13(2), 156–162. doi:10.1038/s41561-019-0511-7

Cornish, V. (1901). On Sand-Waves in Tidal Currents. The Geographical Journal, 18(2), 170. doi:10.2307/1775344

Durán, R., Guillén, J., Ribó, M., Simarro, G., Muñoz, A., Palanques, A., & Puig, P. (2020). Sediment characteristics and internal architecture of offshore sand ridges on a tideless continental shelf (western Mediterranean). Earth Surface Processes and Landforms, 45(14), 3592–3606. doi:10.1002/esp.4986

Franzetti, M., Le Roy, P., Delacourt, C., Garlan, T., Cancouët, R., Sukhovich, A., & Deschamps, A. (2013). Giant dune morphologies and dynamics in a deep continental shelf environment: Example of the banc du four (Western Brittany, France). Marine Geology, 346, 17–30. doi:10.1016/j.margeo.2013.07.014

Lefebvre, A., Herrling, G., Becker, M., Zorndt, A., Krämer, K., & Winter, C. (2022). Morphology of estuarine bedforms, Weser Estuary, Germany. Earth Surface Processes and Landforms, 47(1), 242–256. doi:10.1002/esp.5243

Miramontes, E., Jouet, G., Thereau, E., Bruno, M., Penven, P., & Guerin, C., et al. (2020). The impact of internal waves on upper continental slopes: insights from the Mozambican margin (southwest Indian Ocean). Earth Surface Processes and Landforms, 45(6), 1469–1482. doi:10.1002/esp.4818

Parsons, D. R., Best, J. L., Orfeo, O., Hardy, R., Kostaschuk, R., & Lane, S. N. (2005). Morphology and flow fields of three-dimensional dunes, Rio Paraná, Argentina: Results from simultaneous multibeam echo sounding and acoustic Doppler current profiling. Journal of Geophysical Research: Earth Surface, 110(F4). doi:10.1029/2004JF000231

Scheiber, L., Lojek, O., Götschenberg, A., Visscher, J., & Schlurmann, T. (2021). Robust methods for the decomposition and interpretation of compound dunes applied to a complex hydromorphological setting. Earth Surface Processes and Landforms, 46(2), 478–489. doi:10.1002/esp.5040

Zomer, J. Y., Naqshband, S., Vermeulen, B., & Hoitink, A. J. F. (2021). Rapidly Migrating Secondary Bedforms Can Persist on the Lee of Slowly Migrating Primary River Dunes. Journal of Geophysical Research: Earth Surface, 126(3), e2020JF005918. doi:10.1029/2020JF005918

Renewable infrastructure in a field of dunes: changes to near bed turbulence & sediments

C. Unsworth *School of Ocean Sciences, Bangor University, UK – christopher.unsworth@bangor.ac.uk*
M. A. Austin *School of Ocean Sciences, Bangor University, UK – m.austin@bangor.ac.uk*
K. Van Landeghem *School of Ocean Sciences, Bangor University, UK – k.v.landeghem@bangor.ac.uk*.
A. Couldrey *HR Wallingford, UK – a.couldrey@hrwallingford.com*
R. Whitehouse *HR Wallingford, UK – r.whitehouse@hrwallingford.com*

ABSTRACT: The world's shallow continental shelves are currently experiencing a rapid pace of development from the growth of offshore renewable energy. Our ability to predict the response to new seabed infrastructure is limited by our models of flow and sediment transport which were created and validated assuming a uniform flow structure. We present field results from a deployment in the eastern Irish Sea where profiles of flow and turbulence were measured and used to drive a range of suspended sediment models. The range of models, and the various ways of forcing them, are tested against measured suspended sediment concentrations from a calibrated multi-frequency acoustic backscatter system. It was found that the bed shear stress as measured via 2D depth averaged approximations (with velocities from a bed mounted ADCP), as well as the TKE method (from a near bed ADCP) was the most accurate, whilst law of the wall approximation performed poorly. We found that the method of Garcia and Parker (1992) family of methods produced the most accurate measure of suspended sediments. Transport near the threshold of motion (30% of measurements) was poorly represented by all combinations of methods. The highest suspended sediment concentrations (10% of measurements) were also poorly predicted, likely due to the changing bed level which occurred during these high concentration events.

1INTRODUCTION

The movement of sediment on the seabed is still one of the most challenging processes to accurately model and predict (Egan et al., 2019; Salim et al., 2018; Tang et al., 2019) (Dey et al., 2020; Tsai & Huang, 2019). One of the most pressing issues for predicting sediment transport in marine and coastal environments is understanding the effects of new offshore wind farm infrastructure on both the structure of the flow, the subsequent effect on sediment transport, and the change to the seabed.

A typical assumption when applying sediment transport models is the use of mean flow parameters, usually assuming the form of the turbulent boundary layer. The emplacement of new infrastructure on the seabed forms a natural laboratory for flow and sediment transport processes to be investigated, notably because of two effects: 1) the creation of a localised source of pressure drag and non-equilibrium turbulence and 2) the subsequent effect on the form of the seabed. These effects cause two main problems for estimating sediment transport: 1) localised turbulence generation lowers the bulk flow velocity and 2), localized sources of turbulence tend to generate non-equilibrium flow and sediment transport fields, which are not part of the assumptions in the sediment transport models.

Here we use a recently collected suite of acoustic data from a seabed lander deployed in a field of dunes which had a section of seabed electricity cable attached to it. We use the data to test a variety of methods for estimating bed shear stress and suspended sediment concentrations and ask which methods work well in this environment.

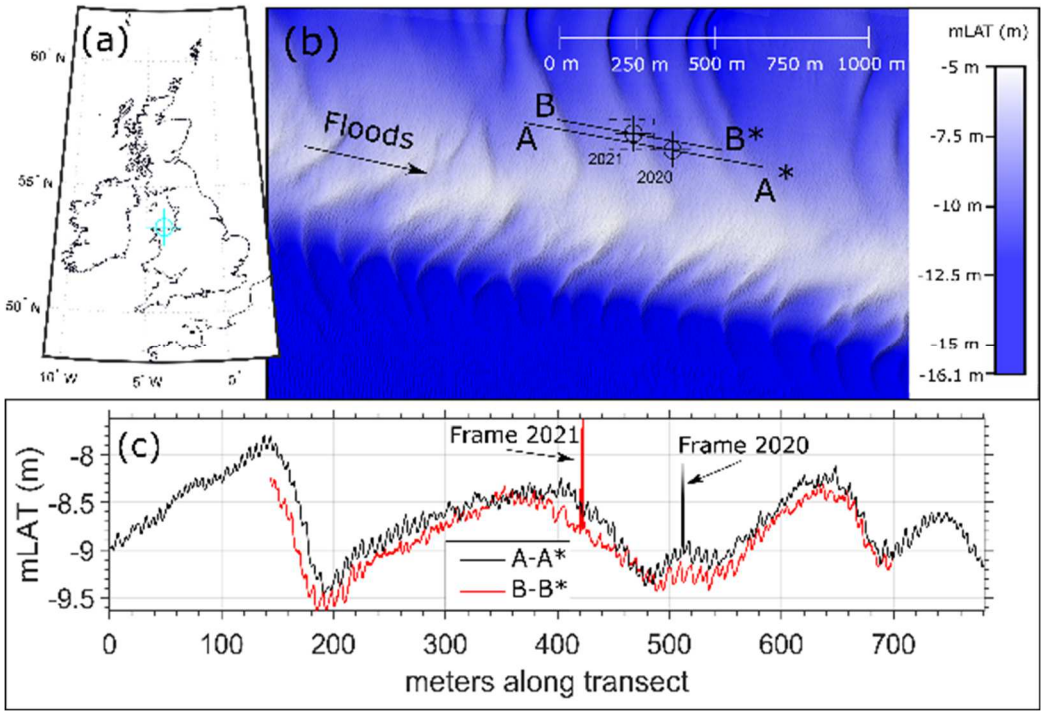

Figure 1. (a) location of site, (b) 2 m Bathymetry of "constable Bank", with instrument frame locations and bedform profiles highlighted. (c) location of frames and bedforms measured during the surveys.

2METHODS

2.1 Field Site

The study site was on the Constable Bank in the Irish Sea 6 km off the coast of North Wales, UK (53° 22.5616' N, 3° 43.6308' W, Figure 1, see end of document). This location is known to have active bedform migration and is close to existing and proposed offshore wind farms. The site has a semi-diurnal macro tidal regime, mean tidal ranges of 7.2 m at springs and 3.8 m at neaps (measured at Llandudno, https://ntslf.org). Dominant flood and ebb directions are 100° and 270 – 290°, respectively. Two separate field deployments were conducted, one in September 2020 and one in July 2021. Repeated vessel mounted Multibeam Echosounder (MBES) surveys were performed during the surveys to map bedform migration. Tides during the 2020 surveys were during the autumnal equinox and thus were some of the largest of the year, whilst tides during the 2021 surveys had an average tidal range for the site. Significant wave heights during the start of each deployment were 1 to 1.5 m high with 3 second periods, lowering to calm conditions towards the end of each deployment.

Grain size at the field site was measured from 11 Shipeck grab samples taken before deployments, was found to be a consistent uniform sand with a median grain size of 244 µm (Figure 2).

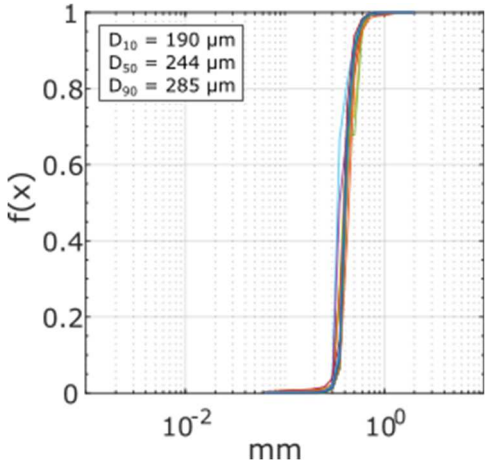

Figure 2. Grain size distributions of 11 grab samples from both surveys at the location of the instrument frames.

Thresholds of motion were calculated via the modified Shields curve (Soulsby, 1997):

$$D^* = D_{50}\left(\frac{(S-1)g}{\nu^2}\right)^{1/3} Eq.\ 1$$

$$\theta^*_{crit} = \frac{0.3}{1+1.2D^*} + 0.055(-0.02D^*) Eq.\ 2$$

$$\theta^*_{sus} = \frac{0.3}{1+D^*} + 0.1(-0.05D^*) Eq.\ 3$$

where D_{50} is the median grain diameter, g is the acceleration due to gravity, ν is the kinematic viscosity of the sea water (at 15°C, 1.1384 x10-6 m^2 s^{-1} and s = 2.58 for quartz grains in seawater.

2.2 Data collected

A suite of acoustic data was collected from a bespoke seabed lander which had a section of undersea electricity cable attached at one end (Figure 3). The data presented here are from AQD-1, the ABS, and the upward facing Sig1K.

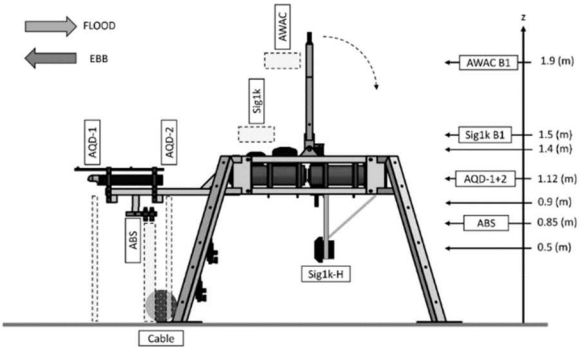

Figure 3. Schematic of the instrument lander. Dashed outlines indicate location of measurements used in the survey, "B1" indicates the location of the first bin of data. The section of cable is fixed to the base of the left side of the lander.

The combination of upward and downward facing ADCP's allows for the mean and near bed flow structure to be measured, including any effects from the bedforms on the flow field as well as the effects of the cable and instrument lander on the ebb tide velocities, especially near the bed. Standard thresholds for correlation and amplitude were set for ADCP's, which removed < 5% of data, velocity spikes were filtered out using a gradient threshold of 0.14 m s^{-2}. Removed values were replaced with linearly interpolated values, if the gap between good values was smaller than 4 data points. Velocities were collected in beam coordinates and converted in post processing. A local three-velocity component (UVW) coordinate system was applied using the median flood tide direction for each instrument, so that $\bar{U}$ is maximised and $\bar{V}$ over time is minimised, and were decomposed into burst-mean (with overbar) and turbulent components (with prime)

$$U = (\bar{U} + u')[v; w]. Eq.\ 4$$

3RESULTS

3.1 Bedforms

The seabed bathymetry at Constable Bank consists of sedimentary bedforms of two main scales. The larger scale bedforms in and around the lander site have an average length of 194 m by 0.94 m high (range from 0.8 – 1.5 m high, 200 – 300 m long), which have an orientation of 150° (Figure 1). Superimposed on these larger bedforms are smaller dunes of a scale 19 m long and 0.16 m high with a dominant angle of 100°, which is in line with the dominant flood tide direction. The location of the bedform crests changed less than 0.1 m between the surveys in 2020 and 2021. Their shape changed during the tides in a similar way to estuarine bedforms (Lefebvre et al., 2022). The size, shape and orientation of these smaller bedforms indicates there would be no/ or little significant flow separation from the larger host bedforms (Herbert et al., 2015). The height of the larger bedforms is roughly equal to the height of the instrument frame (1.4 m) so near bed and upward facing ADCP's will be measuring the turbulent boundary layer generated from the bedforms (Dyer, 1986; McLean et al., 1999; Nowell & Church, 1979).

3.2 Enhanced turbulence and suspended sediments

Given the directional setup of the experiment, we expect floods to have "natural" flows, whilst data collected during the ebb tides will also contain the turbulent wakes from the instrument frame and cable. The example profiles in Figure 4 are from the 2nd tide of the 2020 deployment and show the expected higher near-bed suspended sediment concentrations, and a steeper near bed velocity profile in ebbs.

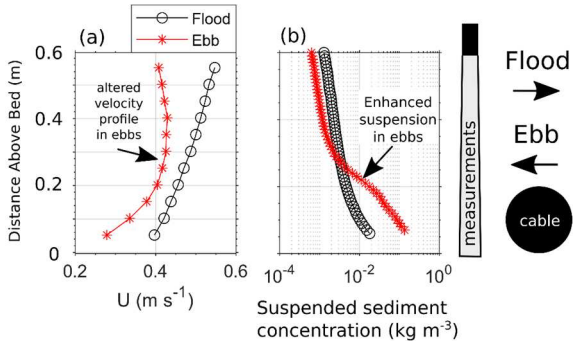

Figure 4. Examples of burst average (10 minute) velocity profiles (a) and suspended sediment concentrations (b). Flood tides measure "natural" flows whereas ebbs are affected by the instrument frame and electricity cable, illustrated on the right.

Such alteration of the near bed velocity profile should have affects on the estimating of bed shear stress via standard methods.

3.3 Estimating bed shear stress

For an estimate of bed shear stress using depth average properties, we used the 2D approximation with a Chezy coefficient (C') based on the bed sediment samples and flow depth (Baas et al., 2000; Van den Berg & Van Gelder, 1993):

$$\theta'_a = \frac{\rho_w \bar{U}^2}{(\rho_s - \rho_w)(C')^2 D_{50}} \quad Eq.\ 5$$

$$C' = 18\,log(\frac{4h}{D_{90}}) \quad Eq.\ 6$$

where ρ_w is the density of sea water, ρ_s is the density of the sediment, h is the flow depth. This method is the default for the 2D version of *Telemac*, for example. The method used in *MIKE21*, uses a manning's *M* for roughness:

$$\theta'_b = C\rho\bar{U}^2, \quad \text{Eq. 7}$$

$$C = \frac{g}{(Mh^{1/6})^2} \quad \text{Eq. 8}$$

where *M* was set to 32 $m^{1/3}s^{-1}$.

We calculate two estimates of bed shear stress suing the law of the wall (*LoW*) method, one with the upward facing ADCP (LoW_{Up}) and downward facing ADCP (LoW_{down}) via the usual equation:

$$u(z) = \frac{u_*}{\kappa}\left[ln\left(\frac{z-h}{z_0}\right)\right] \quad Eq.\ 9$$

Where u_* is the shear velocity, $\kappa = 0.41$ is the von Karmon constant, z is the vertical coordinate, z_0 is the roughness height, and bed shear stress is:

$$\tau_b = \rho u_*^2 \quad Eq.\ 10$$

this calculation was perfumed on the burst averaged by first selecting to lowest 5 velocities to regress, calculated the R^2, and if the fit was better than a set threshold ($R^2 = 0.85$), the next datapoint above was added to the regression until the threshold was passed. At which the previous iteration was used to get u_* and z_0. This procedure produced values for ~ 80 % of all measurements.

Alternatively, bed shear stress can be calculated from near bed turbulence data, which have been shown to perform well in complex flows where the assumptions in the law of the wall and 2D approximations are invalid (Biron et al., 2004; Kim et al., 2000; Pope et al., 2006; Williams et al., 1999).

Here we used the Reynolds Stressed based covariance method outlined by (Klipp, 2018):

$$TKE = \sqrt{\overline{u'w'}^2 + \overline{v'w'}^2} \quad Eq.\ 11$$

$$\tau_b = \sqrt{TKE} \quad Eq.\ 12$$

The TKE method outlined by via (Soulsby & Dyer, 1981):

$$TKE = 0.5\rho(\overline{u'^2} + \overline{v'^2} + \overline{w'^2}) \quad Eq.\ 13$$

$$\tau_b = 0.19TKE \quad Eq.\ 14$$

and the inertial dissipation method (Tennekes & Lumley, 1972)

$$u_* = (\varepsilon kz)^{1/3} \quad Eq.\ 15$$

Where dissipation (ε) can be calculated from (Scannell et al., 2017) for both tide and waves, and assuming a balance of production and dissipation.

The law of the wall-based methods shows by far the largest scatter for any value of $\bar{U}$ for either floods or ebbs (Figure 5a) – likely due to the presence of a turbulent wake in due to the bedforms on both phases of the tide or the extra effects of the wake from the cable and

instrument lander are present in the ebb tide. 2D-depth averaged methods show the least scatter due to their inputs having the least noise (Figurer 5a).

The turbulence-based methods of estimating u^* all produce different trends, but with roughly the same amount of scatter per value of $\overline{U}$. The *Klipp* method seems to perform worse in ebbs than floods, suggesting that the turbulence coming from the frame and cable are negatively affecting the results from this method. The TKE and dissipation-based method should produce similar values (assuming a balance between production and dissipation of turbulence) but it is clear that on both floods and ebbs the dissipation-based method consistently underpredicts u^* - possibly due to the amount of turbulence generated locally by the lander and the bedforms field.

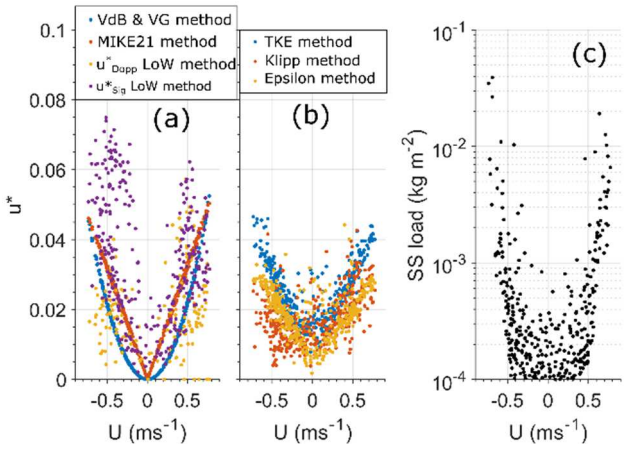

Figure 5 (a) and (b) display the variation of estimates for u* based upon the profile averaged mean velocity from the upward facing Sig1k and Law of the Wall method on the Sig1k and AQD-1 data (a), and (b) methods based upon turbulence Figure 5 (c) display measured suspended sediment loads from the ABS. $\overline{U} > 0$ = floods, < 0 = ebbs.

3.4 Estimating suspension

Next, we compare a range of methods for estimating near bed suspended sediment concentrations; the methods of: (Einstein, 1950; Rijn, 2007; Smith & McLean, 1977) and the (Garcia & Parker, 1991) "family" of methods (de Leeuw et al., 2020; Wright et al., 2005). We use the range of methods of estimating u^* outlined in section 3.3 to drive those models. We do this to try and get a measure of how good a measure of u^* is needed to predict suspended sediment concentrations in an environment where bedforms and infrastructure are on the seabed.

Regressions of observed and predicted near bed suspended sediment concentrations are shown in Figure 6 (at the end of the document). From these comparisons we suggest that the Garcia & Parker (1991) method, and its' decedents Wright et al., (2005) and de Leeuw et al., (2020) are the most sensible methods of estimating near bed suspended sediment concentration. All other methods show major differences in predicted vs measured concentrations at any value.

Plotting the distributions of predicted suspended sediment concentrations (Figure 7) allows a comparison of SSC methods and u^* methods to be compared at the same time. For example, if a SSC model was perfect, but the u^* data used was not, it would still not show the same distribution as the measured data. One key finding here is the highest and lowest concentrations are poorly predicted by any combination of methods.

Using the 2D methods with Garcia and Parker (1991) only *Eq.* 5-6 does well at the higher concentrations, but poorly for ~ 60% of the distribution, whilst *Eq. 7-8* performs well for 70 % of the distribution but the shape of the distribution at the high concentrations is poor. The TKE method has a better distribution at the higher concentrations and shows an excellent distribution down to 10^{-6} kg m^3, where the threshold of motion and the noise flood of the ABS begin to be reached.

The methods of Einstein, 1950; Rijn, 2007; Smith & McLean, 1977, appear to do well at the highest concentrations but considering that these models overpredict concentrations for the rest of the distribution, it seems likely that they provide the right results at high concentrations for the wrong reasons.

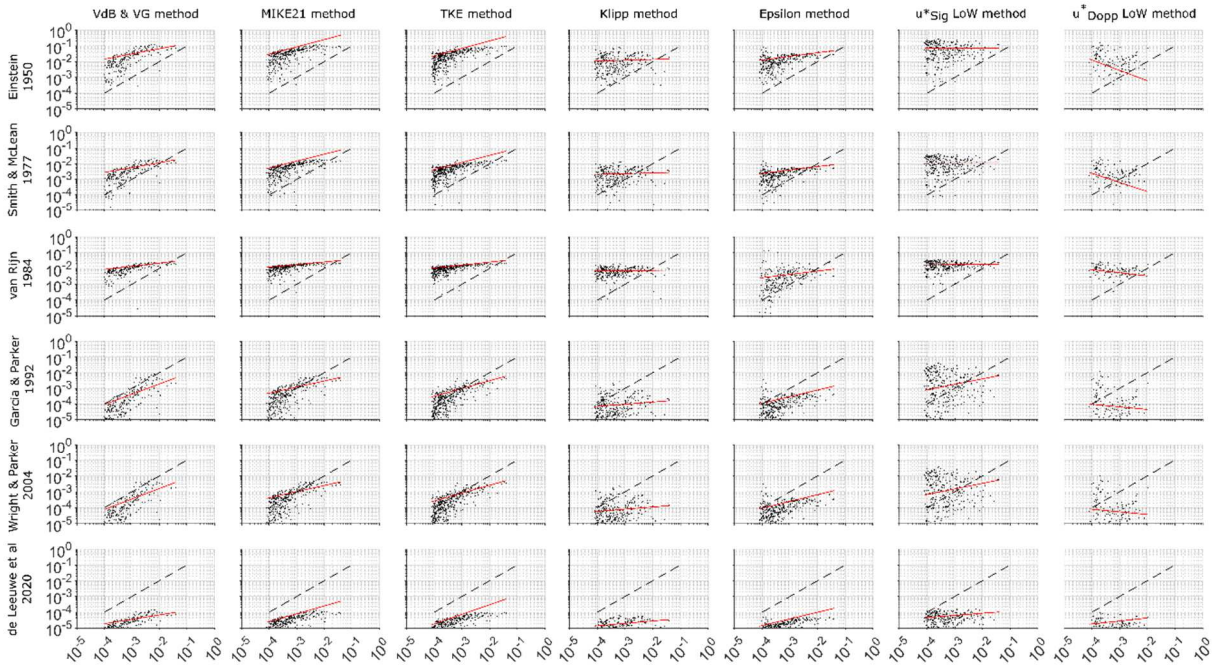

Figure 6. Comparisons between methods of estimating bear shear stress (right to left) and suspended sediment methods (top to bottom. X axis are measured values of SSC, Y axis is the predicted values. 1:1 slope is provided as a dashed line. Values are in log10 kg m-3. Red lines show a best fit from a robust linear regression.

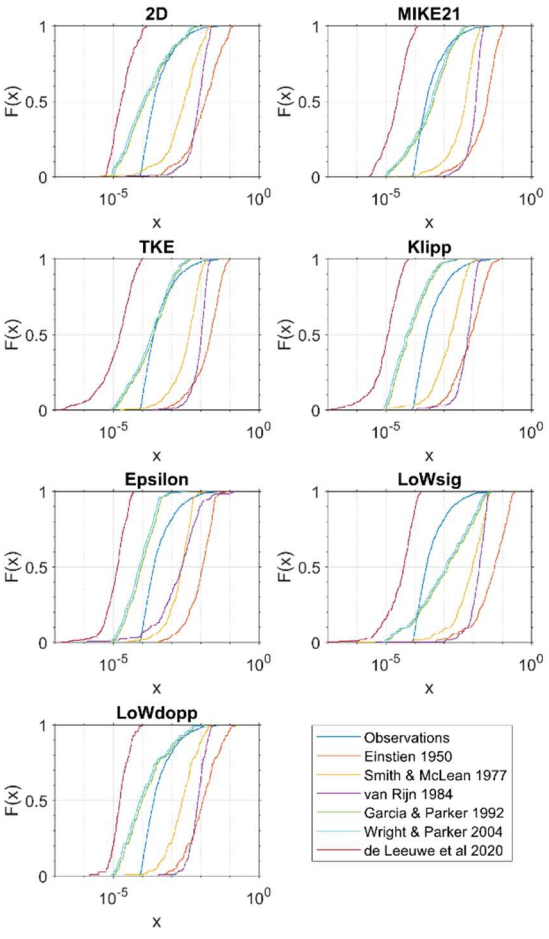

Figure 7. Distributions of measured and predicted near bed suspended sediment concentrations. X axis is concentration in kg m-3 and the y axis is the cumulative distribution of measurements.

4 DISCUSSION

Given the complex bathymetry of the site, and the additional drag produced from the lander and cable during ebb tides, it is perhaps surprising that the 2D methods of estimating bed shear stress (used with Garcia and Parker 1991) estimated near-bed suspended sediment concentrations similarly well to the TKE method which used near bed turbulence measurements. The data from the upward facing Sig1k (used to drive the 2D method) implicitly incorporates both the Eulerian and Lagrangian effects of the bedforms and sand bank on tidal forcing and local flow velocity – something which not all models incorporate. The result highlights that if given good-quality data, the 2D methods do work well.

Given that the TKE performs roughly as well as the 2D methods, one could conclude that near bed turbulence effects on suspending sediment in this deployment are minimal. The higher near-bed suspended sediment concentrations (Figures 4 and 5) would indicate that this does not seem likely.

The highest concentration of near-bed suspended sediment, which were underpredicted by any of the Garcia and Parker family of models (Figure 6), is likely due to the enhanced suspension from the cable and the instrument frame (Figure 3). One of the assumptions of the method is that there is a local equilibrium in the suspension (i.e., no erosion and deposition) which may not be true here as the seabed inevitably adjusted to the presence of the frame. The turbulence generated by the frame appears to have not been fully captured by the near-bed instruments in a way which would lead to equally high predictions of suspended sediment concentrations via the turbulence-based method.

5CONCLUSIONS

At present we conclude that for estimating suspended sediment concentrations (and thus bed shear stresses), both the depth averaged methods, and the near bed method (via TKE) are about as good in this environment. The Law of the wall-based methods should be avoided. We will investigate next how of the performance of the 2D models is due to 1) the velocities being driven by the ADCP data 2) the low noise of the input compared to the nosier (but theoretically more accurate) near bed turbulence methods.

6ACKNOWLEDGEMENTS

This work was funded by the EPSRC Supergen ORE Flexible Fund grant FF2020-1095 and the ECOWind-ACCELERATE project (NE/X008886/1). AJC and RJSW also acknowledge provision of matching funds from the HR Wallingford strategic Scour Research Programme. The team thanks Ben Powell, Aled Owen, and the crew of the RV Prince Madog for facilitating this fieldwork under difficult working conditions due to COVID-19 restrictions.

7REFERENCES

Baas, J. H., van Dam, R. L., & Storms, J. E. a. (2000). Duration of deposition from decelerating high-density turbidity currents. Sedimentary Geology, 136(1–2), 71–88. https://doi.org/10.1016/S0037-0738(00)00088-9

de Leeuw, J., P. Lamb, M., Parker, G., Moodie, A. J., Haught, D., G. Venditti, J., & Nittrouer, J. A. (2020). Entrainment and suspension of sand and gravel. Earth Surface Dynamics, 8(2), 485–504. https://doi.org/10.5194/esurf-8-485-2020

Dey, S., Ali, S. Z., & Padhi, E. (2020). Hydrodynamic Lift on Sediment Particles at Entrainment: Present Status and Its Prospect. Journal of Hydraulic Engineering, 146(6), 03120001. https://doi.org/10.1061/(asce)hy.1943-7900.0001751

Dyer, K. R. (1986). Coastal and estuarine sediment dynamics. John Wiley & Sons.

Egan, G., Cowherd, M., Fringer, O., & Monismith, S. (2019). Observations of Near-Bed Shear Stress in a Shallow, Wave- and Current-Driven Flow. Journal of Geophysical Research: Oceans, 124(8), 6323–6344. https://doi.org/10.1029/2019JC015165

Einstein, H. A. (1950). The bed-load function for sediment transportation in open channel flows. Technical report 1026, Soil Conservation Service.

Garcia, M., & Parker, G. (1991). Entrainment of Bed Sediment into Suspension. In Journal of Hydraulic Engineering (Vol. 117, Issue 4, pp. 414–435). https://doi.org/10.1061/(ASCE)0733-9429(1991)117:4(414)

Herbert, C. M., Alexander, J., & Martínez de Álvaro, M. J. (2015). Back-flow ripples in troughs downstream of unit bars: Formation, preservation and value for interpreting flow conditions. Sedimentology, 62(7), 1814–1836. https://doi.org/10.1111/sed.12203

Klipp, C. (2018). Turbulent friction velocity calculated from the Reynolds stress tensor. Journal of the Atmospheric Sciences, 75(4), 1029–1043. https://doi.org/10.1175/JAS-D-16-0282.1

Lefebvre, A., Herrling, G., Becker, M., Zorndt, A., Krämer, K., & Winter, C. (2022). Morphology of estuarine bedforms, Weser Estuary, Germany. Earth Surface Processes and Landforms, 47(1), 242–256. https://doi.org/10.1002/esp.5243

McLean, S. R., Wolfe, S. R., & Nelson, J. M. (1999). Spatially averaged flow over a wavy boundary revisited. Journal of Geophysical Research: Oceans, 104(C7), 15743–15753. https://doi.org/10.1029/1999jc900116

Nowell, A., & Church, M. A. (1979). Turbulent flow in a depth-limited boundary layer. Journal of Geophysical Research-Oceans, 84(C8), 4816–4824.

Rijn, L. van. (2007). Unified view of sediment transport by currents and waves. II: Suspended transport. Journal of Hydraulic Engineering, 133(6). http://ascelibrary.org/doi/abs/10.1061/(ASCE)0733-9429(2007)133:6(668)

Salim, S., Pattiaratchi, C., Tinoco, R. O., & Jayaratne, R. (2018). Sediment Resuspension Due to Near-Bed Turbulent Effects: A Deep Sea Case Study on the Northwest Continental Slope of Western Australia. Journal of Geophysical Research: Oceans, 123(10), 7102–7119. https://doi.org/10.1029/2018JC013819

Scannell, B. D., Rippeth, T. P., Simpson, J. H., Polton, J. A., & Hopkins, J. E. (2017). Correcting surface wave bias in structure function estimates of turbulent kinetic energy dissipation rate. Journal of Atmospheric and Oceanic Technology, 34(10), 2257–2273. https://doi.org/10.1175/JTECH-D-17-0059.1

Smith, J. D., & McLean, S. R. (1977). Spatially averaged flow over a wavy surface. Journal of Geophysical Research, 82(12), 1735–1746.

Soulsby, R. (1997). Dynamics of Marine Sands. Thomas Telford Publications.

Soulsby, R. L., & Dyer, K. R. (1981). The form of the near-bed velocity profile in a tidally accelerating flow. Journal of Geophysical Research, 86(C9), 8067. https://doi.org/10.1029/JC086iC09p08067

Tang, C., Li, Y., Acharya, K., Du, W., Gao, X., Luo, L., & Yu, Z. (2019). Impact of intermittent turbulent bursts on sediment resuspension and internal nutrient release in Lake Taihu, China. Environmental Science and Pollution Research, 26(16), 16519–16528. https://doi.org/10.1007/s11356-019-04847-2

Tennekes, H., & Lumley, J. L. (1972). A first course in turbulence. MIT press.

Tsai, C. W., & Huang, S. H. (2019). Modeling Suspended Sediment Transport Under Influence of Turbulence Ejection and Sweep Events. Water Resources Research, 55(7), 5379–5393. https://doi.org/10.1029/2018WR023493

Van den Berg, J. H., & Van Gelder, A. (1993). A new bedform stability diagram, with emphasis on the transition of ripples to plane bed in flows over fine sand and silt. Special Publication of the International Association of Sedimentologists, 17, 11–21.

Wright, S., Parker, G., & Asce, M. (2005). Simplified Stratification Model. Journal of Hydraulic Engineering, 130(8), 796–805. https://doi.org/10.1061/(ASCE)0733-9429(2004)130

Bedload quantification by passive acoustic measurement: case of an isolated dune

M. Vah *LOMC, UMR 6294 CNRS, Université Le Havre Normandie, Le Havre, France, melanie.vah@univ-lehavre.fr*
M. Ouzaouit *LOMC, UMR 6294 CNRS, Université Le Havre Normandie, Le Havre, France*
H. Besnard *LOMC, UMR 6294 CNRS, Université Le Havre Normandie, Le Havre, France*
A. Jarno *LOMC, UMR 6294 CNRS, Université Le Havre Normandie, Le Havre, France*
B. Morvan *LOMC, UMR 6294 CNRS, Université Le Havre Normandie, Le Havre, France*
F. Marin *LOMC, UMR 6294 CNRS, Université Le Havre Normandie, Le Havre, France*

ABSTRACT: A preliminary study is performed in a non-tiltable current flume to evaluate bedload transport quantification by passive acoustic measurement with an hydrophone. Tests are conducted with a medium sandand a pre-formed isolated dune as bedform and for different current forcing. Bedload transport is evaluated by two methods: dune-tracking and passive acoustic measurement. Promising results are obtained comparing the root-mean-square pressure from acoustic signals and bedload transport based on excess bottom shear stress. Results from dune tracking method also highlights the sediment supply limitation induced by the isolated dune.

1 INTRODUCTION

Passive acoustics measurements using hydrophones can assess bedload transport quantification during long periods with high temporal resolution as well as during high turbid eventswhich is not possible with optical methods. Research on bedload quantification with hydrophone have been mainly conductedon natural streams and used to quantifygravel bedload (Geay et al. 2017, 2020,Krein et al. 2016). In-situ preliminary studies to estimate bedload transport using passive acoustics measurements were performed by Blanpain et al. 2015 over sands and by Homrani et al. 2019 over coarse shelly sediment of median diameter 1.25mm. The need of laboratory experiments was pointed out in the last study to go further in the analysis.

Thorne 1985 and 1986, based on laboratory experiments in a rotative drum proposed an empirical law to link the number of grain collisions to the root-mean-square pressure. This approach is widely used in the literature. According to Wenz 1962, bedload transport acoustics signal is higher than 20 kHz for sand. Belleudy et al. 2010 have shown that the frequency of bedload transport acoustic signal is increasing when the sediment diameter is decreasing.

Although the difficulties to separate the different components of acoustic signals, in particular to isolate the component related to sediment transport, the hydrophone measurements are simple to implement. Furthermore, in-situ bedload transport quantification is a challenge. Monitoring thebedload transport when submarine dunes migrate is particularly important. It was shown that bedload transport can be correlated to dune migration velocity under unlimited sediment supply as well as under limited sediment supply (Vah et al. 2020). An isolated dune is a particular case of a dune field under sediment supply limitation considering only one dune.

This study is based on experimental tests carried out in a flume under unidirectional current. The case of an isolated dune isstudied. A comparison between results obtained with acoustic and dune tracking methods is performed. The main objective of this preliminary work is to evaluate acoustic measurement possibilities to quantify sand bedload transport in a flume experiment.

2 EXPERIMENTAL SETUP AND TESTS CONDITIONS

Experiments are conducted under unidirectional flow in a non-tilting current flume. The flume is 10.7 m long and 0.49 m wide (Fig. 1). A honeycomb-shaped screen isinstalled in the upstream part of the flume (Fig. 1) to ensure uniform flow conditions.

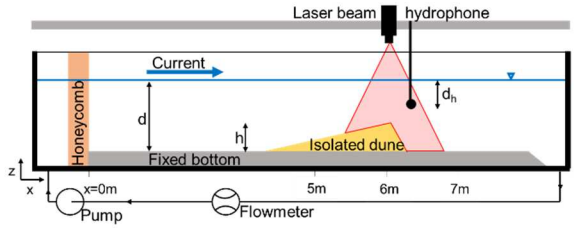

Figure 1. Schematic side view of the current flume

The laser beam is placed above the free surface, laterally centered to the flume at x=6m, where x is the distance from the honeycomb measured in the horizontal direction.A high-resolution digital camera (Basler acA2500-60um, 2048 × 2592 pixels) with a 16 mm focal length is used. It is fixed on a tripod and positioned on the side of the flume at x=6m, inclined from vertical with an angle equal to 50° to visualize the laser plane on a distance of 70 cm. The image resolution was 0.27 mm per pixel. Images are acquiredat a frequency of 0.5Hz with an exposure time of 80,000µs.

A spherical omnidirectional hydrophone (Brüel&Kjær® Type 8105) is placed vertically at x=6.2 m, at a distance d_h below the free surface and at 10 cm from the flume median vertical plane in order to limit perturbation of the free surface near the laser beam.At the beginning of test, the hydrophone is situated above the end of the lee side.It is coupled to a conditioning amplifier (Nexus Type 2692) with 10 mV/Pa calibration on a frequency range extended from 10 Hz to 100 kHz.Data were acquired using an oscilloscope (Teledyne Lecroy Waverunner HRO 66ZI) with a sampling of 2M/sec. Acquisition duration is fixed to 10 s.

Water level far from the isolated dune is set to d=0.25m for present tests. Dune height at equilibrium is noted h. Dune length is equal to approximately 1.2m.

Post-processing for dune tracking method is performed using images acquired with a high-resolution camera. Dune position is extracted after calibration from the position of the laser beam on the images. Migration of the isolated dune is estimated from the crest displacement. Dune height h at equilibrium is also measured. These two parameters allow to calculate the bedload transport rate.

Two different isolated dunes are created in the flume: a mobile one and a fixed one. The mobile dune is composed of medium sediment from a quarry with a medium diameter D_{50} equals to 617µm. This sediment is well-sorted, based on Soulsby 1997 criterion with a density of s=2.65. The fixed dune is composed oflarge pebbles (diameter between 2 to 6 cm) covered with small pebbles with a diameter from 4 to 6 mm to obtain the smallest possible bottom rugosity for a fixed dune under present hydrodynamic forcing.During all the tests on the fixed dune, no pebbles movement are observed.

The same experimental procedure is used for the two series of tests, with a mobile anda fixed dune:

- The dune is manually pre-formed
- Current is turned on with an acceleration phase of 1 minute to reach to desired flow value.
- Acquisition of images for dune tracking measurement is started. Acoustics acquisitions of 10s are triggeredwith a one-minute period.
- After 10 to 15 min the current is turned off.

No image acquisition is performed for tests with the fixed dune.

Conditions of the tests with the mobile isolated dune are given in table 1. The same

Table 1: Tests conditions with the mobile isolated dune. Parameters are given at equilibrium.

test	U (m/s)	h (m)	d_h (m)
1	0.3	0.08	0.075
2	0.32	0.074	0.075
3	0.34	0.075	0.075
4	0.36	0.073	0.075
5	0.38	0.074	0.1
6	0.4	0.08	0.1

tests are conducted with the fixed dune for the same flow velocities. Fixed dune height is equal to 0.085m for all the tests. An additional test was performed without flow to obtain the ambient noise.

For the mobile isolated dune, the angle of the lee side is 32° at equilibrium for all the tests, which corresponds to the avalanche angle and the angle of the stoss side near the crest is 1.5°.

For all the tests the flow regime is turbulent with a Reynolds number larger than 5000. The shear Reynolds number is defined in Equation 1.

$$R_* = \frac{u_*' k_s}{\nu} \quad (1)$$

where u'∗ is the bed shear velocity calculated from Equation 2 given below, k_s is the roughness height with $k_s=2.5D_{50}$ (Nielsen 2009) and ν the fluid kinematic viscosity;

$$\frac{u(z)}{u_*'} = \frac{1}{\kappa}\ln\left(\frac{z}{z_0}\right) \quad (2)$$

where z is the distance from the bed in the vertical direction, u(z) is the flow velocity at a distance z from the bed, κ=0.4 is the von Karman constant and z_0 is a length scale.

For all the tests, the shear Reynolds number R_* is higher than 70 at dune crest which correspond to a rough turbulent flow regime (Sleath 1984). The length scale z_0 may be estimated using Equation 3.

$$z_0 = \frac{k_s}{30} \quad (3)$$

The effective Shields parameter θ' is obtained with Equation 4:

$$\theta' = \frac{u_*'^2}{(s-1)gD_{50}} \quad (4)$$

where g is the acceleration due to the gravity.

The effective Shields parameter is calculated at equilibrium state and at the dune crest.

The critical Shields number $\theta_c$corresponding to the Shields number at the sediment motion threshold is obtained for the D_{50}=617µm sedimentfrom Vah et al. 2022 and θ_c = 0.0373.

Dimensionless bedload sediment transport is calculated from Equation 5.

$$\Phi = \frac{Q_s}{\sqrt{(s-1)g\,D_{50}^3}} \quad (5)$$

where Q_s is the dimensional bedload transport [m²/s].

Charru 2006 showed theoretically that Φ is proportional to $\theta'^{3/2}$, based on a conservation equation and an erosion-deposition model. Bedload transport is compared with a formulation based on the excess of shear stress (Eq. 6), with m a dimensionless parameter. This equation is based on the one proposed by Meyer-Peter and Müller 1948.

$$\Phi = m(\theta' - \theta_c)^{3/2} \quad (6)$$

3 BEDLOAD TRANSPORT USING DUNE TRACKING METHOD

Results obtained for dimensionless bedload transport from tests with the mobile isolated dune are shown in Figure 2 and in Table 2.

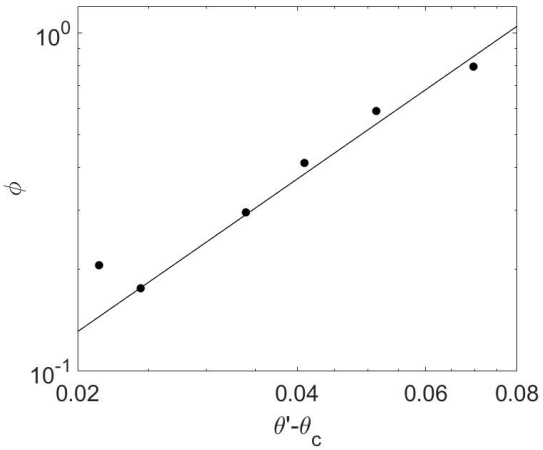

Figure 2. Dimensionless bedload transport. The black line represents the best fit obtained.

Equation 6 has been fitted to the present data and the best value for the parameter m is m=46.3 with a correlation coefficient R^2=0.96.

The power coefficient proposed by Charru 2006 is still available for present data for bedload transport of an isolated dune.

Based on experiments under infinite sediment supply conditions and bedforms naturally formed with the current conditions in the flume from a flat bottom, Meyer-Peter and Müller 1948 and Vah et al. 2020 found, respectively, m=8 and m=6.

The present study is in limited supply sediment conditions. Conclusions for this supply condition found by Vah et al. 2020 in a flume for the same sediment are the following ones: bedforms formed in supply limited sediment condition are smaller and their migration velocities are higher than ones under infinite supply condition for the same hydrodynamics conditions. Here the isolated dune is largely bigger than the one that would havenaturally been formedin the flume. Due to mass conservation, sediment bedload transport is higher in this case than expected for this sediment and this range of excess shear stress under infinite supply conditions. This explains the larger value found for the coefficient m than the one predicted by Meyer-Peter and Müller 1948 or Vah et al. 2020

4 BEDLOAD TRANSPORT USING PASSIVE ACOUSTIC METHOD

For acoustic measurements, a high pass filter is applied on acoustic signal with a 10 kHz cut off frequency (Blanpain et al. 2015). Signal below 10 kHz is assumed to be due toturbulence, free surface, electric noise as well as bedload for particles larger than 1 cm (Thorne 1985, 1986, Geay 2013). Then, the root-mean-square pressure (P_{rms}) is calculated on each acoustic acquisition.

The empirical formulation proposed by Thorne 1985, 1986 to link frequency peak (F_{peak})of the acoustic signal to bedload particle size, for uniform grain size distributions is given in Equation 7.

$$F_{peak} = \frac{224}{D_{50}^{0.9}} \quad (7)$$

For the sediment size considered in this study, Equation 7 gives F_{peak}=173 kHz. As the acoustics signal is sampled at a lower frequency (100 kHz), the validation of this empirical law for this set of experiments in a flume is not possible.

Despite the weakerfrequency sampling compared to the one forsome similar works (frequency sampling of 314 kHz for Blanpain et al. 2015 and Homrani et al. 2019 and of 600 kHz for Thorne 1985, 1986), the objective is to questionif correlation between bedload and acoustic signal can however be detected. Indeed, if the acoustic signal is maximum at F_{peak}=173 kHz, the frequency content of the acoustic signal associated to the sand transport is extended on a wide range.

The mean P_{rms} value estimated for each testisplotted as a function of the excess of shear stress (Fig. 3).

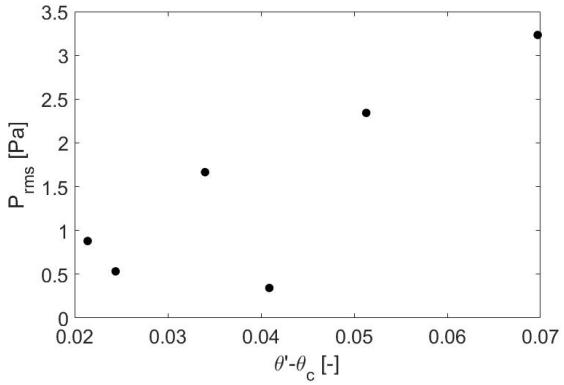

Figure 3. Mean P_{rms} values as a function of the excess shear stress.

Table 2: Dimensionless bedload transport for experimental tests

test	u'∗ [m/s]	θ' [-]	Φ [-]
1	0.0242	0.0587	0.206
2	0.0248	0.0617	0.176
3	0.0267	0.0713	0.295
4	0.0280	0.0782	0.413
5	0.0297	0.0886	0.588
6	0.0327	0.107	0.796

To fit present values, tests 2 and 4 are removed due to the low P_{rms}value found for these two tests. These outliersmay result from a problem during acquisition such as the presence of air bubbles on the hydrophone. Data are fitting with Equation 8 with a good regression coefficient.

$$P_{rms} = \text{a}\,(\theta' - \theta_c)^{3/2} + b \qquad (8)$$

where a=148 Pa and b=0.6 Pa (R^2=0.98).

P_{rms} is also evaluated for the test without flow (only ambient and electric noise), this value is equal to coefficient b in Equation 8. To reduce background noise on data, the P_{rms} value without flow is removed from the P_{rms}values with flow. In spite of the few amounts of testing, it is shown that P_{rms}tends to be proportional to bedload transport.

The same post-processing is applied on acoustic data acquired with the fixed dune and no correlation with the excess bed shear stress was found.

5 CONCLUSIONS

Conclusions on this preliminary work can be resumed as:

- Sediment bedload transport quantification using dune tracking method is consistent with formulations from the literature. The sediment supply limitation which is the consequence of the isolated dune induces larger values for bedload transport than expected using Meyer-Peter and Müller 1948 formulation.
- Even if the acoustic signature of grain collision may be partial due to the weak frequency sampling, mean rms pressure is globally a relevant indicator of bedload transport.

New laboratory tests are necessary to confirm these preliminary results in controlled conditions with various sediments or other bed configurations and a higher sampling frequency.

6 ACKNOWLEDGEMENT

The authors acknowledge the Interreg VA France (Channel) England Program, which funds the TIGER project, the MODULLES project from France EnergiesMarines and the Normandy region which funds this study.

This work was initiated by France Energies Marines, with support from the French government, under the “Investissements d’Avenir” programme managed by the French National Research Agency ANR.

7 REFERENCES

Belleudy, P., Valette, A., Graff, B., 2010. Passive hydrophone monitoring of bedload in river beds: First trials of signal spectral analysis, inBedload-Surrogate Monitoring Technologies, U.S. Geol. Surv. Sci. Invest. Rep. 2010–5091, edited by J. R. Gray, J. B. Laronne, and J. D. G. Marr,pp. 67–84, U.S. Geological Surv., Reston, Va.

Blanpain, O., Demoulin, X., Waeles, B., Ravilly, M., Garlan, T., Guyomard, P., 2015. Passive acoustic measurement of bedload discharge features on a sandy seafloor, Proceedings of the Institue of Acoustics.

Charru, F., 2006. Selection of the ripple length on a granular bed sheared by a liquid flow. Phys Fluids 18(12):121508

Geay, T., 2013. Mesure acoustique passive du transport par charriage dans les rivières. Sicences de la Terre. Université de Grenoble.

Geay, T., Belleudy, P., Gervaise, C., Habersack, H., Aigner, J., Kreisler, A., Seitz, H., Laronne, J.B.,2017. Passive acoustic monitoring of bed loaddischarge in a large gravel bed river. J. Geophys. Res. Earth Surf., 122, 528–545,doi:10.1002/2016JF004112.

Geay, T., Zanker, S., Misset, C., Recking, A., 2020. Passive acousticmeasurement of bedload transport: Toward a global calibration curve?.Journal of Geophysical Research: Earth Surface, 125, e2019JF005242. https://doi.org/10.1029/2019JF005242

Homrani, S., Floc’h, F., Le Dantec, N. L., Demoulin, X., Delacourt, C., 2019. Vessel-mounted hydrophone measurements to estimate bedload transport of coarse shelly sediments. In Coastal Sediments 2019: Proceedings of the 9th International Conference (pp. 1621-1630).https://doi.org/10.1142/9789811204487_0140

Krein, A., Schenkluhn, R., Kurtenbach, A., Bierl, R., Barrière, J., 2016. Listen to the sound of moving sediment in a small gravel-bed river. International Journal of Sediment Research, 31(3), 271-278.https://doi.org/10.1016/j.ijsrc.2016.04.003

Meyer-Peter, E., Müller, R., 1948. Formulas for bed-load transport. IAHSR 2nd meeting, Stockholm, appendix 2. IAHR

Nielsen, P., 2009. Coastal and estuarine processes: advanced series on oceanengineering, Vol. 29. World Scientific: Singapore.

Sleath, J.F.A., 1984. Sea bed mechanics. Wiley: New York.

Soulsby, R., 1997. Dynamics of marine sands: a manual for practical applications.Thomas Telford: Guildford.

Thorne, P. D., 1985. The measurement of acoustic noise generated by moving artificial sediments. Journal of the Acoustical Society of America 78, 1013. doi: 10.1121/1.393018

Thorne, P. D., 1986. Laboratory and marine measurements on acoustic detection of sediment transport. Journal of the Acoustical Society of America 80, 899. doi: 10.1121/1.393913

Vah, M., Jarno, A., Le Bot, S., Ferret, Y., Marin, F., 2020. Bedload transport and bedforms migration under sand supply limitation. Environmental Fluid Mechanics, 20(4), 1031–1052. https://doi.org/10.1007/s10652-020-09738-6

Vah, M., Khoury, A., Jarno, A., Marin, F., 2022. A visual method for threshold detection ofsediment motion in a flume experiment without humaninterference. Earth Surface Processes and Landforms,1–12. https://doi.org/10.1002/esp.5346

Wenz, G. M., 1962. Acoustic ambient noise in the ocean: Spectra and sources. The Journal of the Acoustical Society of America, 34(12), 1936-1956.https://doi.org/10.1121/1.1909155

Two-dimensional subaqueous dune dynamics under unidirectional flows

A. Valance, *Institut de Physique de Rennes, CNRS, Université de Rennes, Rennes, France – alexandre.valance@univ-rennes1.fr*
S. Kiki, *Institut de Physique de Rennes, CNRS, Université de Rennes, Rennes, France*
N. Le Dantec, *Laboratoire Géoscience Océan, Institut Universitaire Européen de la Mer, Plouzané, France*

ABSTRACT: Two-dimensional subaqueous dunes under the shearing of a turbulent flow are investigated experimentally and theoretically. Experiments reveal the existence of steady-state dunes migrating with constant speed. We identified two different morphological regimes. For small dune, the height of the dune varies almost linearly with its mass. In contrast, for large dune, the height and length scale as the square root of the dune mass resulting in a scale invariant dune shape. Adapting aeolian dune models based on the concept of the saturation length to subaqueous sediment transport, we derive theoretical predictions that are in quantitative agreement with our experimental data and allow to infer the saturation length from the experiments.

1 INTRODUCTION

Dunes are sedimentary bodies widely spread in Earth environments. They are found in sand deserts as well as in sea floors. An interesting feature of dunes is that their morphologies provide pieces of information about climatic conditions since they are modeled by ambient streams (Partelli et al. 2014, Courrech du Pont 2015).

Since the pioneer work of Bagnold (1941) on dune morphogenesis, it is known that dunes are generated by aerodynamic or hydrodynamic instability which amplifies any surface irregularities of a granular bed due to a phase shift between the basal shear stress and the bed topography (Sauerman et al 2001, Charru & Mouilleron-Arnoud 2002). This destabilizing mechanism is however balanced on one hand by the gravity force which tends to settle particles and on the other hand by the sediment transport dynamics. Several models for dune formation (Kroy et al 2022, Andreotti et al. 2002 b, Charru et al 2006) have indeed emphasized that the transport dynamics react to a local change of the basal fluid shear stress with a finite spatial lag, often referred to as the saturation length. This saturation process introduces a stabilizing mechanism for dune growth and sets the wavelength of the most unstable wavelength.

One important issue is to determine the relevant physical mechanisms that govern this saturation process. This leads to controversial propositions for the saturation during the last decades. Assuming the balance between particle inertia and fluid drag force dominates the dynamics of particle transport, Andreotti et al. (2002b) suggested that the saturation length is governed by the drag length which corresponds to the distance needed for a particle initially at rest to reach the fluid velocity. This hypothesis has been validated for aeolian sand dune on Earth and Mars (Claudin & Andreotti 2006). Alternative mechanisms have been proposed for subaqueous transport. In particular, Lajeunesse et al. (2006) suggested that the saturation length is set by the deposition length which corresponds to the length travelled by a mobile particle before being trapped by the bed. More recently, Pähtz et al. (2013, 2014) proposed a general theoretical expression for the saturation length that takes into account the relaxation of the fluid and particle speed and particle concentration.

Recent models of dune morphogenesis are based on particle transport description that accounts for this relaxation process via the introduction of a saturation length. These models show that there exists a minimum dune size set by the saturation length and revealed different morphologies for small (i.e., of order the saturation length) and large (i.e., much larger than the saturation length) dunes (Kroy et al, 2002, Andreotti et al. 2002b). Small dunes, sometimes called smooth heaps, domes or proto-dunes are weakly asymmetric and do not exhibit slip face. Large dunes are characterized by asymmetric profiles with well-developed slip face and scale invariant shapes.

These model predictions have been derived for aeolian sand dune. It turns out that the latter model can be easily adapted for investigating subaqueous dunes. This is confirmed by the 2D dune experiments conducted by Groh et al. (2008, 2009) for testing the model of Kroy et al. (2002) developed for aeolian sand dunes. They found a fairly good qualitative agreement between their experimental results and the prediction of the model concerning the migration speed of the steady-state dune. In particular, they confirmed that the migration speed scales like the square root of the dune mass. However, no attempt has been made for a quantitative comparison between the morphological features (height, length, aspect ratio) of the experimental dunes and model predictions.

Several questions arise for the case of subaqueous dunes. Are the models developed for aeolian dunes relevant for describing subaqueous dunes? Do the models have the capability to provide predictions in quantitative agreement with the experimental results? Are the model predictions sensitive to the nature of the transport law? What is the experimental saturation length for subaqueous particle transport? The objective of this study is to provide a detailed picture of steady-state subaqueous dunes both experimentally and theoretically.

Thanks to dune experiments achieved in a quasi-two-dimensional flume, we investigated single steady-state dunes and characterize their shape and migration speed as a function of their size and flow strength. In addition, we adapted the aeolian dune models to describe subaqueous dunes and computed steady-state dune profiles. Finally, we propose a method to assess experimentally the saturation length from a comparison with model predictions.

2 EXPERIMENTS

In this section, we present our experimental results. We first describe our experimental set-up and then present the main morphological and kinematic features of steady dunes according to their size and flow strength.

2.1 Set-up

The subaqueous dune experiments are conducted in a closed channel inspired from that of Groh et al. 2008 (see Figure 1). The channel is composed by two 900 mm long rectilinear sections closed by semi-circular junctions. The cross-section of the channel is a 90mm×90mm except for the forefront rectilinear section where the width is reduced to 6 mm. The dunes are formed and observed within the narrow section. This allows to consider that the dunes are two-dimensional.

The flow is set by a propeller which is installed in the large section of the channel. We thus have a flow driven by pressure gradient with no free surface. In the configuration we investigated so far, the flow in the narrow section is fully turbulent. We checked by particle image velocimetry that the flow close to the bottom wall obeys a classical logarithmic profile:

$$U(z) = \frac{u^*}{\kappa} \ln\left(\frac{z}{z_0}\right) \quad (1)$$

where $\kappa \approx 0.41$ is the Von Kármán constant, u_0* is the wall friction velocity and z_0 the hydrodynamic roughness.

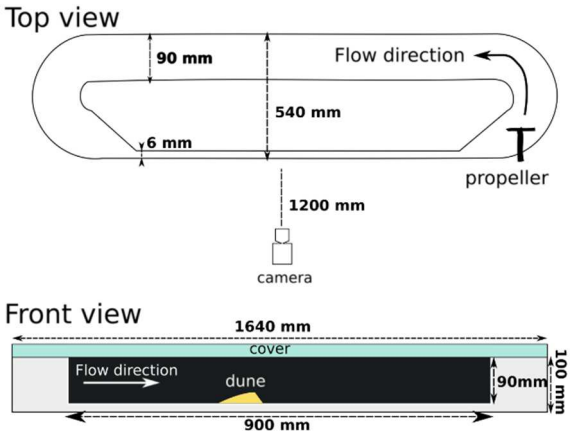

Figure 1. Scheme of the flume (top and front view).

Thanks to the determination of the flow profile throughout the whole height, it is possible to find a relationship between the friction velocity u_0* and the depth-averaged velocity $\langle U_0 \rangle$. We find $u_0^* \approx 0.064 \langle U_0 \rangle$. The strength of the flow is controlled by the propeller rotation rate.

The granular material used for the dunes are spherical glass beads with a median diameter d = 0.4 mm and a bulk density ρ_p = 2500 kg/ m^3. These particles are entrained by the flow when the latter exceeds a mean velocity $\langle U_{0c} \rangle \approx$ 0.336 m/s, which corresponds to a critical friction velocity $u_c^* \approx 0.0215$ and a critical Shields number $S_c \approx 0.08$, as summarized in Table 1.

Table 1: Critical values for incipient motion

d (mm)	$\langle U_{0c} \rangle$ (m/s)	u_c^* (m/s)	S_c
0.4	0.336	0.021	0.08

An experimental run consists of the following steps. First, the channel is filled with water before introducing a given mass m_0 of glass beads in the narrow part of the channel. The initial pile has a triangular shape and its surface area A_0 is proportional to its mass m_0: $A_0 \approx (113 \text{mm}^2/\text{g}) \times m_0$. Once the pile is formed, the propeller is turned on to the desired rotation rate and the dune morphodynamics is documented via a Nikon D610 Reflex camera with a resolution of 6016 × 4016 pixels. The spatial resolution is 0.12 mm per pixel and the images are captured with a rate of one image per second.

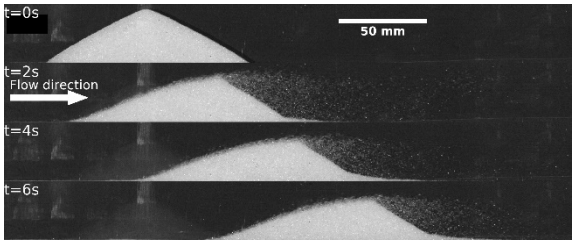

Figure 2. Successive snapshots illustrating the morphodynamics of a dune starting from an initial triangle shape. Experimental parameters: m_0 = 15 g, $\langle U_0 \rangle \approx$ 0.43 m/s.

From the captured images (see Fig. 2), we can extract the dune profile by a classic method thanks to the contrast between the dune and the dark background. We can thus easily document the temporal evolution of the height H, length L, area A and position of the dune. On the example illustrated in Fig. 2, we observe that the height, length and area of the dune reach after a very short transient (less than 1s) stationary values. Similarly, the migration speed of the dune is quickly stabilized..

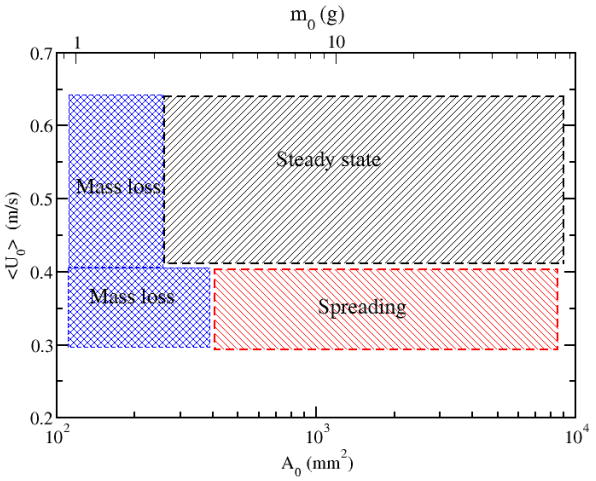

Figure 3. Regime map in the diagram ($\langle U0 \rangle$, A_0): Three scenarios are observed including spreading, steady state and mass loss.

We investigate a range of dune mass from 2 to 50g and a range of mean flow velocity from 0.3 to 0.55m/s (i.e., $0.8 < S_0/S_c < 3.5$). We identify three different regimes: (i) a spreading regime, (ii) a steady-state regime and (iii) a regime with mass loss. The observed behaviors are reported in the phase diagram $\langle U_0 \rangle$ versus A_0 (see Fig. 3). For flow velocities ranging from 0.4m/s to

0.65m/s (i.e., $1.5<S_0/S_c<3.5$) and dune mass $m_0>2g$, the dune reaches a steady-state where its shape becomes stationary and its migration speed constant. In the following, we will document essentially the steady-state regime and disregard the other regimes.

2.2 Height, length and aspect ratio of the steady dune

The variation of the height H, length L and aspect ratio R=H/L of steady-state dunes exhibit two different behaviors according to the dune size (see Fig. 4). For small dunes (i.e., $A_0<1000$ mm^2), H, L and R can be locally described by scaling laws as a function of the dune area A_0:

$$\frac{H}{d} = K_H \left(\frac{A_0}{d^2}\right)^{\alpha} \qquad (2)$$

$$\frac{L}{d} = K_L \left(\frac{A_0}{d^2}\right)^{\beta} \qquad (3)$$

$$R = K_R \left(\frac{A_0}{d^2}\right)^{\gamma} \qquad (4)$$

with $\gamma=\beta-\alpha$. The scaling exponents α and β exhibit a weak dependence with the dune size: α decreases progressively from 0.85 down to 0.5 with increasing dune size while and β increases from 0.35 up to 0.5. In contrast, for large dunes (i.e., A_0 >1000 mm^2), the scaling exponents do not show any variation and we get: $\alpha = \beta = 0.5$ and $\gamma=0$. This regime corresponds to the asymptotically large dune regime where the aspect ratio is invariant. The coefficients K_H, K_L and K_R appearing in the scaling laws are found to increase slightly with increasing flow strength.

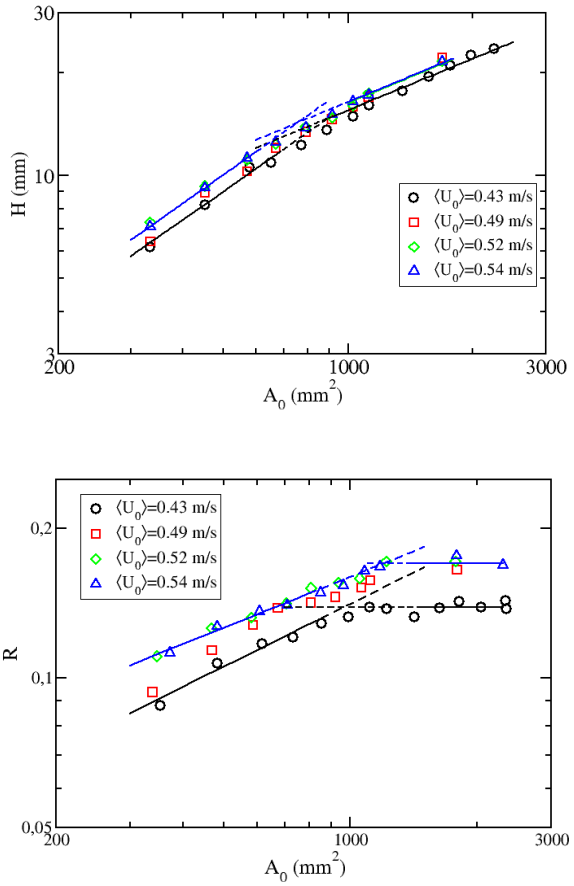

Figure 4: Height H and aspect ratio R of the steady dune as a function of the dune area for different flow strengths (< U_0 >=0.43,0.49,0.52 and 0.54 m/s).

2.3 Dune shape

Fig. 5a presents the profiles of steady-state dune at a given flow strength (<U_0>≈ 0.43 m/s and S_0/S_c= 1.6) for various dune mass ranging from 2g to 20g. Except for the smallest dune (m_0=2g), the dune profiles are asymmetric with a well-developed slip face in the downstream side. The local slopes associated to the dune profiles are shown in Fig. 5b. We observe an increase of the slope with increasing dune size both on upstream and downstream faces. The maximum slope of the upstream and downstream faces increases with increasing dune size in the small dune regime and saturates in the large dune regime to a value of 17° and 35°, respectively. These asymptotic values increase with increasing flow strength. For the largest flow strength, we investigate (S_0/S_c=2.4), the maximum slope on the upstream and downstream face are 20° and

40°, respectively. The strength of the flow has thus a non-negligible effect of the angle of the downstream slip face.

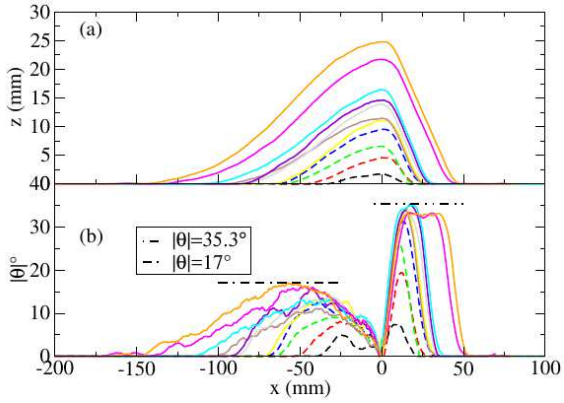

Figure 5: Profiles of steady-state dunes for a given flow strength $\langle U_0 \rangle \approx$ 0.43m/s (S_0/S_c= 1.6): From the bottom to the top, the mass m_0 are respectively 2, 3, 4, 5, 6, 7, 8, 9, 10, 16 and 20g. (b) Local slopes of the steady-state profiles.

Fig. 6 shows the dune profiles rescaled in both direction by their length L. This figure illustrates the gradual transition to the large dune regime which is scale invariant.

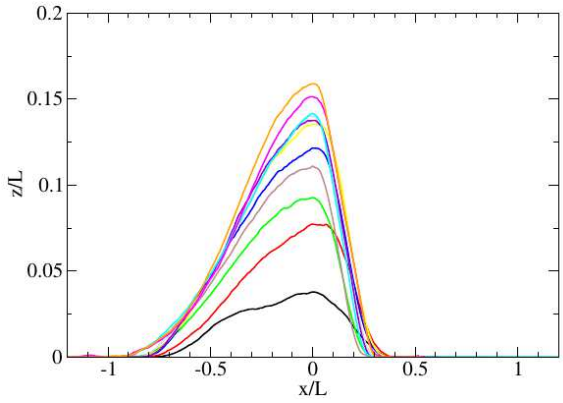

Figure 6: profiles of steady-state dune rescaled by their length L in both directions. From the bottom to the top, the mass m_0 are respectively 2, 3, 4, 5, 6, 7, 8, 9, 10, 16 and 20g. Experimental parameters: $\langle U_0 \rangle \approx$ 0.43 m/s.

2.4 Migration speed

The migration speed of steady-state dunes as a function of the dune size is shown in Fig. 7a for different flow strengths. It decreases with increasing dune size and increases with increasing flow strength as expected. We observe a single scaling regime for small and large dunes:

$$\frac{V}{[(s-1)gd]^{\frac{1}{2}}} = K_v \left(\frac{A_0}{d^2}\right)^{-\frac{1}{2}} \qquad (5)$$

where $s=\rho_p/\rho_{fluid}$. The scaling exponent is −1/2, which is in agreement with the observations by Groh et al. (2008, 2009) for subaqueous dunes. This result is also consistent with the prediction of the dune model for large dune regime.

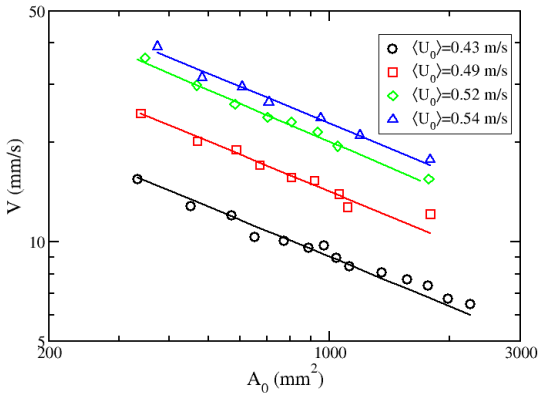

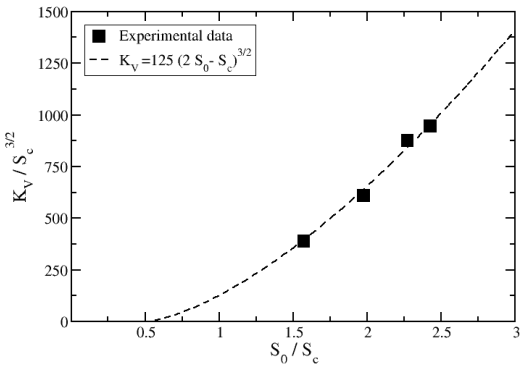

Figure 7: (a) Migration speed of the steady dune as a function of the dune area for different flow strengths. (b) Coefficient K_v (see eq. 5) as a function of the Shields number S_0.

The coefficient K_V which encodes the influence of the flow strength is shown in Fig. 7b and is found to obey the following power law:

$$K_v = K_{v0}(2S_0 - S_c)^{\frac{3}{2}} \qquad (6)$$

K_V is linked to the mass flux Q_{crest} at the top of the dune. In the large dune regime, the latter can be easily calculated:

$$Q_{crest} = V \times H = K_v \times K_H = 65\, Q_0 (2S_0 - S_c)^{\frac{3}{2}} \qquad (7)$$

We recall that the law of Meyer-Peter and Müller for the saturated flux is given by $Q_{MPM}=8Q_0\ (S_0 - S_c\ )^{3/2}$. We thus find a law similar to that of Meyer-Peter and Müller with a 3/2 exponent. The factor 2 which multiplies the Shields number can be interpreted as the shear stress increase factor at the top of the dune. This value is in agreement with the measurements by Charru & Franklin (2012). We can note that the proportionally factor in Eq. (7) is much higher than that in the law of Meyer-Peter and Müller flow (65 against 8).

3 THEORETICAL MODELING

We used the theoretical continuum model developed by Kroy et al.(2002) for aeolian sand dunes and adapted it to the situation of subaqueous dunes. The model is explained in details in S. Kiki (2019). We recall here briefly the main assumptions of the model.

3.1 Model equation

The equation describing the temporal evolution of a sand heap on a flat and horizontal substrate subject to the shearing of a turbulent flow is inferred from mass conservation and reads:

$$\frac{\partial h(x,t)}{\partial t} = -\frac{1}{\rho_b}\frac{\partial Q(x,t)}{\partial x} \qquad (8)$$

where h(x, t) and Q(x,t) are the local height and mass flux, respectively, at position x and time t. ρ_b is the bulk density of the dune. We assume that the mass flux Q_{sat} at saturation (or equilibrium) is given by the empirical formulation of Meyer-Peter and Müller (1948) :

$$Q_{sat} = Q_{MPM} = 8Q_0(S(x,t) - S_c)^{\frac{3}{2}} \quad (9)$$

For unsteady or non-uniform conditions, the particle flux is not necessarily equal to the saturated flux because the relaxation towards the saturated value is not instantaneous. For non-uniform flow conditions, the case we are interested in, the relaxation process can be simply modeled by (Andreotti et al., 2002b, 2010, Valance et al., 2005a,b):

$$\frac{\partial Q(x,t)}{\partial x} = \frac{Q(x,t) - Q_{sat}(x,t)}{l_{sat}} \qquad (10)$$

where l_{sat} is the saturation length and sets the characteristic length scale for the relaxation process. To compute the saturated flux at any position along the dune profile, it is necessary to assess the local fluid shear stress τ at the bed. To do this, we employ the approximated formulation of Jackson et al. (1975) which reads:

$$\frac{\tau(x,t)}{\tau_0} = 1 + A\int_{-\infty}^{+\infty} \frac{dx'}{\pi x'}\frac{\partial h}{\partial x}(x - x') + B\,\frac{\partial h}{\partial x}(x) \qquad (11)$$

where τ_0 is the unperturbed fluid shear stress upstream the dune (note that $\tau/\tau_0=S/S_0$). We define the corresponding Shields number $S_0=\tau_0/(\rho_p-\rho_{fluid}\ )gd$, which characterizes the basal shear stress in the absence of dune. Eq. (11) is valid in the limit of small relief, that is $H/L << 1$. $\mathcal{A}$ and $\mathcal{B}$ are parameters which depend logarithmically on the dune size. More specifically, they depend on the relative roughness of the dune z_0/L where z_0 is the hydrodynamical roughness of the sand bed surface. If the range of variation of the ratio z_0/L is limited to one decade, $\mathcal{A}$ and $\mathcal{B}$ can be fairly considered as constant parameters. For our purpose, we will use two sets of parameters ($\mathcal{A}$, $\mathcal{B}$): (4.2, 2) and (4.2, 3.8) (see Kiki 2019). The first set is obtained from a simple turbulent model based on the Prandtl turbulent length and the second one from a more elaborated turbulent model (Frederick & Hanratty 1988). For calculating both sets of values, we took $L/z_0 \sim 10^4$ which corresponds to our experimental conditions. Note that for terrestrial aeolian dune, $\mathcal{A}$ and $\mathcal{B}$ are slightly different: $\mathcal{A}=4$ and $\mathcal{B}=1$.

Eqs. (8-11) form a close set of equations for the dune morphodynamics. This description is very similar to that developed by Kroy et al (2002). However, we should emphasize that we disregard two mechanisms that are included in the original model: i) the phenomenon of flow separation and ii) the avalanche process at the lee side. These mechanisms have been recognized to be important for a detailed description of the equilibrium dune shape. However, we have shown (Kiki, 2019) that those are in fact of secondary importance for predicting the height, length and migration speed of equilibrium dune shape.

3.2 Model predictions

The model reveals the existence of three distinct regimes: an asymptotical small and large dune regime, and a cross-over regime. The asymptotical small dune regime is characterized by a linear increase of the equilibrium height and aspect ratio as a function of the dune area:

$$H = \frac{2A_0}{\lambda_c} \; and \; R = \frac{2A_0}{\lambda_c^2} \quad (12)$$

where λ_c is the cut-off wavelength deduced from the linear stability analysis of a flat bed ($\lambda_c = (2\pi\mathcal{A}/\mathcal{B})l_{sat}$). The small regime is observed for $A_0 < 3\ l_{sat}^2$. In contrast, in the asymptotical large dune regime ($A_0 > 100\ l_{sat}^2$), the height varies as the square root of the dune area whereas the aspect ratio is invariant:

$$H = K_H^{\infty} A_0^{\frac{1}{2}} \; and \; R = \frac{K_H^{\infty 2}}{2} \quad (13)$$

The proportionality coefficient K_H^{∞} depends on $\mathcal{A}$, $\mathcal{B}$ and S_0/S_c but not on l_{sat}. The transition or cross-over regime occurs for intermediate dune sizes ($3\ l_{sat}^2 < A_0 < 100\ l_{sat}^2$) as shown in Fig. 9.

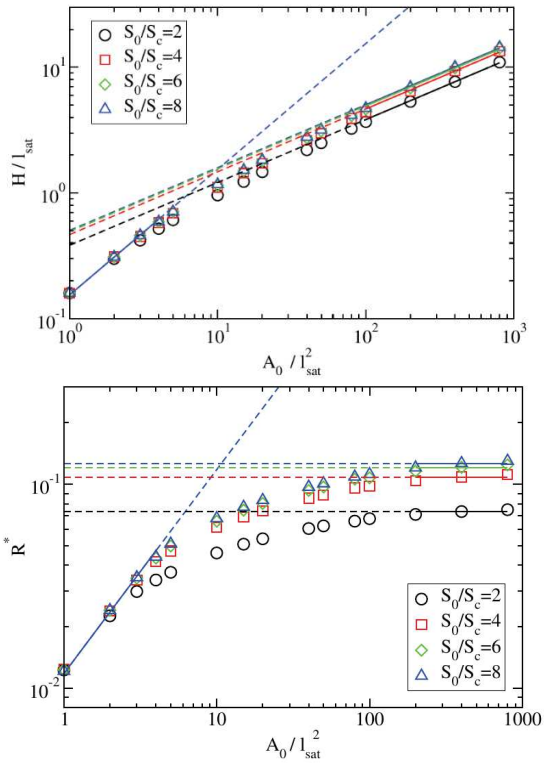

Figure 8: Height (a) and aspect ratio (b) of steady dune as a function of the dune size for different flow strengths. Model parameters: $\mathcal{A}$=4.2 and $\mathcal{B}$=2.

3.3 Discussion

The large dune regime observed in the experiments do correspond to the asymptotically large dune regime of the model. In contrast, the small dune regime identified in the experiments do not match with the asymptotically small dune regime of the model but corresponds to the crossover regime between the two asymptotical regimes. A detailed comparison of the model with the experiments in the asymptotically large dune indicate that the relevant values for the model parameters are: $\mathcal{A}$=4.2 and $\mathcal{B}$=3.8 (i.e., those corresponding from the model of Frederick & Hanratty 1988). Comparison made in the cross-over regime allows to determine the saturation length l_{sat}. The procedure is explained in details in S. Kiki 2018.

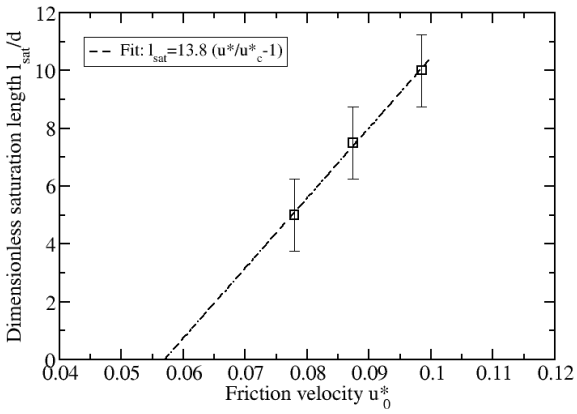

Figure 9: saturation length l_{sat} as a function u_0* inferred from comparison between experiments and model predictions.

One way to do this is to determine the value of l_{sat} which gives the best agreement between the experimental equilibrium heights and those predicted by the model for a given ratio S_0/S_c. The same procedure can be carried out with the length of the dune or aspect ratio. The outcome of these adjustments suggests that the saturation length increases with the strength of the flow. We go from 2mm for S_0/S_c=1.6 to 4 mm for S_0/S_c=2.5. This evolution seems to follow a linear law with the friction velocity u_0*.

These results also indicate a proportionality between l_{sat} and the friction velocity u_0*:

$$\frac{l_{sat}}{d} = \frac{53}{\left((s-1)gd\right)^{\frac{1}{2}}}(u_0* - u_c*) \quad (14)$$

which is compatible with a saturation length governed by a deposition length as proposed by Lajeunesse et al. (2010).

4 CONCLUSIONS

We have investigated steady-state subaqueous sand dune experimentally and theoretically. The proposed model predicts the existence of two asymptotic regimes for small and large dunes, as suggested by previous models and a cross-over regime for intermediate dune sizes. In the small dune regime, the dune length is set by the saturation length and the dune height scales linearly with the dune mass. In the large dune regime, the dune profile is scale invariant: both height and length of the dune increases as the square root of the dune mass. Experiments confirm the existence of different regimes. We indeed identified clearly the cross-over regime and the large dune regime where the dune profile is scaling invariant. The cross-over regime teaches us about the scale of the saturation length. A comparison between experimental and theoretical dune profiles in this regime allowed us to assess the experimental saturation length. Our results suggest that the saturation length is governed by the deposition length rather the drag length.

5 REFERENCES

Andreotti, B., and Claudin, P. (2002). The European Physical Journal B 28, 341.

Andreotti, B., Claudin, P., and Douady, S. (2002). The European Physical Journal B 28, 321.

Bagnold, R. A. (1941). The physics of blown sand and desert dunes. London: Methuen.

Charru, F. (2006). Selection of the ripple length on a granular bed sheared by a liquid flow. Physics of fluids 18, 121508.

Courrech Dupont, S. (2015). Dune morphodynamics. Comptes Rendus Physique 16, 118.

Groh, C., Wierschem, A., Aksel, N., Rehberg, I., and Kruelle, A.C. (2008). Barchan dunes in two dimensions: Experimental tests for minimal models. Phys. Rev. E 78, 021304.

Groh, C., Rehberg, I., and Kruelle, A.C. (2009). How attractive is a barchan dune. New J. Phys. **11** 023014.

Jackson, P. S, and Hunt, J. C. R (1975). Turbulent Wind Flow over a Low Hill. Quart. J. R. Met. Soc. 101, 929.

Kiki, S, 2018. Caractérisation de la morphologie des dunes aquatiques dans des écoulements unidirectionnels et alternatifs. PhD Thesis. University of Rennes.

Kroy, K., Sauermann, G., and H. J. Herrmann, H.J. (2002). Minimal model for aeolian sand dunes. Phys. Rev. E 66, 031302.

Lajeunesse, E., Malverti, L. and Charru, F. (2010). Bed load transport in turbulent flow at the grain scale: Experiments and modeling . Journal of Geophysical Research: Earth Surface 115, 2003–2012.

Meyer-Peter, E. and Müller, R. (1948). Formula for the bedload transport. Proceedings of the 3rd Meeting of the International Association of Hydraulic Research.

Parteli, E.J., Durán, O., Bourke, M. C., Tsoar H., Pöschel, T. and Herrmann, H. (2014). Origins of barchan dune asymmetry: Insights from numerical simulations. Aeolian Research 12, 121.

Sauermann, G., Kroy, K. and Herrmann, H.J (2001). Continuum saltation model for sand dunes. Phys. Rev. E 64, 031305.

Valance, A. and Langlois, V. (2005). Ripple formation over a sand bed submitted to a laminar shear flow. Eur. Phys. J. B 43, 283–294.

Valance, A. (2005). Ripple formation over a sand bed submitted to a turbulent shear flow. Eur. Phys. J. B 45, 433–442.

On elevation and migration: a model for sandbank dynamics in sediment-scarce seas

T.J. van Veelen *University of Twente, Enschede, The Netherlands – t.j.vanveelen@utwente.nl*
P.C. Roos *University of Twente, Enschede, The Netherlands – p.c.roos@utwente.nl*
S.J.M.H. Hulscher *University of Twente, Enschede, The Netherlands – s.j.m.h.hulscher@utwente.nl*

ABSTRACT: Tidal sandbanks are large-scale dynamic bedforms observed in shallow seas with varying sediment supply. Their dynamics have often been studied under the assumption that sediment supply is unrestricted. However, this is invalid for banks in sediment-scarce seas, like the Flemish and Norfolk banks in the North Sea. Here, we show using a process-based idealized model how sediment scarcity affects the cross-sectional shape and migration speed. We find that sediment scarcity reduces the height of sandbanks and changes bank asymmetry when a residual current is present. Furthermore, the migration rate of banks increases. Our findings are especially relevant in the context of continued sand extraction in sediment-scarce seas, and help understand sandwave dynamics around sandbanks.

1 INTRODUCTION

Tidal sandbanks are large-scale marine bedforms in shallow seas that migrate under asymmetric tidal forcing. They are frequently observed in conjunction with sandwaves. Due to their large size of ten of metres in height, tens of kilometres in length and kilometres in width (Dyer & Huntley, 1999, de Swart & Yuan, 2018), their dynamics determine the environmental conditions (e.g. water depth and flow characteristics) relevant for sand waves. They are also an attractive location for sand extraction and an important ecological habitat for marine species (Wyns et al., 2021).

Observations have identified that sandbanks are regularly located in sediment-scarce seas. For examples, the Flemish banks lie on top of a layer of hard clay, which is exposed in the troughs (Hademenos et al., 2019). Gravel has also been observed in the troughs between the Norfolk Banks (Caston, 1972). Sand extraction for coastal nourishments and industry will further reduce the sediment budget. Therefore, it is important to understand how tidal sandbank dynamics depend on the available sediment budget.

So far, sandbanks have often been studied under the assumption of infinite sediment supply. Under these conditions, process-based models have explained the initial growth of sandbanks as a free instability of the flat bed (Huthnance 1982a, Hulscher et al., 1993), and have shown that sandbanks may evolve towards static or dynamic equilibria (Roos et al., 2004, Yuan et al, 2017). Under asymmetrical forcing (e.g. residual current or M4-tide) sandbanks attain asymmetrical cross-sectional shapes and exhibit migration in the order of meters per year. However, these results come from models ignoring conditions of sediment scarcity.

Huthnance (1982ab) did consider the effects of sediment scarcity in his models of equilibrium cross-sections (1982a) and sandbank evolution (1982b). He concluded that sediment scarcity led to lower and narrower sandbanks. He also found that sediment scarcity was important for attaining equilibrium profiles, together with the presence of wind waves. However, his results were based on simplified hydro-dynamic conditions (no Coriolis effects and block flow). It is unclear whether his results hold under more complex tidal conditions.

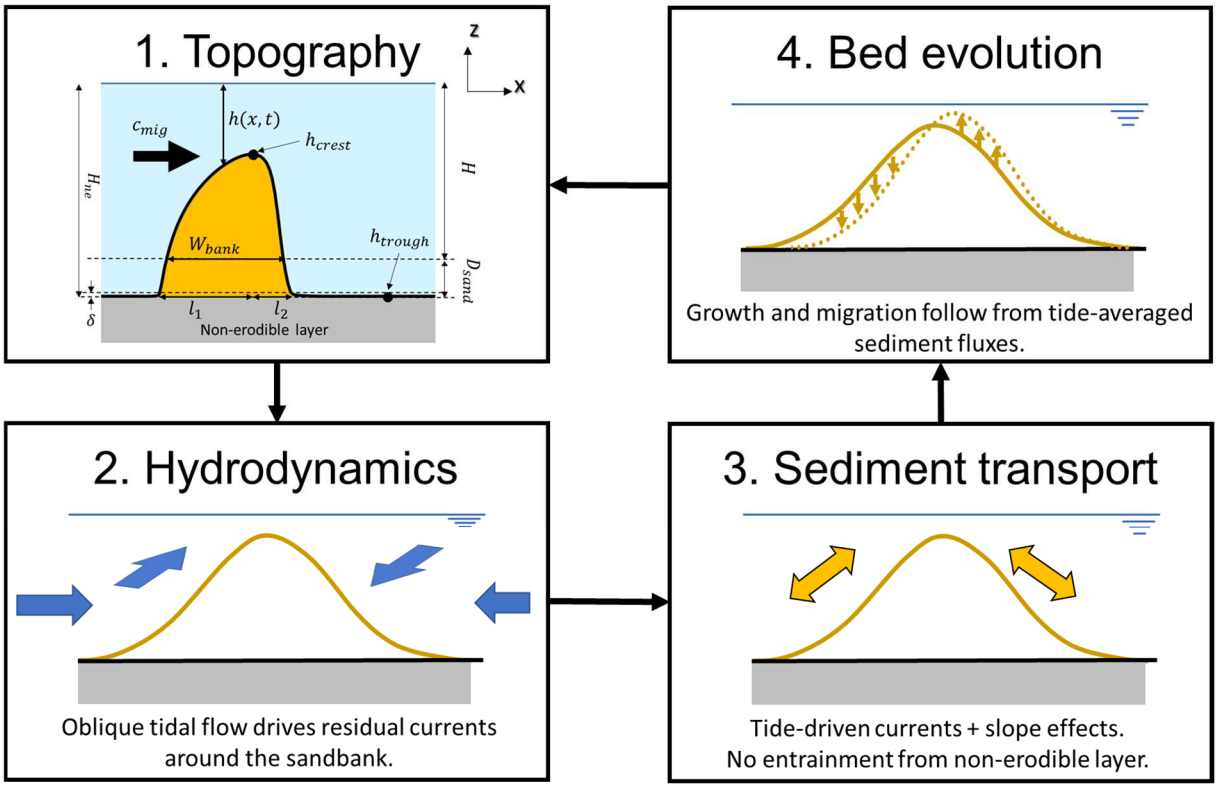

Figure 1. Schematisation of the four stages of the morphological loop in our process-based model. Stage 1 is the topography. The corresponding hydrodynamic solution given a tidal forcing is computed in stage 2. This leads to a solution for sediment transport in stage 3. Importantly, no sediment can be entrained from the non-erodible layer. Stage 4 solves the bed evolution based on the divergence of tide-averaged sediment transport. The evolved bed then serves as the new topography for the next iteration of the loop.

In order to overcome our limited understanding of sandbank dynamics under sediment scarcity, we present a process-based idealized model in which we restrict sediment availability via a non-erodible layer. We apply this model to study the cross-sectional shape and migration speed in sediment-scarce seas.

2 METHODS

Following previous models (Roos et al., 2004, Yuan et al, 2017, van Veelen et al, 2018), we keep our morphodynamic model as simple as possible, while still including the essential physics to understand tide-topography interactions and the resulting sediment transport. Our model includes tidal flow (including a residual current), and accounts for Coriolis effects, bottom friction, suspended sediment transport. We only consider the dynamics over the cross-section of the bank, as we focus on cross-sectional shapes in this study. Finally, all dynamics are depth-averaged, as bank evolution is driven by horizontal circulation cells (Huthnance, 1982a).

Sediment scarcity is included via a uniform non-erodible layer which limits the thickness of the sand layer (D_{sand}). Sand cannot be picked up where the non-erodible layer is exposed, but the non-erodible layer does not affect sediment transport when it is covered by sand.

We simulate the evolution of the topography $z = -h(x,t)$ over time based on the morphological loop (Fig. 1). The hydrodynamics are solved using the shallow water equations. Then, we compute sediment transport using the sediment advection-diffusion equation, given by

$$\frac{\partial c}{\partial t} + \frac{\partial (cu)}{\partial x} = \gamma (c_e - c). \quad (1)$$

$c(x,t)$ is the depth-integrated sediment concentration. u is the flow velocity in cross-

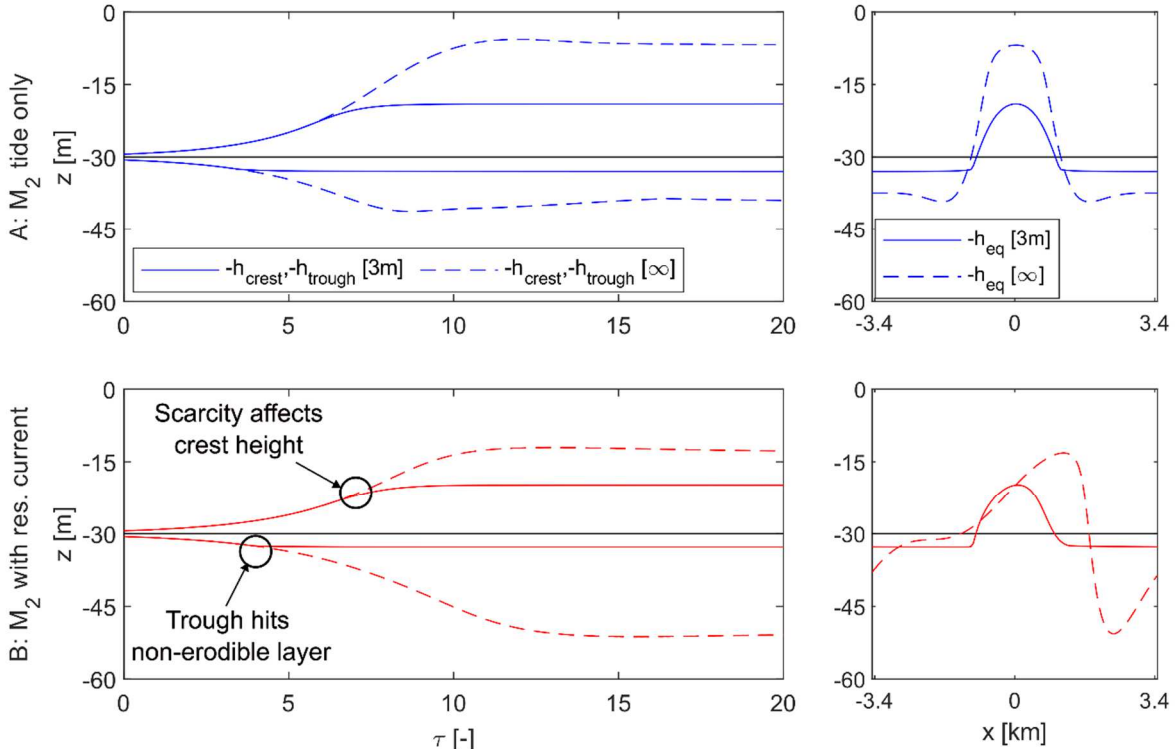

Figure 2. Left: Evolution of crest height and trough depth over morphological time τ with sand layer thickness of 3m and ∞ (denoted between square brackets). Every τ-unit is approximately 280 years. Some conditions ran for longer than $\tau = 20$ to reach equilibrium. Right: Equilibrium cross-sectional profiles for D_{sand} = 3m and D_{sand} = ∞ under conditions A (top) and B (bottom). All plots show mean water depth $z = -H$ as a solid black line.

bank direction, γ is a deposition coefficient, and

$$c_e = \alpha_s \mu_s (u^2 + v^2) \quad (2)$$

is the entrainment concentration with sediment transport coefficient α_s, sediment limiter μ_s, and velocities in cross-bank and along-bank directions u and v. $\mu_s(h)$ is 0 when the non-erodible layer is exposed ($h = H_{ne}$), ranges between 0 and 1 in the buffer layer ($H_{ne} - \delta \leq h \leq H_{ne}$), and is 1 when sufficient sand is available. Finally, the bed evolution is obtained via Exner's equation.

The solution method is pseudo-spectral in space and time. The initial topography is given by a sinusoidal bank with amplitude $0.02H$ and with a wavelength and orientation in accordance with the fastest growing mode from linear theory (e.g., Hulscher et al., 1993). The simulation continues until a morphodynamic equilibrium is reached.

3 RESULTS

3.1 Overview of simulations

We run our model for two types of conditions. Condition A is forced by an M_2-tidal flow with an amplitude of 0.6 m/s. Condition B is characterized by an M_2-tidal flow amplitude of 0.57 m/s and a residual current of 0.03 m/s. Furthermore, both conditions have a mean water depth of H = 30 m, and are located at a latitude of 52°N. Each condition is repeated with a sand layer thickness varying between 1.5 m and infinity (i.e., non-erodible layer not present).

3.2 Evolution towards equilibrium

The evolution towards a morphodynamic equilibrium for both conditions with D_{sand} = 3 m and ∞ is shown in Figure 2. Sediment scarcity affects bank evolution from the moment that the non-erodible layer is exposed in the trough. The trough cannot

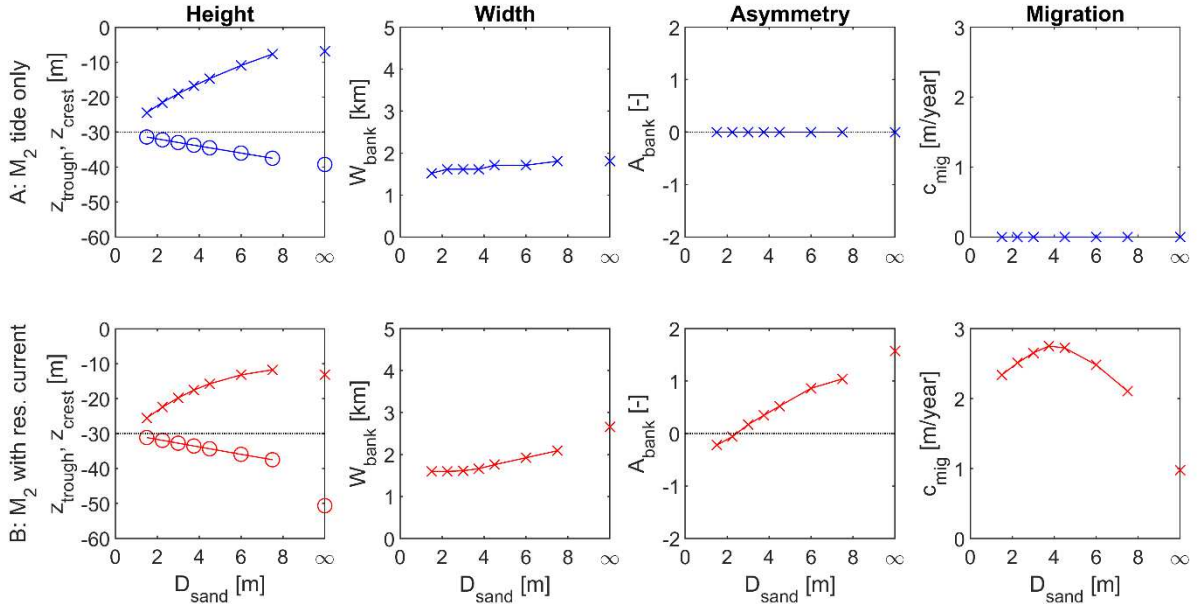

Figure 3. Influence of sand layer thickness D_{sand} on various properties of the equilibrium bank shape: crest and trough elevation z_{crest} and z_{trough}, bank width W_{bank}, bank asymmetry A_{bank}, migration speed c_{mig}.

erode beyond the non-erodible layer. As shown in Fig.2, the crest height is not affected until much later in the simulation. Importantly, the equilibrium crest height and trough depth are both of lower amplitude when sediment is scarce.

3.3 Cross-sectional equilibrium shape

The relation between sand scarcity and shape parameters z_{crest} and z_{trough}, width W_{bank}, and asymmetry $A_{bank} = \log(l_1/l_2)$ (see Fig. 1) is presented in Figure 3. The height is much more sensitive to scarcity than width. Our results indicate that equilibrium profiles become lower rather than narrower when sediment supply reduces.

When a residual current is present (conditions B), the asymmetry is affected by the scarcity. The lee side flattens with a thinner sand layer, as also shown by the equilibrium cross-sections in Figure 2 (bottom right). When sand is very scarce (here $D_{sand} < 2.5$m), the asymmetry may even flip. This means that the stoss side is steeper than the lee side rather than the other way around as is observed when $D_{sand} = \infty$.

3.4 Migration

Our results show that sandbanks migrate faster when a non-erodible layer is present (Fig. 3d). All our runs with a non-erodible layer exhibit higher migration rates than when sediment supply is unlimited. There is a maximum: highest migration rates are obtained with $D_{sand} = 3.75$ m under the conditions studied here. The migration rate reduces when the sand layer is either thinner or thicker. Note that migration can only occur when the tidal flow is asymmetric (i.e. condition B).

4 CONCLUSIONS

Tidal sandbanks are large-scale bedforms, whose dynamics affect the flow characteristics for sandwaves and other bedforms. Here, we have included a non-erodible layer in a process-based idealised model in order to study how sediment scarcity affects the cross-sectional shape and migration speed.

Our results show that the equilibrium values of the crest height and trough depth reduce when sediment becomes scarcer, whereas the width of the banks is less sensitive to scarcity. During the development process, the trough depth is immediately affected when the non-erodible layer is exposed, whereas the crest height will not be affected by scarcity until much later in our simulation.

The migration rate increases under sediment-scarce conditions. Our results suggest that there exists a sand layer thickness for which the migration rate reaches a maximum. It is recommended that this is further explored in future research.

5 ACKNOWLEDGEMENT

This work was carried out on the Dutch national e-infrastructure with the support of SURF Cooperative.

6 REFERENCES

Caston, V.N.D., 1972. Linear sand banks in the Southern North Sea. Sedimentology 18, 63-78.

De Swart, H.E., Yuan, B., 2019. Dynamics of offshore tidal sand ridges, a review. Env. Fluid Mech. 19(5), 1047-1071.

Dyer, K.R., Huntley, D.A., 1999. The origin, classification and modelling of sand banks and ridges. Cont. Shelf Res. 19(10), 1285-1330.

Hademenos, V., Stafleu, J., Missiaen, T., Kint, L., Van Lancker, V.R.M., 2019. 3D subsurface characterisation of the Belgian Continental Shelf: A new voxel modelling approach. Netherl. J. of Geosci. 98, E1.

Hulscher, S.J.M.H., de Swart, H.E., de Vriend, H.J., 1993. The generation of offshore tidal sand banks and sand waves. Cont. Shelf Res. 13, 1183–1204.

Huthnance, J.M., 1982a. On one mechanism forming linear sand banks. Est. Coast. Shelf Sci. 14, 79-99.

Huthnance, J.M., 1982b. On the formation of sand banks of finite extent. Est. Coast. Shelf Sci. 15, 277-299.

Roos, P.C., Hulscher, S.J.M.H., Knaapen, M.A.F., Van Damme, R.M.J., 2004. The cross-sectional shape of tidal sandbanks: Modeling and observations. JGR Earth Surf. 109, F02003.

Van Veelen, T.J., Roos, P.C., Hulscher, S.J.M.H., 2018. Process-based modelling of bank-breaking mechanisms of tidal sandbanks. Cont. Shelf Res. 167, 139-152.

Wyns, L., Roche, M., Barette, F., Van Lancker, V.R.M., Degrendele, K., Hostens, K., De Backer, A., 2021. Near-field changes in the seabed and associated macrobenthic communities due to marine aggregate extraction on tidal sandbanks: A spatially explicit bio-physical approach considering geological context and extraction regimes. Cont. Shelf Res. 229, 104546.

Yuan, B., de Swart, H.E., Panadès, C., 2017. Modeling the finite-height behavior of off-shore tidal sand ridges, a sensitivity study. Cont. Shelf Res. 137, 72-83.

Sedimentology of a large field of lunate shaped bedforms in the Fehmarn Belt, Baltic Sea

C. Winter *Institute of Geosciences, CAU Kiel, Germany – christian.winter@ifg.uni-kiel.de*
G. Díaz-Mendoza *Institute of Geosciences, CAU Kiel, Germany – giuliana.diaz@ifg.uni-kiel.de*
M. Becker *Institute of Geosciences, CAU Kiel, Germany – marius.becker@ifg.uni-kiel.de*
K. Krämer *Institute of Geosciences, CAU Kiel, Germany – knut.kraemer@ifg.uni-kiel.de*

ABSTRACT: We discuss formation mechanisms of bedforms in the Fehmarn Belt, Western Baltic Sea based on their morphology and sedimentology. Characterised by the isolated occurrence and their lunate or crescentic shape at some instances the morphology resembles barchanoid dunes. The central part is of height O(1m) and often two tails of lengths in O (100 m) predominantly open towards the South-East, suggesting an active migration towards this direction. New data from a multibeam echo sounder survey, sediment cores and subbottom profiles reveal morphodynamics, sedimentology, and the internal bedding and challenge previous assumptions on the formation and dynamics of the bedforms.

1 INTRODUCTION

In the microtidal Western Baltic Sea, the occurrence of different bedform fields has been observed in earlier studies. Besides a prominent compound bedform field in medium to coarse sands (Feldens et al. 2014, Krämer et al., this volume), other assemblages of large, flow transverse bedforms occur in water depths exceeding 20 m (Fig. 1).

Figure 1. Location of the investigation area in the Western Baltic Sea. The white line surrounds the lunate bedform field. Indicated in red are the positions of short sediment cores. The scale bar is 30 km.

These low-relief bedforms have been reported in a region of about 217 km² in the central Fehmarn Belt. Their height is 0.5–1.0 m and about 50 m wide. The distance between the individual features is in the order of a few hundred meters. The crescentic planform geometry resembles barchanoid dunes, often with two tails of lengths in O(100 m) opening towards the E or SE.

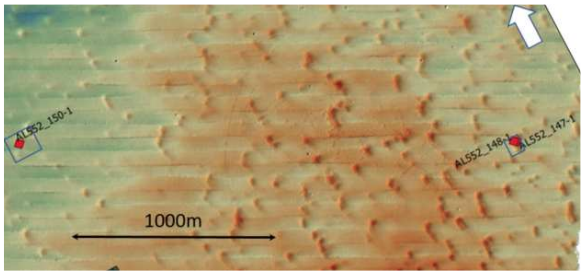

Figure 2. MBES bathymetry subset of the lunate bedform field in between different core locations NE of Fehmarn island (ref Fig. 1)

Jensen et al. (2003) termed these features *isolated sand-silt waves* because of their solitary occurrence in muddy to fine sediments. Based on a limited set of observations, they were first described as “NE-SW striking ridges of considerable length” without a clear asymmetry or preferred orientation. The authors noted that the features occur on various substrates ranging from late glacial clay in the western part of the Fehmarn Belt to Holocene marine mud in the eastern part of the strait.

The whole extension of the so called *lunate bedform field* was revealed by a large scale multibeam echo sounder (MBES)

mapping in the framework of the environmental impact assessment for the large Fehmarn Belt tunnel construction (FEHY, 2013). In water depths of about 25 m, many similar bedforms of characteristic shape were identified as regularly spaced with distances between individual features of a few hundred meters, on an area of 217 km² (Fig. 1). The report assesses the bed roughness and speculates on a high activity of the bedforms i.e., migrations in the order of several meters per annum towards the NE or SW, however, based on a rather crude assessment of local sediment transport potential.

The lunate bedforms are also briefly mentioned in a habitat mapping report by Schwarzer & Unverricht (2020). They observed 350 of these features by side-scan-sonar mappings and subbottom profiling, described their heights of about one meter, a width of 50 m and a mean distance of 145 m between individual forms. The authors also mention internal cross-beddings that suggest a migration towards the NW during their formation. Underwater videos showed a high abundance of shells and living bivalves on the bedforms – in their study, interpreted as an indicator of recent low dynamics.

Although the existence, distribution, and role as roughness elements on the local hydrodynamics has been described before, the discussion on the genesis, morphology, and dynamics of these bedforms are still not conclusive.

The morphology and sedimentology of these bedforms is interesting, as they resemble a unique and characteristic morphological feature of the geodiversity of the Fehmarn Belt: Amongst active bedform fields (Krämer et al., this volume), adjacent remnants of paleo fluvial systems (Feldens & Schwarzer, 2012), and in a region of complex habitats and extensive human impact.

Analyses of new high resolution bathymetric observations, shallow sub-bottom profiling, and sediment analyses of individual bedforms contribute to the discussion on the formation and transport mechanisms. Data from sediment cores and subbottom profilers reveal the sedimentology, internal bedding, and cross-stratification of the central bedforms.

2 METHODS

Research cruises with the German research vessel ALKOR to the Fehmarn Belt were conducted in 2020, 2021 and 2022. During the expeditions, the bedform field was investigated by multibeam echo sounder mapping, parametric echo sounder profiles, gravity coring and bed surface sediment grab sampling. Grain size distributions were measured in the CAU Kiel, sedimentology laboratory.

We used a NORBIT - iWBMS STX with RTK positioning to measure high-resolution bathymetry of a part of the bedform field. The sound velocity profile was corrected by regular updates based on CTD casts.

Subbottom profiles were measured with a hull-mounted Innomar SES parametric echo sounder. Settings were optimised for high-resolution data of the first few meters below the seafloor.

Short sediment cores were taken with a gravity corer. Additionally, bed surface samples were taken by Van Veen grab sampling. RTK GNSS positioning and very good navigation by the captain and helmsman allowed the precise sampling of the bedform at defined positions.

Sediment grain size distributions of surface and core samples were measured with a Beckman Coulter LS 13320 Laser Diffraction Particle Size Analyzer in the range of 0,017 µm to 2000 µm.

3 RESULTS

During a series of expeditions, an area of about 6 km² was (re-)mapped with multibeam and parametric echo sounders. The processed high-resolution bathymetry confirms the existence of individual bedforms in heights in the order of one meter, which often feature a crescentic shape with a density of about 50 bedforms/km². Where present, the extremities (“*horns*”) resemble the shape of

barchanoid dunes, opened towards the SE. Successive surveys indicate little or no mobility of the bedforms.

In the high-resolution MBES data, sharp, angular features, predominately on the Western side of the bedforms, are present. Based on earlier and recent underwater camera observations, these are interpreted as accumulations of mussels and shell fragments, which were also observed on top of the bedforms.

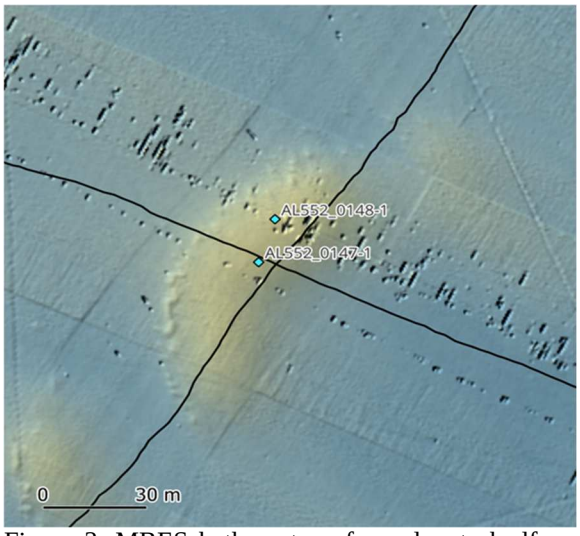

Figure 3. MBES bathymetry of one lunate bedform and position of cores 147-1 and 148-1 near the crest of a lunate bedform. Straight lines N-S and WSW-ENE are trawling marks. Wiggles and gaps at the overlap of NW-SE bathymetric profiles are hydroacoustic artefacts.

The parametric echo sounder reveals subbottom horizontal bedding without characteristic anomalies like acoustic blanking, faults, or others below and between the bedforms (Fig. 4). The internal structure of the bedforms above a continuous horizontal reflector is characterised by internal cross-bedding in multiple sets. The predominant internal bedding is dipping towards the NW, while some sets are also in the opposite direction. These subbottom features are similar at all investigated bedforms.

Several surface samples in between and across the lunate bedforms classified the upper centimeters as silty sand, with varying fractions of 65 to 85% sand, 12 to 30% silt, and less than 7 % clay. Crest samples had up to 10% higher sand content than the surrounding areas (Steinert, 2020).

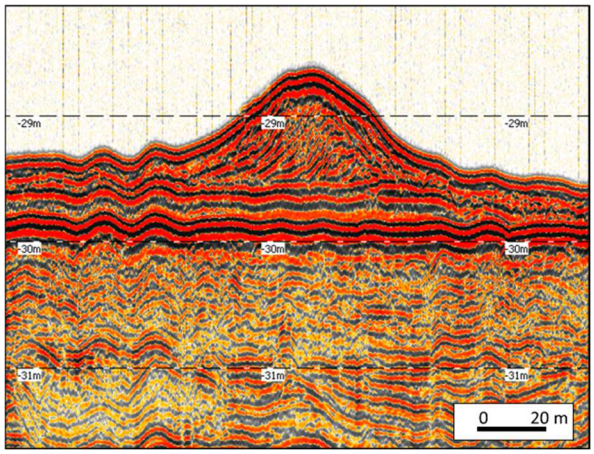

Figure 4. Subbottom profile across the centre of a lunate bedform driven from NW (left) to SE (right). Horizontal lines indicate meter distance in the vertical.

A gravity core taken near the crest of of one of the bedforms (Fig. 3) shows differences between sediments of the bedform, sediments at the base, and the layers below: The bedform itself is composed of bioturbated silty sand with layers of complete and fragmented bivalve and gastropod shells. Below is a layer of 0.2 m of grey muddy sediment, interpreted as a freshwater gyttja deposit. The layers below feature beddings of silty sands and sandy silts in variable thicknesses.

4 DISCUSSION

Previous studies have described the occurrence of a large number of *low-relief bedforms* in the central Fehmarn Belt in the Western Baltic Sea. Their origin, drivers, and development remain speculative so far. Although the lunate or crescentic shapes and isolated occurrence suggest formation in sediment-starved conditions (cf. *barchanoid dunes*) and mobility towards the SE, other characteristics and new field data question this approach.

In this area the (recent) environment is not sediment starved. Mobile fine sands and silts are abundant in variable thickness, also between the individual bedforms.

Furthermore, the interpretation of internal cross-beddings observed in subbottom profiler data does not support SE migration of the bedforms.

In fact, no (residual) mobility was observed throughout three years of observation, although the central Fehmarn Belt is prone to higher current velocities (and sediment transport rates), compared adjacent areas of Mecklenburg Bay and Kiel Bay .

If no connection to recent forcing can be drawn, the bedforms may be relict features. Their origin would then be connected to different stages of paleo-environmental conditions throughout the complex Baltic Sea history (Feldens & Schwarzer, 2012). Besides local emergence, the discussion of the origin and formation mechanisms of relict features must then consider other possibilities, including the breaching of formerly continuous 2D ridges, the various shapes of periglacial geomorphology, aeolian formation during sea level lowstands, and erosive rather than depositional formation. Dating of the sedimentary layers is required, to confirm or reject any of these possible scenarios of bedform formation.

Other ideas on bedform development have been discussed earlier. In FEHY (2013) also pockmarks were mentioned as possible generation mechanisms. In fact, Krämer et al. (2017) show shapes and distributions of pockmarks of somehow similar widespread and low relief character - however, in much different high energetic conditions, other sediments, and with clear subbottom indicators for fluid seepage. The latter are missing in the Fehmarn Belt observations. Also, the resemblance to crescentic comet marks was mentioned; however, no initiation mechanism is evident to support this theory.

Observations of the high abundance of complete and fragmented shells in and above bedforms need better interpretation. Dedicated studies are currently investigating the mutual interaction of seafloor fauna and bedform formation. Further work covers AMS ^{14}C dating of bivalve shell and plant remains for an age model of the sediment cores.

5 CONCLUSIONS

We discuss the origin and development of a large field of low-relief bedforms in the central Fehmarn Belt in the Western Baltic Sea. Despite high-resolution data on the morphology, sedimentology of the features, formation mechanisms and the mutual interactions with sea floor fauna remain inconclusive.

6 ACKNOWLEDGEMENTS

The authors thank captain and crew of R/V ALKOR for their excellent support. We thank the organisers of the MARID conferences for keeping up the spirit and providing a home for bedform enthusiasts.

7 REFERENCES

FEHY (2013). Fehmarnbelt Fixed Link EIA. Marine Soil - Baseline. Seabed Morphology of the Fehmarnbelt Area. Report No. E1TR0056 – Volume I

Feldens, P., Diesing, M. Schwarzer, K., Heinrich, C., Schlenz, B. (2014) Occurrence of flow parallel and flow transverse bedforms in Fehmarn Belt (SWBaltic Sea) related to the local palaeomorphology, Geomorphology

Feldens, P., Schwarzer, K. (2012) The Ancylus Lake stage of the Baltic Sea in Fehmarn Belt: Indications of a new threshold?. Continental Shelf Research, 35. pp. 43-52.

Jensen, J. B., Kuijpers, A., Lemke, W. (2003). Seabed sediments and current-induced bedforms in the Fehmarn Belt—Arkona Basin. In: ICES. 2003. Proceedings of the Baltic Marine Conference, Rønne, Denmark, 22–26 October 1996. ICES Cooperativen Research Report No. 257. 334 pp.

Krämer, K., et al. (2017) Abrupt emergence of a large pockmark field in the German Bight, southeastern North Sea. Scientific Reports 7

Kraemer K., Becker, M., Winter, C. (this volume) Bedform transition related to sediment supply and transport capacity in the SW Baltic. Proceedings of Conference Marine and River Dune Dynamics – MARID VII – 1-3 April 2023 - Rennes, France

Schwarzer K., Unverricht, D. (2020) Abschlussbericht FFH – LRT-Kartierung Fehmarn Ost. Institut für Geowissenschaften, Christian-Albrechts-Universität, Kiel (unpublished, in German), 72p

Steinert, A. (2020) Entstehung der barchanförmigen Bodenformen im Fehmarnbelt. BSc Thesis. Institute of Geosciences (unpublished), 58p.

Clay winnowing associated with wave–current ripple dynamics on cohesive sand–clay beds

X. Wu *University of Hull, Hull, U.K. – x.wu@hull.ac.uk*
J. Malarkey *School of Ocean Sciences, Bangor University, Menai Bridge, U.K. – j.malarkey@bangor.ac.uk*
F. Fernández *Department of Civil and Environmental Engineering, The Pennsylvania State University, State College, USA – roberto@psu.edu*
J. H. Baas *School of Ocean Sciences, Bangor University, Menai Bridge, U.K. – j.baas@bangor.ac.uk*
D. R. Parsons *Loughborough University, Loughborough, U.K. – d.parsons@lboro.ac.uk*

ABSTRACT: A full understanding of ripple dynamics in sand–clay mixtures is essential to improve existing ripple predictors, especially under combined wave–current conditions. We conducted a series of experiments in a large recirculating flume, with initial clay contents, C_0, ranging from 0 to 18.3%, in the Total Environment Simulator at the University of Hull. The experimental results reveal that winnowing-induced clay loss from beds is associated with two distinct types of equilibrium combined-flow ripples, separated by a discontinuity at C_0 = 10.6%: large clean-sand ripples and small, flat ripples. Most importantly, for the first time, we combine earlier experimental results to quantify the influence of both clay and hydrodynamic forcing on ripple morphology. Additionally, the present experiments show the difference in clay winnowing efficiency over flat and rippled beds under different flow conditions and will prove beneficial in stimulating further research focusing on the factors controlling the clay winnowing process.

1 INTRODUCTION

Flume studies concerning ripple dynamics on beds of well-sorted clean sand under different flow conditions (e.g., Pedocchi and García, 2009, Perillo et al., 2014) have provided high-quality process information for developing empirical formulae to predict ripple dimensions. However, the existing ripple predictors are of limited use for the majority of estuarine and coastal environments, where sediment almost universally consists of mixtures of cohesive clay and non-cohesive sand. More recently, researchers have therefore focused on ripple dynamics within substrates composed of mixtures of sand and clay under currents and waves (Baas et al., 2013, Wu et al., 2018). Moreover, Wu et al., (2022) studied the influence of clay on ripple development under combined wave-current flows and highlighted the significant decrease in ripple dimensions with an initial clay content, C_0, greater than 10.6%. While these studies have identified the role clay winnowing from the bed has played in ripple development, it is still unclear which factors control clay winnowing efficiency. Therefore, the present study extends Wu et al.'s (2022) research, with further experiments under a wider range of hydrodynamic conditions. The specific objectives were: (1) to compare ripple development on beds with similar clay content under different hydrodynamic conditions; (2) to compare clay winnowing efficiency, based on quantifying bed clay content during ripple development, under different types of flow conditions.

2 METHODS

2.1.1 Experiment setup

The experiments were undertaken in a recirculating flume tank, the Total Environment Simulator at the University of Hull. Three equal channels, 11 m long and 1.6 m wide, were separated by brick walls, 0.2 m high, in the tank (Figure 1). Combined flow conditions were maintained during the

experiments and flow velocities in each channel were measured by a 25 Hz Vectrino profiler. Freshwater was used in all experiments, with a water depth of 0.4 m. A 2-MHz ultrasonic ranging sensor (URS), containing 32 probes, monitored the bedform evolution in the test section (Figure 1).

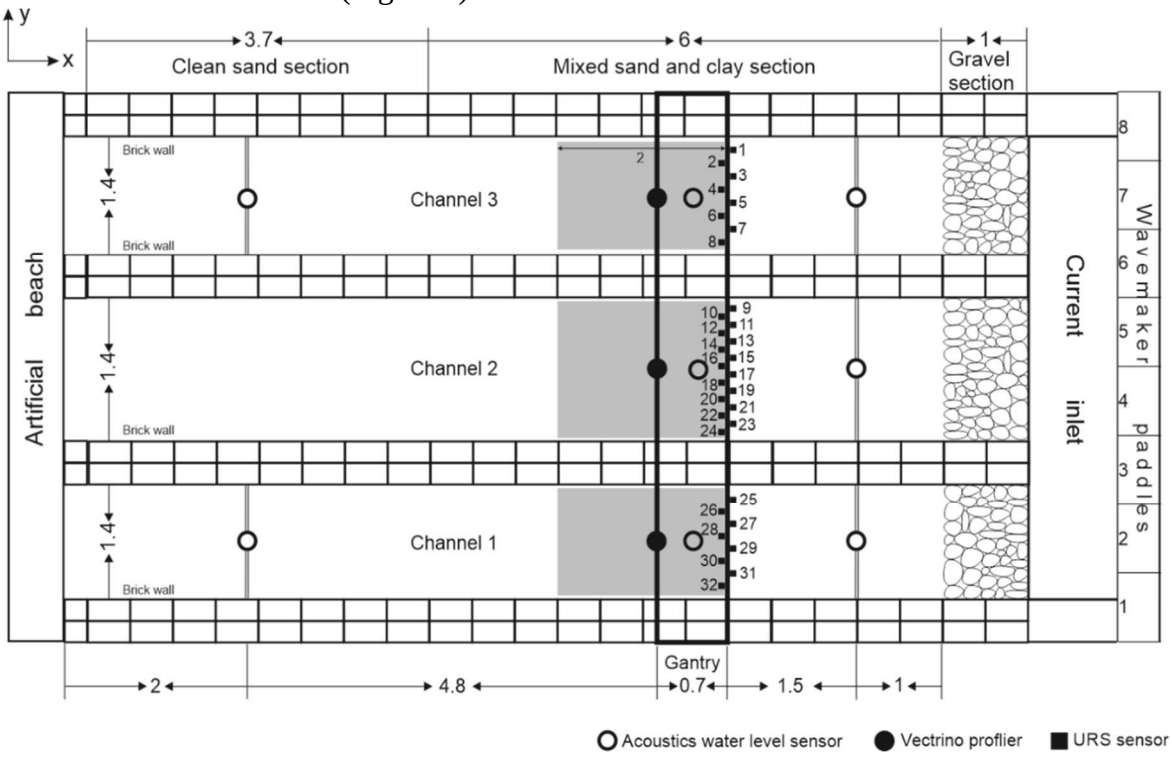

Figure 1. Plan view of the experimental setup. The grey area was scanned by an Ultrasonic Range System (URS) with numbered sensors (black squares). White and black circles denote acoustic water level sensors and Vectrino profilers, respectively. Dimensions are in metres.

2.2 Experimental procedure

Wu et al.'s (2022) wave-dominated flow condition (WC1), with a depth-average current, U_c ~ 0.16 m s^{-1}, and wave velocity amplitude, U_o ~ 0.32 m s^{-1}, was added to in this paper with two further flow conditions (WC2 and WC3) with U_c ~ 0.3 m s^{-1} and U_o ~ 0.27 and 0.13 m s^{-1} (Table 1). The flow conditions are numbered according to increasing relative current strength from WC1-WC3. The experiments involved different mass concentrations of initial clay, C_0, in each of the three channels, with the same flow conditions for each channel. The bed was composed of a well-sorted sand with a median diameter, D_{50}, of 0.45 mm and cohesive kaolinite clay with D_{50} = 0.089 mm. The order of the experiments was from high to low clay content, by taking advantage of the natural winnowing of the bed during the experiment.

To ensure homogeneity in the mixed section of each channel (Figure 1), the clay was mixed into the sand using a handheld mixer and levelled between runs. A terrestrial 3D laser scanner was used to scan the sediment bed in each channel before and after the run, without water in the tank. Ripple development was recorded using an Ultrasonic Range System (URS) and pre- and post-experiment sediment cores were collected from the bed using syringes with a diameter of 20 mm and a maximum length of 90 mm. Channel 1 of Run A2 and Channel 2 of Run B4 were excluded from the analysis, because the sediment in these channels was not sufficiently well mixed.

2.3 Data processing

Raw bed elevation profiles (BEPs) recorded from each URS scan, were analysed using a standard 'peaks and troughs' procedure to identify individual ripple heights, η, and wavelengths, λ, and their mean values, λ_t and η_t, at time, t, to construct

the development curves of ripple dimensions and determine

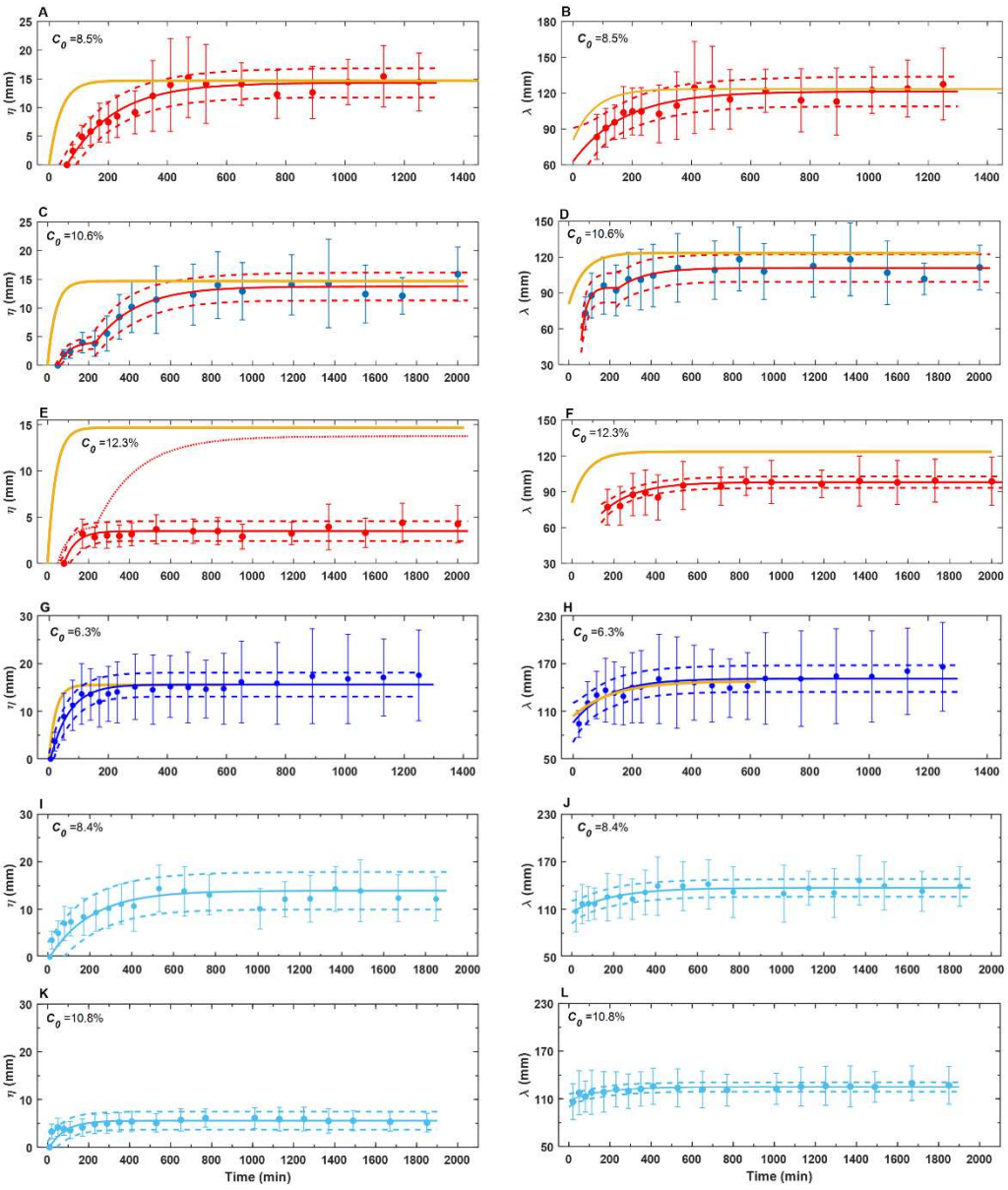

Figure 2. Development of ripple height and wavelength for WC1 (red dots in A - F) (Wu et al., 2022), WC3 (dark blue dots in G – H) and WC2 (light blue dots in I - L) for different values of C_0. The vertical lines denote one standard deviation from the mean dimension. Red, dark and light blue lines are based on fitting to Equations 1 and 2, and dashed lines are their corresponding 95% confidence intervals. The yellow lines are best-fit curves for the clean-sand counterparts, under WC1 and WC3 conditions.

equilibrium bedform dimensions, following Wu et al.'s (2022) procedure:

$$\frac{\eta_t}{\eta_e} = 1 - 0.1^{\frac{t-t_i}{T_\eta - t_i}}, \quad (1)$$

$$\frac{\lambda_t - \lambda_i}{\lambda_e - \lambda_i} = 1 - 0.1^{\frac{t-t_i}{T_\lambda - t_i}}, \quad (2)$$

where η_e and λ_e, are the equilibrium height and wavelength, T_η and T_λ are the equilibrium time for the height and wavelength, t_i is the initiation time and λ_i is the initial wavelength. The ripples were also characterised by their steepness (RS) = η_e/λ_e, and ripple symmetry index (RSI) = λ_s/λ_l, where λ_s and λ_l are the length of the stoss and lee side of the ripple (RSI < 1.3 for symmetric and 1.3 < RSI < 1.5 for quasi-asymmetric ripples, Perillio et al., 2014) (Table 1).

Table 1 Experimental parameters and bedform characteristics

Run /Channel	Flow code[1]	Duration (min)	C_0 (%)	U_o (m s^{-1})	U_c (m s^{-1})	η_e (mm)	T_η (mm)	λ_e (mm)	T_λ (mm)	RSI	RS	Plan view
A1/2	WC1	1970	0	0.32	0.16	14.4	90	123.6	170	1.4	0.12	2D
A3/1	WC1	1250	5.7	0.32	0.19	14.7	125	126.5	330	1.4	0.12	2D
A3/2	WC1	1250	8.5	0.31	0.16	14.3	432	121.4	456	1.4	0.11	2D
A2/2	WC1	1250	10.6	0.33	0.19	13.7	678	110.9	540	1.3	0.14	2D
A3/3	WC1	2000	11.6	0.31	0.15	4.1	271	108.5	382	1.5	0.05	3D
A2/3	WC1	2000	12.3	0.33	0.2	3.5	211	98	499	1.5	0.04	3D
B1/2	WC3	600	0	0.14	0.31	15.5	53	147.9	302	1.5	0.11	2D
B4/1	WC3	1250	2.5	0.13	0.25	14.8	71	144.8	330	1.5	0.11	2D
B4/3	WC3	1250	6.4	0.12	0.29	15.6	151	152	342	1.5	0.1	2D
B2/1	WC3	650	9.9	0.13	0.31	-	-	-	-	-	-	-
B2/2	WC3	650	13.1	0.14	0.29	-	-	-	-	-	-	-
B2/3	WC3	650	18.3	0.13	0.31	-	-	-	-	-	-	-
B3/1	WC2	1850	8.4	0.27	0.32	13.9	471	137	465	1.4	0.09	2D
B3/2	WC2	1850	10.8	0.27	0.3	5.6	273	125	377	1.6	0.04	3D
B3/3	WC2	1850	16.3	0.27	0.31	-	-	-	-	-	-	-

[1]Flow code number signifies increasing relative current strength compared to WC1.

Sediment cores from the initial flat bed and the ripple crests and troughs were sliced into 5- and 10-mm intervals for grain size analysis using a Malvern Mastersizer 2000. Crest and trough cores were combined to form one continuous profile through the active layer (ripple crest down to trough) and into the substrate beneath. The measured clay content, C, in the sediment cores was further processed to acquire the total amount of clay removed from the bed, I, by integrating the clay deficit, defined as $C_{def} = C_0 - C$, from the lowest reference level, $z = -b$ up to the crest level, $z = 0$.

3 RESULTS

3.1 Ripple development

Under WC1 conditions, increasing C_0 slowed ripple development compared to the clean-sand case (Figure 2A-D). This is particularly true for C_0 = 10.6%. Ripples experienced two stages of development; the ripple height and wavelength only grew to 3.9 and 96.2 mm at t = 170 min, thereafter, the ripples experienced a period of relatively rapid, yet gradually decelerating, growth in the next approximately 7 hours, reaching η_e = 13.7 mm and λ_e = 110.9 mm with 2D plan view geometry (Figure 2C – D, Table 1). For C_0 = 12.3%, the initial ripple height growth trend was similar to its 10.6% counterpart until t = 230 min. However, thereafter, the ripples experienced weak growth in the remainder of the experiment. The equilibrium ripples were asymmetric and 3D, with η_e = 3.5 mm and λ_e = 98 mm (Table 1).

For C_0 = 6.4% under WC3 conditions, the ripples developed to similar equilibrium dimensions as their clean-sand counterparts, η_e = 15.6 mm and λ_e = 152.5 mm (Figure 2C, D), and the bed was again covered in 2D, quasi-asymmetric ripples (Table 1).

For C_0 = 8.4% under WC2 conditions, ripple dimensions experienced a gradual development period of around seven hours before reaching stability, with η_e of 7.1 and λ_e of 110.8 mm (Figure 2I and J). Equilibrium ripples retained similar geometries to those developed under WC3 conditions, characterised by 2D plan forms and quasi-asymmetric cross sections (Table 1).

For C_0 = 10.8% (WC2), the ripple height was 3.3 mm at t = 20 min, followed by a period of slow growth up to η_e = 5.6 mm at t = 230 min, beyond which the ripple height grew no further (Figure 2K). The small ripples formed were 3D with discontinuous, sinuous crestlines in plan view. In cross-section, these ripples were slightly asymmetric and of limited steepness, with RSI = 1.6 and RS = 0.04 (Table 1).

3.2 Comparison of pre- and post-experiment vertical bed clay content

Under WC1 conditions, for C_0 = 10.6%, at the end of the experiment, the sediment cores reveal 100% clay loss in the active layer (ripple crest down to the ripple trough); there was a layer, with thickness of ~ 60 mm of reduced clay, beneath the ripple base (Figure 3A). The equivalent clean-sand depth (black horizontal dashed line), $d_c = I/C_0$, was 43 mm. Compared to the ripple height, d_c gives an indication of how much clean sand is available for ripples to grow (Wu et al., 2022). Small ripples, for the C_0 = 12.3% case, retained 8% clay near the base, with a thin layer of reduced clay content beneath the ripple base (Figure 3B).

Similarly, under WC3 condition, for C_0 = 6.4%, the clay content in the active layer of the ripples was zero and a layer of reduced clay content extended down to c. 80 mm by the end of the experiment (dark blue symbols and lines in Figure 3C), with d_c = 57 mm, more than two times the ripple height.

In the C_0 = 8.4% (WC2) case, a small amount of clay, approximately 2.8%, remained at the base of the ripples at the end of the experiment (Figure 3E). Compared to the C_0 = 8.4% case, the base of the small ripples, for C_0 = 10.8%, contained a higher amount of clay (9.8%) and d_c = 10.1 mm (Figure 3F).

No ripples formed for $C_0 \geq$ 9.9% under WC3 conditions and C_0 = 16.3% under WC2 conditions (Table 1). Sediment cores collected from the flat beds after these experiments show vertically-constant clay loss from the entire bed (Figure 3D, G). On beds with C_0 = 16.3% and 18.3%, there was an approximate 10% reduction in clay content and d_c was approximately 17 mm and 15 mm, respectively.

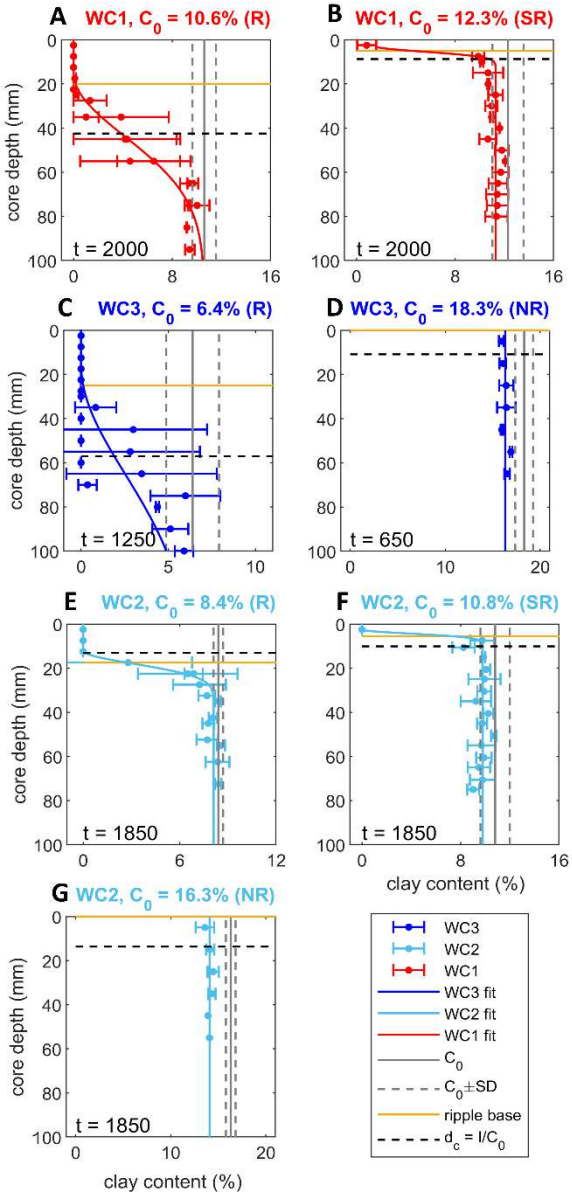

Figure 3. Vertical profiles of clay content in cores collected from beds in the mixed sand-clay section post experiment under WC1 conditions (A - B), WC3 conditions (C - D), and under WC2 conditions (E - G). The red, dark and light blue solid lines are the fits to WC1/WC3/WC2 clay content at each depth. The grey vertical solid and dashed lines represent mean initial clay content and one standard deviation from the mean. The horizontal bars denote one standard deviation of the mean clay content at that depth. The yellow lines represent the ripple base. The dashed horizontal black line is the equivalent clean-sand depth.

4 DISCUSSION

4.1 The effect of clay and hydrodynamic conditions on ripple dimensions

The ripple steepness and wavelength for all cases are listed in Table 1; there are two quite distinct constant steepness groupings, η_e/λ_e, related to the large and small ripples with a change at $C_0 = 10.6\%$. For large ripples the steepness decreases with increasing current strength: $\eta_e/\lambda_e \sim 0.12$, for $U_c \sim 0.16$ m s^{-1}, WC1; and 0.103, for $U_c \sim 0.3$ m s^{-1}, WC2 and WC3 (Tables 1). This is the current shearing the tops off the ripple crests with increasing effect, such that for the strongest current the steepness is only just above the threshold for oscillatory boundary-layer separation ($\eta_e/\lambda_e > 0.1$). The small ripples have a steepness of ~ 0.04. While there is a sudden change in ripple steepness and height, there is a gradual decrease in wavelength with increasing C_0, for $C_0 \geq 8.5\%$.

4.2 Quantifying the clay loss

Significant clay loss beneath equilibrium ripples was observed on beds with $C_0 \leq 10.6\%$ (Figure 3A, C). However, such deep cleaning of the bed clay was considerably weakened in the $C_0 = 8.4\%$ (WC2) case, despite the increased hydrodynamic forcing (Figure 3E).

We quantified the clay loss under different flow conditions by calculating the mass flux of clay out of the bed, $F_b = I/t_d$, where t_d, is the experiment duration. For large ripples this gives $F_b \sim 3.5\times10^{-6}$ g mm^{-2}min^{-1}, under WC1 and WC3 conditions, compared to 9.4×10^{-7} g mm^{-2}min^{-1} under WC2 conditions. This latter value is comparable to that being removed from small-rippled beds in the WC1 and WC2 cases, with $F_b \sim 8.5\times10^{-7}$ g mm^{-2}min^{-1}. This difference in deep cleaning between WC2 and WC3 is also seen in the cases where no ripples formed, even though the fluxes are two orders of magnitude smaller: $F_b \sim 5\times10^{-8}$ g mm^{-2}min^{-1} for WC3 and $F_b = 2\times10^{-8}$ g mm^{-2}min^{-1} for WC2.

5 CONCLUSIONS

The following conclusions are drawn:

1. The experimental results reveal that two distinct types of equilibrium ripples develop. For $C_0 \leq 10.6\%$, large 2D, quasi asymmetric equilibrium ripples develop, with dimensions similar to their clean-sand counterparts; for $C_0 > 10.6\%$, small, flat, and more asymmetric equilibrium ripples develop.
2. There were two quite distinct constant steepness groupings associated with this change at $C_0 = 10.6\%$, with a value 0.04 for the small ripples. For larger ripples, the steepness decreased with increasing current strength. The ripple wavelength decreases for $C_0 > 8.5\%$.
3. Winnowing-induced deep cleaning of bed clay under large ripples occurred under WC1 and WC3 conditions, but was inhibited under WC2 conditions, which is reflected in a reduction of the clay flux out of the bed by a factor of four.

6 ACKNOWLEDGEMENT

We acknowledge funding by the European Research Council under the European Union's Horizon 2020 research and innovation program (grant no. 725955). Participation of R. Fernández was also supported by the Leverhulme Trust and Leverhulme Early Career Researcher Fellowship (grant ECF-2020-679).

7 REFERENCES

Baas, J. H., Davies, A. G. & Malarkey, J. 2013. Bedform development in mixed sand–mud: The contrasting role of cohesive forces in flow and bed. Geomorphology, 182, 19-32.

Pedocchi, F. & García, M. 2009. Ripple morphology under oscillatory flow: 2. Experiments. Journal of Geophysical Research: Oceans, 114.

Perillo, M. M., Best, J. L. & Garcia, M. H. 2014. A new phase diagram for combined-flow bedforms. Journal of Sedimentary Research, 84, 301-313.

Soulsby, R. (1997). Dynamics of marine sands: A manual for practical applications. Thomas Telford.

Wu, X., Baas, J. H., Parsons, D. R., Eggenhuisen, J., Amoudry, L., Cartigny, M., Mclelland, S., Mouazé, D. & Ruessink, G. 2018. Wave Ripple Development on Mixed Clay - Sand Substrates: Effects of Clay Winnowing and Armoring. Journal

of Geophysical Research: Earth Surface, 123, 2784-2801.

Wu, X., Fernández, R., Baas, J.H., Malarkey, J. & Parsons, D.R. 2022. Discontinuity in equilibrium wave-current ripple size and shape and deep cleaning associated with cohesive sand-clay beds. Journal of Geophysical Research Earth Surface, 127, e2022JF006771.

Interaction between two scales of fluvial bedforms and its impact on sediment transport dynamics

J.Y. Zomer *Wageningen University & Research, Wageningen, Netherlands – judith.zomer@wur.nl*
B. Vermeulen *Wageningen University & Research, Wageningen, Netherlands – bart.vermeulen@wur.nl*
A.J.F. Hoitink *Wageningen University & Research, Wageningen, Netherlands – ton.hoitink@wur.nl*

ABSTRACT: In many river systems worldwide, multiple scales of bedforms are observed to coexist, where trains of secondary bedforms are superimposed on larger primary dunes. To date, this secondary scale remains poorly studied. This study aims to characterize secondary bedforms based on a large bathymetric dataset from the Dutch river Waal. Secondly, a field campaign has been completed based on which the dynamics and interaction of two scales are investigated.

1 INTRODUCTION

In fluvial environments, dunes are a key element in various flow processes on multiple scales. They induce flow separation at the bed, control hydraulic roughness, and affect local sediment transport dynamics. With this, dunes exert a strong control on the navigability of a river, and on the stability of infrastructure.

Fluvial dunes have been the topic of extensive research in the past decades. This research has almost exclusively been focused on one scale of larger, formative dunes. In many fluvial systems worldwide, the presence of a secondary scale of bedforms has been reported (Carling et al, 2000; Cisneros et al., 2020; Galeazzi et al., 2018; Harbor, 1998; Parsons et al., 2005; Wilbers & Ten Brinke, 2003, Baranya et al., 2023), which remain comparatively poorly studied to date. Trains of small, secondary dunes can be superimposed on larger, primary dunes, which is why they may interact.

In many studies, secondary dunes or bedforms were merely considered to be an artefact of the larger scale dunes, which is then referred to as a compound dune. Recent work has shed more light on the secondary dune scale. Two different processes have been observed and described that lead to the superimposition of secondary bedforms. Firstly, secondary bedforms have been observed to emerge during the falling limb of a flood wave. The newly emerged, secondary scale is then considered to be the active bedform scale, which is in equilibrium with the decreased discharge (Martin & Jerolmack, 2013). The primary dunes at that stage of the discharge wave have become inactive, and are slowly cannibalized. Two scales of bedforms have also been observed under steady flow conditions however (Zomer et al., 2021). In steady flow, it is expected that the secondary scale develops in the boundary layer that establishes over the primary dune (Ashley, 1990). Previous work has further shown that secondary bedforms are not limited to the primary dune stoss, but can persist over the full length of the primary dune (Galeazzi et al., 2018; Zomer et al., 2021). Secondary bedforms can have steep lee side angles and are thus likely to cause flow separation and affect local flow and sediment transport dynamics (Zomer et al., 2021) and also affect primary dune development (Reesink and Bridge, 2007). Both field and laboratory studies have indicated that secondary bedforms migrate comparatively fast, and the bedload sediment transport associated with the small scale equals or even exceeds transport associated with primary dune migration (Zomer et al., 2021; Venditti et al., 2005).

Many questions remain unanswered. Whereas the primary dune scale has been studied extensively, a comprehensive characterization of secondary dunes has remained elusive to date. Previous work has been limited to field studies at small spatial

and temporal scales, or flume studies. It is unknown how the two scales interact and affect each other's development on a large scale. Finally, it is unclear what the impact of the presence of a secondary scale is on the total sediment transport dynamics, and how dune tracking should be applied in systems where two scales actively migrate.

This study has two main aims. Firstly, we aim to characterize secondary bedforms based on a large bathymetric dataset that has been acquired in the Dutch river Waal, the main branch of the Rhine river. Secondly, a dedicated field campaign has been completed in the river Waal, near Tiel, based on which we study the dynamics of dunes at two scales, their interaction, and the impact on sediment transport and consequences for dune tracking.

2 METHODS

2.1 Secondary bedform characterization: separation of bathymetric data representing two bedforms scales.

The characterization of the secondary bedforms was based on a biweekly bathymetric dataset, acquired through multibeam echo sounding (MBES). These data were provided by the Dutch Ministry of Infrastructure and Environment (Rijkswaterstaat) for the Waal river. The data were interpolated on a 0.1 × 1.0 m grid and subsequently processed following the method of Zomer et al., (2022). With this method, the bathymetric data is separated into a signal representing secondary bedforms and a signal representing the underlying bathymetry, including primary dunes. The first step of this procedure is to decompose the initial bathymetric signal based on a LOESS (locally estimated scatter plot smoothing) algorithm (Greenslate et al., 1997; Schlax and Chelton, 1992). Steep primary dune slopes are preserved by implementing breaks in the previously fitted LOESS curve. The steep lee slopes are subsequently fitted with a sigmoid function (Figure 1). Following the separation of scales, secondary and primary bedforms are

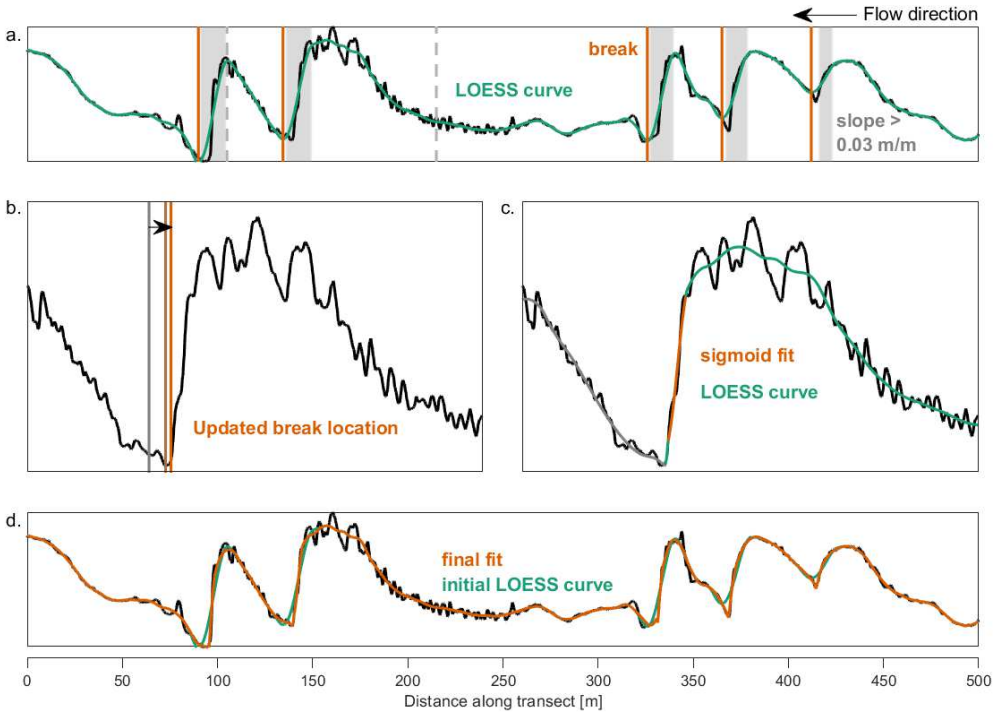

Figure 1. Adopted from Zomer et al. (2022). Schematic overview of the tool developed by Zomer et al. (2022). a) A bed elevation profile with the initially fitted LOESS curve. The vertical orange lines indicate the locations of breaks at steep primary lee slopes. b) The exact location of the break is updated; c) the steep primary lee slope is approximated with a sigmoid function; d) the bed elevation profile with the initial LOESS curve (green) and the final fit (orange).

identified based on zero-crossing (Zomer et al., 2022; Van der Mark and Blom, 2007).

2.2 Field campaign

To further study the interaction between dune scales and the effect of secondary bedforms on sediment transport dynamics and the applicability of dune tracking, a field campaign was set up. This campaign included 10 measurement days distributed over a range of discharges, between November 2021 and March 2022. Per day, a reach of approximately 400 m was scanned to enable characterization of primary dunes. In addition to that, repeated bed elevation scans took place over a cross-sectional transect, in order to track dynamics of secondary bedforms over the full width of the river. Also, repeated scans were taken over three longitudinal transects. The aim of this was to enable tracking of the dynamics of secondary bedforms over primary dunes. The field campaign further included velocity measurements (ADCP), water samples, and river bed samples.

3 RESULTS

A first question to be answered was whether secondary bedforms were restricted to specific hydraulic conditions and river sections. To answer this, we determined what fraction of the river bed was covered by secondary bedforms (Figure 2). Figure 2 indicates that secondary bedforms are ubiquitous throughout the Waal river, both at a small and large discharge. This indicates that the secondary scale is an important element in the river system and it is vital to consider their impact on sediment transport dynamics, river bed development and hydraulic roughness.

Secondary, the characteristics of both primary and secondary dunes were determined. Figure 3 shows the median values (averaged per timestep over a reach of one kilometer) and the interquartile range. The results indicate that secondary bedforms increase in height and length, and lee slopes become steeper with increasing discharge. The lee side slopes develop up to around 20 degrees. It is therefore likely that secondary bedforms cause flow separation. The variability in dune size is large and has been shown previously to inversely correlate to primary dune size (Zomer et al., 2021). Primary dunes increase in height and lee slope steepness, but their lengths decrease with increasing discharge, similar to previous findings by Lokin et al., (2022).

In some cases, secondary bedforms persist over the whole length of the primary dune where in other cases secondary bedforms disintegrate at the primary lee slope. As this likely impacts the total sediment transport dynamics and applicability of dune tracking, we further studied this. The primary dune dataset was separated into primary dunes onto which secondary bedforms persist over the full length of the primary dune, and a set

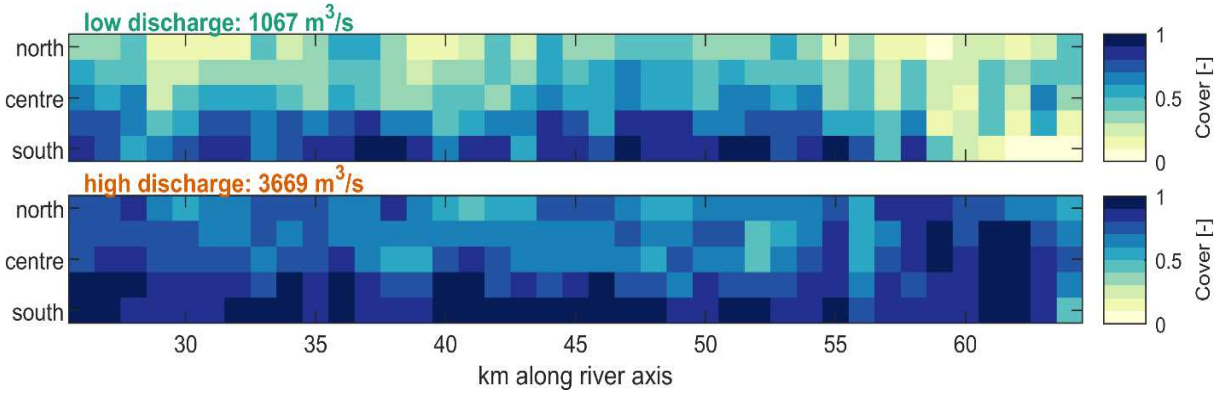

Figure 2. The fraction of the river bed covered by secondary bedforms. The river divided in sections based on kilometers along the river axis and 5 sections distributed over the width of the river.

of primary dunes where secondary bedforms did not persist.

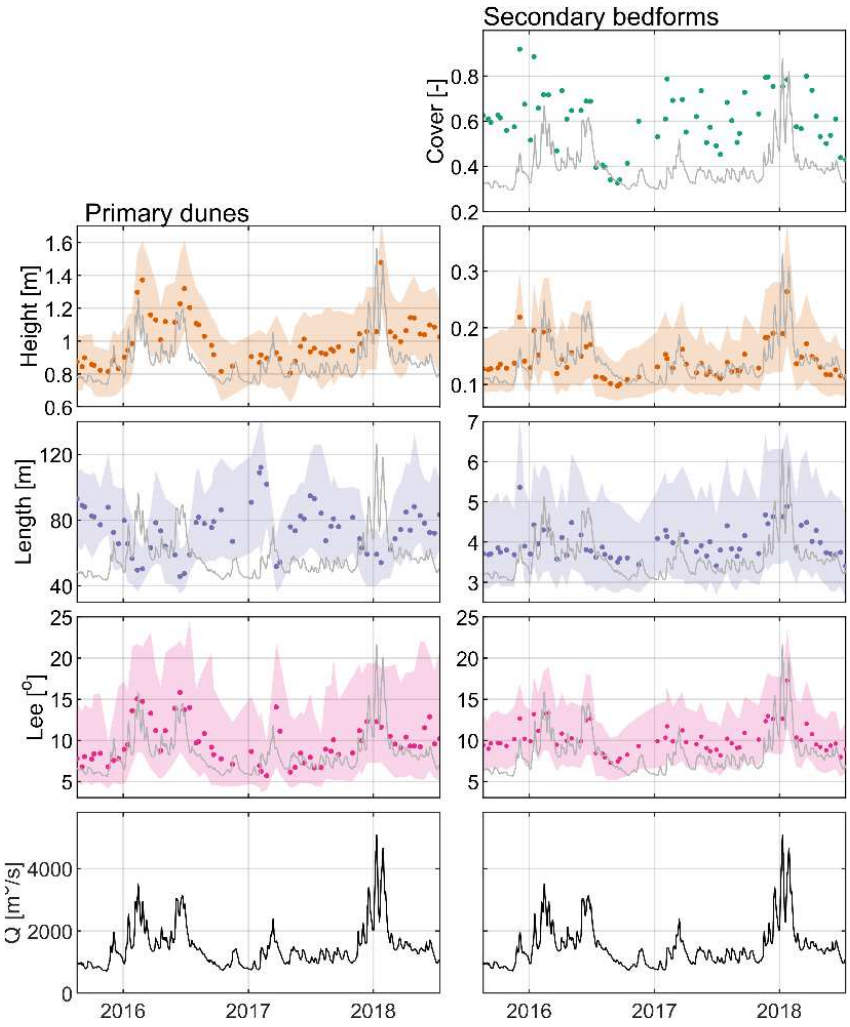

Figure 3. The properties of primary (right panels) and secondary (left panels) dunes over time. The dots indicate median values for all dunes identified in one kilometer, per timestep. The transparent, colored areas indicate the interquartile range.

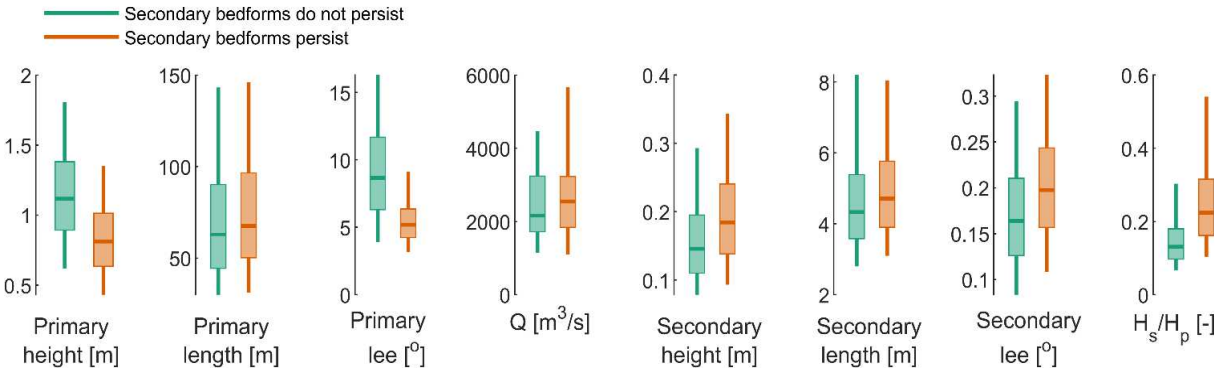

Figure 4. The characteristics of primary dunes over which secondary bedforms persist (orange) and over which secondary bedforms do not persist (green). The averaged properties of secondary bedforms on these dunes are shown in panels e-g.

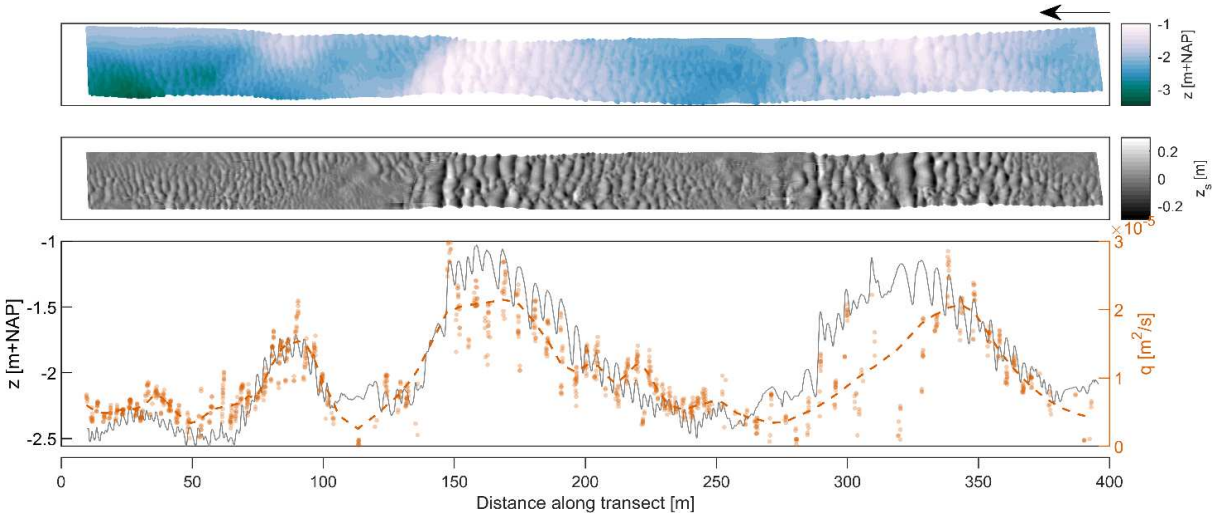

Figure 5. Top panel: Bed elevation of a longitudinal transect. Middle panel: The secondary morphology of the transect. Bottom panel: A bed elevation profile from the longitudinal transect (grey). For each secondary bedform an associated transport is determined for each combination of bed elevation scans (6 timesteps in total). A LOESS curve is fitted through the individual datapoints (orange, intermittent line).

These two primary dune groups were compared with each other. Figure 4 indicates that primary dunes over which secondary bedforms persist are lower in height and have less steep lee side slopes. The secondary bedforms on these primary dunes are slightly larger.

4 ONGOING WORK AND OUTLOOK

The field campaign was designed to further study the dynamics of the two dune scales, which is not possible based on the biweekly dataset, and to specifically study the relationship with sediment transport and the interaction between dune scales. Bedload sediment transport by both primary and secondary dunes were separately determined. For both scales, sediment transport increases with increasing discharge. In the studied area, the transport rates are similar in magnitude.

In the case that the secondary bedforms disintegrate at the primary dune lee, we expect that the secondary bedforms are the agency by which the primary dune migrates. Sediments transported by secondary bedforms then fully contribute to the migration of the primary dune, excluding sediments going into suspension at the dune crest. In cases where secondary bedforms persist over the full length of the primary dune, however, it is unclear what the interaction between the two dune scales is. Preliminary results (figure 5) indicate that sediment transport associated with secondary bedform migration increases over the primary dune stoss, towards the crest. This is expected to cause net erosion of the dune stoss. The sediment transport associated with secondary bedform migration decreases along the primary dune lee, indicating net deposition. This might indicate the mechanisms by which the primary dune migrates.

5 ACKNOWLEDGEMENT

This study is part of the research program Rivers2Morrow, which is funded by the Dutch Ministry of Infrastructure and Water Management and its executive organization Rijkswaterstaat. We thank Rijkswaterstaat-CIV for providing the data used in this study.

6 REFERENCES

Ashley, G. M. (1990). Classification of large-scale subaqueous bedforms; a new look at an old problem. Journal of Sedimentary Research, 60(1), 160–172. https://doi.org/10.2110/jsr.60.160

Baranya, S., Fleit, G., Muste, M., Tsubaki, R., & Józsa, J. (2023). Bedload estimation in large sand-bed rivers using Acoustic Mapping Velocimetry (AMV). Geomorphology, 424, 108562.

Carling, P., Golz, E., Orr, H., & Radecki-Pawlik, A. (2000). The morphodynamics of fluvial sand dunes in the river rhine, near Mainz, Germany. i. sedimentology and morphology. Sedimentology, 47(1), 227–252. https://doi.org/10.1046/j.1365-3091.2000.00291.

Cisneros, J., Best, J., Van Dijk, T., de Almeida, R. P., Amsler, M., & Boldt, J. (2020). Dunes in the worlds big rivers are characterized by low-angle lee-side slopes and a complex shape. Nature Geoscience, 13(2), 156–162. https://doi.org/10.1038/s41561-019-0511-7

Galeazzi, C. P., Almeida, R. P., Mazoca, C. E., Best, J. L., Freitas, B. T., Ianniruberto, M., et al. (2018). The significance of superimposed dunes in the Amazon River: Implications for how large rivers are identified in the rock record. Sedimentology, 65(7), 2388–2403. https://doi.org/10.1111/sed.12471

Harbor, D. J. (1998). Dynamics of bedforms in the lower Mississippi River. Journal of Sedimentary Research, 68(5), 750–762. https://doi. org/10.2110/jsr.68.750

Lokin, L. R., Warmink, J. J., Bomers, A., & Hulscher, S. J. M. H. (2022). River dune dynamics during low flows. Geophysical research letters, 49(8), e2021GL097127.

Martin, R. L., & Jerolmack, D. J. (2013). Origin of hysteresis in bed form response to unsteady flows. Water Resources Research, 49(3), 1314-1333.

Parsons, D. R., Best, J. L., Orfeo, O., Hardy, R. J., Kostaschuk, R., & Lane, S. N. (2005). Morphology and flow fields of three-dimensional dunes, Rio Paraná, Argentina: Results from simultaneous multibeam echo sounding and acoustic doppler current profiling. Journal of Geophysical Research, 110(F4), F04S03. https://doi.org/10.1029/2004JF000231

Reesink, A., & Bridge, J. (2007). Influence of superimposed bedforms and flow unsteadiness on formation of cross strata in dunes and unit bars. Sedimentary Geology, 202(1–2), 281–296. https://doi.org/10.1016/j.sedgeo.2009.09.014

Schlax, M. G., & Chelton, D. B. (1992). Frequency domain diagnostics for linear smoothers. Journal of the American Statistical Association, 87(420), 1070–1081.

Van der Mark, C., & Blom, A. (2007). A new and widely applicable tool for determining the geometric properties of bedforms. Water Engineering and Management, 1568–4652.

Venditti, J. G., Church, M., & Bennett, S. J. (2005b). Morphodynamics of small-scale superimposed sand waves over migrating dune bedforms. Water Resources Research, 41(10), W10423. https://doi.org/10.1029/2004WR003461Greenslat e et al., 1997

Wilbers, A., & Ten Brinke, W. (2003). The response of subaqueous dunes to floods in sand and gravel bed reaches of the Dutch Rhine. Sedimentology, 50(6), 1013–1034. https://doi.org/10.1046/j.1365-3091.2003.00585.x

Zomer, J., Naqshband, S., Vermeulen, B., and Hoitink, A. (2021). Rapidly migrating secondary bedforms can persist on the lee of slowly migrating primary river dunes, J. Geophys. Res.-Earth Surf., 126, e2020JF005918, https://doi.org/10.1029/2020JF005918

Zomer, J. Y., Naqshband, S., & Hoitink, A. J. (2022). A tool for determining multiscale bedform characteristics from bed elevation data. Earth Surface Dynamics, 10(5), 865-874, https://doi.org/10.5194/esurf-10-865-2022.